technische universität
dortmund

Dissertation

Towards Squaramide-based Coordination Cages with Catalytic Activity

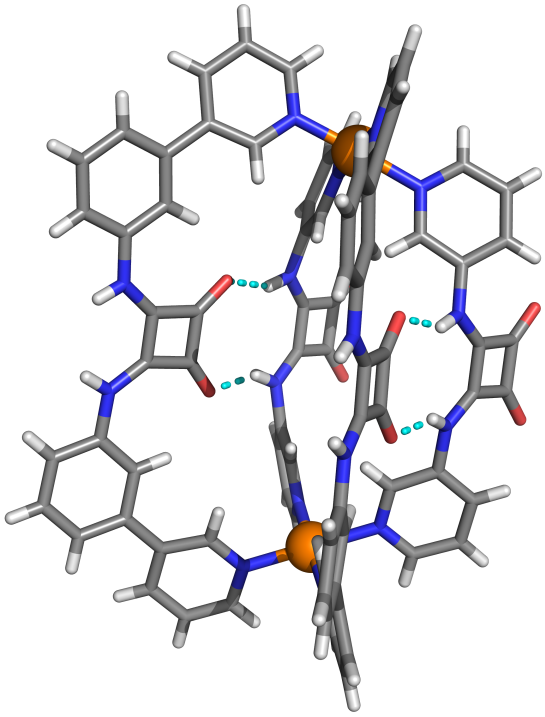

by

M. Sc. Ertuğrul Yalçın

prepared at the

Department of Chemistry and Chemical Biology

of TU Dortmund University

Dortmund 2025

I dedicate this PhD thesis to my family
and I want to thank my dear friend
Umut Yasin Gemici
for his never ending support and always being there for me no matter where I was.
May his soul rest in peace.

Inna lillahi wa inna ilayhi raji'un. [2:156]
Verily we belong to Allah, and verily to Him do we return. [2:156]

The work presented here has been prepared at the Department of Chemistry and Chemical Biology of the TU Dortmund University under the supervision of Prof. Dr. Guido H. Clever.

Supervisor:	**Prof. Dr. Guido H. Clever** Department of Chemistry and Chemical Biology, TU Dortmund University, Otto-Hahn-Str.6, 44227 Dortmund
Co-Supervisor:	**Prof. Dr. Lars Schäfer** Department of Chemistry and Biochemistry, Ruhr University Bochum, Universitätsstraße 150, 44801 Bochum
Date of Submission:	25.02.2025

Eidesstattliche Versicherung (Affidavit)

_____ _____

Name, Vorname
(Surname, first name)

Matrikel-Nr.
(Enrolment number)

Belehrung:

Wer vorsätzlich gegen eine die Täuschung über Prüfungsleistungen betreffende Regelung einer Hochschulprüfungsordnung verstößt, handelt ordnungswidrig. Die Ordnungswidrigkeit kann mit einer Geldbuße von bis zu 50.000,00 € geahndet werden. Zuständige Verwaltungsbehörde für die Verfolgung und Ahndung von Ordnungswidrigkeiten ist der Kanzler/die Kanzlerin der Technischen Universität Dortmund. Im Falle eines mehrfachen oder sonstigen schwerwiegenden Täuschungsversuches kann der Prüfling zudem exmatrikuliert werden, § 63 Abs. 5 Hochschulgesetz NRW.

Die Abgabe einer falschen Versicherung an Eides statt ist strafbar.

Wer vorsätzlich eine falsche Versicherung an Eides statt abgibt, kann mit einer Freiheitsstrafe bis zu drei Jahren oder mit Geldstrafe bestraft werden, § 156 StGB. Die fahrlässige Abgabe einer falschen Versicherung an Eides statt kann mit einer Freiheitsstrafe bis zu einem Jahr oder Geldstrafe bestraft werden, § 161 StGB.

Die oben stehende Belehrung habe ich zur Kenntnis genommen:

Official notification:

Any person who intentionally breaches any regulation of university examination regulations relating to deception in examination performance is acting improperly. This offence can be punished with a fine of up to EUR 50,000.00. The competent administrative authority for the pursuit and prosecution of offences of this type is the chancellor of the TU Dortmund University. In the case of multiple or other serious attempts at deception, the candidate can also be unenrolled, Section 63, paragraph 5 of the Universities Act of North Rhine-Westphalia.

The submission of a false affidavit is punishable.

Any person who intentionally submits a false affidavit can be punished with a prison sentence of up to three years or a fine, Section 156 of the Criminal Code. The negligent submission of a false affidavit can be punished with a prison sentence of up to one year or a fine, Section 161 of the Criminal Code.

I have taken note of the above official notification.

_____ _____

Ort, Datum
(Place, date)

Unterschrift
(Signature)

Titel der Dissertation:
(Title of the thesis):

_____

_____

_____

Ich versichere hiermit an Eides statt, dass ich die vorliegende Dissertation mit dem Titel selbstständig und ohne unzulässige fremde Hilfe angefertigt habe. Ich habe keine anderen als die angegebenen Quellen und Hilfsmittel benutzt sowie wörtliche und sinngemäße Zitate kenntlich gemacht.
Die Arbeit hat in gegenwärtiger oder in einer anderen Fassung weder der TU Dortmund noch einer anderen Hochschule im Zusammenhang mit einer staatlichen oder akademischen Prüfung vorgelegen.

I hereby swear that I have completed the present dissertation independently and without inadmissible external support. I have not used any sources or tools other than those indicated and have identified literal and analogous quotations.

The thesis in its current version or another version has not been presented to the TU Dortmund University or another university in connection with a state or academic examination.*

*Please be aware that solely the German version of the affidavit ("Eidesstattliche Versicherung") for the PhD thesis is the official and legally binding version.

_____ _____

Ort, Datum
(Place, date)

Unterschrift
(Signature)

Abstract

This thesis explores two main topics: the computational study of strain in heteroleptic coordination cages and the incorporation of squaramide functionalities into coordination cages to investigate their host-guest properties.
The computational study aimed at expanding the understanding of the thermodynamic driving forces behind the non-statistical self-assembly of *cis*-$[Pd_2L_2L'_2]$ and *trans*-$[Pd_2L_2L'_2]$ nanocages. Previous studies on Pd^{II}-based homo- and heteroleptic cages composed of a carbazole ligand with either an elongated or non-elongated phenanthrene ligand were analyzed using NMR spectroscopy, ESI-MS and single-crystal X-ray analysis. The findings of these studies raised the question of whether differences in ring strain could be reproduced through gas-phase electronic energy comparisons via DFT geometry optimization. To address this, cage-to-cage transformations were examined, and ligands excised from heteroleptic cages were compared with their fully relaxed counterparts to assess strain in self-assembled coordination cages. This work extends these studies to acridone- and inverted carbazole-based ligands paired with the respective phenanthrene ligands. The calculations revealed that acridone- and inverted carbazole-based ligands preferentially form heteroleptic coordination cages with elongated phenanthrene ligands rather than with the shorter phenanthrene ligands. Additionally, the incorporation of diketopyrrolopyrrole-based ligands in *trans*-$[Pd_2L_2L'_2]$ cages featuring self-penetrated motifs was examined. Computational studies demonstrated that the release of strain upon transformation of a self-penetrated homoleptic diketopyrrolopyrrole cage to a heteroleptic cage plays a significant role in driving the preferential formation of the heteroleptic structures.

Hydrogen bonding is a key noncovalent interaction that influences molecular recognition and catalytic processes. Squaramides are well-known hydrogen bond receptors and catalysts, possessing both hydrogen bond donor and acceptor groups. The second focus of this thesis is the heteroleptic cage formation of squaramide-based ligands with square-planar Pd(II) cations. Poorly soluble squaramide-based ligands assembled into a distinct assembly in DMSO-d_6. To enhance the likelihood of observing the effects of hydrogen bonding on host-guest interactions, derivatives of squaramide-based ligands were synthesized and formed analogous heteroleptic *cis*-$[Pd_2L_2L'_2]$ cages in CD_2Cl_2. The resulting assemblies were analyzed using NMR spectroscopy, ESI-MS and single-crystal X-ray crystallography. When two squaramide ligands were combined, the formation of a heteroleptic cage was observed. X-ray analysis revealed that the hydrogen bond donor functionalities of one squaramide is oriented outward, with intramolecular hydrogen bonding occurring within the cage. This raised the question of whether such intramolecular hydrogen bonding contributes to a cooperative effect in guest binding. To investigate this, a reference cage was designed by pairing a squaramide-based ligand with a benzothiadiazole-based ligand, forming a distinct heteroleptic cage with

the same topology. Computational studies suggested that the cooperative effect of intramolecular hydrogen bonding is more pronounced when two squaramide units are involved in intramolecular hydrogen bonding. To validate this, binding constants for neutral guest molecules were determined via ^{1}H NMR titration experiments and compared across the two different cage systems. The results confirmed a cooperative effect in guest binding, particularly for caffeine and β-nitrostyrene. Additionally, the host-guest properties of the assembled coordination cages were examined with chloride, disulfonate and phosphate anions. However, attempts to determine binding constants for anions to the solely squaramide-based heteroleptic cage in CD_2Cl_2 revealed broadening in the ^{1}H NMR spectra, suggesting aggregation, likely due to ion pairing effects. Nevertheless, binding constants for two disulfonates with the benzothiadiazole-based cage were successfully obtained, demonstrating a binding constant that is an order of magnitude stronger than for other palladium-based cages. In addition, the incorporation of 1,3-squaramides with a piperazine linker into coordination cages with Pd^{II} was investigated. The self-assembled structures and their host-guest complexes were analyzed using NMR spectroscopy, ESI-MS and single-crystal X-ray crystallography. A ring-like topology with the molecular formula $[Pd_3\mathbf{L}_6]^{6+}$ was characterized. Binding constants for Allura Red and ferrocene-1,1'-disulfonate were determined via ^{1}H NMR titration experiments. Cyclic voltammetry experiments showed that the redox event of Pd_3L_6 is electrochemically reversible, whereas the free ligand exhibits no reversibility.

Abstract (Deutsche Version)

Diese Arbeit lässt sich in zwei Hauptthemen gliedern: die Computer-gestützten Berechnung von Spannungen in heteroleptischen Koordinationskäfigen und die Integrierung von Quadratsäureamid-Funktionalitäten in Koordinationskäfige zur Untersuchung ihrer Wirt-Gast-Eigenschaften.

Die computergestützte Studie erweitert das Verständnis der thermodynamischen Triebkräfte hinter der nicht-statistischen Selbstassemblierung von *cis*-$[Pd_2L_2L'_2]$- und *trans*-$[Pd_2L_2L'_2]$-Nanokäfigen. Vorangehende Untersuchungen an Pd^{II}-basierten homo- und heteroleptischen Käfigen, die aus einem Carbazol-Liganden und einem entweder verlängertem oder nicht verlängertem Phenanthren-Liganden bestehen, wurden mittels NMR-Spektroskopie, ESI-MS und Einkristall-Röntgenanalyse durchgeführt. Diese Studien warfen die Frage auf, ob Unterschiede in der Ringspannung durch elektronische Energievergleiche in der Gasphase mittels DFT-Geometrieoptimierung reproduziert werden können. Zur Klärung dieser Frage wurden dort einerseits die Käfig-zu-Käfig-Transformationen untersucht und andererseits die jeweiligen Liganden aus heteroleptischen Käfigen herausgeschnitten und mit ihren geometrie-optimierten Liganden verglichen, um die Spannungen in selbst-assemblierten Koordinationskäfigen zu quantifizieren. Diese Arbeit erweitert diese Untersuchungen auf Acridon- und invertierte Carbazol-basierte Liganden in Kombination mit den entsprechenden Phenanthren-basierten Liganden. Die Berechnungen zeigten, dass Acridon- und invertierte Carbazol-Liganden bevorzugt heteroleptische Koordinationskäfige mit verlängerten Phenanthren-Liganden bilden, anstatt mit kürzeren Phenanthren-Liganden. Darüber hinaus warfen Diketopyrrolopyrrol-Liganden in *trans*-$[Pd_2L_2L'_2]$-Käfigen mit selbstpenetrierenden Motiven die Frage auf, ob Ringspannungen eine Rolle bei der Bildung dieser heteroleptischer Käfige spielen. Computergestützte Studien zeigten, dass die Reduktion von Spannung des selbstpenetrierenden homoleptischen Diketopyrrolopyrrol-Käfigs zugunsten eines heteroleptischen Käfigs einen entscheidenden Faktor in der heteroleptischen Käfigformation darstellt.

Der zweite Schwerpunkt dieser Arbeit liegt in der Implementierung von Quadratsäureamiden in Koordinationskäfige. Quadratsäureamide sind bekannte Wasserstoffbrückenrezeptoren und Katalysatoren, die sowohl Wasserstoffbrücken-Donor- als auch Akzeptorgruppen aufweisen. Ziel dieser Arbeit ist die Bildung heteroleptischer Käfige aus Quadratsäureamid-basierten Liganden und quadratisch-planaren Pd^{II}-Kationen sowie die Untersuchung ihrer Wirt-Gast-Chemie. In DMSO-d_6 zeigten Quadratsäureamid-basierte Liganden eine Selbstassemblierung zu heteroleptischen Käfigen. Um die Auswirkungen von Wasserstoffbrücken-bindungen auf Wirt-Gast-Wechselwirkungen gezielt zu untersuchen, wurden Quadratsäureamid-Derivate synthetisiert, die in CD_2Cl_2 analoge heteroleptische *cis*-$[Pd_2L_2L'_2]$- Käfige bildeten. Die resultierenden Assemblierungen wurden mithilfe von NMR-Spektroskopie, ESI-MS und Einkristall-Röntgenanalyse

charakterisiert. Die Kristallstruktur eines heteroleptischen Käfigs, der aus vier Quadratsäureamid-Liganden aufgebaut war, zeigte, dass die Wasserstoffbrücken-Donorfunktionalitäten von zwei Quadratsäureamiden nach außen gerichtet waren und intramolekulare Wasserstoffbrücken innerhalb des Käfigs gebildet wurden. Dies warf die Frage auf, ob diese intramolekularen Wechselwirkungen zu einem kooperativen Effekt bei der Gastbindung führen. Zur Untersuchung dieses Effekts wurde ein Referenzkäfig mit identischer Topologie entworfen, indem ein Quadratsäureamid-basierter Ligand mit einem Benzothiadiazol-basierten Liganden kombiniert wurde. Berechnungen legten nahe, dass der kooperative Effekt der intramolekularen Wasserstoffbrückenbindung bei zwei Quadratsäureamid-Liganden stärker ausgeprägt ist. Um dies experimentell zu zeigen, wurden die Bindungskonstanten für neutrale Gastmoleküle mittels ^{1}H-NMR-Titrationen bestimmt und zwischen den Käfigsystemen verglichen. Die Ergebnisse zeigten einen deutlichen kooperativen Effekt bei der Gastbindung, insbesondere für Koffein und β-Nitrostyrol. Darüber hinaus wurden die Wirt-Gast-Eigenschaften der Koordinationskäfige mit Chlorid-, Disulfonat- und Phosphatanionen untersucht. Die Titration von diesen Anionen in CD_2Cl_2 führte jedoch zu verbreiterten Signalen in den ^{1}H-NMR-Spektren, was auf Aggregations- und Ionenpaarungseffekte hindeutet. Dennoch konnten für zwei Disulfonate Bindungskonstanten mit dem Benzothiadiazol-basierten Käfig bestimmt werden, die im Vergleich zu anderen Palladium-basierten Koordinationskäfigen eine signifikant stärkere Bindung zeigten. Darüber hinaus wurde die Integrierung von 1,3-Quadratsäureamiden mit Piperazin-Linker in Pd^{II}-Koordinationskäfige untersucht. Die Selbstassemblierungen und ihre Wirt-Gast-Komplexe wurden mittels NMR-Spektroskopie, ESI-MS und Einkristall-Röntgenanalyse analysiert. Eine ringförmige Topologie mit der Molekularformel $[Pd_3\mathbf{L}_6]^{6+}$ wurde charakterisiert. Die Bindungskonstanten für Allura Red und Disulfonat-Ferrocen wurden durch ^{1}H-NMR-Titrationsexperimente bestimmt. Cyclovoltammetrie-Experimente zeigten, dass das Redoxevent elektrochemisch reversibel ist, während der freie Ligand keine Reversibilität aufweist.

Contents

Part I

Squaramide-based Coordination Cages

1 Introduction

1.1 Historical background of Hydrogen Bonding

Hydrogen bonding (HB), which can occur both within a molecule (intramolecular) and between molecules (intermolecular), is an interaction that plays a crucial role in various chemical and biological processes. [1] The concept of hydrogen bonding emerged in the early 20th century and its understanding has deepened over time through advancements in both theoretical and experimental chemistry. [2]

In 1920, Latimer and Rodebush recognized the consistent pattern in HB, noting its directional and linear nature, where hydrogen atoms interact with lone pairs on electronegative atoms. [3] This discovery facilitated the development of principles for designing hydrogen bonds, enhancing the understanding and visualization of structures and functions in various hydrogen bonding systems. [3]

This breakthrough was strongly influenced by two recent findings at the time. One of those key findings is the work of G. N. Lewis on theory of valence and chemical structures. Lewis introduced the concept of electron-pair sharing and stated that hydrogen atoms with their relatively weak electron density could form attractive interactions with more electronegative atoms. [4][5] Therefore, Lewis provided the fundamental concept of HB, which served as a foundation for further development of this idea.

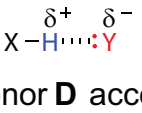

Figure 1.1. Illustration of a hydrogen bond between a donor **D** and acceptor **A** shown. The corresponding partial charges δ are shown.

The other significant contribution to the hydrogen bond research was the discovery of X-Ray diffraction analysis in year 1895. With the X-ray analysis it was possible to observe hydrogen bonds between proton-sharing atoms, which were in close proximity. [6]

This led to the realization that HBs could impact the three-dimensional arrangement of molecules and molecular fragments. [7] As a result, competition arose among various research groups to unravel key structural features of biomolecules. Notable discoveries included the structure of DNA's double helix (1953, Watson and Crick), the α-helix structure (1951, Pauling, Corey and Branson) and the β-sheet structure (1950, Pauling and Corey) of proteins (see figure 1.2). [8][9][10] These discoveries further led to increased investigations and developments regarding HB patterns in organic crystals. [11] The elucidation of the secondary structure of DNA occurred during the peak of the initial applications of crystallography in

chemistry and provided the groundwork for the discovery of numerous principles for designing hydrogen bonds.

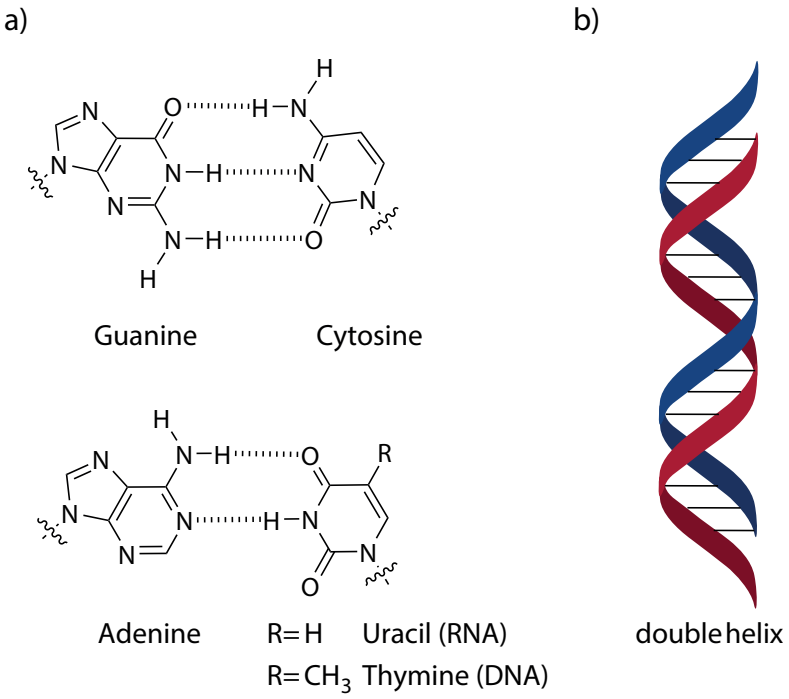

Figure 1.2. Illustration of: a) a Watson-Crick base pair with the respective nucleobases and their base pairs. b) two strands consisting of DNA are twisted and are forming a double helix.

These principles have since been widely applied in areas such as molecular recognition, catalysis, organic synthesis, and supramolecular chemistry. [12][13][14][15][16]

Within the broader field of catalysis, asymmetric catalysis has emerged as a particularly important subfield. Asymmetric catalysis focuses on facilitating chemical reactions that produce chiral molecules with high enantioselectivity, which is essential in pharmaceuticals. [17] Over the past decades, HB has played a pivotal role in advancing this area by enabling precise control over reaction pathways. [13] Notable HB donors include squaramides and thioureas (see figure 1.3).

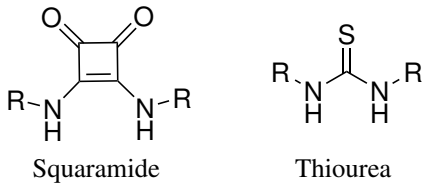

Figure 1.3. Illustration of thiourea and squaramide functionalities with an organyl group R.

The synthesis of squaramides will be discussed first, followed by a comparison with their well-known competitor, thiourea.

1.1.1 Synthesis of Squaramides

Squaramides are derivatives of the conformationally rigid cyclobutene ring consisting of two carbonyl hydrogen-bond acceptors and two amide nitrogen hydrogen-bond donors. This compact molecular framework possesses distinctive physical and chemical properties, making it an exceptionally valuable as a tool in a wide range of areas including bioconjugation, molecular recognition, catalysis and self-assembly. [18][19][20][21][22]

Originally synthesized by Cohen et al. in 1959 through the hydrolysis of dichlorotetrafluorocyclobutene, squaric acid (diketocyclobutenediol) serves as the precursor for squaramides. [23]. Over time, alkyl esters have become valuable tools for bioconjugation and serve as crucial starting materials for synthesizing mono- and di-substituted squaramides, squaraine dyes and more recently, thiosquaramides. [24][25][26] In 1963, West et al. attributed the stability and aromaticity of the dianionic diketocyclobutene to cyclic delocalization of π-electrons within the four-membered ring. [27] While much theoretical work has focused on understanding the aromaticity of $C_nO_n^{2-}$ systems, the easy synthesis of alkyl squarates has made squaramide synthesis more accessible today. [28][29][30]

One particularly handy trait is their capability for sequential substitution by amines. The initial substitution reaction increases aromatic stabilization compared to the parent alkyl squarate, making the mono-substituted intermediate less reactive and enabling easy access to unsymmetrical squaramides. [28] Unsymmetrical aliphatic squaramides can be synthesized by aliphatic amine condensation starting from dialkoxysquarate. Additionally, unsymmetrical squaramides can be obtained by aromatic amine condensation, however, longer reaction times in comparison to aliphatic amine condensation were observed due to the reduced nucleophilicity of aromatic amines (0.3 h-2 h in comparison to 50 h, see figure 1.4). [31]

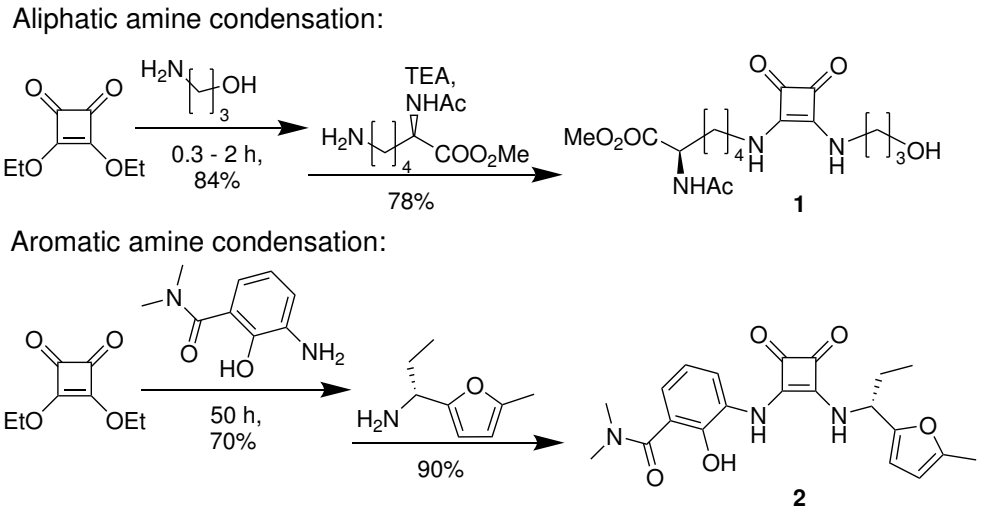

Figure 1.4. Reaction conditions: in EtOH and at rt. **2** was developed by the Schering–Plough Research Institute and utilized in the treatment of various inflammatory diseases. [32][33]

It has been previously reported that reactions with aromatic amines can yield two products: 1,3-squaraine and 1,2-squaramide (see **5** and **6** in figure 1.5). [31] The proposed reaction mechanism shows that the squaric ester **3** can react as an electrophile either in a direct 1,2-addition to the carbonyl or via a conjugate 1,4-addition, which depends on choice of nucleophile and reaction conditions. [31] Predicting the exact process of the initial step from converting squaric ester **3** to mono-squaramide **4** is challenging. Both a 1,2-addition followed by loss of ROH (e.g. R= Me) and a direct 1,4-displacement of ROH could result in the same intermediate **4**. However, in the subsequent step where the second ROH is leaving the squarate functionality, two different products can be obtained depending on the regiochemistry of the amine addition. A 1,4-addition leads to the formation of bis-squaramide **6**, while a 1,2-addition results in the corresponding squaraine **5**. [34]

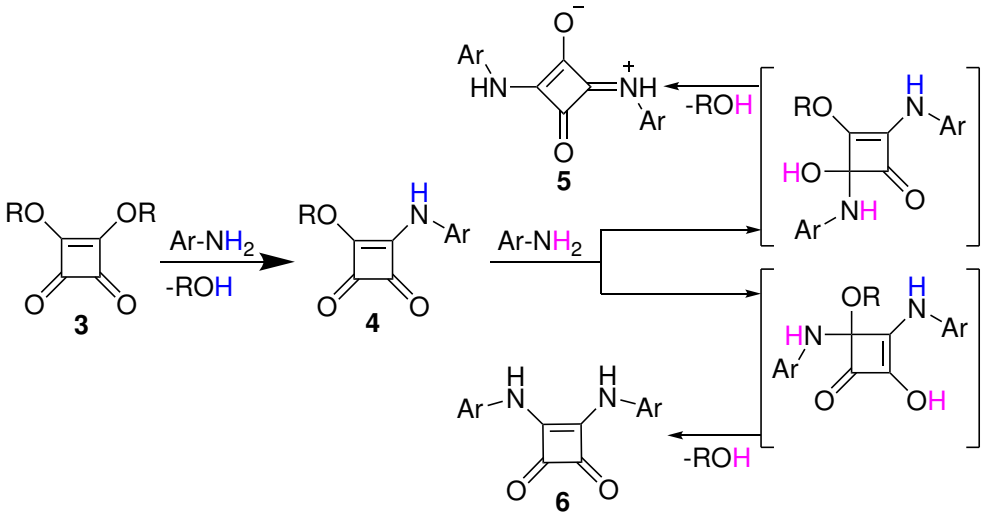

Figure 1.5. Proposed reaction mechanism of a squaric ester **3** with an aryl amine Ar-NH_2. [31] Chosen colors are only for a clearer illustration of the proposed reaction mechanism.

Notably, the Taylor group explored methods to optimize aromatic-substituted squaramide synthesis by minimizing undesired by-products. They demonstrated that Lewis acids can catalyze the addition of anilines and 2-pyridylamines to diethylsquarate, allowing for milder reaction conditions and preventing the formation of squaraine by-products. Diethylsquarate reacted successfully with electron-poor bis-trifluoromethyl aniline in the presence of zinc(II) trifluoromethanesulfonate ($Zn(OTf)_2$), yielding squaramide with a high yield of 80% and without observing monoester or squaraine isomer (see figure 1.6). [24]

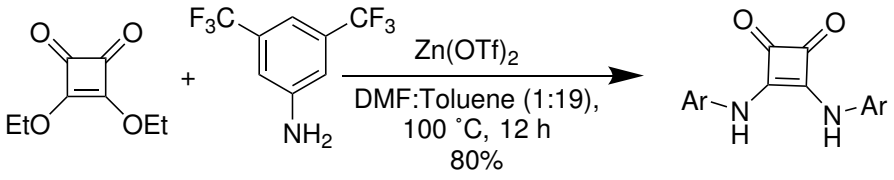

Figure 1.6. Lewis acid catalyzed squaramide synthesis reported by Taylor et al.. [24]

Following the brief discussion of squaramide synthesis, their structural features and properties will now be examined in comparison to thiourea, a well-established hydrogen bond donor. [35]

1.1.2 Squaramides Under Closer Inspection

Thioureas and squaramides share a common feature in their amide nitrogen. In both functionalities, one of the nitrogen lone pairs can delocalize through the carbon-oxygen double bond, which restricts the rotation of the C-N bond (see **I** and **II** in a) in figure 1.7).

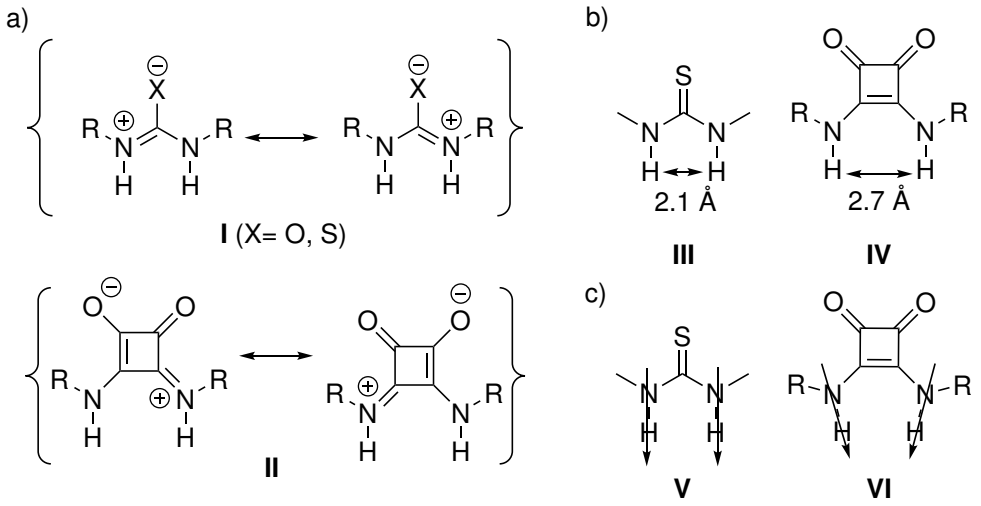

Figure 1.7. Difference of (thio)urea and squaramide: a) comparison of zwitterionic forms of (thio)urea and squaramide structure, b) comparison of Hydrogen bond spacing distances in N,N'-dimethylthiourea and N,N'-dimethylsquaramide (calculated at the 6-31G*basis set level), c) comparison of arrangements of the hydrogen bonds in thioureas and squaramides. [36]

A distinctive property of squaramides, however, is their ability to further delocalize a nitrogen lone pair into the cyclobutenedione ring system. This delocalization imparts aromatic character to the four-membered ring, consistent with Hückel's rule ([4n + 2] π electrons, n = 0). Analysis using computational methods, like the nucleus-independent chemical-shift (NICS) method confirmed that squaramides exhibit partial aromatic character. [37] This leads to increased conformational restriction, making the carbonyl and amine groups in squaramides align in the same plane. [28] In addition, a crystallographic study supported this fact by showing that nitrate binds to the squaramide through strong hydrogen

bonds formed with the two oxygen atoms, which are nearly coplanar (see a) in figure 1.8). [38]

Furthermore, NICS analysis showed that HB with squaramides can enhance the aromaticity of their four-membered ring, arising from electron delocalization induced by hydrogen bond formation. [39] This effect provides advantageous thermodynamic stability, which is particularly beneficial for self-assembly and molecular recognition processes. [40][41] Moreover, squaramides have the capability to interact with negatively charged species, like carboxylates and nitrates, forming robust associations in polar solvents. [42][43] Moreover squamides show superiority over thiourea in halide binding. [44]

Another notable difference between thioureas and squaramides is the spacing between their N-H groups, which was shown by the Takemoto and Rawal groups that the distance between the N-H groups in N,N'-dimethylthiourea is approximately 2.13 Å, while in N,N'-dimethylsquaramide it is around 2.72 Å (see **III** and **IV** in b) in figure 1.7). [45][20] Additionally, the structure of the cyclobutenedione ring also causes a convergent orientation of the N-H groups, tilting each by approximately 6° (see **V** and **VI** in c) in figure 1.7). This unique property observed in the squaramide recognition unit may lead to greater linearity in HB for some substrates and offer different binding properties in the transition states compared to urea/thiourea, which leads to a better enantiocontrol in asymmetric catalysis. [20][36]

Moreover, the primary distinction between squaramides and their urea/thiourea is their dual capability for both ionic- and hydrogen-bonding. While ureas and thioureas show binding affinity to anions, their ability to recognize cations is restricted. In comparison, the squaramide functionality shows duality and readily engages in ditopic binding (see a) in figure 1.8). [39][46]

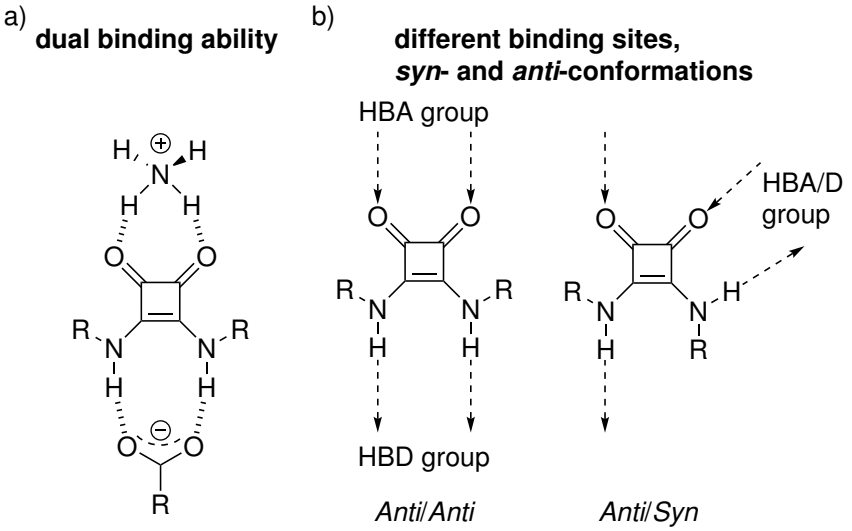

Figure 1.8. Illustration of ditopic- and hydrogen-bonding sites of squaramides. a) duality binding and b) *anti*/*anti*- and *anti*/*syn*-conformations. The three different HB sites of squaramide over the HBD functionality, HBA functionality or HBA/D functionality are shown in b). [36]

In bid to support the ditopic binding abillity of squaramides, theoretical explanations suggest that the heightened recognition of cations arises from the increased aromaticity of the four-membered ring during complexation. [39] In addition to their ditopic binding capabilities, squaramides exhibit various binding modes that can lead to different conformers, such as *anti/anti* and *anti/syn*. These conformers can potentially enable diverse supramolecular self-assembly motifs through HB. The different conformations of *bis*-secondary squaramides have been studied by NMR, revealing that in solution, *bis*-secondary squaramides generally adopt an *anti/anti* conformation, where both NH groups are positioned in an *anti*-orientation relative to the carbonyl oxygen. [37] However, in specific cases, a *anti/syn* conformation has been observed, facilitated by intramolecular HB (see chapter 1.2 for further information). [47] Furthermore, *syn/syn* conformation is theoretically possible, but experimentally not observed due to steric hindrance from amine substituents. [48] X-ray crystallography studies have provided insights into the solid-state conformations of squaramides. These studies consistently show that squaramides prefer the *anti/anti* conformation and support the results of the NMR studies. [49].

As discussed in chapter 1.1, hydrogen bond donors play a crucial role in asymmetric catalysis, with significant potential applications in the pharmaceutical industry. [17] The following chapter explores the application of thioureas and squaramides, particularly as asymmetric catalysts.

1.1.3 Hydrogen Bond Donors in one Glance: Thiourea and Squaramides

Several hydrogen-bond donor catalysts are reported to date, but most of them are based on thiourea building blocks, which established a strong presence in asymmetric catalysis. [35] The numerous reactions catalyzed by thioureas underscore their importance as motif (e.g. Strecker reaction, Micheal addition, Morita-Baylis-Hillmann reaction, Friedel-Crafts reaction, Petasis reaction, Pictet-Spengler cyclization and Diels-Alder reaction). [50][45][51][52][53][54][55] While chiral thioureas have been found to be a valuable resource for discovering catalysts, other motifs with Hydrogen bond (H-bond) donor properties have received much less attention (diols, dipeptides, cinchona alkaloid derivatives, phosphoric acids, guanidinium ions and amidinium ions). [56][57][58][59][60][61]

Drawing parallels with anion-receptor studies, it's notable that the adoption of squaramide functionality as a significant player in asymmetric catalysis happened almost a decade after their urea/thiourea competitor. [13][20] The realization of their potential and diverse applications of squaramide organocatalysts as a "game-changer" made a significant presence with the groundbreaking research by the Rawal et al. in 2008 on the development of cinchona-squaramide-based organocat-

alysts. [20] Since then, squaramides and thioureas have found applications in both anion recognition and catalysis (see figure 1.9). [44][62][63][64][65][66]

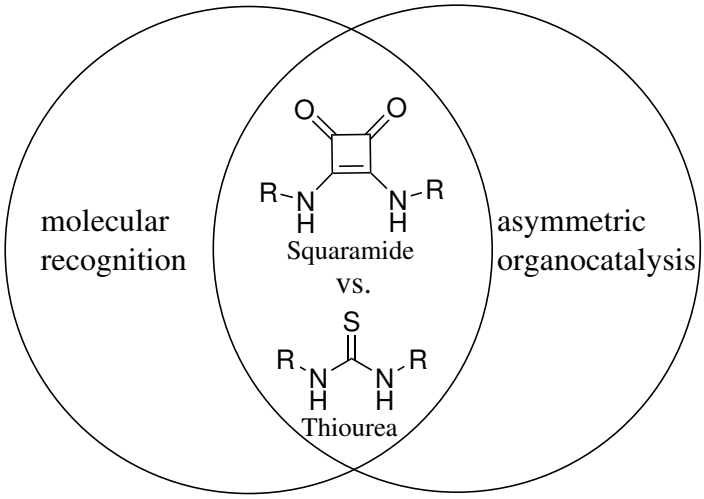

Figure 1.9. Thiourea and squaramide functionality with an organic residue R. [36]

Notably, squaramides have demonstrated their superiority over thioureas as a hydrogen-bond donor asymmetric catalysts, showcasing a broader substrate scope, higher yield and better enantioselectivity, while also being reported to exhibit superiority in terms of catalyst loading, faster turnover and shorter reaction times compared to thioureas. [20][65][67]

In catalysis, turnover frequency TOF is an important parameter, which can be correlated with catalyst acidity and is defined as the ability of a catalyst to donate protons (Brønsted acidity) or accept electron pairs (Lewis acidity) during a chemical reaction. [68] In some cases catalytic activity increases with acidity of the hydrogen bond donor catalyst. [68] Therefore the acid strength of the catalyst can be a crucial parameter for catalytic activity. [69] As mentioned above chiral squaramide catalysis showed excellent catalytic performance rather than their competitor thiourea.

One of factor for the superiority of the squaramides was claimed to be their higher acidity. For a long time there were no quantitative studies of pK_a values of squaramides. In 2014, Xiang et al. determined by UV spectrophotometric titrations pK_a values for catalytic active squaramides and compared those with corresponding thioureas in DMSO. [69] Squaramides were reported to have lower pK_a values compared to their thiourea analogues, possibly explaining why squaramide catalysts can achieve higher activity levels in a variety of asymmetric transformations, even with lower loadings. [70]

Therefore, after being underreported in the field of organocatalysis, squaramides have significantly gained research interest across diverse areas of chemical and biological sciences. [34][71][72]

In summary, compared to thiourea, the squaramide functionality exhibits significant differences in pK_a, rigidity, hydrogen bond spacing, hydrogen bond

angle and duality. [69][20] These characteristics, along with their synthetic versatility, conformational rigidity and relative stability, have spurred considerable research in recent years to explore the potential of this highly valuable framework. Squaramides, in particular, have garnered attention as organocatalysts due to these attributes, as well as their ability to activate a variety of substrates such as carbonyl, nitro, nitrile, and imino compounds by HB (see figure 1.10). [73]

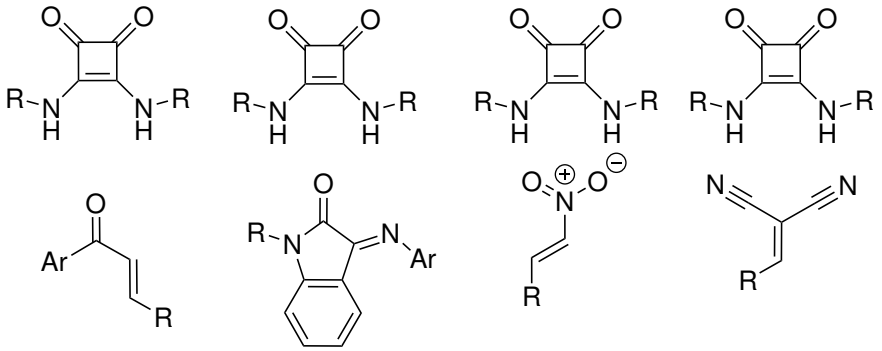

Figure 1.10. Substrates activated by squaramide-based organocatalysts. [74]

However, squaramides have not yet fully been explored in the context of self-assembled supramolecular structures such as coordination cages, which is a subfield of supramolecular chemistry. This work deals with filling this void (see chapter 2 for more details).

1.2 General Information: Supramolecular Chemistry

Supramolecular chemistry focuses on highly complex and functional molecular systems formed through the assembly of individual components. [75] These supramolecular structures are stabilized by intermolecular non-covalent interactions, including hydrogen bonds, π-stacking interactions, electrostatic forces, hydrophobic effects and mechanical bonds. [76]

A pivotal moment in the history of supramolecular chemistry was the discovery of crown ethers, which catalyzed the rapid growth of this field. In 1987, Jean-Marie Lehn, Charles J. Pedersen, and Donald J. Cram were jointly awarded the Nobel Prize in Chemistry for their groundbreaking work in developing and utilizing molecules capable of highly selective structure-specific interactions.

The origins of this achievement date back to 1967, when Charles J. Pedersen reported that a cyclic molecule he had synthesized significantly increased the solubility of potassium salts in nonpolar solvents. [77] This molecule was later named "crown ether". Two years later, Jean-Marie Lehn discovered cryptands, which exhibit an even higher affinity for metal cations due to their three-dimensional structure. [78] Further advancements came in 1979 with Donald J. Cram's publication on spherands, a new class of macrocycles. [79] Spherands consist of six phenylene units connected via their meta-positions, offering unique structural and functional properties (see figure 1.11).

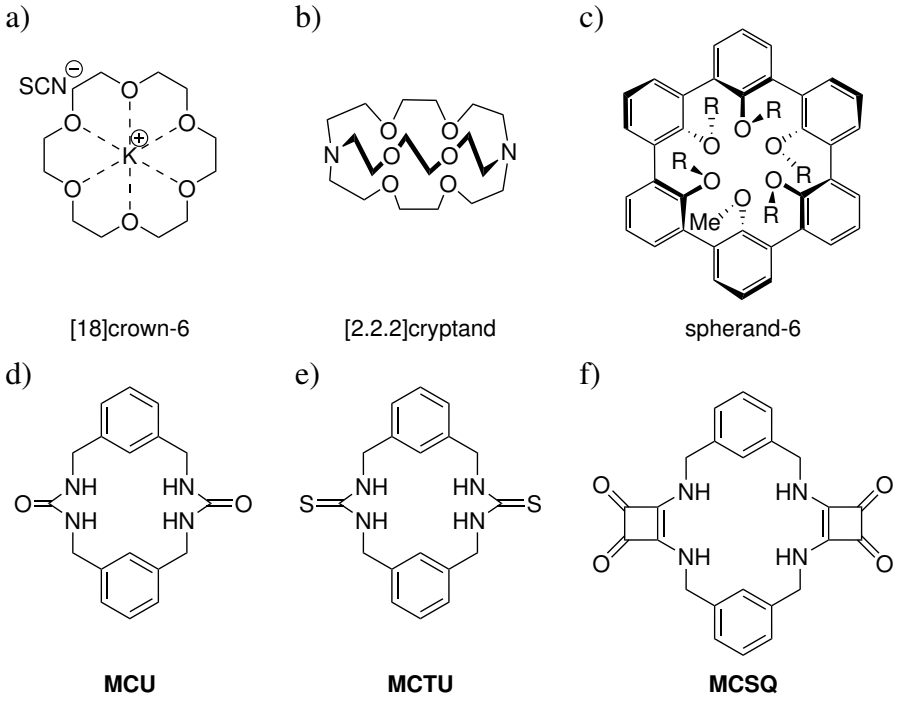

Figure 1.11. Illustration of the macrocyclic molecules a)-c) which led to the award of the Noble Prize in chemistry in 1987. a) crown ether obtained by Pedersen, b) cryptand investigated by Lehn, c) spherand-6 investigated by Cram. [78][79]. d)-f) show different macrocycles with HB functionalities.

The six phenylene units of spherand-6 are functionalized with methoxy groups, whose oxygen atoms are oriented toward the center of the macrocycle. Due to this preorganization of oxygen atoms, spherands exhibit significantly higher binding affinities to Li^+ and Na^+ compared to crown ethers or cryptands. [80][81] Building upon the principles of selective binding observed in cation binding receptors, researchers have turned their attention to exploring macrocyclic compounds with HB functionalities, which offer promising avenues for anion recognition. [82]

Inspired by the previous mentioned pioneering works on macrocycles, molecular structures featuring HB functionalities, such as urea- and squaramide-based macrocycles, have been explored for their ability to bind anionic molecules. [83][84][85] Recently, Shimizu et al. compared the crystal structures of a squaramide-based macrocycle **MCSQ** and its (thio)urea analogs **MCU** and **MCTU** (see d)–f) in figure 1.11). [86] Their analysis revealed that all squaramide functionalities in the crystal structures adopt a *trans-trans* conformation. Moreover, in the solid state, **MCSQ** forms a "head-to-tail" hydrogen-bonding assembly. Specifically, only one carbonyl oxygen of the squaramide engages in hydrogen bonding with the NH functionality of an adjacent squaramide molecule (see a) in figure 1.12). [86]

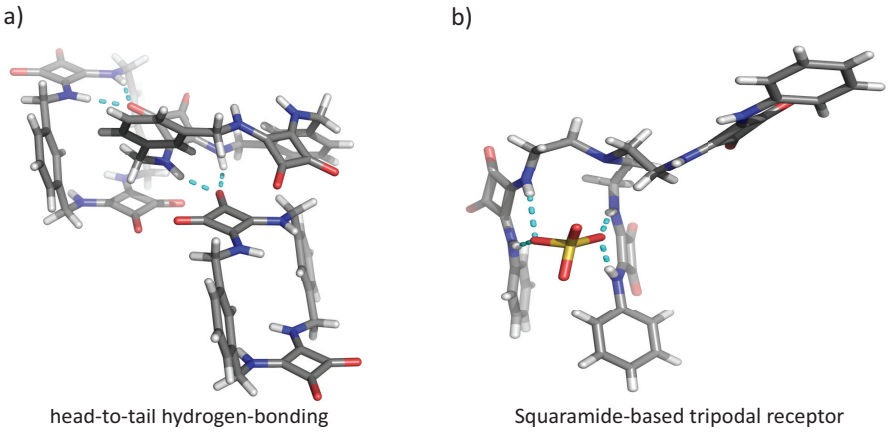

Figure 1.12. Illustration of X-ray structure of squaramide-based macrocycle **MCSQ**, which shows intermolecular HB. [86] b) shows a squaramide-based tripodal, which binds SO_4^{2-} by HB. X-ray structures are shown. For clarity, one of two disordered SO_4^{2-}, two TBA cations and the second tripodal molecule are omitted. [87]

Another interesting molecular class besides the macrocycles are tripodal molecules. In particular, squaramide-based tripodal receptors are versatile compounds in supramolecular chemistry, offering significant potential for selective anion recognition and extraction. [87][88] Their design leverages the strong H-bond-donating ability of squaramide moieties, with a tripodal configuration providing preorganization and multiple binding sites for enhanced selectivity and affinity. These receptors demonstrate high binding strength, particularly for sulfate and phosphate anions, through the formation of multiple H-bonds. [87] Wang et al. reported a squaramide-based tripod, which binds selectively

SO_4^{2-} (see b) in figure 1.12). Recent advancements, such as integrating crown ether units have enhanced their versatility by enabling simultaneous cation and anion binding and tunable selectivity based on its counter ion. [89]

Noteworthy developments in supramolecular chemistry were not confined to host-guest chemistry. One particularly fascinating area is molecular machinery, which has garnered significant attention from chemists, especially in the last two decades. The foundation for molecular machines was laid by Jean-Pierre Sauvage in 1983, with the introduction of a novel approach for the synthesis of catenane structures consisting of two or more mechanically interlocked rings. [90] In earlier work, Edel Wasserman successfully synthesized catenanes. However, the process was laborious and required numerous synthesis steps. [91] Sauvage revolutionized the field by significantly improving the yield and accessibility of catenanes through the use of metal ions such as copper(I) as templates (see a) in figure 1.13).

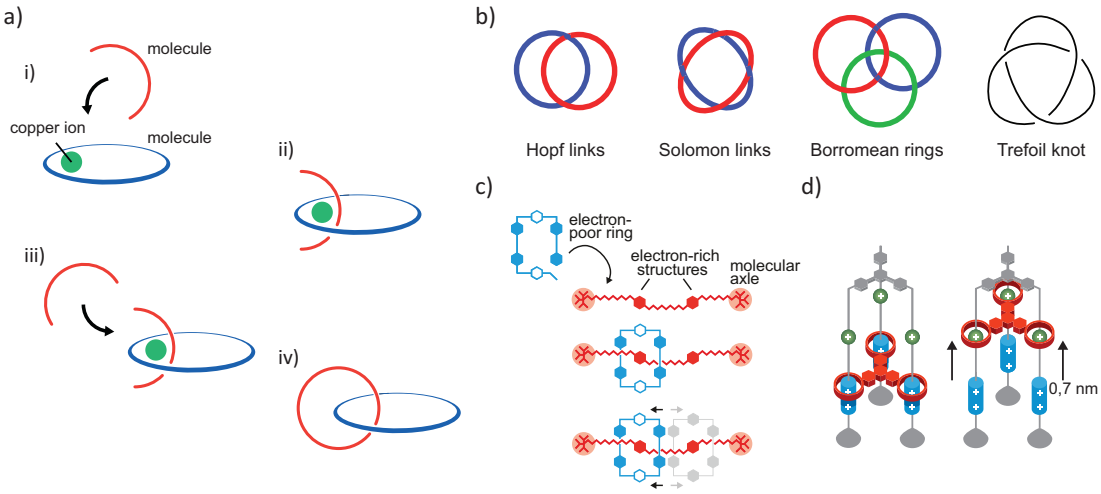

Figure 1.13. a) Conceptual drawing of synthesis of a catenane by using copper(I) as a template. Adapted from [92]. © Johan Jarnestad/The Royal Swedish Academy of Sciences. b) Depiction of hopf link (catenane), the solomon links, the borromean rings and trefoil knot. [93] c) Conceptual drawing of shuttle-rotaxane consisting of a electron-poor ring and a electron-rich structure. Adapted from [92]. © Johan Jarnestad/The Royal Swedish Academy of Sciences. d) Visual representation of pH-switchable molecular elevator. Adapted from [92]. © Johan Jarnestad/The Royal Swedish Academy of Sciences.

In the first step, the cyclic molecule coordinates to a copper ion (i)). Subsequently, the copper ion facilitates the gathering of a second molecule (ii)), followed by a third molecule linking to the crescent-shaped structure (iii)). Finally, the catenane is obtained through demetallation in the presence of KCN (iv)) (see a) in figure 1.13). [94] This strategy enabled the synthesis of new intertwined structures, including links and knots. Notable examples include solomon links, borromean rings and the trefoil knot (see b) in figure 1.13). [95][96][97] Catenanes can be described as hopf links, as their two rings are interlocked exactly once.

Another intriguing class of supramolecular structures are rotaxanes. [98] Rotaxanes consist of a dumbbell-shaped molecule threaded through a macrocycle. In 1991, J. Fraser Stoddart reported a shuttle-rotaxane based on an electron-deficient ring and electron-rich regions of a linear molecule. This molecule is equipped with sterically bulky groups at its ends, serving as stoppers (see c) in figure 1.13). [99] The ring can move back and forth along the molecular axle in response to temperature variations. In subsequent years, J. Fraser Stoddart introduced more complex systems, such as the molecular muscle and the molecular elevator (see d) in figure 1.13). [100][101]

Another fascinating category of molecular machines is molecular motors. In 1999, Ben L. Feringa reported the first molecular motor, which is made of two unidirectional paddle-like rotating molecules. [102] These molecules are connected by a double bond with steric hindrance from the methyl groups ensuring that the rotors rotate in only one direction. Upon irradiation, distinct helical conformations are observed (see a) in figure 1.14).

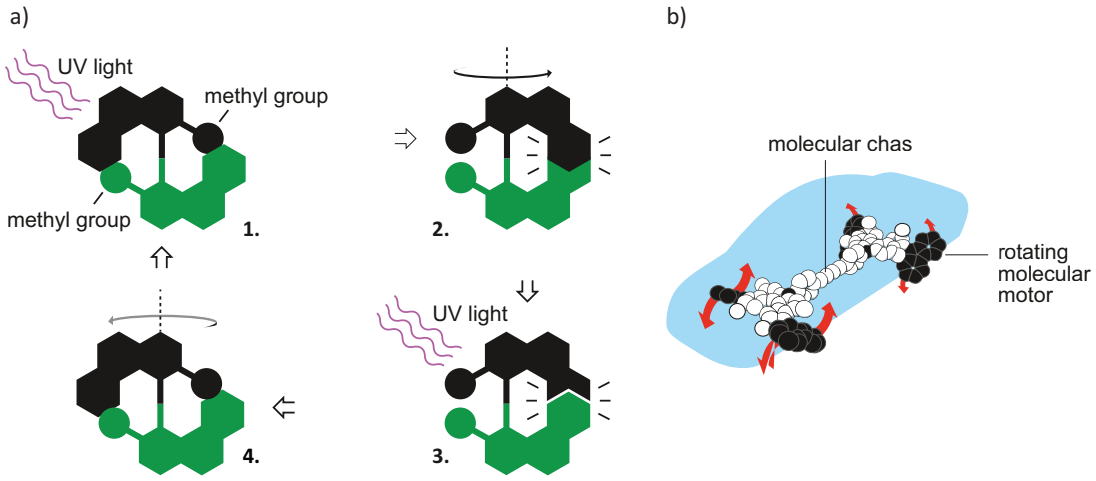

Figure 1.14. Illustration of: a) the principle of a rotating molecular motor, featuring paddle-like components connected by a double bond, with steric hindrance directing unidirectional rotation under irradiation. b) a molecular nanocar equipped with four molecular motors acting as wheels, all connected to a central molecular chassis. Adapted from [92]. © Johan Jarnestad/The Royal Swedish Academy of Sciences.

Moreover, in 2011, Ben L. Feringa reported the development of a molecular nanocar consisting of four molecular motors connected to a central molecular chassis (see b) in figure 1.14). Scanning tunneling microscopy revealed that the nanocar was capable of unidirectional motion on a Cu(111) surface. To trigger the molecular motors to perform a full 360° rotation, both UV-light irradiation and temperature changes were required. [102]

Over the years, this field progressed rapidly, leading up to in 2016, when Bernard L. Feringa, Jean-Pierre Sauvage, and J. Fraser Stoddart were jointly awarded the Nobel Prize in Chemistry "for the design and synthesis of molecular machines".

In the previous chapters, the crucial role of HB in our surroundings and in science has been briefly discussed. The properties of the key-player in HB thiourea and squaramide have been compared and the superiority of squaramide over the as long known as golden-standard in organocatalysis thiourea has been explained. A brief introduction to supramolecular chemistry and some exciting work has been presented. The next chapter will explore how the unique properties of squaramides contribute to the formation of supramolecular structures stabilized by non-covalent interactions.

Squaramides under the Scope of Supramolecular Chemists

As previous mentioned squaramides raised the attention of scientist from different fields due their unique properties and modular synthetic accessibility. [73][34] Therefore, it is not surprising that squaramides have sparked the curiosity of supramolecular chemists, leading to their exploration in the context of supramolecular assemblies. Notably, the work of Prohens et al. based on an unsymmetrical squaramide **6a** (see a) in figure 1.15).

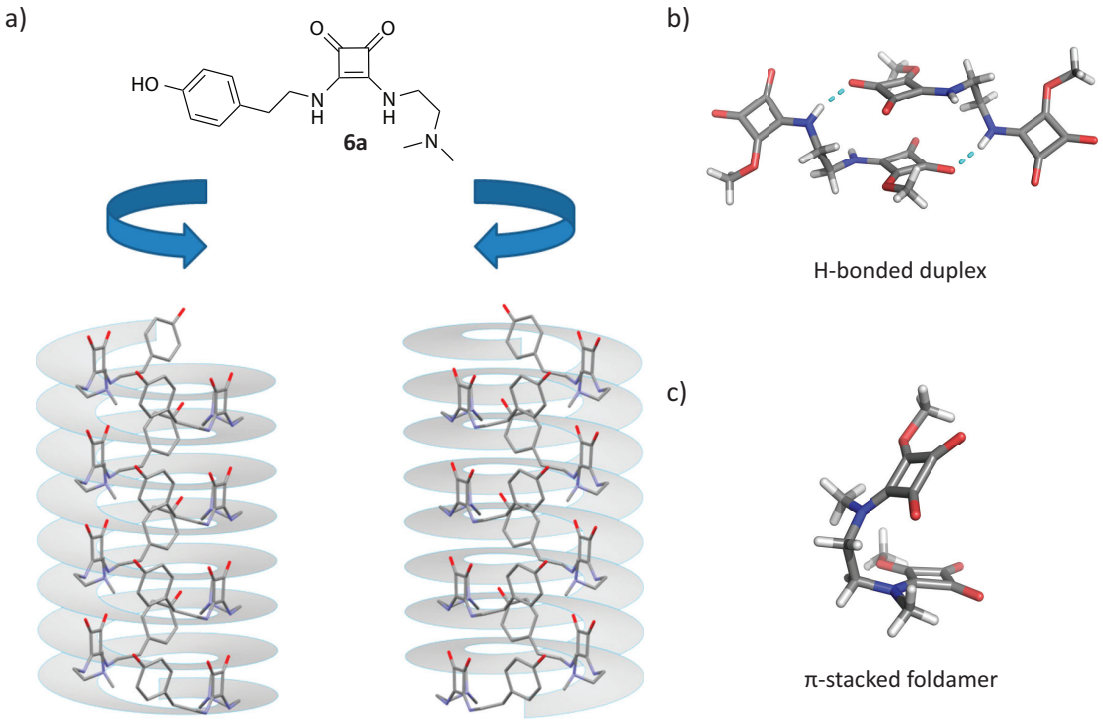

Figure 1.15. a) Illustration of clock and anticlockwise rotation of the two different helices in the racemic crystal of **6a**. Adapted from [103] (© 2013 American Chemical Society). Illustration of intermolecular aggregation controlled by varying ability of HB and π-stacking by b) ethylenediamine to form a H-bonded duplex and c) with *N,N´*-dimethylethane-1,2-diamine (DMEDA) to form a π-stacked foldamer. X-ray structures are shown. [104]

They were able to show intramolecular HB in a "head-to-tail" interaction. Thereby, they observed a racemic mixture of alternating clock/anticlockwise rotating helices in solid state, which are formed through an unprecedented combination of strong squaramide-squaramide (NH-O interaction) and amine-phenol (N-HO interaction) interactions. The authors also observe CH-π interaction between the methylamino group and the aromatic ring. [103] This work shows the potential of squaramides as interesting framework for self-assembly structures.

Eight years later, Patwari et al. demonstrated intermolecular aggregation controlled by the varying HB and π-stacking abilities of a bis-squaramide. The bridging length between the two squaramide units was adjusted using methyl or ethyl groups, while primary and secondary diamine linkers were employed to

further modulate HB capability. They found out that ethylenediamine-based bis-squaramide is interacting by NH-O hydrogen bonds leading to unfolded duplex-like structures. In contrast, for DMEDA-based bis-squaramides, the absence of NH groups reduces NH-O bonding, allowing π-stacking to take precedence and resulting in folded structures (see b) and c) in figure 1.15). [104]

The squaramide-based assemblies mentioned earlier rely on intermolecular HB and are held together through head-to-tail interactions, enabled by the dual hydrogen bond donor and acceptor properties of squaramides. These assemblies can extend into head-to-tail chains with enhanced average bond strength, a phenomenon known as "hydrogen bond cooperativity". [105][106][107][108] This effect arises from the polarization of squaramides, when interacting with strong dipoles, which further promotes HB. [109] Such cooperativity is a key feature in supramolecular systems, underlying behaviors such as the high polarity of alcohols as solvents and the characteristic nucleation-elongation pattern observed in polymerization processes. [110][111][112]

Furthermore, cooperativity has been observed in intramolecular HB networks. For instance, cooperative polarization between multiple aligned urea and thiourea units has been shown to enhance the catalytic activity of terminal NH groups. [113][114][115] Recent studies by Cockroft and Hunter et al. have quantitatively measured cooperativity in OH-based H-bonded chains and amide interactions with donors or acceptors. [116][117][118][119] Successive intramolecular H-bonds cooperatively polarize terminal H-bond donors or acceptors, enhancing their interactions with complementary molecules. This polarization increases with the number of HB groups and therefore promotes stronger intermolecular interactions and self-aggregation, which are influenced by the length of the intramolecular H-bonded arrays.

Webb et al. investigated cooperative intra- and intermolecular HB in scaffolded squaramide arrays, examining how molecular design and structure influence these interactions. [120]

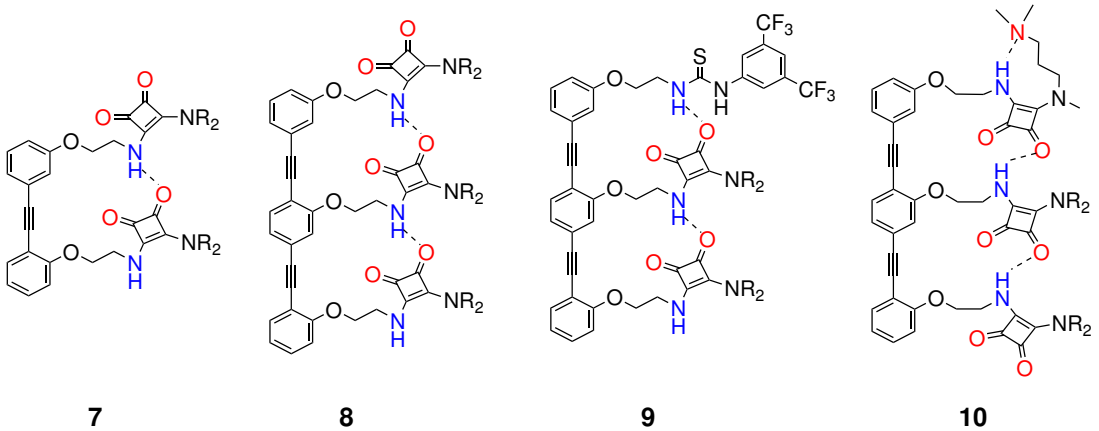

Figure 1.16. Illustration of some of squaramide-based arrays. **10** was found to be in *antiparallel* conformation. [120]

Their study focused on squaramide arrays linked to oligo-(phenylene-ethynylene) backbones of varying lengths and capping groups (see figure 1.16; R= C_8H_{17}). By comparing binding constants obtained from ^{1}H-NMR titrations with DMSO, they demonstrated that longer squaramide arrays exhibited stronger cooperative polarization of terminal HB groups due to successive intramolecular HB. X-ray analysis further revealed that enhanced polarization extends to intermolecular interactions, thereby strengthening self-aggregation. The self-aggregation was also analyzed through dilution experiments using ^{1}H-NMR spectroscopy. Additionally, they examined the effect of capping groups, showing that capping squaramide arrays with strong H-bond donors or acceptors show reduced intermolecular interactions and consequently decreased aggregation. [120]

Various squaramide-based assemblies utilizing inter- and intramolecular interactions were explored, showcasing the versatility and tunability of squaramides in creating diverse supramolecular architectures and enhancing cooperativity through intramolecular HB. While squaramides are promising building blocks for supramolecular assemblies, relying solely on HB to form organic cages is less viable for future host-guest chemistry. Such cages are prone to decomposition depending on the solvent or competitive guest. This may explain why only a few well-defined supramolecular cages formed through HB have been reported.

Examples include a few capsules formed via multiple ring threading and a limited number of H-bonded cages, such as those formed by calix[4]resorcinarenes, tris(guanidinium)nitrate clusters and PO_4^{3-} anions. [121][122][123][124][125][126]

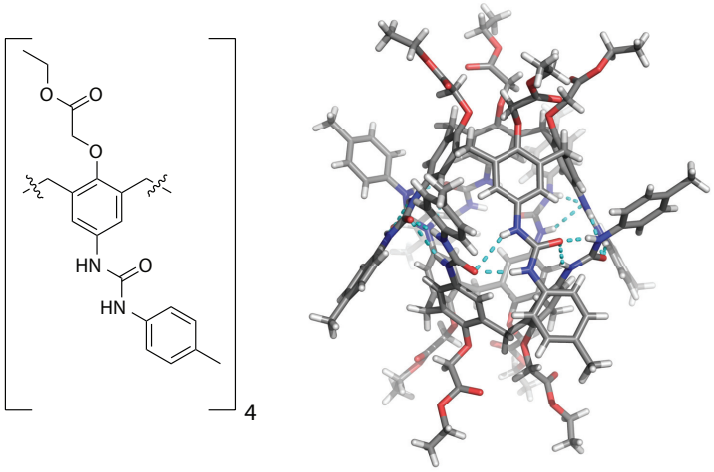

Figure 1.17. Illustration of dimer formation of calix[4]arenes, which is functionalized with urea. It is stabilized by 16 hydrogen-bonds between NH and C=O groups in apolar solvents without external H-bond acceptors. X-ray structure is shown. [127]

The cooperativity of intramolecular HB offers significant potential for host-guest chemistry within supramolecular cages. Coordination cages, composed of organic ligands and metal ions forming a cavity, exhibit unique properties and represent a promising class of supramolecular assemblies. Despite their potential, the role

of intramolecular HB in such systems remains unexplored. This thesis focuses on the formation and study of a squaramide-based coordination cage utilizing intramolecular HB with an emphasis on investigating its host-guest chemistry. In chapter 1.3 the supramolecular coordination cages are introduced.

1.3 Supramolecular Coordination Cages

Supramolecular coordination cages are discrete, three-dimensional structures formed through the self-assembly of metal ions and organic ligands via coordination bonds, often designed to encapsulate guest molecules and facilitate applications in areas such as catalysis, molecular recognition and drug delivery.[128][129][130]

Supramolecular coordination cages are particularly fascinating, because the use of metal cations enables the formation of geometric topologies in supramolecular assemblies that would be exceedingly tedious to achieve through conventional organic synthesis alone. [131][132][128][133] In addition, the open cavity of these three-dimensional coordination structures imparts unique properties, resulting in novel functions and characteristics. Many coordination cages are positively charged due to their construction from neutral ligands coordinated to positively charged metal ions, which often enables the encapsulation of anions. [133][134] Furthermore, neutral or reactive guest molecules can be stabilized within these cages and unreactive molecules can be activated for further reactions. [135][136] The versatility of supramolecular coordination cages extends to applications such as molecule separation from mixtures, gas separation, and catalytic activity, which will be explained in detail in chapter 1.6. [137][138][139][140][141] These attributes underscore the immense significance of coordination cages in host-guest chemistry. [142]

One of the key features that enable these diverse applications is the wide array of distinct geometric topologies achievable in supramolecular structures. The topology of these assemblies can be influenced by factors such as the choice of metal ion or the shape of the ligands (see figure 1.18).

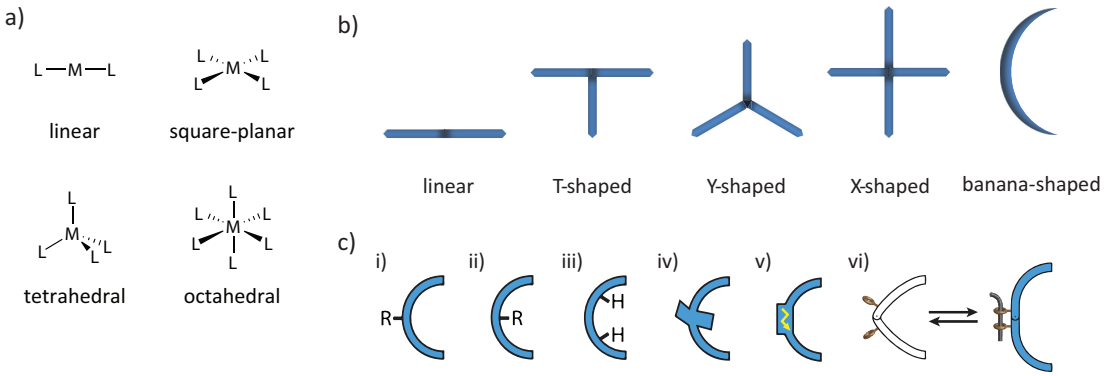

Figure 1.18. a) Illustration of the various coordination geometries. b) schematic illustration of different ligand geometries as building block c) graphical representation of functionalized ligands, which include substitution in i) exterior or ii) endohedral positions, iii) the placement of hydrogen-bond donors inside the cavity, iv) the introduction of steric bulk around the ligand backbone, v) redox activity and vi) ligand backbones, which are photo-switchable. Adapted from [143]. © The Royal Society of Chemistry 2014.

A thorough understanding of the geometric properties of both metal ions and ligands is essential to creating a variety of structures. Different metal ions can adopt specific coordination geometries, including linear (e.g. silver(I)), tetrahedral (e.g. Cu(I)), square planar (e.g. palladium(II)) or octahedral (e.g. iron(II)) (see a) in figure 1.18). [144] In addition, the geometry of the ligand plays a crucial role in the assembly of coordination complexes. Ligands can feature donor atoms such as oxygen or nitrogen and can be categorized as bis-, tris-, or tetrakis-dentate building blocks. The ligand's structure, including its shape and bite angle, introduces further variability (see b) in figure 1.18).

By carefully selecting appropriate building blocks and metal cations, the predictability of the resulting supramolecular assembly increases significantly. One particularly intriguing ligand geometry is the bis-monodentate concave banana-shaped ligand. This type of ligand allows for diverse functionalization (see c) in figure 1.18). Moreover, the banana-shaped ligand proves to be a reliable choice, as it provides accessible cavities due to its symmetrical and spatial arrangement around the coordination center. [145] This feature, combined with its utility in host-guest chemistry, underscores the potential of such ligands in the design of coordination cages. The coordination cages formed by banana-shaped ligands are introduced in chapter 1.4.

1.4 Coordination Cages Formed by Banana-Shaped Ligands

One common class of ligands in supramolecular chemistry are the banana-shaped ligands, which are distinguished by their concave shape and terminal donor groups (see previous chapter 1.3). Additionally, they are typically symmetric and often possess a rigid aromatic backbone. The backbone and the terminal donor group are typically connected by linkers such as alkyne units, phenyl units, amide units or single bonds. [146] These ligands are capable of forming self-assembled cages with square planar metal centers such as palladium(II). By considering the ligands' bite angle, a M_2L_4 stoichiometry can be achieved, where the donor atoms and the metal centers align collinearly. However, various other self-assembled structures are possible (see a) in figure 1.19).

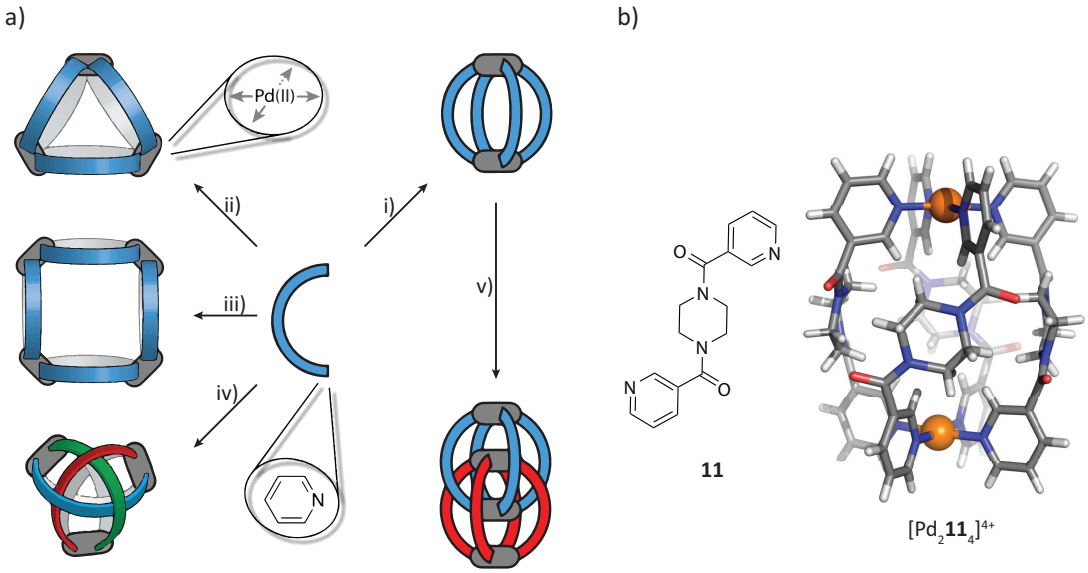

Figure 1.19. a) Schematic illustration of various coordination cages, which are obtained with banana-shaped ligands and palladium(II) with square-planar coordination geometries. Schematic depicting of $[Pd_nL_{2n}]$ (n = 2–4) cages including i) simple $[Pd_2L_4]$ cage, ii) $[Pd_3L_6]$ and iii) $[Pd_4L_8]$ rings, iv) a double-trefoil knot with intertwined ligands $[Pd_3L_6]$, and v) interpenetrated $[Pd_4L_8]$ cage. Adapted from [143]. © 2014 The Royal Society of Chemistry. b) illustration of X-ray structure of coordination cage $[Pd_2\mathbf{11}_4]^{4+}$. [147]

The monomeric $[M_2L_4]$ coordination cage is the most commonly observed structure. In this assembly, all available metal coordination sites are occupied by four ligands, which bridge the two metal cations. The resulting coordination cage contains a cavity due to the concave nature of the ligands. This cavity is spherical in shape and the assembly-structure is often referred to as a lantern-shaped coordination cage.

In figure 1.19 b), an example of a $[M_2L_4]$ coordination cage with a piperazine backbone and an amide linker, synthesized by Chand et al., is presented. [147]

This coordination cage with the molecular formula $[Pd_2\mathbf{11}_4]^{4+}$ is formed through the square-planar arrangement of four ligands **11** with two Pd(II), resulting in a coordination cage containing a cavity. Chand et al. reported that ligand **11** adopts both *syn* and *anti* conformations in solution, but in the case of the coordination cage $[Pd_2\mathbf{11}_4]^{4+}$, only the *anti* conformation was observed through X-ray analysis. [147]

As shown in a) in figure 1.19, banana-shaped ligands can also form M_3L_6 rings (ii), M_4L_8 rings (iii), double-trefoil knots (iv) and interpenetrated double cages M_4L_8 (v). [148] However, most of these cages are constructed using a single type of ligand, which often limits their functionality. Functionality can be enhanced, for example by employing multiple ligand types in the assembly process. In chapter 1.5, heteroleptic coordination cages, consisting of at least two different types of ligands, will be introduced. The use of multiple ligand types allows for the incorporation of additional functionalities into the coordination cages, presenting exciting possibilities for future applications.

1.5 Hetereoleptic Coordination Cages

In nature, enzymes catalyze reactions by binding smaller molecules in a regio- and enantioselective manner. These macromolecular hosts are characterized by their low symmetry and the presence of multiple functional groups. Inspired by nature, supramolecular scientists have increasingly focused on creating structures with diverse functionalities and low symmetry. [149][150][151][152] Several approaches can be employed to design structures with multiple functionalities. One method is organic covalent synthesis, which often involves multi-step procedures followed by laborious purification processes. [149] Alternatively, multicomponent reactions or dynamic covalent self-assembly offer promising routes to achieve functional diversity. [153][154]

In recent years, metal-mediated self-assembly has garnered significant attention. [155] However, the formation of distinct heteroleptic cages through this method is particularly challenging due to its entropic disfavor. Despite this difficulty, advances in controlling self-sorting behaviors such as narcissistic, integrative, and statistical self-sorting have enabled the formation of well-defined coordination cages. These behaviors are illustrated in a) in figure 1.20.

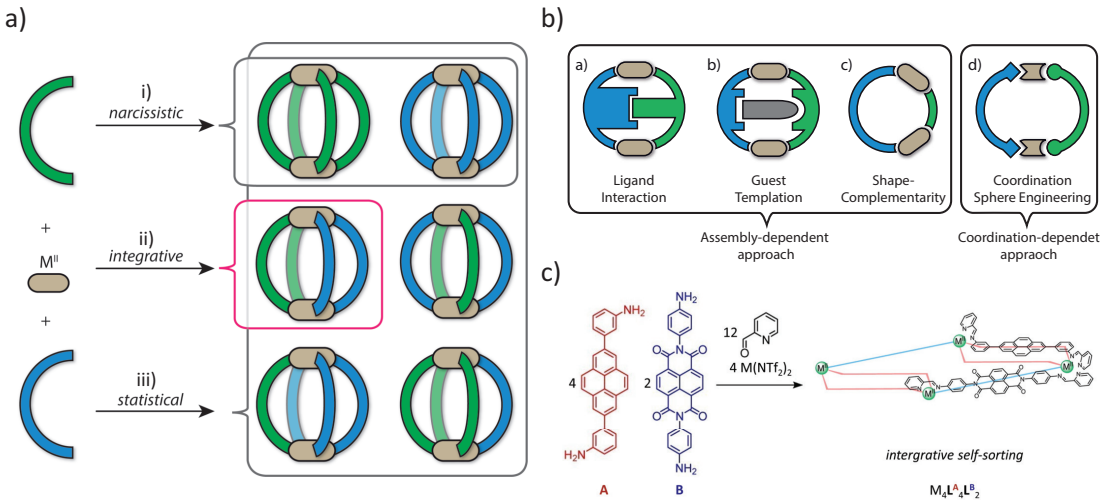

Figure 1.20. a) Three different self-sorting behaviors in coordination-cage formation. Reproduced from [155]. © 2017 The Royal Society of Chemistry. b) different approaches for coordination-driven heteroleptic self-assemblies. Reproduced from [155]. © 2017 The Royal Society of Chemistry. c) self-assembly by using π-π stacking between the ligands. Mixing of **A**, **B**, 2-formylpyridine and $Zn(NTf_2)_2$ in a ratio of 2:1:6:2 provided $Zn_4\mathbf{L}^{\mathbf{A}}{}_4\mathbf{L}^{\mathbf{B}}{}_2$. Only two ligands are shown for clarity. M= Fe^{II}, Co^{II} and Zn^{II}. Reproduced from [156]. © 2015 American Chemical Society.

In narcissistic self-sorting, ligands form only homoleptic cages during coordination-driven self-assembly (see i) in a) in figure 1.20). In contrast, statistical self-sorting results in the formation of all possible cage assemblies as a statistical mixture, predominantly comprising heteroleptic cages (see iii) in a) in figure 1.20). Integrative self-sorting, however, produces a single heteroleptic cage. This process

is entropically unfavorable, which requires that the enthalpic stabilization of the heteroleptic cage compensates for the associated entropic penalty. To overcome this entropic penalty, various strategies have been reported. These approaches can be broadly categorized into coordination-based and assembly-based methods (see b) in figure 1.20). One effective strategy involves the incorporation of a guest template, which selectively stabilizes a specific structure. For instance, in 1999, Albrecht et al. studied the self-sorting of alkyl-bridged catechol ligands in Ti^{III} helicates. They demonstrated that the multiple catechol oxygen atoms facilitated the binding of alkali cations, enabling the regulation of self-sorting outcomes. The addition of Li^{+} to a narcissistic mixture induced the formation of a system containing a heteroleptic species along with both homoleptic species. [157]

In 2015, Yoshizawa et al. demonstrated integrative self-sorting using an anthracene-based ligand and fullerene as a templating guest. Initially, the anthracene-based ligand **12** and its elongated version **13** were independently formed homoleptic coordination cages. However, when the homoleptic cages were mixed without the guest template, a statistical mixture of coordination cages spontaneously formed. The introduction of C_{60} to this mixture induced guest encapsulation and a distinct reorganization into a specific heteroleptic cage product. [158][159]

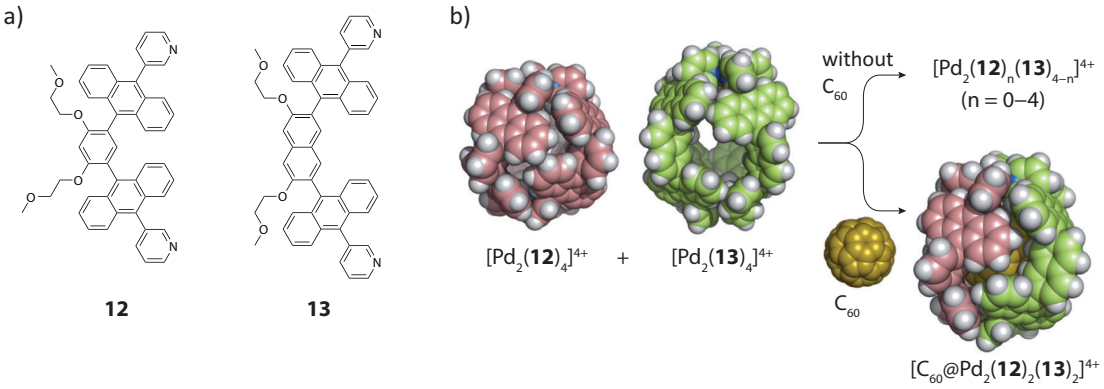

Figure 1.21. Illustration of two anthracene-based ligands **12** and **13**. [158][159]. Adapted from [155] © The Royal Society of Chemistry.

Another approach for achieving distinct heteroleptic cages via integrative self-sorting relies on interactions between adjacent ligands during heteroleptic cage assembly. These interactions such as π-stacking between ligands, play a critical role. In 2015, Nitschke et al. reported a heteroleptic self-assembly process that utilized π-π stacking interactions between electron-rich and electron-poor subunits in the presence of divalent metal cations (e.g., Fe^{II} and Co^{II}). This approach successfully facilitated the formation of heteroleptic cages (see c) in figure 1.20). [156] The use of steric hindrance and π-π stacking interactions, both between the guest and ligand as well as among ligands themselves, provides a highly effective tool for the self-assembly of heteroleptic cages. However, these

approaches can also hinder guest binding due to the occupied cavity of the self-assembled structure. Consequently, alternative strategies are required to enable host-guest interactions within the cavity of heteroleptic cages. One particularly promising approach for achieving integrative self-sorting in heteroleptic assemblies is shape complementarity, which is discussed in detail in chapter 1.5.1.

1.5.1 Heteroleptic Cage Formation using Shape-Complementarity

In 2014, Fujita et al. studied the heteroleptic self-assembly of two bis-monodentate pyridyl ligands with different lengths, but similar bite angles of approximately 120° (see **14** and **15** in b) in figure 1.22). [160]

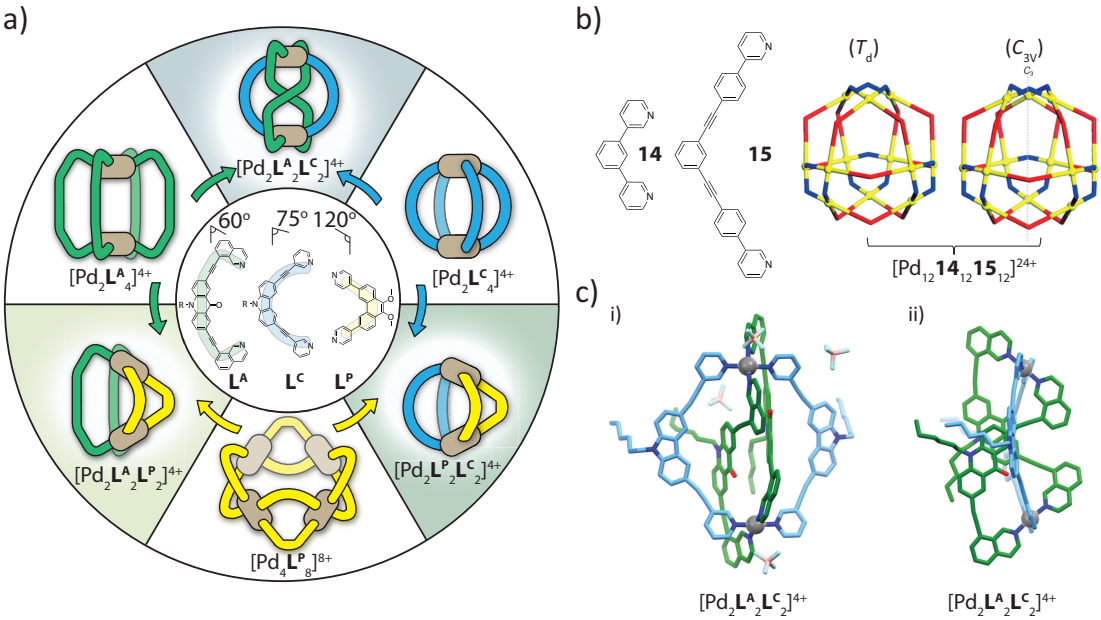

Figure 1.22. a) Illustration of bis-monodentate banana-shaped ligands $\mathbf{L^A}$, $\mathbf{L^C}$ and $\mathbf{L^P}$. Their heteroleptic cage formation due to shape-complementarity approach is schematic shown. R= hexyl substituent. Adapted from [161]. © 2017 Wiley-VCH Verlag GmbH & Co. KGaA, Weinheim. b) illustration of integrative self-sorting of **14** and **15** provided two geometrical isomers of the heteroleptic structure $[Pd_{12}\mathbf{14}_{12}\mathbf{15}_{12}]^{24+}$. Adapted from [160]. © 2014 Wiley-VCH Verlag GmbH & Co. KGaA, Weinheim. c) illustration of X-ray crystal structure of *trans*-$[Pd_2(\textit{anti}\text{-}\mathbf{L^A})_2\mathbf{L^C}_2]^{4+}$: i) shows the occupied cavity and ii) shows the side view. Reproduced from [161]. © 2017 Wiley-VCH Verlag GmbH & Co. KGaA, Weinheim.

Fujita and colleagues reported the Pd^{II}-mediated heteroleptic cuboctahedral self-assembly of $[Pd_{12}\mathbf{14}_{12}\mathbf{15}_{12}]^{24+}$, which exhibited a clean NMR spectrum, when the ligands **14** and **15** were mixed with Pd^{II} in a 1:1:1 ratio. Diffusion-ordered spectroscopy (DOSY) confirmed the presence of a single species in solution and CSI-TOF-MS analysis revealed no homoleptic species. Analytical data suggested the formation of a heteroleptic self-assembled complex $[Pd_{12}\mathbf{14}_{12}\mathbf{15}_{12}]^{24+}$ with T_d

symmetry. However, X-ray analysis revealed a slightly different isomeric structure with C_{3v} molecular symmetry. The authors attributed this to the coexistence of geometrical isomers of the heteroleptic self-assembly structures in solution.

Another research group that makes use of shape complementarity to form heteroleptic cages is the Clever group, focusing on controlling geometric parameters such as the bite angles of banana-shaped ligands in their assembly. In 2016, Clever et al. reported the self-assembly of the shape-complementary acridone-based ligand $\mathbf{L^A}$ and phenanthrene-based ligand $\mathbf{L^P}$, which formed both homoleptic and heteroleptic coordination cages mediated by Pd^{II}. These ligands have bite angles of 60° and 120°, respectively (see a) in figure 1.22). [145] They demonstrated that the heteroleptic cage could be formed through multiple self-assembly routes, including direct combination of the ligands with Pd^{II} (1:1:1), cage-to-cage transformations and cage rearrangement induced by ligand addition. The latter was observed only when $\mathbf{L^P}$ was added to the strained homoleptic cage of $\mathbf{L^A}$. Additionally, the accessible cavity of the heteroleptic cage $[Pd_2\mathbf{L^A}_2\mathbf{L^P}_2]^{4+}$ exhibited a strong binding affinity for concave-shaped disulfonate guests. [145]

In 2017, Bloch et al. expanded on the shape-complementarity concept by discovering a novel heteroleptic coordination cage (with a "doubly bridged figure-eight" topology. *Trans*-$[Pd_2(anti\text{-}\mathbf{L^A})_2\mathbf{L^C}_2]^{4+}$ was formed through Pd^{II}-mediated assembly of the carbazole-based ligand $\mathbf{L^C}$ and $\mathbf{L^A}$ (see a) in figure 1.22). The carbazole-based ligand $\mathbf{L^C}$ formed a homoleptic cage, when mixed with Pd^{II} cations in a 1:2 ratio. However, mixing $\mathbf{L^A}$ and $\mathbf{L^C}$, which both exhibit a bend angle of 75°, in a 1:1:1 ratio with Pd^{II} yielded the *trans*-$[Pd_2(anti\text{-}\mathbf{L^A})_2\mathbf{L^C}_2]^{4+}$ coordination cage (see a) in figure 1.22). NOESY experiments indicated that one isoquinoline moiety of each $\mathbf{L^A}$ ligand was twisted. X-ray analysis revealed that the cavity of *trans*-$[Pd_2(anti\text{-}\mathbf{L^A})_2\mathbf{L^C}_2]^{4+}$ was occupied by the backbones of two $\mathbf{L^A}$ molecules, which exhibited π-stacking interactions. These interactions forced BF_4^- counterions to leave the cavity (see c) in figure 1.22). Moreover, Bloch et al. reported the heteroleptic cage $[Pd_2\mathbf{L^P}_2\mathbf{L^C}_2]^{4+}$, consisting of ligands $\mathbf{L^P}$ and $\mathbf{L^C}$ (see a) in figure 1.22). Several years later Regeni et al. used a diketopyrrolopyrrole-based ligand with isoquinoline as a donor group to form a heterolepic cage with a "doubly bridged figure-eight" topology. [150][162]

Worth to mention that Bloch et al. further showed that Pd(II)-based heteroleptic coordination cages demonstrate a shape-specific guest-binding ability due to their unique structure of their cavity and the metal centers, which act as anchors for charged anionic molecules. This property is exemplified by the differential binding of two naphthalene disulfonate isomers, which are the linear 2,7-naphthalene disulfonate and the bent 2,6-naphthalene disulfonate. The cage's cavity structure enables selective recognition and binding based on the distinct shapes of these guest molecules, highlighting the significant influence of cavity geometry on host-guest interactions. [145]

In chapter 1.5, various approaches for achieving control over integrative self-sorting to form self-sorted heteroleptic cages with banana-shaped ligands were discussed. Shape-complementarity appears promising for maintaining the cavity necessary for potential host-guest chemistry. However, the study of supramolecular self-assemblies is often time-consuming and challenging due to the complex ligand synthesis and optimization of self-assembly conditions.

To streamline the planning of promising self-assemblies and support experimental data, computational calculations have proven valuable. In recent years, advances in microprocessor technology and the widespread availability of sophisticated electronic structure programs have led to a significant increase in the use of theoretical calculations to complement experimental research. Moreover, the previously tedious and error-prone process of editing input files for electronic structure programs, which often required expertise in computational chemistry, is now being replaced by software with user-friendly graphical interfaces. These advancements make theoretical calculations increasingly accessible to researchers with limited experience in computational chemistry. [163] As previously mentioned, strain plays a significant role in coordination cage formation. To quantify this driving force and gain a deeper understanding of self-assemblies, examining strain is highly beneficial. In chapter 5, the fundamentals of electronic structure calculations and the concept of strain and its calculation in coordination cages will be introduced.

Coordination cages have a cavity, which allows host-guest chemistry and make different applications possible such as molecular recognition, stabilization of reactive species or catalysis. [164][165][166][167] In following chapter 1.6 catalysis in coordination cages will be introduced.

1.6 Catalysis in Coordination Cages

In nature, enzymes exhibit remarkable efficiency in catalyzing diverse processes while maintaining high selectivity. Catalysis operates on the principle of the catalyst interacting with the transition state and stabilizing it, thereby reducing the energy required for the substrate to transition from the ground state to the transition state. This reduction in energy facilitates an increase in the reaction rate. Importantly, the catalyst itself remains chemically unchanged throughout the process. A catalyst influences the kinetics of a reaction without affecting its thermodynamics. [168]

Various examples of supramolecular catalysis involving both unimolecular and bimolecular reactions demonstrated the utility of coordination cages as catalysts. Examples include cage-catalyzed aza-Cope rearrangements and Nazarov cyclization for unimolecular reactions, as well as Diels-Alder reactions, hydrolysis of orthoformates, Michael addition, Knoevenagel condensation and asymmetric hydroformylation for bimolecular reactions. [169][170][171][172][173]

Thereby, supramolecular catalysis presents three distinct approaches, each utilizing a coordination cage as a "reaction vessel":

Firstly, in the "cavity-directed" approach, catalysis occurs solely within the cavity without additional catalytically active functionalization. The cavity facilitates substrate pre-orientation, leading to faster reaction rates and high regioselectivity. Additionally, the cavity can stabilize intermediates, accelerate reactions, and enable novel reaction pathways. For bimolecular reactions, the host increases the local concentration of reaction partners by preferentially encapsulating them within its nanometer-sized cavity, driven by a solvophobic effect.

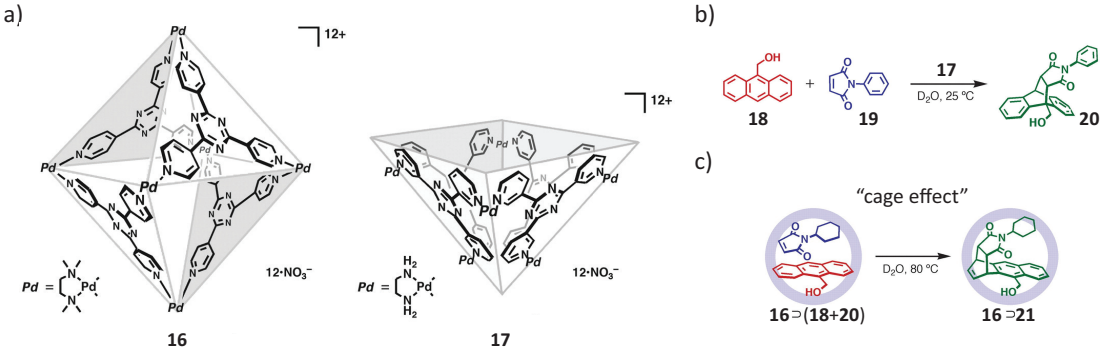

Figure 1.23. a) Illustration of coordination cages **16** and **17** from Fujita group. b) And c) Diels-Alder reaction of **18** and **19**. Reproduced from [169]. © 2006 American Association for the Advancement of Science.

In 2006, Fujita et al. reported an octahedral $[Pd_6\mathbf{L}_4]^{4+}$ coordination cage in water that could catalyze the Diels–Alder reaction of 9-hydroxymethylanthracene (**18**) and *N*-phenylmaleimides (**19**) at the less favored 1,4-position (see a) and c) in figure 1.23). To confirm that the reaction outcome was influenced by the cavity of $[Pd_6\mathbf{L}_4]^{4+}$, Fujita's group conducted a control experiment in the absence of the

enclosed cavity (see **17** in a) and b) in figure 1.23). This experiment demonstrated that without the enclosed cavity of **16**, the typical product the 9,10-adduct was formed. Thus, the regioselectivity observed in the presence of **16** can be described as a so-called "cage effect". [169]

Another noteworthy work was reported in 2010 by Raymond et al., describing the catalytic conversion of 1,4-pentadien-3-ol to cyclopentadiene within an anionic coordination cage formed by Ga(III) and bis-catechol ligands. This Nazarov cyclization exhibited an astonishing acceleration in an aqueous medium by a factor of 2.1 x 10^6, a feat typically achievable only in enzyme systems. This enhancement was attributed to several factors, including guest uptake facilitated by the hydrophobic effect, substrate pre-organization, stabilization of the transition state owing to the negative charge of the cage and an increase in the alcohol function's basicity. [174]

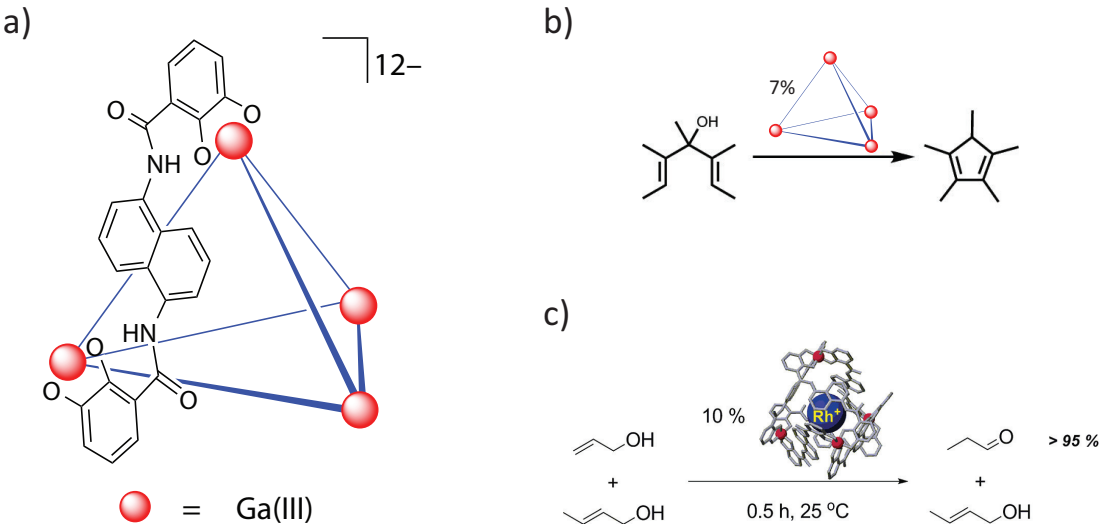

Figure 1.24. a) Illustration of supramolecular tetrahedral assembly of the Raymond cage and b) the catalyzed Nazarov cyclization. Reproduced from [174]. © 2010 American Chemical Society. c) Illustration of the supramolecular tetrahedral assembly encapsulated a rhodium complex and were found to be catalytically active for the isomerization of allylic alcohols. Reproduced from [175]. © 2007 American Chemical Society.

Secondly, a separate molecule is introduced into the cavity as a catalyst, enhancing reactivity within the specialized environment. This catalyst may be bound covalently or non-covalently within the cavity. The catalysis occurs on the catalyst itself, while the cavity controls substrate interactions, regioselectivity, and stereoselectivity. Ideally, the coordination cage efficiently ejects the product, mitigating catalyst deactivation due to "product inhibition".

In 2007, Raymond et al. used the previously mentioned gallium-based cage and reported the selective encapsulation of a rhodium complex, which performed as a catalyst within the coordination cage. After comparing the performance of the encapsulated catalyst with its free counterpart in a series of reactions, they

observed that the encapsulated catalyst not only facilitated the reactions with high efficiency, but also displayed remarkable selectivity for substrates based on their size and shape (see c) in figure 1.24).

Thirdly, a catalytically active functionality is either attached to the ligands or provided by a free coordination site at the metal center. This setup allows the catalyst to activate the substrate while preventing catalyst aggregation and increasing its local concentration. In the following, the implementation of H-bond-based coordination cages with catalytic activity will be introduced.

Catalysis by Hydrogen bonding in Coordination Cages

In nature, enzymes play a central role as catalysts due to their efficiency and selectivity. [176] HB plays a crucial role in numerous biological processes. [177]

In 2018, the Lusby working group showed that a relatively simple cationic Pd(II) coordination cage can catalyze a reaction via hydrogen bonds by stabilizing the transition state. This $[Pd_2\mathbf{L}_4]^{4+}$ cage showed high activity, regioselectivity, chemoselectivity, and low product inhibition when catalyzing the Diels-Alder reaction of benzoquinone and a diene (see a) in figure 1.25). [178][179][180]

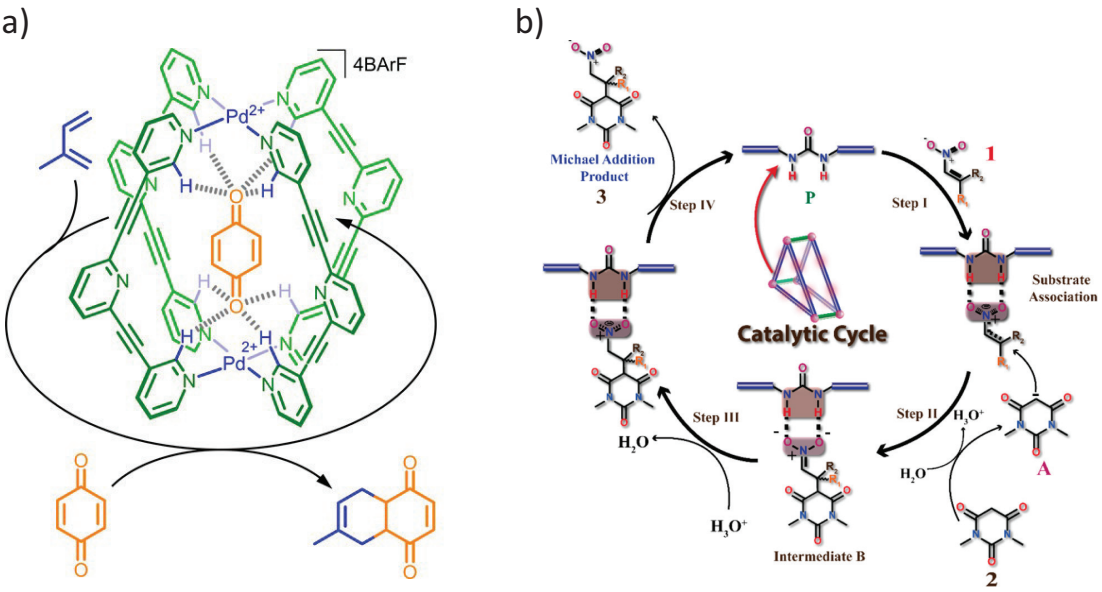

Figure 1.25. a) Illustration of the lantern-shaped coordination cage $[Pd_2\mathbf{L}_4]^{4+}$ from Lusby group. Reproduced from [179]. © 2018 American Chemical Society. b) Assumed catalytic cycle for the Michael addition reactions in the presence of prism-shaped coordination cage **P**. Reproduced from [181]. © 2016 American Chemical Society.

In recent years, organic catalysts based on HB have shown that they can be a alternative to enzyme catalysts and as previously mentioned, urea in particular stands out among the various HB catalysts due to its non-toxicity and thermal stability. [182] One problem with urea functions is their intermolecular interaction, which significantly reduces the catalytic efficiency (self-quenching).

The Mukherjee group was able to overcome this problem with a prism-shaped coordination cage. This discrete structure is functionalized with urea and can bind guests via hydrogen bonds and act as a catalyst. [181] The catalyst could be recovered by filtration and reused without showing any loss of catalytic activity for several recycling cycles. Due to the H-bonds between the urea function and nitroolefins (guest), the substrate molecules could be activated by the prism P (host). This host-guest system is the first heterogeneous catalyst that enables the urea-promoted Michael addition of water-soluble nitroolefins with dimethylbarbituric acid in an aqueous medium. Furthermore, the prism as a catalyst in the Diels-Alder reaction. This coordination cage is the first of its kind and shows that supramolecular coordination cages are promising candidates to study the behavior of biologically active cavities as they occur in nature (e.g. in enzymes).

The previously mentioned examples rely on HB interactions between the neutral guest and the coordination cage for substrate activation. An example, while not catalytic, that demonstrates molecular recognition and host-guest chemistry based on HB within a palladium-based coordination cage is reported by the Clever group.

The Clever group designed a modular family of heteroleptic coordination cages $[Pd_2\mathbf{L^A}_2\mathbf{L^B}_2]^{4+}$. Thereby, those coordination cages were assembled from carbazole-based banana-shaped ligands ($\mathbf{L^A}$) and aromatic ligands ($\mathbf{L^B}$) with diverse backbones and lengths. The cages were characterized by NMR spectroscopy, ESI mass spectrometry and X-ray diffraction. The secondary amine of the carbazole moiety was functionalized with amides or methyl groups and then tested for their ability to bind hydrogen bond acceptors such as alkyl- and aryl phosphate ester salts. The binding constants were determined by ^{1}H-NMR titrations, which suggested that binding was primarily driven by H-bond formation with additional contributions from ionic interactions and π–π stacking, supported by MD simulations and ion-mobility mass spectrometry. [183]

Binding anionic guest into a cationic coordination cage is not astonishing. However, coordination cages are often formed in H-bond competitive solvents such as DMSO or DMF and it is known that the solvent plays a crucial role in modulating HB interactions. [184] Future research on HB-based host-guest chemistry in coordination cages should focus on enhancing their solubility in less competitive solvents. This advancement could facilitate the binding of neutral molecules and unlock their potential for enabling various organocatalytic reactions. Achieving this goal is challenging, as the self-assembly of coordination cages is often influenced by their counterions and the choice of solvent. [185][186][187]

The limited works of H-bond-based palladium coordination cages and the squaramide as a promising building block were briefly introduced. In the future, squaramide-based coordination cages could be an important step at developing H-Bond functionalized coordination cages in molecular recognition and catalysis.

The next chapter 2 will highlight the scope of this thesis.

2 Scope of this Thesis

One of the primary goals of the Clever group is to develop novel frameworks for coordination cages and increase their complexity by forming heteroleptic cages.

As previously mentioned, HB has been well-known for decades, with squaramides, in particular, gaining significant attention in various research fields since 2008. Squaramides have especially risen in prominence as organocatalysts. However, squaramides have not yet explored in context of coordination cages. This work deals with filling this void by synthesizing squaramide-based bis-monodentate banana-shaped ligands. The limited works of H-bond-based palladium coordination cages were briefly introduced and triggers curiosity to explore squaramide-based coordination cages, which could have potential to show also their presence in coordination cages as HB functionality.

The scope of this thesis is to design and synthesize a squaramide-based heteroleptic coordination cage and investigate its host-guest properties, focusing on HB interactions. Initial studies will explore interactions with anionic guests, with a long-term goal of extending these investigations to neutral guests. To achieve stronger binding constants, using cooperativity appears to be a promising approach. Therefore, two squaramide-based ligands were proposed to form a coordination cage. Given the close proximity of the ligands within the cage, intramolecular interactions and cooperative effects are anticipated.

The characterization of the structures is mainly examined by one- and two-dimensional NMR spectroscopy. Furthermore, ESI mass spectrometry, ^{1}H-DOSY NMR experiments and X-ray analysis were used to characterize the coordination cages and their host-guest complexes.

Especially the following points were examined during the squaramide part of this doctoral research:

- Design, synthesis, self-assembly, and characterization of squaramide-based ligands and their heteroleptic coordination cage using NMR, ESI-MS, and X-ray diffraction
- Guest-binding studies of various organic disulfonate and phosphate ester salts via NMR and ESI-MS
- Synthesizing derivatives of squaramide-based ligands to increase their solubility and, analogous to the previous points, studying the binding of neutral molecules with and without cooperativity effect
- Design and synthesis of ligands, which are based on squaraine dyes and 1,3-squaramides
- Expanding of strain calculations of $[Pd_2\mathbf{L}_2\mathbf{L}'_2]^{4+}$ coordination cages

3 Results and Discussion

3.1 Squaramide-based Coordination Cages

In previous chapters 1, squaramides were introduced as a potential hydrogen-bonding functionality in coordination cages. As previously mentioned, the unique properties and synthetic accessibility of diverse squaramide derivatives make them highly attractive for various applications, including self-assembly, organocatalysis, molecular recognition, medicinal chemistry and bioconjugation. [44][19][188][22] These qualities underline their utility, versatility and future potential. [189][190][191]

In chapter 1.2, the enhancement of cooperativity through intramolecular HB in squaramide-based structures was introduced. In a simple $[Pd_2\mathbf{L}_2\mathbf{L}'_2]^{4+}$ coordination cage, two ligands can come into close proximity. To increase the probability of intramolecular HB within the coordination cage, the structure can be composed entirely of squaramide-based ligands. Calculations of the electrostatic potential maps of an isolated squaramide-based ligand and its dimer show that intramolecular HB enhances the polarization of terminal hydrogen-bonding groups (see figure 4.167 in chapter 4.3.8).

To study the cooperative effects of squaramide functionality within coordination cages, two easily accessible squaramide-based ligands were synthesized. The synthetic routes are depicted in figure 3.1.

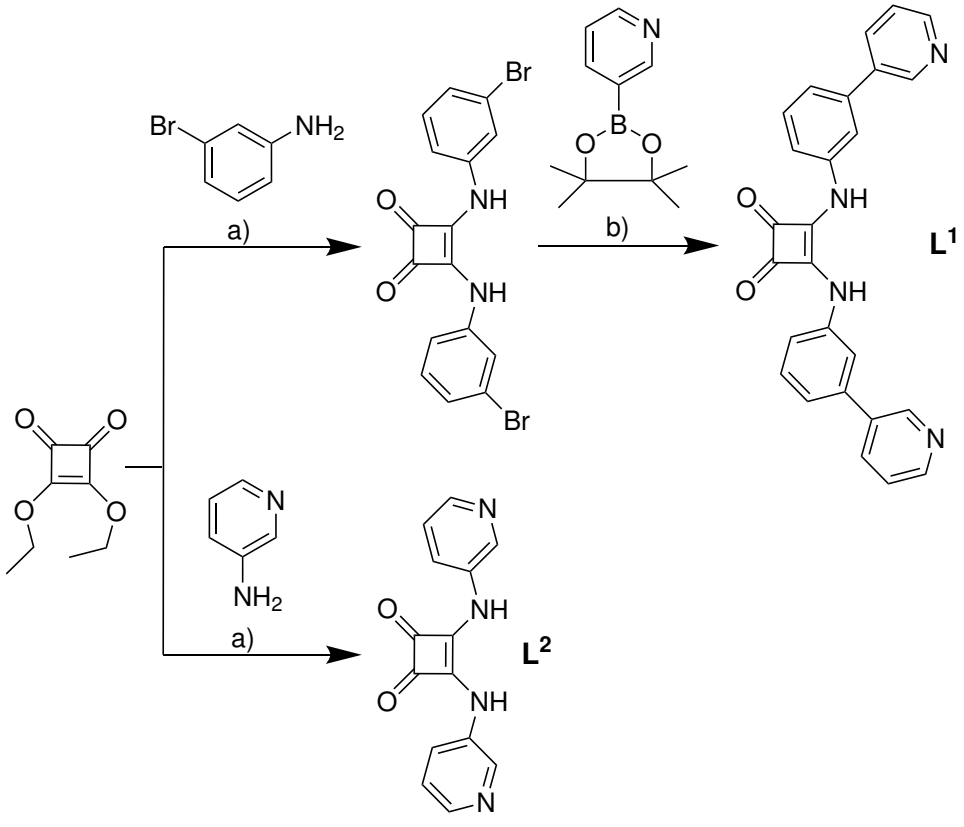

Figure 3.1. Reaction conditions: a) $Zn(CF_3SO_3)_2$, 12 h, 100 °C, toluene/DMF (5:1), b) $Pd(PPh_3)_4$, K_3PO_4, 12 h, 100 °C, DMF/H_2O (3:1).

Starting from diethyl squarate and appropriately substituting with respective aromatic amines, the squaramide-based ligands 3,4-bis(pyridin-3-ylamino)cyclobut-3-ene-1,2-dione ($\mathbf{L^2}$) and 3,4-bis((3-(pyridin-3-yl)phenyl)amino)cyclobut-3-ene-1,2-dione ($\mathbf{L^1}$) were successfully synthesized. For detailed synthetic procedures and characterization data see the experimental section in chapter 4.2.4.

The first synthetic step, common to both ligands, involves the addition of an aromatic amine to diethyl squarate with $Zn(OTf)_2$. This method, previously developed by Taylor et al., is based on an "addition-elimination" mechanism (see figure 1.5 in chapter 1.1).

Homoleptic Coordination Cage Formation of $\mathbf{L^1}$ and $\mathbf{L^2}$

The experiments on homoleptic coordination cage formation with $\mathbf{L^1}$ and $\mathbf{L^2}$ revealed differing behaviors. While $\mathbf{L^1}$ did not form a distinct species (see figure 4.98 in chapter 4.3.2 with ^{1}H-NMR spectrum of reaction mixture), $\mathbf{L^2}$ successfully formed a $[Pd_2\mathbf{L^2}_4]^{4+}$ coordination cage according to NMR and ESI-MS data (see chapter 4.3.1 for experimental data suggesting the structure). The homoleptic coordination cage $[Pd_2\mathbf{L^2}_4]^{4+}$ shows a clean ^{1}H NMR spectrum in DMSO-d_6. No splitting of ligand signals in ^{1}H NMR spectrum of cage was observed, which indicates an assembly of a highly symmetric molecule (see b) in figure 3.2).

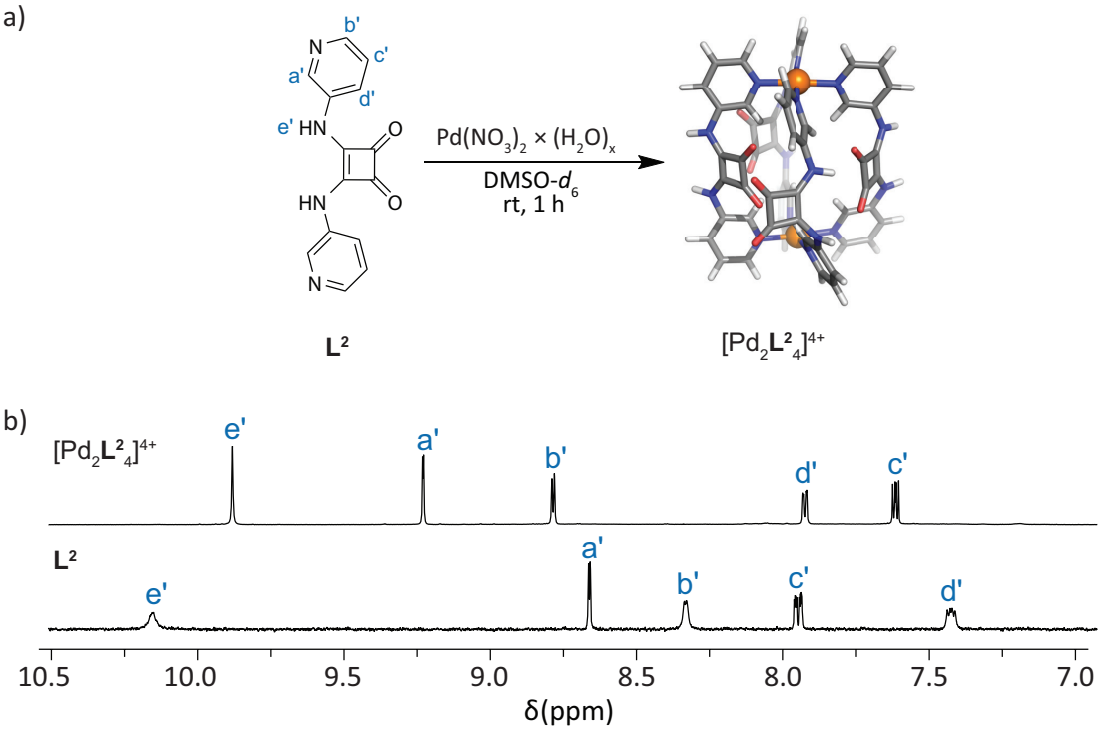

Figure 3.2. a) Coordination cage formation of $[Pd_2\mathbf{L^2}_4]^{4+}$. Calculated on PM6 level. b) ^{1}H-NMR spectra (500 MHz, 298 K, DMSO-d_6) of $\mathbf{L^2}$ and $[Pd_2\mathbf{L^2}_4]^{4+}$.

All proton signals, except for c´ and e´, exhibit a downfield shift during complexation. Notably, protons a´ and b´ undergo significant downfield shifts, which can be attributed to their close proximity to the coordination center. This

effect arises because electron density from the nitrogen is relocated towards the coordination bond, leading to deshielding and, consequently, a pronounced downfield shift.

However, this $[Pd_2\mathbf{L^2}_4]^{4+}$ cage should feature a relatively small cavity, likely encapsulating its counterion to compensate the positive charge from the two Pd(II) cations.

Future plans focus on enhancing solubility of the coordination cage in nonpolar solvents, such as dichloromethane, to strengthen HB interactions. This will be achieved by introducing solubilizing groups onto the ligand structure. However, this approach may crowd the surroundings of the cage, hindering the formation of distinct coordination cages. Therefore, the initial focus shifted to heteroleptic coordination cage studies. Heteroleptic cages incorporating $\mathbf{L^1}$, which feature a phenyl spacer between the pyridine and squaramide group, should increase the spatial separation between the two different ligands within the coordination cage.

3.1.1 Heteroleptic Coordination Cage Formation of $[Pd_2L^1{}_2L^2{}_2]^{4+}$

Then the heterolepic coordination cage formation of $\mathbf{L^1}$ and $\mathbf{L^2}$ has been examined (see figure 3.3).

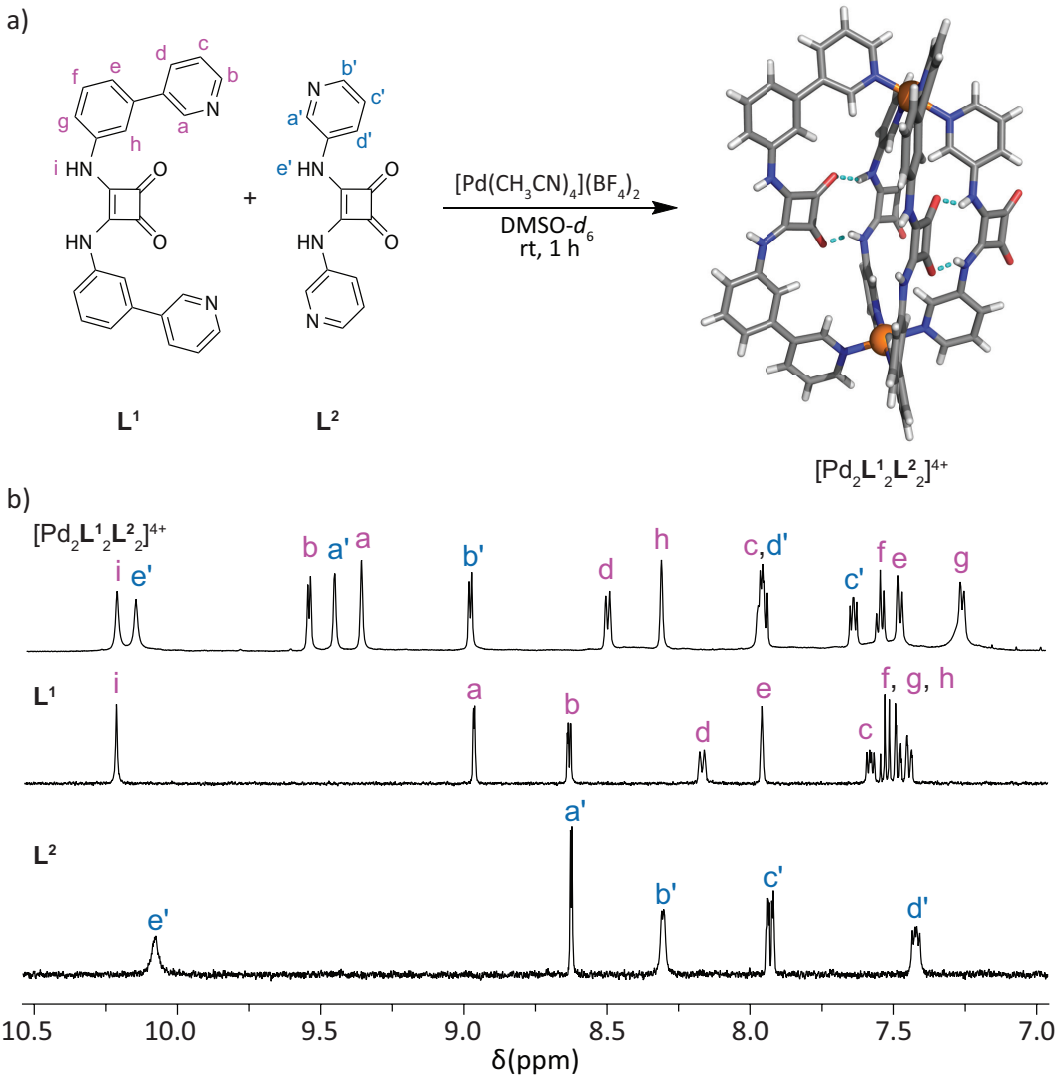

Figure 3.3. a) Coordination cage formation of $[Pd_2\mathbf{L^1}_2\mathbf{L^2}_2]^{4+}$ illustrated with the internal HB highlighted by dashes in X-ray structure. b) ^{1}H-NMR spectra (500 MHz, 298 K, DMSO-d_6) of $\mathbf{L^1}$, $\mathbf{L^2}$ and $[Pd_2\mathbf{L^1}_2\mathbf{L^2}_2]^{4+}$.

The heteroleptic cage experiment involving $\mathbf{L^1}$ and $\mathbf{L^2}$ yielded a distinct set of signals in the ^{1}H-NMR spectrum in DMSO-d_6. Signals a, b, d, a´, b´, and d´ in the aromatic region were downfield-shifted due to complexation. Notably, protons a, b, a´, and b´ experienced intense downfield shifts, caused by their close proximity to the coordination center. Furthermore, ESI-MS analysis suggested the formation of a $[Pd_2\mathbf{L^1}_2\mathbf{L^2}_2(BF_4)_n]^{(4-n)+}$ (n = 0–2) species (see a) in figure 3.4). Additionally, the ^{1}H DOSY NMR spectrum confirms that all assigned proton signals of $[Pd_2\mathbf{L^1}_2\mathbf{L^2}_2]^{4+}$ belong to the same molecule with a similar diffusion coefficient (see b) in figure 3.4).

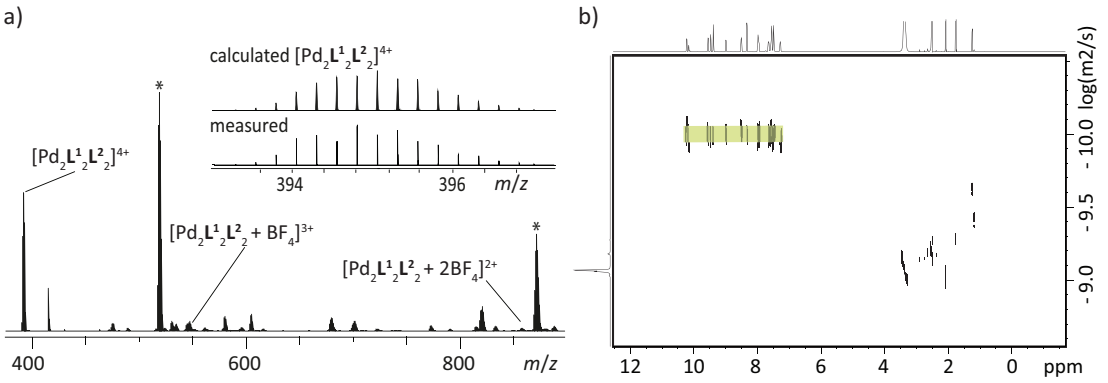

Figure 3.4. a) ESI-MS of $[Pd_2\mathbf{L^1}_2\mathbf{L^2}_2]^{4+}$. b) ^{1}H DOSY NMR spectrum (500 MHz, 298 K, DMSO-d_6) of $[Pd_2\mathbf{L^1}_2\mathbf{L^2}_2]^{4+}$. $D([Pd_2\mathbf{L^1}_2\mathbf{L^2}_2]^{4+}) = 1.02 \cdot 10^{-10}\,\frac{m^2}{s}$, $r_H([Pd_2\mathbf{L^1}_2\mathbf{L^2}_2]^{4+}) = 9.75\,Å$. $*$ could be not assigned to a specific species.

The determined diffusion coefficient D of $[Pd_2\mathbf{L^1}_2\mathbf{L^2}_2]^{4+}$ is equal to $1.02{\cdot}10^{-10}\,\frac{m^2}{s}$, and further with the Stokes-Einstein equation (see equation 3.1) the hydrodynamic radius $r_H = 9.75\,Å$ was determined. [192]

$$D = \frac{k_B T}{6\pi\eta r_H} \tag{3.1}$$

With T as the temperature, k_B the Boltzmann constant ($1.3806488 \cdot 10^{-13} JK^{-1}$), η the dynamic viscosity of the solvent and r_H as the hydrodynamic radius of the diffusible molecules ($\eta_{DMSO} = 0.219\,mPa{\cdot}s$ at 25 °C). [193][194] The determined r_H of $[Pd_2\mathbf{L^1}_2\mathbf{L^2}_2]^{4+}$ is 9.75 Å, which is larger than that of previously reported heteroleptic cages $[Pd_2\mathbf{L^C}_2\mathbf{L^P}_2]^{4+}$ with 9.1 Å (see figure 1.22 in chapter 1.5.1). [161] That suggests that a cage of the type $[Pd_2L_4]^{4+}$ was formed.

The lantern-shaped structure of $[Pd_2\mathbf{L^1}_2\mathbf{L^2}_2]^{4+}$ was confirmed by single crystal analysis (see a) figure 3.3). The X-ray structure of $[Pd_2\mathbf{L^1}_2\mathbf{L^2}_2]^{4+}$ suggests that the NH functionalities of $\mathbf{L^2}$ are pointing inside of the cavity and forming an intramolecular H-bond to the carbonyl oxygen of the backbone of $\mathbf{L^1}$ (see a) figure 3.3). At the same time, the NH functionalities of $\mathbf{L^1}$ are pointing outside of the cavity, which was confirmed by NOESY spectrum since proton signal i shows a NOESY signal contact to g (see a) in figure 3.5). However, NH of $\mathbf{L^2}$ with the proton signal assignment e´ shows NOESY signals contact to a´ and d´. This occurs because the pyridine group of $\mathbf{L^2}$ is a bit rotated in comparison to the squaramide backbone of $\mathbf{L^2}$ (see b) n figure 3.5). As expected, NOESY analysis shows that proton signal a correlates with a´ and b with b‘, due to the close proximity at the Pd(II) centers. Moreover, NOESY analysis confirms that proton a is inside pointing inside of the cavity since it shows a NOESY contact to proton h.

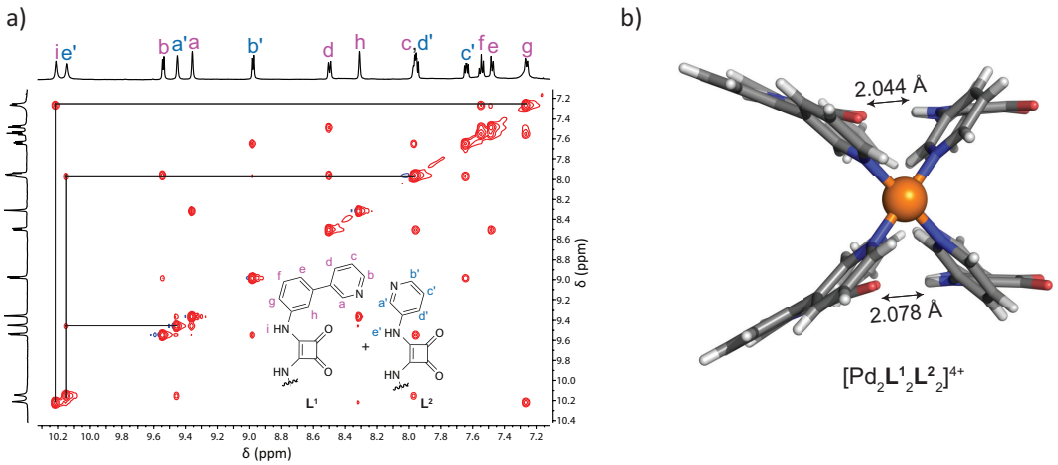

Figure 3.5. a) ^{1}H-^{1}H NOESY spectrum (600 MHz, 298 K, DMSO-d_6) of $[Pd_2\mathbf{L^1}_2\mathbf{L^2}_2]^{4+}$. b) Top view of the X-ray structure of $[Pd_2\mathbf{L^1}_2\mathbf{L^2}_2]^{4+}$ with the NH-O distance shown.

3.1.2 Host-guest Chemistry of $[Pd_2\mathbf{L^1}_2\mathbf{L^2}_2]^{4+}$

The host-guest chemistry of $[Pd_2\mathbf{L^1}_2\mathbf{L^2}_2]^{4+}$ with anionic guests was studied due to its cationic nature. Various disulfonates, which are typical anionic guests for palladium-based coordination cages, have been examined. [145][195][196][197]

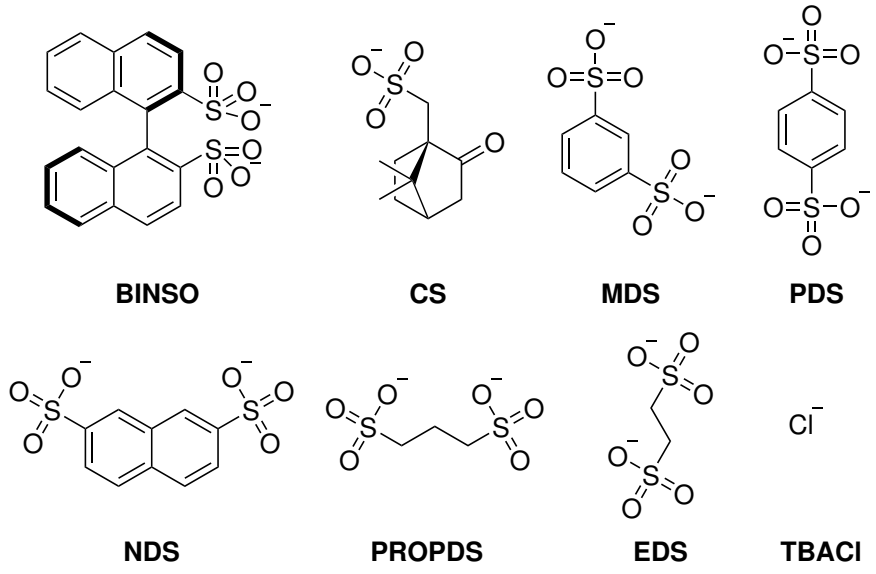

Figure 3.6. Illustration of screened organic disulfonate guests and **TBACl** to $[Pd_2\mathbf{L^1}_2\mathbf{L^2}_2]^{4+}$ in DMSO-d_6. With TBA as a counterion except for **BINSO** with K^+.

Some guests lead to a broadening of signals upon titration or resulted in overlapping of signals (see from figure 4.105 until 4.108 in chapter 4.3.3 for ^{1}H-NMR spectra).

One particularly noteworthy guest is Cl^-, as Cl^- is a fundamental anion in various biological systems, making it an interesting target for anion receptor studies. [198] Its relatively small size and high charge density facilitate strong electrostatic

interactions and HB with receptors. [199][200] However, encapsulating Cl^- into coordination cages is not so trivial since it typically leads to the decomposition of coordination cages. In the literature, squaramide-based organic receptors have been shown to bind Cl^- via HB and to exhibit superior affinity for Cl^- compared to ureas. [44][201][202] Therefore Cl^- was chosen as a potential guest. The NMR titration of Cl^- to $[Pd_2\mathbf{L^1}_2\mathbf{L^2}_2]^{4+}$ showed decomposition from 1 eq. since new signals were rising and the intensity of the $[Pd_2\mathbf{L^1}_2\mathbf{L^2}_2]^{4+}$ was significantly decreasing upon titration (see figure 4.175 in chapter 4.3.3 for ^{1}H-NMR spectra).

The anionic guest that showed interaction with $[Pd_2\mathbf{L^1}_2\mathbf{L^2}_2]^{4+}$ without decomposing it during the ^{1}H-NMR titration and allowed the determination of a binding constant was (*R*)-1,1'-binaphthalene-2,2'-disulfonate **BINSO**. The binding constant was determined by Bindfit. [203] With the 1:1 fitter a binding constant of (13870 ± 3745) M^{-1} was determined (the shown error represents the goodness of fit). I. Regeni reported a family of coal-tar dyes-based coordination cages, which interact with **BINSO**, but due to broadening of the signals in the ^{1}H-NMR spectra during titration no binding constant was obtained. [195] Similarly, K. Ebbert observed a comparable phenomenon in a family of diketopyrrolopyrrole-based heteroleptic cages featuring fluorenone- and carbazole-based ligands. [196] To the best of my knowledge, no binding constants for **BINSO** to heteroleptic palladium-based coordination cages have ever been reported. So this work could represent the first determination of a binding constant by ^{1}H-NMR titration for **BINSO** to a heteroleptic palladium-based coordination cage in DMSO-d_6. However, ESI-MS did not provide information about the host-guest complex. **BINSO** carries an axial chirality. In the literature, it is known that a guest can transform their chirality to the coordination cage. [204] In the CD spectra of the host-guest complex of **BINSO** and $[Pd_2\mathbf{L^1}_2\mathbf{L^2}_2]^{4+}$, a new absorption maximum of around 332 nm is observed, suggesting a chirality transfer from the guest to the host (see figure 4.114 in chapter 4.3.3 for ^{1}H-NMR spectra).

Two additional disulfonates that demonstrated interactions with $[Pd_2\mathbf{L^1}_2\mathbf{L^2}_2]^{4+}$ in the ^{1}H-NMR titration and provided a binding constant are naphthalene-2,7-disulfonate **NDS** and benzene-1,4-disulfonate **PDS** (see figure 3.7).

The 1:1 fitter was used to determine the binding constant of both host-guest complexes, and both titration curves show a saturation after 1 eq. (see figure 4.124 in chapter 4.3.3). In a previous work, W. Bloch showed that **NDS** binds to the hetroleptic cage ($[Pd_2\mathbf{L}_2\mathbf{L'}_2]^{4+}$) consisting of an acridone- and phenanthrene-based ligand with a binding constant of 5200 M^{-1}. [145] In the case of $[Pd_2\mathbf{L^1}_2\mathbf{L^2}_2]^{4+}$ a binding constant of (31021 ± 4653) M^{-1} was obtained, which is more than 5 folds larger than the previous mentioned example.

In the case of **PDS** a binding constant of (12620 ± 1010) M^{-1} was obtained. In the work of A. Walther, a binding constant for **PDS** to a palladium-based coordination cage ($[Pd_2\mathbf{L}_4]^{4+}$) is reported. He could determine a binding constant

by UV-Vis titration to a elongated azulene-based coordination cage of (6557± 262) M^{-1}. [197] Although those are two different methods to determine the binding constant, it can be qualitatively interpreted that $[Pd_2\mathbf{L^1}_2\mathbf{L^2}_2]^{4+}$ seems to bind **PDS** stronger. For both cases, a binding constant of **NDS** and **PDS** to $[Pd_2\mathbf{L^1}_2\mathbf{L^2}_2]^{4+}$ was determined and showed higher affinity in comparison to the previously mentioned coordination cages. [145][197] This may be attributed to the more favorable distance between the cationic Pd(II) centers in $[Pd_2\mathbf{L^1}_2\mathbf{L^2}_2]^{4+}$, which likely facilitates stronger interactions with the anionic sulfonates.

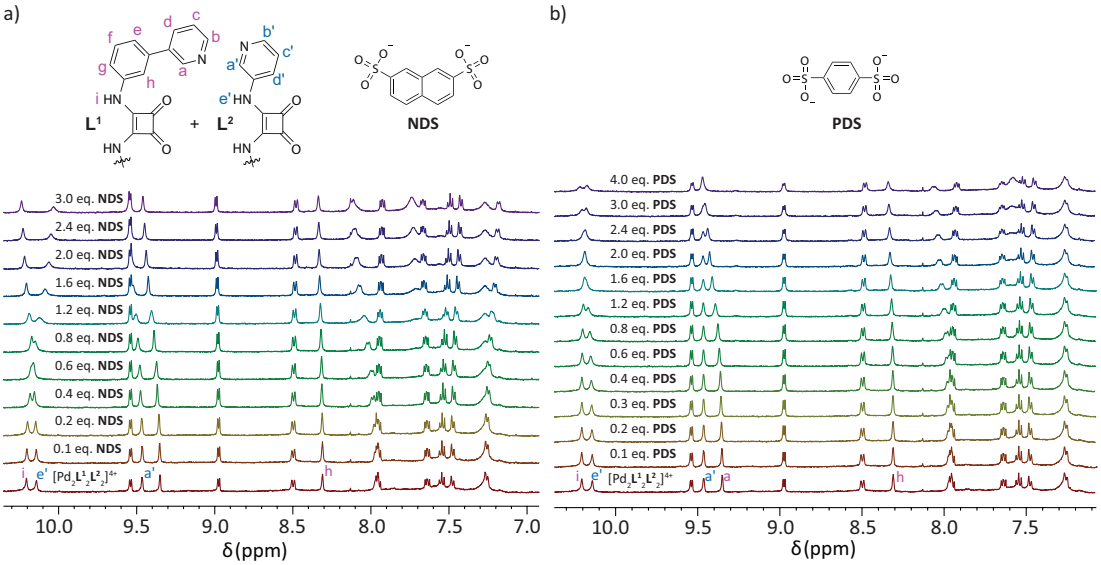

Figure 3.7. ^{1}H-NMR (500 MHz, 298 K, DMSO-d_6) titration of **NDS** and **PDS** to 0.63 mM $[Pd_2\mathbf{L^1}_2\mathbf{L^2}_2]^{4+}$. TBA as counter ions for **NDS** and **PDS**. For ESI-MS see figure 4.119 in chapter 4.3.3.

As mentioned in chapter 1.6 the Clever group showed that phosphate esters such as diphenyl phosphate **DPP**, dibenzyl phosphate **DBnP**, dibutyl phosphate **DBuP** and diethyl phosphate **DEP** can bind to a series of heteroleptic cages with a secondary NH function (see figure 3.8 for the mentioned phosphate esters). [183]

The strongest binding constant of (2062 ± 31) M^{-1} was observed for **DPP** in DMSO-d_6. MD simulations emphasized that π-interactions play a important role in the guest binding.

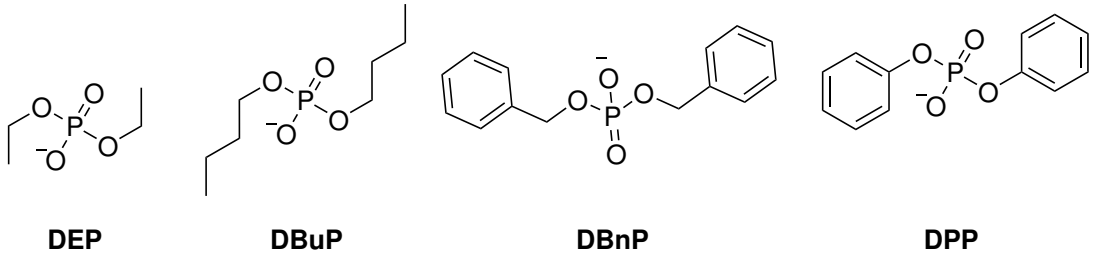

Figure 3.8. Illustration of screened phosphate esters to $[Pd_2\mathbf{L^1}_2\mathbf{L^2}_2]^{4+}$. TBA as a counterion.

Analogous to that work, different phosphate esters have been screened by ^{1}H-NMR titration (see figure 3.8 and for ^{1}H-NMR spectra see figures 4.176, 4.177 and

4.178 in chapter 4.3.3). But only for **DPP**, a significant chemical shifting in the ^{1}H-NMR titration was observed and provided a binding constant (see a) in figure 3.9). The determined binding constant for **DPP** is $(64 \pm 2)\,M^{-1}$ (see figure 4.124 in chapter 4.3.3). ESI-MS indicates the presence of host-guest complexes of $[Pd_2\mathbf{L^1}_2\mathbf{L^2}_2]^{4+}$, consisting of either one or two **DPP** guests (see figure 4.123 in chapter 4.3.3). This observation aligns with a similar trend previously noted, where **DPP** was also identified as the strongest binding guest among the tested phosphate esters. [183] In that work, this trend can be explained by the combined significant contribution of HB and π-interactions between the guest and the ligands of the coordination cage. It is worth emphasizing that the binding site of $[Pd_2\mathbf{L^1}_2\mathbf{L^2}_2]^{4+}$ is most likely oriented outwards due to intramolecular interactions. As a result, the chance for π-interactions is likely reduced or more challenging compared to cases where the NH functionalities point inward towards the cavity, and therefore the guest binding occurs inside the cavity. So it is likely that with the lack of π-interactions and in DMSO as a competitive hydrogen bond acceptor, the binding constant of **DPP** to $[Pd_2\mathbf{L^1}_2\mathbf{L^2}_2]^{4+}$ is very weak.

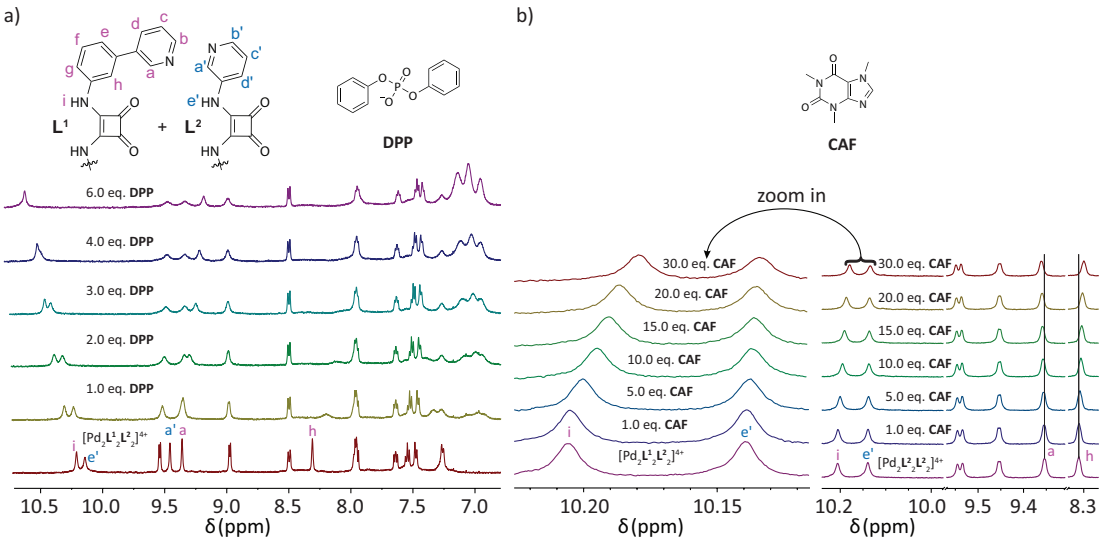

Figure 3.9. ^{1}H-NMR (500 MHz, 298 K, DMSO-d_6) titration of **DPP** and **CAF** to 0.63 mM $[Pd_2\mathbf{L^1}_2\mathbf{L^2}_2]^{4+}$. TBA as counter ion for **DPP**. For ESI-MS see figure 4.123 in chapter 4.3.3.

Next a neutral guest was studied. Caffeine, containing two carbonyl oxygens that could theoretically enhance its binding affinity to NH functionalities, exhibited gradual signal shifts during titration in DMSO-d_6. However, this did not result in a measurable binding constant (see b) in figure 3.9). The observed shifts could potentially be attributed to a dilution effect or to a very weak interaction. This is further supported by the binding curve, which does not exhibit saturation in the ^{1}H-NMR spectra. When an attempt was made to fit the data, the resulting fit resembled a flat curve rather than having enough curvature to be reliably plotted, which indicates the absence of significant binding (see figure 4.124 in chapter 4.3.3).

The heteroleptic cage incorporating ligands $\mathbf{L^1}$ and $\mathbf{L^2}$, which feature squaramide moieties, was successfully synthesized and tested for guest binding. While it exhibits superior binding affinity for certain disulfonate guests compared to previously reported palladium-based coordination cages, it performs poorly in binding phosphate esters and neutral guests. Therefore, structural modifications were pursued to enhance its performance.

Moreover, the X-ray structure of this squaramide-based heterolpetic coordination cage reveals intramolecular interactions between the squaramide functionalities. These interactions are theoretically expected to enhance the HB donor ability of the outer squaramide groups through cooperativity. However, the solubility of squaramide-based ligands is generally poor in most apolar solvents. Additionally, the solvent selected for examining hydrogen bonding between the host and guest should not be highly competitive. Thus, the next step was to improve the solubility of these ligands in low-polarity solvents, such as dichloromethane (DCM), by attaching solubilizing groups like polyethylene glycol (PEG) chains. PEG chains are known to enhance solubility not only in polar solvents such as water but also in nonpolar solvents like chloroform. [205] The straightforward synthetic accessibility of PEG chains makes them ideal candidates as solubilizing groups. It is anticipated that incorporating a more soluble ligand will facilitate the formation of the coordination cage in a less competitive solvent, such as DCM.

3.1.3 Ligand Synthesis of L^{1peg} and L^{2peg}

The synthesis route for PEG-modified $\mathbf{L^2}$ is illustrated in figure 3.10. To prevent excessive steric hindrance around the coordination center and at the squaramide functionality, the meta position of pyridine-3-amine was chosen for substitution. Consequently, 5-aminopyridin-3-ol was selected as the starting material. Following a series of reactions, the PEG-modified ligand $\mathbf{L^{2peg}}$ was successfully synthesized.

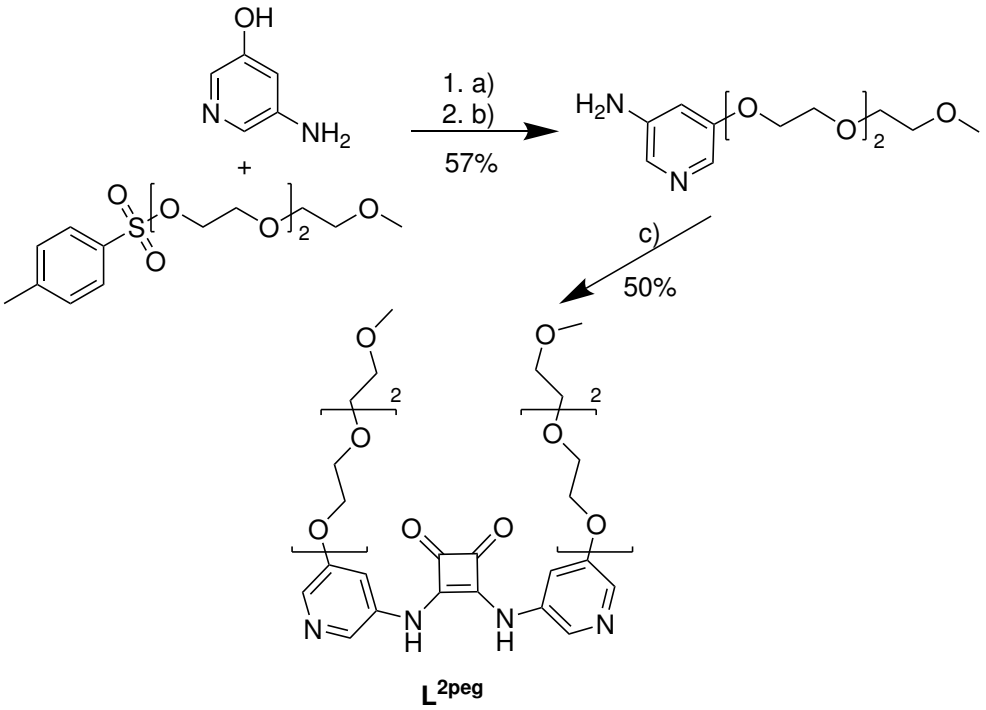

Figure 3.10. Illustration of synthesis of ligand $\mathbf{L^{2peg}}$. Reaction conditions: a) NaOtBu, 30 min, rt, THF b) 12 h, 70 °C, c) diethyl squarate, NEt_3, 12 h, 84 °C, toluene.

Notably, the reaction of PEG-modified aminopyridin-3-ol with diethyl squarate and $Zn(OTf)_2$ resulted in low yield of the target product and series of unidentified side products, which were not further investigated in this study. However, this issue was resolved by using NEt_3 in toluene, yielding $\mathbf{L^{2peg}}$ with good efficiency (50%). [31] Detailed synthetic procedures and characterization data for $\mathbf{L^{2peg}}$ can be found in the experimental section in chapter 4.2.3.

It is worth noting that achieving a sufficient total yield during ligand synthesis is an important factor. Synthesis planning, reaction monitoring, workup and purification are time-intensive processes. Additionally, optimizing conditions for coordination cage formation, guest screening and conducting control experiments require substantial amounts of ligand material, which is typically not recoverable from the coordination cage. Consequently, good yields and effective purification methods for ligands are essential and can significantly impact ligand design and coordination cage research.

The synthesis route for PEG-modified derivatives of $\mathbf{L^{1peg}}$ is presented in figure 3.11.

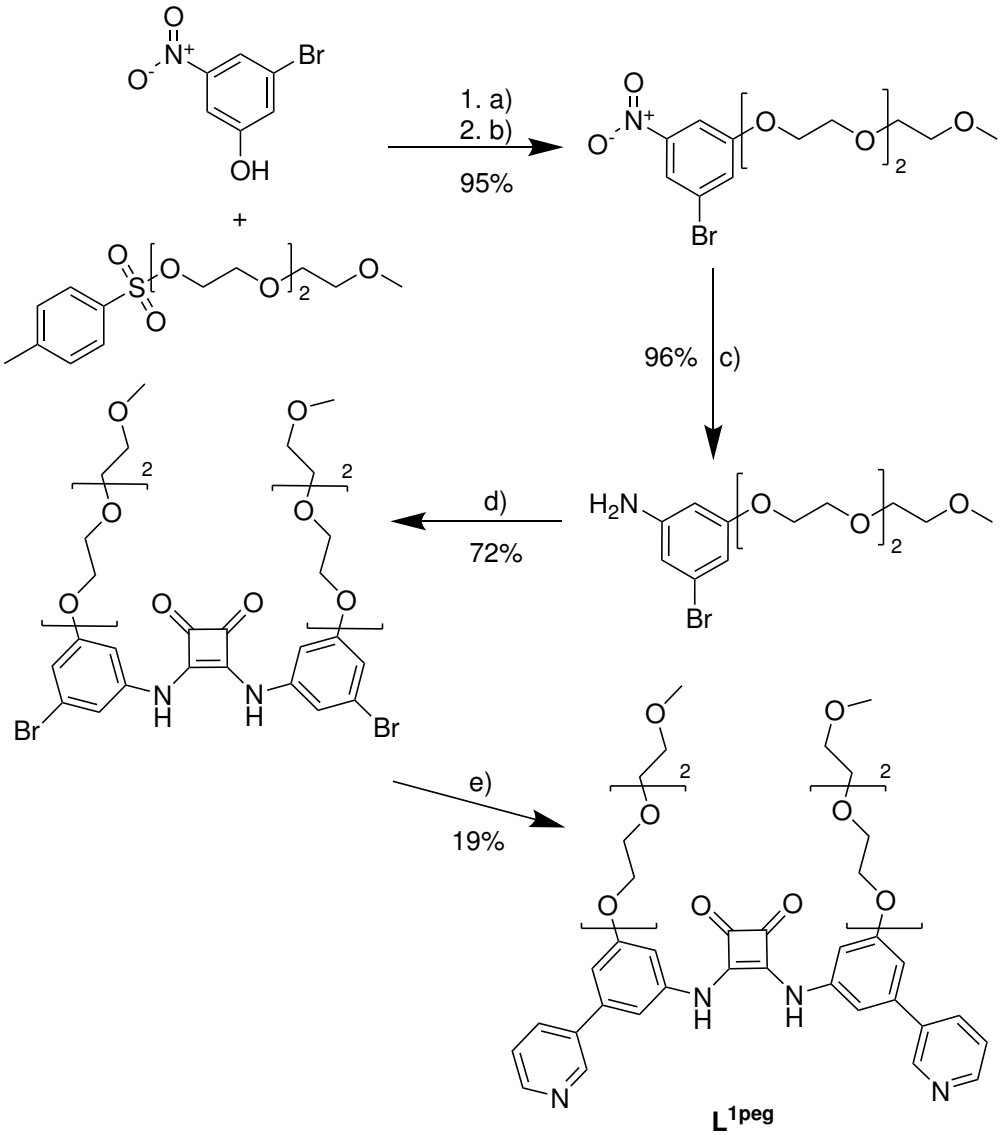

Figure 3.11. Illustration of synthesis of ligand $\mathbf{L^{1peg}}$. Reaction conditions: a) NaOtBu, 30 min, rt, THF b) 12 h, 70 °C, c) $SnCl_2$, 3 h, rt ⟶ reflux, EtOAc, d) diethyl squarate, NEt_3, 12 h, 82 °C, toluene, e) 3-pyridineboronic acid pinacol ester $Pd(PPh_3)_4$, K_3PO_4, 12 h, 100 °C, THF/H_2O (3:1).

Starting with 3-bromo-5-nitrophenol, the hydroxyl group was substituted with a PEG moiety, followed by the reduction of the nitro group to an amine using $SnCl_2$, yielding excellent results in both steps. Through subsequent reactions, the PEG-modified ligand $\mathbf{L^{1peg}}$ was successfully synthesized with an impressive overall yield of 71% across four synthetic steps. The final step in the synthesis of $\mathbf{L^{1peg}}$ involved a Pd(II)-catalyzed cross-coupling reaction. Future studies could focus on optimizing this step by adjusting reaction parameters such as temperature, solvent, and palladium precursors. Additionally, screening alternative phosphine ligands

could improve the yield. Detailed synthetic procedures and characterization data are provided in the experimental section in chapter 4.2.6.

After both PEG-modified squaramide based ligands $\mathbf{L^{2peg}}$ and $\mathbf{L^{1peg}}$ were synthesized, the coordination cage formation was examined.

Homoleptic coordination cage experiments revealed that neither $\mathbf{L^{2peg}}$ nor $\mathbf{L^{1peg}}$ formed distinct coordination cages in DMSO-d_6 and CD_3CN (see chapters 4.3.4 and 4.3.5). This result aligns with previous findings indicating that $\mathbf{L^1}$ does not form a distinct coordination cage, making the lack of homoleptic cage formation by $\mathbf{L^{1peg}}$ unsurprising. However, it was previously demonstrated that $\mathbf{L^2}$ forms a distinct homoleptic coordination cage in DMSO-d_6. A plausible explanation for this discrepancy could be the steric hindrance introduced by the bulky PEG groups, which may interfere with the formation of the relatively compact homoleptic coordination cage.

Then the heterolepic coordination cage formation with $\mathbf{L^{2peg}}$ and $\mathbf{L^{1peg}}$ was examined.

3.1.4 Formation of Coordination Cage of $[Pd_2L^{1peg}{}_2L^{2peg}{}_2]^{4+}$

As mentioned in chapter 3.1.1, selecting a less competitive HB solvent is favorable for observing HB interactions between a squaramide-based coordination cage and a neutral guest. For this reason, CD_2Cl_2 was chosen as the solvent, similar to its use in reported studies on squaramide-based organocatalysts. [73][184][206] Figure 3.12 illustrates the heteroleptic cage formation of $\mathbf{L^{2peg}}$ and $\mathbf{L^{1peg}}$ in CD_2Cl_2. For clarity, the PEG chains are omitted and marked by curved hyphens in the subsequent figures.

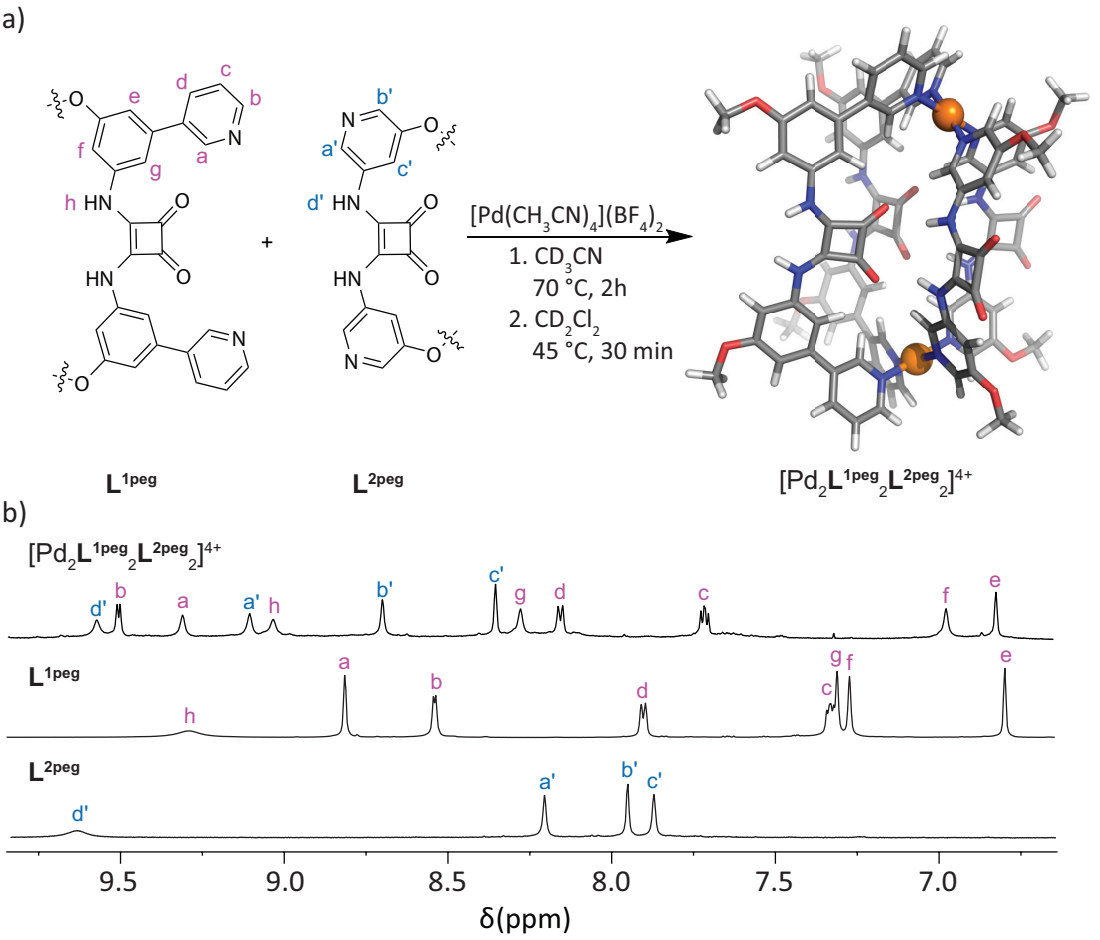

Figure 3.12. a) Heteroleptic coordination cage formation of $[Pd_2\mathbf{L^{1peg}}_2\mathbf{L^{2peg}}_2]^{4+}$. PEG chains omitted for clarity and calculated on PM6 level. b) ^{1}H-NMR spectra (700 MHz, 298 K, CD_2Cl_2) of $\mathbf{L^{1peg}}$, $\mathbf{L^{2peg}}$ and $[Pd_2\mathbf{L^{1peg}}_2\mathbf{L^{2peg}}_2]^{4+}$.

Direct attempts to form $[Pd_2\mathbf{L^{1peg}}_2\mathbf{L^{2peg}}_2]^{4+}$ in CD_2Cl_2 probably result in the cage aggregation that is supported by the signal bordering in the ^{1}H-NMR spectrum (for ^{1}H-NMR spectra see figure 4.142 in chapter 4.3.8). Consequently, the heteroleptic cage of $\mathbf{L^{2peg}}$ and $\mathbf{L^{1peg}}$ was initially assembled in CD_3CN (for ^{1}H-NMR spectra see figure 4.143 in chapter 4.3.8). After solvent removal, CD_2Cl_2 was added (details are provided in chapter 4.3.8).

As anticipated, proton signals a, b, a´, and b´ exhibited significant downfield shifts, attributed to their proximity to the coordination center, as previously

explained. NOESY analysis confirmed correlations between proton signals b and b´, as well as a and a´, reflecting their spatial proximity at the coordination center. Contacts between signals a and g, and d and e in the NOESY spectrum further support the proposed structure shown in figure 3.12. Furthermore, NOESY analysis suggests that the conformation of the squaramides in $[Pd_2\mathbf{L^{1peg}}_2\mathbf{L^{2peg}}_2]^{4+}$ is identical to that in $[Pd_2\mathbf{L^{1}}_2\mathbf{L^{2}}_2]^{4+}$. This conclusion is supported by the correlation between NH proton signal h and proton signal f (see figure **??** in chapter 4.3.8). Additionally, the NH proton signal d´ correlates with a´ in the NOESY spectrum. These observations strongly indicate consistency with the conformation observed in $[Pd_2\mathbf{L^{1}}_2\mathbf{L^{2}}_2]^{4+}$, suggesting that an intramolecular H-bond between the squaramides is highly likely in CD_2Cl_2 solution.

The ESI-MS spectrum displayed peaks corresponding to $[Pd_2\mathbf{L^{1peg}}_2\mathbf{L^{2peg}}_2]^{4+}$ and contamination by Cl^- (see a) in figure 3.13). Additionally, the ^{1}H DOSY NMR spectrum confirmed that all assigned proton signals of $[Pd_2\mathbf{L^{1}}_2\mathbf{L^{2}}_2]^{4+}$ belong to the same molecule, as evidenced by their similar diffusion coefficients (see b) in figure 3.13).

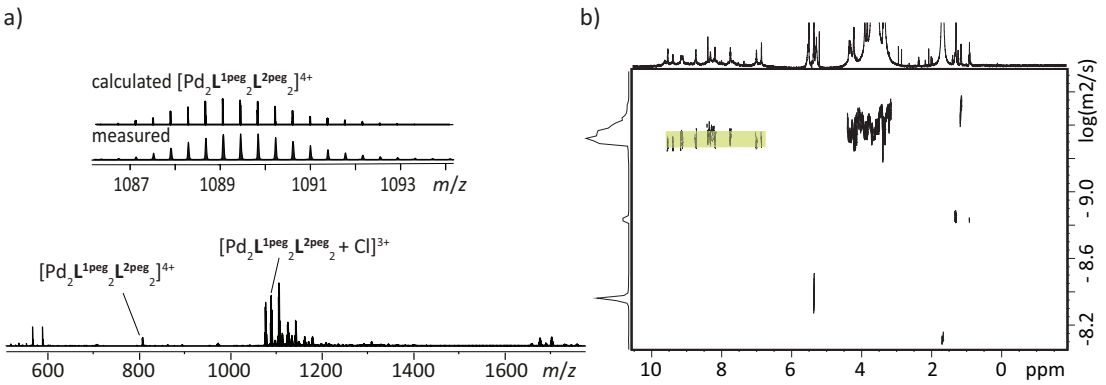

Figure 3.13. a) ESI-MS of $[Pd_2\mathbf{L^{1peg}}_2\mathbf{L^{2peg}}_2]^{4+}$. b) ^{1}H DOSY NMR spectrum (500 MHz, 298 K, CD_2Cl_2) of $[Pd_2\mathbf{L^{1peg}}_2\mathbf{L^{2peg}}_2]^{4+}$. $D([Pd_2\mathbf{L^{1peg}}_2\mathbf{L^{2peg}}_2]^{4+}) = 4.85{\cdot}10^{-10}\,\frac{m^2}{s}$, $r_H([Pd_2\mathbf{L^{1peg}}_2\mathbf{L^{2peg}}_2]^{4+}) = 10.46\,Å$.

The Stokes-Einstein relation was used to determine r_H of $[Pd_2\mathbf{L^{1peg}}_2\mathbf{L^{2peg}}_2]^{4+}$, with the viscosity of CD_2Cl_2 with $\eta = 4.3 \cdot 10^{-3}\,Pa \cdot s$ at 293 K. [207] The calculated r_H for $[Pd_2\mathbf{L^{1peg}}_2\mathbf{L^{2peg}}_2]^{4+}$ is 10.46 Å, which is larger than the r_H of $[Pd_2\mathbf{L^{1}}_2\mathbf{L^{2}}_2]^{4+}$ (9.75 Å). This observation suggests that the PEG-modified squaramide coordination cage was successfully obtained, as the PEG chains are expected to increase the hydrodynamic radius of the coordination cage.

In the literature it is reported that low polarity solvents such as dichloromethane (DCM) can promote ion pairing, a phenomenon in which oppositely charged ions associate in solution to form distinct complexes. [208] This interaction is driven by electrostatic attractions between cations and anions. [208]

Lusby et al. investigated the influence of counterions on a lantern-shaped palladium-based coordination cage in various solvents such as CD_3CN, CD_3OD,

CD_3NO_2 and CD_2Cl_2, and found that guest binding, which occurs inside the cavity by HB, constantly significantly increases when large, non-coordinating counterions are used. One of the reasons for this enhancement is because a bulky counterion cannot fit inside the cavity and therefore significantly decreases the competition with the guest for binding or blocking the binding site in the cavity. [178] In their study, Lusby et al. screened various neutral guests such as quinones compounds featuring two carbonyl oxygens capable of interacting with the C-H groups of the coordination cage through HB. The highest binding constants were observed in CD_2Cl_2, when tetrakis[3,5-bis(trifluormethyl)phenyl]borate $BArF^-$ was used as the counterion. $BArF^-$ is a weakly coordinating anion featuring four fluorinated aryl groups arranged tetrahedrally around a central boron atom.

That is why the cage formation of $[Pd_2\mathbf{L^{1peg}}_2\mathbf{L^{2peg}}_2]^{4+}$ with various counterions such as OTf^-, PF_6^-, and $BArF^-$ were examined. However, no distinct cage formation was observed (see figure 4.145 and figure 4.146 in chapter 4.3.8). Consequently, the subsequent host-guest chemistry studies were conducted using the well-characterized $[Pd_2\mathbf{L^{1peg}}_2\mathbf{L^{2peg}}_2]^{4+}$ with BF_4^- as the counterion.

Chapter 3.1.5 deals with the host-guest chemistry of $[Pd_2\mathbf{L^{1peg}}_2\mathbf{L^{2peg}}_2]^{4+}$.

3.1.5 Host-guest Chemistry of $[Pd_2L^{1peg}{}_2L^{2peg}{}_2]^{4+}$

Anionic Guests

First, host-guest chemistry of $[Pd_2\mathbf{L^{1peg}}_2\mathbf{L^{2peg}}_2]^{4+}$ with anions was examined. NMR titration of Cl^- showed no significant shift in the proton signals, and after the addition of 1 equivalent, new signals began to emerge, indicating the decomposition of the coordination cage (see figure 4.147 in chapter 4.3.8).

Previously, binding constants for **PDS** and **NDS** were successfully determined for $[Pd_2\mathbf{L^1}_2\mathbf{L^2}_2]^{4+}$ in DMSO-d_6. However, for $[Pd_2\mathbf{L^{1peg}}_2\mathbf{L^{2peg}}_2]^{4+}$ in CD_2Cl_2, titration with these guests led to broadening of the proton signals (for **PDS**, see a) in figure 3.14). This result suggests that **PDS** and **NDS** may induce aggregation of $[Pd_2\mathbf{L^{1peg}}_2\mathbf{L^{2peg}}_2]^{4+}$, likely due to enhanced ion pairing in CD_2Cl_2.

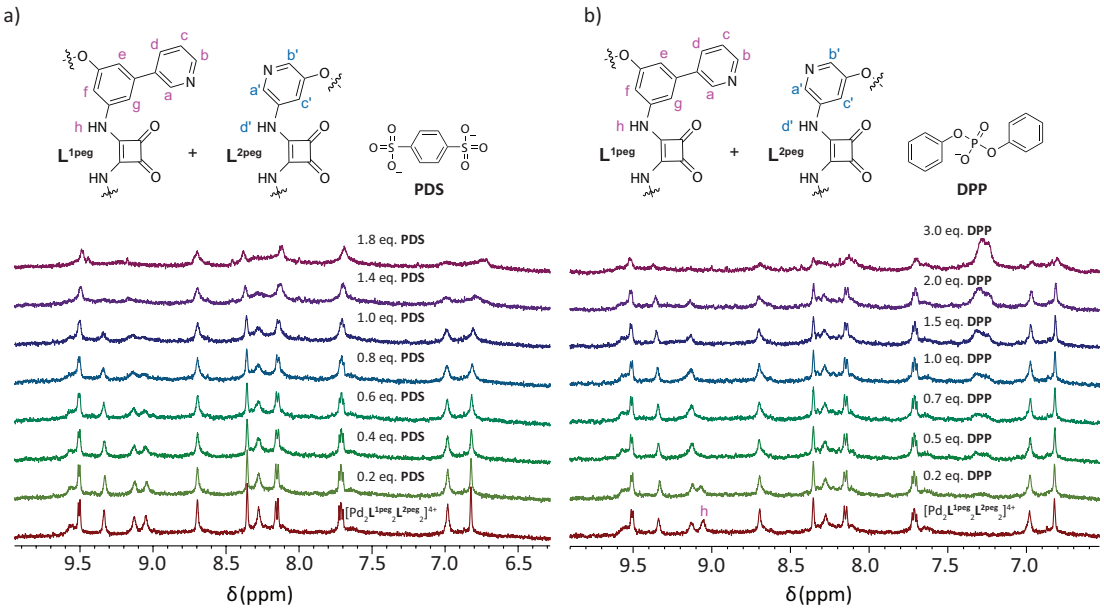

Figure 3.14. ^{1}H-NMR spectra (500 MHz, 298 K, CD_2Cl_2) of NMR titration of a) **PDS** to 0.24 mM $[Pd_2\mathbf{L^{1peg}}_2\mathbf{L^{2peg}}_2]^{4+}$ and b) **DPP** to 0.24 mM $[Pd_2\mathbf{L^{1peg}}_2\mathbf{L^{2peg}}_2]^{4+}$.

The phosphate guests **DEP**, **DBuP**, **DBnP** and **DPP** showed a common trend in ^{1}H-NMR spectra: the NH signal h shifted until 0.5 equivalents (or 0.4 eq.) and then overlapped with another signal (for **DPP** see b) in figure 3.14, and the other mentioned guests can be found in chapter 4.3.8). After the addition of 1 equivalent, the intensity of the signals of $[Pd_2\mathbf{L^{1peg}}_2\mathbf{L^{2peg}}_2]^{4+}$ decreased and broadened. These observations suggest interactions between the phosphate guests and the coordination cage, but also may suggest the presence of aggregation. Control experiments involving the titration of phosphate guests into solutions of $\mathbf{L^{1peg}}$ and $\mathbf{L^{2peg}}$ in CD_2Cl_2 revealed intense shifts up to 2.95 ppm of the NH signals upon titration (see from figure 4.154 until 4.161 in chapter 4.3.8 for ^{1}H-NMR spectra). Proton signals in the aromatic region also intensely shift. The presence of cationic Pd(II) eliminates the significant signal shifts and shows a

broadening in the ^{1}H-NMR spectra, therefore this finding supports the hypothesis that aggregation likely occurs due to intermolecular ion pairing between phosphates and Pd(II) coordination cages.

Another reason for the increased aggregation behavior of $[Pd_2\mathbf{L^{1peg}}_2\mathbf{L^{2peg}}_2]^{4+}$ compared to $[Pd_2\mathbf{L^{1}}_2\mathbf{L^{2}}_2]^{4+}$ could be the cooperative effect of intramolecular HB enhanced by guest binding. Intramolecular HB is known to promote aggregation, as discussed in chapter 1.2. [120] It is worth emphasizing that the squaramide functionality possesses both hydrogen-acceptor and hydrogen-donor sites, and each of these functionalities points outward in $[Pd_2\mathbf{L^{1peg}}_2\mathbf{L^{2peg}}_2]^{4+}$. When an anionic guest binds to the cationic coordination cage, it reduces the overall charge, thereby decreasing Coulomb repulsion between aggregates. This reduction in repulsion may favor aggregation by HB between host-guest complexes.

Neutral Guests

Following the binding of an anionic guest, neutral guests carrying two carbonyl oxygens, which could theoretically enhance their binding affinity to the NH functionalities, were screened (see figure 3.15). A guest lacking carbonyl functionality but containing a nitro group, namely [(*E*)-2-nitroethen-1-yl]benzene (**NVB**) was included in the study. **NVB** has been reported in the literature to be activated by H-bond-based organocatalysts or, as previously noted, by urea-based coordination cages. [209][181]

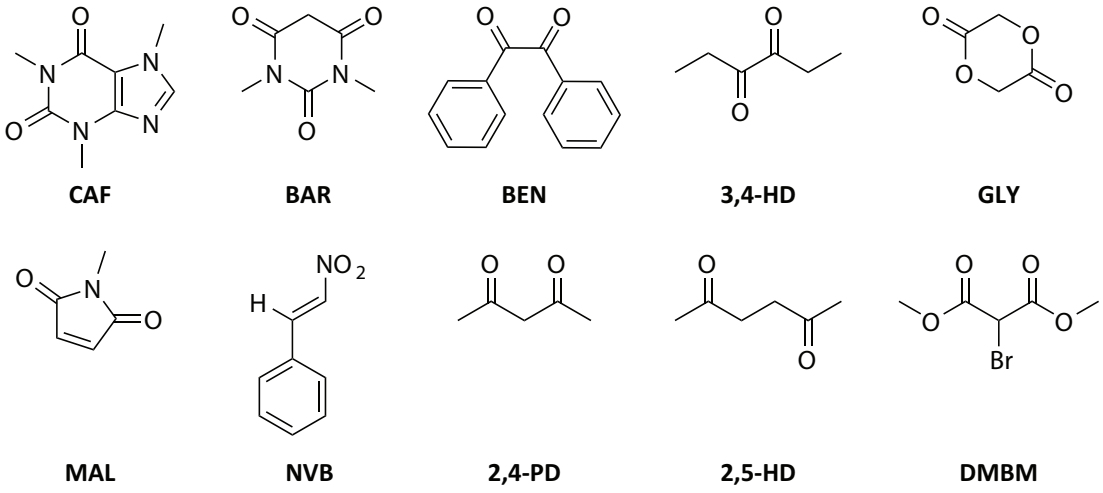

Figure 3.15. Illustration of screened neutral molecules to 0.3 mM $[Pd_2\mathbf{L^{1peg}}_2\mathbf{L^{2peg}}_2]^{4+}$ in CD_2Cl_2.

For the ^{1}H-NMR spectra of the screening see figure 4.163 in chapter 4.3.8. Guests that showed significant shifts compared to others during the screening include **CAF**, **NVB**, **2,5-HD**, and **DMBM**. These guests were subsequently used in NMR titration experiments with $[Pd_2\mathbf{L^{1peg}}_2\mathbf{L^{2peg}}_2]^{4+}$ to determine binding constants.

Interestingly, the screening results suggest that the two carbonyl groups in a guest must be separated by at least one atom to effectively interact with the

squaramide moieties of the coordination cage. The guest **BAR** likely interacts too weakly with the squaramide due to the distinct orientation of its carbonyl oxygens compared to **CAF**. Furthermore, **CAF** could benefit from additional noncovalent interactions between its methyl group at the alpha position and the carbonyl oxygen group from the squaramide ligand. [210][211] Differences in the electron properties arising from structural variations also likely contribute to the differing binding affinities of **BAR** and **CAF**.

In figure 3.16 the NMR titration results for **CAF** and **NVB** are presented. The shifts observed for proton signals a, a´ and h are highlighted using vertical reference lines relative to the proton signal of $[Pd_2\mathbf{L^{1peg}}_2\mathbf{L^{2peg}}_2]^{4+}$.

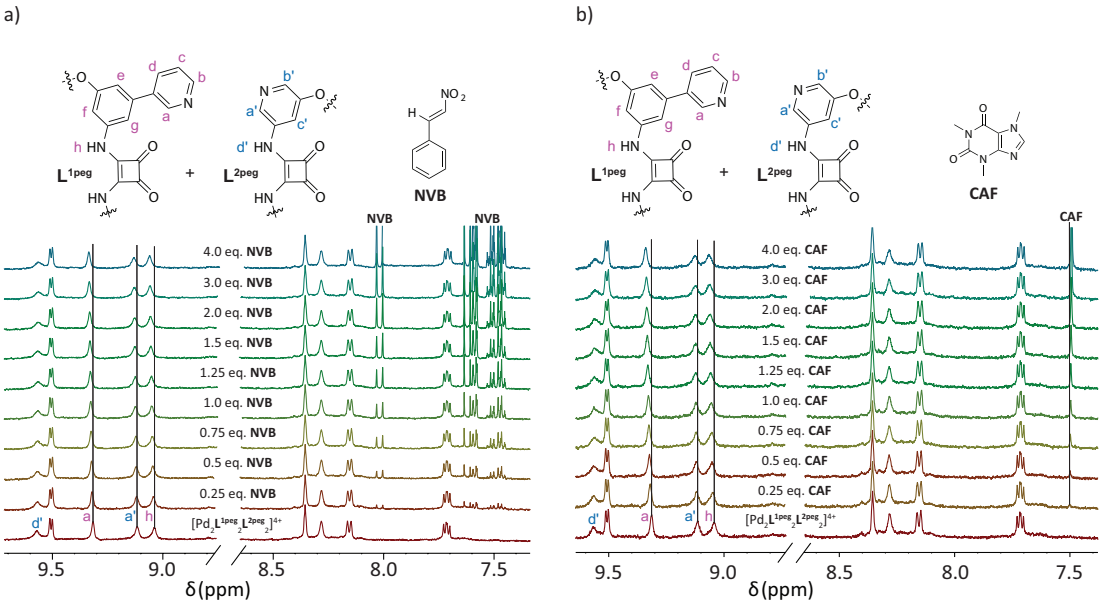

Figure 3.16. Illustration of ^{1}H-NMR (500 MHz, 298 K, CD_2Cl_2) titration of **NVB** and **CAF** to 0.3 mM $[Pd_2\mathbf{L^{1peg}}_2\mathbf{L^{2peg}}_2]^{4+}$. For Bindfit plots see figure 4.165 in chapter 4.3.8.

The NH proton signal d', which points inward toward the cavity, shows no significant shift, likely because it is engaged in intramolecular hydrogen bonding. This suggests that guest binding occurs externally.

Both titration experiments were repeated three times, yielding average binding constants of (5194 ± 312) M^{-1} for **NVB** and (6185 M ± 433) M^{-1} for **CAF** with $[Pd_2\mathbf{L^{1peg}}_2\mathbf{L^{2peg}}_2]^{4+}$ (see table 4.2 in chapter 4.3.8). During titration, the proton signal of **CAF** in the aromatic region is shifting. A control experiment involving the titration of the same volume of solvent (CD_2Cl_2) to **CAF** showed no shifts, suggesting that the shifts are indeed due to interactions with $[Pd_2\mathbf{L^{1peg}}_2\mathbf{L^{2peg}}_2]^{4+}$ (see figure 4.166 in chapter 4.3.8). However, NOESY signals between **CAF** and $[Pd_2\mathbf{L^{1peg}}_2\mathbf{L^{2peg}}_2]^{4+}$ were not observed.

Then the binding constants for **2,5-HD** and **DMBM** with $[Pd_2\mathbf{L^{1peg}}_2\mathbf{L^{2peg}}_2]^{4+}$ were determined by NMR titration. These experiments were repeated twice, yielding average binding constants of (8722 ± 1308) M^{-1} for **2,5-HD** and (4390 ±

615) M^{-1} for **DMBM** (see table 4.2 in chapter 4.3.8). These findings suggest that greater spacing between carbonyl groups enhances the binding affinity toward $[Pd_2\mathbf{L^{1peg}}_2\mathbf{L^{2peg}}_2]^{4+}$.

The introduction of PEG chains successfully led to the formation of the heteroleptic coordination cage $[Pd_2\mathbf{L^{1peg}}_2\mathbf{L^{2peg}}_2]^{4+}$, as confirmed by NMR and ESI-MS analysis. However, its host-guest behavior in CD_2Cl_2 was influenced by ion pairing effects and aggregation, particularly in the presence of anionic guests. While neutral guests with carbonyl functionalities exhibited promising interactions. Moreover, NMR titration analysis showed that the externally pointing NH proton signal shifted significantly, whereas the internally pointing NH proton signal exhibited no significant shifting. This raises the question of whether the intramolecular hydrogen bond, observed in the X-ray structure of $[Pd_2\mathbf{L^{1}}_2\mathbf{L^{2}}_2]^{4+}$, plays a role in guest binding.

To investigate the cooperativity effect of the squaramides in $[Pd_2\mathbf{L^{1peg}}_2\mathbf{L^{2peg}}_2]^{4+}$, it would be desirable to have a reference cage that lacks intramolecular interactions. This reference cage served as a comparison for the binding constants of neutral molecules. For the reference coordination cage, bis(3-pyridyl)benzothiadiazole ($\mathbf{L^{BDT}}$) was selected as a shape-complementary ligand. The formation and photophysical properties of $\mathbf{L^{BDT}}$ are well-documented in the literature. [212] As a photosensitizer, $\mathbf{L^{BDT}}$ was expected to impart fluorescence to the cage. [213] Combining multiple functionalities within a single cage through shape-complementarity is a promising approach. However, due to non-radiative relaxation pathways of Pd(II), no fluorescence was observed for the coordination cage in chapter 3.1.6. [214]

3.1.6 Formation of Coordination Cage of $[Pd_2L^{1peg}{}_2L^{BDT}{}_2]^{4+}$

In figure 3.17 the heteroleptic cage formation of $\mathbf{L^{1peg}}$ and $\mathbf{L^{BDT}}$ in CD_2Cl_2 is shown.

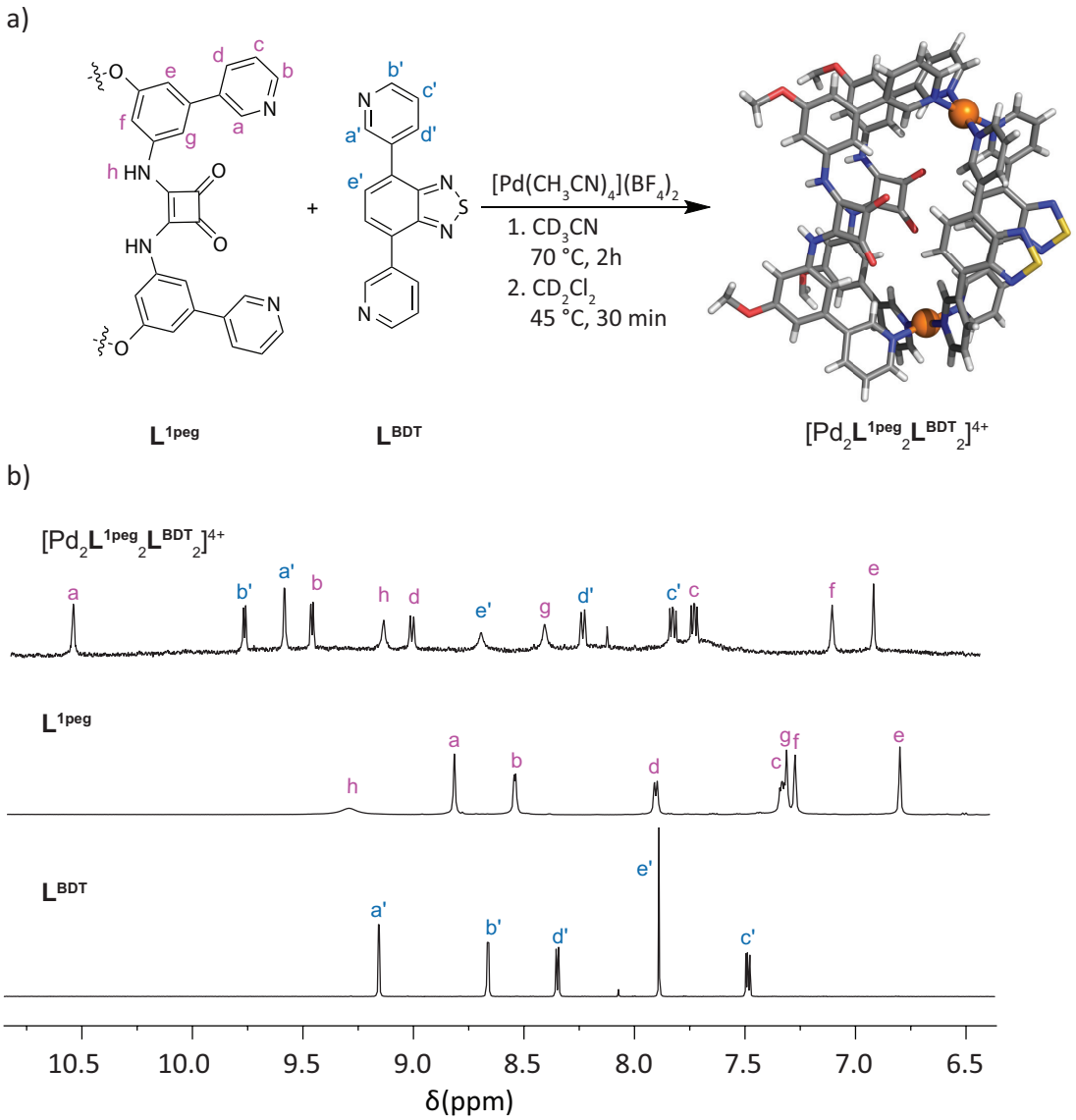

Figure 3.17. a) Coordination cage formation of $\mathbf{L^{1peg}}$ and $\mathbf{L^{BDT}}$ to $[Pd_2\mathbf{L^{1peg}}{}_2\mathbf{L^{BDT}}{}_2]^{4+}$. X-ray structure of $[Pd_2\mathbf{L^{1peg}}{}_2\mathbf{L^{BDT}}{}_2]^{4+}$ is shown. b) ^{1}H-NMR spectra (700 MHz, 298 K, CD_2Cl_2) of $\mathbf{L^{1peg}}$, $\mathbf{L^{BDT}}$ and $[Pd_2\mathbf{L^{1peg}}{}_2\mathbf{L^{BDT}}{}_2]^{4+}$.

Analogous to the coordination cage formation of $[Pd_2\mathbf{L^{1peg}}{}_2\mathbf{L^{2peg}}{}_2]^{4+}$, first the heteroleptic cage of $\mathbf{L^{1peg}}$ and $\mathbf{L^{BDT}}$ was formed in CD_3CN (for ^{1}H-NMR spectra see figure 4.174 in chapter 4.3.9). Following the removal of CD_3CN, CD_2Cl_2 was added to the mixture (for details see chapter 4.3.9). As expected, proton signals a, b, a´ and b´ show an intense downfield shifting due to close proximity of the coordination center.

ESI-MS analysis suggested the formation of $[Pd_2\mathbf{L^{1peg}}{}_2\mathbf{L^{BDT}}{}_2(BF_4)_n]^{(4-n)+}$ (n = 0–2) species with a $[Pd_2\mathbf{L}_2\mathbf{L´}_2]^{4+}$ stoichiometry (see a) in figure 3.18). Furthermore, ^{1}H DOSY NMR spectrum confirms that all assigned proton signals of

$[Pd_2\mathbf{L^{1peg}}_2\mathbf{L^{BDT}}_2]^{4+}$ belong to same molecule with a similar diffusion coefficient (see b) in figure 3.18). The Stokes-Einstein relation was used to determine r_H of $[Pd_2\mathbf{L^{1peg}}_2\mathbf{L^{BDT}}_2]^{4+}$ with a viscosity of CD_2Cl_2 of η=4.3 · 10^{-3} Pa · s at 293 K and Diffusion coefficients of D= 5.28·10^{-10} $\frac{m^2}{s}$. [207] The determined r_H of $[Pd_2\mathbf{L^{1peg}}_2\mathbf{L^{BDT}}_2]^{4+}$ is 9.61 Å, which is slightly smaller than that of $[Pd_2\mathbf{L^{1}}_2\mathbf{L^{2}}_2]^{4+}$ (9.75 Å).

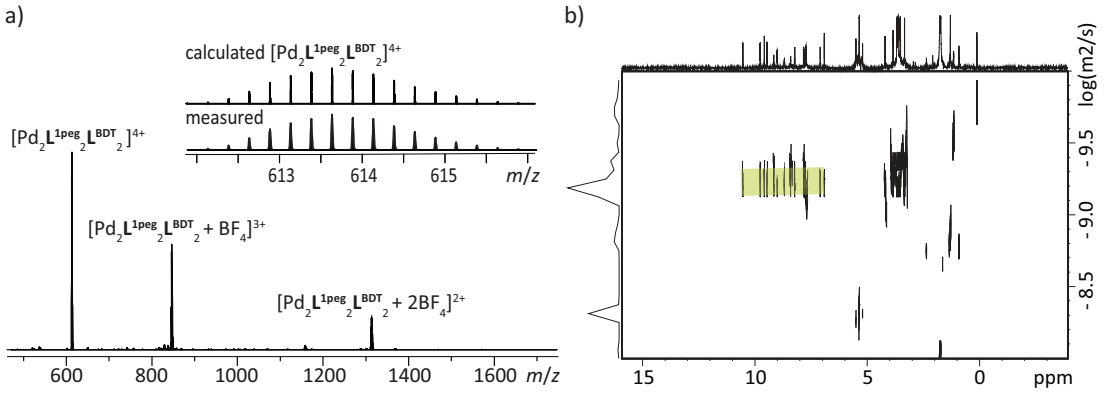

Figure 3.18. a) ESI-MS of $[Pd_2\mathbf{L^{1peg}}_2\mathbf{L^{BDT}}_2]^{4+}$. b) ^{1}H DOSY NMR spectrum (500 MHz, 298 K, CD_2Cl_2) of $[Pd_2\mathbf{L^{1peg}}_2\mathbf{L^{BDT}}_2]^{4+}$.

To further investigate the conformation, a NOESY analysis was conducted. The analysis suggests that the thiadiazole group points outward from the cavity, as evidenced by the observed NOESY contact signal between e´ and a (see figure 3.19). The conformation of the squaramides in $[Pd_2\mathbf{L^{1peg}}_2\mathbf{L^{BDT}}_2]^{4+}$ remains consistent with that in $[Pd_2\mathbf{L^{1}}_2\mathbf{L^{2}}_2]^{4+}$, as indicated by the correlation between the NH proton signal h and proton signal f. In addition to that, the NOESY analysis confirmed the correlation of proton signal b to b´ and a to a´ due to the proximity at the coordination center.

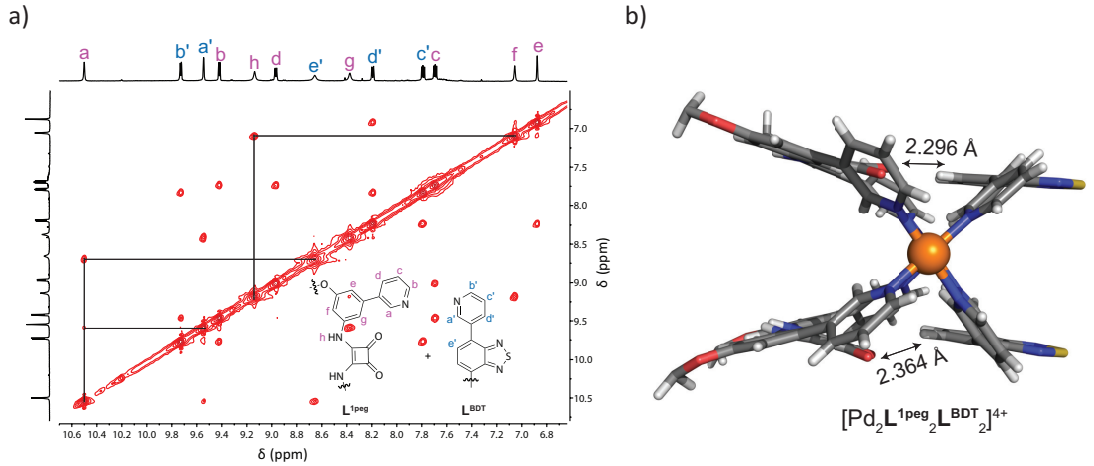

Figure 3.19. a) ^{1}H-^{1}H NOESY spectrum (600 MHz, 298 K, CD_2Cl_2) of $[Pd_2\mathbf{L^{1peg}}_2\mathbf{L^{BDT}}_2]^{4+}$. b) top view of the preliminary X-ray structure of $[Pd_2\mathbf{L^{1peg}}_2\mathbf{L^{BDT}}_2]^{4+}$ with the NH-O distance shown.

The X-ray structures show that the distance between the CH group from the phenyl backbone and the carbonyl oxygen is between 2.296-2.364 Å. Therefore,

the intramolecular HB distance within $[Pd_2\mathbf{L^{1peg}}_2\mathbf{L^{BDT}}_2]^{4+}$ is greater than that in $[Pd_2\mathbf{L^{1peg}}_2\mathbf{L^{2peg}}_2]^{4+}$ (2.044-2.078 Å).

3.1.7 Host-guest Chemistry of $[Pd_2\mathbf{L^{1peg}}_2\mathbf{L^{BDT}}_2]^{4+}$

Anionic Guests

Since $[Pd_2\mathbf{L^{1peg}}_2\mathbf{L^{BDT}}_2]^{4+}$ carries a positive charge due to the palladium (II) cations, it is anticipated to interact preferentially with anionic guests. To enable direct comparison with previous studies, the same set of anions were screened through NMR titration.

In the titration of Cl^- no significant shifts were observed and upon titration decomposing was observed. By the end of the titration, signal broadening was evident and only free $\mathbf{L^{BDT}}$ remained in the ^{1}H-NMR spectrum probably due to broadening of signals of $\mathbf{L^{1peg}}$ in the ^{1}H-NMR spectra (see figure 4.175 in chapter 4.3.9).

^{1}H-NMR spectra of the NMR titration of **NDS** and **PDS** to $[Pd_2\mathbf{L^{1peg}}_2\mathbf{L^{BDT}}_2]^{4+}$ are shown in figure 3.20.

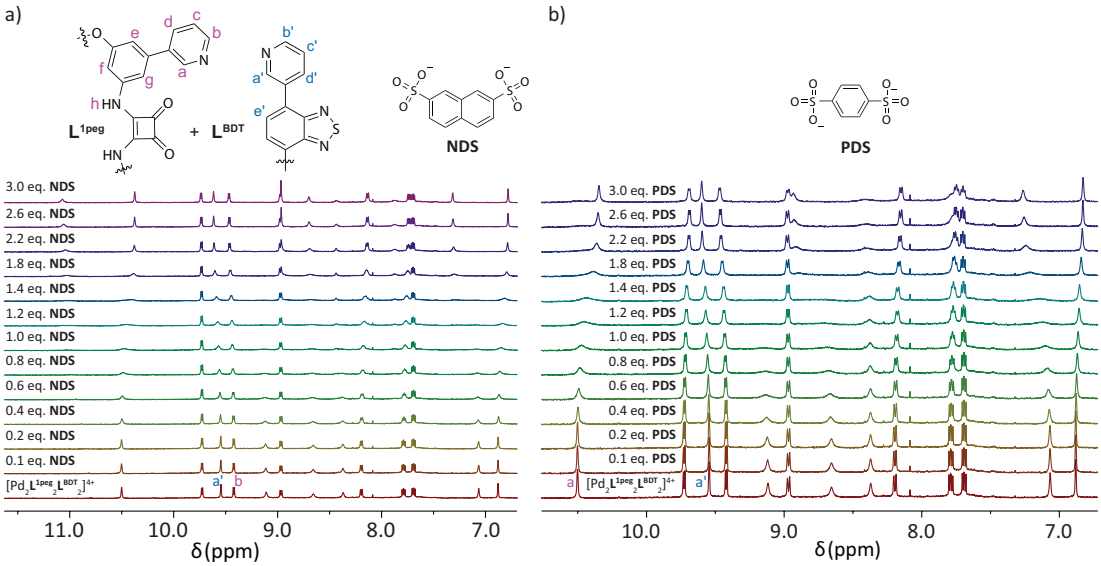

Figure 3.20. ^{1}H-NMR (500 MHz, 298 K, CD_2Cl_2) titration of **NDS** and **PDS** to 0.3 mM $[Pd_2\mathbf{L^{1peg}}_2\mathbf{L^{BDT}}_2]^{4+}$. TBA as counter ions for **NDS** and **PDS**.

Plotting the NMR titration data for both titrations resulted in sigmoidal curves with identifiable inflection points. The 1:1 binding model failed to fit the data, while the 2:1 binding model produced negative values, indicating an error in the fitting process. Therefore, the 1:2 fitter (host:guest) was used to fit the titrations and provided a binding constant for **NDS** of K_{11} equals to $(191649 \pm 105407)\,M^{-1}$ and K_{12} with $(110343 \pm 37517)\,M^{-1}$. Furthermore, the binding constant for **PDS** of K_{11} equals to $(352498 \pm 49350)\,M^{-1}$ and K_{12} with $58254 \pm 4660)\,M^{-1}$ was obtained (see figure 4.182 in chapter 4.3.9).

The host-guest complexes of **PDS** and **NDS** with $[Pd_2\mathbf{L^{1peg}}_2\mathbf{L^{BDT}}_2]^{4+}$ was observed in ESI-MS (see figure 4.183 and figure 4.184 in chapter 4.3.9).

Analogous to the previous chapter, phosphates esters have been screened. In the NMR titrations of phosphate esters with $[Pd_2\mathbf{L^{1peg}}_2\mathbf{L^{BDT}}_2]^{4+}$, a consistent broadening and shifting of the NH signal was observed during titration. Additionally, at the end of the titration (after 3 equivalents), an unidentified species appeared. However, attempts to determine reliable binding constants using sharp, shifting signals such as a, a´, e´, and g up to 3 equivalents were unsuccessful because the titration plots did not reach saturation (see figures 4.176, 4.177, 4.178, and 4.179 in chapter 4.3.9). Moreover, ESI-MS experiments did not reveal information about host-guest complexes in these cases.

Neutral Guests

Analogous to the previous chapter, neutral molecules with two carbonyl groups, as well as **NVB**, were screened (see figure 3.21; for ^{1}H-NMR spectra, see figures 4.185 and 4.186 in chapter 4.3.9).

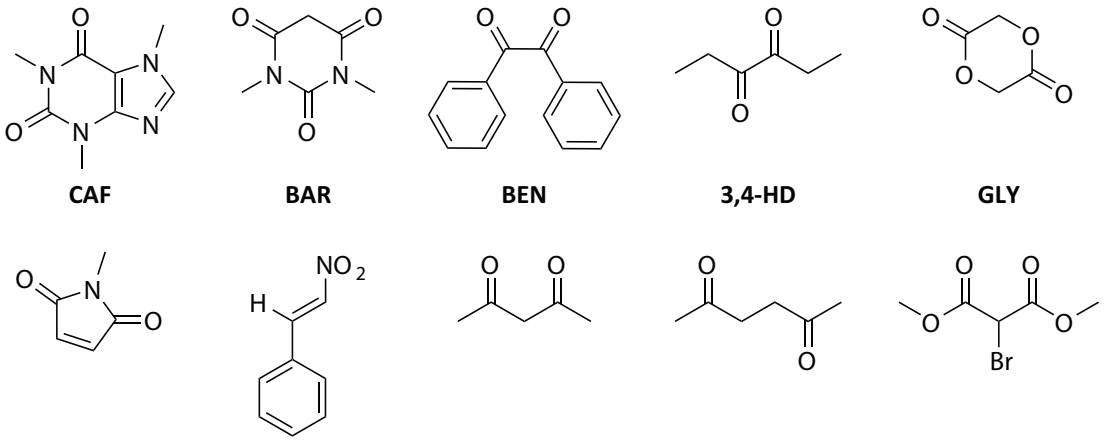

Figure 3.21. Illustration of screened neutral molecules to 0.3 mM $[Pd_2\mathbf{L^{1peg}}_2\mathbf{L^{BDT}}_2]^{4+}$ in CD_2Cl_2.

CAF and **NVB** showed a significant shifting and that is why a NMR titration to $[Pd_2\mathbf{L^{1peg}}_2\mathbf{L^{BDT}}_2]^{4+}$ was conducted (see figure 3.22).

The NMR titration of **CAF** and **NVB** was repeated twice. The average binding constant of **CAF** to $[Pd_2\mathbf{L^{1peg}}_2\mathbf{L^{BDT}}_2]^{4+}$ is $(4009 \pm 361)\,M^{-1}$ while the for **NVB** it is equal to $(4037 \pm 565)\,M^{-1}$ (see table 4.4 and figure 4.188 in chapter 4.3.9).

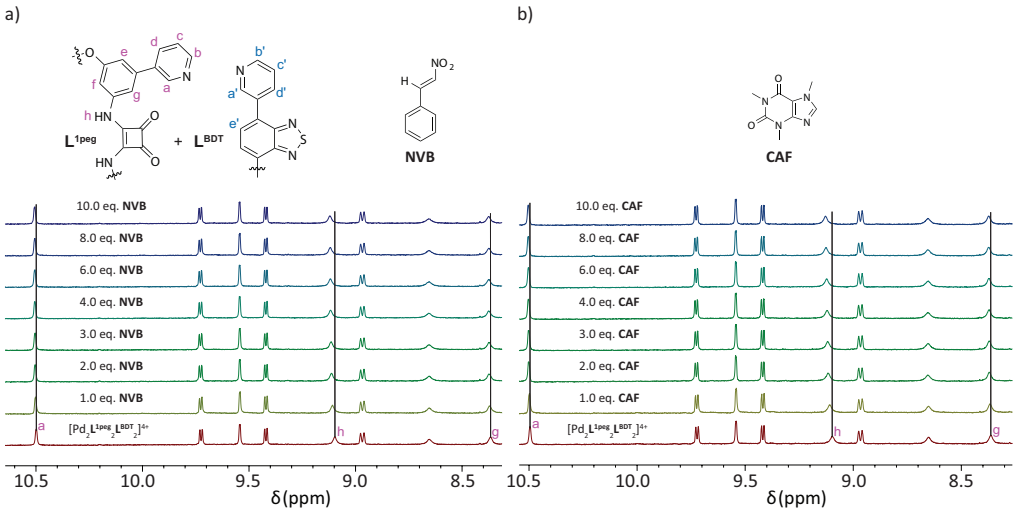

Figure 3.22. ^{1}H-NMR (500 MHz, 298 K, CD_2Cl_2) titration of **NVB** and **CAF** to 0.3 mM $[Pd_2\mathbf{L^{1peg}}_2\mathbf{L^{BDT}}_2]^{4+}$.

Influence of Cooperativity on Guest Binding by Intramolecular HB

The obtained binding constants for the respective coordination cages were compared to evaluate the extent of a cooperativity effect (see table 3.1).

Table 3.1: Obtained average binding constants K_a from the NMR titration of **CAF** and **NVB** to $[Pd_2\mathbf{L^{1peg}}_2\mathbf{L^{2peg}}_2]^{4+}$ and $[Pd_2\mathbf{L^{1peg}}_2\mathbf{L^{BDT}}_2]^{4+}$ in CD_2Cl_2.

$[Pd_2\mathbf{L^{1peg}}_2\mathbf{L^{2peg}}_2]^{4+}$		$[Pd_2\mathbf{L^{1peg}}_2\mathbf{L^{BDT}}_2]^{4+}$	
K_a(**CAF**)	K_a(**NVB**)	K_a(**CAF**)	K_a(**NVB**)
$(6185 \pm 433)\,M^{-1}$	$(5194 \pm 312)\,M^{-1}$	$(4009 \pm 361)\,M^{-1}$	$(4037 \pm 565)\,M^{-1}$

The comparison of K_a values between the two coordination cages and their respective guests reveals that the binding constants for $[Pd_2\mathbf{L^{1peg}}_2\mathbf{L^{2peg}}_2]^{4+}$ are higher, which could indicate a stronger effect of cooperativity. As previously mentioned, titration of the solvent alone with **CAF** did not result in any shift. In contrast, NMR titrations of **CAF** with both coordination cages showed a shift in the proton signal of **CAF** in the aromatic region, suggesting an interaction with the coordination cage. However, the host-guest complex was not detected in ESI-MS analysis and no NOESY signals between the respective guests and hosts were observed.

To study the cooperative effect of intramolecular H-bonds in $[Pd_2\mathbf{L^{1peg}}_2\mathbf{L^{2peg}}_2]^{4+}$ and $[Pd_2\mathbf{L^{1peg}}_2\mathbf{L^{BDT}}_2]^{4+}$ on the HB ability of the squaramide moieties, a theoretical investigation was performed using the X-ray geometries of $[Pd_2\mathbf{L^1}_2\mathbf{L^2}_2]^{4+}$ and $[Pd_2\mathbf{L^{1peg}}_2\mathbf{L^{BDT}}_2]^{4+}$ (with PEG moieties omitted). In the case of $[Pd_2\mathbf{L^1}_2\mathbf{L^2}_2]^{4+}$, only the positions of hydrogen atoms were optimized using the ωB97XD/def2SVP level of theory to ensure their correct placement. For the $[Pd_2\mathbf{L^{1peg}}_2\mathbf{L^{BDT}}_2]^{4+}$ cage, the bond lengths and angles of the squaramide unit were additionally optimized due to the lower quality of the X-ray structure.

To confirm the presence of intramolecular HB and estimate their energies, an Atoms-In-Molecules (AIM) analysis was performed. [215] The cooperative effect of intramolecular hydrogen bonds was assessed through electrostatic surface potential distribution calculations. The AIM method confirmed the presence of intramolecular hydrogen bonds in both cages by locating appropriate bond critical points (BCPs): for all four possible intramolecular hydrogen bonds between the squareamide moieties in $[Pd_2\mathbf{L^1}_2\mathbf{L^2}_2]^{4+}$ and between the squaramide and BDT moieties in $[Pd_2\mathbf{L^{1peg}}_2\mathbf{L^{BDT}}_2]^{4+}$ (see figure 4.168 in chapter 4.3.8). The estimation of hydrogen bond energy was conducted using the electron density at the BCP, following the method proposed by S. Emamian and T. Lu (see table 4.3 in chapter 4.3.8). [216] The obtained results indicate that the total intramolecular hydrogen bond strength in $[Pd_2\mathbf{L^1}_2\mathbf{L^2}_2]^{4+}$ is almost three times higher than in $[Pd_2\mathbf{L^{1peg}}_2\mathbf{L^{BDT}}_2]^{4+}$. This should lead to stronger polarization of the squaramide moiety within the cages, which correlates with the higher maximum electrostatic surface potential of the squaramide in $[Pd_2\mathbf{L^1}_2\mathbf{L^2}_2]^{4+}$ compared to $[Pd_2\mathbf{L^{1peg}}_2\mathbf{L^{BDT}}_2]^{4+}$ (see figure 3.23). The latter also implies the higher hydrogen bond donating ability of $[Pd_2\mathbf{L^1}_2\mathbf{L^2}_2]^{4+}$ cage.

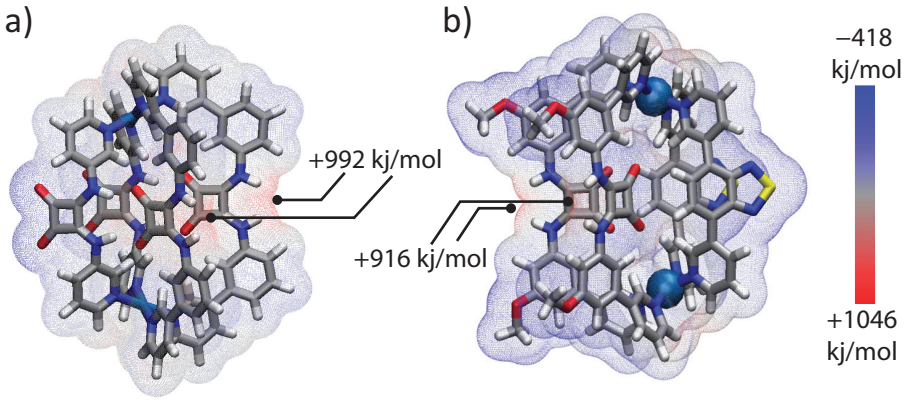

Figure 3.23. Electrostatic potential distribution for the X-ray geometries of cages a) $[Pd_2\mathbf{L^1}_2\mathbf{L^2}_2]^{4+}$ and b) $[Pd_2\mathbf{L^{1peg}}_2\mathbf{L^{BDT}}_2]^{4+}$. Calculated on ωB97X-D/def2-SVP level by A. S. Mikherdov.

The higher binding affinity of $[Pd_2\mathbf{L^{1peg}}_2\mathbf{L^{2peg}}_2]^{4+}$ than $[Pd_2\mathbf{L^{1peg}}_2\mathbf{L^{BDT}}_2]^{4+}$ as shown in table 3.1 can be explained by the greater cooperativity effect of the stronger intramolecular HB of $[Pd_2\mathbf{L^{1peg}}_2\mathbf{L^{2peg}}_2]^{4+}$.

3.1.8 Conclusion and Outlook

Ligands based on 1,2-squaramide functionalities were successfully synthesized and incorporated as ligands in Pd(II)-based supramolecular assemblies. Notably, interesting structural features were observed when combining two different squaramide-based ligands into a distinct heteroleptic assembly, as intramolecular HB was observed in the X-ray structure. A benzothiadiazole-based ligand was identified as a shape-complementary partner, forming a distinct structure in com-

bination with a squaramide-based ligand, which showed also intramolecular HB in the X-ray structure. However, calculations supported that the intramolecular HB of two squramides leads to a stronger polarization. Derivatives of 1,2-squaramide bearing solubilizing PEG chains were successfully synthesized and integrated into Pd(II)-based supramolecular assemblies, significantly enhancing their solubility in DCM. It was observed that 1,2-squaramide-based ligands without a phenyl spacer do not form a homoleptic coordination cage after introducing the bulky PEG groups, probably due to steric hindrance. The squaramide-based supramolecular assemblies were characterized using spectroscopic, spectrometric and diffraction techniques to evaluate their structures, particularly their conformations. Due to the cationic nature of the Pd(II)-based coordination cages, different disulfonates were screened and showed a significant higher binding affinity than previously reported Pd(II)-based coordination cages. In addition to that, phosphate esters were screened, but showed a low binding affinity in DMSO-d_6 and signal broadening in CD_2Cl_2 in NMR experiments. Signal broadening in ^{1}H-NMR spectra of host-guest experiments in CD_2Cl_2 could be caused by ion pairing and aggregation, which seem to be possible limitations of this system in CD_2Cl_2. To get use of the squaramide functionality in the coordination cage in CD_2Cl_2, neutral molecules especially containing two carbonyl oxygens and a nitroalkene were screened for binding affinity studies. To investigate the cooperativity effect of this intramolecular interaction, NMR titrations were conducted, and the binding constants of neutral molecules were compared among squaramide-based cages with varying strengths of intramolecular interactions. These binding studies and theoretical calculations revealed that the stronger intramolecular interactions in the fully squaramide-based coordination cage may contribute to its higher binding affinities for both guests.

Based on these studies, the next step could be to expand the investigation of neutral molecules containing two carbonyl oxygens by systematically analyzing the distance between the carbonyl oxygens and their electronic properties. Furthermore, exploring caffeine derivatives in greater detail could provide deeper insights into their interactions and potential applications.

Attempts to obtain water-soluble heteroleptic coordination cages incorporating PEG-modified 1,2-squaramide-based ligands were unsuccessful. Future studies should focus on evaluating the water solubility of PEG-modified ligand systems and their potential to form distinct coordination cages in aqueous environments. This would enable the use of the well-established hydrophobic effect for encapsulating neutral molecules and, in the long term, facilitate their use in chemical reactions.

3.2 Towards 1,3-Squaramide-based Coordination Cages

Incorporating stimuli-responsive components into self-assembled cages to create dynamic self-assembly structures capable of reversible electronic or structural changes has recently gained attention, as it allows greater control over chemical processes. [217][218][219] This could mean changing their properties in response to an external stimulus, such as pH, light or electrochemically. [220] Therefore, redox-active ligands have been implemented into coordination cages and studied in a broad range of applications due to their catalytic activity and electrochemical properties. [221][222][223] A redox-active coordination cage can serve as an electron mediator, transferring electrons to specific substrates within its cavity and accelerating various organic transformations. [224][225][226][227][228][229] Furthermore, one interesting feature is that they can reversibly encapsulate and release guest molecules in response to a redox-stimulus. [230][231][232][233]

For example, Goeb et al. showed that π-extended tetrathiafulvalene-based (TTF) ligand $\mathbf{L^{TEG}}$ can form a polycationic coordination cage $[Pd_4\mathbf{L^{TEG}}_2]^{8+}$, which disassembles upon oxidation and reassembles upon reduction through drastic conformational changes. The self-assembly of that coordination cage is performed with *cis*-Pd(dppf)$(OTf)_2$ (dppf = bis-(diphenylphosphino) ferrocene) (see a) in figure 3.24).

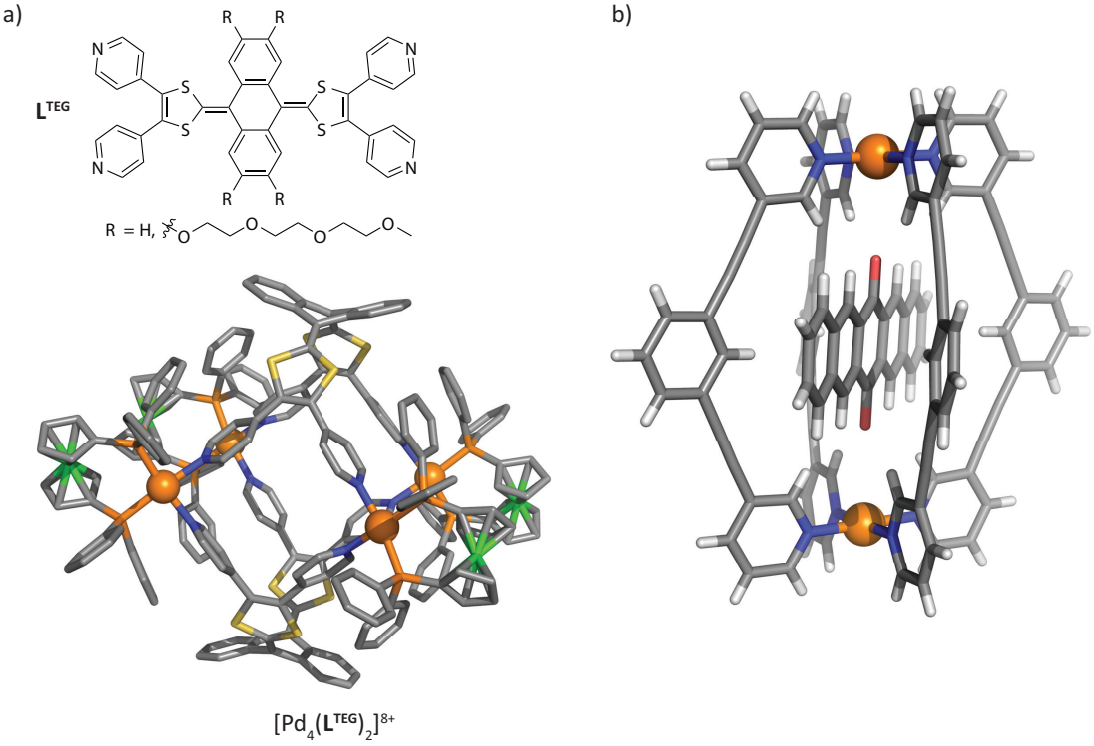

Figure 3.24. a) illustration of $\mathbf{L^{TEG}}$ and X-ray structure of $[Pd_4\mathbf{L^{TEG}}_2]^{8+}$. [233]. b) illustration of Pd_2L_4 host and encapsulated guest pentacenequinone. X-ray structure taken from [178].

This reversible process makes it possible to control the binding and release of anionic guests. Hereby the dramatic geometrical change of the π-extended TTF ligand from a butterfly shaped neutral state to a planar di-cationic structure plays a key role. [233][234] Furthermore, as examined by CV studies, $\mathbf{L}^{\mathbf{TEG}}$ can also form a charge neutral Pt-based coordination cage $[Pt_4\mathbf{L}^{\mathbf{TEG}}{}_2]$, which is more stable than $[Pd_4\mathbf{L}^{\mathbf{TEG}}{}_2]$ and releases a neutral guest during the oxidation process without disassembling the coordination cage. [230]

In 2020, the Lusby group demonstrated that binding commercially available quinones within a simple palladium-based lantern-shaped coordination cage in CD_2Cl_2 creates catalytic activity that neither the quinones nor the cage possess independently (see b) in figure 3.24). They proposed that encapsulating the quinone inside the cage would raise its redox potential, enabling electron transfer from a free substrate and creating radical-cation reactivity. This approach allows a wider range of reactants and avoids product inhibition, although it loses substrate and product selectivity due to lack of confinement. Notably, the cage anodically shifts the quinone's redox potential by 1 V, supported by chemical oxidation and cyclic voltammetry, and protects the reduced semiquinone from protonation, transforming quinones into catalytic single-electron acceptors. This highlights the potential of coordination cages for stabilizing highly reactive species and catalyzing complex transformations. [235]

Recently, the Shi Group introduced a phenothiazine-based stable polyradical cationic palladium coordination cage, which was obtained by a post-synthetic oxidation process and characterized by NMR and EPR. [236] Besides $[Pd_3\mathbf{L}^{\mathbf{PT}}{}_4]^{4+}$, the polyradical cage $[Pd_2\mathbf{L}^{\mathbf{PT}}{}_4]^{4\bullet+}$ was isolable and characterized by single-crystal X-ray diffraction analysis. Also worth mentioning is that the chemical oxidation of $[Pd_3\mathbf{L}^{\mathbf{PT}}{}_4]^{4+}$ to $[Pd_2\mathbf{L}^{\mathbf{PT}}{}_4]^{4\bullet+}$ by $AgSbF_6$ is reversible.

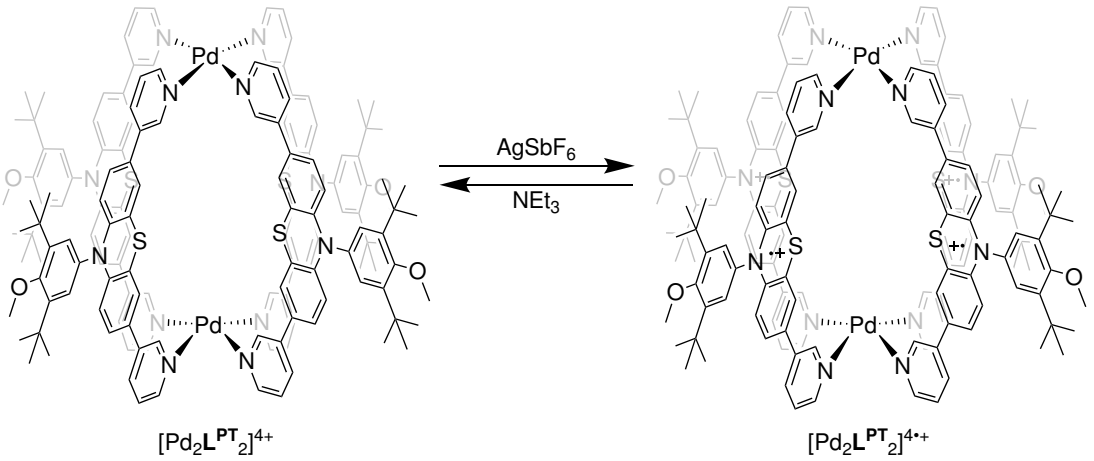

Figure 3.25. Chemical oxidation of $[Pd_2\mathbf{L}^{\mathbf{PT}}{}_4]^{4+}$ to $[Pd_2\mathbf{L}^{\mathbf{PT}}{}_4]^{4\bullet+}$ by $AgSbF_6$ and reversal by NEt_3. [236]

Clever et al. formed a double cage based on a statistical mixture of phenothiazine- and anthraquinone-based ligands. The double cage were chemically oxidized by

Fe(III). Furthermore, the double cage could be recovered by reduction with Zn powder, which has been confirmed with the observation of the specific double cage signals in the ^{1}H-NMR spectrum. [237] Clever et al. previously reported interpenetrated double-cage with eight phenothiazine donors and four Pd(II) centers, which remained stable during 8-fold oxidation by Cu(II) and by Fe(III). This work showed that the creation of a more positively charged species in a palladium-based coordination cage does not necessarily lead to Coulomb-driven decomposition. [238]

In the examples mentioned above, the organic ligands (or guest) in these assemblies undergo oxidation or reduction, generating reactive ionic radicals that are challenging to isolate yet essential for studying electron transfer and radical-driven reactions. [236][228][225][229] This has ignited interest among supramolecular chemists in incorporating such ligands into cages. Additionally, the natural curiosity of supramolecular chemists continues to drive the exploration of new architectures and the integration of novel molecules into coordination cages to investigate their effects on cage formation and host-guest chemistry.

Coordination Cage Formation of 1,3-Squaramide-based Ligands

In 1968, Ziegenbein et al. showed the condensation reaction of squaric acids and secondary amines, and others followed after a short time. [239][240][241]. Then, in 1977 Hünig et al. reported the redox properties of squaramides. [242] After a long gap in studies on squaramides for energy storage, Hansmann et al. examined squaramides, focusing on isolating and stabilizing radical cations. They systematically optimized the squaramide structure, achieving remarkable stability and high redox potentials in squaric acid quinoxalines. [243] Shortly afterward, Toste group highlighted squaric acid quinoxalines as effective multielectron catholytes for use in redox flow batteries. [244]

Inspired by the work of the Hansmann group on 1,3-Squaramides (1,3-SQA) and their electrochemical properties, this chapter is dealing with the implementation of 1,3-SQA ligands into palladium-based redox-active coordination cages. In the future this could allow controlled host-guest chemistry through a redox-stimulus. This chapter focuses firstly on finding a suitable ligand to form a coordination cage, then on its host-guest chemistry and finally on CV studies.

Synthesis of methyl-phenyl substituted 1,3-SQA is reported in the literature. [245] As a starting point, this easily accessible building block was chosen and intuitively a terminal meta-pyridine substituent was synthesized. Therefore, $\mathbf{L^3}$ was synthesized by Marcel E. Baumert, and then its coordination cage formation was studied (see figure 3.26).

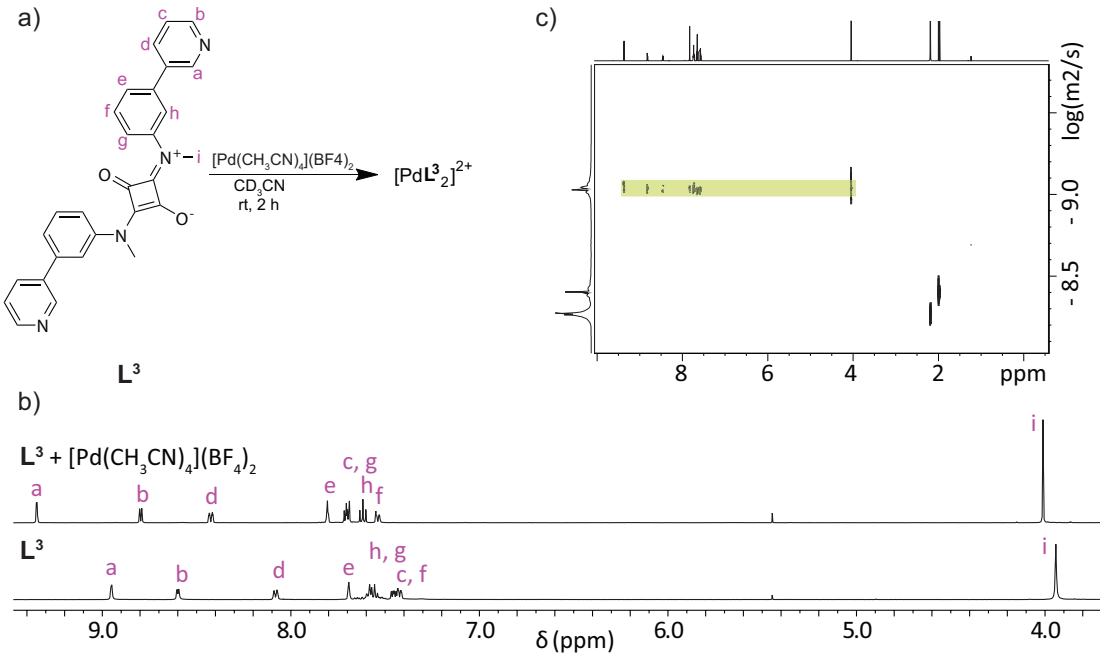

Figure 3.26. a) Homoleptic cage formation experiment of $\mathbf{L^3}$, b) ^{1}H-NMR spectrum (500 MHz, 298 K, CD_3CN) of the homoleptic cage of $\mathbf{L^3}$ and c) ^{1}H DOSY NMR spectrum (500 MHz, 298 K, CD_3CN) of the coordination cage formation experiment of $\mathbf{L^3}$. $D = 9.39 \cdot 10^{-10} \frac{m^2}{s}$, $r_H = 6.96$ Å.

In the ^{1}H-NMR spectrum, a downfield shift, especially for signals a, b, and d, is observed due to deshielding of these protons by the coordination of nitrogen to Pd(II). In the ESI-MS, a mononuclear complex, $[Pd\mathbf{L^3}_2]^{2+}$, was detected (see figure 4.191 in chapter 4.3.10). ^{1}H-DOSY NMR spectrum shows that the signals belong to one species but the obtained $r_H = 6.96$ Å suggests that a mononuclear assembly was obtained by chelation.

Subsequently, another 1,3-SQA was tested, selected for its straightforward synthetic accessibility. Piperazine was chosen as a flexible linker to create concave binding vectors, though it is unlikely to form a chelate complex (for the 1,3-SQA ligand featuring a piperazine linker between the backbone and the donor group, namely $\mathbf{L^4}$, see a) in figure 3.27). [195]

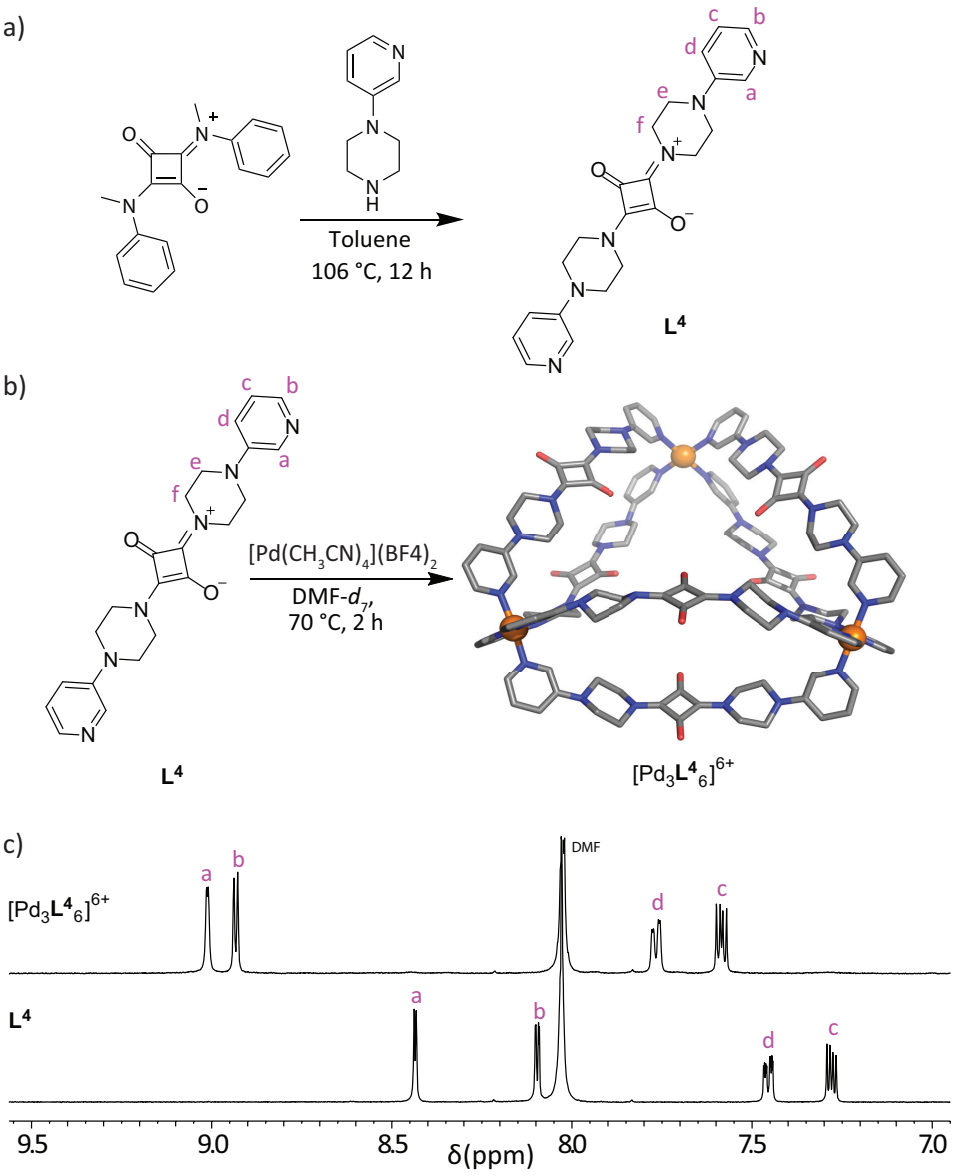

Figure 3.27. a) Synthesis of $\mathbf{L^4}$, b) X-ray crystal structure of $[Pd_3\mathbf{L^4}_6]^{6+}$ c) ^{1}H-NMR spectrum (500 MHz, 298 K, DMF-d_7) of $\mathbf{L^4}$ and $[Pd_3\mathbf{L^4}_6]^{6+}$.

The coordination cage consisting of the ligand $\mathbf{L^4}$ shows a clean ^{1}H NMR spectrum in DMF-d_7. After adding $[Pd(CH_3CN)_4](BF_4)_2$ solution to the ligand solution, the 4 signals of NMR signals in the aromatic area are downfield shifted due to the complexation, but especially proton **a** and **b** show an intense downfield shit because of their close proximity to the coordination center. Due to that, electron density of the nitrogen is being relocated to the coordination bond and is therefore deshielded, and an intense downfield shift is observed.

In ESI-MS $[Pd_3\mathbf{L^4}_6(BF_4)_n]^{(6-n)+}$ (n=0-4) was observed (see a) in figure 3.28). Therefore, a ring topology was suggested and then confirmed by single crystal analysis. Furthermore, ^{1}H DOSY NMR spectrum is shown in b) in figure 3.28 and confirms that all assigned proton signals of the homoleptic species of $\mathbf{L^4}$ belong to same molecule with a similar diffusion coefficient.

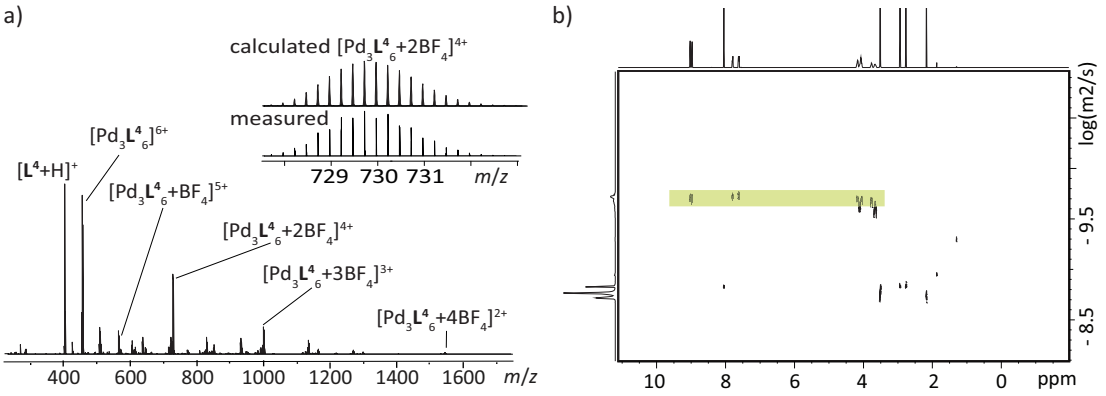

Figure 3.28. a) ESI-MS of $[Pd_3\mathbf{L^4}_6]^{6+}$. b) ^{1}H DOSY NMR spectrum (500 MHz, 298 K, DMF-d_7) of the homoleptic cage of $\mathbf{L^4}$. $D([Pd_3\mathbf{L^4}_6]^{6+}) = 1.91 \cdot 10^{-10}\,\frac{m^2}{s}$, $r_H([Pd_3\mathbf{L^4}_6]^{6+}) = 13.47\,Å$.

Apart from this, the self-assembly of the coordination cage was also examined in DMSO-d_6 and CD_3CN, but no single set of signals corresponding to a well-defined species in ^{1}H NMR spectra was confirmed (see figures 4.199 in chapter 4.3.11). However, the self-assembly in DMSO-d_6 was found to be miscible with D_2O and provided a clean ^{1}H NMR spectrum of the coordination cage, for which ESI-MS suggested the same chemical formula $[Pd_3\mathbf{L^4}_6]^{6+}$ as the coordination cage formation of $\mathbf{L^4}$ in DMF-d_7 (see figures 4.197 and 4.198 in chapter 4.3.11).

Also, the possibility of the formation of a lantern shaped cage by using isoquinoline instead of the pyridine donor group was examined, hypothesizing that the ligands could twist to achieve this. But a clean coordination cage formation could not be established, probably due to steric hinderance. (see figures 4.215 and 4.216 in chapter 4.3.12). [195]

After $[Pd_3\mathbf{L^4}_6]^{6+}$ was well-characterized in DMF-d_7, the following work focused on its host-guest chemistry in this solvent. $[Pd_3\mathbf{L^4}_6]^{6+}$ features a ring topology with two openings at the top and bottom, enabling it to encapsulate and interact with large guest molecules. Moreover, its positive charge, attributed to the palladium(II) cations, makes it particularly suited for screening with various large anionic guests.

In figure 3.29 the ^{1}H-NMR titration for the host-guest complexes of the anionic guests ferrocene-1,1'-disulfonate (**FCS**) and Allura Red (**AR**) to $[Pd_3\mathbf{L^4}_6]^{6+}$ are shown. Beside **AR**, other azo-dyes such as trypan blue, chromotrope, amaranth and naphthol blue black have been screened as well, which also carry multiple negative charges due to sulfonate groups, but they lead to precipitation (see figures 4.200, 4.201 and 4.202 in chapter 4.3.11).

Figure 3.29 shows that the HG complexes of $[Pd_3\mathbf{L^4}_6]^{6+}$, with **FCS** and **AR** respectively show the most significant shifting for signal of proton a, which is pointing inside of the cavity. The NMR titration of **FCS** to $[Pd_3\mathbf{L^4}_6]^{6+}$ shows a saturation of the signal shifts after addition of 1.7 eq. guest, while the addition

of **AR** leads to a broadening of signal of proton a (for close-up spectrum see figure 4.203 in chapter 4.3.11).

Then, the association constant was determined by Bindfit. [203] For $[Pd_3\mathbf{L^4}_6]^{6+}$ with **FCS**, the protons d, c, b, and a have been plotted with 1:1 bind model, which provided an association constant of $(5474 \pm 383)\,M^{-1}$.

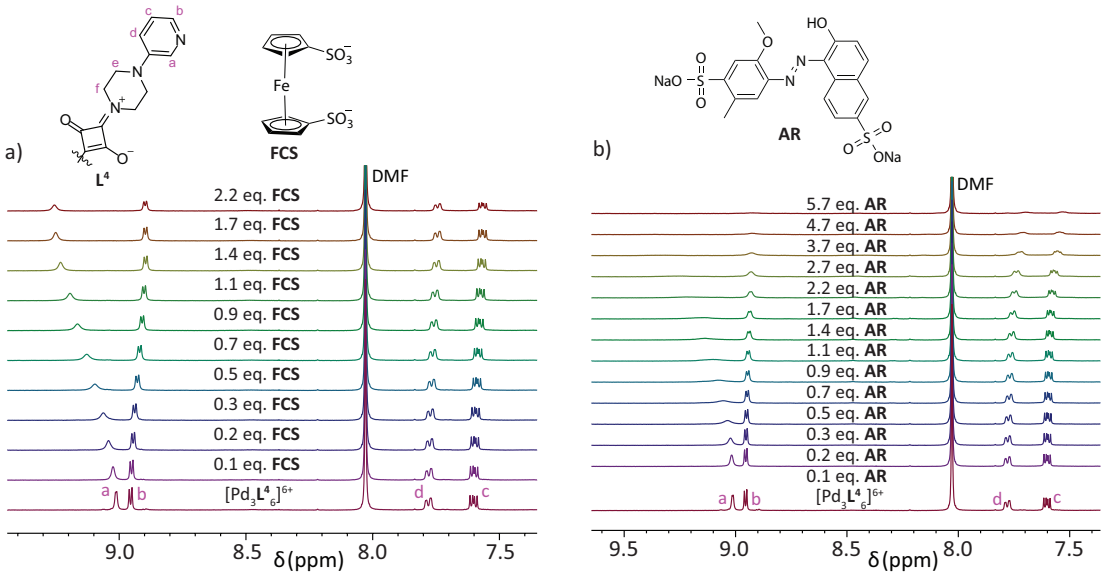

Figure 3.29. ^{1}H-NMR (500 MHz, 298 K, DMF-d_7) titration of allura red (**AR**) and ferrocene-1,1'-disulfonate (**FCS**) to 0,63 mM $[Pd_3\mathbf{L^4}_6]^{6+}$. TBA as counter ions for **FCS**.

In the work of K. Ebbert, a fluorenone-based ligand $\mathbf{L^A}$ and a phenyl-based ligand $\mathbf{L^B}$ was used to form a heteroleptic ring $[Pd_3\mathbf{L^A}_3\mathbf{L^B}_3]^{6+}$. The host-guest complex of $[Pd_3\mathbf{L^A}_3\mathbf{L^B}_3]^{6+}$ with azo-dyes was examined by NMR and UV-Vis analysis, but in that work the addition of **AR** to the coordination assembly led to a broadening and overlapping of signals, and therefore no binding constant could be determined. Despite that, CSI-MS analysis suggested a 2:1 ratio of host to guest. [196] In this work, the signal of proton a is also broadening during the titration, but it was possible to obtain a binding constant. For the host-guest complex of $[Pd_3\mathbf{L^4}_6]^{6+}$ with **AR**, association constants were determined by analyzing the chemical shift of the signal of the inside-pointing proton a. Using a 2:1 binding model and a sigmoidal plot, K_{11} was calculated as $(9410 \pm 1223)\,M^{-1}$ and K_{21} as $(796 \pm 111)\,M^{-1}$. The difference between K_{11} and K_{21} exceeds one order of magnitude, reflecting a significantly stronger affinity for the first binding event compared to the second (see figure 4.204 in chapter 4.3.11 for Bindfit analysis of the titrations).

Various attempts to obtain the ESI-MS spectra of the host-guest complex of $[Pd_3\mathbf{L^4}_6]^{6+}$ with **AR** failed. Then, crystals of HG complex were grown to examine the interaction in solid state, which can give information about the binding motive of the guest to the host. Single crystals could be grown by slow vapor crystallization by diffusion of Et_2O into DMF $[Pd_3\mathbf{L^4}_6]^{6+}$. Surprisingly, $[Pd_4\mathbf{L^4}_8]^{8+}$

was observed with **AR** in a 1:2 ratio (see figure 3.30). The different nuclearity could be a solid state effect, which is a result of highly dense packing of molecules. A transformation of $[Pd_3\mathbf{L^4}_6]^{6+}$ to $[Pd_4\mathbf{L^4}_8]^{8+}$ during the titration of **AR** is not expected since the two sets of signals should be distinguishable by NMR.

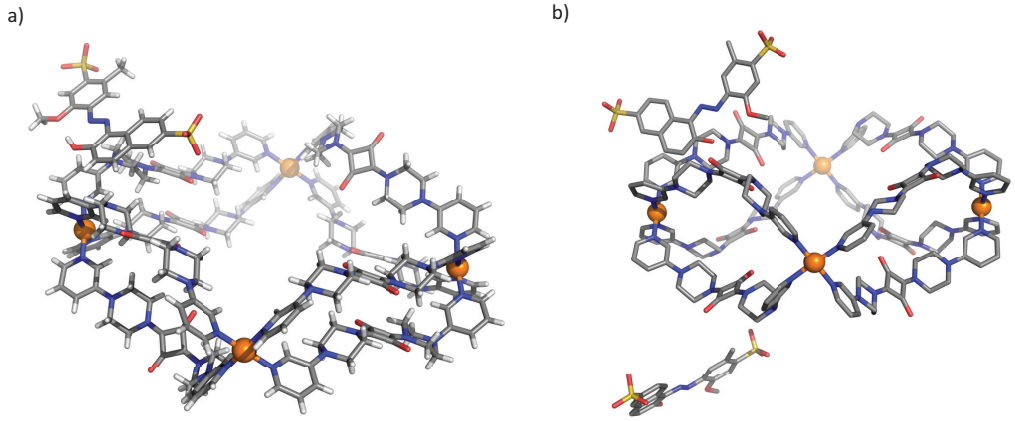

Figure 3.30. Illustration of X-Ray structures of the HG complex consisting of **AR** and $[Pd_4\mathbf{L^4}_8]^{6+}$ obtained by slow vapor crystallization by diffusion of Et_2O into DMF. a) guest outside binding and b) HG complex with a lower symmetry space group P-1 with two **AR**.

The binding constant of **AR** to $[Pd_3\mathbf{L^4}_6]^{6+}$, determined through ^{1}H-NMR analysis, is substantial enough to warrant further investigation of the binding interactions using UV-Vis spectroscopy. [246] Additionally, if charge-transfer contributes to the host-guest interaction, it should be detectable through UV-Vis analysis.

UV-Vis Studies

The host-guest complex of **AR** and $[Pd_3\mathbf{L^4}_6]^{6+}$ was examined by UV-Vis spectroscopy. For that, a titration was performed after the stability of $[Pd_3\mathbf{L^4}_6]^{6+}$ was shown at UV-Vis concentration (see figure 4.206 in chapter 4.3.11). However, isosbestic points could not be determined from the titration of **AR** to $[Pd_3\mathbf{L^4}_6]^{6+}$, but isosbestic points were observed by the titration of $[Pd_3\mathbf{L^4}_6]^{6+}$ to **AR** (see figure 3.31 and figure 4.207 in chapter 4.3.11).

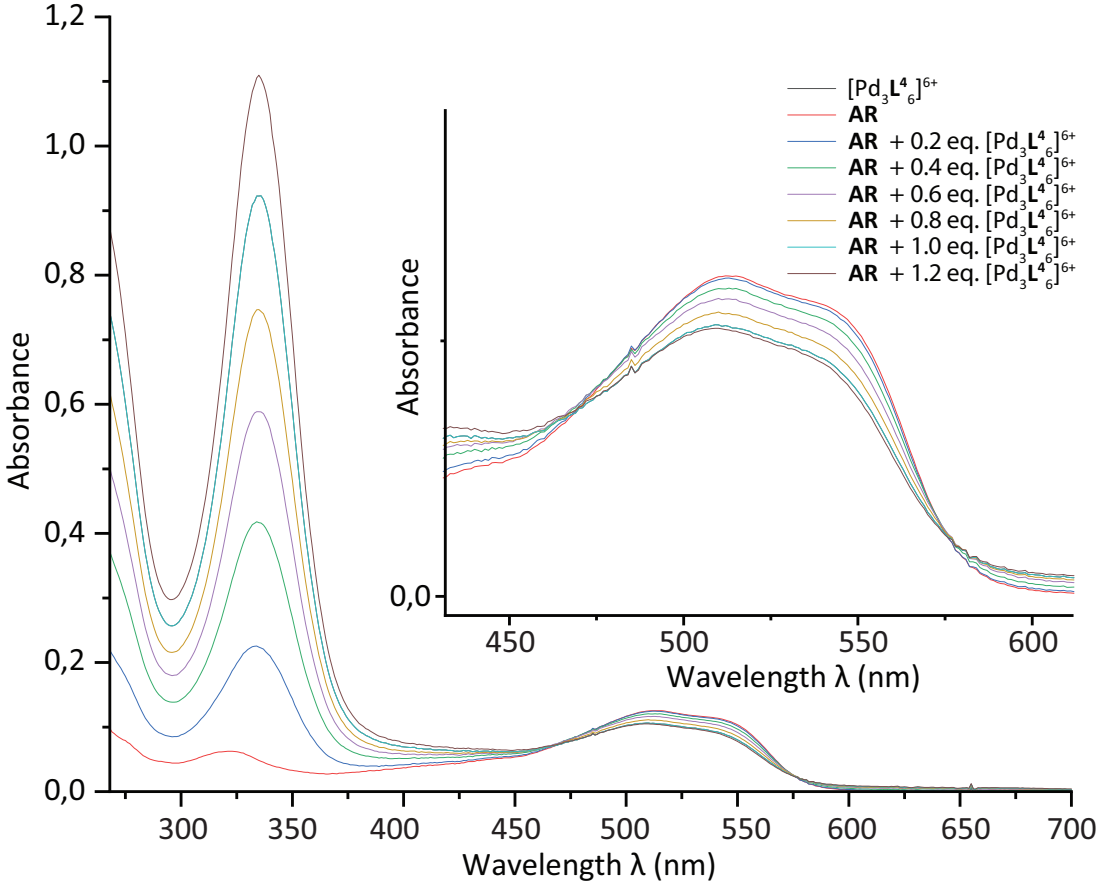

Figure 3.31. UV-Vis absorption spectra of reverse titration of $[Pd_3\mathbf{L^4}_6]^{6+}$ to **AR**. Concentration of $[Pd_3\mathbf{L^4}_6]^{6+}$ 35 μM, DMF-d_7 and with a cuvette of 0.2 cm optical path.

The addition of $[Pd_3\mathbf{L^4}_6]^{6+}$ to **AR** led to no color change, which is also shown in the constant absorption maximum of the dye at λ= 512 nm upon titration. The titration shows two isosbestic points, one at λ= 471 nm and the second at λ= 577 nm. While the HG-complex is forming, the absorption band is decreasing, which could indicate the interaction between $[Pd_3\mathbf{L^4}_6]^{6+}$ and **AR**. But fitting the UV-Vis titration data using Bindfit did not provide satisfying results since the errors of the plot were too high (see figure 4.208 in chapter 4.3.11).

CV Studies

First, $[Pd_3\mathbf{L^4}_6]^{6+}$ was examined under CV conditions with an excess of electrolyte solution by ^{1}H-NMR analysis to be sure that the cage is stable under those conditions (see a) in figure 4.209 in chapter 4.3.11). Then CV studies of $[Pd_3\mathbf{L^4}_6]^{6+}$ and the free ligand $\mathbf{L^4}$ were examined (details about CV in chapter 4.1.2; all CVs in this chapter were performed by Marcel E. Baumert). The cyclic voltammogram of $[Pd_3\mathbf{L^4}_6]^{6+}$ is electrochemically reversible, while ligand $\mathbf{L^4}$ is not (see a) in figure 3.32). This suggests that the oxidation state is stabilized by the palladium(II).

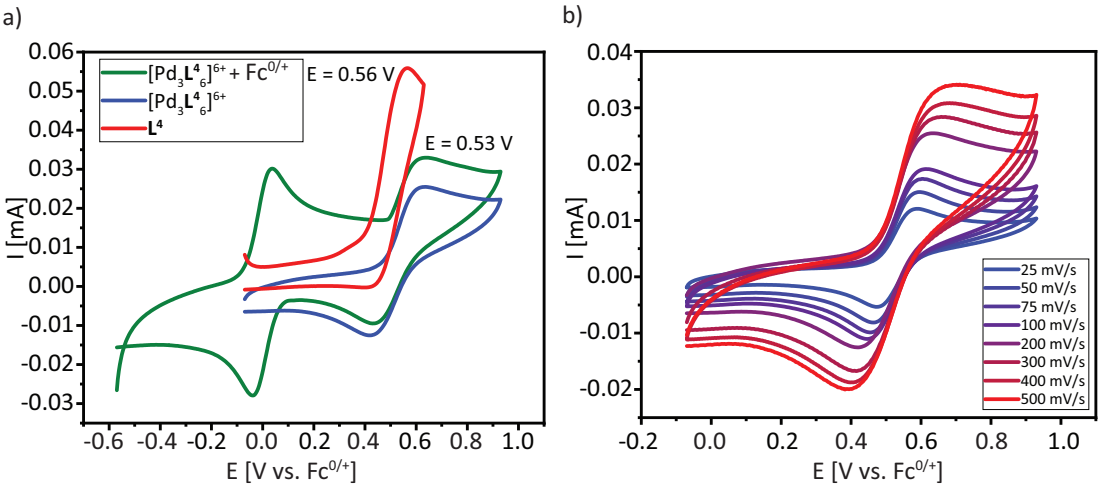

Figure 3.32. a) CV of $[Pd_3\mathbf{L^4}_6]^{6+}$ and $\mathbf{L^4}$, b) CV of $[Pd_3\mathbf{L^4}_6]^{6+}$ dependent on scan rate. 0.63 mM $[Pd_3\mathbf{L^4}_6]^{6+}$ in DMF (0.1 mM $n-Bu_4NPF_6$).

Then, different scan rates were applied to show that the voltammogram of $[Pd_3\mathbf{L^4}_6]^{6+}$ is electrochemical reversible since the applied potential (E) correlates with response, which is the resulting current (I) (see b) in figure 3.32). So forming a coordination cage with $\mathbf{L^4}$ enables that the CV is reversible, which is probably due to the change of electronic properties of the ligand by coordinating to the palladium-center. The host-guest (HG) complexes comprising $[Pd_3\mathbf{L^4}_6]^{6+}$ with **AR** and Benzoquinone (**BQ**) were studied separately using cyclic voltammetry (CV). Initial CV measurements of the guests alone revealed that **AR** exhibits electrochemical irreversibility, whereas **BQ** demonstrates electrochemical reversibility.

The HG complex consisting of $[Pd_3\mathbf{L^4}_6]^{6+}$ and **AR** showed an electrochemical irreversible cyclic voltammogram, while the HG complex of **BQ** is electrochemical reversible. In the case of the latter one, the spectra indicate an oxidation event at the $[Pd_3\mathbf{L^4}_6]^{6+}$, which is most likely to occur at the coordinated ligand of $[Pd_3\mathbf{L^4}_6]^{6+}$ (see b) figure 3.33).

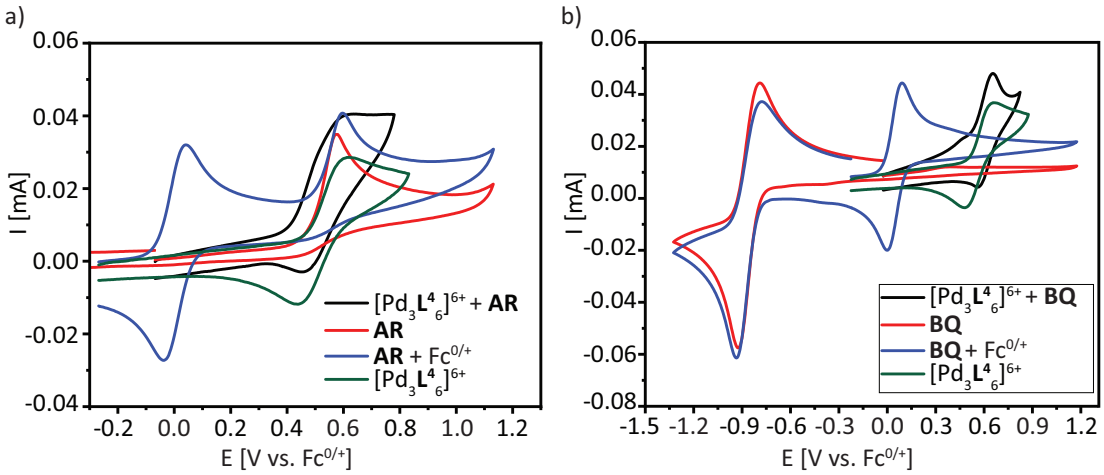

Figure 3.33. CV of 0.63 mM $[Pd_3\mathbf{L^4}_6]^{6+}$ in DMF (0.1 mM *n*-Bu_4NPF_6). a) CV of $[Pd_3\mathbf{L^4}_6]^{6+}$ and **AR**. b) CV of $[Pd_3\mathbf{L^4}_6]^{6+}$ and **BQ**. HG complexes respectively formed with 2 eq. **AR** and 4 eq. **BQ**.

Comparing the redox event of **BQ** and **BQ** with $[Pd_3\mathbf{L^4}_6]^{6+}$ (referenced to $Fc^{0/+}$) shows potential shift of 0.05 V at CV (see figure 4.210 in chapter 4.3.11). This indicates an electrochemical change in **BQ** when combined with $[Pd_3\mathbf{L^4}_6]^{6+}$ during CV. However, as no interaction between **BQ** and $[Pd_3\mathbf{L^4}_6]^{6+}$ is observed in solution by ^{1}H-NMR (see figure 4.209 in chapter 4.3.11), the CV change is not significant. A stronger interaction between **BQ** and $[Pd_3\mathbf{L^4}_6]^{6+}$ in solution would likely result in a more substantial shift in the electron potential of **BQ**. Interactions involving a neutral molecule, such as benzoquinone, could occur via HB in nonpolar solvents, which can be confirmed by ^{1}H-NMR analysis. Additionally, the influence of counterions must be considered, as they can significantly affect cationic coordination cages in nonpolar solvents. [178]

3.2.1 Conclusion and Outlook

In conclusion, the 1,3-SQA-based coordination cage with piperazine-linker $[Pd_3\mathbf{L^4}_6]^{6+}$ was formed and characterized in solution by ^{1}H-NMR, in gas phase by ESI-MS, and in solid state by single crystal analysis. The HG chemistry of $[Pd_3\mathbf{L^4}_6]^{6+}$ with big anionic guests such as azo-dyes has been examined. Then a binding stoichiometry of 2:1 (H:G) and the binding constants of **AR** to $[Pd_3\mathbf{L^4}_6]^{6+}$ were determined. In addition to that, binding stoichiometry of 1:1 and the binding constant of **FCS** to $[Pd_3\mathbf{L^4}_6]^{6+}$ was determined. Crystallization of the HG complex of **AR** and $[Pd_3\mathbf{L^4}_6]^{6+}$ led to a HG complex of **AR** and $[Pd_4\mathbf{L^4}_8]^{8+}$. The CV studies showed that the ligand $\mathbf{L^4}$ is chemically irreversible, while $[Pd_3\mathbf{L^4}_6]^{6+}$ is chemically reversible. Different HG complexes were examined by CV, but only the HG complex of $[Pd_3\mathbf{L^4}_6]^{6+}$ and **BQ** seems to be electrochemically reversible.

In the future, a heteroleptic cage based on $\mathbf{L^4}$ and a ligand with hydrogen-bonding functionality or a ligand with a big π-surface should be aimed for, because then encapsulating of a neutral guest should be much more promising.

In addition to that, a new coordination cage which is based on squaric acid quinoxaline ligands should be examined (see figure **??**). The ligand $\mathbf{L^{PJ1}}$ features the same base geometry as as $\mathbf{L^{BDT}}$ and therefore could be used to form heteroleptic cages with squaramide-based ligand $\mathbf{L^{1peg}}$, as shown in chapter 3.1.6. Using the squaramide ligand $\mathbf{L^{1peg}}$ to bind a guest by HB should be considered. Furthermore, the redox properties of the coordination cage with $\mathbf{L^{PJ1}}$ should be examined, since the redox properties of squaric acid quinoxaline-based structures were studied. [243][244] Combining two distinct properties by using ligands with different functionalities could be a fruitful approach, exemplifying how the heteroleptic cage strategy can combine multiple functionalities into a single cage structure.

3.3 Catalysis in Gallium-Cages

As mentioned in chapter 1.6, the use of coordination cages in catalysis represents an exciting application. Utilizing the hydrophobic effect as a driving force to encapsulate guests and increase local concentration in a bimolecular reaction is a well established approach in this field. [247][248][167][249][250] The work presented in this chapter was carried out during a research stay at *UC Berkeley* from January 8th to March 25th, 2024, within the Toste Group. The primary objectives of this research stay were to learn the synthesis and cage formation procedures for a catechol-based ligand and a gallium(III) coordination cage, as well as to investigate catalysis using these coordination cages.

Besides the synthesis, the cage formation differs dramatically from cage formation with pyridine-based ligands, since the pyridine donor group is not sensitive to oxidation in comparison to the catechol donor group.

Extensive research on catechol chemistry has focused on its oxidation, underscoring the well-studied nature and significance of catechol oxidation processes across various applications, particularly as wet adhesive material. [251][252][253][254][255] In particular, the oxidation of catechol to quinone is well studied. [256][257]

The first part of this work focused on the synthesis of the catechol-based ligands (see synthesis route a) in figure 3.34). [258]

To prevent the oxidation of catechol groups, the coordination cage was assembled under an inert atmosphere and the solvents were degassed (see b) in figure 3.34).

Ligand $\mathbf{L^5}$ was synthesized and the coordination cage $[Ga_4\mathbf{L^5}_6]^{12-}$ formed according to the literature (for ^{1}H-NMR spectrum see figure 4.219 and figure 4.220 in chapter 4.3.13). [258]

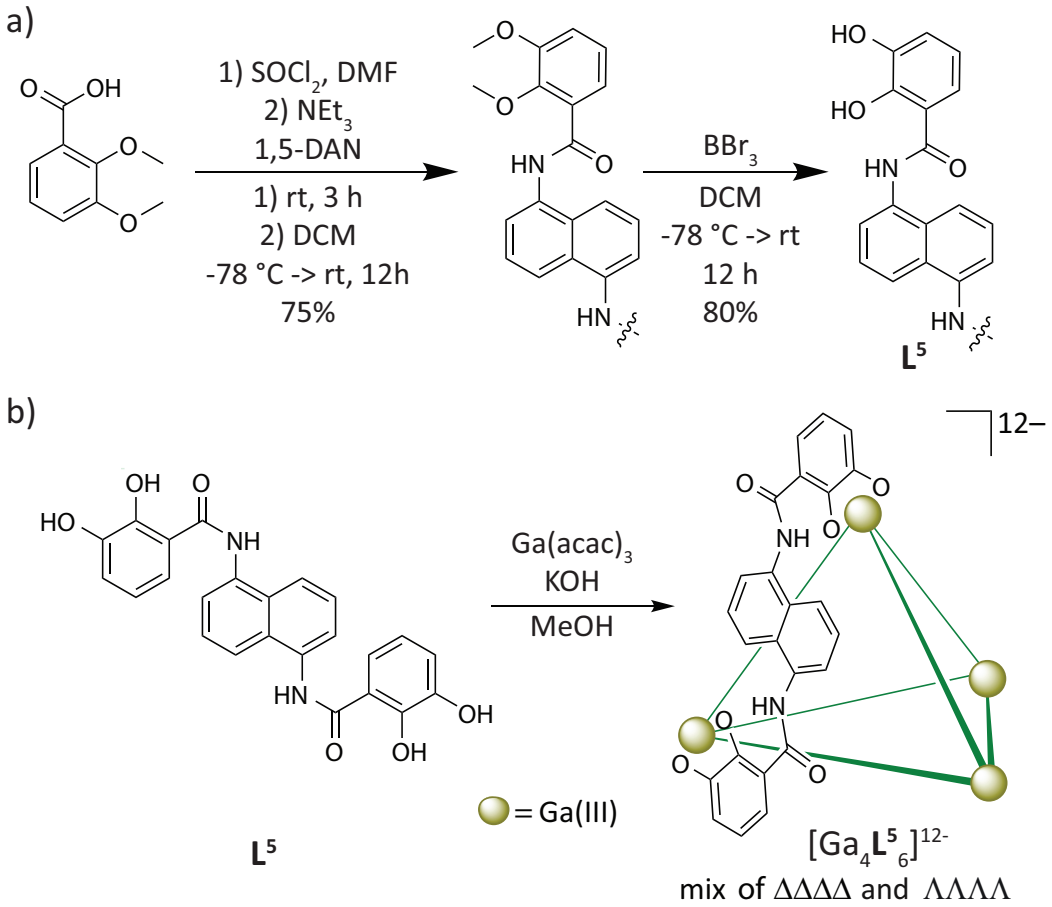

Figure 3.34. Illustration of a) synthesis of catechol-based ligand $\mathbf{L^5}$ and b) coordination cage formation of $[Ga_4\mathbf{L^5}_6]^{12-}$. [258]

After $\mathbf{L^5}$ and $[Ga_4\mathbf{L^5}_6]^{12-}$ were successfully reproduced the main goal was to study catalysis within coordination cages, which is described in section 3.3.1.

3.3.1 Synthesis of a enantiopure Ligand and its Formation of an Enantiopure M_4L_6 Supramolecular Host

In 2022, Toste group reported a series of anionic enantiopure gallium(III)-based coordination cages, which could catalyze aza-Darzens reaction up to 99% *ee*. [259] Based on this work, the chiral ligand was synthesized to form an enantiopure coordination cage and then to investigate enantioselective catalysis. The synthesis route, according to the reported procedure, is shown in figure 3.35. [259] First, the synthesis of the reported ligand was studied, and hereafter the enantiopure coordination cage was formed.

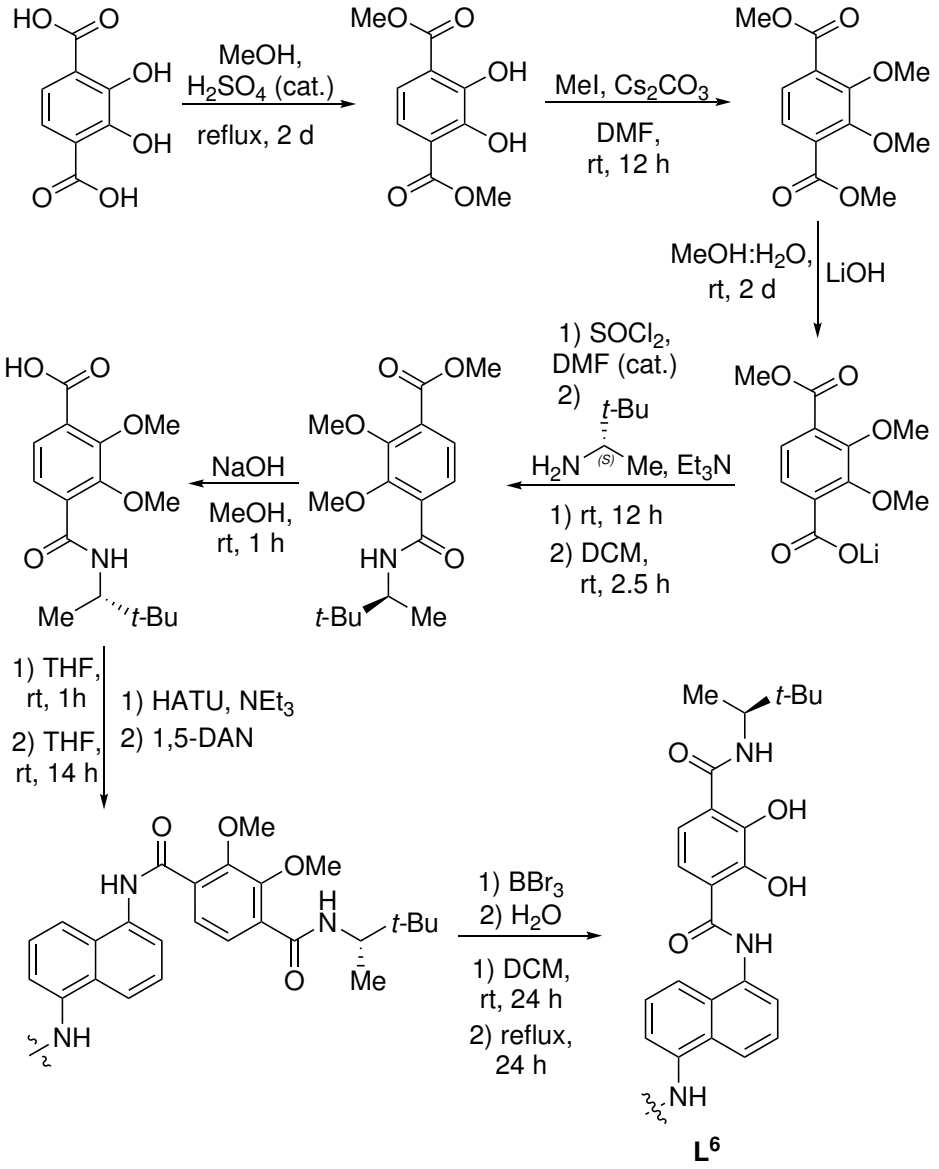

Figure 3.35. Illustration of the synthesis route of ligand $\mathbf{L^6}$. [259]

After the chiral ligand $\mathbf{L^6}$ was synthesized, the enantiopure coordination cage $[Ga_4\mathbf{L^6}_6]^{12-}$ was assembled under an inert N_2-atmosphere using degassed solvents.

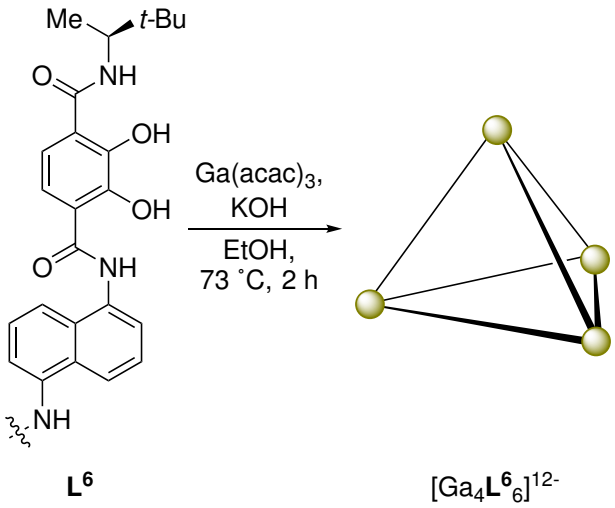

Figure 3.36. Coordination cage formation of enantiopure coordination cage $[Ga_4\mathbf{L^6}_6]^{12-}$. [259]

After $[Ga_4\mathbf{L^6}_6]^{12-}$ was formed, tetraethylphosphonium (PET) was introduced as a positively charged guest to block the cavity. This was confirmed by the characteristic ^{1}H-NMR signal shifts of the encapsulated PET at -1.3 ppm and -1.63 ppm, consistent with previously reported literature (see figure 4.226 in chapter 4.3.13). [259]

In the following chapter 3.3.2, the previous work of enantioselective reduction with $[Ga_4\mathbf{L^6}_6]^{12-}$ will be briefly described. Hereafter, my research topic, the reduction of 2-(hydroxymethyl)indole with $[Ga_4\mathbf{L^6}_6]^{12-}$, will be discussed.

3.3.2 Indole Reduction Catalyzed by an Enantiopure M_4L_6 Supramolecular Host

The reduction of oximes to hydroxylamines is of significant interest, as hydroxylamines are prevalent in pharmaceuticals and agrochemicals. [260] However, this process presents synthetic challenges, due to the low reactivity of the oxime C=N bond and the potential cleavage of the relatively weak N–O bond. [261]

Chiral boranes have been shown to produce mixtures of hydroxylamines and their over-reduction products. [261][262][263] In 2020, Cramer et al. introduced the first transition-metal-catalyzed asymmetric reduction of oximes, which was later followed by Ir- or Ni-catalyzed methods. [264][265][266][267] The limited number of reports on this topic has motivated the Toste group to investigate the reduction of oximes using an enantiopure coordination cage.

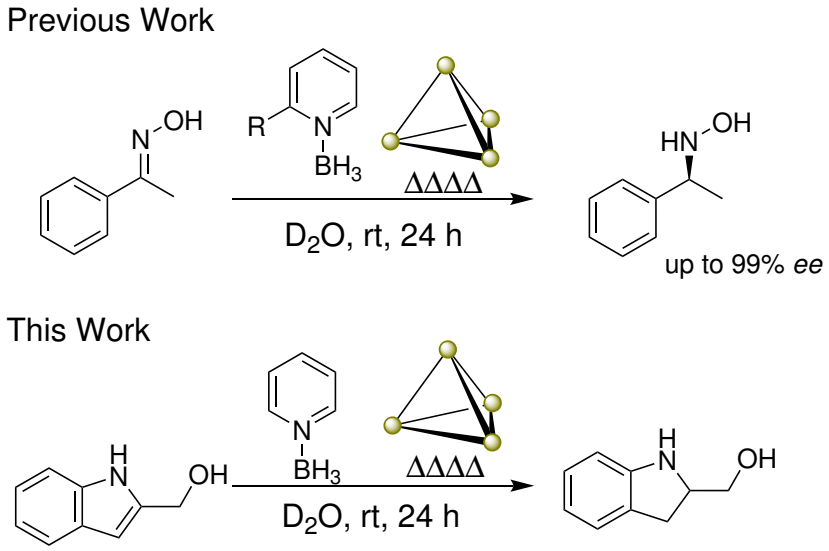

Figure 3.37. Shown oxime reduction to hydroxylamines and indole reduction to indolines by a enantiopure coordination cage with pyridine borane as reductant. [268]

Heafner et al. from the Toste group expanded the scope of substrates to include aliphatic oximes and *N*-containing heterocyclic oximes, achieving excellent enantioselectivities of up to 99% *ee* (see previous work in figure 3.37). Subsequently, the Toste group sought a new substrate class: the reduction of indoles to indolines. This reduction reaction is well-studied due to the use of indolines in pharmaceutical products. [269] Although existing methods achieve good diastereoselectivity or enantioselectivity, the Toste group hypothesized that an enantiopure host could mediate both enantioselective and diastereoselective reductions of indoles. [270][271] Preliminary results, however, showed that the enantiopure coordination cage provided diastereoselectivity but lacked enantioselectivity in the reduction of 2,3-methyl-indole. Consequently, my work focuses on enhancing the enantioselectivity of the reduction of indoles to indolines (see figure 3.37). [268]

In chapter 3.3.3 the indole reduction mediated by a supramolecular host and pyridine borane as reductant is described.

3.3.3 Substrate Synthesis for Enantioselective Reduction

As mentioned earlier, the previous study on the reduction of oximes to hydroxylamines, the starting material contained an OH functionality. Heafner et al. hypothesized that this group could act as a directing group for enantioselectivity. Consequently, an indole with an OH functionality in proximity to the chiral center, similar to the substrates used in the earlier oxime studies, was selected for further investigation (see a) in figure 3.38). Due to this, the synthesis of 2-(hydroxymethyl)indole was chosen as the starting point.

After 2-(hydroxymethyl)indole (**22**) was synthesized according to the procedure described in the literature, the racemic mixture product of the reduction of **22** to the respective indoline **23** was carried out (see b) in figure 3.38). Subsequently, the chiral HPLC analysis conditions have been optimized for a clear peak seperation within the chiral HPLC chromatogram (obtained chiral HPLC chromatogram shown in figure 4.229 in chapter 4.3.13)).

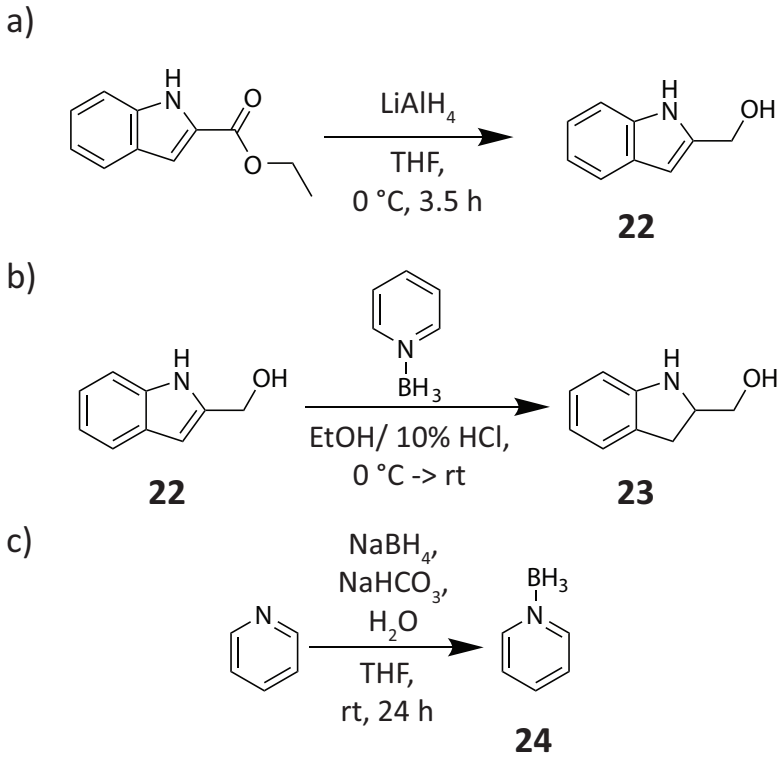

Figure 3.38. a) Synthesis of **22**, b) racemic reduction to **23** and c) synthesis of pyridine borane **24**. ^{1}H-NMR spectra in agreement with the literature. [272][273][274]. See figures 4.227, 4.228 and 4.230 in chapter 4.3.13).

Lastly, pyridine borane **24** was synthesized (see c) in figure 3.38). After the chiral HPLC conditions were optimized, the enantioselective reduction of **22**, mediated by an enantiopure supramolecular coordination cage, was examined in chapter 3.3.4.

3.3.4 Enantioselective Reduction of 2-(hydroxymethyl)indole

The enantioselective reduction of **22** was studied using $[Ga_4\mathbf{L^6}_6]^{12-}$ and pyridine borane as a stoichiometric reductant under aqueous and mild conditions (see a) figure 3.39).

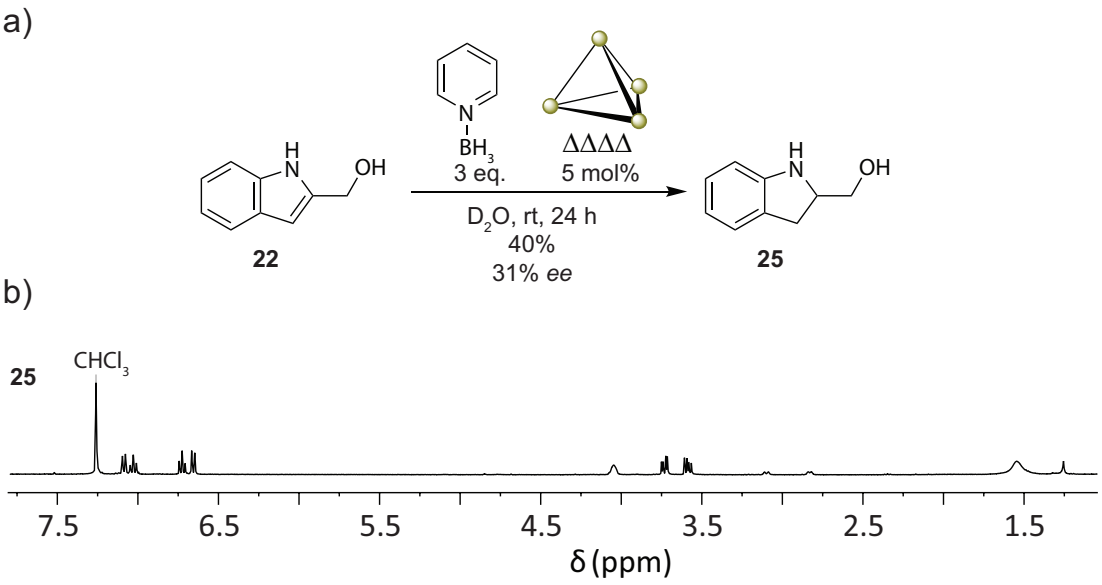

Figure 3.39. a) Enantioselective catalysis of reduction **22** to **25** mediated by $[Ga_4\mathbf{L^2}_6]^{12-}$ with pyridine borane. b) ^{1}H-NMR (500 MHz, 298 K, $CDCl_3$).

After 24 h, the reaction was quenched by adding PET, and the reaction mixture was extracted with $CDCl_3$. A 40% conversion was determined by ^{1}H-NMR spectroscopy using 1,3,5-trimethoxybenzene (TMB) as an internal standard. The reaction mixture was then purified by column chromatography (prep TLC; 3% MeOH/97% DCM) to isolate **25** (see b) figure 3.39).

In the literature, both metal-free and acid-mediated deuterium insertion into indoles have been reported; however, the acid-mediated process typically requires high temperatures of around 80 °C. [275][276] In contrast, the Toste group observed deuterium insertion into various indole derivatives at temperatures as low as rt and 45 °C using $[Ga_4\mathbf{L^5}_6]^{12-}$ or $[Ga_4\mathbf{L^6}_6]^{12-}$ in buffered D_2O, as suggested by ^{1}H-NMR analysis. [277][268] The Toste group suggests that deuterium insertion into indoles is part of the approximate reduction cycle (see figure 4.223 in chapter 4.3.13). Deuterium insertion was also observed for **25** and a 31% enantiomeric excess (*ee*) was determined by chiral HPLC analysis (see figure 4.231 in chapter 4.3.13). A control experiment using a blocked cavity of $[Ga_4\mathbf{L^6}_6]^{12-}$ with PET showed no conversion of indole (^{1}H-NMR analysis), demonstrating that the observed enantiomeric excess is a result of the cage effect. This finding highlights the potential of using enantiopure hosts for enantioselective catalysis.

Outlook

Further investigation should focus on increasing the enantioselectivity with the use of pyridine boranes, as their interaction with indole within the host is likely to be influenced by their steric and electronic properties. For further investigations, pyridine boranes were synthesized (see figure 3.40. For ^{1}H-NMR spectra see figures 4.232, 4.233, and 4.234 in chapter 4.3.13).

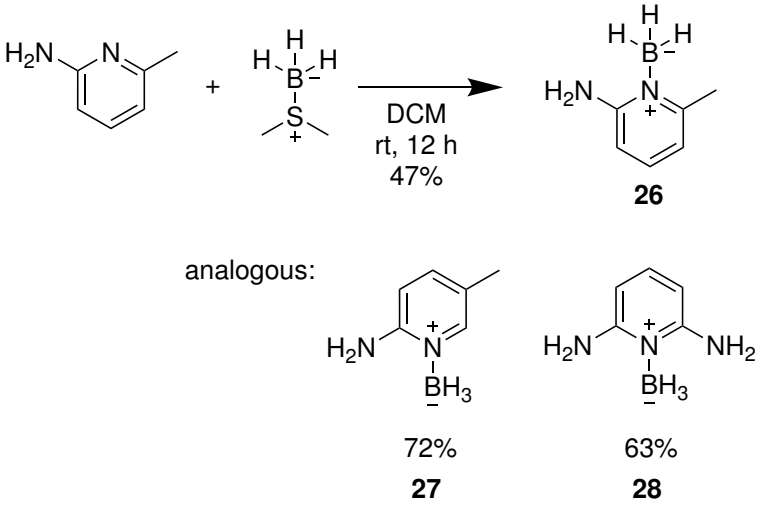

Figure 3.40. Synthesis of **26**, **27** and **28**. The respective yield is shown. The synthesis procedure has been modified from previous literature. [278]

Due to time constraints, the derivatives of pyridine borane were synthesized, but not screened for the enantioselective reduction of 2-(hydroxymethyl)indole.

4 Experimental Section

4.1 General Information

4.1.1 Theory for Binding Studies

This chapter gives a brief introduction to binding studies. Detailed information can be found in the literature. [246][280][281]
An essential question in supramolecular systems is determining stoichiometry, which can be a complex task. Historically, the Job plot has been a widely used method for determining the stoichiometry of complexes. [282] However, recent studies by researchers such as Jurczak and Thordarson have highlighted potential inaccuracies and misleading results associated with the Job plot. Both researchers recommend using residual distribution analysis to achieve more reliable stoichiometric determinations. [283][284]
In the past, experimental data were often plotted manually, leading to reliance on linear equations or expressions. Modern computational tools, however, have revolutionized this process by enabling automated calculations through corresponding algorithms. Thordarson and co-workers emphasize the value of freely accessible web portals for facilitating such analyses. One notable example is the *OpenDataFit* platform, developed by Thordarson and hosted on the website *supramolecular.org*, which includes the tool *BindFit*. [203] With *BindFit*, users can fit titration data using various host-guest binding models and employ the effective Nelder-Mead algorithm for optimization. [285] Additionally, Thordarson et al. advise fitting data across multiple models and comparing residuals to identify the most accurate binding model.

The benefits of free-access web portals are evident: they offer fast and convenient tools for analyzing data, saving significant time when data are pre-processed. These platforms also allow users to test and compare multiple binding models, enabling them to select the most appropriate approach for their specific systems.

NMR titration has notable advantages, including the ability to directly observe changes in host-guest interactions through NMR spectra. This method provides reliable and accurate results for binding studies. However, it does have limitations. NMR titration cannot directly provide thermodynamic parameters, which must instead be approximated using the Van't Hoff method. Additionally, NMR titration is limited to binding constants (K_a) up to approximately 10^5 M^{-1}. [246]

Association constant of a 1:1 equilibria

The equilibrium of a host-guest system HG with one guest G with one host H is described in equation 4.1.

$$\mathrm{H} + \mathrm{G} \overset{K_\mathrm{a}}{\rightleftarrows} \mathrm{HG} \tag{4.1}$$

Using the law of mass action, the association constant K_a can be determined with the respective concentrations (see equation 4.2)

$$K_\mathrm{a} = \frac{[\mathrm{HG}]}{[\mathrm{H}][\mathrm{G}]} \tag{4.2}$$

With the equation for the initial concentration for the host concentration $[\mathrm{H}]_0$ and initial guest concentration $[\mathrm{G}]_0$, the association constant can be further described as in equation 4.5.

$$[\mathrm{H}]_0 = [\mathrm{H}] + [\mathrm{HG}] \tag{4.3}$$

$$[\mathrm{G}]_0 = [\mathrm{G}] + [\mathrm{HG}] \tag{4.4}$$

$$K_\mathrm{a} = \frac{[\mathrm{HG}]}{([\mathrm{H}]_0 - [\mathrm{HG}]) \cdot ([\mathrm{G}]_0 - [\mathrm{HG}])} \tag{4.5}$$

In an NMR titration with fast exchange system as examined in this work, the chemical shift δ of HG appears as the weighted average of the chemical shift of free host and free HG complex. [HG] can be calculated with the observed chemical shift δ, initial chemical shift of host δ_H and chemical shift of host-guest complex δ_HG (see equation 4.8).

$$\delta = \delta_\mathrm{H}(1-\chi) + \delta_\mathrm{HG} \cdot \chi \tag{4.6}$$

$$\rightarrow [\mathrm{H}]_0 \cdot (\delta - \delta_\mathrm{H}) = [\mathrm{HG}] \cdot (\delta_\mathrm{HG} - \delta_\mathrm{H}) \tag{4.7}$$

$$\leftrightarrow [\mathrm{HG}] = \frac{[\mathrm{H}]_0(\delta - \delta_\mathrm{H})}{\delta_{\mathrm{HG}-\delta_\mathrm{H}}} \tag{4.8}$$

Hereby χ describes the ratio of complexed host at the equilibrium over the total host. In this work, the investigated host-guest systems are all in a fast exchange compared to the ^{1}H-NMR timescale. the binding constant or so-called association constant K_a was obtained obtained by plotting the Δ of the chemical shifts of the coordination cage proton signals against the guest concentration and the data was fitted by using the software *Bindfit*. [203][246] More detailed information and the determination of the association constant of a 1:2 or 2:1 host-guest equilibrium is described in the literature. [246]

4.1.2 Measuring instruments

Nuclear Magnetic Resonance Spectroscopy (NMR)

The NMR spectroscopic data was measured on the spectrometers Bruker AV 500 Avance NEO, AV 500 Avance III HD, AV 600 Avance III HD and AV 700 Avance III HD. The chemical shifts were calibrated on deuterated solvents as internal standard (CD_3CN 1.94 ppm, $CDCl_3$ 7.26 ppm, DMSO-d_6 2.50 ppm). For the ^{13}C NMR spectra the signals of the solvents were used as the internal standard (CD_3CN: 1.32, 118.26 ppm, $CDCl_3$: 77.00 ppm, DMSO$-d_6$: 39.52 ppm). The chemical shift δ is given in ppm, the coupling constants J in Hz. All spectra were recorded at 25 °C, if not mentioned otherwise. [286]

Electron Spray Ionisation Mass Spectrometry (ESI-MS)

The Mass Spectrometry (MS) measurements were on a Bruker ESI-TOF MS spectrometer including ESI-MS (positive / negative mode). The timsTOF consist of a time-of-flight analyser with upstream trapped ion mobility spectrometry. An Agilent ESI low concentration tuning mix has been used for calibration of tims and TOF units. Mass spectrometry data is given as mass/charge ratio (m/z) as well as the relative intensity with regard to the base peak (I = 100). [287][288]

Trapped Ion Mobility ESI Mass Spectrometry

Ion mobility measurements were performed on a Bruker timsTOF instrument combining a trapped ion mobility (TIMS) with a time-of-flight (TOF) mass spectrometer in one instrument.

After the generation of ions by electrospray ionization (ESI, analyte concentration: 0.07 mM, solvent: MeCN, capillary voltage: 2500 V, end plate offset voltage: 500 V, nebulizer gas pressure: 0.3 bar, dry gas flow rate: 3.0 l/min, dry temperature: 200 °C) the desired ions were orthogonally deflected into the TIMS cell consisting of an entrance funnel, the TIMS analyzer (carrier gas: N_2, temperature: 305 K, entrance pressure: 2,55 mbar, exit pressure: 0,89 mbar, IMS imeX ramp end: 1.6 1/K0, IMS imeX ramp start: 0.4 1/K0). As a result, the ions are stationary trapped. After accumulation (accumulation time: 80.0 ms), a stepwise reduction of the electric field strength leads to a release of ion packages separated by their mobility. After a subsequent focusing, the separated ions are transferred to the TOF-analyzer. [289][290][291]

UV-Vis

Standard UV-Vis measurment data was obtained from Agilent 8453 DAD UV-Visible Spectrophotometer, using standard quartz glass cuvettes suitable for the ultra-violet and visible light spectra. Thermal denaturation experiments and

thermal difference spectra were measured with the JASCO V-650 and JASCO V-750 UV-Vis Spectrophotometer, both equipped with the PAC-743 Automatic 6/8-position Peltier Cell Changer.

Cyclic Voltammetry

The CVs were measured with a Gamry Instruments Reference 600+ and integrated iR compensation using the positive feedback method. Samples were measured under inert atmosphere in a nitrogen glovebox at room temperature in dry solution of the respective solvent containing $n-Bu_4NPF_6$ (0.1 M). Electrochemical grade nBu_4NPF_6 was molten under vacuum prior to use. The setup consisted of a three- neck flask with a three-electrode setup containing a glassy carbon working electrode (GC: CH Instruments, ALS Japan; A = 7.1 mm^2), a platinum wire as a counter electrode, and an $Ag/AgNO_3$ reference electrode (0.01 M $AgNO_3$ in 0.1 M $n-Bu_4NPF_6$ in MeCN). The reference electrode was freshly prepared by using a fritted sample holder (Vycor glass), which was activated by storing it in a DMF solution for one night, followed by diluted HCl (1 M) for one night, dried and stored in DMF for at least one additional night. To the fritted sample holder was added a freshly prepared 0.01 M $AgNO_3$/0.1 M $n-Bu_4NPF_6$ solution in MeCN and a silver wire. The working electrode was cleaned before measuring a new compound by standard methods: washed with water, polished with an alox-slurry (0.05 μm), washed with millipore water, sonicated in HPLC grade EtOH for 3 minutes, rinsed with millipore water and HPLC grade EtOH, and dried. Initially a blank sample only containing electrolyte in the respective solvent (0.1 M) was measured and the potential cycled for 3-5 scans until a stable and clean potential was reached. Then the 3-neck cell was emptied and a specific amount of a compound was dissolved in 3 mL THF added and the CV measured. The system was furthermore (doubly) referenced internally by addition of ferrocene.

All CV in this thesis have been measured at rt (scanned towards anodic potentials) and with 200 mV/s (iR compensation = 259 Ohm) and referenced internally against ferrocene (**Fc**).

Circular Dichroism

Circular dichroism spectra were recorded on an Applied Photophysis qCD Chirascan CD spectrometer.

GPC

Recycling gel permeation chromatography was carried out using Japan Analytical Industry NEXT and LaboACE instruments equipped with JAIGEL 1-HH and 2-HH columns (20 mm × 600 mm) at a flow rate of 7 mL/min.

X-ray Analysis

Crystal preparation, measurement and refinement was performed by Dr. J. J. Holstein.

Bruker D8 venture (in-house) Single crystal X-ray diffraction data was collected on a *Bruker D8 venture* equipped with an *Incoatec microfocus* source (Iμs 3.0) using CuK_α or MoK_α radiation on a four axis κ-goniometer, equipped with an *Oxford Cryostream 800* and a *Photon II* detector.

P11 DESY (synchrotron) Single crystal X-ray diffraction data was collected at macromolecular beamline *P11*, *Petra III*, *DESY*, Germany. Samples were mounted using the *Stäubli TX60L* robotic arm. A wavelength of $\lambda = 0.6889$ Å was chosen using a liquid N_2 cooled double crystal monochromator. Single crystal X-ray diffraction data was collected at 80(2) K on a single axis goniometer, equipped with an *Oxford Cryostream 800* a *Pilatus 6M fast*.

4.2 General Synthesis

Squaramide-based Ligands

4.2.1 Synthesis of Ligand L^2

Synthesis of L^2

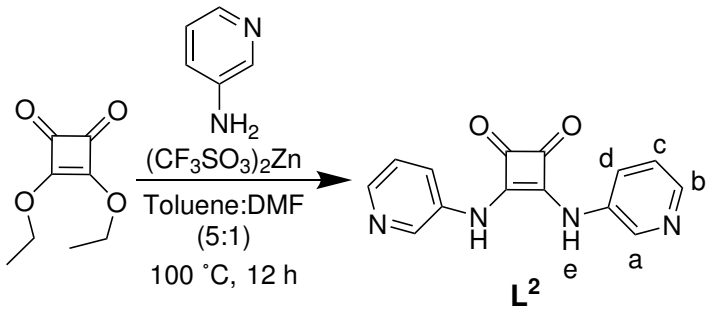

Figure 4.1. Synthesis of $\mathbf{L^2}$.

3,4-diethoxycyclobut-3-ene-1,2-dione (500.00 mg, 434.78 μL, 2.94 mmol, 1.0 eq.) was added to pyridin-3-amine (594.58 mg, 6.32 mmol, 2.2 eq.), $(CF_3SO_3)_2Zn$ (213.62 mg, 0.59 mmol, 0.2 eq.) and then dissolved in toluene:DMF (5:1). The mixture was stirred and heated at 100 °C for 12 h. The suspension was filtered, washed with toluene and CH_3CN and then the residual solvent was removed *in vacuo*. The crude product was purified by gel permeation chromatography (DMF). The product $\mathbf{L^2}$ (112.0 mg, 0.42 mmol, 14 %) was obtained as a yellow solid.

^{1}H-NMR (600 MHz, 298 K, DMSO$-d_6$): δ (ppm)= 10.08 (s, 1H, e), 8.62 (d, $J = 2.7$ Hz, 1H, a), 8.31 (dd, $J = 4.7, 1.4$ Hz, 1H, b), 7.93 (ddd, $J = 8.3, 2.8, 1.4$ Hz, 1H, d), 7.42 (dd, $J = 8.3, 4.7$ Hz, 1H, c).

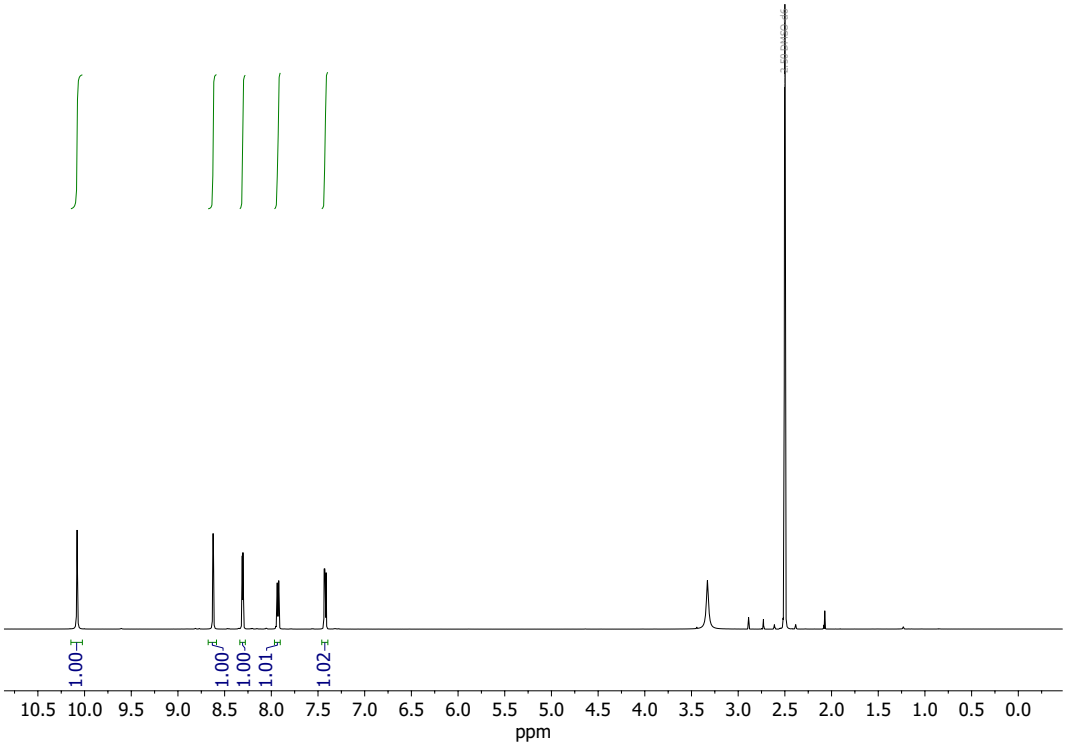

Figure 4.2. ^{1}H-NMR Spectrum (600 MHz, 298 K, DMSO$-d_6$) of **L^2**.

^{13}C-NMR (151 MHz, 298 K, DMSO$-d_6$): δ (ppm)= 182.31, 165.99, 144.35, 140.39, 135.16, 125.89, 123.98.

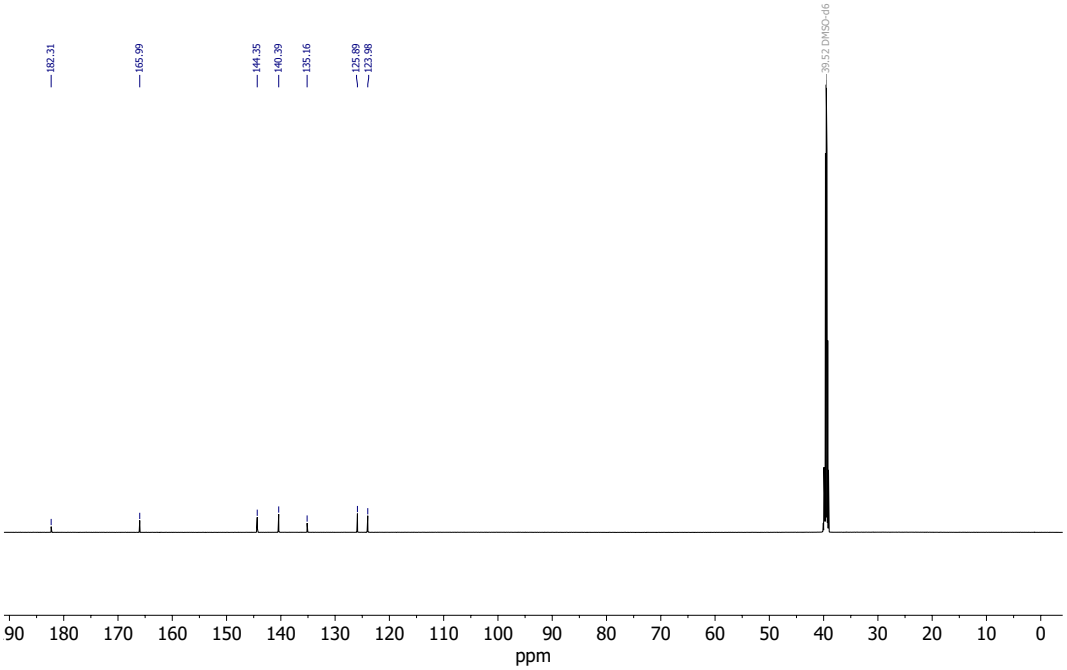

Figure 4.3. ^{13}C-NMR Spectrum (151 MHz, 298 K, DMSO$-d_6$) of **L^2**.

Synthesis of L^2

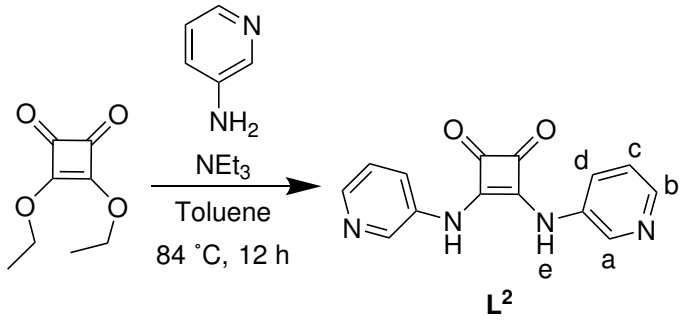

Figure 4.4. Synthesis of L^2.

3,4-diethoxycyclobut-3-ene-1,2-dione (1.00 g, 869.57 μL, 5.88 mmol, 1.0 eq.) was added to pyridin-3-amine (1.27 g, 13.52 mmol, 2.3 eq.), NEt_3 (3.01 mL, 23.51 mmol, 4.0 eq.) and then dissolved in toluene. The mixture was stirred and heated at 84 °C for 12 h. The suspension was filtered and washed with acetone then the residual solvent was removed *in vacuo*. The product $\mathbf{L^2}$ (1.32 g, 4.95 mmol, 84,3 %) was obtained as a yellow solid.

^{1}H-NMR (600 MHz, 298 K, DMSO$-d_6$): δ (ppm)= 10.07 (s, 1H, e), 8.62 (dd, J = 2.7, 0.7 Hz, 1H, a), 8.31 (dd, J = 4.7, 1.4 Hz, 1H, b), 7.92 (ddd, J = 8.3, 2.8, 1.4 Hz, 1H, c), 7.42 (ddd, J = 8.3, 4.7, 0.8 Hz, 1H, d).

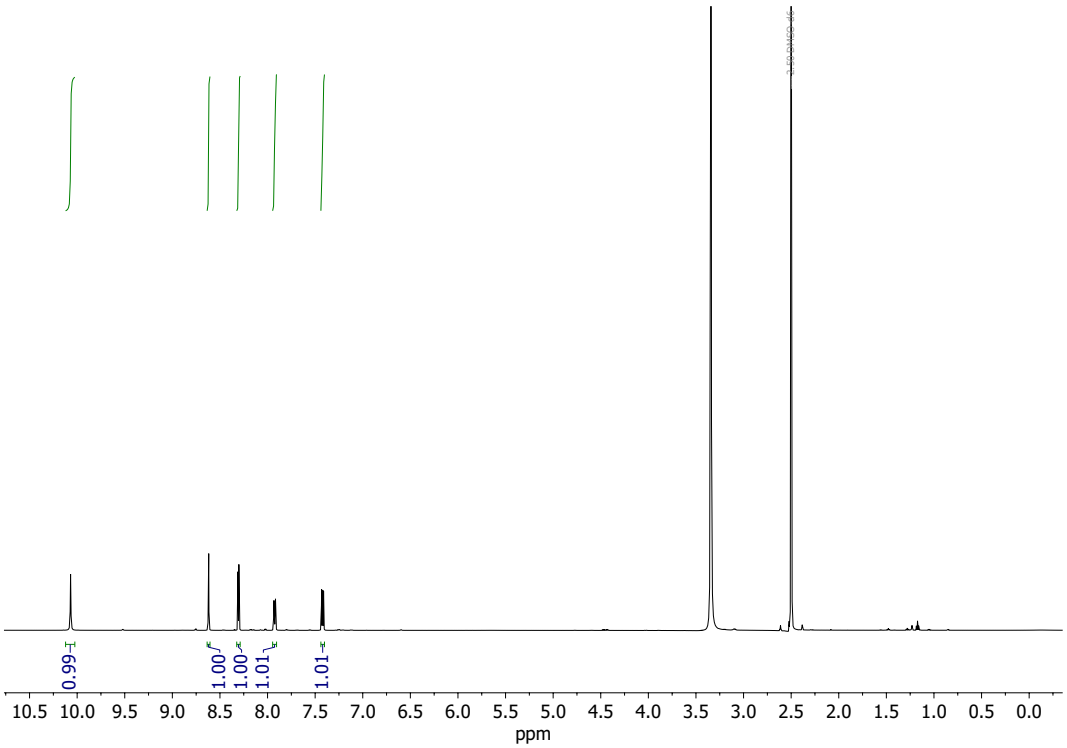

Figure 4.5. ^{1}H-NMR Spectrum (600 MHz, 298 K, DMSO$-d_6$) of **L^{2}**.

^{13}C-NMR (151 MHz, 298 K, DMSO$-d_6$): δ (ppm)= 182.34, 166.01, 144.38, 140.42, 135.17, 125.91, 124.00.

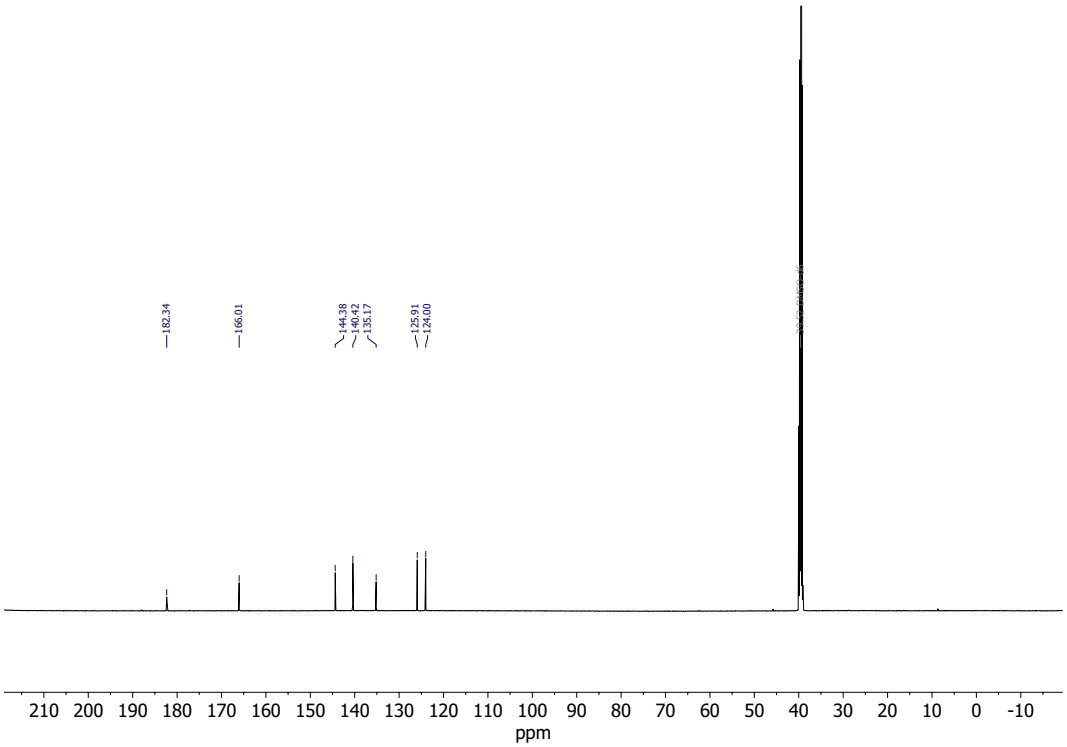

Figure 4.6. ^{13}C-NMR Spectrum (151 MHz, 298 K, DMSO$-d_6$) of **L^{2}**.

4.2.2 Synthesis of derivatives of Ligand L^2

Synthesis of L^{2ph}

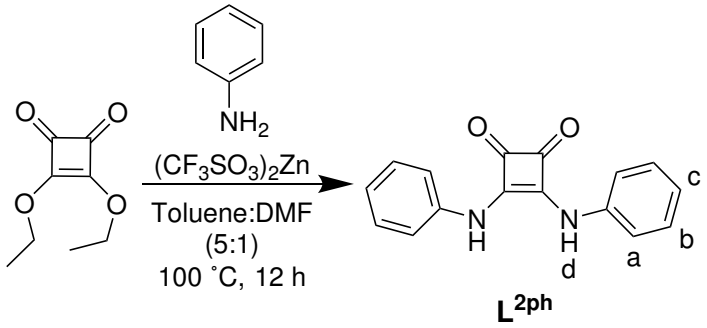

Figure 4.7. Synthesis of $\mathbf{L^{2ph}}$.

3,4-diethoxycyclobut-3-ene-1,2-dione (1.00 g, 869.57 μL, 5.88 mmol, 1.0 eq.) was added to aniline (1.18 g, 12.63 mmol, 2.15 eq.), $(CF_3SO_3)_2Zn$ (363.51 mg, 1.18 mmol, 0.2 eq.) and then dissolved in toluene:DMF (5:1). The mixture was stirred and heated at 100 °C for 12 h. The suspension was filtered and washed with toluene and CH_3CN and then the residual solvent was removed *in vacuo*. The product $\mathbf{L^{2ph}}$ (667.0 mg, 2.52 mmol, 43 %) was obtained as a yellow solid.

^{1}H-NMR (600 MHz, 298 K, DMSO$-d_6$): δ (ppm)= 9.88 (s, 1H, d), 7.50 (dt, J= 7.7 Hz, 1.1 Hz, 2H, a), 7.39 (dd, J= 8.6, 7.3 Hz, 2H, b), 7.11 – 7.08 (m, 1H, c).

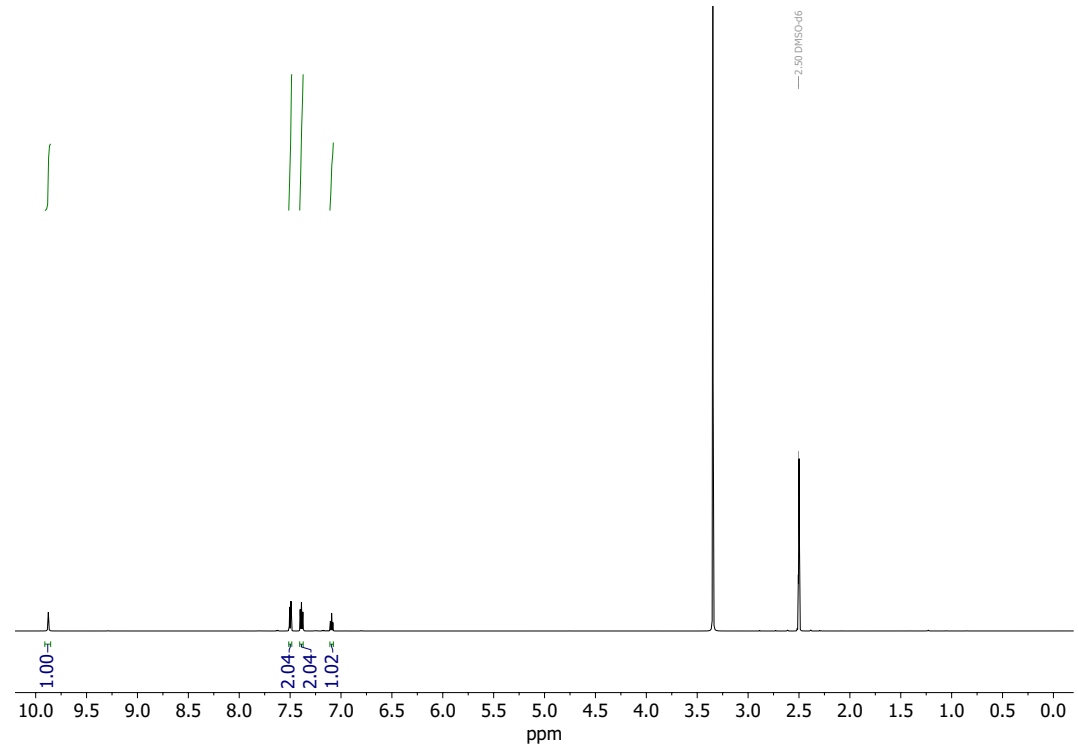

Figure 4.8. ^{1}H-NMR Spectrum (600 MHz, 298 K, DMSO$-d_6$) of **L^{2ph}**.

^{13}C-NMR (151 MHz, 298 K, DMSO$-d_6$): δ (ppm)= 181.61, 165.66, 138.54, 129.43, 123.34, 118.49.

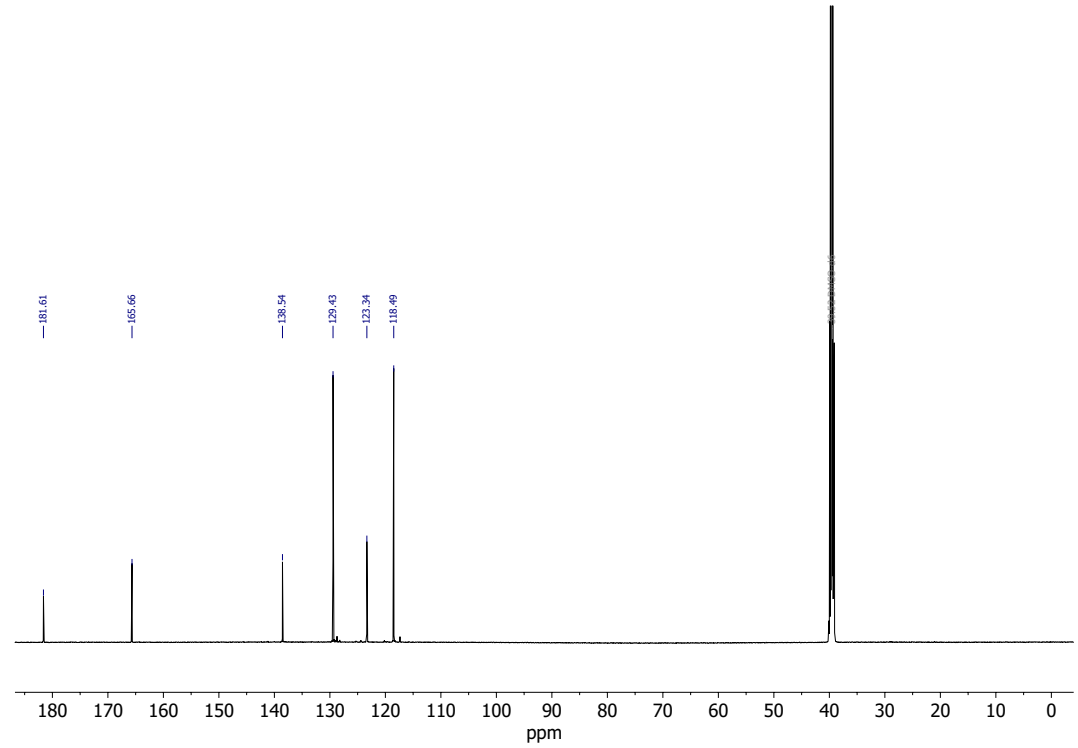

Figure 4.9. ^{13}C-NMR Spectrum (151 MHz, 298 K, DMSO$-d_6$) of ligand **L^{2ph}**.

Synthesis of L^{2f}

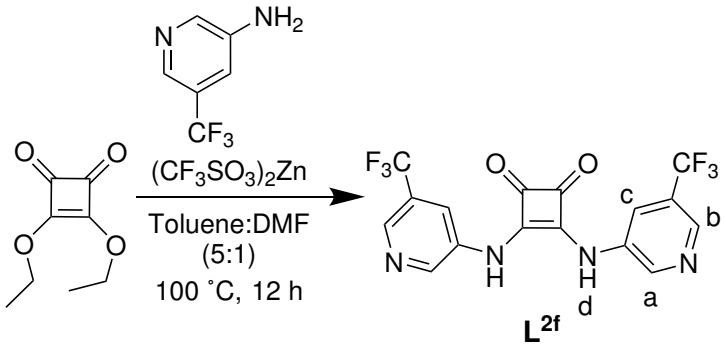

Figure 4.10. Synthesis of $\mathbf{L^{2f}}$.

3,4-diethoxycyclobut-3-ene-1,2-dione (1.00 g, 869.57 μL 5.88 mmol, 1.0 eq.) was added to 5-(trifluoromethyl)pyridin-3-amine (2.00 g, 12.34 mmol, 2.1 eq.), $(CF_3SO_3)_2Zn$ (427.24 mg, 1.18 mmol, 0.2 eq.) and then dissolved in toluene:DMF (5:1). The mixture was stirred and heated at 100 °C for 12 h. The suspension was filtered and washed with toluene and CH_3CN and then the residual solvent was removed *in vacuo*. The product $\mathbf{L^{2f}}$ (164.44 mg,0.41 mmol, 7 %) was obtained as a yellow solid.

^{1}H-NMR (600 MHz, 298 K, DMSO$-d_6$): δ (ppm)= 10.46 (s, 1H, d), 8.79 (d, J = 2.5 Hz, 1H, a), 8.68 – 8.65 (m, 1H, b), 8.29 (t, J = 2.3 Hz, 1H, c).

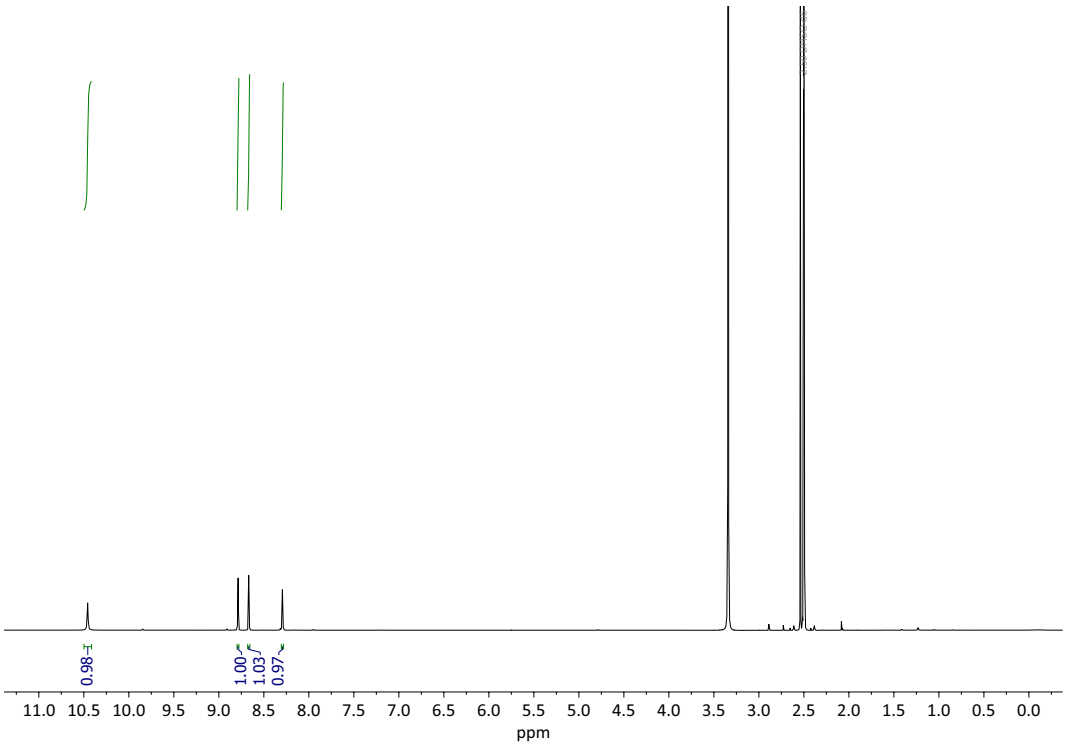

Figure 4.11. ^{1}H-NMR Spectrum (600 MHz, 298 K, DMSO$-d_6$) of **L^{2f}**.

^{13}C-NMR (151 MHz, 298 K, DMSO$-d_6$): δ (ppm)= 183.33, 166.05, 144.23, 140.26, 135.37, 125.52, 124.33, 122.52.

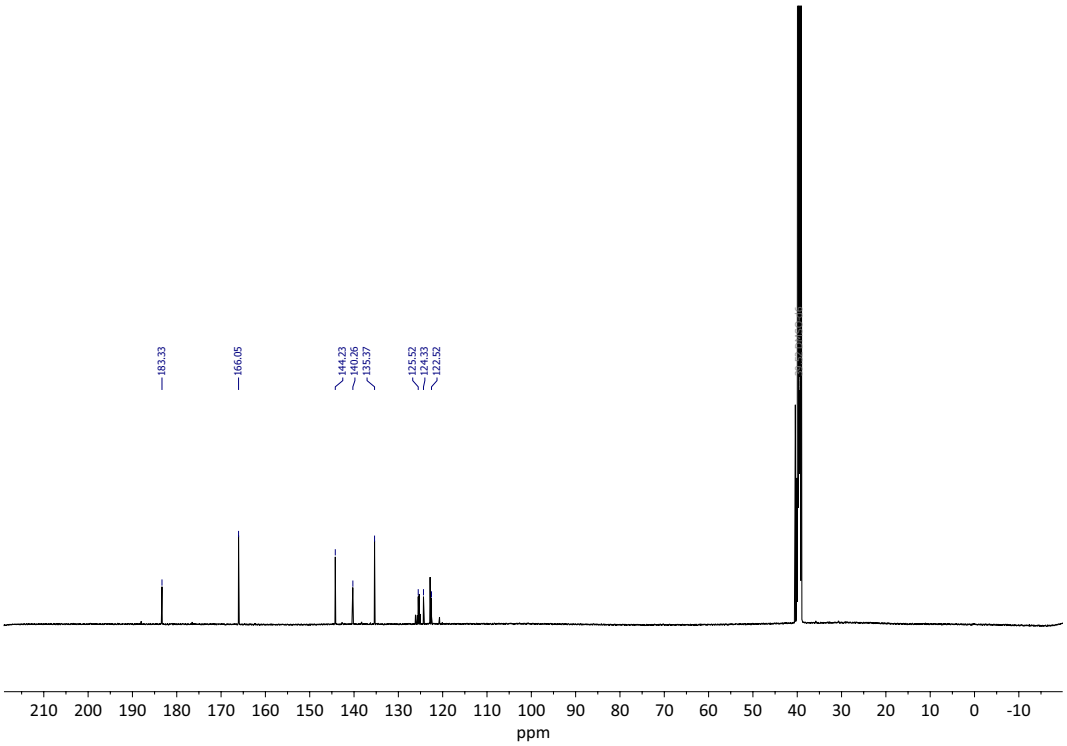

Figure 4.12. ^{13}C-NMR Spectrum (151 MHz, 298 K, DMSO$-d_6$) of **L^{2f}**.

Synthesis of L^{2L}

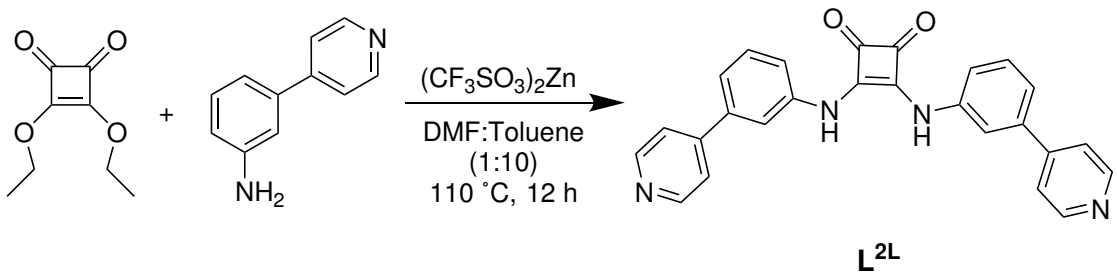

Figure 4.13. Synthesis of L^{2L}.

3,4-diethoxycyclobut-3-ene-1,2-dione (100.00 mg, 0.59 mmol, 1.0 eq.) was added to 3-(pyridin-4-yl)aniline (210.06 mg, 1.23 mmol, 2.1 eq.), $(CF_3SO_3)_2Zn$ (21.36 mg, 0.06 mmol, 0.1 eq.) and then dissolved in toluene:DMF (10:1). The mixture was stirred and heated at 110 °C for 12 h. The suspension was filtered and washed with toluene and CH_3CN and then the residual solvent was removed *in vacuo*. The product was not obtained.

4.2.3 Synthesis of Ligand L^{2peg}

Synthesis of P0

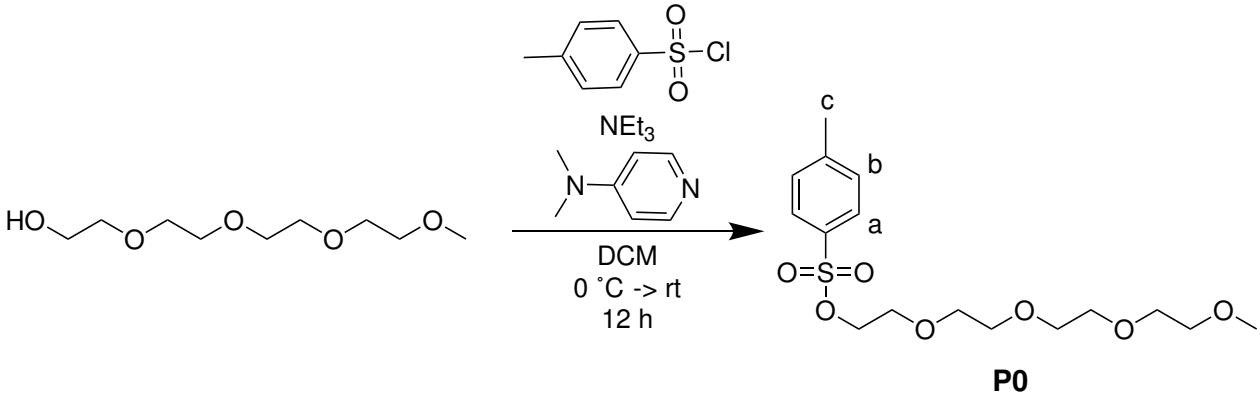

Figure 4.14. Synthesis of **P0**.

2,5,8,11-tetraoxatridecan-13-ol (5.00 g, 24.01 mmol, 1.0 eq.) was mixed with NEt_3 (7.29 g, 726.00 μL, 72.03 mmol, 3.0 eq.) in DCM at rt. Then DMAP (293.32 mg, 2.40 mmol, 0.1 eq.) and 4-methylbenzenesulfonyl chloride (2.75 g, 14.51 mmol, 0.6 eq.) were added dropwise to the solution at 0 °C. After warming to r, the resulting reaction mixture was stirred for 12 h. The solution was washed with 1 M HCl and H_2O. After drying over $MgSO_4$, filtration and removing the solvent *in vacuo*, the product **P0** (6.60 g, 18.21 mmol, 76 %) was obtained as a colorless viscous liquid.

^{1}H-NMR (500 MHz, 298 K, CD_3CN): δ (ppm)= 7.81 – 7.76 (m, 2H, a), 7.46 – 7.42 (m, 2H, b), 4.13 – 4.09 (m, 2H), 3.61 – 3.59 (m, 2H), 3.54 – 3.50 (m, 6H), 3.48 (s, 4H), 3.47 – 3.44 (m, 2H), 3.28 (s, 3H), 2.44 (s, 3H, c).

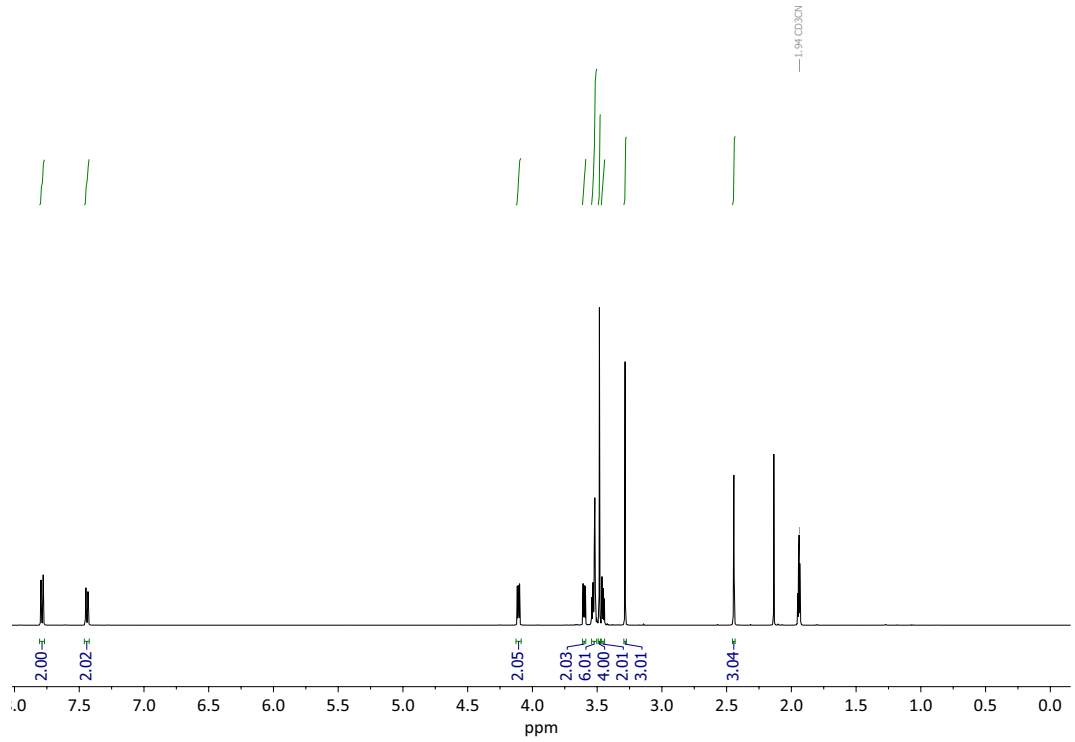

Figure 4.15. ^{1}H-NMR Spectrum (500 MHz, 298 K, CD_3CN) of **P0**.

^{13}C-NMR (151 MHz, 298 K, CD_3CN): δ (ppm)= 144.60, 131.99, 129.22, 126.98, 70.77, 69.35, 69.34, 69.28, 69.17, 69.15, 67.37, 57.07, 19.83.

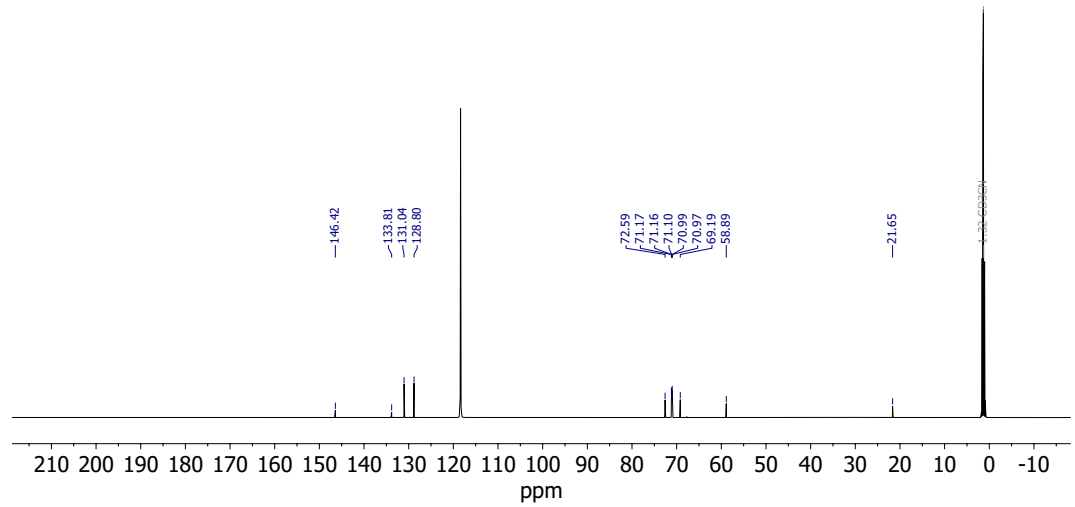

Figure 4.16. ^{13}C-NMR Spectrum (151 MHz, 298 K, CD_3CN) of **P0**.

Synthesis of P1

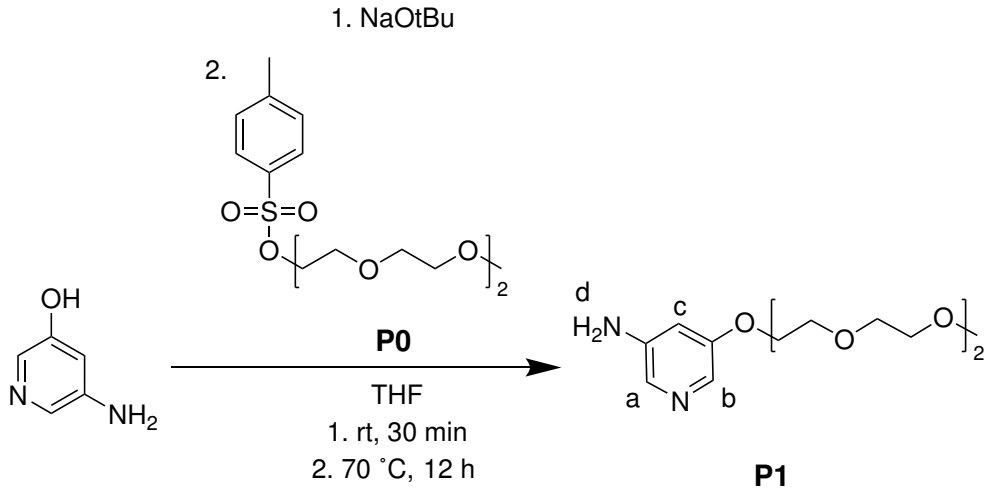

Figure 4.17. Synthesis of **P1**.

5-aminopyridin-3-ol (200.00 mg, 1.82 mmol, 1.0 eq.) was dissolved in THF and stirred with NaOtBu (349.10 mg, 3.63 mmol, 2.0 eq.) at rt for 30 min. **P0** (987.42 mg, 2.72 mmol, 1.5 eq.) was added to the suspension and stirred at 70 °C for 12 h. The suspension was filtered and then the solvent was removed *in vacuo* and the residue was purified by means of column chromatography (SiO_2, MeOH:DCM 1:99 → 13:87). The product **P1** (310.00 mg, 1.03 mmol, 57 %) was obtained as a viscous liquid.

^{1}H-NMR (500 MHz, 298 K, CD_3CN): δ (ppm)= 7.54 (d, J = 2.1 Hz, 1H, b), 7.45 (d, J = 2.5 Hz, 1H, a), 6.49 (t, J = 2.4 Hz, 1H, c), 5.29 (s, 2H, d), 4.05 – 4.01 (m, 2H), 3.73 – 3.70 (m, 2H), 3.59 – 3.56 (m, 2H), 3.54 – 3.49 (m, 8H), 3.43 – 3.41 (m, 2H), 3.23 (s, 3H).

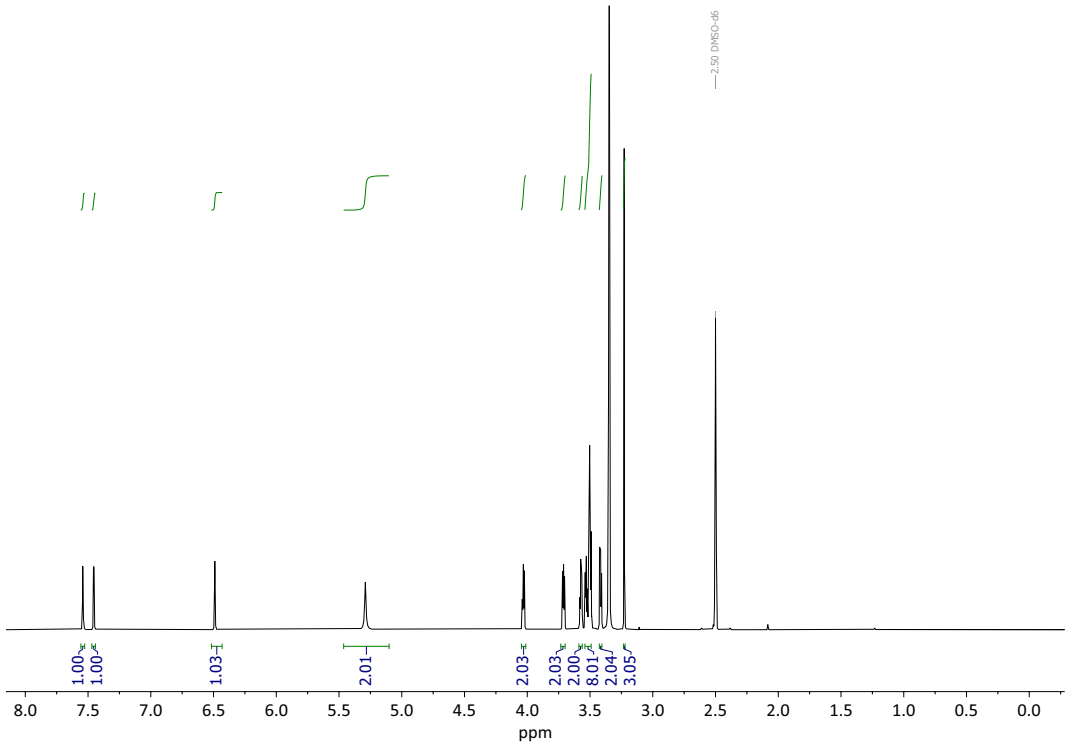

Figure 4.18. ^{1}H-NMR Spectrum (500 MHz, 298 K, CD_3CN) of **P1**.

^{13}C-NMR (151 MHz, 298 K, CD_3CN): δ (ppm)= 155.29, 145.76, 129.32, 124.96, 105.22, 71.28, 69.93, 69.83, 69.80, 69.78, 69.58, 68.88, 67.04, 58.05.

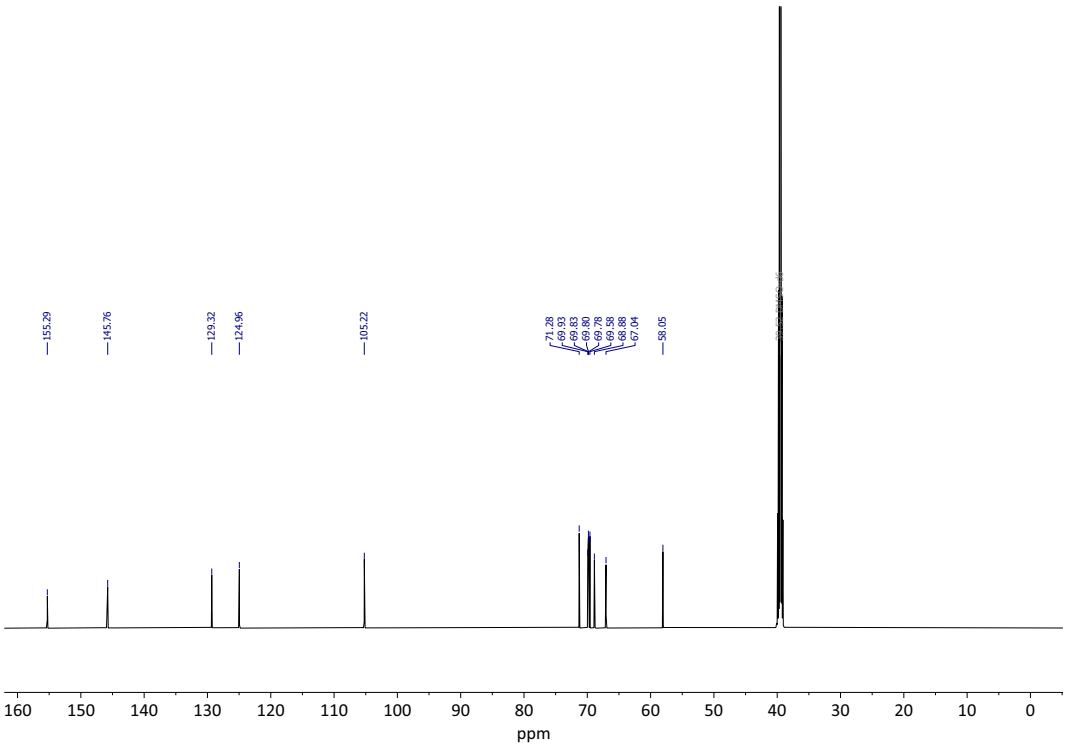

Figure 4.19. ^{13}C-NMR Spectrum (151 MHz, 298 K, DMSO$-d_6$) of ligand **P1**.

Synthesis of L^{2peg}

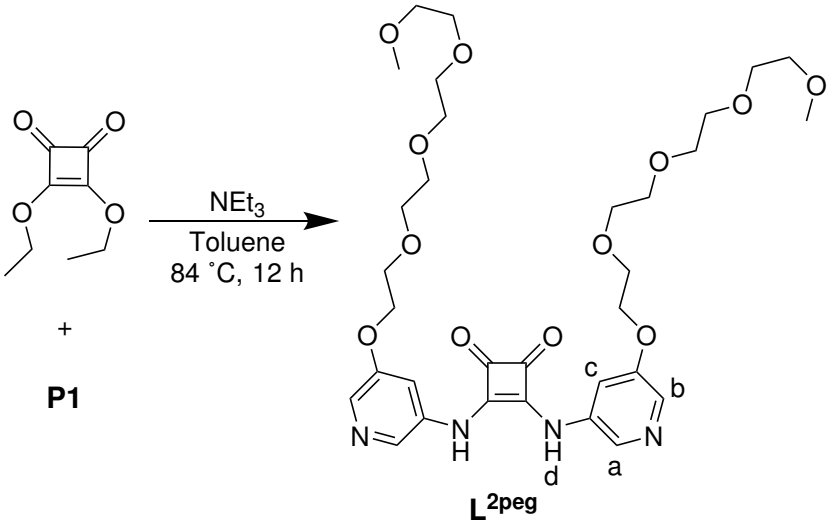

Figure 4.20. Synthesis of $\mathbf{L^{2peg}}$.

3,4-diethoxycyclobut-3-ene-1,2-dione (72.17 μL, 0.49 mmol, 1.0 eq.) was added to **P1** (306.66 mg, 1.02 mmol, 2.1 eq.), (NEt_3 (3.5 mL, 27.31 mmol, 56.0 eq.) and then dissolved in toluene. The mixture was stirred and heated at 84 °C for 12 h. The residue was purified by means of column chromatography (SiO_2, MeOH:DCM 5:95 $\rightarrow$ 20:80). The product $\mathbf{L^{2peg}}$ (166.00 mg, 0.24 mmol, 50 %) was obtained as a brown viscous liquid.

^{1}H-NMR (500 MHz, 298 K, CD_3CN): δ (ppm) = 10.41 (s, 1H, d), 8.28 (d, J = 2.2 Hz, 1H, a), 7.99 (d, J = 2.5 Hz, 1H, b), 7.81 (t, J = 2.3 Hz, 1H, c), 4.24 – 4.16 (m, 2H), 3.84 – 3.81 (m, 2H), 3.67 – 3.64 (m, 2H), 3.61 – 3.58 (m, 2H), 3.56 – 3.54 (m, 6H), 3.47 – 3.45 (m, 2H), 3.27 (s, 3H).

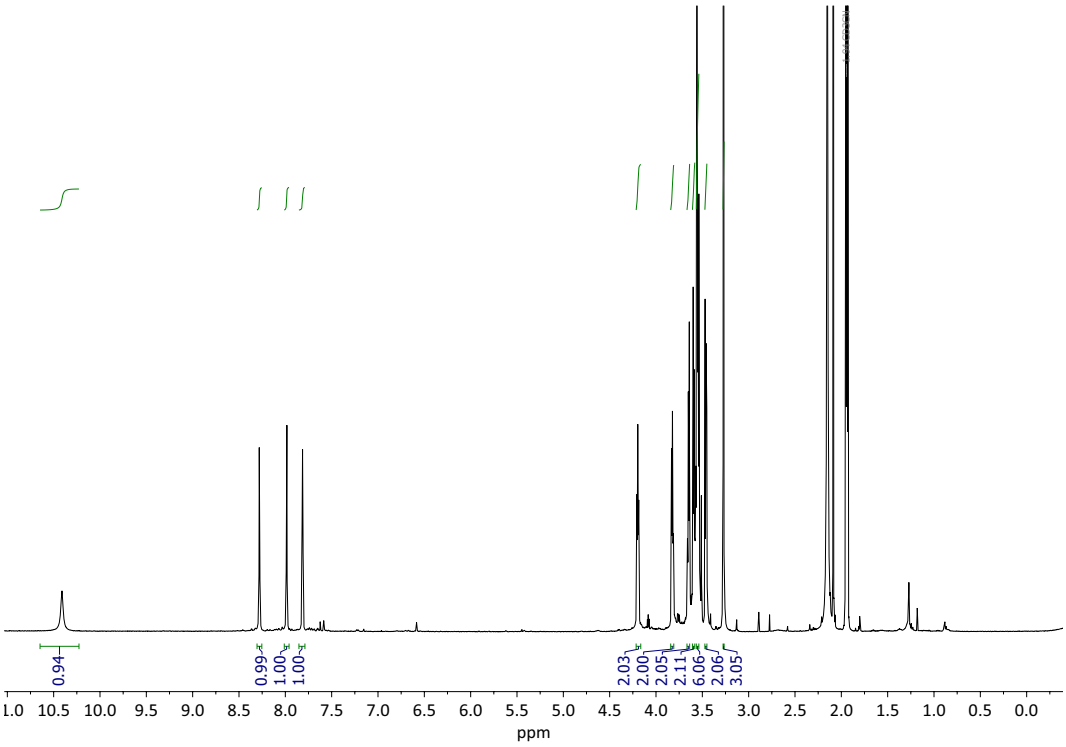

Figure 4.21. ^{1}H-NMR Spectrum (500 MHz, 298 K, CD_3CN) of $\mathbf{L^{2peg}}$.

^{13}C-NMR (151 MHz, 298 K, DMSO$-d_6$): δ (ppm) = 181.79, 166.23, 155.08, 136.17, 132.28, 132.11, 110.94, 71.29, 69.94, 69.84, 69.80, 69.78, 69.59, 68.68, 67.69, 58.06.

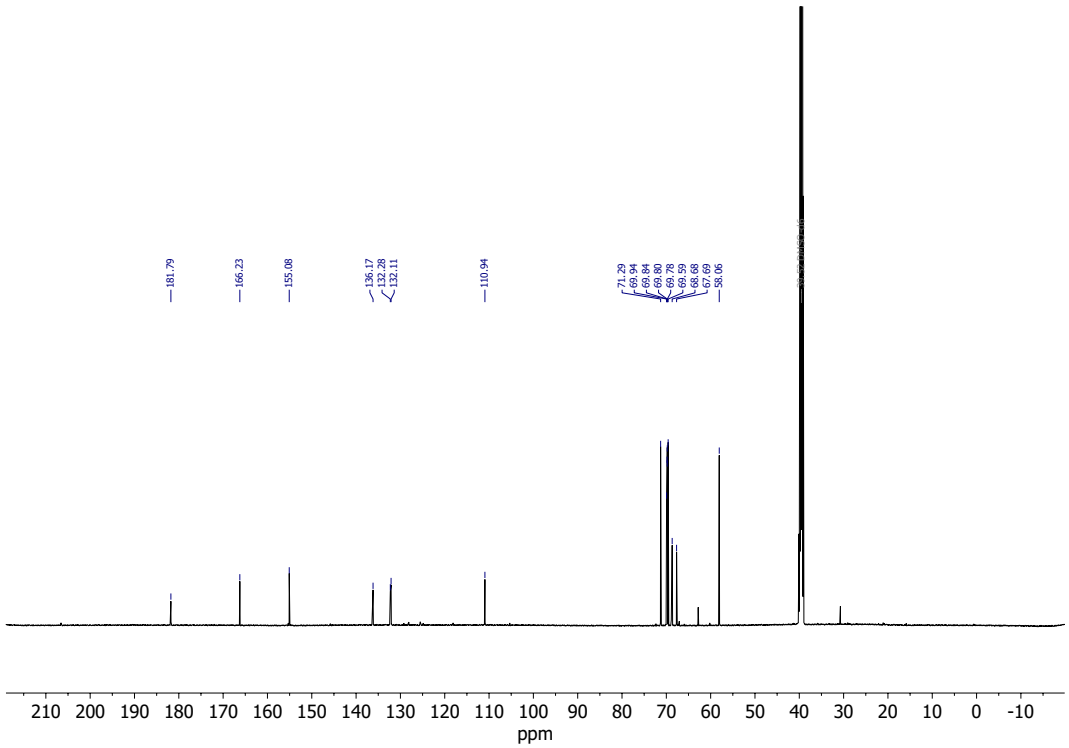

Figure 4.22. ^{13}C-NMR Spectrum (151 MHz, 298 K, DMSO$-d_6$) of $\mathbf{L^{2peg}}$.

4.2.4 Synthesis of Ligand L[1]

Synthesis of P2

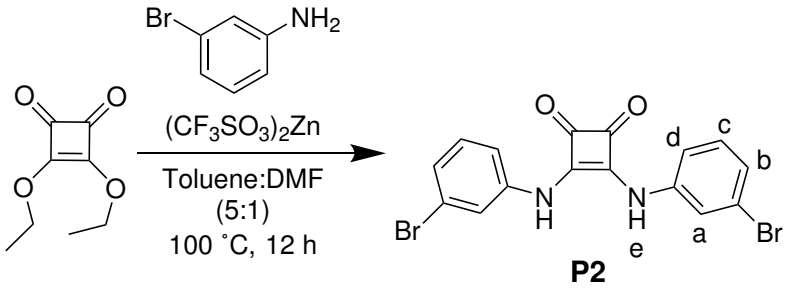

Figure 4.23. Synthesis of **P2**.

3,4-diethoxycyclobut-3-ene-1,2-dione (500.00 mg, 2.94 mmol, 1.0 eq.) was added to 3-bromoaniline (1.06 g, 6.17 mmol, 2.1 eq.), $(CF_3SO_3)_2Zn$ (213.62 mg, 0.59 mmol, 0.2 eq.) and then dissolved in toluene:DMF (5:1). The mixture was stirred at 100 °C for 12 h. The suspension was filtered and washed with toluene and CH_3CN and then the residual solvent was removed *in vacuo*. The product **P2** (1.11 g, 2.63 mmol, 90 %) was obtained as a grey solid.

^{1}H-NMR (600 MHz, 298 K, DMSO$-d_6$): δ (ppm) = 11.62 (s, 1H, e), 8.09 (t, J = 1.9 Hz, 1H, b), 7.76 (m, 1H, a), 7.38 – 7.29 (m, 2H, c, d).

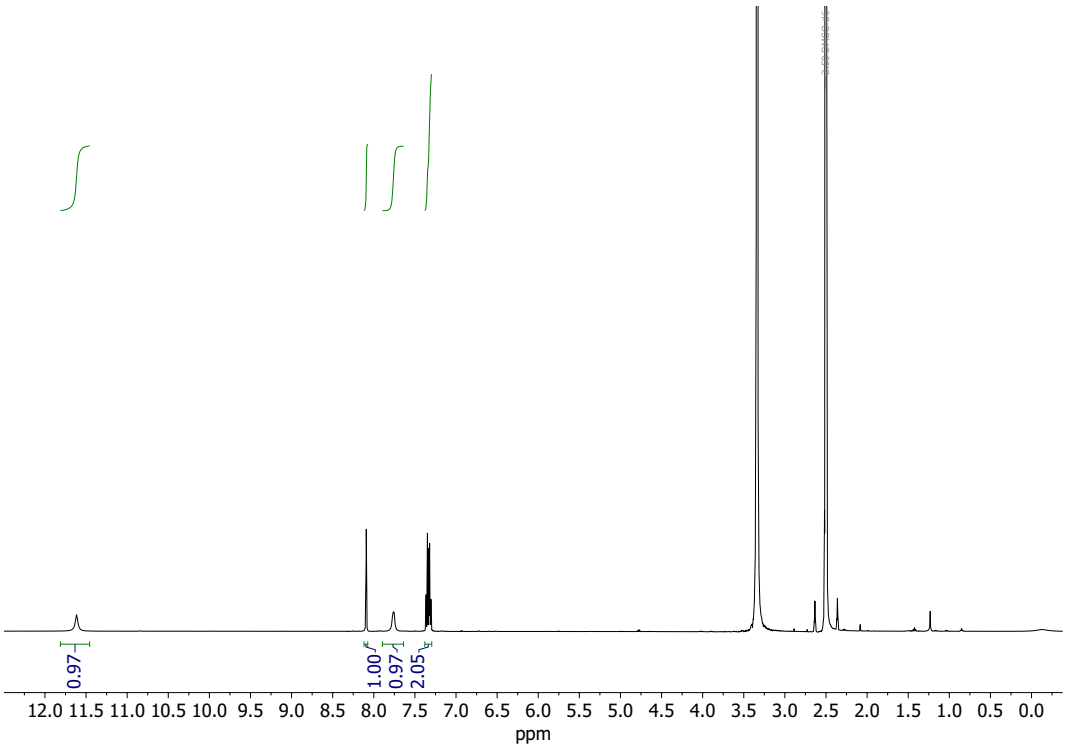

Figure 4.24. ^{1}H-NMR Spectrum (600 MHz, 298 K, DMSO$-d_6$) of **P2**.

^{13}C-NMR (151 MHz, 298 K, DMSO$-d_6$): δ (ppm) = 177.93, 139.98, 131.63, 127.52, 122.90, 122.88, 122.47, 119.22.

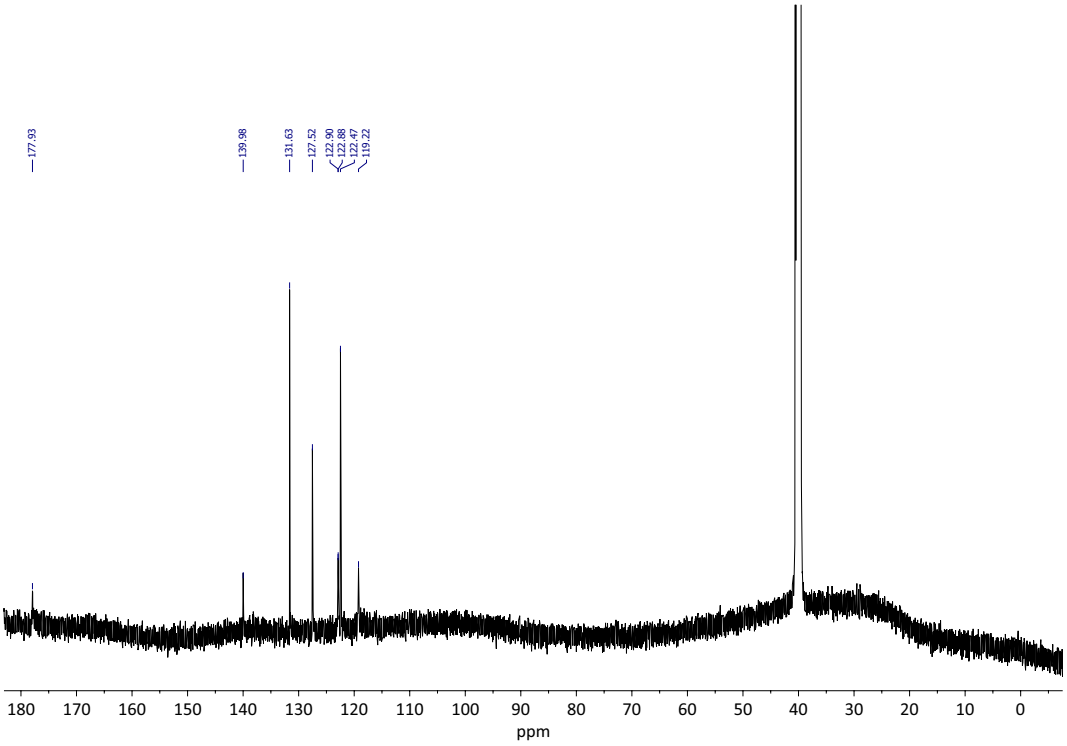

Figure 4.25. ^{13}C-NMR Spectrum (151 MHz, 298 K, DMSO$-d_6$) of **P2**.

Synthesis of P2

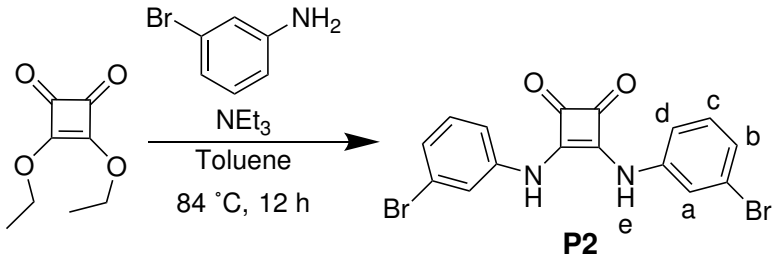

Figure 4.26. Synthesis of **P2**.

3,4-diethoxycyclobut-3-ene-1,2-dione (1.00 g, 869.57 μL, 5.88 mmol, 1.0 eq.) was added to 3-bromoaniline (2.33 g, 13.52 mmol, 2.3 eq.), (NEt_3 (3.01 mL, 23.51 mmol, 4.0 eq.) and then dissolved in toluene. The mixture was stirred and heated at 84 °C for 12 h. The suspension was filtered and washed with acetone then the residual solvent was removed *in vacuo*. The product **P2** (521.0 mg, 4.95 mmol, 21 %) was obtained as a grey solid.

^{1}H-NMR (600 MHz, 298 K, DMSO$-d_6$): δ (ppm) = 10.01 (s, 1H, e), 7.79 (t, J = 1.9 Hz, 1H, a), 7.37 – 7.30 (m, 2H, c, d), 7.26 (dt, J = 7.3, 1.7 Hz, 1H, b).

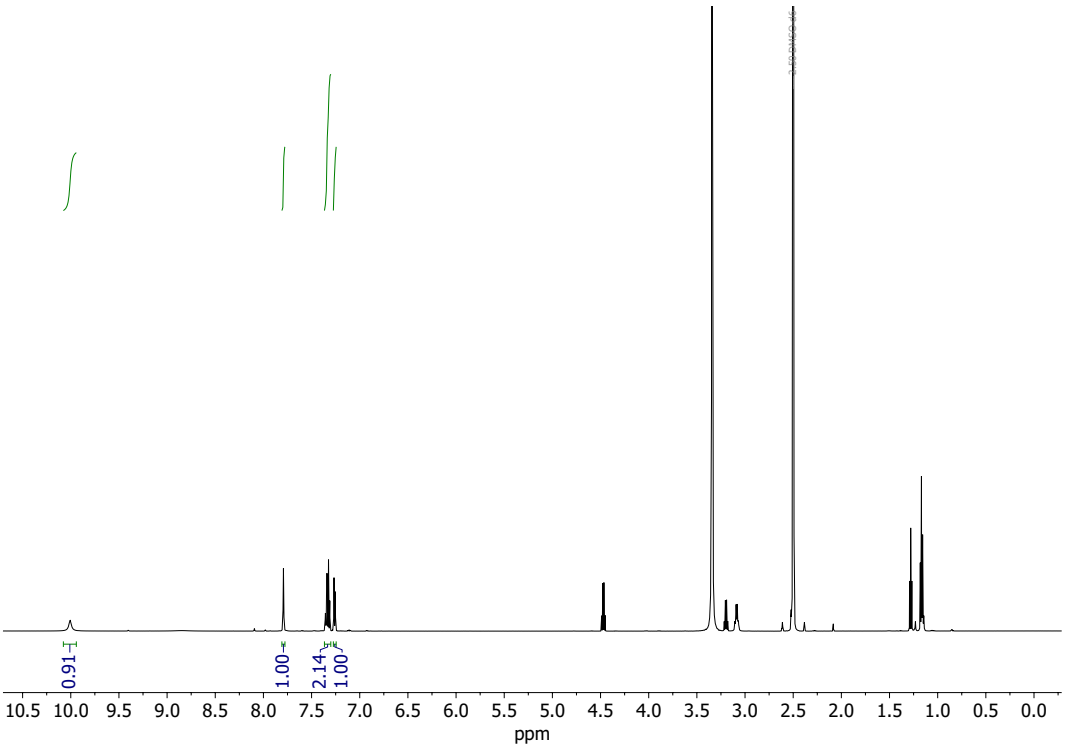

Figure 4.27. ^{1}H-NMR Spectrum (600 MHz, 298 K, DMSO$-d_6$) of **P2**.

^{13}C-NMR (151 MHz, 298 K, DMSO$-d_6$): δ (ppm) = 182.14, 165.61, 140.02, 131.29, 125.93, 122.20, 121.23, 117.55.

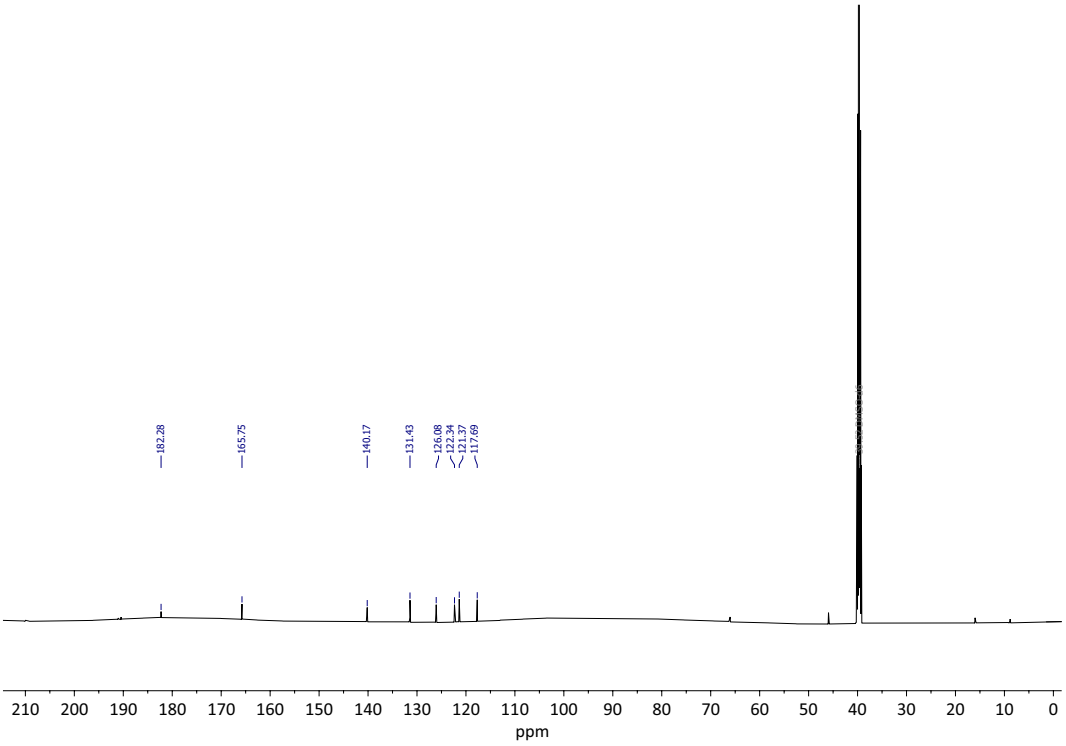

Figure 4.28. ^{13}C-NMR Spectrum (151 MHz, 298 K, DMSO$-d_6$) of **P2**.

Synthesis of L^1

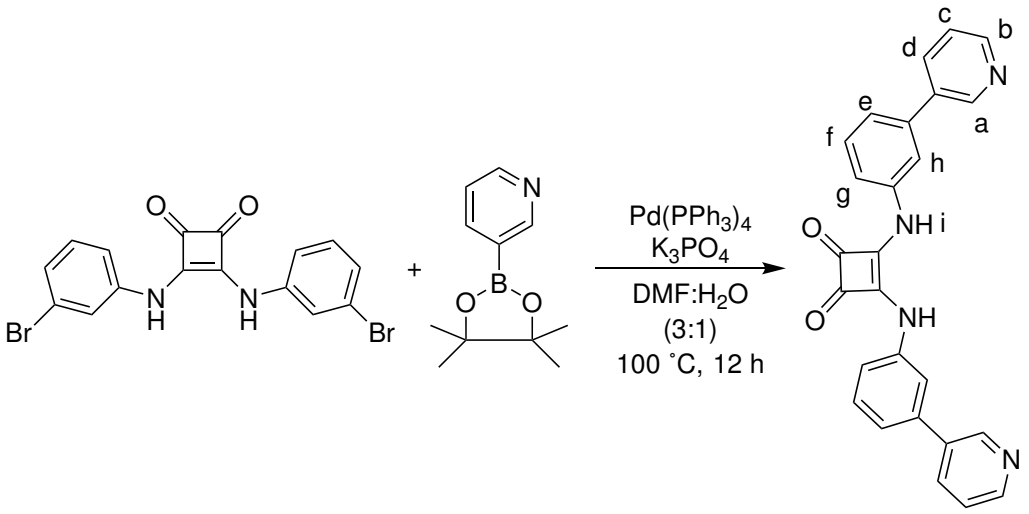

Figure 4.29. Synthesis of $\mathbf{L^1}$.

3-(4,4,5,5-tetramethyl-1,3,2-dioxaborolan-2-yl)pyridine (1.21 g, 5.92 mmol, 2.5 eq.) was added to **P2** (1.0 g, 2.37 mmol, 1.0 eq.), $Pd(PPh_3)_4$ (273.79 mg, 0.24 mmol, 0.1 eq.) and K_3PO_4 (2.01 g, 9.48 mmol, 4.0 eq.) and then dissolved in DMF/H_2O (3:1) and degassed. The mixture was stirred and heated at 100 °C for 12 h in a pressure flask. The solvent was removed *in vacuo* and the residue was purified by means of column chromatography (SiO_2, DCM:DMF 95:5 → 60:40). After adding toluene to the product fraction with residue of DMF the product was filtered. The product $\mathbf{L^1}$ (110.0 mg, 0.26 mmol, 11 %) was obtained as a yellow solid.

^{1}H-NMR (600 MHz, 298 K, DMSO$-d_6$): δ (ppm) = 10.25 (s, 1H, i), 8.96 (dd, J = 2.4, 0.8 Hz, 1H, a), 8.62 (dd, J = 4.8, 1.6 Hz, 1H, b), 8.14 (d, J = 8.0 Hz, 1H, d), 7.96 (t, J = 2.0 Hz, 1H, e), 7.59 – 7.44 (m, 4H, c, f, g, h).

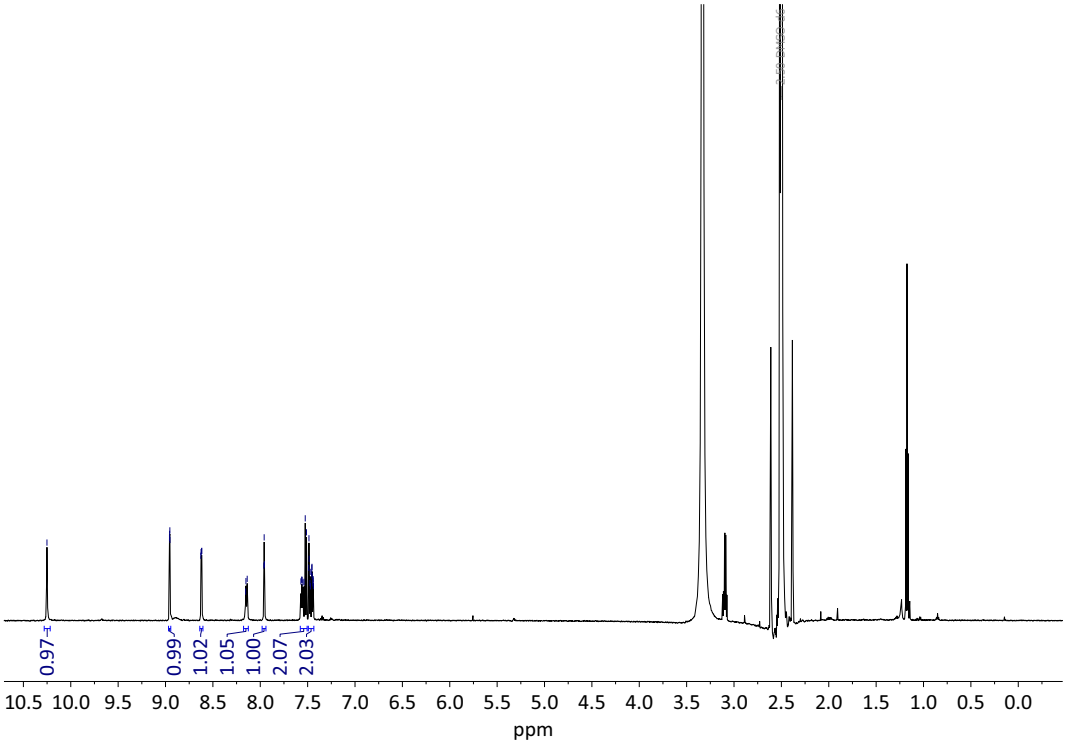

Figure 4.30. ^{1}H-NMR Spectrum (600 MHz, 298 K, DMSO$-d_6$) of **L^1**.

^{13}C-NMR (151 MHz, 298 K, DMSO$-d_6$): δ (ppm) = 182.05, 165.79, 148.81, 147.61, 139.16, 138.18, 135.16, 134.12, 130.23, 123.99, 121.79, 118.23, 117.15.

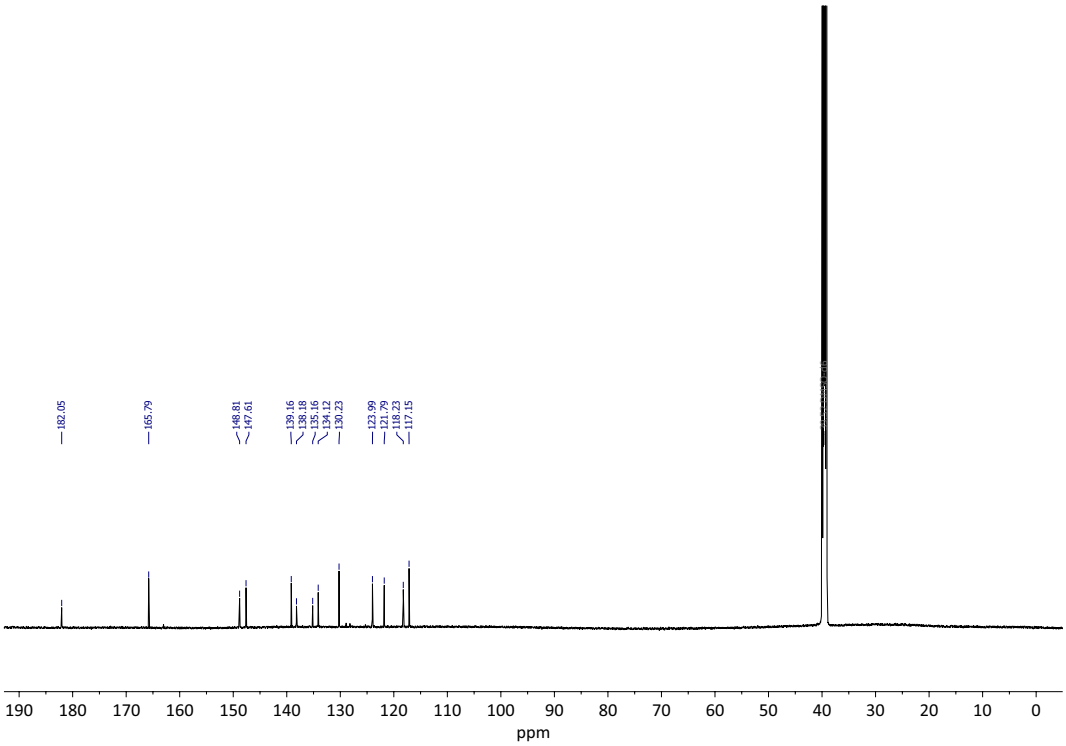

Figure 4.31. ^{13}C-NMR Spectrum (151 MHz, 298 K, DMSO$-d_6$) of **L^1**.

4.2.5 Synthesis of derivatives of Ligand L[1]

Synthesis of P2f

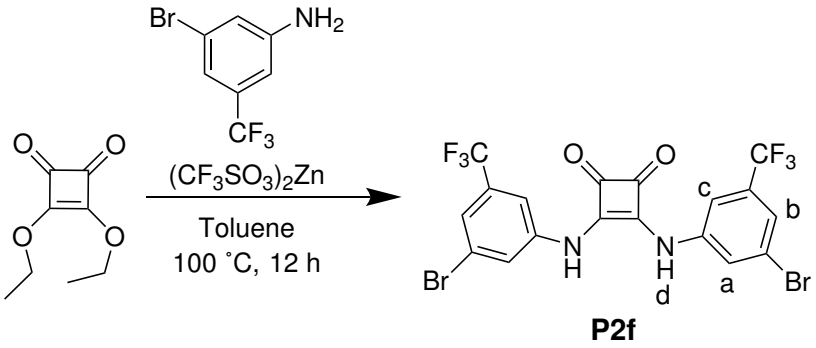

Figure 4.32. Synthesis of **P2f**.

3,4-diethoxycyclobut-3-ene-1,2-dione (1.00 g, 869.57 μL, 5.88 mmol, 1.0 eq.) was added to 3-bromo-5-(trifluoromethyl)aniline (2.96 g, 12.34 mmol, 2.1 eq.), $(CF_3SO_3)_2Zn$ (427.24 mg, 1.18 mmol, 0.2 eq.) and then dissolved in toluene. The mixture was stirred and heated at 100 °C for 12 h. The suspension was filtered and washed with toluene and CH_3CN and then the residual solvent was removed *in vacuo*. The product **P2f** (2.22 g, 3.98 mmol, 68 %) was obtained as a yellow solid.

^{1}H-NMR (600 MHz, 298 K, CD_3CN): δ (ppm)= 8.50 (s, 1H, d), 7.85 – 7.82 (m, 1H, c), 7.69 – 7.67 (m, 1H, b), 7.61 – 7.58 (m, 1H, a).

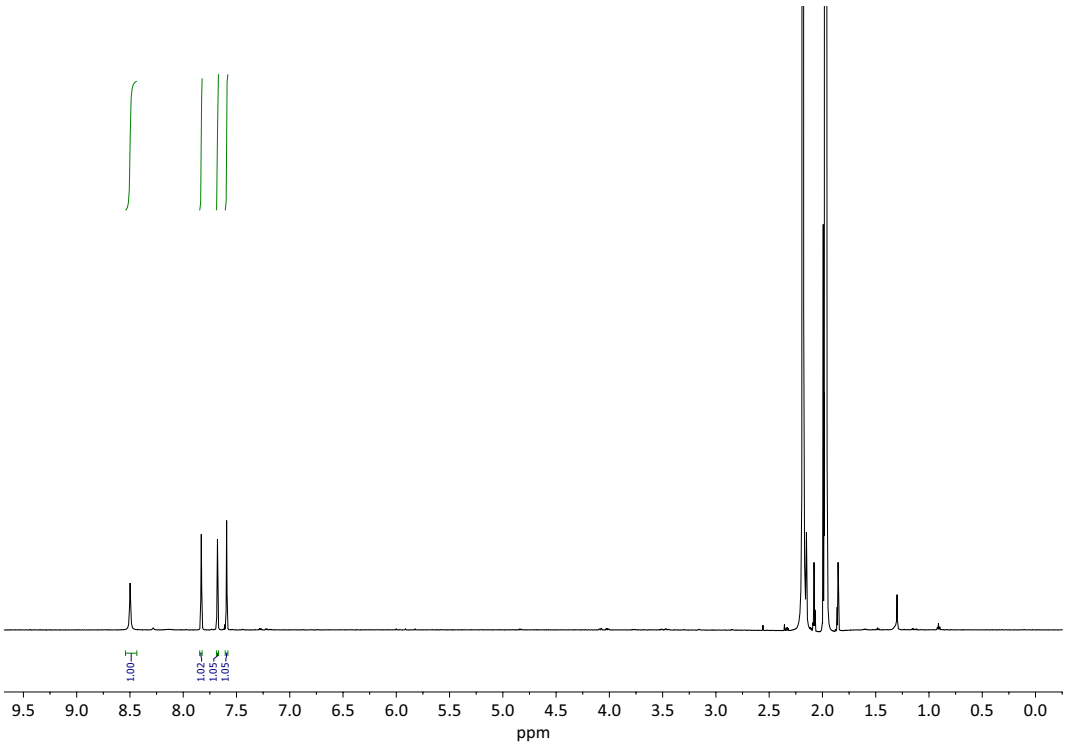

Figure 4.33. ^{1}H-NMR Spectrum (600 MHz, 298 K, CD_3CN) of **P2f**.

^{13}C-NMR (151 MHz, 298 K, DMSO$-d_6$): δ (ppm)= 191.35, 190.76, 184.21, 166.23, 141.37, 125.68, 123.23, 122.50, 115.10.

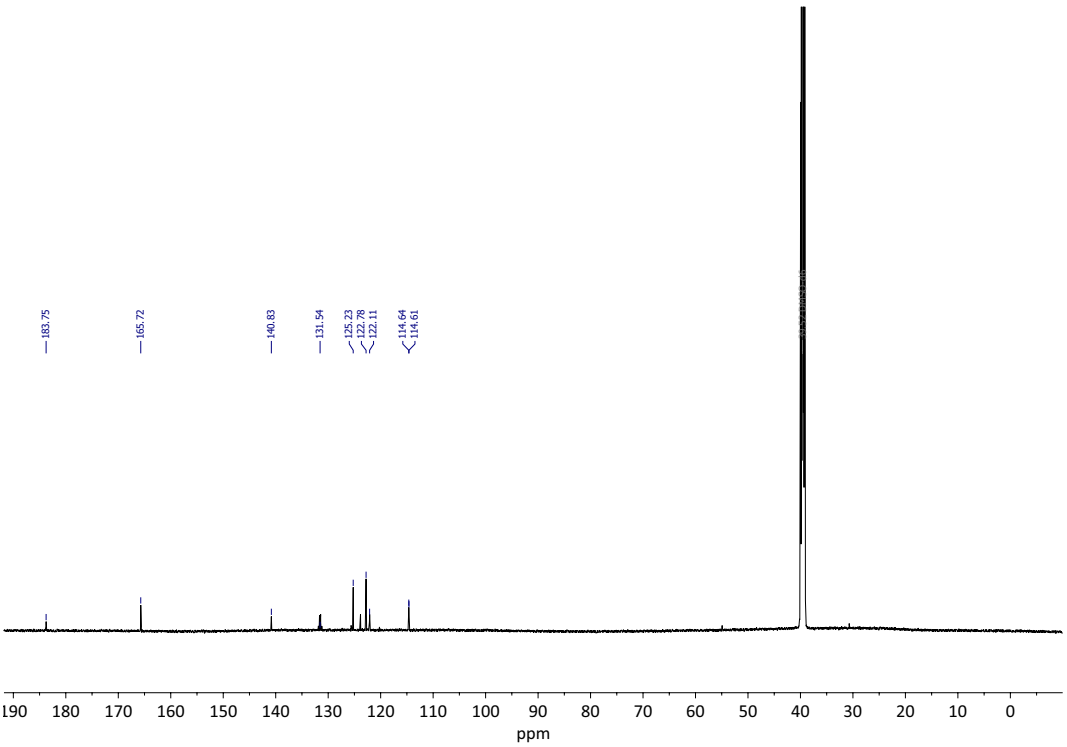

Figure 4.34. ^{13}C-NMR Spectrum (151 MHz, 298 K, DMSO$-d_6$) of **P2f**.

Synthesis of L^{1f}

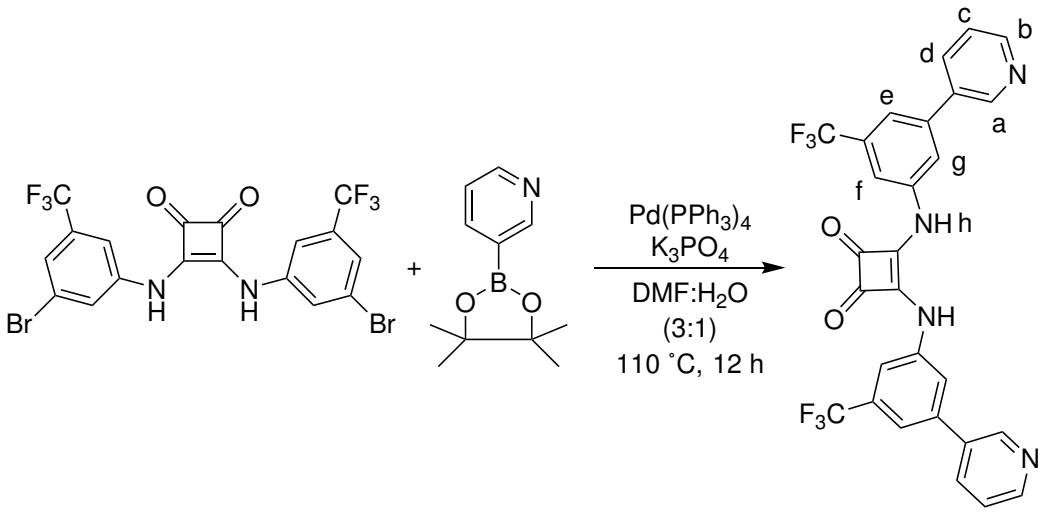

P2f **L^{1f}**

Figure 4.35. Synthesis of L^{1f}.

3-(4,4,5,5-tetramethyl-1,3,2-dioxaborolan-2-yl)pyridine (459.31 mg, 2.24 mmol, 2.5 eq.) was added to **P2f** (500.00 mg, 0.90 mmol, 1.0 eq.), $Pd(PPh_3)_4$ (103.53 mg, 0.09 mmol, 0.1 eq.) and K_3PO_4 (570.53 mg, 2.69 mmol, 4.0 eq.) and then dissolved in DMF/H_2O (3:1) and degassed. The mixture was stirred and heated at 100 °C for 12 h in a pressure flask. The solvent was removed *in vacuo* then the residue was washed with EtOH and CH_3CN. The product $\mathbf{L^{1f}}$ (108.0 mg, 0.19 mmol, 22 %) was obtained as a yellow solid.

^{1}H-NMR (600 MHz, 298 K, DMSO$-d_6$): δ (ppm)= 10.42 (s, 1H h), 8.96 (d, J = 2.5 Hz, 1H, a), 8.64 (dd, J = 4.8, 1.5 Hz, 1H, b), 8.15 (dt, J = 8.1, 1.9 Hz, 1H, d), 7.98 (s, 1H, f), 7.73 (s, 2H, g, e), 7.53 (ddd, J = 8.0, 4.8, 0.9 Hz, 1H, d).

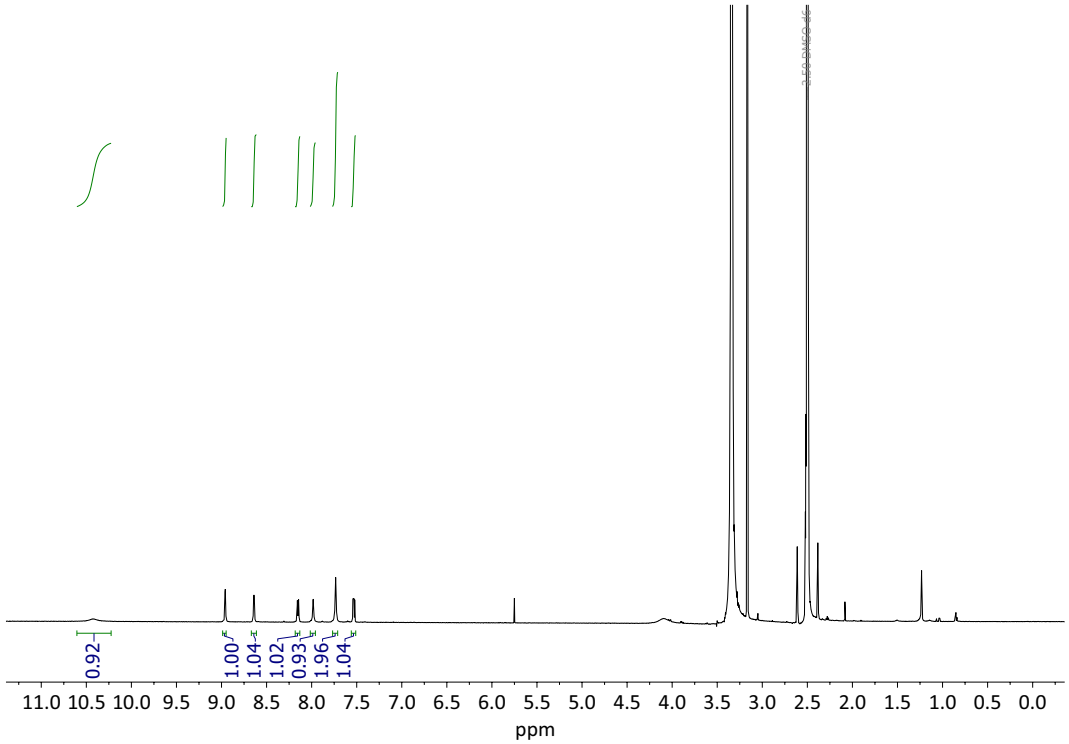

Figure 4.36. ^{1}H-NMR Spectrum (600 MHz, 298 K, DMSO$-d_6$) of **L^{1f}**.

^{13}C-NMR (151 MHz, 298 K, DMSO$-d_6$): δ (ppm)= 183.83, 166.46, 149.97, 148.26, 139.83, 134.92, 134.21, 131.40, 125.14, 124.47, 123.34, 121.45, 118.38, 115.31.

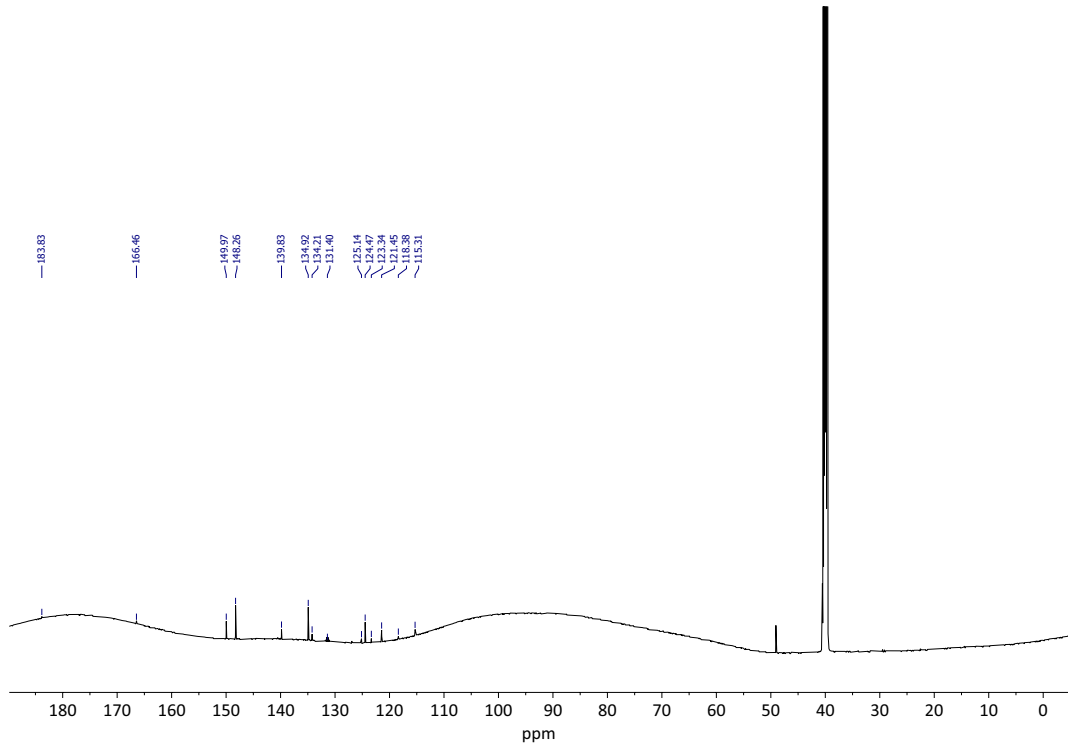

Figure 4.37. ^{13}C-NMR Spectrum (151 MHz, 298 K, DMSO$-d_6$) of $\mathbf{L^{1f}}$.

Synthesis of L^{1a}

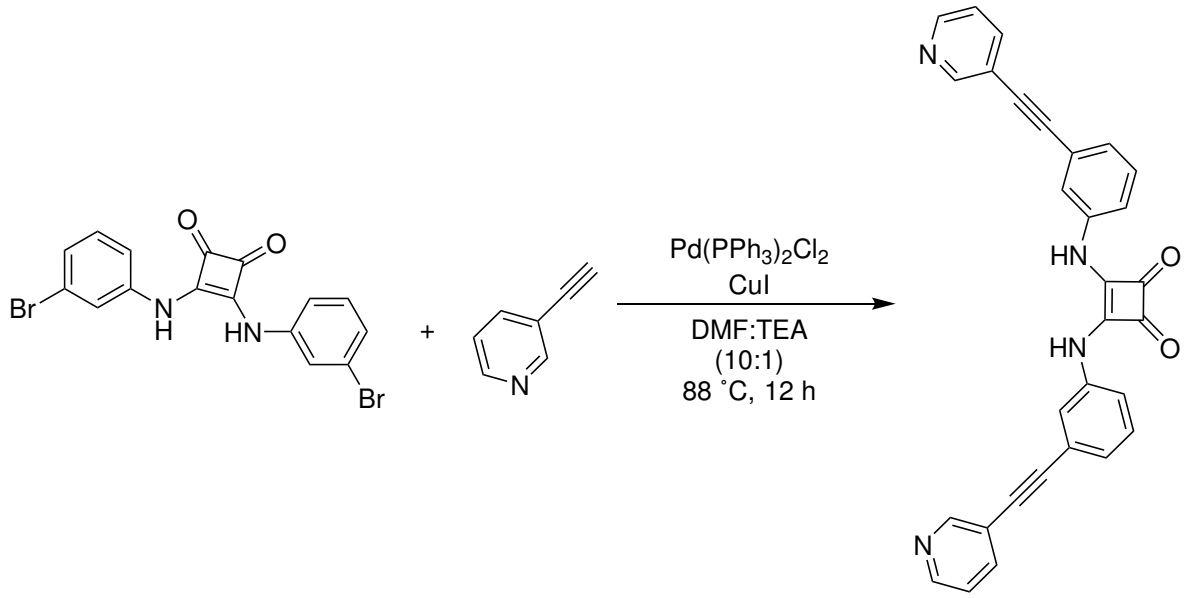

P2 **L^{1a}**

Figure 4.38. Synthesis of L^{1a}.

Ethynyltrimethylsilane (101.80 μL, 0.89 mmol, 2.5 eq.) was added to **P2** (105.00 mg 0.36 mmol, 1.0 eq.), $Pd(PPh_3)_2Cl_2$) (24.94 mg, 0.04 mmol, 0.1 eq.) and CuI (13.54 mg, 0.71 mmol, 0.2 eq.) and then dissolved in DMF/NEt_3 (10:1) and degassed. The mixture was stirred and heated at 88 °C for 12 h under reflux. The solvent was removed *in vacuo* and the residue was purified by means of column chromatography (SiO_2, DMF:DCM 1:20 → 75:25). The solvent was removed *in vacuo*. The product $\mathbf{L^{1a}}$ could not be obtained.

Table 4.1: Screening of different reaction conditions.

entry	pd source	T / °C	base	solvent
1	$Pd(PPh_3)_2Cl_2$)	88	TEA	DMF
2	$Pd(PPh_3)_2Cl_2$)	105	TEA	DMF
3	$Pd(PPh_3)_2Cl_2$)	120	TEA	DMF
4	$Pd(PPh_3)_4$	88	TEA	DMF
5	$Pd(PPh_3)_2Cl_2$)	88	Cs_2CO_3	DMF
6	$Pd(PPh_3)_4$	105	Cs_2CO_3	DMF
7	$Pd(PPh_3)_2Cl_2$)	88	DIPEA	DMF
8	$Pd(PPh_3)_4$	105	DIPEA	DMF

Synthesis of Ligand L^{1p}

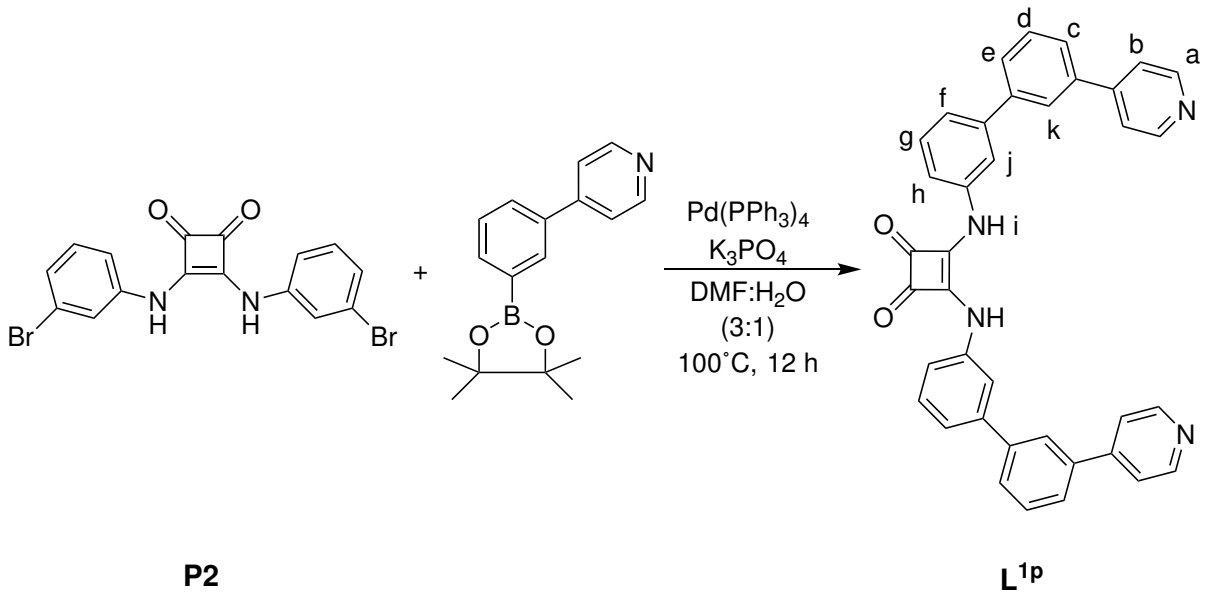

Figure 4.39. Synthesis of $\mathbf{L^{1p}}$.

4-(3-(4,4,5,5-tetramethyl-1,3,2-dioxaborolan-2-yl)phenyl)pyridine (459.64 mg, 1.63 mmol, 2.3 eq.) was added to **P2** (300.0 mg, 0.71 mmol, 1.0 eq.), $Pd(PPh_3)_4$ (82.14 mg, 0.07 mmol, 0.1 eq.) and K_3PO_4 (603.49 mg, 2.84 mmol, 4.0 eq.) and then dissolved in DMF/H_2O (3:1) and degassed. The mixture was stirred and heated at 100 °C for 12 h in a pressure flask. The solvent was removed *in vacuo* and the residue was purified by means of column chromatography (SiO_2, DCM:MeOH 99:1 → 90:10). The product $\mathbf{L^{1p}}$ (40.0 mg, 0.07 mmol, 10 %) was obtained as a grey solid.

^{1}H-NMR (600 MHz, 298 K, DMSO$-d_6$): δ (ppm)= 10.71 (s, 1H, i), 8.78 (d, J = 5.4 Hz, 2H, a), 8.18 (t, J = 1.9 Hz, 1H, j), 8.11 (t, J = 2.0 Hz, 1H, k), 8.05 – 8.00 (m, 2H, b), 7.88 (ddt, J = 15.6, 7.8, 1.3 Hz, 2H, f, h), 7.69 (t, J = 7.7 Hz, 1H, g), 7.55 – 7.47 (m, 3H, c, d, e).

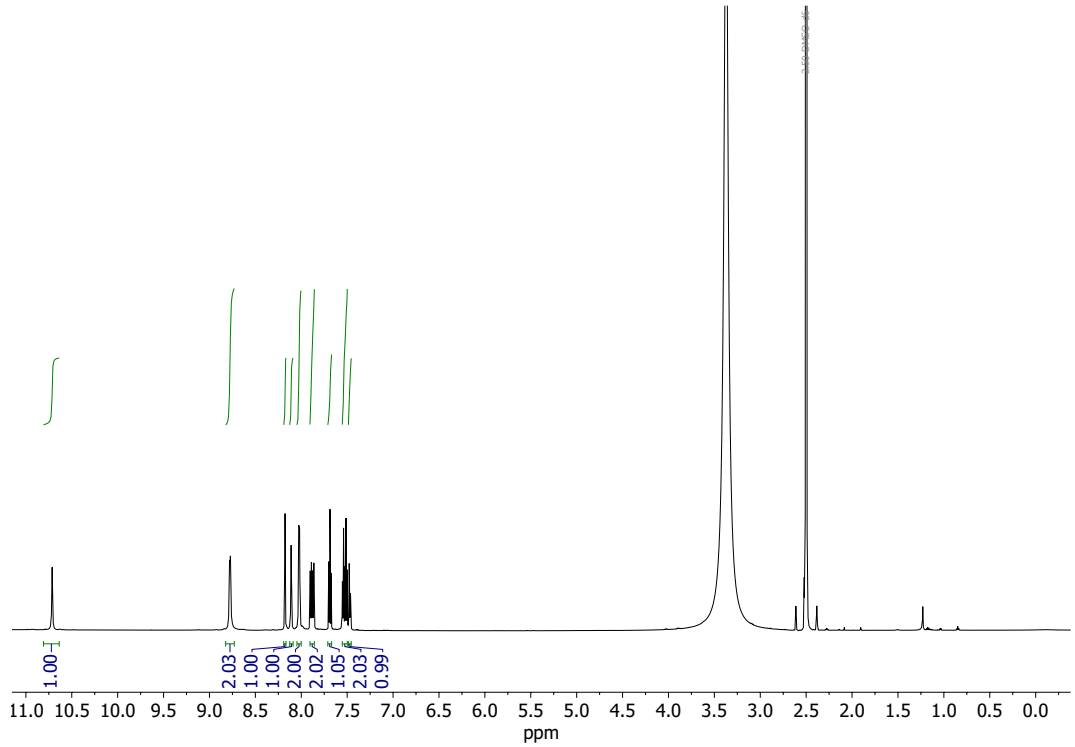

Figure 4.40. ^{1}H-NMR Spectrum (600 MHz, 298 K, DMSO$-d_6$) of **L^{1p}**.

^{13}C-NMR (151 MHz, 298 K, DMSO$-d_6$): δ (ppm)= 182.23, 166.37, 149.81, 148.57, 141.31, 141.16, 139.75, 137.64, 130.56, 130.50, 128.63, 127.05, 126.00, 122.63, 122.26, 118.24, 117.64.

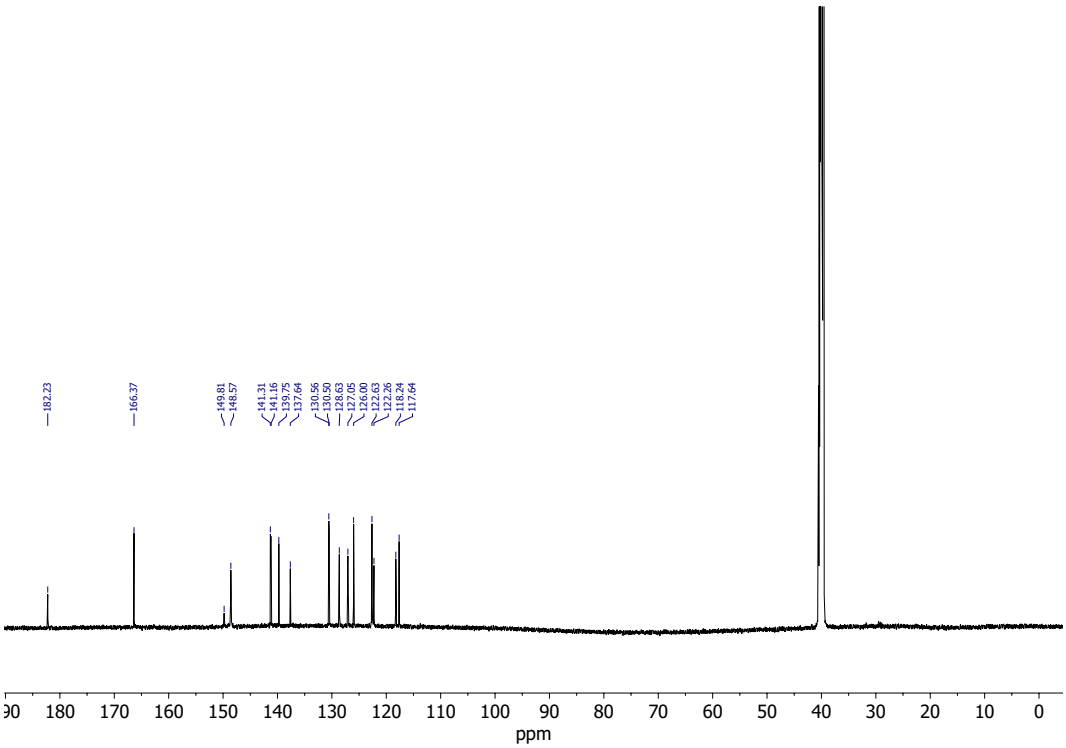

Figure 4.41. ^{13}C-NMR Spectrum (151 MHz, 298 K, DMSO$-d_6$) of $\mathbf{L^{1p}}$.

4.2.6 Synthesis of Ligand L^{1peg}

Synthesis of P3

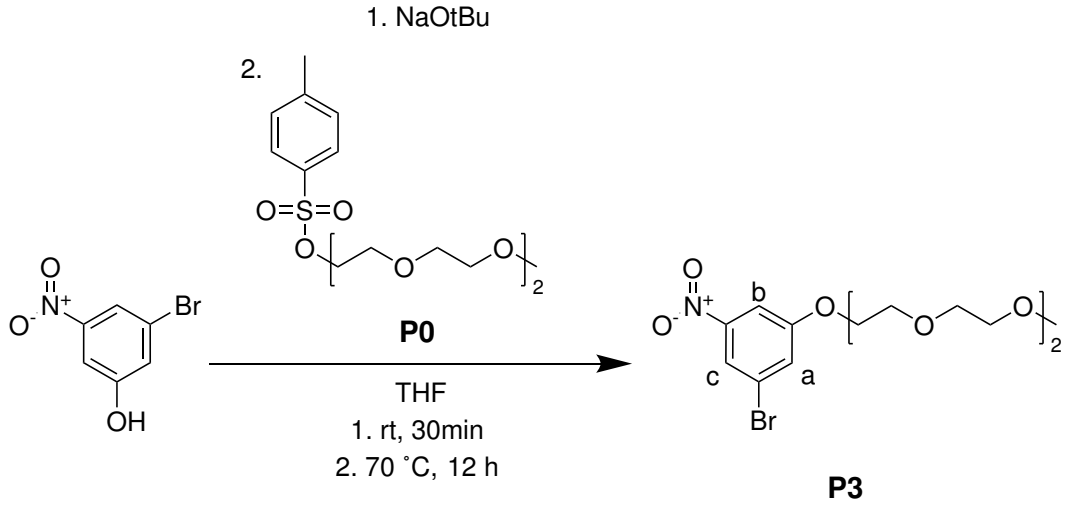

Figure 4.42. Synthesis of **P3**.

3-bromo-5-nitrophenol (2.00 g, 9.17 mmol, 1.0 eq.) was dissolved in THF and stirred with NaOtBu (1.76 g, 18.35 mmol, 2.0 eq.) at rt for 30 min. **325** (4.32 g, 11.93 mmol, 1.3 eq.) was added to the suspension and stirred at 70 °C for 12 h. The suspension was filtered and then the solvent was removed *in vacuo* and the residue was purified by means of column chromatography (SiO_2, ETOAc:n-Pentane 30:70 → 99:1). The product **P3** (3.57 g, 8.74 mmol, 95 %) was obtained as a brown viscous liquid.

^{1}H-NMR (500 MHz, 298 K, CD_3CN): δ (ppm)= 7.95 (t, J = 1.8 Hz, 1H, b), 7.73 (t, J = 2.2 Hz, 1H, a), 7.53 (dd, J = 2.4, 1.6 Hz, 1H, c), 4.23 – 4.20 (m, 2H), 3.81 – 3.78 (m, 2H), 3.63 – 3.61 (m, 2H), 3.57 – 3.55 (m, 2H), 3.54 – 3.52 (m, 6H), 3.46 – 3.44 (m, 2H), 3.28 (s, 3H).

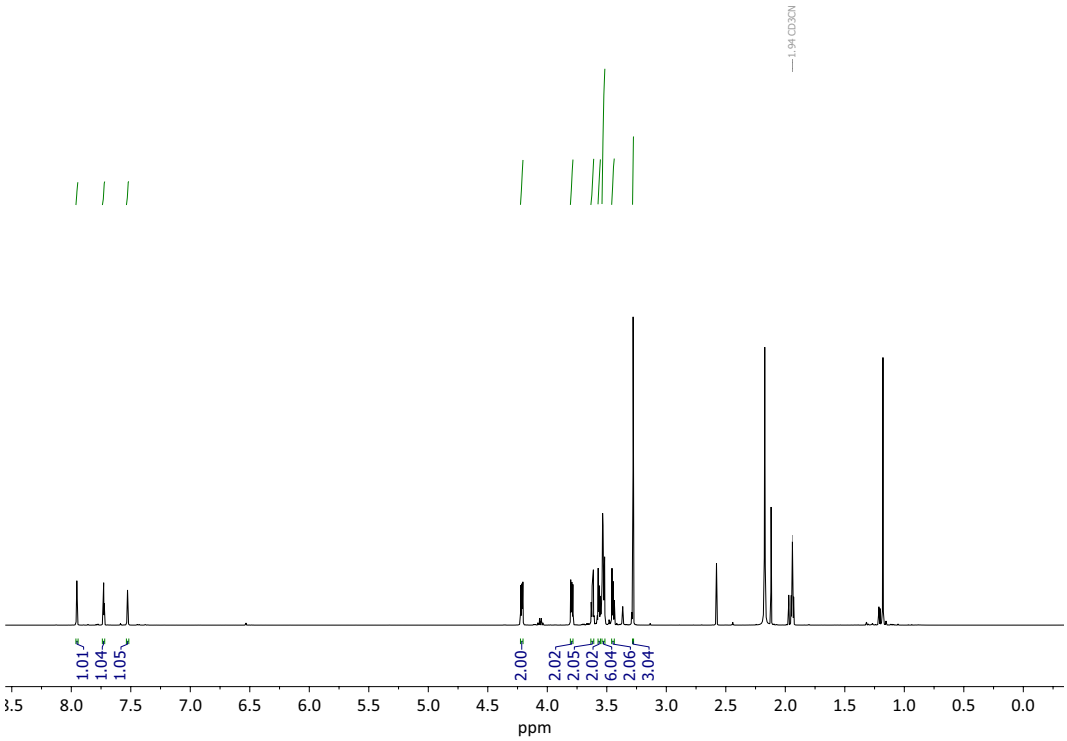

Figure 4.43. ^{1}H-NMR Spectrum (500 MHz, 298 K, CD_3CN) of **P3**.

^{13}C-NMR (151 MHz, 298 K, CD_3CN): δ (ppm)= 161.10, 150.71, 125.18, 123.52, 119.62, 110.02, 72.60, 71.42, 71.21, 71.14, 70.99, 69.96, 69.91, 58.88.

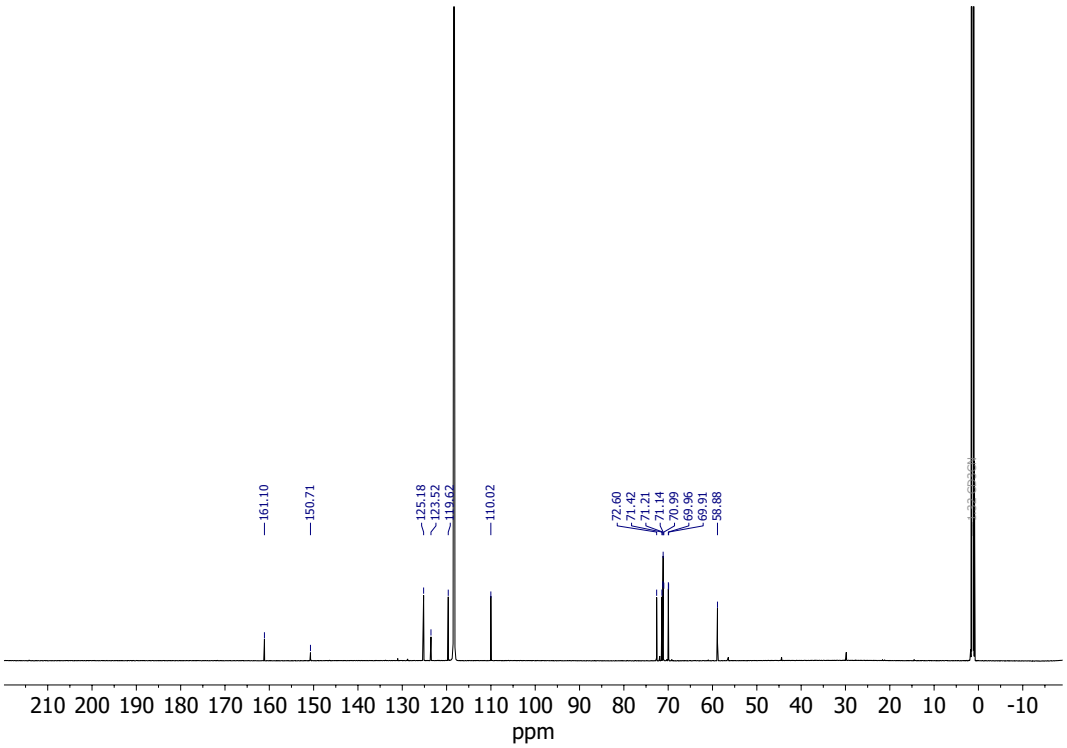

Figure 4.44. ^{13}C-NMR Spectrum (151 MHz, 298 K, CD_3CN) of **P3**.

Synthesis of P4

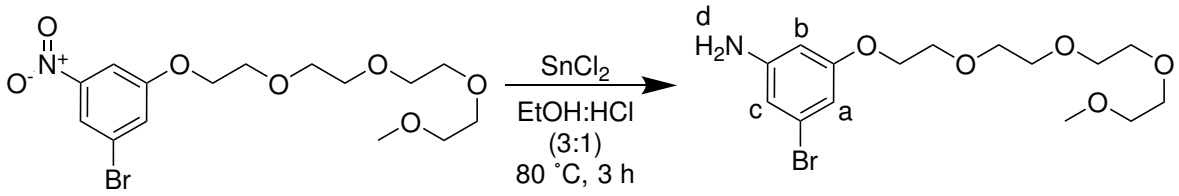

P3 **P4**

Figure 4.45. Synthesis of **P4**.

P3 (1.00 g, 2.45 mmol, 1.0 eq.) was dissolved in EtOH:HCl(30 %)(3:1) and stirred with $SnCl_2$ (2.32 g, 12.25 mmol, 5.0 eq.) at 80 °C for 3 h. The reaction was carefully quenched with a saturated solution of NaOH. The suspension was filtered, washed with water and extracted with DCM. After drying over $MgSO_4$, the solvent was removed *in vacuo*. The product **P4** (888.00 mg, 2.35 mmol, 96 %) was obtained as a brown viscous liquid.

Alternative Synthesis Route

Reduction with Pd/C and H_2 did not provide the desired product.

^{1}H-NMR (500 MHz, 298 K, CD_3CN): δ (ppm)= 6.44 (t, $J = 1.8$ Hz, 1H, b), 6.40 (t, $J = 2.0$ Hz, 1H, a), 6.19 (t, $J = 2.1$ Hz, 1H, c), 4.33 (s, 2H, d), 4.06 – 4.02 (m, 2H), 3.76 – 3.74 (m, 2H), 3.64 – 3.62 (m, 2H), 3.60 – 3.55 (m, 8H), 3.50 – 3.47 (m, 2H).

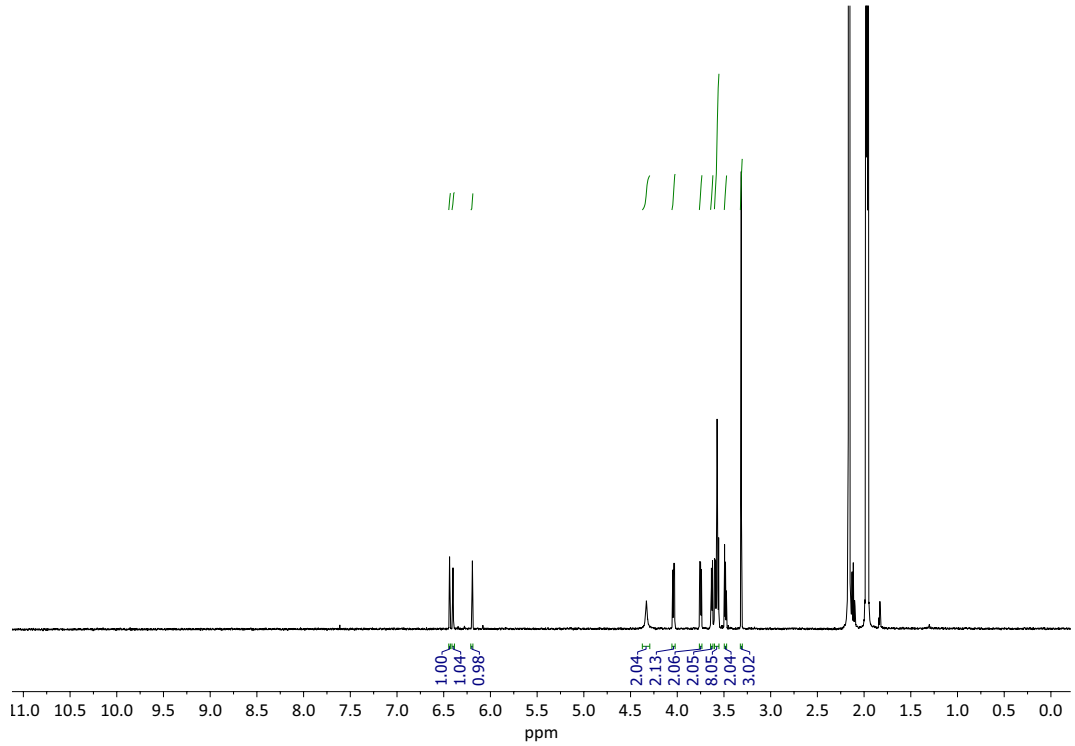

Figure 4.46. ^{1}H-NMR Spectrum (500 MHz, 298 K, CD_3CN) of **P4**.

^{13}C-NMR (176 MHz, 298 K, CD_3CN): δ (ppm)= 161.22, 151.18, 123.24, 110.54, 106.94, 100.00, 72.20, 70.92, 70.79, 70.74, 70.73, 70.58, 69.74, 68.06, 58.46.

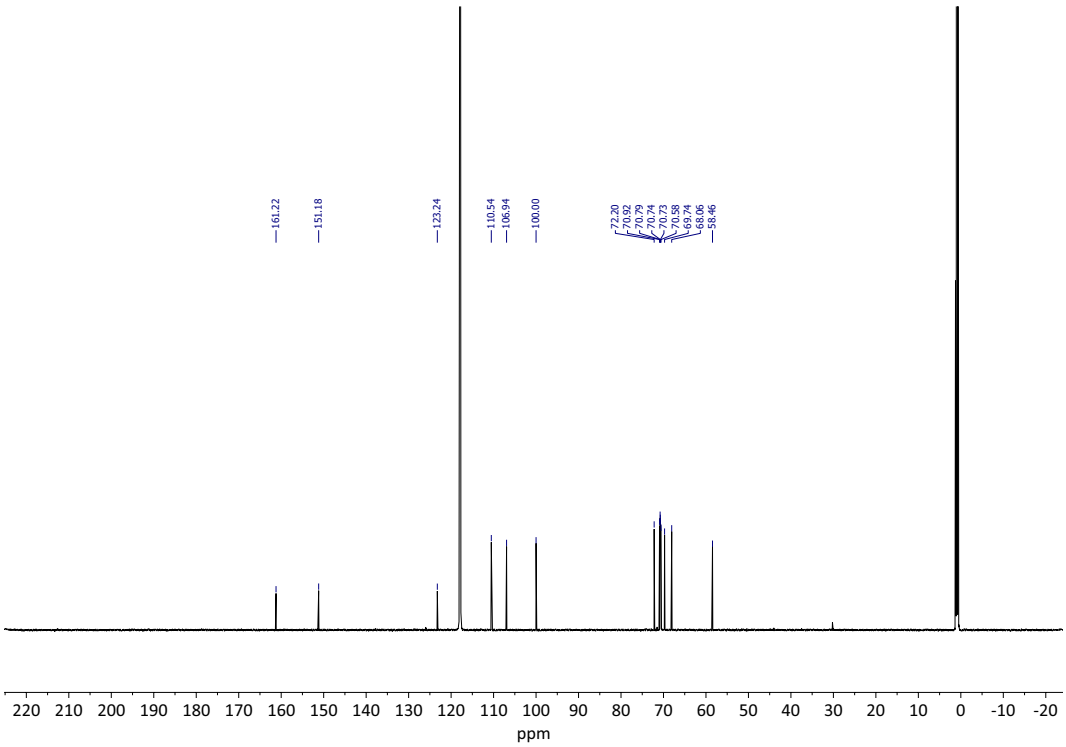

Figure 4.47. ^{13}C-NMR Spectrum (176 MHz, 298 K, CD_3CN) of **P4**.

Synthesis of P5

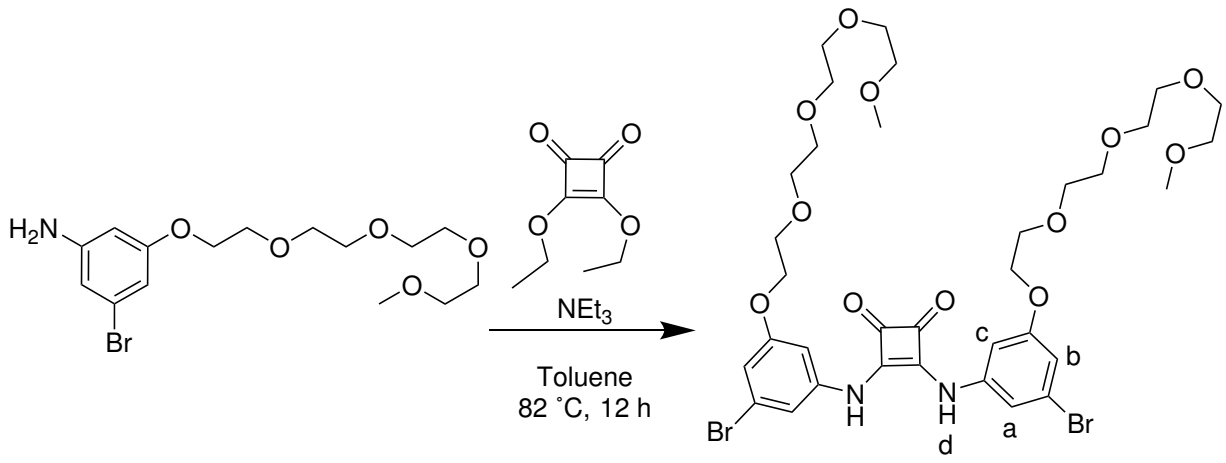

P4 **P5**

Figure 4.48. Synthesis of **P5**.

3,4-diethoxycyclobut-3-ene-1,2-dione (86.96 μL, 0.59 mmol, 1.0 eq.) was added to **P4** (489.05 mg, 1.29 mmol, 2.2 eq.), NEt_3 (3.5 mL, 27.33 mmol, 46.5 eq.) and then dissolved in toluene. The mixture was stirred and heated at 82 °C for 12 h. The residue was purified by means of column chromatography (SiO_2, MeOH:DCM 1:99 $\rightarrow$ 5:95) The product **P5** (365.00 mg, 0.52 mmol, 72 %) was obtained as a brown viscous liquid.

^{1}H-NMR (500 MHz, 298 K, CD_3CN): δ (ppm) = 8.51 (s, 1H, d), 7.17 (t, J = 1.8 Hz, 1H, c), 7.06 (t, J = 2.2 Hz, 1H, b), 6.82 (t, J = 1.9 Hz, 1H, a), 4.11 – 4.09 (m, 2H), 3.78 – 3.76 (m, 2H), 3.65 – 3.62 (m, 2H), 3.60 – 3.58 (m, 2H), 3.56 – 3.53 (m, 6H), 3.45 – 3.43 (m, 2H), 3.26 (s, 3H).

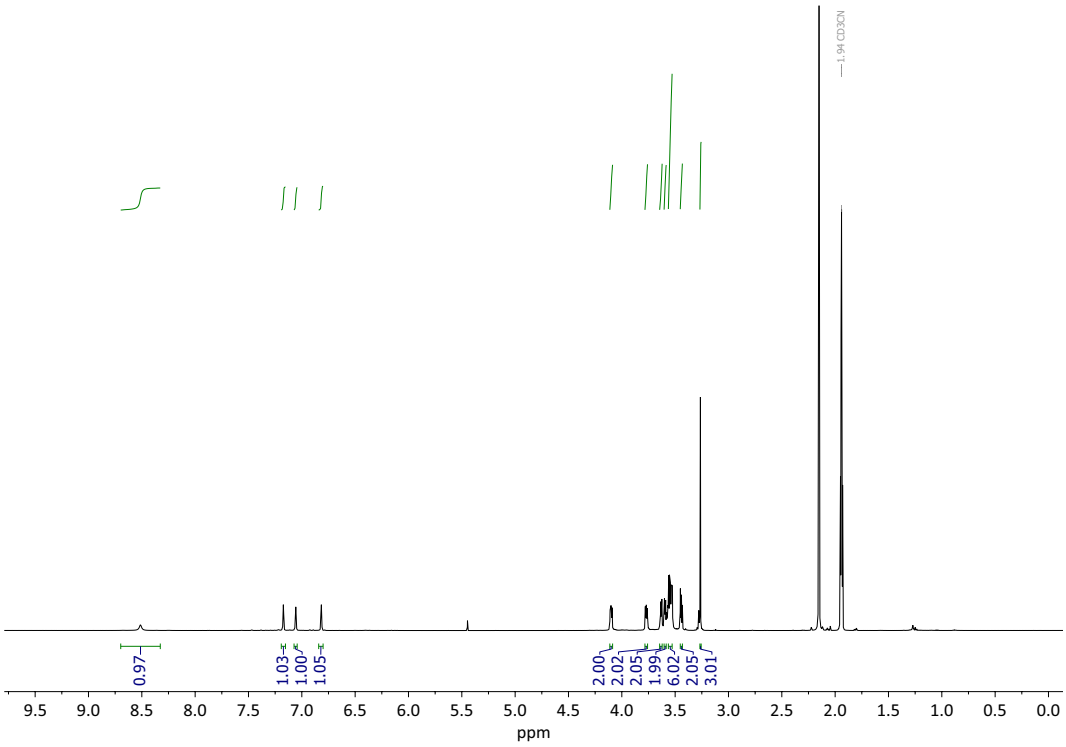

Figure 4.49. ^{1}H-NMR Spectrum (500 MHz, 298 K, CD_3CN) of **P5**.

^{13}C-NMR (151 MHz, 298 K, CD_3CN): δ (ppm) = 183.15, 166.86, 161.35, 141.85, 123.73, 123.71, 115.00, 113.83, 105.29, 105.27, 72.54, 71.32, 71.17, 71.13, 71.06, 70.95, 70.06, 70.03, 69.02, 58.92.

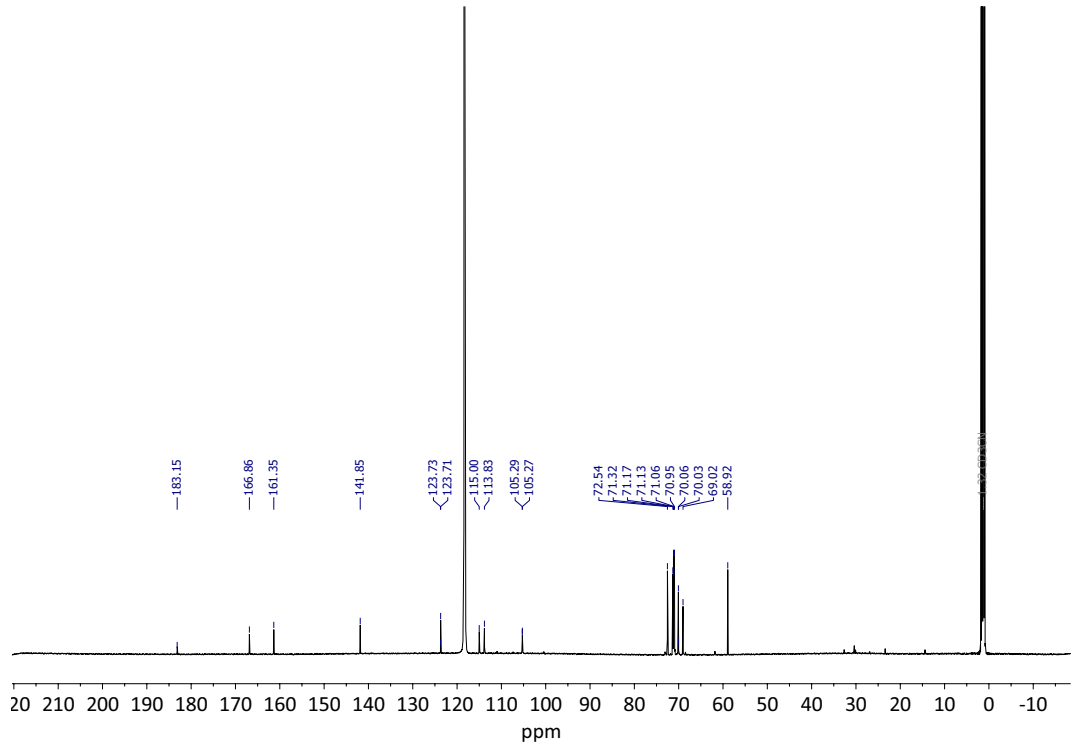

Figure 4.50. ^{13}C-NMR Spectrum (151 MHz, 298 K, CD_3CN) of **P5**.

Synthesis of L^{1peg}

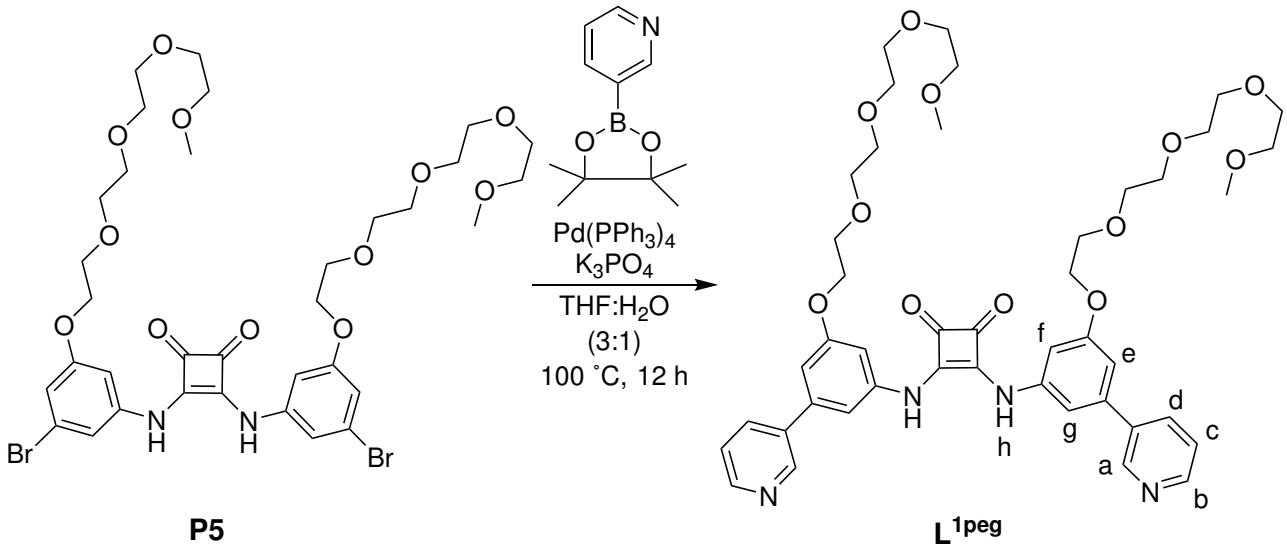

Figure 4.51. Synthesis of L^{1peg}.

4-(3-(4,4,5,5-tetramethyl-1,3,2-dioxaborolan-2-yl)phenyl)pyridine (551.02 mg, 2.69 mmol, 2.5 eq.) was added to **P5** (897.0 mg, 1.07 mmol, 1.0 eq.), $Pd(PPh_3)_4$ (62.10 mg, 0.05 mmol, 0.05 eq.) and K_3PO_4 (912.59 mg, 4.30 mmol, 4.0 eq.) and then dissolved in THF/H_2O (3:1) and degassed. The mixture was stirred and heated at 100 °C for 12 h in a pressure flask. The solvent was removed *in vacuo* and the residue was purified by means of column chromatography (SiO_2, DCM:MeOH 99:1 → 90:10). The product $\mathbf{L^{1peg}}$ (169.0 mg, 0.20 mmol, 19 %) was obtained as a brown viscous liquid.

^{1}H-NMR (500 MHz, 298 K, DMSO$-d_6$): δ (ppm) = 10.04 (s, 1H, h), 8.92 (dd, J = 2.4, 0.9 Hz, 1H, a), 8.59 (dd, J = 4.7, 1.6 Hz, 1H, b), 8.09 (ddd, J = 8.0, 2.4, 1.6 Hz, 1H, d), 7.50 (ddd, J = 7.9, 4.8, 0.8 Hz, 1H, c), 7.35 (t, J = 1.7 Hz, 1H, g), 7.14 (t, J = 2.1 Hz, 1H, f), 7.03 (dd, J = 2.3, 1.4 Hz, 1H, e), 4.24 – 4.17 (m, 2H), 3.81 – 3.77 (m, 2H), 3.63 – 3.60 (m, 2H), 3.57 – 3.54 (m, 2H), 3.52 – 3.48 (m, 6H), 3.41 – 3.39 (m, 2H), 3.21 (s, 3H).

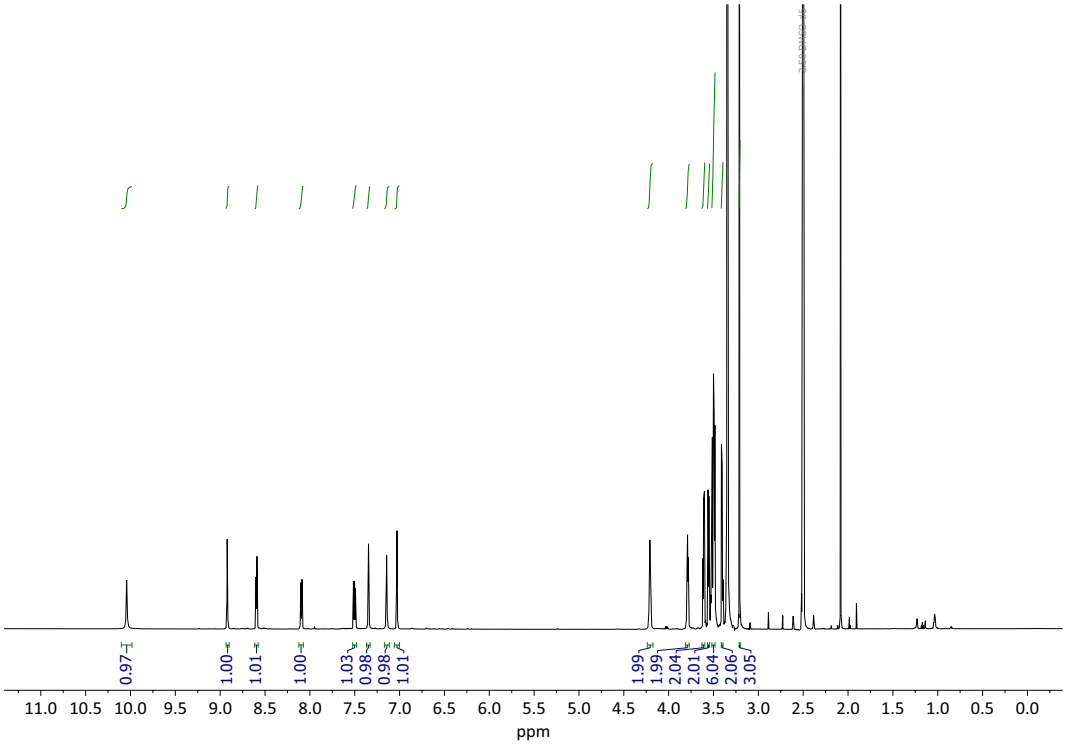

Figure 4.52. ^{1}H-NMR Spectrum (600 MHz, 298 K, DMSO$-d_6$) of $\mathbf{L^{1peg}}$.

^{13}C-NMR (151 MHz, 298 K, DMSO$-d_6$): δ (ppm) = 182.10, 165.80, 159.95, 148.96, 147.69, 140.21, 139.29, 135.09, 134.19, 123.92, 109.62, 108.17, 104.50, 71.27, 69.96, 69.83, 69.81, 69.79, 69.58, 68.87, 67.47, 58.04.

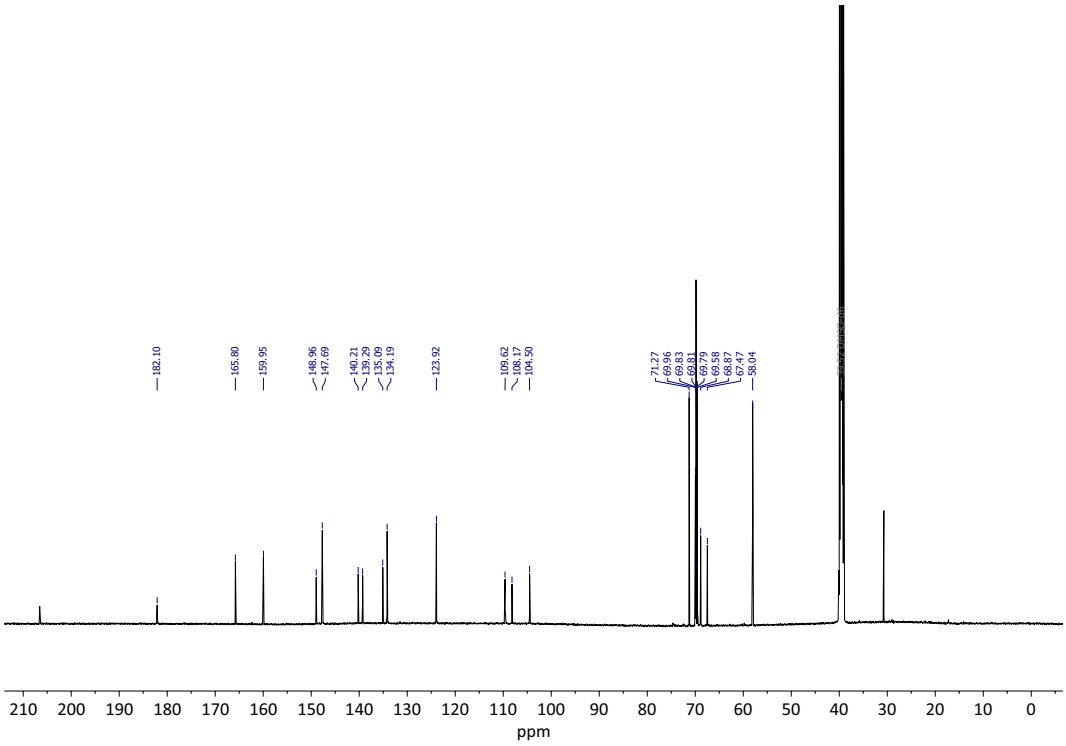

Figure 4.53. ^{13}C-NMR Spectrum (151 MHz, 298 K, DMSO$-d_6$) of $\mathbf{L^{1peg}}$.

4.2.7 1,3-Squaramide-based Ligands

4.2.8 Synthesis of Ligand L^4

Synthesis of L^4

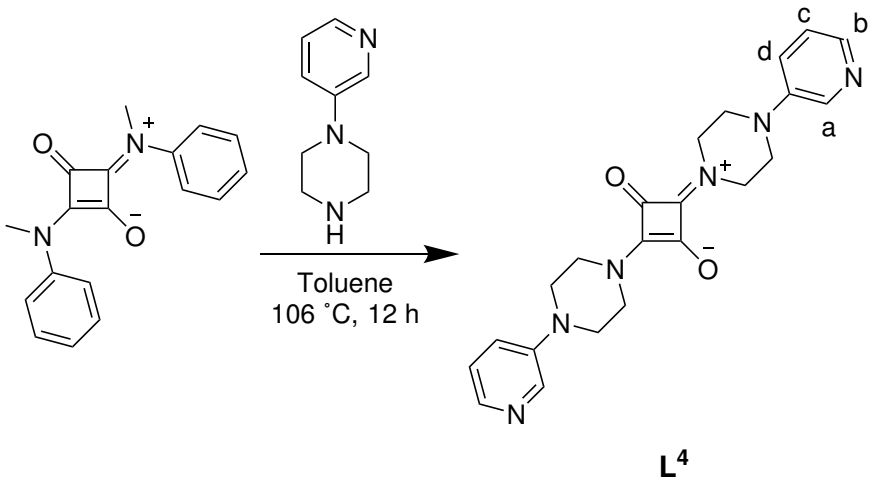

Figure 4.54. Synthesis of $\mathbf{L^4}$.

(*E*)-2-(methyl(phenyl)amino)-4-(methyl(phenyl)iminio)-3-oxocyclobut-1-en-1-olate (200.00 mg, 0.68 mmol, 1.0 eq.) was added to 1-(pyridin-3-yl)piperazine1-(pyridin-3-yl)piperazine (893.34 mg, 5.47 mmol, 8.0 eq.) and then dissolved in toluene. The mixture was stirred and heated at 106 °C for 12 h. The suspension was filtered and washed with cold CH_3CN. After centrifugation with DMF, followed by acetone, the residual solvent was removed *in vacuo*. The product $\mathbf{L^4}$ (174.0 mg, 0.43 mmol, 63 %) was obtained as a bright yellow solid.

^{1}H-NMR (500 MHz, 298 K, CD_3CN): δ (ppm) = 8.30 (d, J = 3.0 Hz, 1H, a), 8.07 (dd, J = 4.6, 1.4 Hz, 1H, b), 7.31 (ddd, J = 8.5, 3.0, 1.4 Hz, 1H, d), 7.23 (ddd, J = 8.4, 4.6, 0.7 Hz, 1H, c), 4.01 – 3.98 (m, 4H), 3.36 – 3.34 (m, 4H).

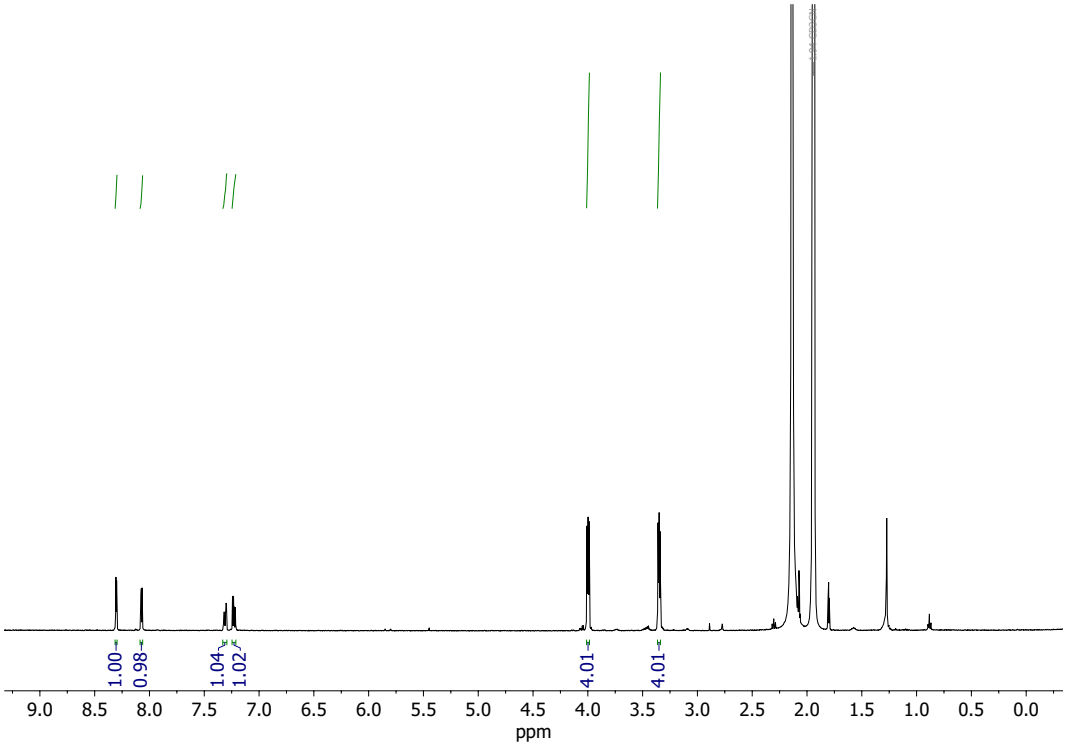

Figure 4.55. ^{1}H-NMR Spectrum (600 MHz, 298 K, CD_3CN) of **L^4**.

^{13}C-NMR (151 MHz, 298 K, CD_3CN): δ (ppm)= 175.15, 169.23, 147.31, 141.48, 139.38, 124.22, 123.72, 49.20, 46.38.

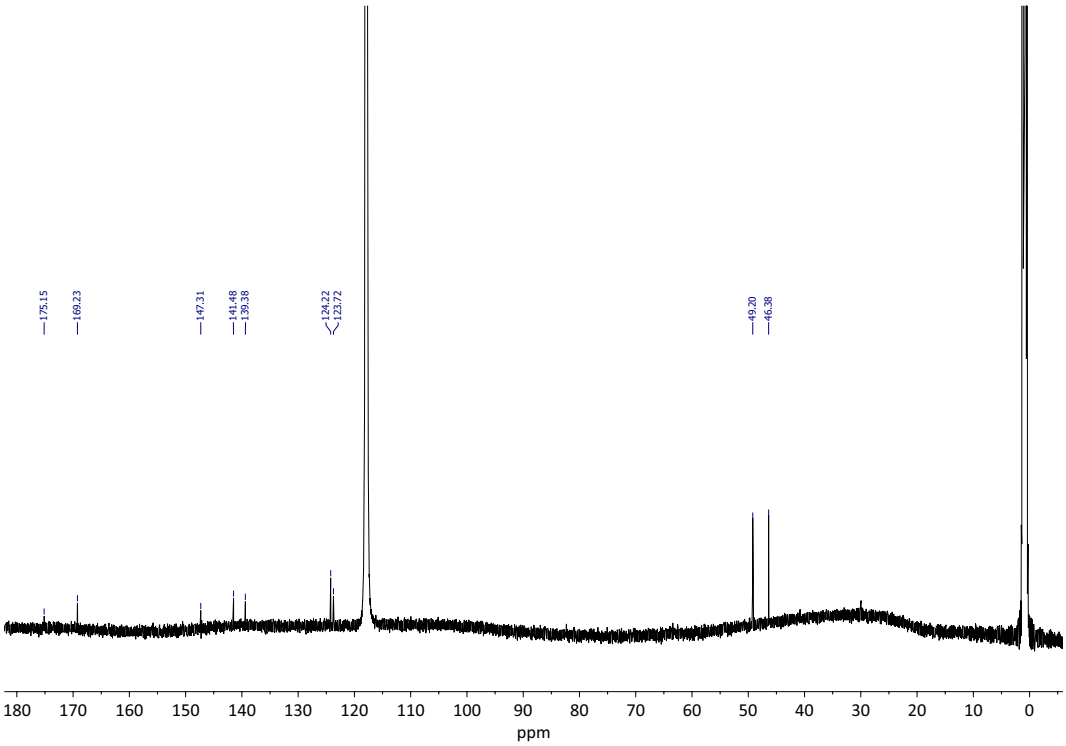

Figure 4.56. ^{13}C-NMR Spectrum (151 MHz, 298 K, CD_3CN) of **L^4**.

4.2.9 Synthesis of Ligand L^{4n}

Synthesis of P6

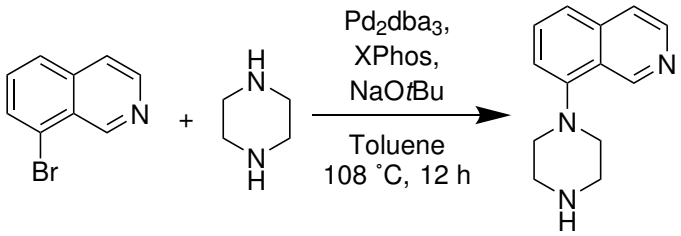

P6

Figure 4.57. Synthesis of **P6** as reported. [195]

8-bromoisoquinoline (2.00 g, 9.61 mmol, 1.0 eq.) was added to piperazine (2,07 g, 24.03 mmol, 2.5 eq.), Pd_2dba_3 (769.02 mg, 0.77 mmol, 0.08 eq.), XPhos (687.40 mg, 1.44 mmol, 0.15 eq.) and NaO*t*Bu (2.07 g, 13.46 mmol, 2,5 eq) and then dissolved in toluene. The mixture was stirred and heated at 108 °C for 12 h under reflux. The reaction mixture was cooled down and then was washed with H_2O and extracted with CH_2Cl_2 (2 x 50 mL). The solvent was removed *in vacuo* and the residue was purified by means of column chromatography (SiO_2, DCM/MeOH/EtOAc 85:10:5 $\rightarrow$ 70:20:10). The product **P6** (1.0 g, 4.69 mmol, 49 %) was obtained as a brown viscous liquid.

Synthesis of L^{4n}

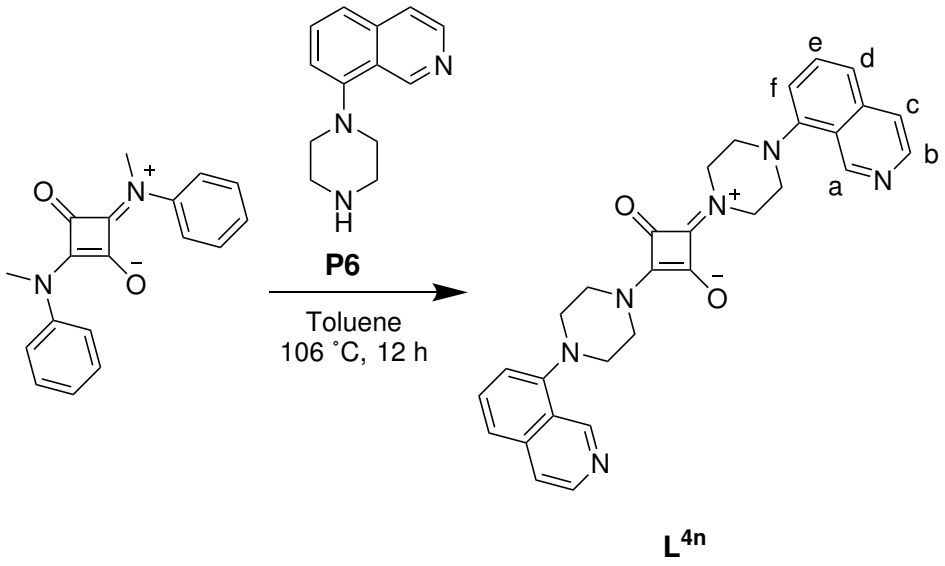

Figure 4.58. Synthesis of L^{4n}.

(*E*)-2-(methyl(phenyl)amino)-4-(methyl(phenyl)iminio)-3-oxocyclobut-1-en-1-olate (200.00 mg, 0.68 mmol, 1.0 eq.) was added to **P6** (583.66 mg, 2.74 mmol, 4.0 eq.) and then dissolved in toluene. The mixture was stirred and heated at 106 °C for 12 h under reflux. The suspension was filtered and washed with CH_3CN and then the residual solvent was removed *in vacuo*. The product $\mathbf{L^{4n}}$ (23.0 mg, 45.58 mmol, 7 %) was obtained as a brownish solid.

^{1}H-NMR (600 MHz, 298 K, CD_3CN): δ (ppm) = 9.54 (s, 1H, a), 8.51 (d, J = 5.7 Hz, 1H, b), 7.72 (dd, J = 5.7, 1.0 Hz, 1H, c), 7.71 – 7.62 (m, 2H, f, d), 7.29 (dd, J = 7.3, 1.2 Hz, 1H, e), 3.48 – 3.46 (m, 4H), 3.43 (t, J = 5.1 Hz, 4H).

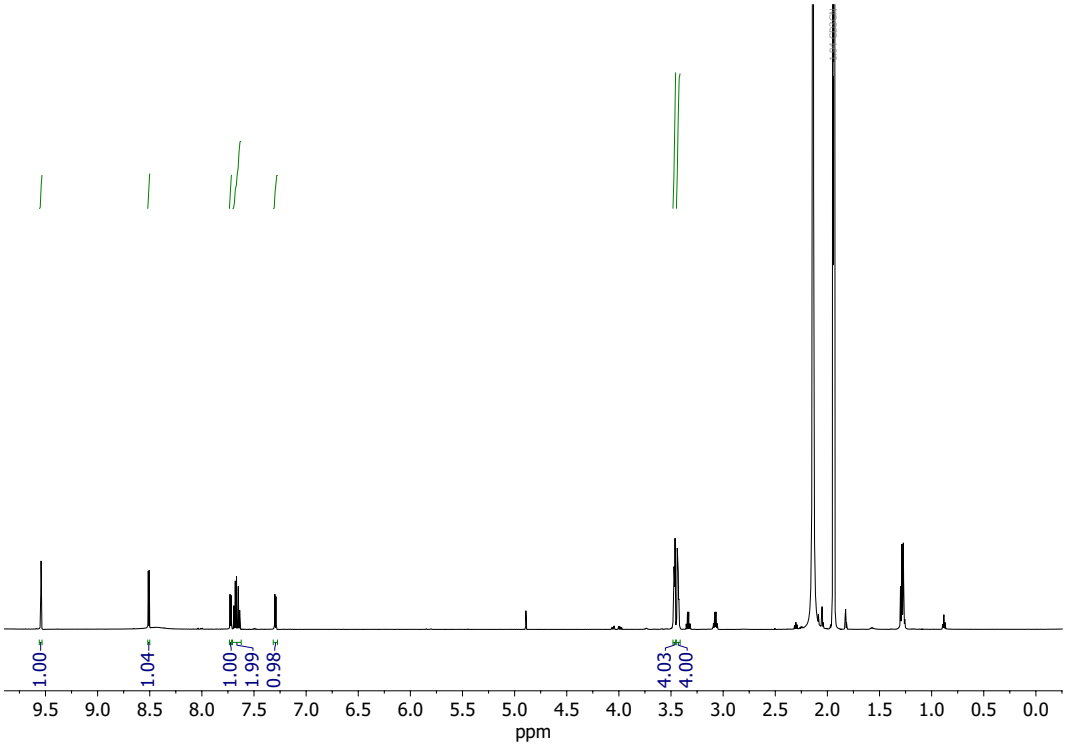

Figure 4.59. ^{1}H-NMR Spectrum (600 MHz, 298 K, CD_3CN) of **L^{4n}**.

^{13}C-NMR (151 MHz, 298 K, CD_3CN): δ (ppm)= 150.16, 149.35, 144.22, 138.29, 131.76, 124.32, 123.72, 121.60, 50.69, 47.06, 45.00, 30.36.

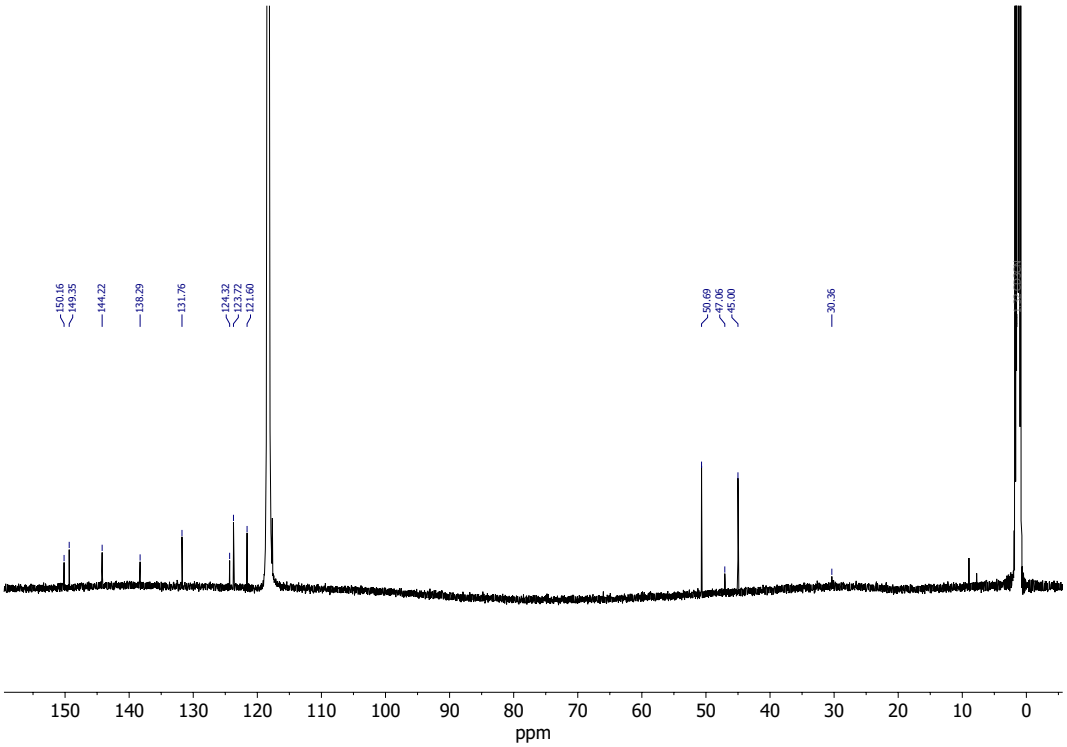

Figure 4.60. ^{13}C-NMR Spectrum (151 MHz, 298 K, CD_3CN) of **L^{4n}**.

4.2.10 Squaraine Dyes-based Ligands

Synthesis of P7

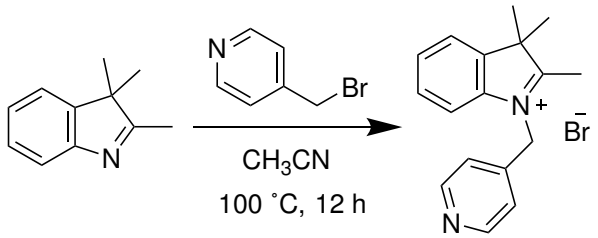

P7

Figure 4.61. Synthesis of **P7**.

4-(Bromomethyl)pyridine (2.70 g, 10.68 mmol, 1.7 eq.) was added to 2,3,3-Trimethylindolenine (1.0 g, 6.28 mmol, 1.0 eq.) then dissolved in CH_3CN. The mixture was stirred and refluxed at 100 °C for 12 h. After cooling down diethylether was added and the precipitate was filtered and washed with cold diethylether. The product could not be obtained.

Synthesis of P8

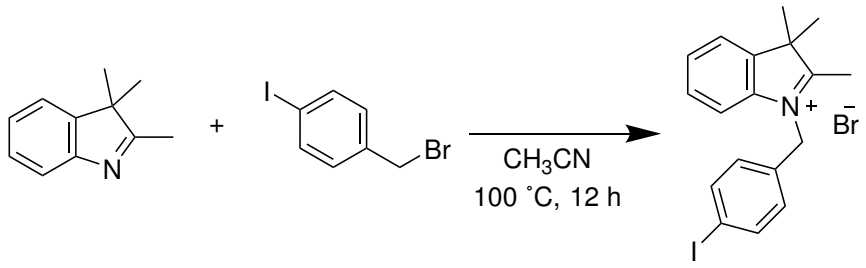

P8

Figure 4.62. Synthesis of **P8**.

1-(bromomethyl)-4-iodobenzene (1.12 g, 3.77 mmol, 1.2 eq.) was added to 2,3,3-Trimethylindolenine (500.00 mg, 3.14 mmol, 1.0 eq.) then dissolved in CH_3CN. The mixture was stirred and refluxed at 100 °C under argon atmosphere for 12 h. The solvent was removed *in vacuo*. The residue was dissolved in DCM and diethylether was added. The precipitate was filtered and washed with cold diethylether. The product could not be obtained.

Synthesis of P9

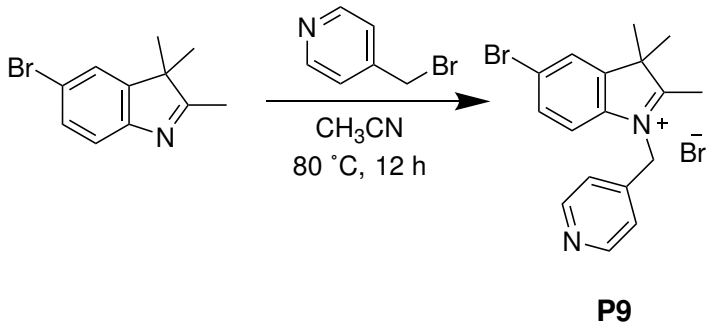

P9

Figure 4.63. Synthesis of **P9**.

4-(Bromomethyl)pyridine (108.36 mg, 0.63 mmol, 1.5 eq.) was added to 5-bromo-2,3,3-trimethyl-3H-indole (100.0 mg, 0.42 mmol, 1.0 eq.) then dissolved in CH_3CN. The mixture was stirred and refluxed at 80 °C for 12 h. After cooling to rt, the precipitate was filtered and washed with cold diethylether. The product could not be obtained.

Synthesis of P10

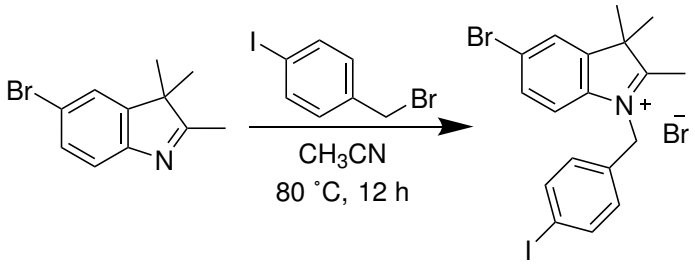

P10

Figure 4.64. Synthesis of **P10**.

1-(bromomethyl)-4-iodobenzene (187.34 mg, 0.63 mmol, 1.5 eq.) was added to 5-bromo-2,3,3-trimethyl-3H-indole (100.0 mg, 0.42 mmol, 1.0 eq.) then dissolved in CH_3CN. The mixture was stirred and refluxed at 80 °C for 12 h. After cooling to rt, the precipitate was filtered and washed with cold diethylether. The product could not be obtained.

Synthesis of P11

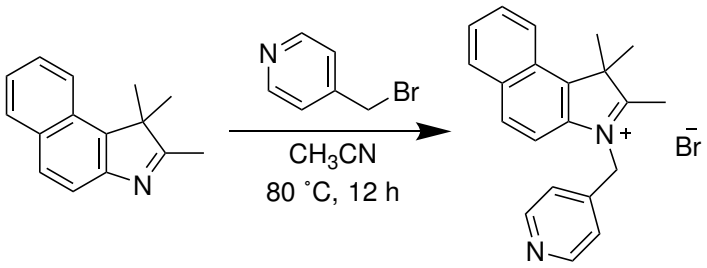

P11

Figure 4.65. Synthesis of **P11**.

4-(Bromomethyl)pyridine (123.29 mg, 0.71 mmol, 1.5 eq.) was added to 1,1,2-trimethyl-1H-benzo[e]indole (100.0 mg, 0.48 mmol, 1.0 eq.) then dissolved in CH_3CN. The mixture was stirred and refluxed at 80 °C for 12 h. After cooling to rt, the precipitate was filtered and washed with cold diethylether. The product could not be obtained.

4.2.11 Synthesis of Ligand L^{sd1}

Synthesis of P12

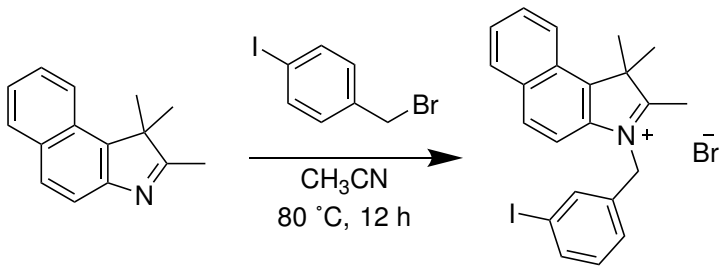

P12

Figure 4.66. Synthesis of **P12**.

1-(bromomethyl)-3-iodobenzene (2.13 g, 7.17 mmol, 1.5 eq.) was added to 1,1,2-trimethyl-1H-benzo[e]indole (1.00 g, 4.78 mmol, 1.0 eq.) then dissolved in CH_3CN. The mixture was stirred and refluxed at 80 °C for 12 h. After cooling to rt, the precipitate was filtered and washed with cold diethylether. The product **P12** (112,1 mg, 0.22 mmol, 46 %) was obtained as a bright green solid.

^{1}H-NMR (600 MHz, 298 K, CD_3CN): δ (ppm) = 8.31 (dt, J = 8.6, 1.0 Hz, 1H), 8.13 (dt, J = 9.2, 1.1 Hz, 2H), 7.84 (m, J = 1.8 Hz, 1H), 7.82 – 7.71 (m, 4H), 7.28 (ddd, J = 7.9, 1.9, 1.0 Hz, 1H), 7.17 (t, J = 7.9 Hz, 1H), 5.79 (s, 2H), 2.94 (s, 3H), 1.85 (s, 6H).

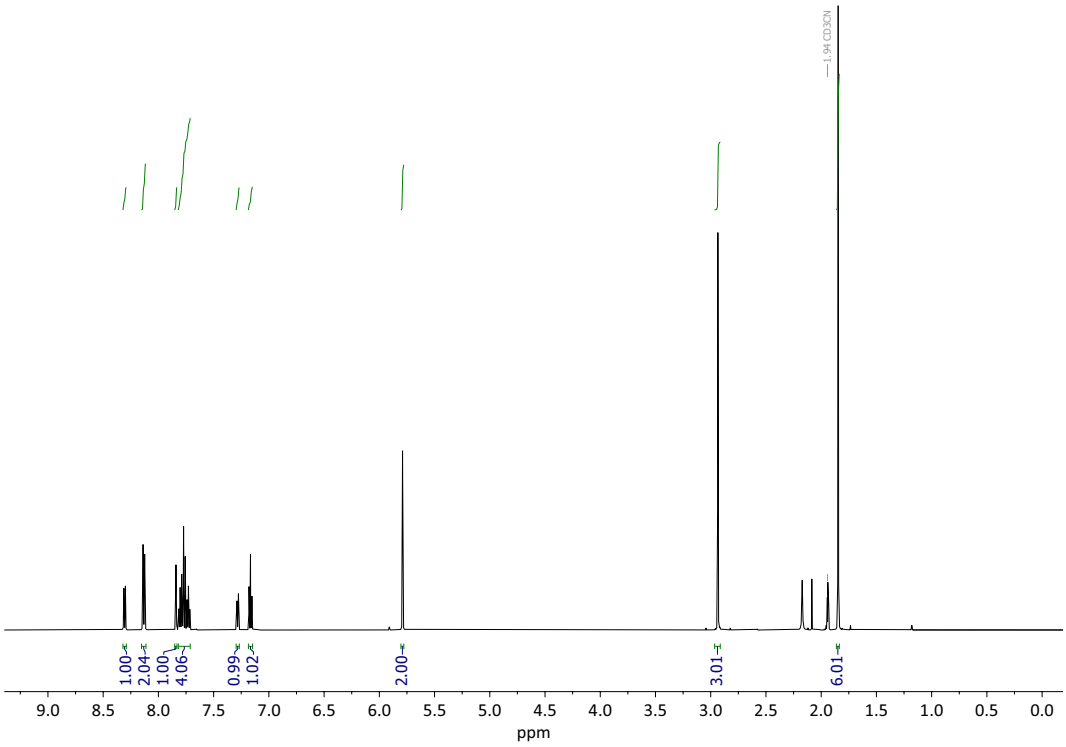

Figure 4.67. ^{1}H-NMR Spectrum (600 MHz, 298 K, CD_3CN) of **P12**.

^{13}C-NMR (151 MHz, 298 K, CD_3CN): δ (ppm)= 199.42, 139.56, 139.19, 138.56, 137.21, 134.67, 134.61, 132.24, 132.20, 130.90, 129.64, 128.79, 128.66, 127.37, 124.40, 114.01, 95.52, 57.38, 51.74, 22.47, 15.39.

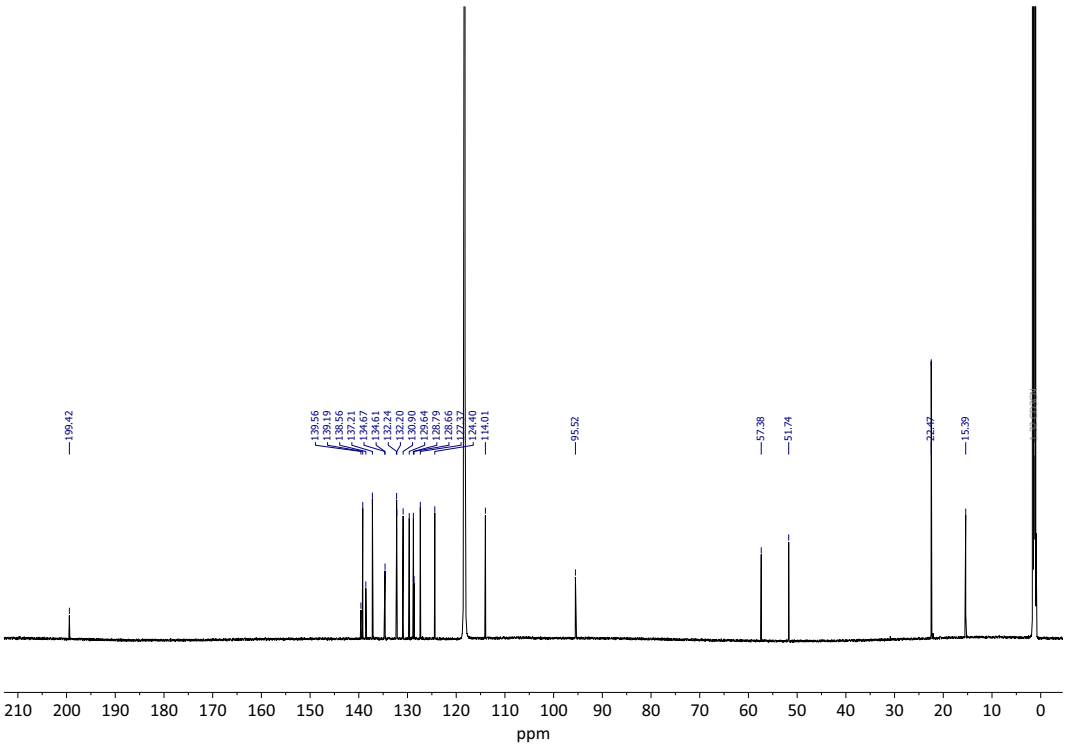

Figure 4.68. ^{13}C-NMR Spectrum (151 MHz, 298 K, CD_3CN) of **P12**.

Synthesis of P13

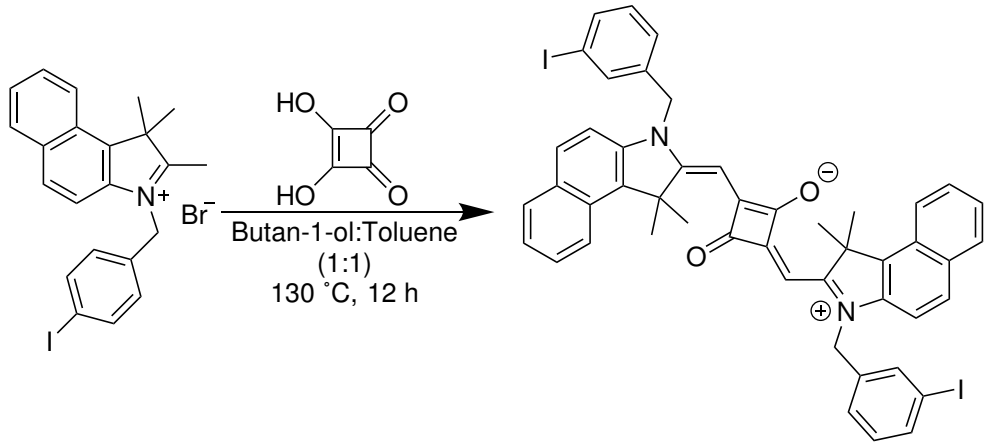

P12 **P13**

Figure 4.69. Synthesis of **P13**.

In a Dean-Stark apparatus **P12** (1.10 g, 2.17 mmol, 2.2 eq.), squaric acid (112,65 mg, 0.99 mmol), toluene (75 mL), 1-butanol (75 mL) were combined and heated to reflux for 12 h. The reaction mixture readily turns deep green. Then the reaction mixture was concentrated *in vacuo*. The residue was purified by means of column chromatography (SiO_2, DCM/MeOH 99:1 → 14:1). The product **P13** (515.9 mg, 0.56 mmol, 56 %) was obtained as a glittering green solid.

Comment: Removing BuOH by distillation or lyophilization!

^{1}H-NMR (600 MHz, 298 K, DMSO$-d_6$): δ (ppm) = 8.27 – 8.25 (m, 2H), 8.02 – 7.98 (m, 4H), 7.70 (m, 2H), 7.67 – 7.63 (m, 6H), 7.47 (ddd, J = 8.0, 6.8, 1.1 Hz, 2H), 7.16 – 7.15 (m, 4H), 5.84 (s, 2H), 5.54 (s, 4H), 2.00 (s, 12H).

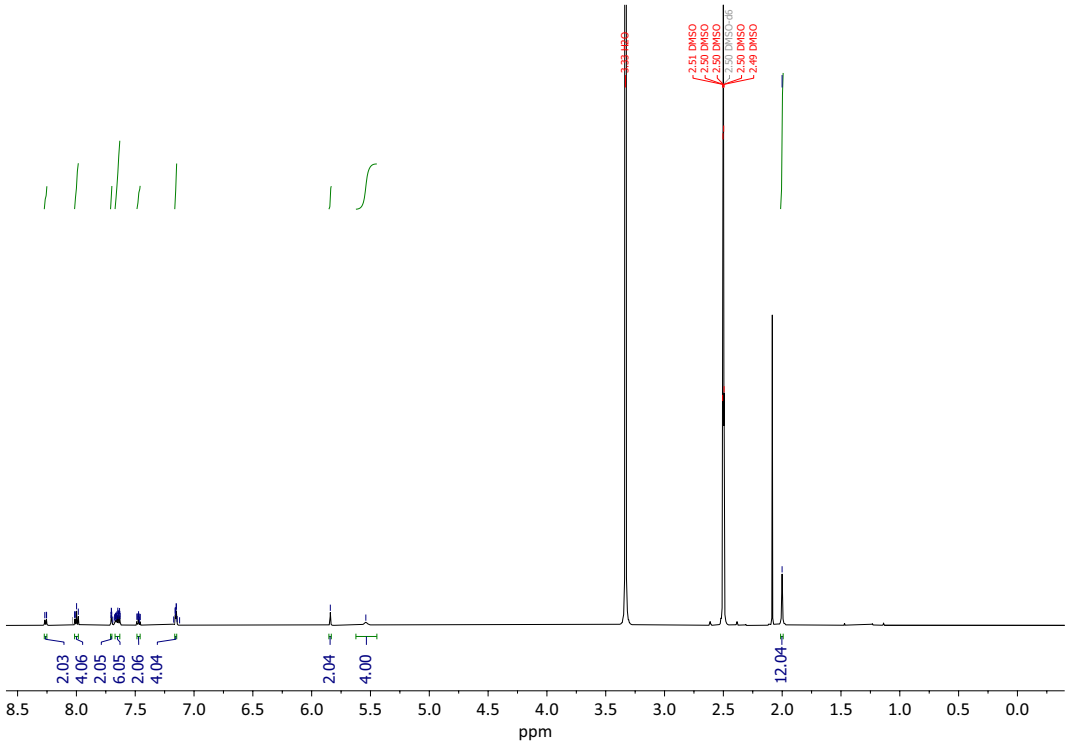

Figure 4.70. ^{1}H-NMR Spectrum (600 MHz, 298 K, CD_3CN) of **P13**.

^{13}C-NMR (151 MHz, 298 K, DMSO$-d_6$): δ (ppm)= 170.86, 139.83, 137.99, 136.32, 135.08, 131.19, 131.02, 130.02, 129.79, 127.97, 127.61, 125.21, 124.40, 122.31, 111.21, 95.37, 50.74, 45.36, 40.06, 39.92, 26.39.

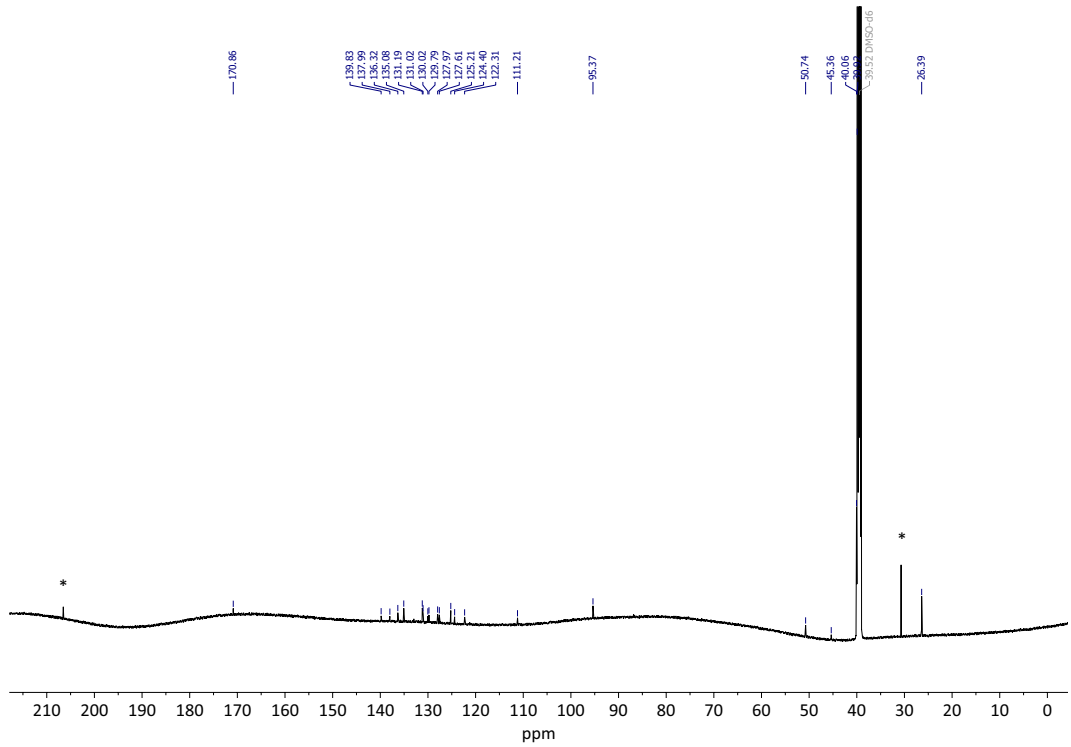

Figure 4.71. ^{13}C-NMR Spectrum (151 MHz, 298 K, DMSO$-d_6$) of **P13**.

Synthesis of L^{sd1}

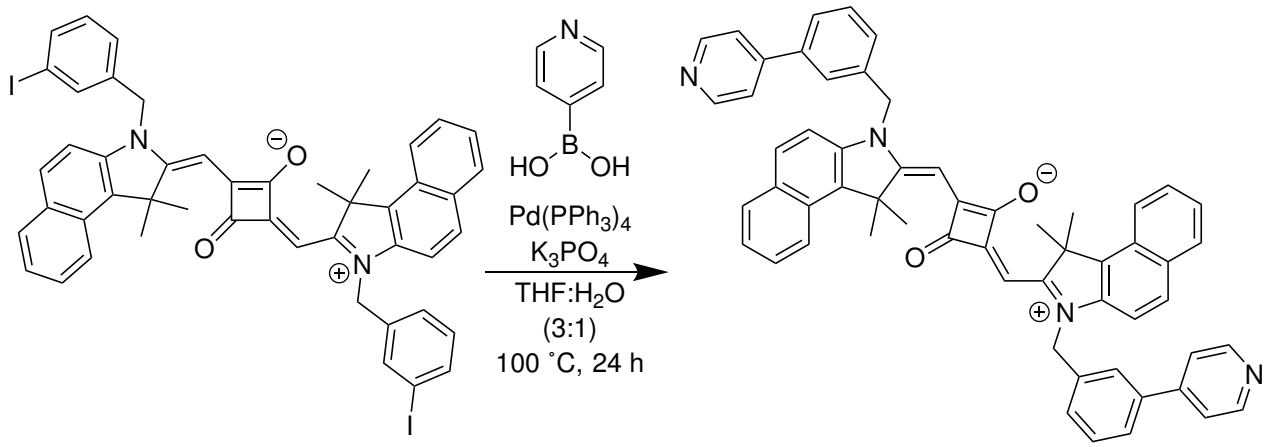

P13 **L^{sd1}**

Figure 4.72. Synthesis of **552**.

Pyridin-4-ylboronic acid (43.68 mg, 0.71 mmol, 2.2 eq.) was added to **P13** (150.00 mg, 0.32 mmol, 1.0 eq.), $Pd(PPh_3)_4$ (18.67 mg, 0.02 mmol, 0.05 eq.) and K_3PO_4 (274.29 g, 1.29 mmol, 4.0 eq.) and then dissolved in THF:H_2O (3:1) and degassed. The mixture was stirred and heated at 100 °C for 24 h in a pressure flask. The solvent was removed *in vacuo* and the residue was purified by means of column chromatography (SiO_2, MeOH/DCM 1:99 → 1:10). Recrystallization from *n*-BuOH provided the product $\mathbf{L^{sd1}}$ (37 mg, 0.45 mmol, 28 %) as a blue solid.

^{1}H-NMR (600 MHz, 298 K, DMSO$-d_6$): δ (ppm) = 8.72 – 8.69 (m, 2H), 8.27 (d, J = 8.4 Hz, 1H), 8.02 – 7.99 (m, 2H), 7.85 (d, J = 1.9 Hz, 1H), 7.79 (dd, J = 16.2, 6.5 Hz, 3H), 7.73 (d, J = 8.9 Hz, 1H), 7.64 (ddd, J = 8.4, 6.8, 1.4 Hz, 1H), 7.52 (t, J = 7.8 Hz, 1H), 7.47 (ddd, J = 8.0, 6.8, 1.0 Hz, 1H), 7.25 (d, J = 7.8 Hz, 1H), 5.93 (s, 1H), 5.64 (s, 2H), 2.01 (s, 6H).

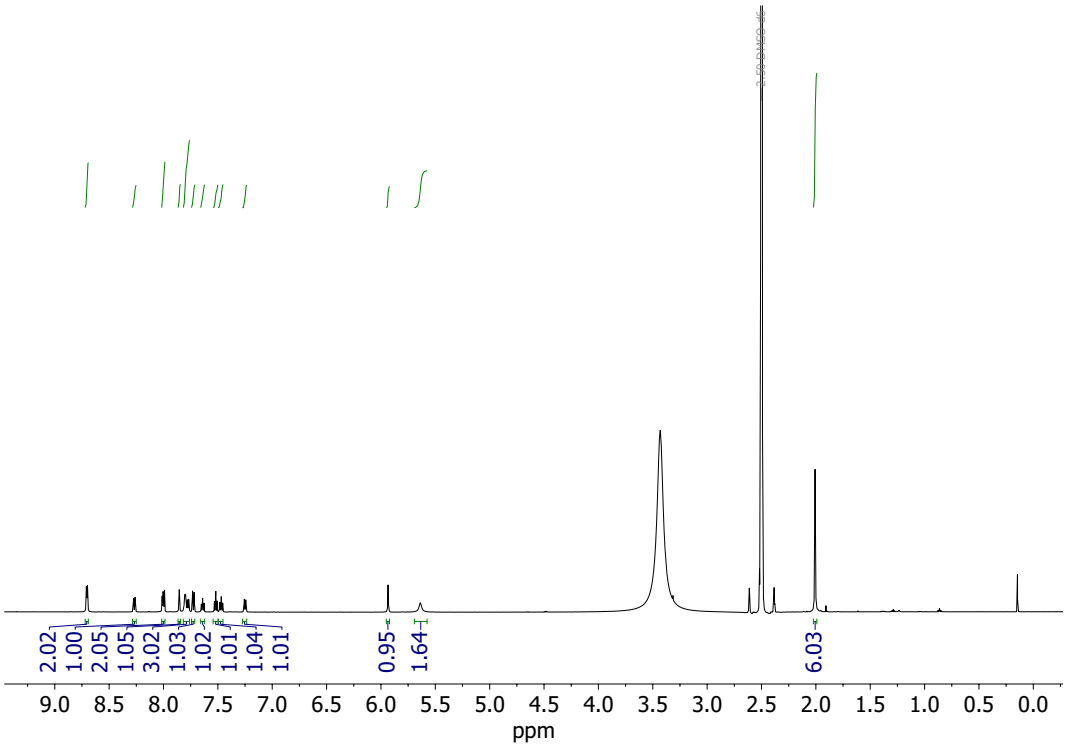

Figure 4.73. ^{1}H-NMR Spectrum (600 MHz, 298 K, CD_3CN) of ligand $\mathbf{L^{sd1}}$.

^{13}C-NMR (151 MHz, 298 K, DMSO$-d_6$): δ (ppm)= 193.75, 178.48, 170.85, 148.92, 139.93, 137.28, 136.57, 133.02, 131.01, 130.11, 130.00, 129.78, 127.99, 127.58, 127.04, 126.47, 125.58, 124.37, 122.32, 121.74, 121.74, 111.28, 86.87, 50.73, 46.17, 26.40.

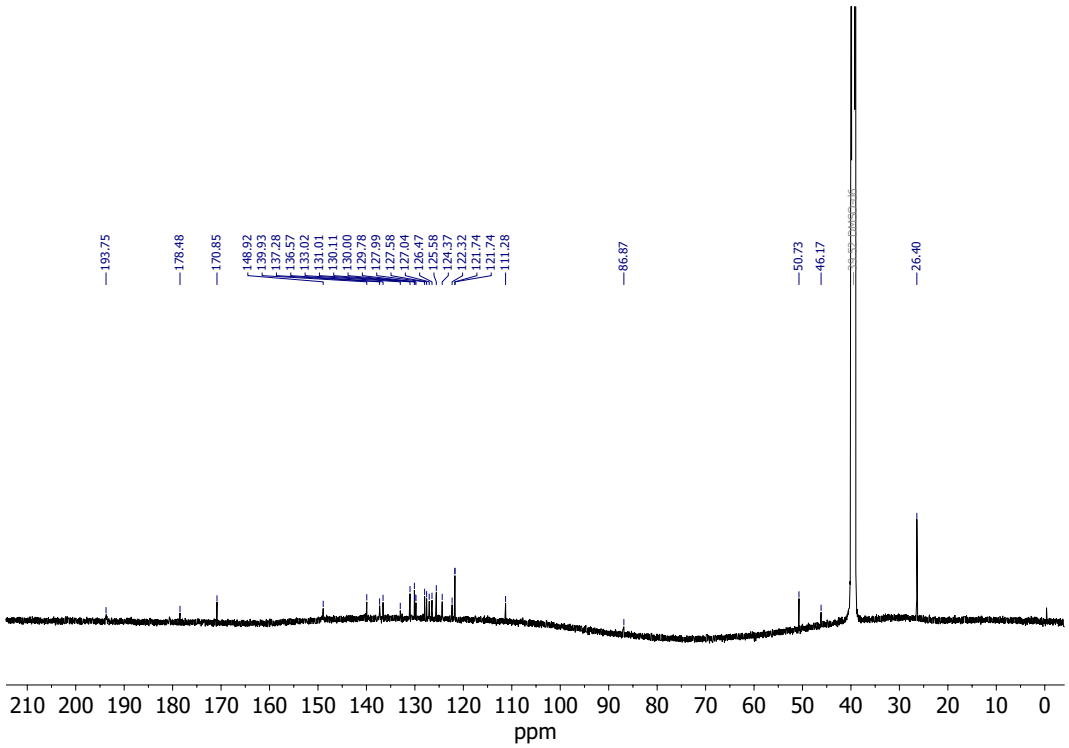

Figure 4.74. ^{13}C-NMR Spectrum (151 MHz, 298 K, DMSO$-d_6$) of ligand $\mathbf{L^{sd1}}$. 10240 scans

4.2.12 Synthesis of Ligand L^{sd2}

4.2.13 Synthesis of P14

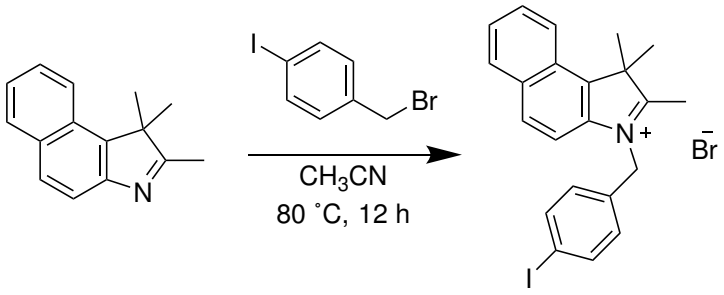

P14

Figure 4.75. Synthesis of **P14**.

1-(bromomethyl)-4-iodobenzene (2.13 g, 7.17 mmol, 1.5 eq.) was added to 1,1,2-trimethyl-1H-benzo[e]indole (1.00 g, 4.78 mmol, 1.0 eq.) then dissolved in CH_3CN. The mixture was stirred and refluxed at 80 °C for 12 h. After cooling to rt, the precipitate was filtered and washed with cold diethylether. The product **P14** (2.03 g, 4.01 mmol, 84 %) was obtained as a bright green solid.

^{1}H-NMR (700 MHz, 298 K, CD_3CN): δ (ppm) = 8.30 (dt, J = 8.5, 1.0 Hz, 1H), 8.14 – 8.11 (m, 2H), 7.81 – 7.76 (m, 4H), 7.72 (ddt, J = 8.1, 6.9, 1.1 Hz, 1H), 7.18 – 7.14 (m, 2H), 5.82 – 5.74 (m, 2H), 2.95 – 2.91 (m, 3H), 1.84 (s, 6H).

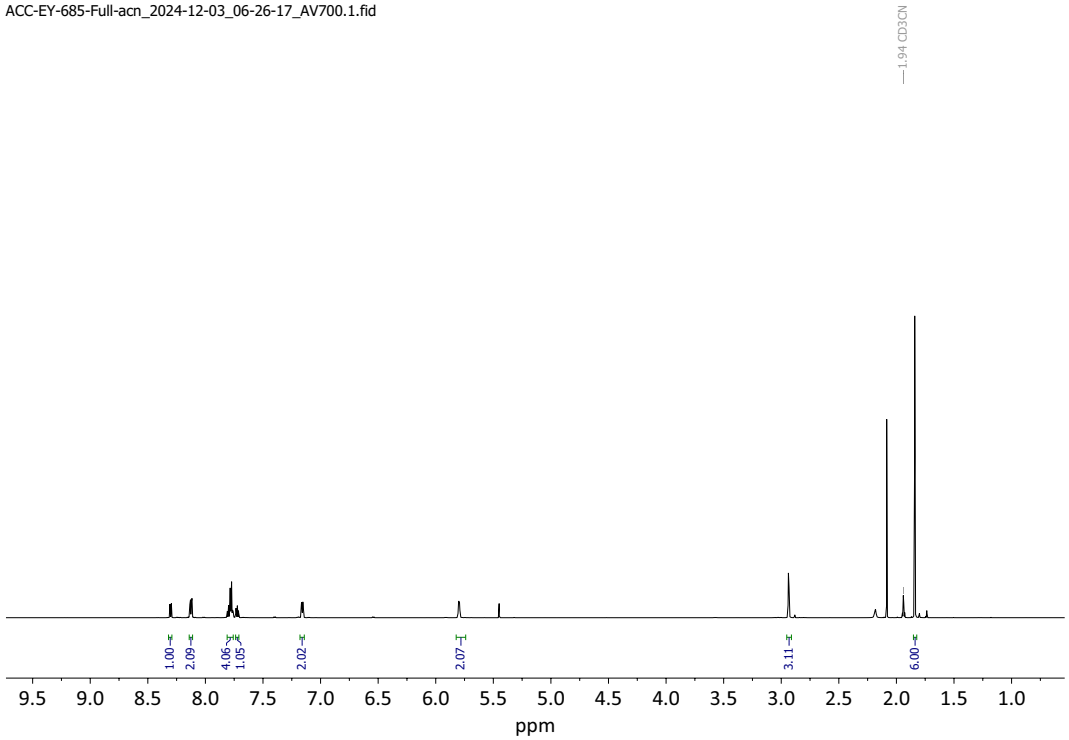

Figure 4.76. ^{1}H-NMR Spectrum (600 MHz, 298 K, CD_3CN) of **P14**.

^{13}C-NMR (151 MHz, 298 K, CD_3CN): δ (ppm)= 99.23, 139.58, 139.43, 139.43, 138.54, 134.64, 132.25, 132.13, 130.88, 130.27, 129.61, 128.75, 128.63, 124.38, 114.07, 95.28, 57.33, 52.14, 22.43, 22.43, 15.41.

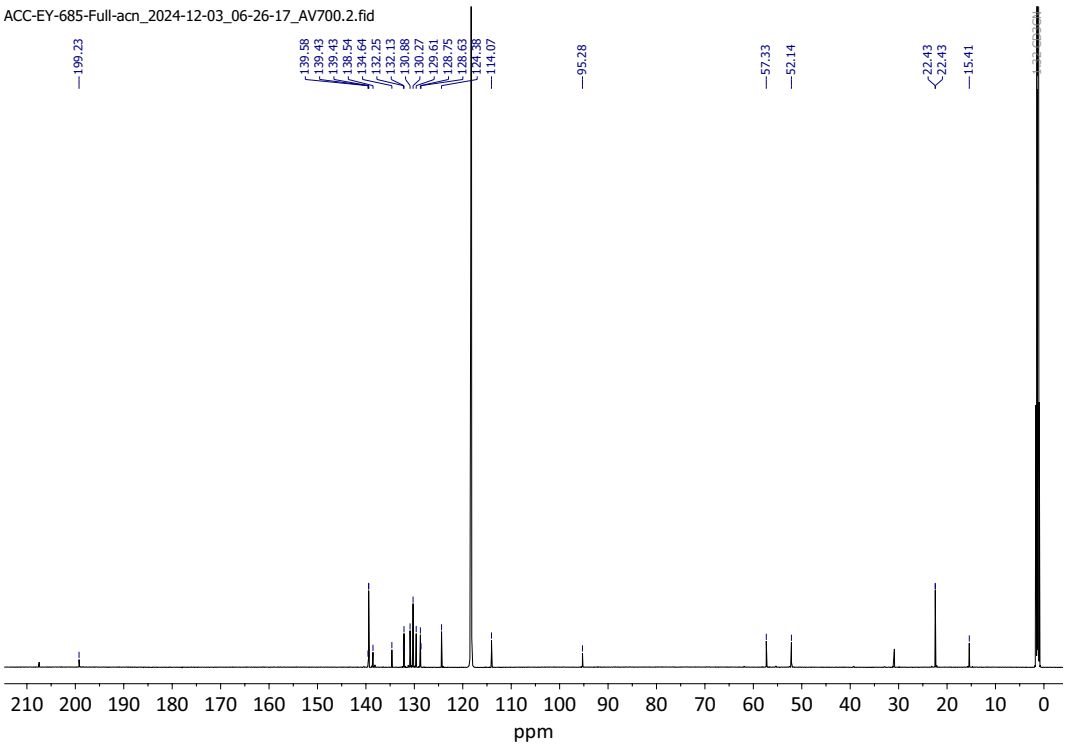

Figure 4.77. ^{13}C-NMR Spectrum (151 MHz, 298 K, CD_3CN) of **P14**.

Synthesis of P15

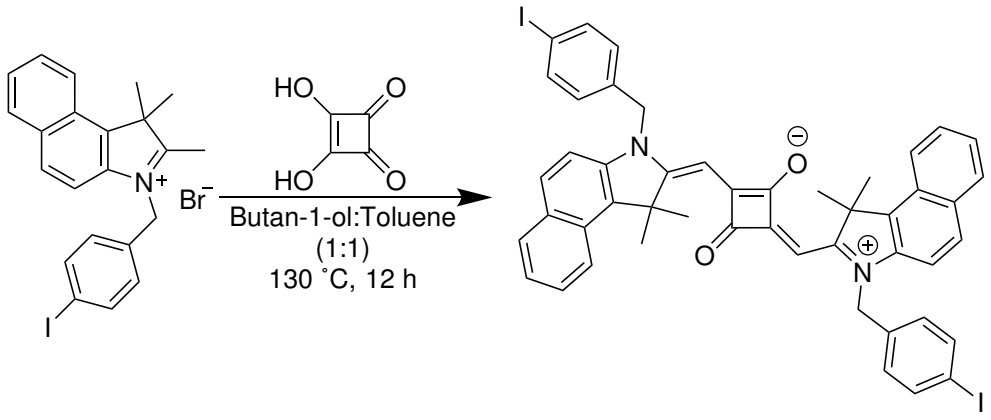

P14 **P15**

Figure 4.78. Synthesis of **P15**.

In a Dean-Stark apparatus **14** (0.62 mg, 1.22 mmol, 2.2 eq.), squaric acid (63,19 mg, 0.55 mmol), toluene (75 mL), 1-butanol (75 mL) were combined and heated to reflux for 12 h. Reaction mixture readily turns deep green. Then the reaction mixture was concentrated *in vacuo*. The residue was purified by means of column chromatography (SiO_2, DCM/MeOH 99:1 → 14:1). The product **P15** (126.9 mg, 0.14 mmol, 24 %) was obtained as a glittering green solid.

Comment: Removing BuOH by distillation or lyophilization!

^{1}H-NMR (600 MHz, 298 K, DMSO$-d_6$): δ (ppm) = 8.02 – 7.97 (m, 2H), 7.75 – 7.72 (m, 2H), 7.66 – 7.62 (m, 2H), 7.47 (ddd, J = 8.0, 6.8, 1.1 Hz, 1H), 7.09 – 7.05 (m, 2H), 5.83 (s, 1H), 5.49 (s, 2H), 1.99 (s, 6H).

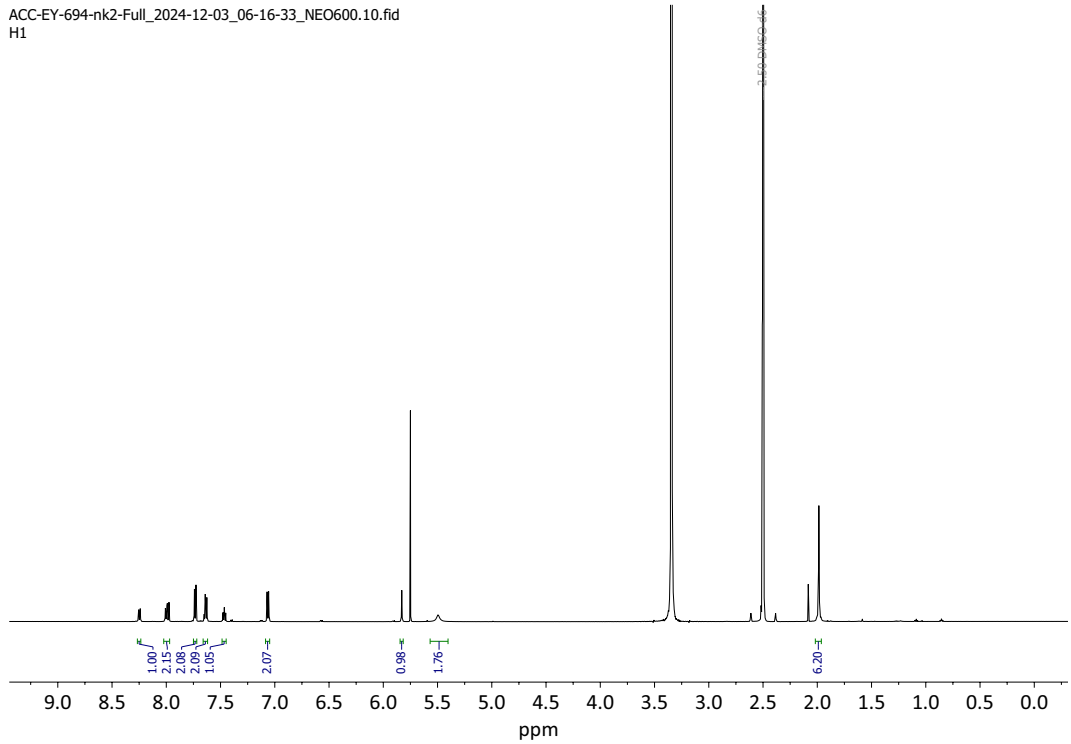

Figure 4.79. ^{1}H-NMR Spectrum (600 MHz, 298 K, CD_3CN) of **P15**.

^{13}C-NMR (151 MHz, 298 K, DMSO$-d_6$): δ (ppm)= 170.80, 139.90, 137.74, 135.29, 131.02, 129.98, 129.78, 128.63, 127.99, 127.60, 124.38, 122.29, 111.23, 93.60, 54.92, 50.73, 45.83, 26.37.

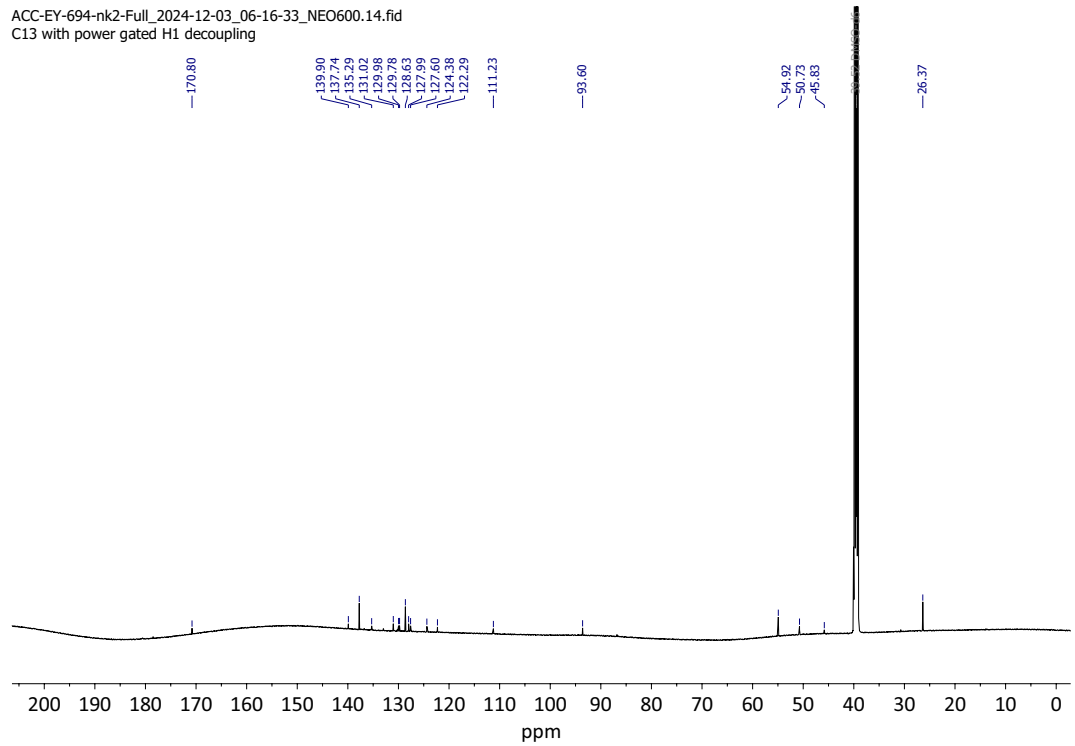

Figure 4.80. ^{13}C-NMR Spectrum (151 MHz, 298 K, DMSO$-d_6$) of **P15**.

Ligand L^{sd2}

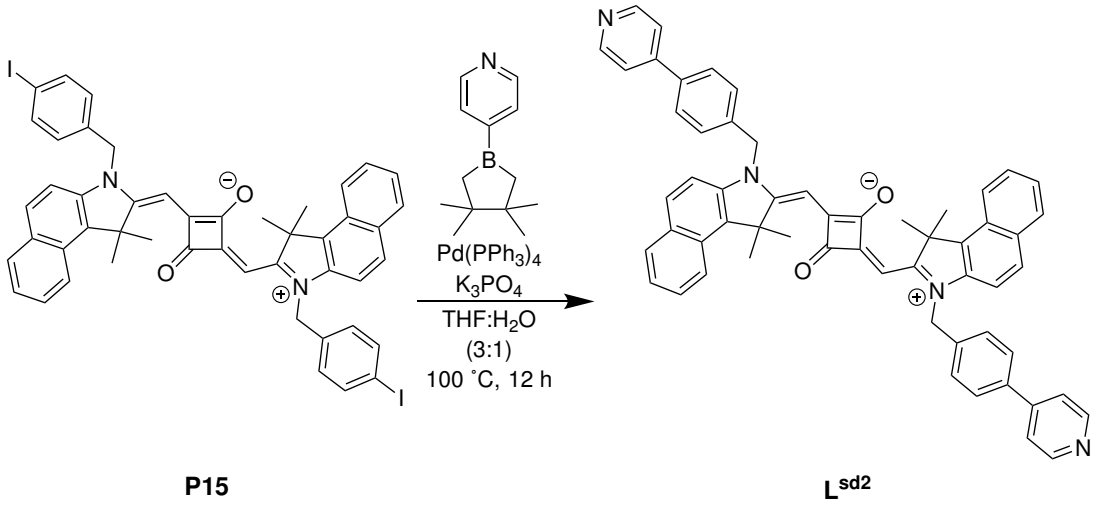

P15 **L^{sd2}**

Figure 4.81. Synthesis of **L^{sd2}**.

4-(4,4,5,5-tetramethyl-1,3,2-dioxaborolan-2-yl)pyridine (29.15 mg, 0.14 mmol, 2.2 eq.) was added to **P15** (60.00 mg, 0.06 mmol, 1.0 eq.), $Pd(PPh_3)_4$ (3.73 mg, 0.01 mmol, 0.05 eq.) and K_3PO_4 (54.86 mg, 0.26 mmol, 4.0 eq.) and then dissolved in THF:H_2O (3:1) and degassed. The mixture was stirred and heated at 100 °C for 12 h in a pressure flask. The solvent was removed *in vacuo* and the residue was purified by means of column chromatography (SiO_2, MeOH/DCM 1:99 → 1:10) provided the product **L^{sd2}** (13 mg, 0.02 mmol, 24 %) as a blue solid.

^{1}H-NMR (600 MHz, 298 K, DMSO−d_6): δ (ppm) = 8.67 (d, J = 5.4 Hz, 2H), 8.28 – 8.24 (m, 1H), 8.02 – 7.99 (m, 2H), 7.86 (d, J = 8.2 Hz, 2H), 7.83 – 7.77 (m, 2H), 7.69 – 7.63 (m, 2H), 7.47 (ddd, J = 8.0, 6.8, 1.1 Hz, 1H), 7.41 (d, J = 8.4 Hz, 2H), 5.89 (s, 1H), 5.63 (s, 1H), 2.02 (s, 6H).

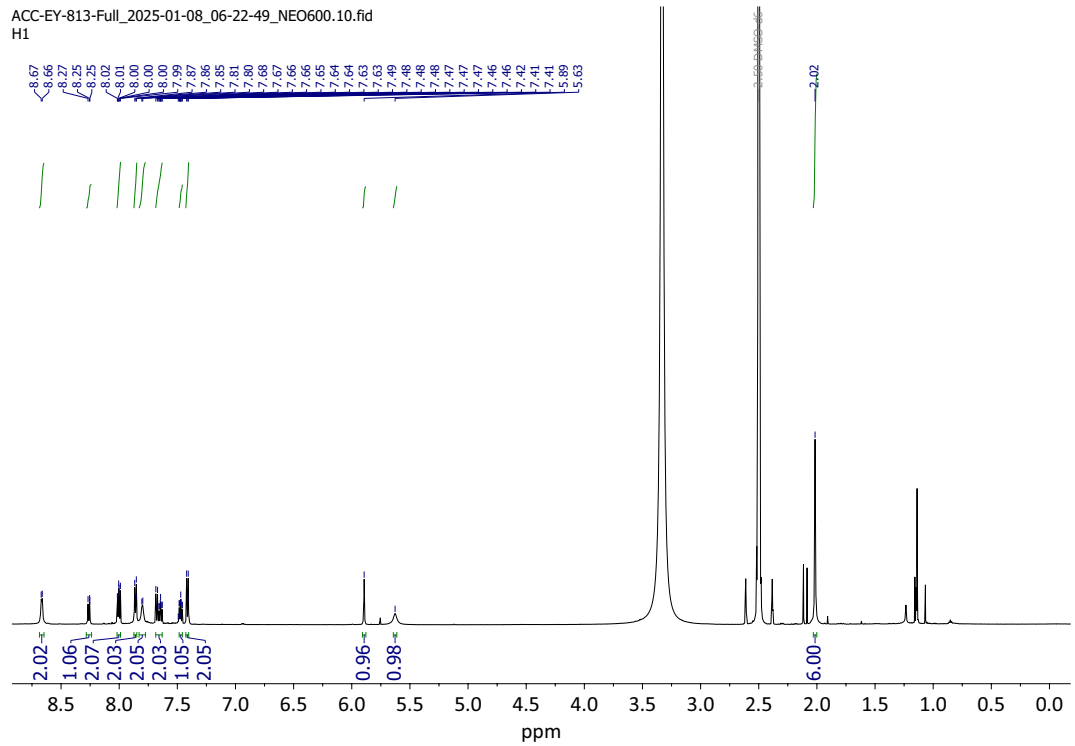

Figure 4.82. ^{1}H-NMR Spectrum (600 MHz, 298 K, DMSO$-d_6$) of $\mathbf{L^{sd2}}$.

Additional Synthesis

Synthesis of L^F

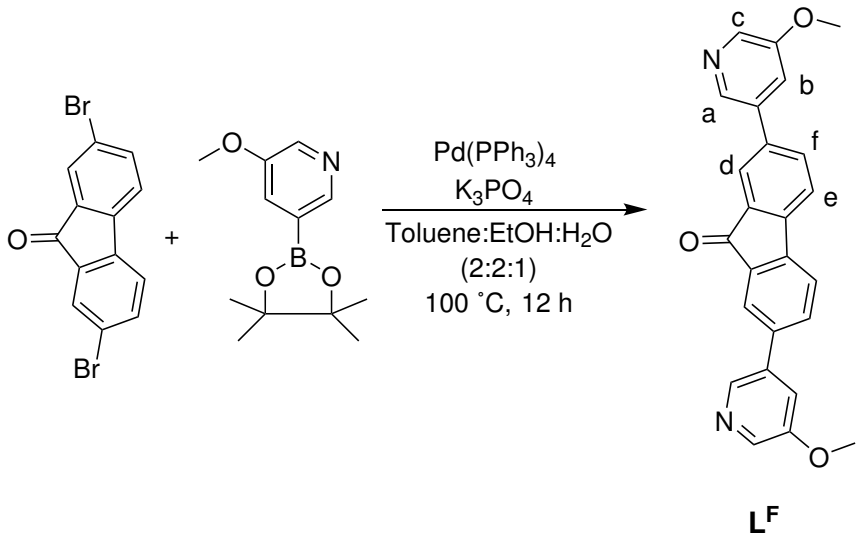

Figure 4.83. Synthesis of L^F.

2,7-dibromo-9H-fluoren-9-one (1.0 g, 2.96 mmol, 1.0 eq.) was added to 3-methoxy-5-(4,4,5,5-tetramethyl-1,3,2-dioxaborolan-2-yl)pyridine (2.09 g, 8.88 mmol, 3.0 eq.), $Pd(PPh_3)_4$ (239.32 mg, 0.21 mmol, 0.07 eq.) and K_3PO_4 (1.88 g, 8.88 mmol, 3.0 eq.) and then dissolved in Toluene:EtOH:H_2O (2:2:1) and degassed. The mixture was stirred and heated at 100 °C for 12 h in a pressure flask. The mixture cooled down to rt then filtered and washed with cold CH_3CN and EtOH. The residual solvent was removed *in vacuo*. The product $\mathbf{L^F}$ (213.0 mg, 0.54 mmol, 18 %) was obtained as an orange solid.

^{1}H-NMR (400 MHz, 298 K, DMSO$-d_6$): δ (ppm) = 8.59 (d, J = 1.9 Hz, 1H, a), 8.33 (d, J = 2.7 Hz, 1H, b), 8.08 – 8.01 (m, 3H, d, e, f), 7.77 (dd, J = 2.8, 1.9 Hz, 1H, c), 3.94 (s, 3H).

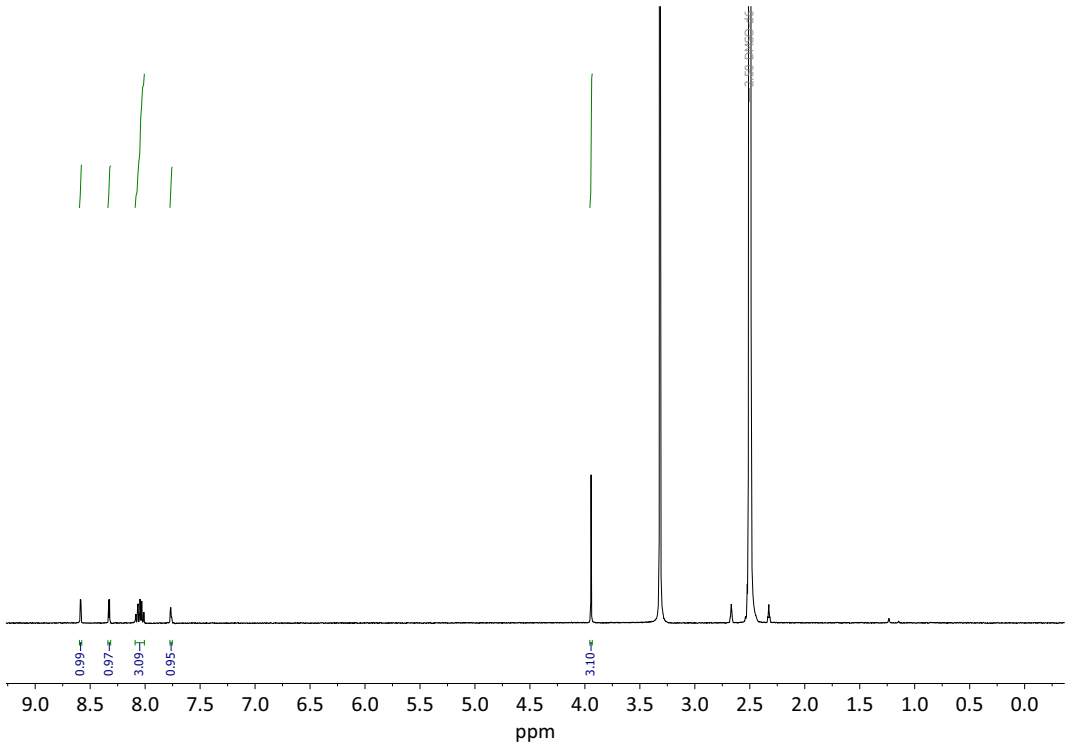

Figure 4.84. ^{1}H-NMR Spectrum (500 MHz, 298 K, DMSO$-d_6$) of ligand $\mathbf{L^F}$.

^{13}C-NMR (151 MHz, 298 K, DMSO$-d_6$): δ (ppm)= 192.99, 156.15, 143.70, 140.10, 138.81, 137.80, 135.72, 134.96, 134.67, 123.19, 122.65, 118.55, 56.21.

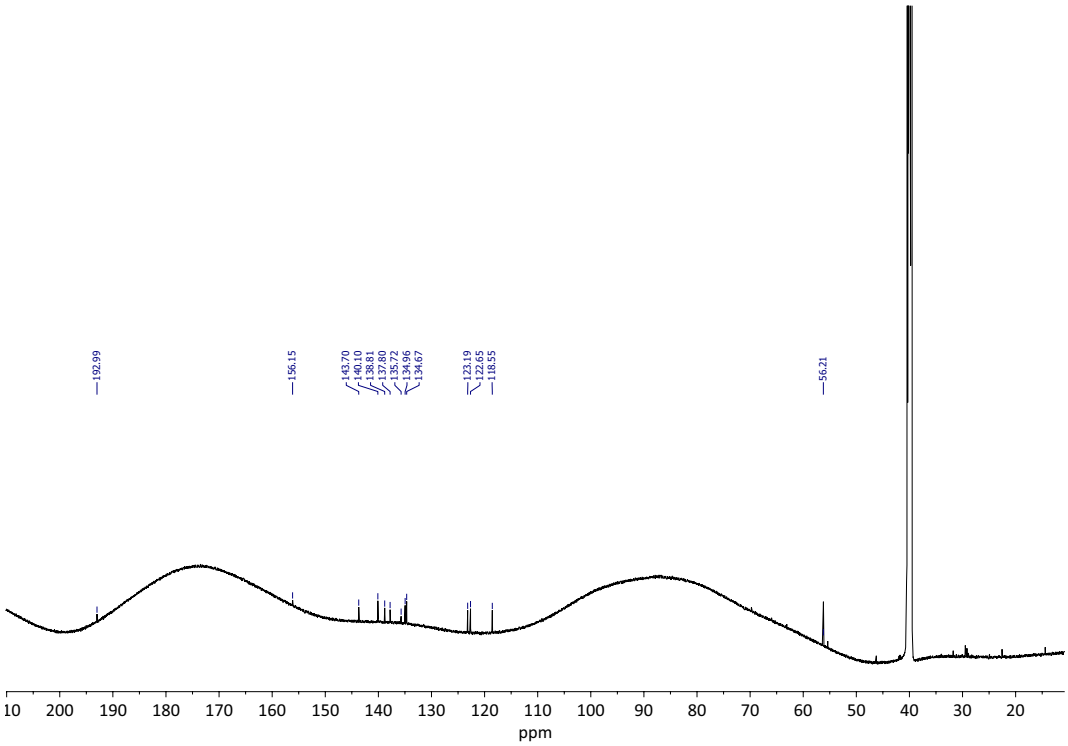

Figure 4.85. ^{13}C-NMR Spectrum (151 MHz, 298 K, CD_3CN) of ligand $\mathbf{L^F}$.

4.2.14 Synthesis of an urea-based backbone

Synthesis of P16

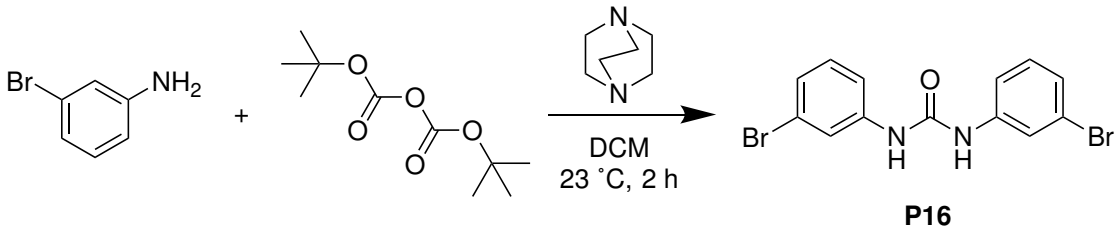

Figure 4.86. Synthesis of **P16**.

3-bromoaniline (316.46 μL, 2.91 mmol, 1.0 eq.) was added to di-tert-butyl dicarbonate (317.18 mg, 1.45 mmol, 0.5 eq.), DABCO (32.60 mg, 0.29 mmol, 0.1 eq.) then dissolved in DCM. The mixture was stirred at rt for 2 h. The reaction mixture was cooled to 0 °C, n−hexane was then added, the resulting white solid was collected and then washed with cold water and Et_2O. The product **P16** (438.64 mg, 1.19 mmol, 41 %) was obtained as a colorless solid.

^{1}H-NMR (600 MHz, 298 K, DMSO$-d_6$): δ (ppm) = 8.93 (s, 1H), 7.84 (t, J = 2.0 Hz, 1H), 7.31 (ddd, J = 8.2, 2.1, 1.0 Hz, 1H), 7.24 (t, J = 8.0 Hz, 1H), 7.16 (ddd, J =J = 7.9, 2.0, 1.0 Hz, 1H).

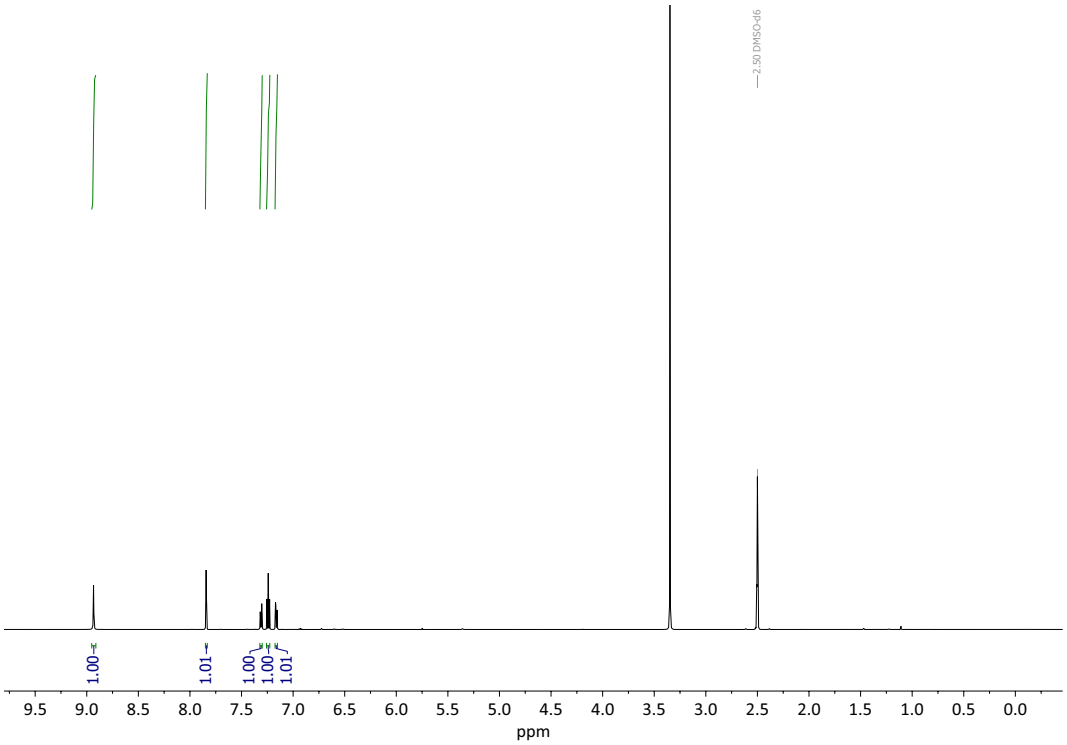

Figure 4.87. ^{1}H-NMR Spectrum (600 MHz, 298 K, DMSO$-d_6$) of **P16**.

^{13}C-NMR (151 MHz, 298 K, DMSO$-d_6$): δ (ppm)= 150.08, 148.93, 135.28, 134.32, 124.84.

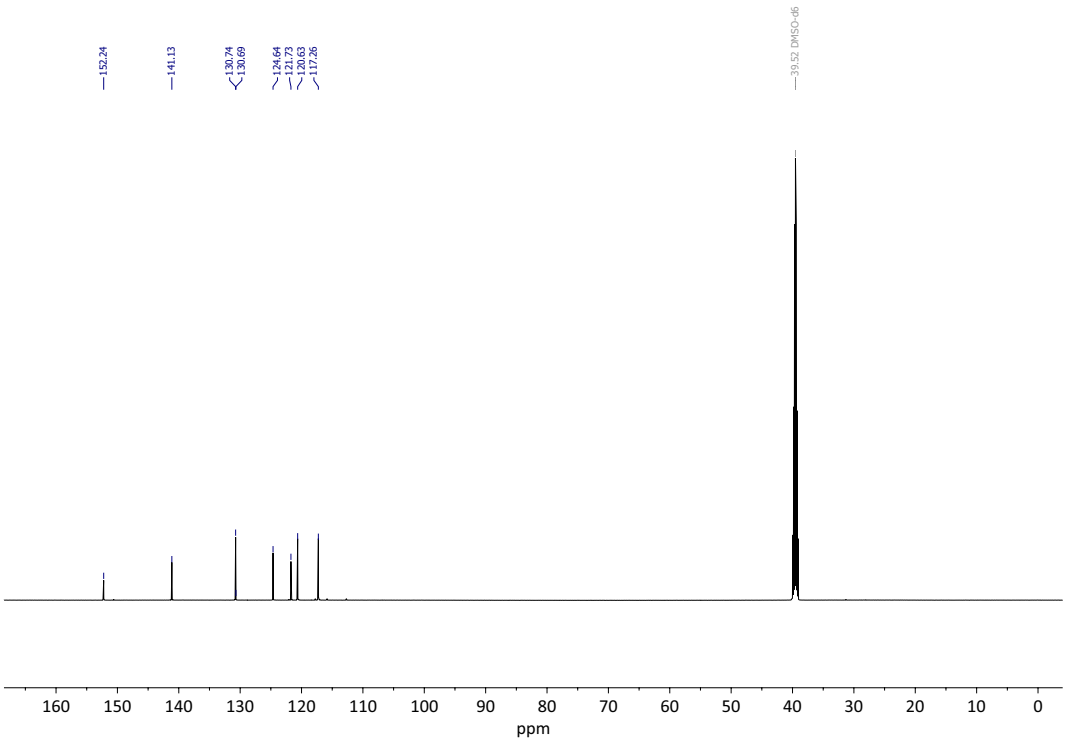

Figure 4.88. ^{13}C-NMR Spectrum (151 MHz, 298 K, DMSO$-d_6$) of **P16**.

4.3 Cage Formations

4.3.1 Homoleptic Coordination Cage Formation of Ligand L^2

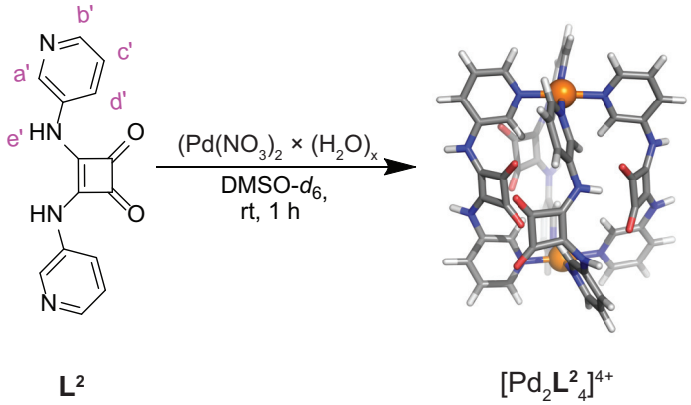

Figure 4.89. Homoleptic cage formation of $\mathbf{L^2}$ in DMSO-d_6. Calculated on PM6 level.

At room temperature 540 μL of $\mathbf{L^2}$ (1.51 mmol, 2.8 mM) in DMSO-d_6 was prepared with 15 mM $[Pd(CH_3CN)_4](BF_4)_2$ (1.13 mmol, 75 μL). The change in chemical shift of the ^{1}H-NMR signals suggest that a homoleptic species has been formed. ^{1}H DOSY NMR confirmed that one species was obtained. Mass spectrometry also suggests that the homoleptic species is formed. In Addition to that, r_H of $[Pd_2\mathbf{L^{59}}_4]^{4+}$ is 8,8 Å so it can be assumed that it is a $[Pd_2\mathbf{L}_4]^{4+}$ species.

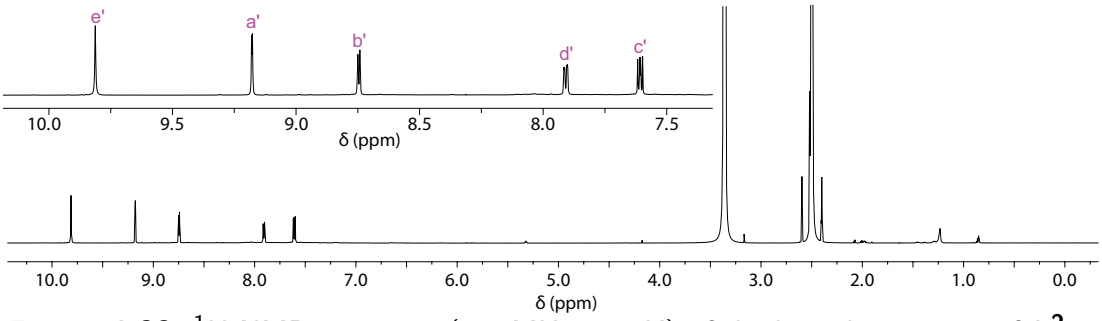

Figure 4.90. ^{1}H-NMR spectrum (500 MHz, 298 K) of the homoleptic cage of $\mathbf{L^2}$ in DMSO-d_6. The aromatic region is shown zoomed in.

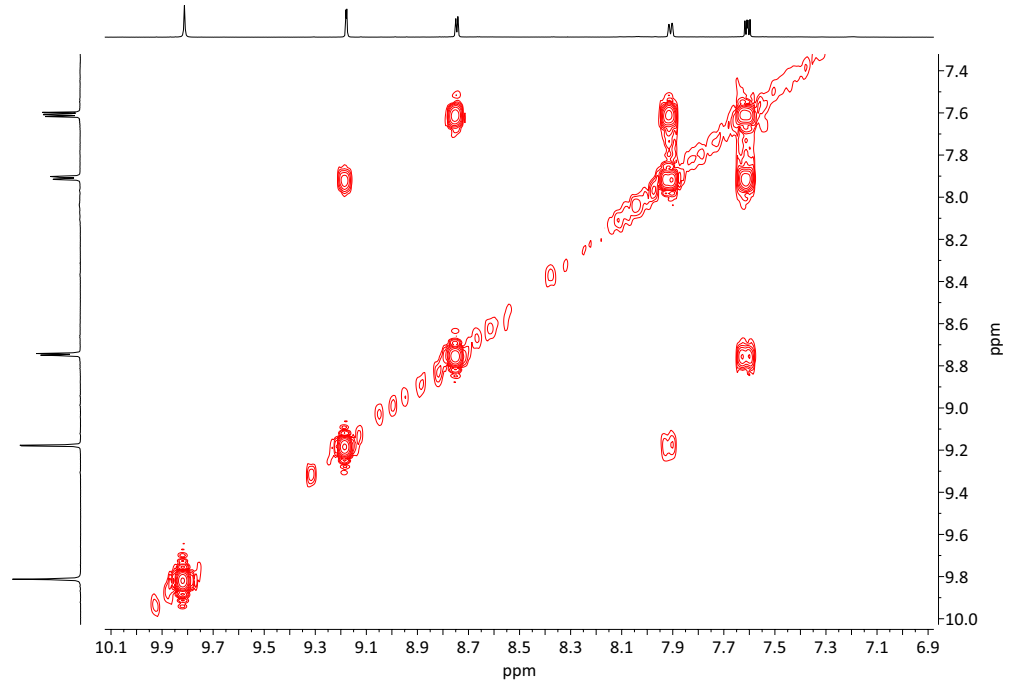

Figure 4.91. ^{1}H-^{1}H COSY spectrum (700 MHz, 298 K, DMSO-d_6) of spectrum of the cage formation of $\mathbf{L^2}$.

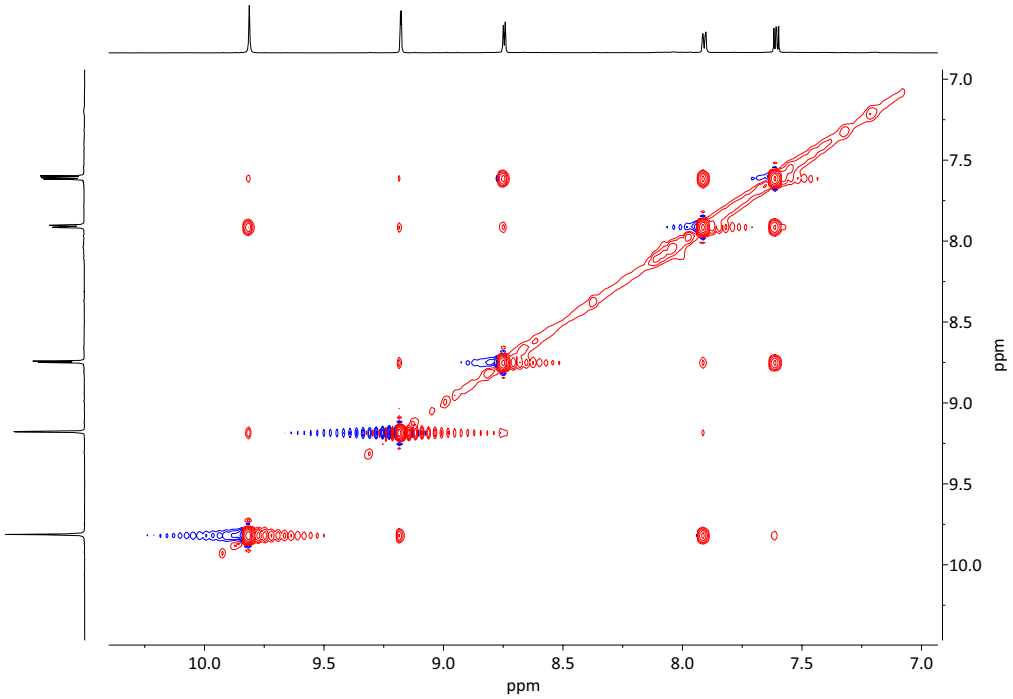

Figure 4.92. ^{1}H-^{1}H NOESY spectrum (700 MHz, 298 K, DMSO-d_6) of spectrum of the cage formation of $\mathbf{L^2}$.

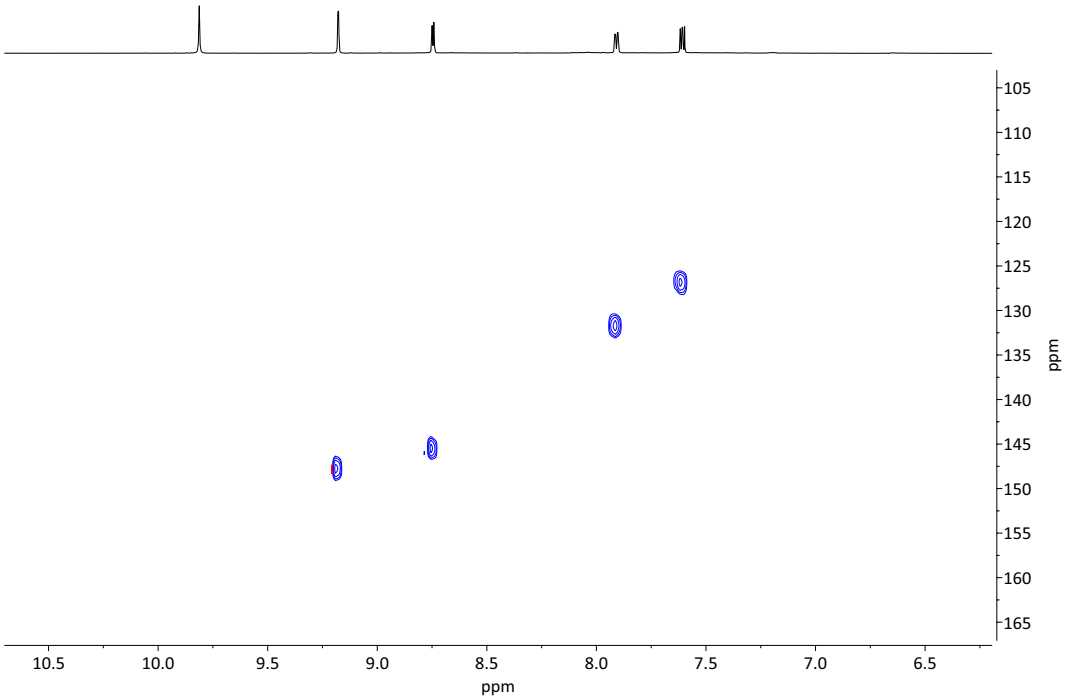

Figure 4.93. ^{1}H-^{13}C HSQC spectrum (700 MHz, 298 K, DMSO-d_6) of spectrum of the cage formation of **L²**.

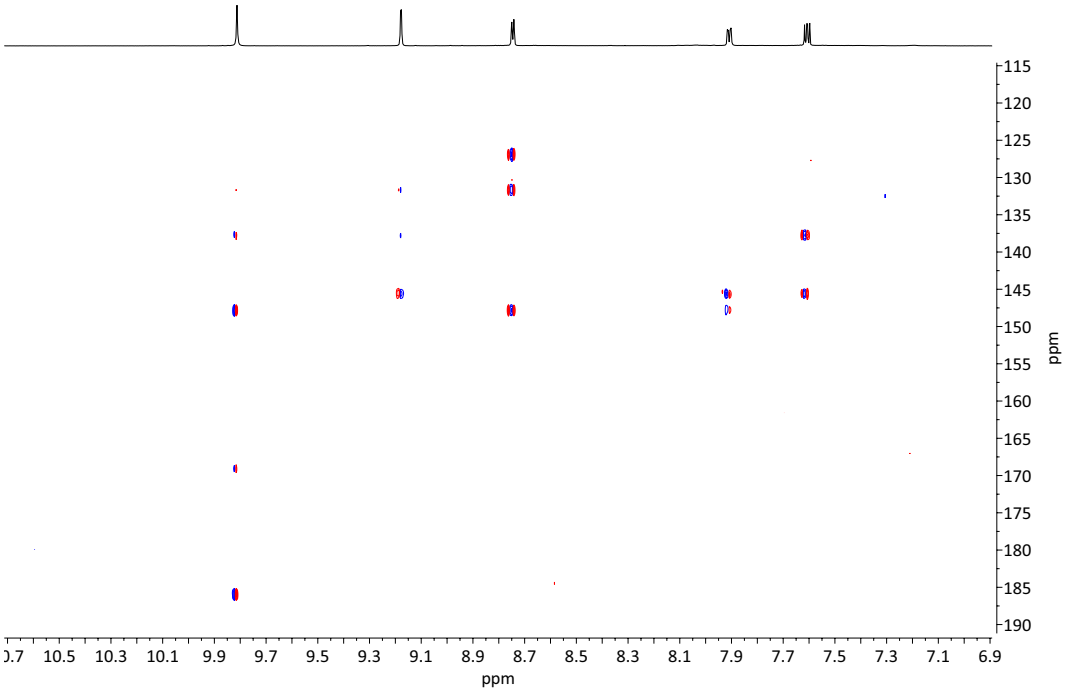

Figure 4.94. ^{1}H-^{13}C HMBC spectrum (700 MHz, 298 K, DMSO-d_6) of spectrum of the cage formation of **L²**.

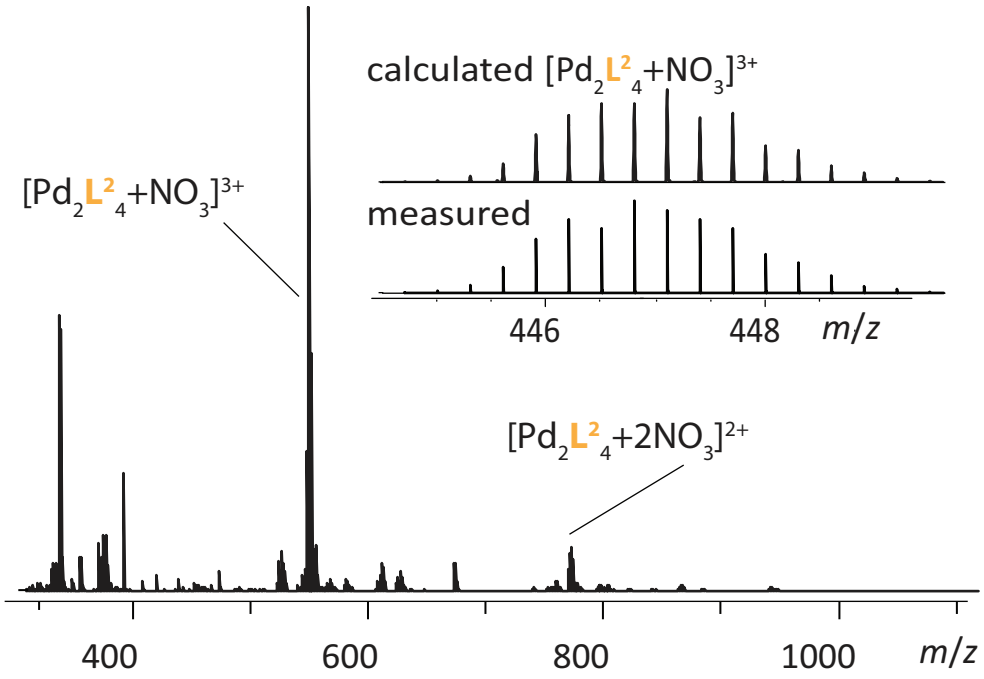

Figure 4.95. Illustration of ESI-MS of $\mathbf{L^2}$ in DMSO-d_6.

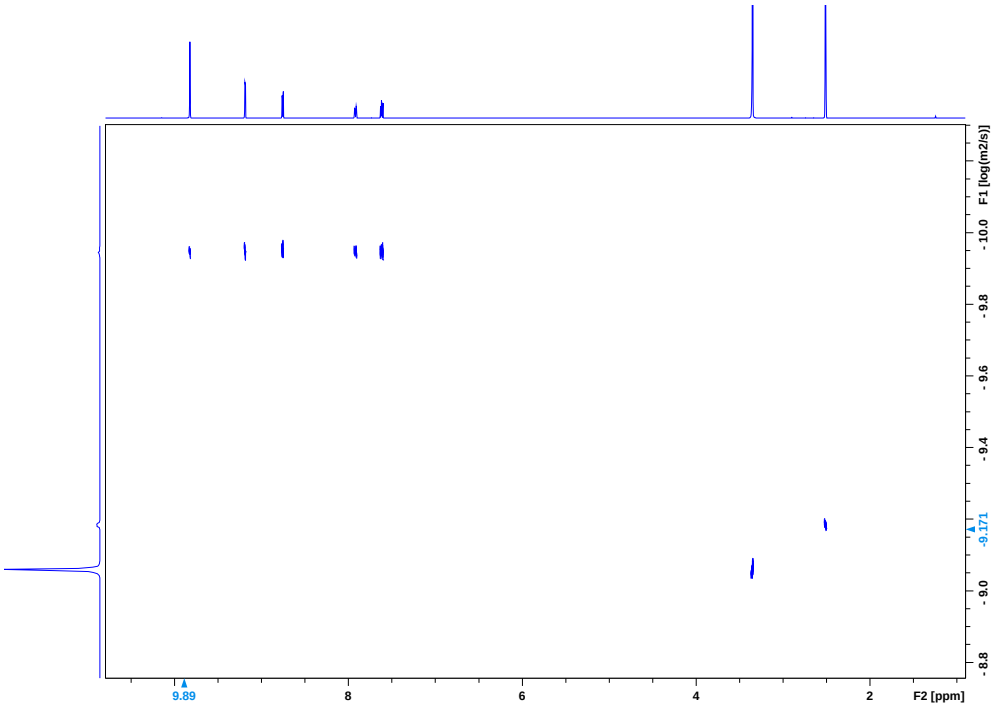

Figure 4.96. ^{1}H DOSY NMR spectrum of the homoleptic species of $\mathbf{L^2}$ in DMSO-d_6.

4.3.2 Homoleptic Coordination Cage Formation with Ligand L^1

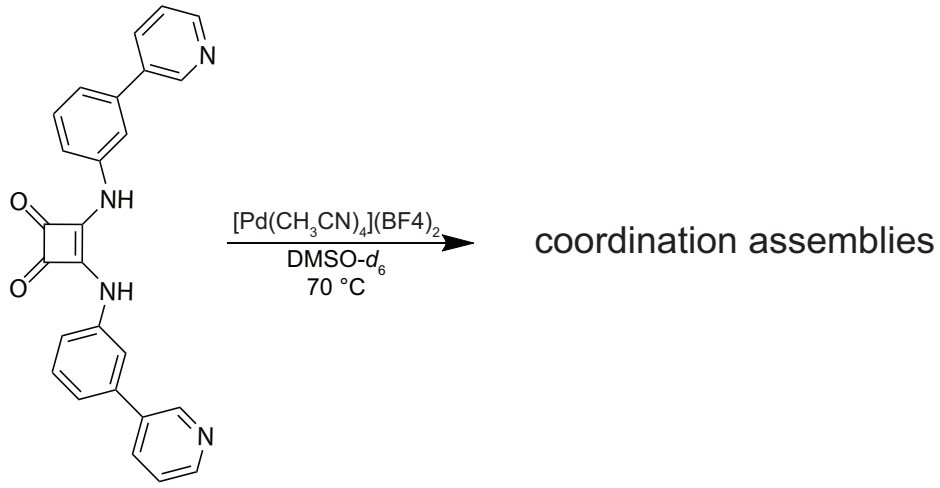

L¹

Figure 4.97. Homoleptic cage formation of $\mathbf{L^1}$ in DMSO-d_6.

540 μL of $\mathbf{L^1}$ (1.52 mmol, 2.8 mM in DMSO has been prepared with 15 mM $[Pd(CH_3CN)_4](BF_4)_2$ (0.90 mmol, 60 μL) heated at 70 °C for 2 h. The coordination cage formation experiment was submitted to ESI-MS measurement but it did not provide any informations about coordination assembly.

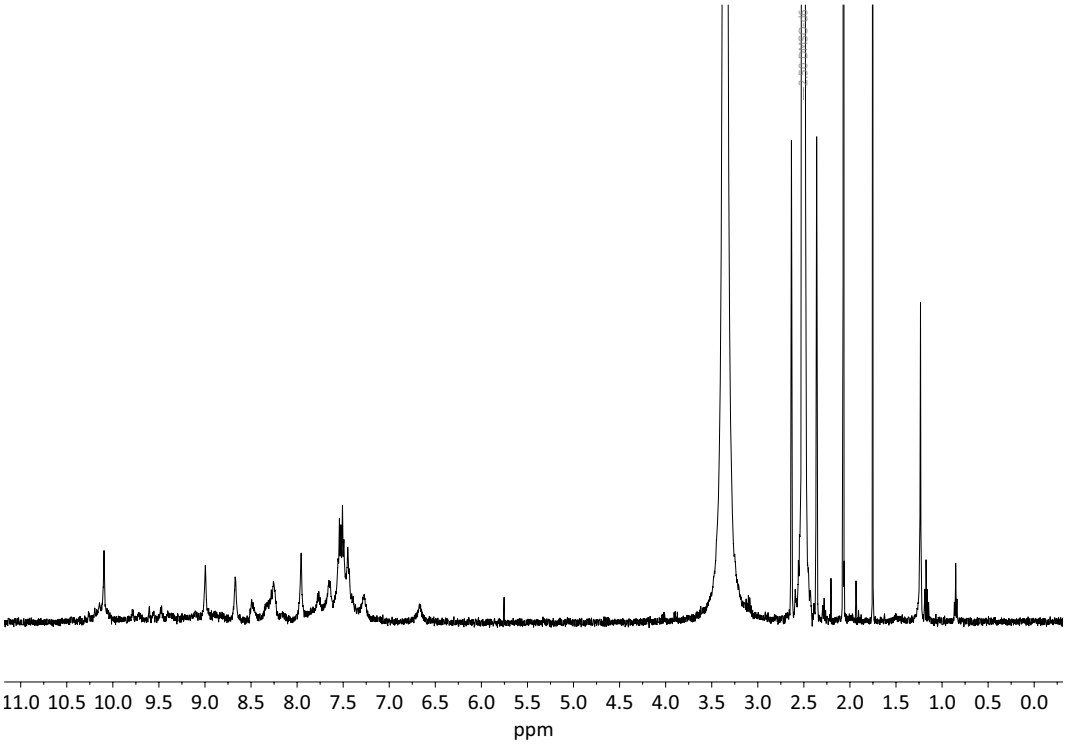

Figure 4.98. ^{1}H-NMR spectrum (500 MHz, 298 K, DMSO) of $\mathbf{L^1}$ with $[Pd(CH_3CN)_4](BF_4)_2$ heated at 70 °C for 2h.

4.3.3 Heteroleptic Coordination Cage het1 Formation with Ligand L^1 and L^2

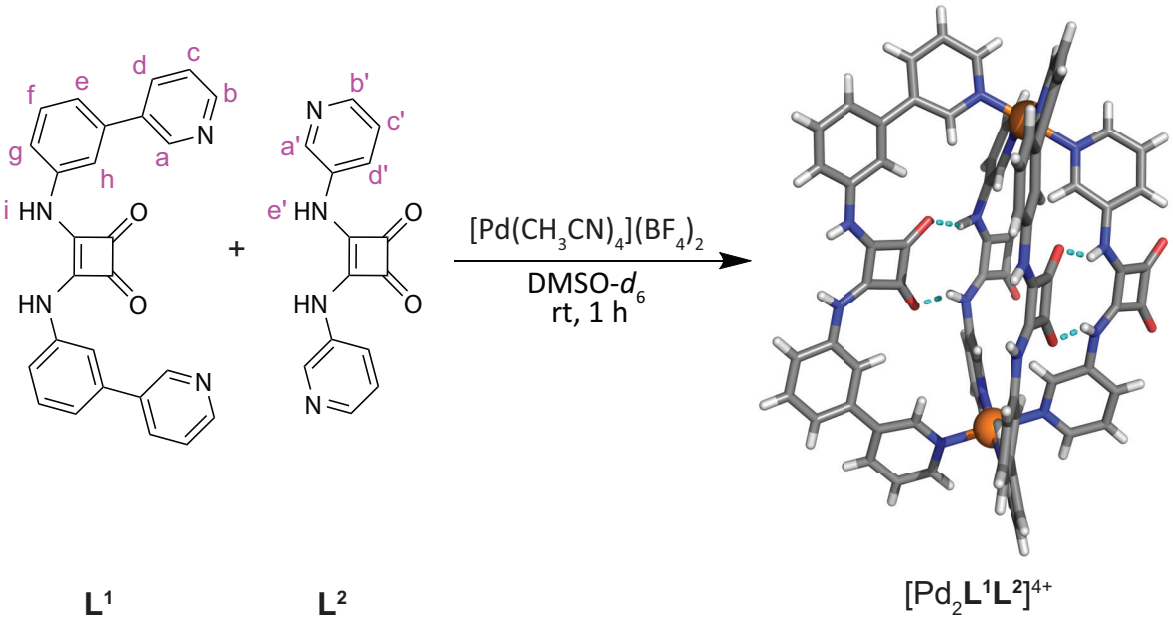

Figure 4.99. Heteroleptic coordination cage formation of $\mathbf{L^2}$ and $\mathbf{L^1}$ in DMSO-d_6. Single-crystal X-ray structure of $[Pd_2\mathbf{L^1}_2\mathbf{L^2}_2]^{4+}$ with BF_4^- as the counter anion. Single-crystal obtained by slow vapour diffusion of Et_2O into a solution DMF-d_7 of $[Pd_2\mathbf{L^1}_2\mathbf{L^2}_2]^{4+}$

At room temperature 270 μL of $\mathbf{L^1}$ (0.76 mmol, 2.8 mM) and 270 μL of $\mathbf{L^2}$ (0.76 mmol, 2.8 mM) in DMSO-d_6 has been prepared with 15 mM $[Pd(CH_3CN)_4](BF_4)_2$ (1.13 mmol, 75 μL). The chemical shifting of the ^{1}H-NMR signals suggest that a coordination species has been formed. ^{1}H DOSY NMR confirmed that one species was obtained. Mass spectrometry also suggests that the coordination cage is formed. In Addition to that, r_H of $[Pd_2\mathbf{L^1}_2\mathbf{L^2}_2]^{4+}$ is 9,8 Å so it can be assumed that it is a $[Pd_2\mathbf{L}_2\mathbf{L}'_2]^{4+}$ species.

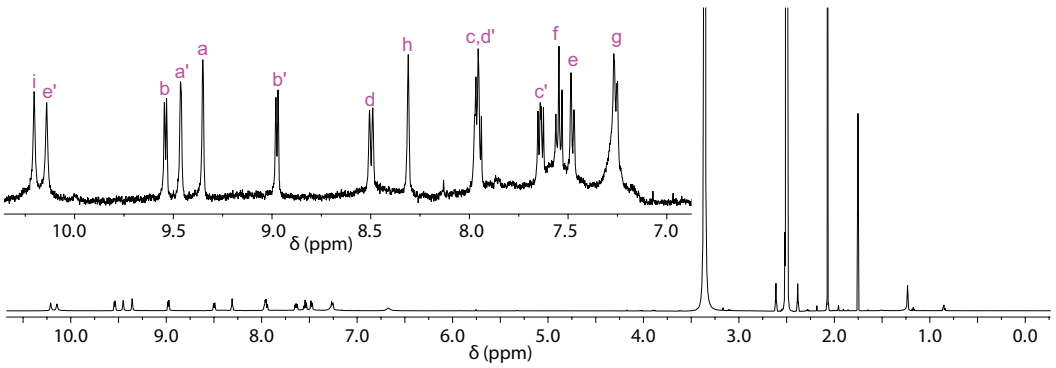

Figure 4.100. ^{1}H-NMR spectrum (500 MHz, 298 K, DMSO-d_6) of $[Pd_2\mathbf{L^1}_2\mathbf{L^2}_2]^{4+}$. The aromatic region is shown zoomed in.

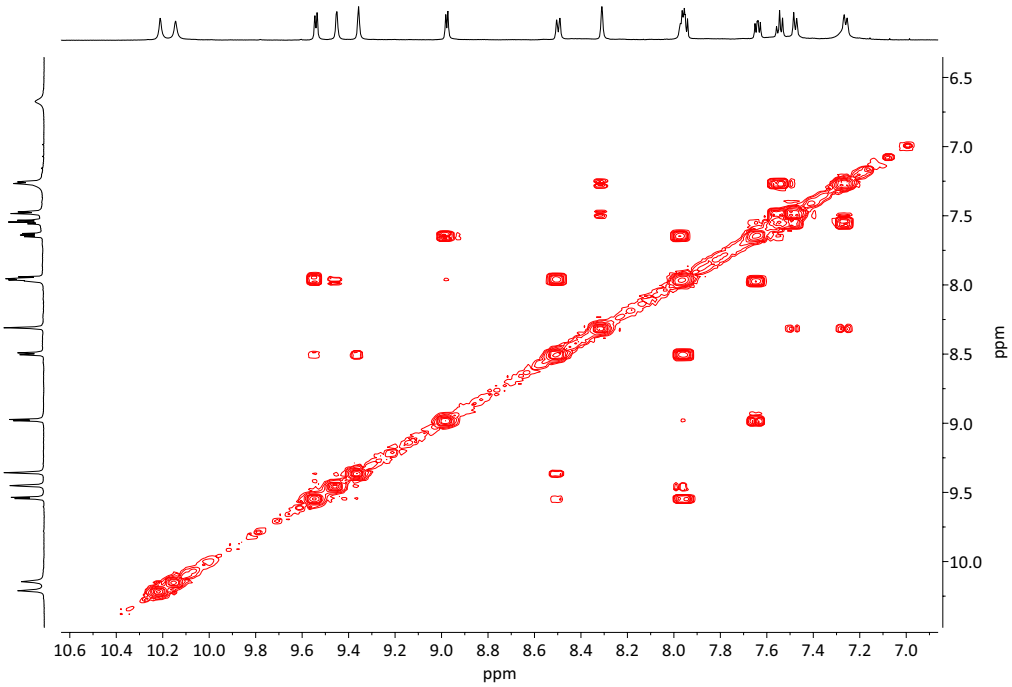

Figure 4.101. ^{1}H-^{1}H COSY spectrum (600 MHz, 298 K, DMSO-d_6) of spectrum of $[Pd_2\mathbf{L^1}_2\mathbf{L^2}_2]^{4+}$.

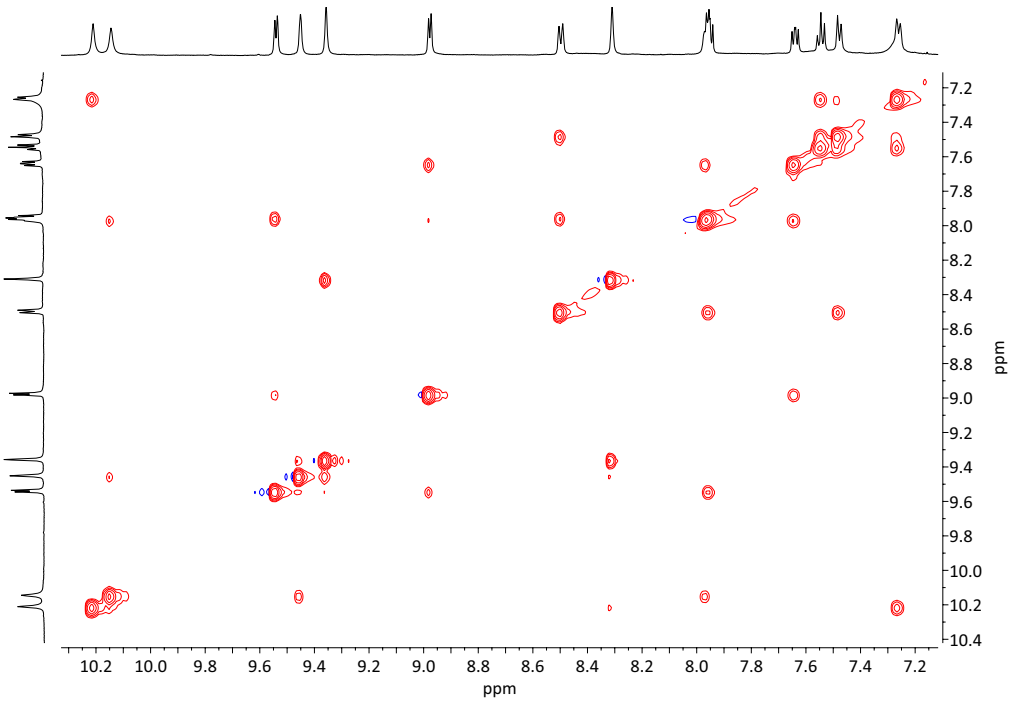

Figure 4.102. ^{1}H-^{1}H NOESY spectrum (600 MHz, 298 K, DMSO-d_6) of spectrum of $[Pd_2\mathbf{L^1}_2\mathbf{L^2}_2]^{4+}$.

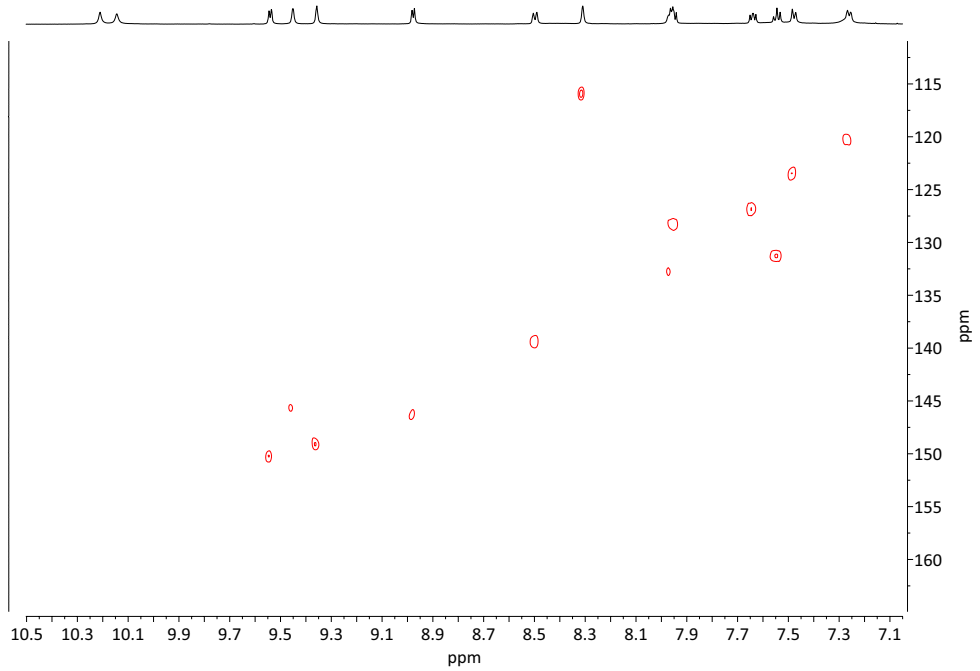

Figure 4.103. ^{1}H-^{13}C NOAH (HSQC, HMBC) spectrum (600 MHz, 298 K, DMSO-d_6) of spectrum of $[Pd_2\mathbf{L^1}_2\mathbf{L^2}_2]^{4+}$.

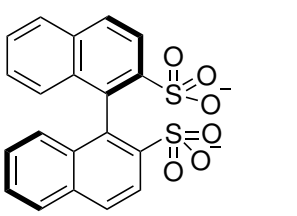

(*R*)-**BINSO**

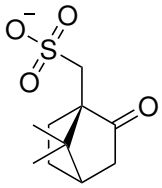

CS

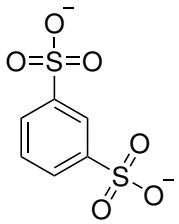

MDS

TBACl

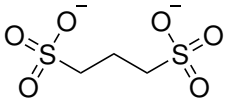

PROPDS

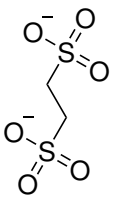

EDS

Figure 4.104. Screeened organic disulfonate guests and **TBACl** to $[Pd_2\mathbf{L^1}_2\mathbf{L^2}_2]^{4+}$ in DMSO$-d_6$.

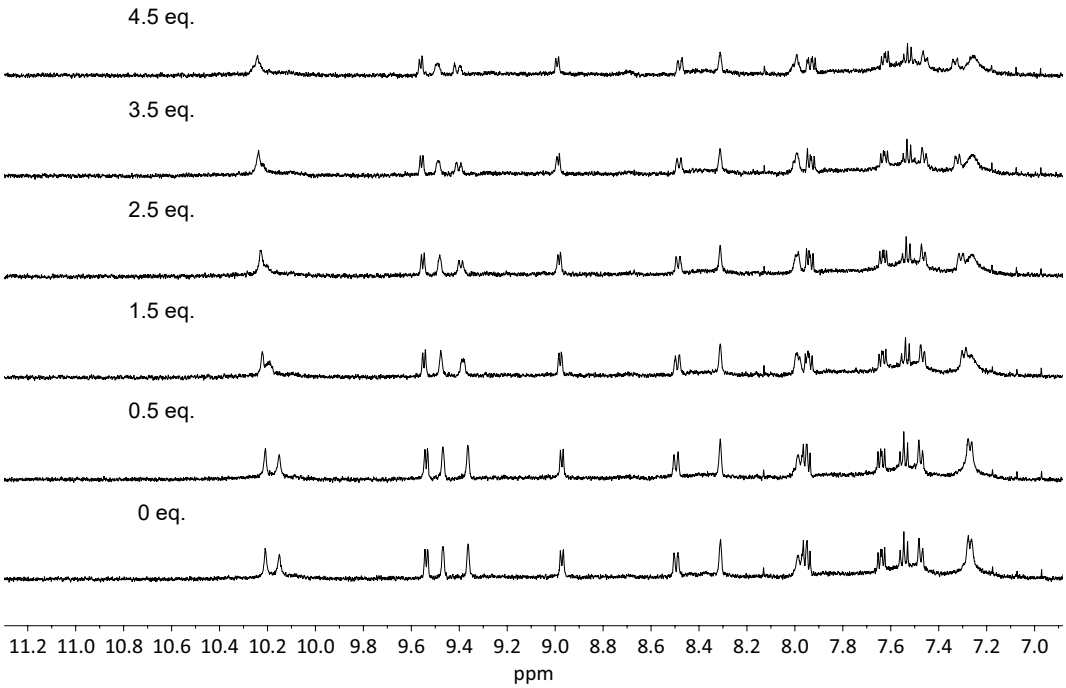

Figure 4.105. ^{1}H-NMR spectrum (500 MHz, 298 K, DMSO$-d_6$) of titration of **CS** to $[Pd_2\mathbf{L^1}_2\mathbf{L^2}_2]^{4+}$.

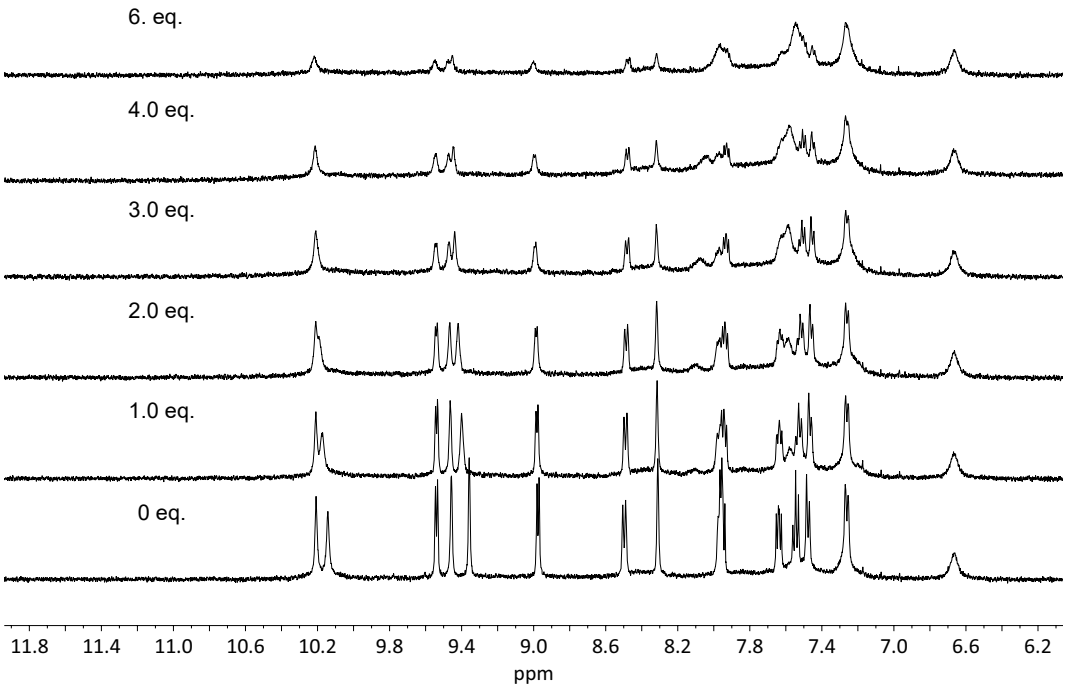

Figure 4.106. ^{1}H-NMR spectrum (500 MHz, 298 K, DMSO$-d_6$) of titration of **MDS** to $[Pd_2\mathbf{L^1}_2\mathbf{L^2}_2]^{4+}$.

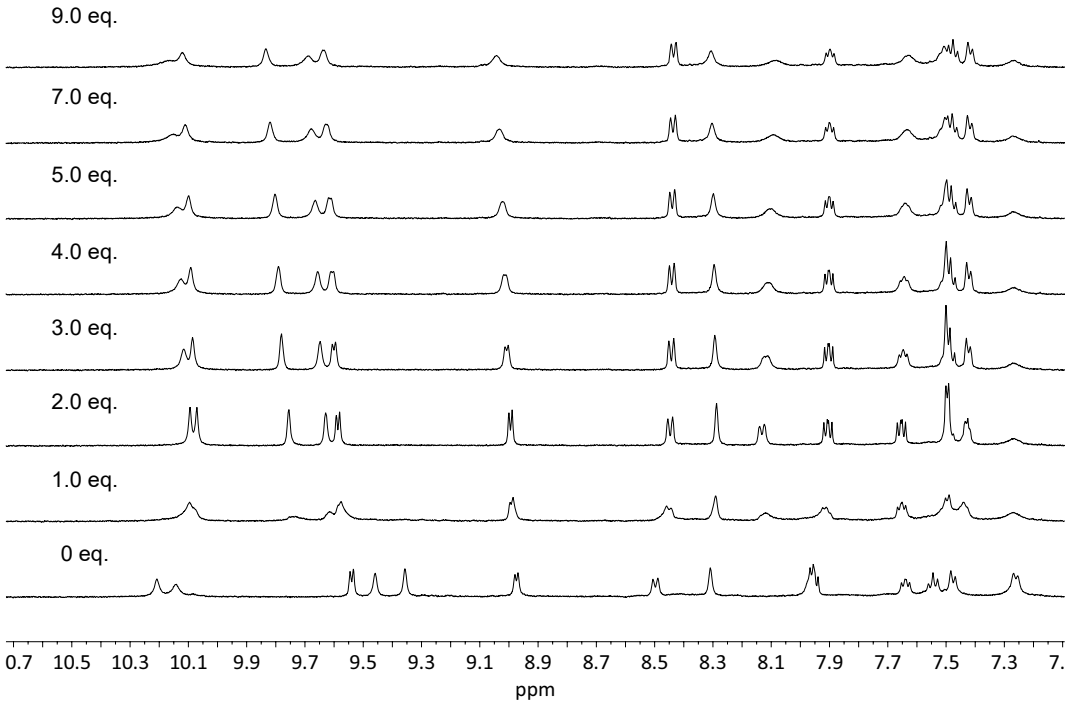

Figure 4.107. ^{1}H-NMR spectrum (500 MHz, 298 K, DMSO$-d_6$) of titration of **EDS** to $[Pd_2\mathbf{L^1}_2\mathbf{L^2}_2]^{4+}$.

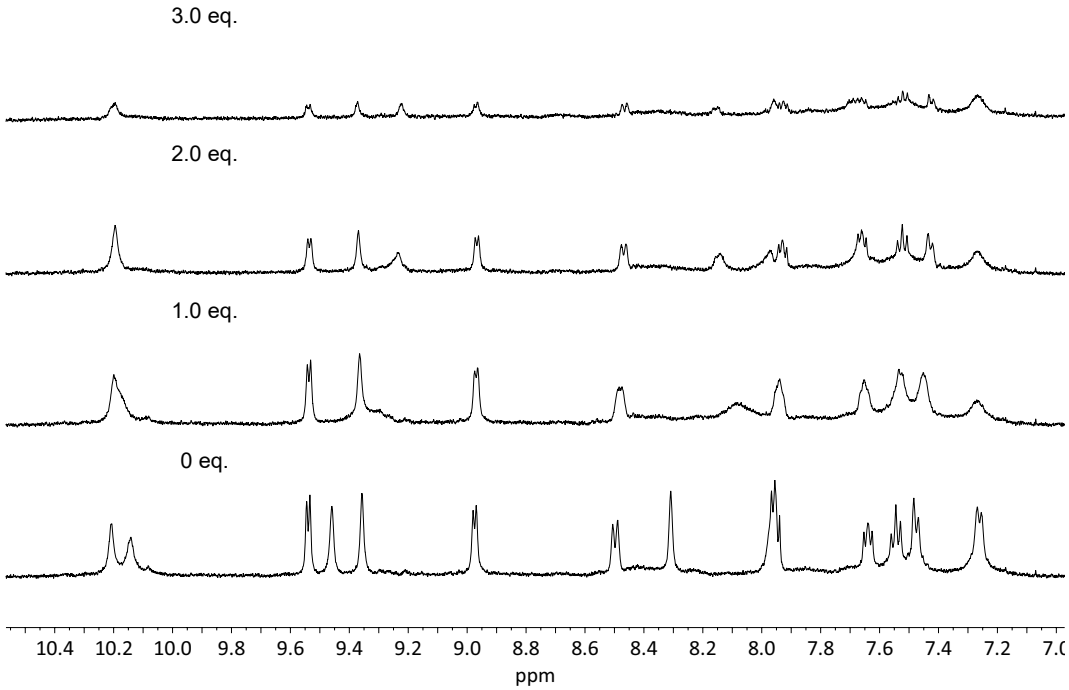

Figure 4.108. ^{1}H-NMR spectrum (500 MHz, 298 K, DMSO$-d_6$) of titration of **PROPDS** to $[Pd_2\mathbf{L^1}_2\mathbf{L^2}_2]^{4+}$.

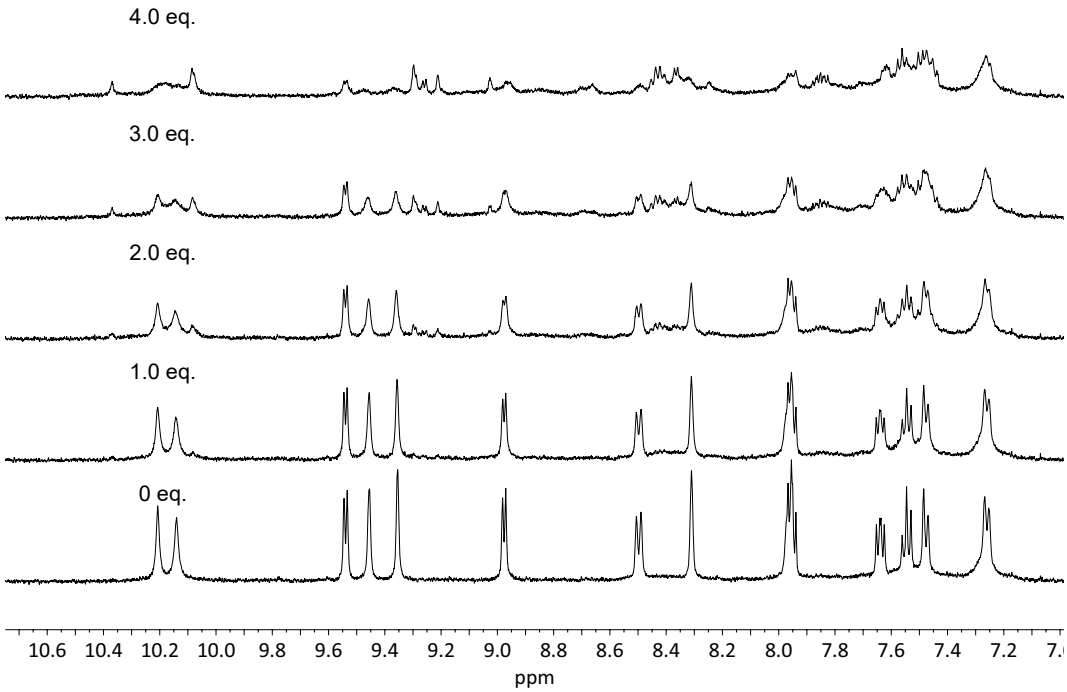

Figure 4.109. ^{1}H-NMR spectrum (500 MHz, 298 K, DMSO$-d_6$) of titration of **TBACl** to $[Pd_2\mathbf{L^1}_2\mathbf{L^2}_2]^{4+}$.

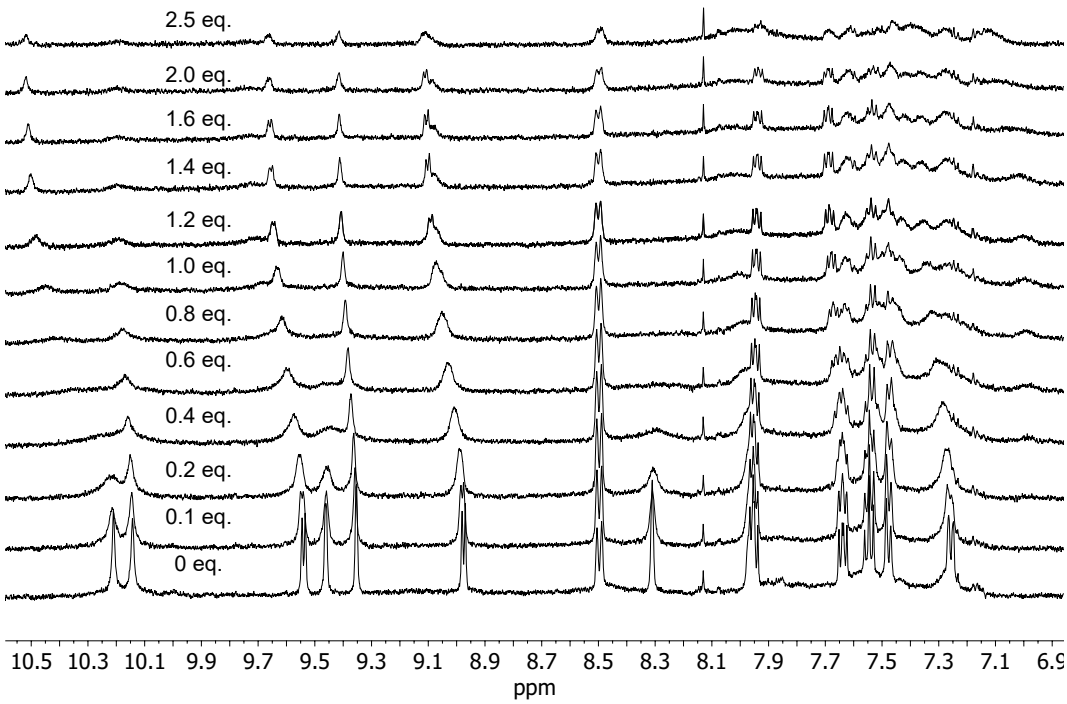

Figure 4.110. ^{1}H-NMR spectrum (500 MHz, 298 K, DMSO$-d_6$) of titration of **BINSO** to $[Pd_2\mathbf{L^1}_2\mathbf{L^2}_2]^{4+}$. K^+ as counter ions for **BINSO**.

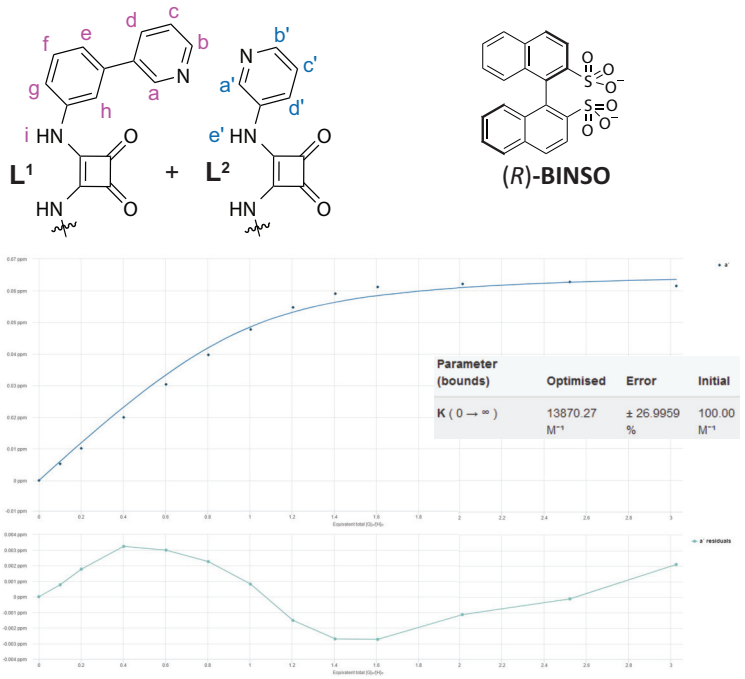

Figure 4.111. Illustration of binding analysis result obtained by BindFit (Fitter: 1:1) titration of **BINSO** to $[Pd_2\mathbf{L^1}_2\mathbf{L^2}_2]^{4+}$. K^+ as counter ions for **BINSO**. Proton signals a´ have been plotted

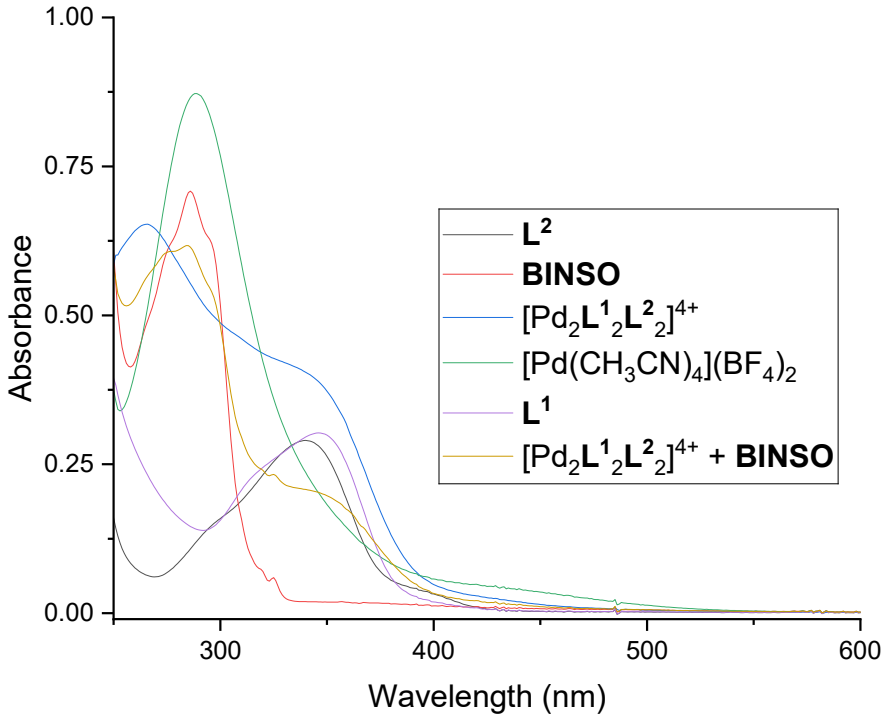

Figure 4.112. Illustration of UV-Vis titration of **BINSO** to $[Pd_2\mathbf{L^1}_2\mathbf{L^2}_2]^{4+}$ in DMSO$-d_6$. Concentration of $[Pd_2\mathbf{L^1}_2\mathbf{L^2}_2]^{4+}$ is 25 μM and with a cuvette of 0.2 cm optical path.

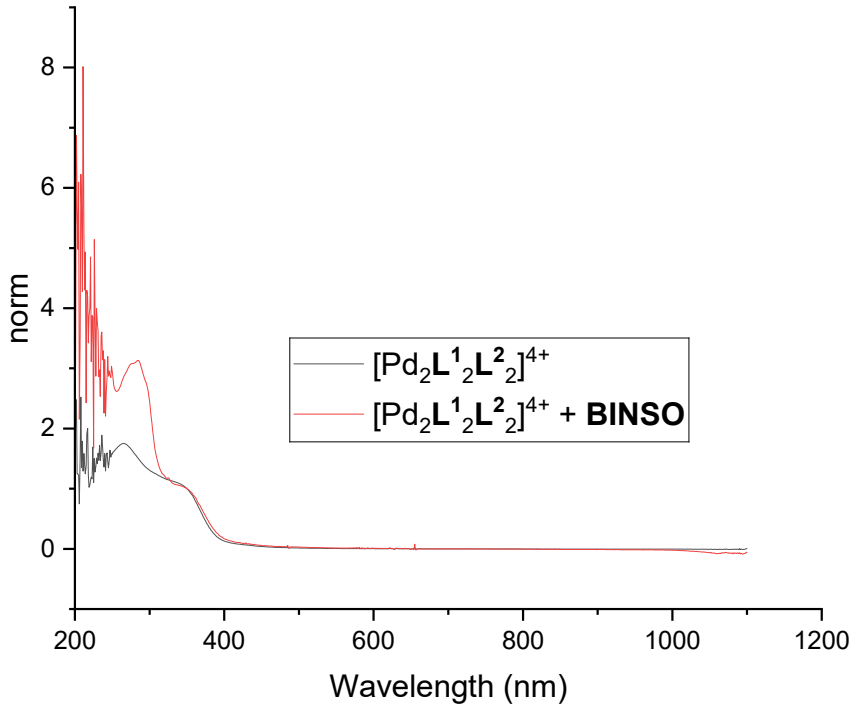

Figure 4.113. Illustration of normed UV-Vis spectra of **BINSO** to $[Pd_2\mathbf{L^1}_2\mathbf{L^2}_2]^{4+}$ in DMSO$-d_6$. Concentration of $[Pd_2\mathbf{L^1}_2\mathbf{L^2}_2]^{4+}$ is 25 μM and with a cuvette of 0.2 cm optical path.

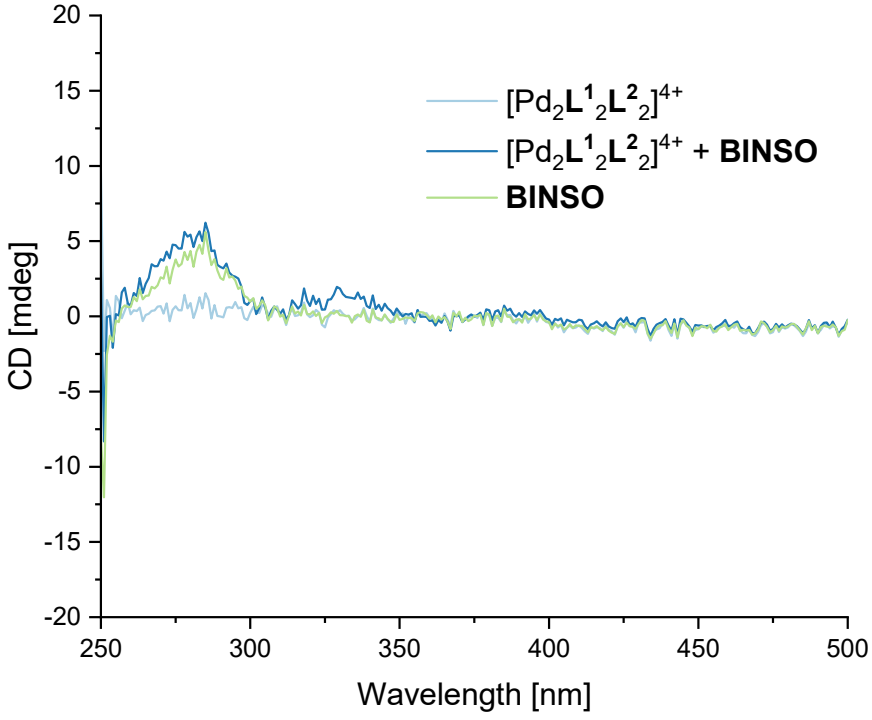

Figure 4.114. Illustration of CD spectra of **BINSO** to $[Pd_2\mathbf{L^1}_2\mathbf{L^2}_2]^{4+}$ in DMSO$-d_6$. Concentration of $[Pd_2\mathbf{L^1}_2\mathbf{L^2}_2]^{4+}$ is 25 μM and with a cuvette of 0.2 cm optical path.

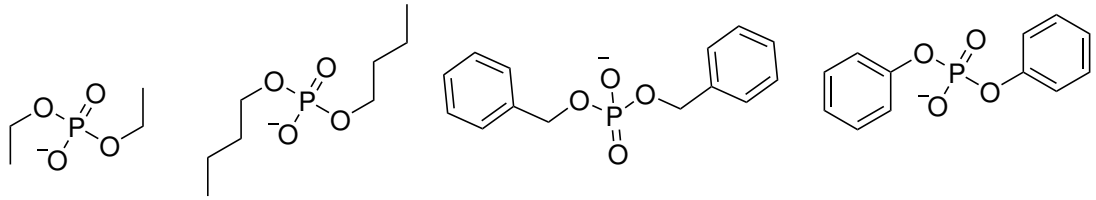

DEP **DBuP** **DBnP** **DPP**

Figure 4.115. Illustration of screened phosphate esters to $[Pd_2\mathbf{L^1}_2\mathbf{L^2}_2]^{4+}$.

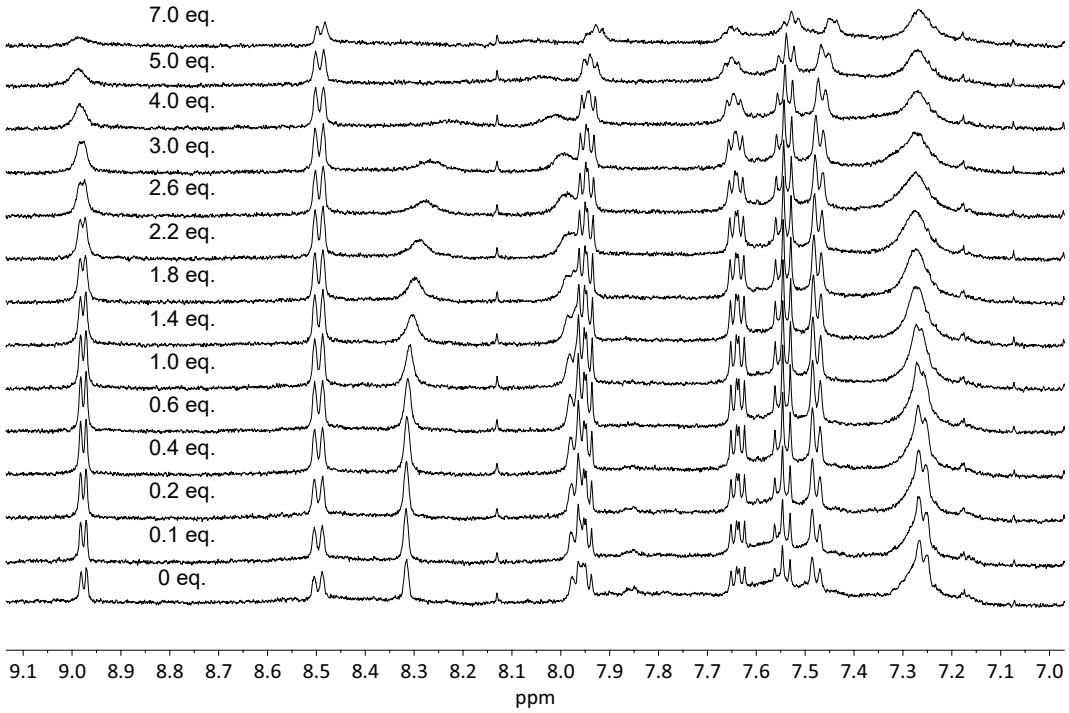

Figure 4.116. ^{1}H-NMR spectrum (500 MHz, 298 K, DMSO$-d_6$) of titration of **DEP** to $[Pd_2\mathbf{L^1}_2\mathbf{L^2}_2]^{4+}$.

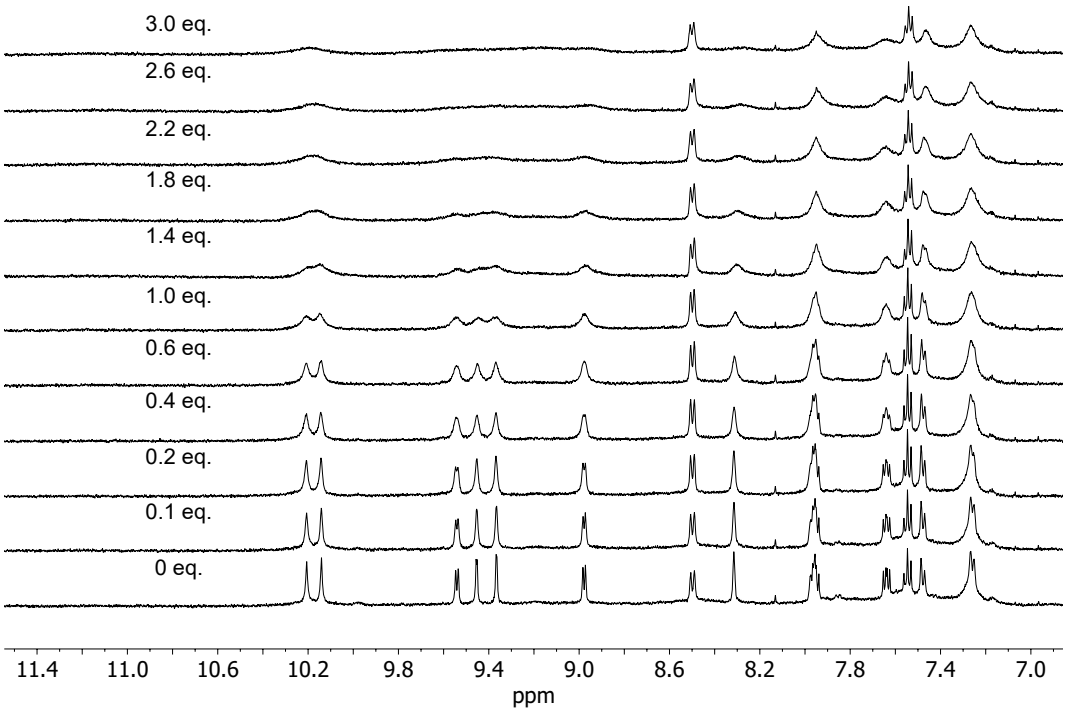

Figure 4.117. ^{1}H-NMR spectrum (500 MHz, 298 K, DMSO$-d_6$) of titration of **DBuP** to $[Pd_2\mathbf{L^1}_2\mathbf{L^2}_2]^{4+}$.

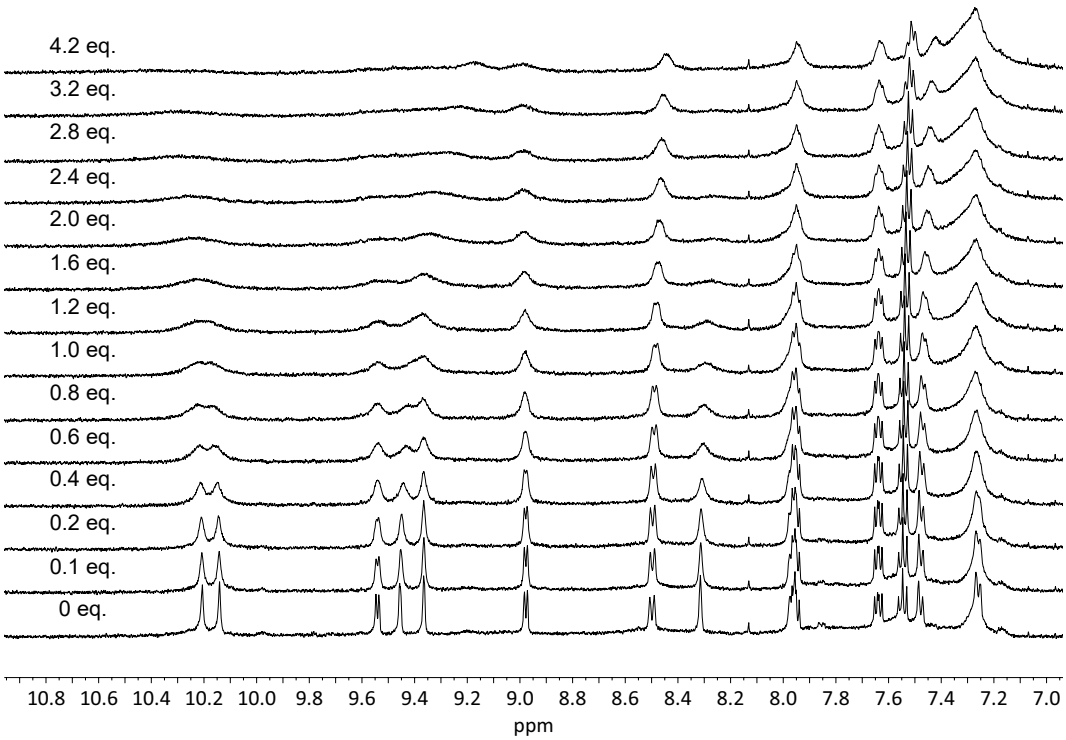

Figure 4.118. ^{1}H-NMR spectrum (500 MHz, 298 K, DMSO$-d_6$) of titration of **DBnP** to $[Pd_2\mathbf{L^1}_2\mathbf{L^2}_2]^{4+}$.

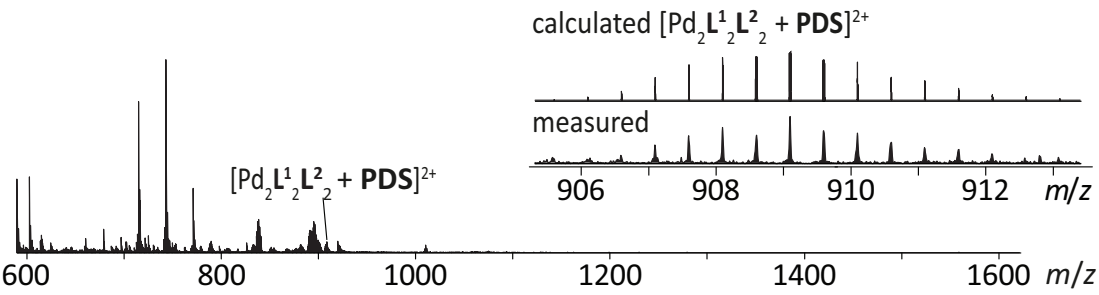

Figure 4.119. Illustration of ESI-MS of $[Pd_2\mathbf{L^1}_2\mathbf{L^2}_2]^{4+}$ and **PDS**.

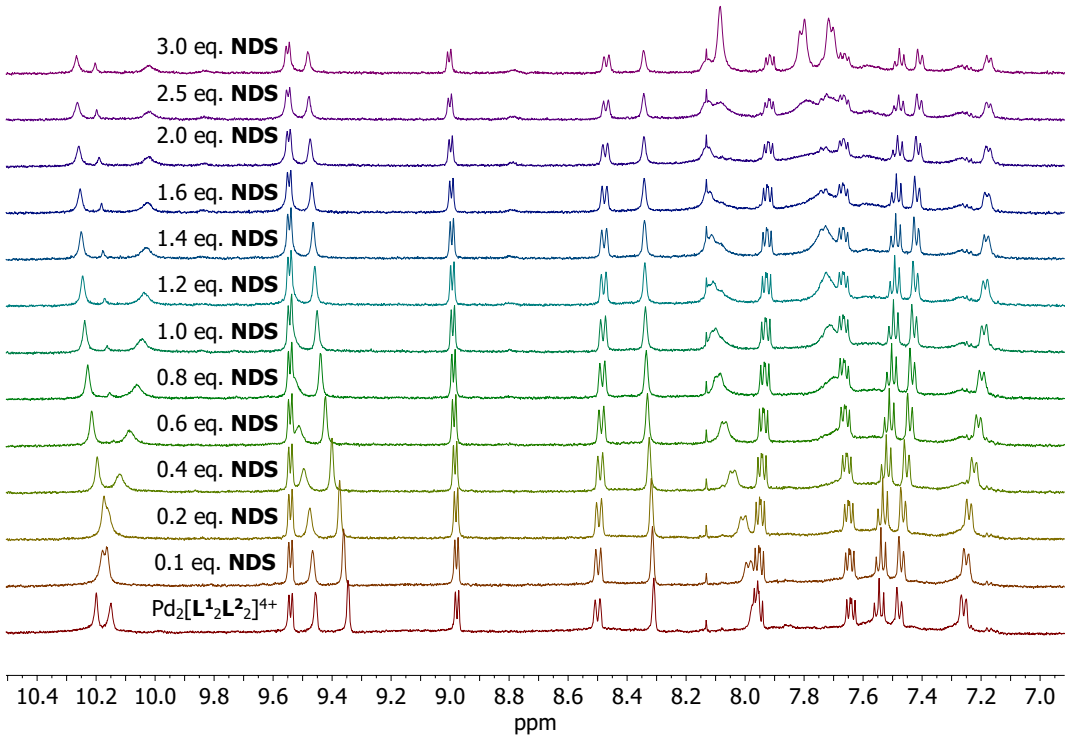

Figure 4.120. ^{1}H-NMR spectrum (500 MHz, 298 K, DMSO$-d_6$) of titration of **NDS** to $[Pd_2\mathbf{L^1}_2\mathbf{L^2}_2]^{4+}$. TBA as counter ions for **NDS**.

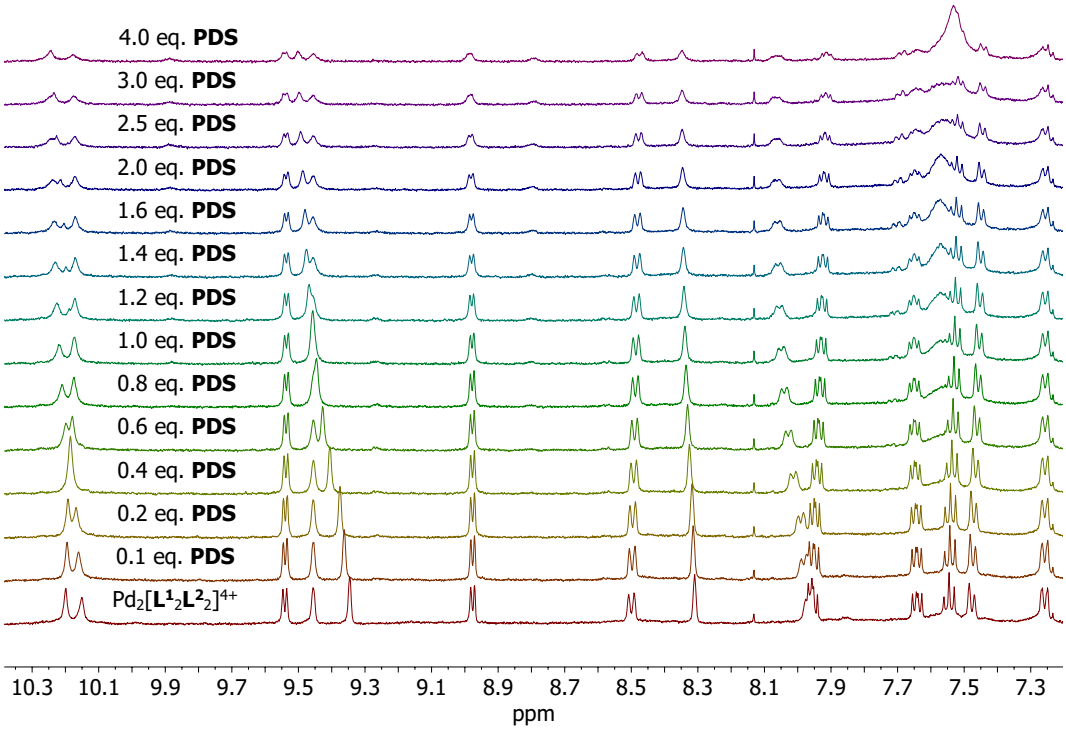

Figure 4.121. ^{1}H-NMR spectrum (500 MHz, 298 K, DMSO$-d_6$) of titration of **PDS** to $[Pd_2\mathbf{L^1}_2\mathbf{L^2}_2]^{4+}$. TBA as counter ions for **PDS**.

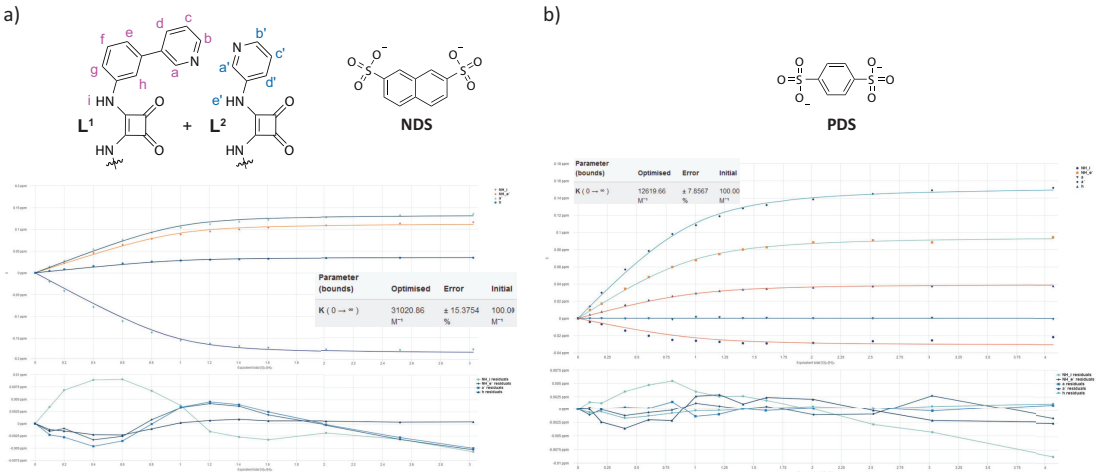

Figure 4.122. Illustration of binding analysis result obtained by BindFit (Fitter: 1:1) titration of **NDS** and **PDS** to $[Pd_2\mathbf{L^1}_2\mathbf{L^2}_2]^{4+}$. TBA as counter ions for **NDS** and **PDS**. a) Proton signals i, e´, a´ and h have been plotted. b) Proton signals i, e´, a, a´ and h have been plotted.

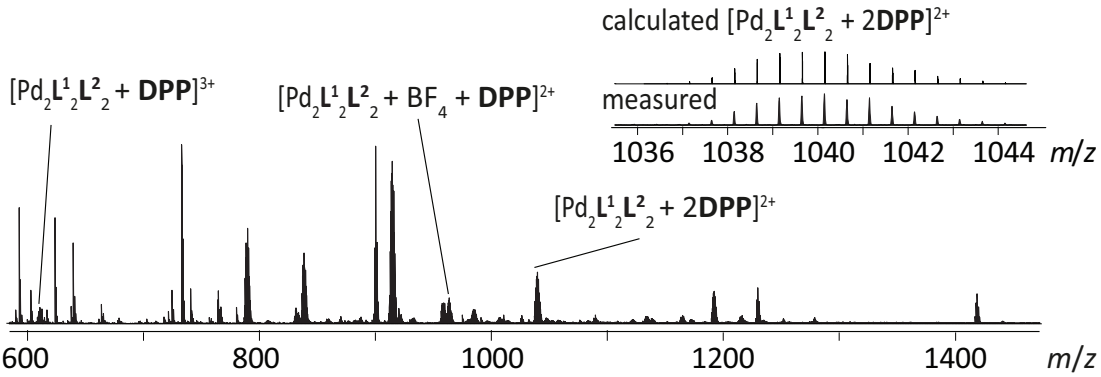

Figure 4.123. Illustration of ESI-MS of $[Pd_2\mathbf{L^1}_2\mathbf{L^2}_2]^{4+}$ and **DPP**.

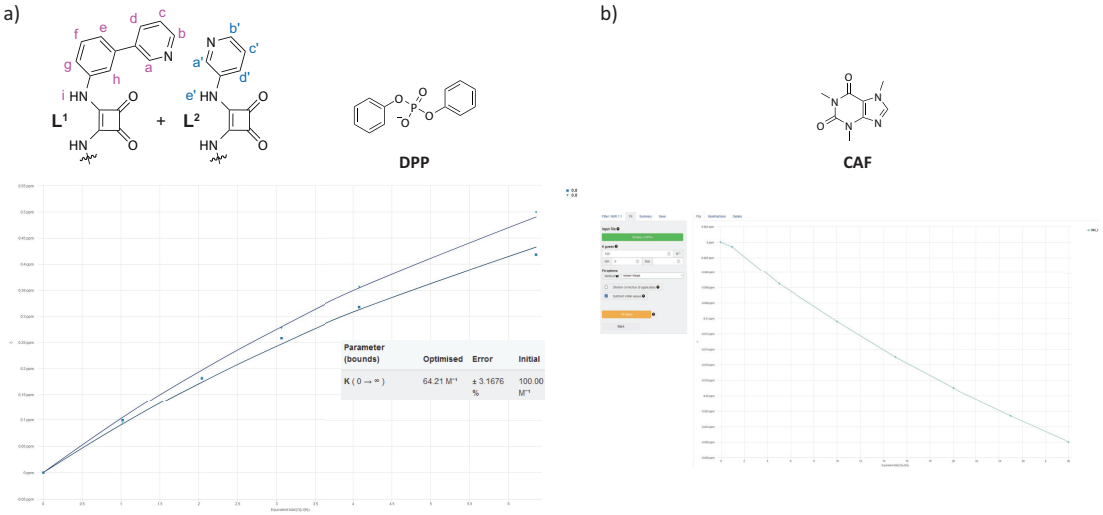

Figure 4.124. Illustration of binding analysis result obtained by BindFit (Fitter: 1:1) titration of **DPP** and **CAF** to $[Pd_2\mathbf{L^1}_2\mathbf{L^2}_2]^{4+}$. TBA as counter ion for **DPP**.

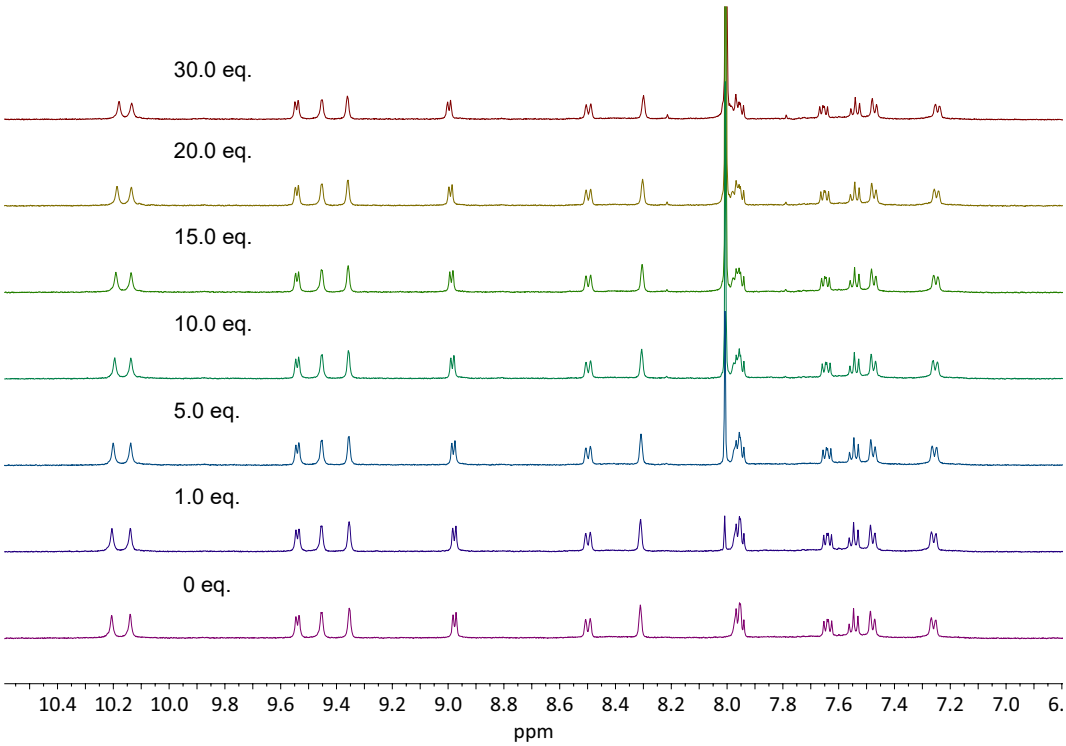

Figure 4.125. ^{1}H-NMR spectrum (500 MHz, 298 K, DMSO$-d_6$) of titration of **CAF** to $[Pd_2\mathbf{L^1}_2\mathbf{L^2}_2]^{4+}$.

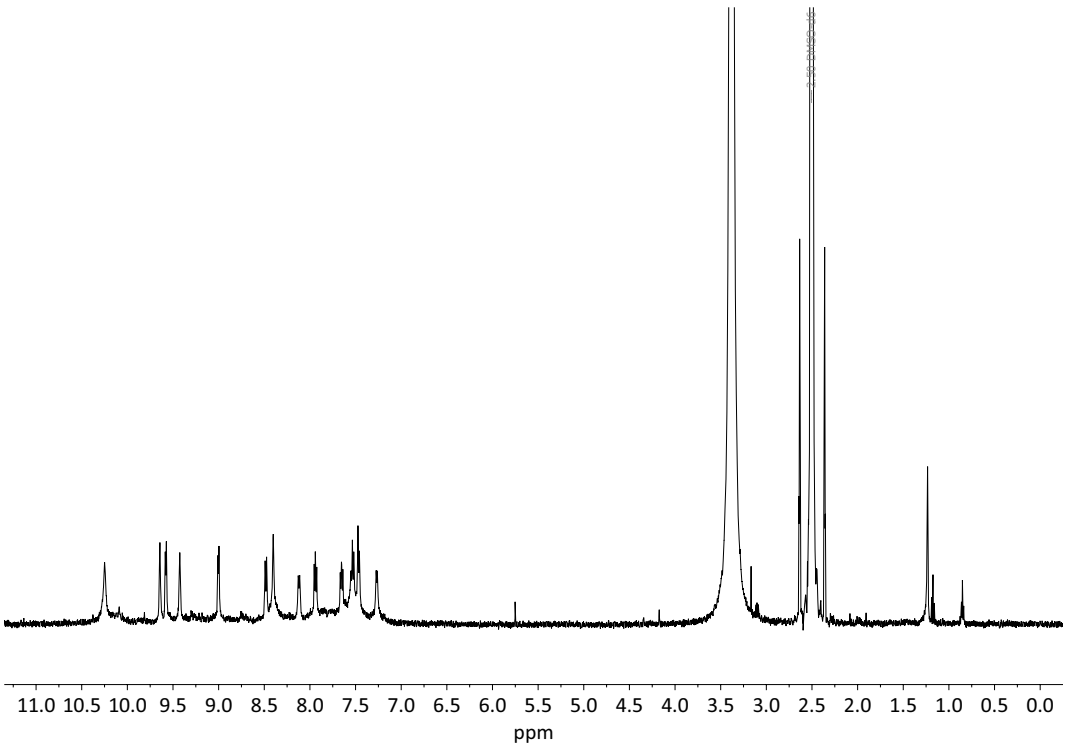

.

Figure 4.126. ^{1}H-NMR spectrum (500 MHz, 298 K, DMSO$-d_6$) of $[Pd_2\mathbf{L^1}_2\mathbf{L^2}_2]^{4+}$ formed with $PdNO_3 \cdot (H_2O)_x$

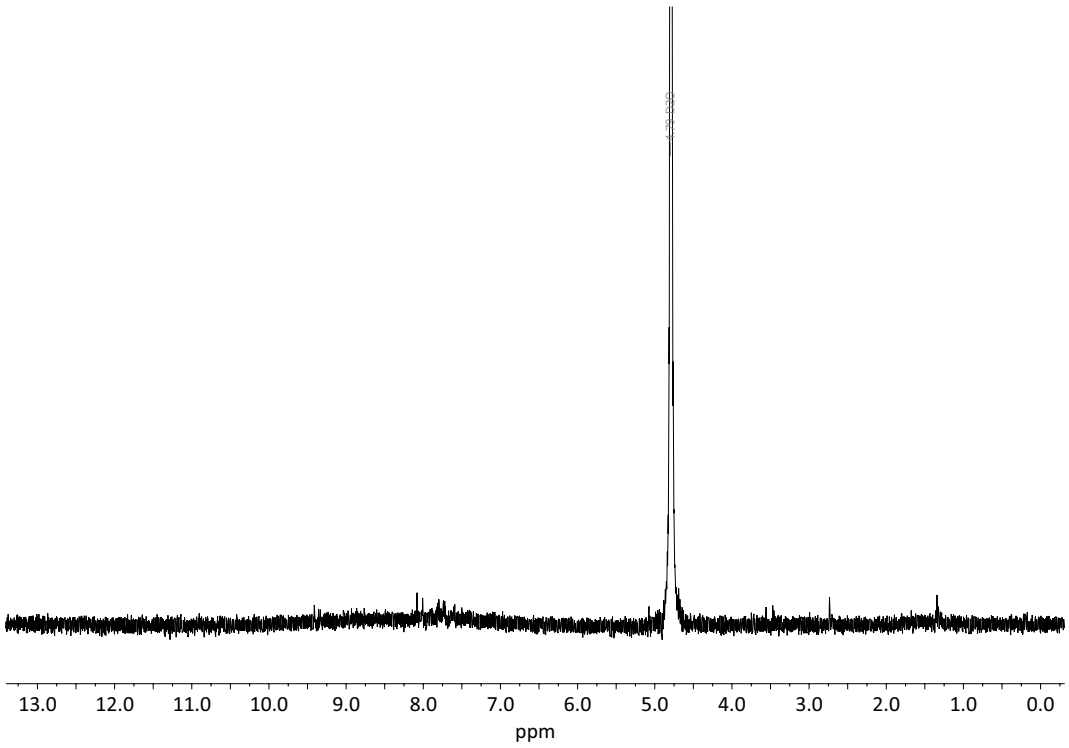

.

Figure 4.127. ^{1}H-NMR spectrum (500 MHz, 298 K, D_2O) of $[Pd_2\mathbf{L^1}_2\mathbf{L^2}_2]^{4+}$ formed with $PdNO_3$ x H_2O

4.3.4 Homoleptic Coordination Cage Formation with L^{1peg}

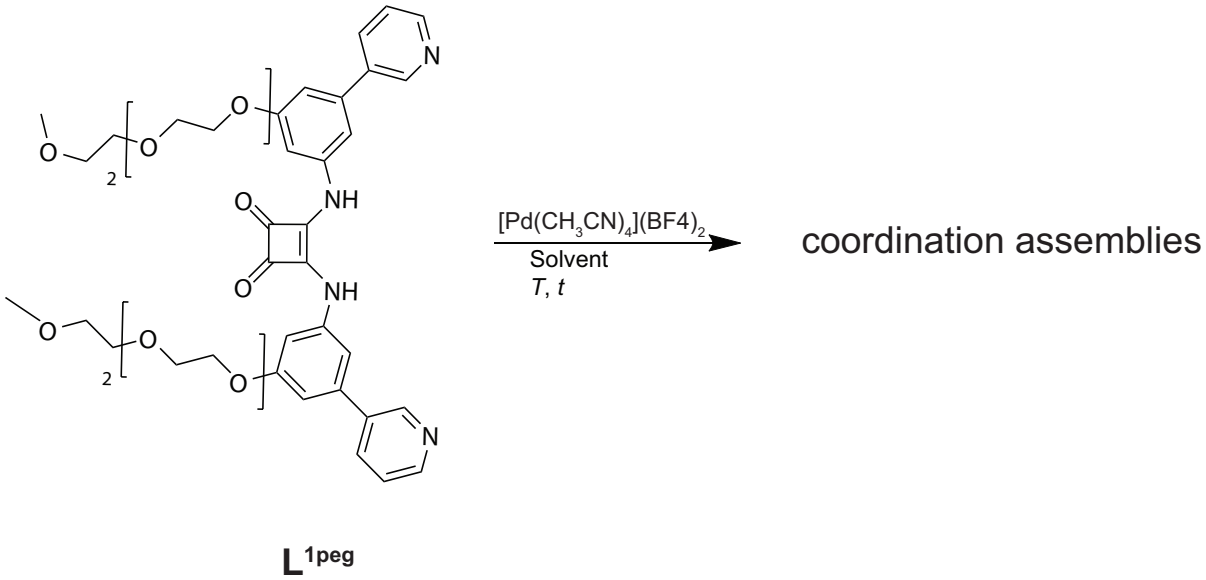

Figure 4.128. Heteroleptic coordination cage formation of $\mathbf{L^{1peg}}$.

540 μL of $\mathbf{L^{1peg}}$ (1.52 mmol, 2.8 mM in respective solvent (DMSO, CD_3CN) has been prepared with 15 mM $[Pd(CH_3CN)_4](BF_4)_2$ (0.90 mmol, 60 μL) for 2 h at room temperature and afterwards heated to 70 °C for 2 h. At each step no clear homoleptic coordination species was observed. Each coordination cage formation experiment was submitted to ESI-MS measurement but it did not provide any informations about coordination assembly structures.

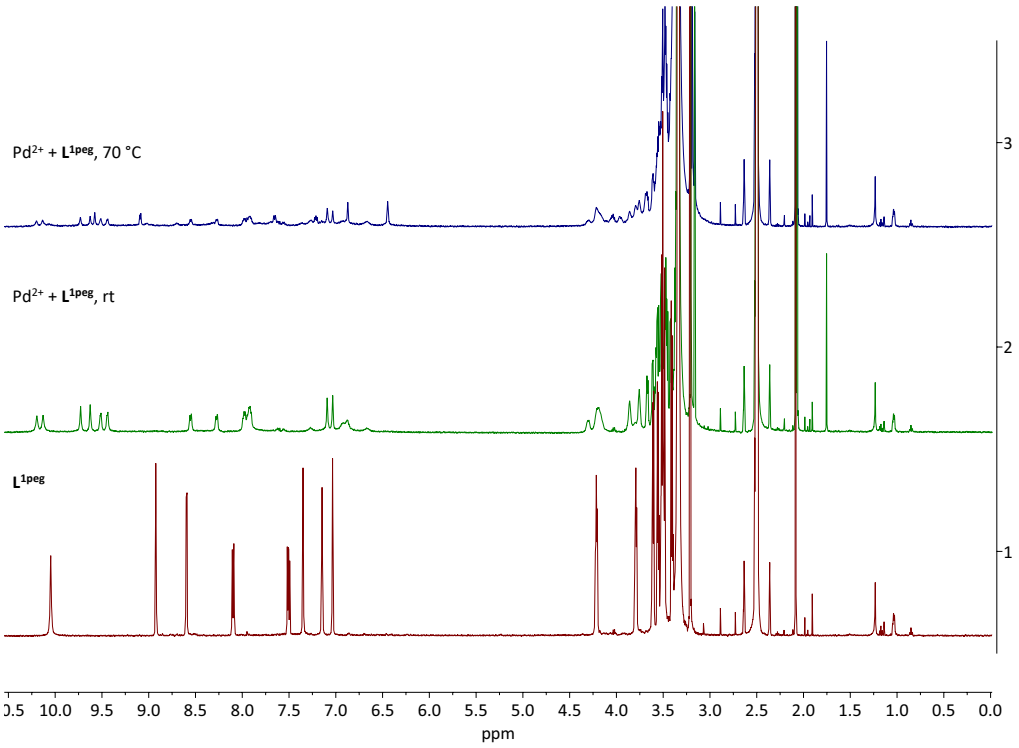

Figure 4.129. ^{1}H-NMR spectrum (500 MHz, 298 K, DMSO) of $\mathbf{L^{1peg}}$ and respectively with $[Pd(CH_3CN)_4](BF_4)_2$ at rt and 70 °C.

For the cage formation in CD_3CN, the procedure was carried out analogously.

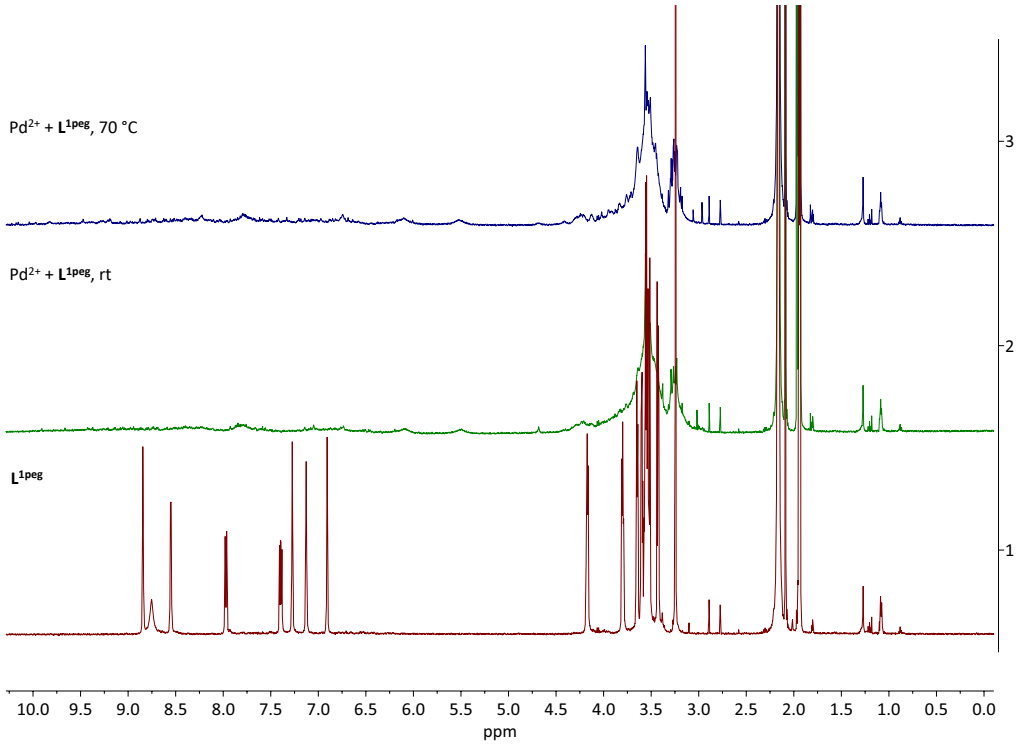

Figure 4.130. ^{1}H-NMR spectrum (500 MHz, 298 K, CD_3CN) of **L^{1peg}** and respectively with $[Pd(CH_3CN)_4](BF_4)_2$ at rt and 70 °C.

4.3.5 Homoleptic Coordination Cage Formation with L^{2peg}

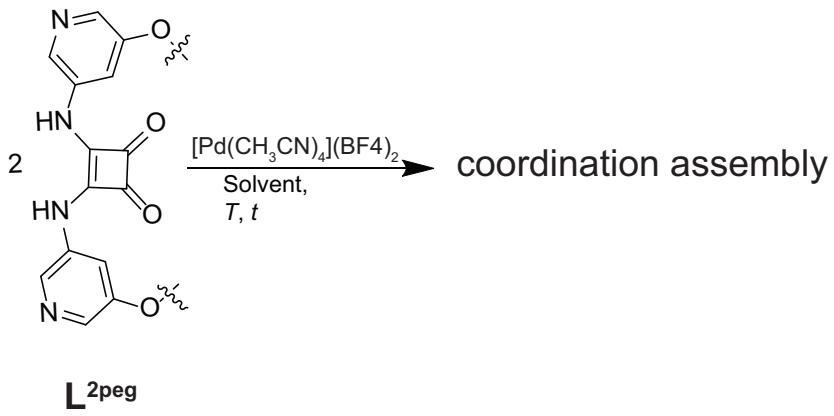

Figure 4.131. Homoleptic coordination cage formation of $\mathbf{L^{2peg}}$.

540 μL of $\mathbf{L^{2peg}}$ (1.52 mmol, 2.8 mM in DMSO has been prepared with 15 mM $[Pd(CH_3CN)_4](BF_4)_2$ (0.90 mmol, 60 μL) for 2 h at room temperature and afterwards heated to 70 °C for 2 h. The NH-signal of $\mathbf{L^{2peg}}$ is shifting but the aromatic signals of $\mathbf{L^{2peg}}$ are shifting only slightly which suggests that the counterion is interacting with the NH group. That is why 4 eq. of BF_4^- was added to a solution of the free ligand. Only a slight shift of the NH signal was observed.

Each coordination cage formation experiment was submitted to ESI-MS measurement but it did not provide any informations about coordination assembly structure.

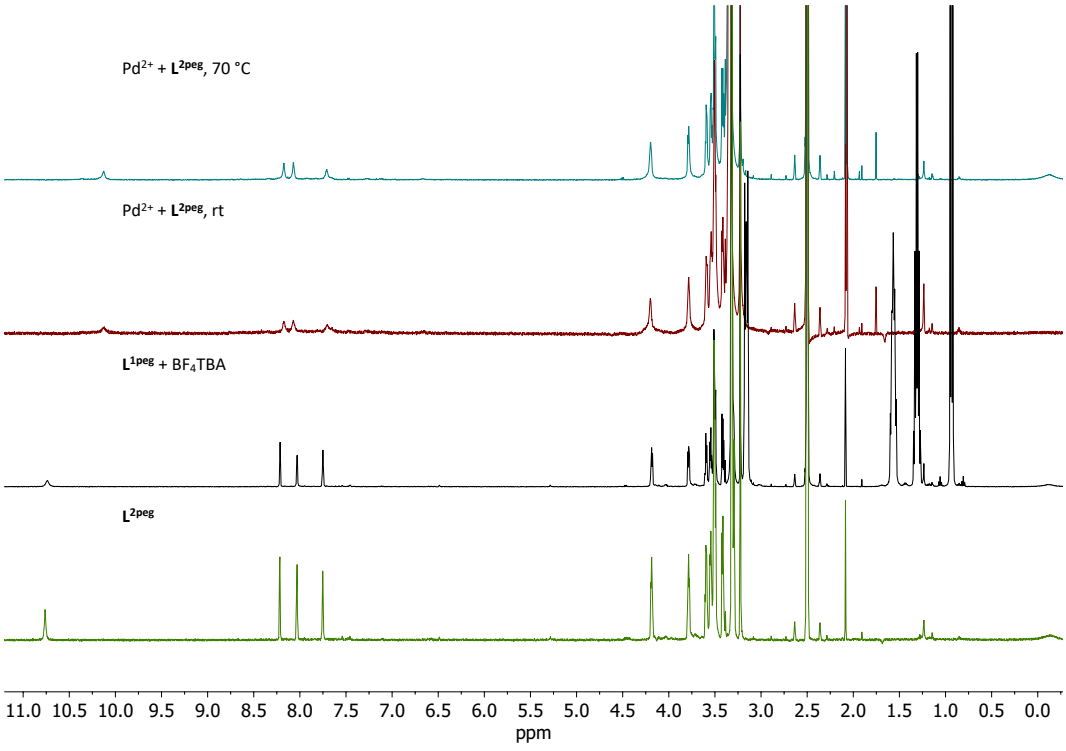

Figure 4.132. ^{1}H-NMR spectrum (500 MHz, 298 K, DMSO$-d_6$) $\mathbf{L^{2peg}}$ and respectively with $[Pd(CH_3CN)_4](BF_4)_2$ at rt and 70 °C.

Other counterions such as PF_6^-, NO_3^-, OTf^- have been screened but the ^{1}H-NMR could not be distinguished or did not show a clear formation of one coordination assembly.

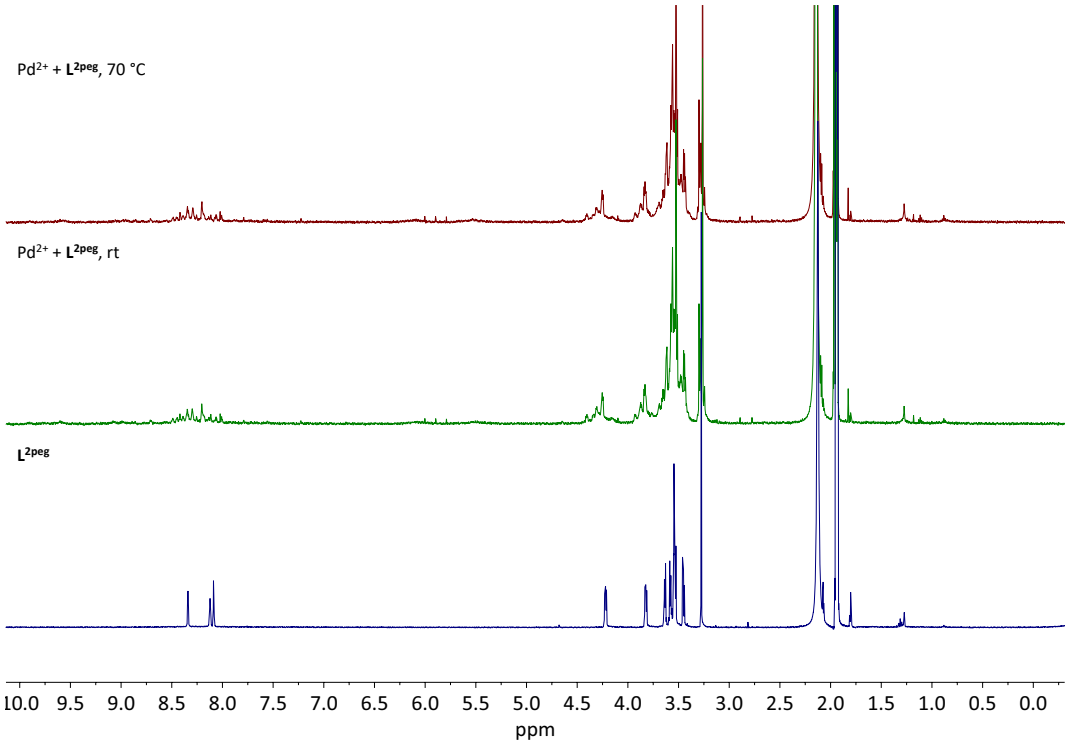

Figure 4.133. ^{1}H-NMR spectrum (500 MHz, 298 K, CD_3CN) $\mathbf{L^{2peg}}$ and respectively with $[Pd(CH_3CN)_4](BF_4)_2$ at rt and 70 °C.

4.3.6 Heteroleptic Coordination Cage Formation with L^{2peg} and L^2

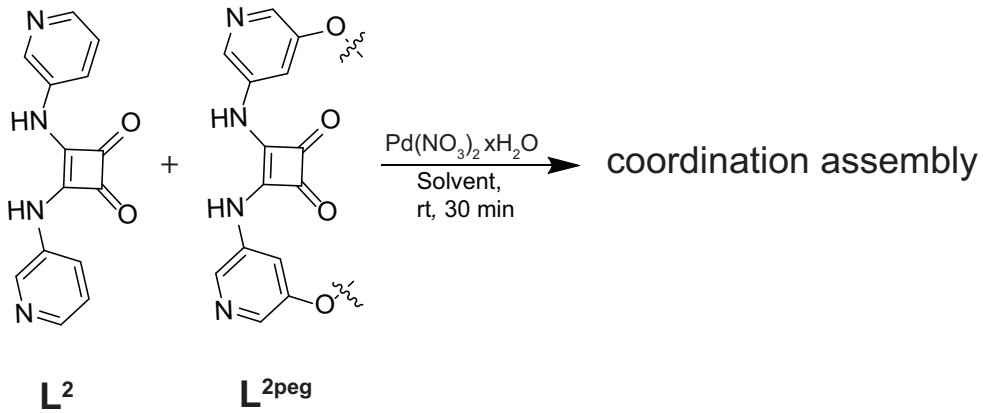

Figure 4.134. Heteroleptic coordination cage formation of $\mathbf{L^{2peg}}$ and $\mathbf{L^2}$.

Cage formation was done analogously to a heteroleptic cage formation in chapter 4.3.3.

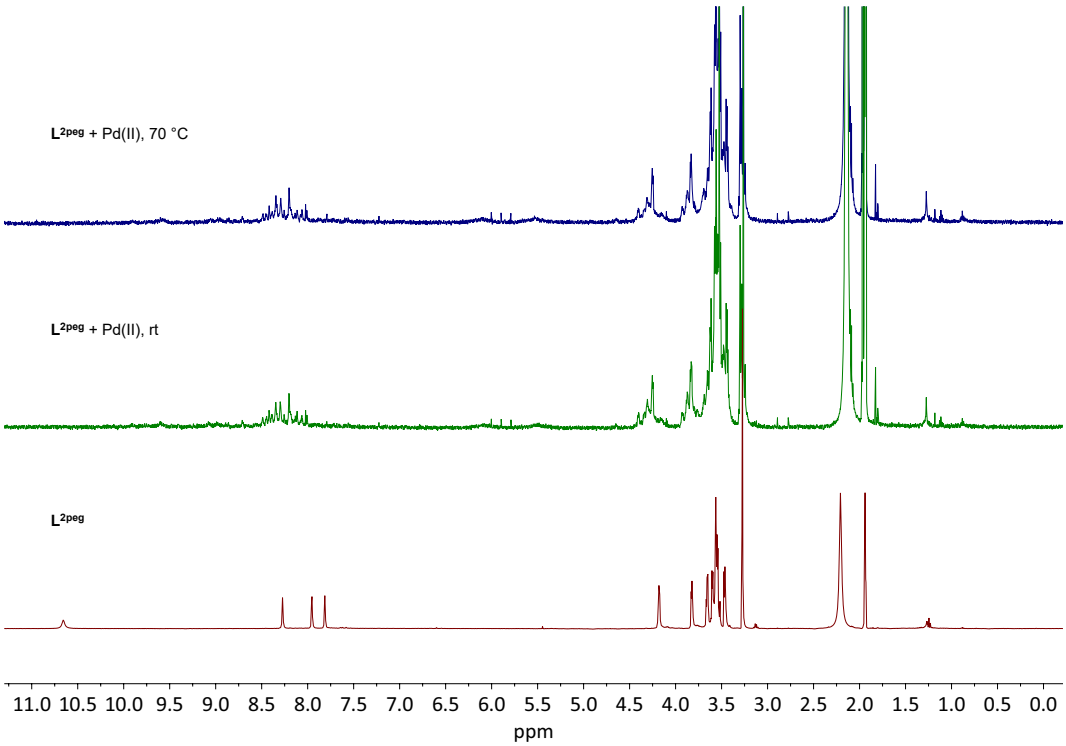

Figure 4.135. ^{1}H-NMR spectra (500 MHz, 298 K, CD_3CN) of homoleptic coordination cage formation of $\mathbf{L^{2peg}}$.

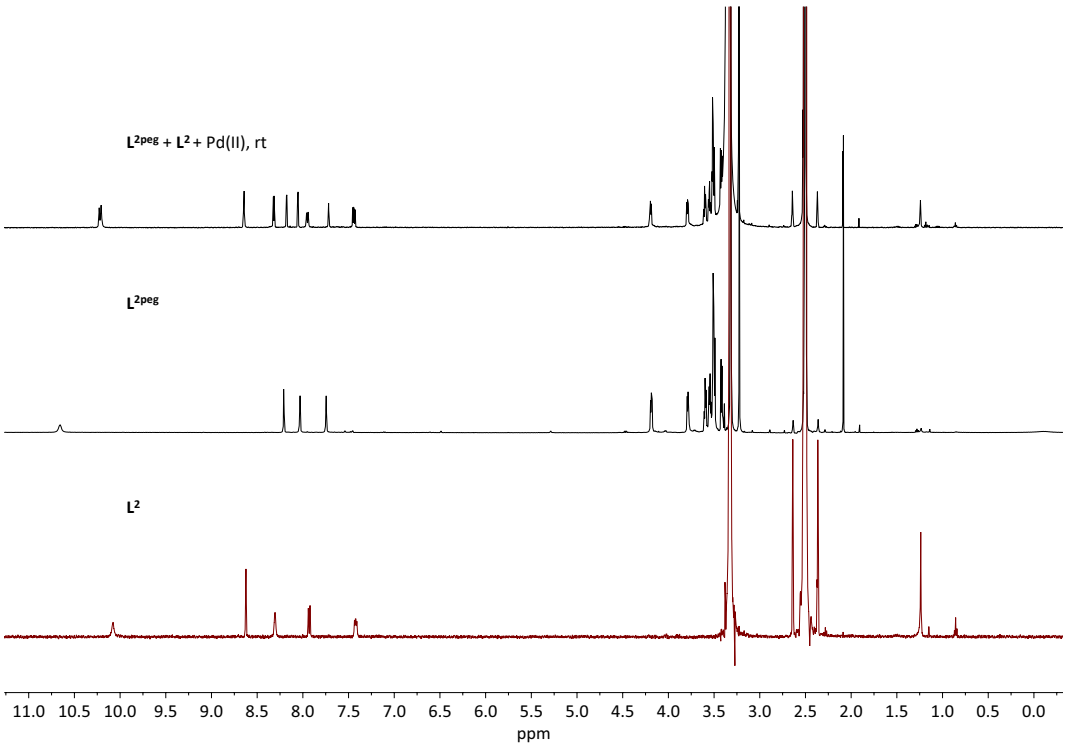

Figure 4.136. ^{1}H-NMR spectra (500 MHz, 298 K, DMSO$-d_6$) of coordination cage formation of $\mathbf{L^{2peg}}$ and $\mathbf{L^{2}}$ at rt.

4.3.7 Heteroleptic Coordination Cage Formation with L^{2peg} and L^1

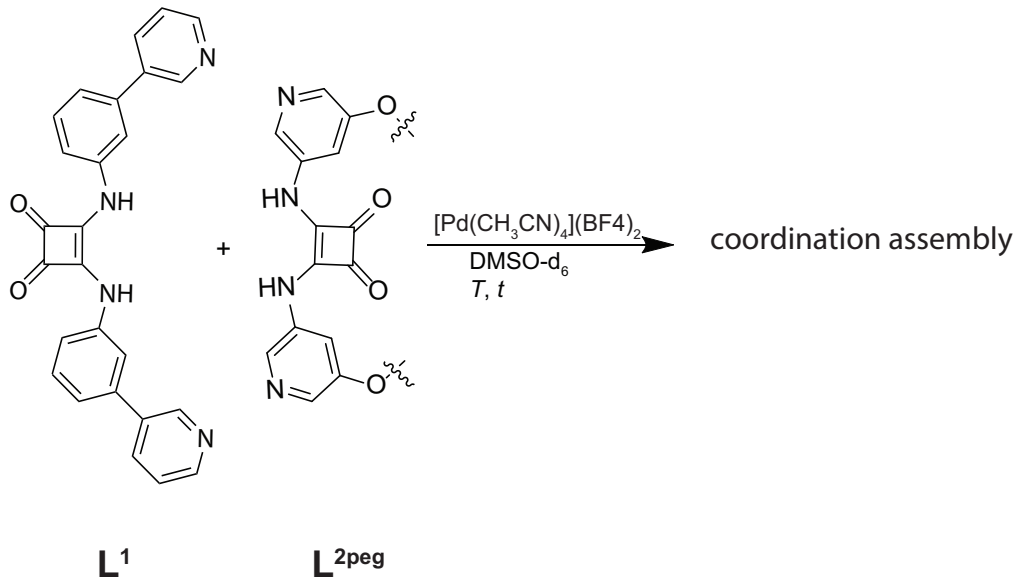

Figure 4.137. Heteroleptic coordination cage formation of L^{2peg} and L^1.

The procedure was carried out analogously to the heteroleptic coordination cage formation.

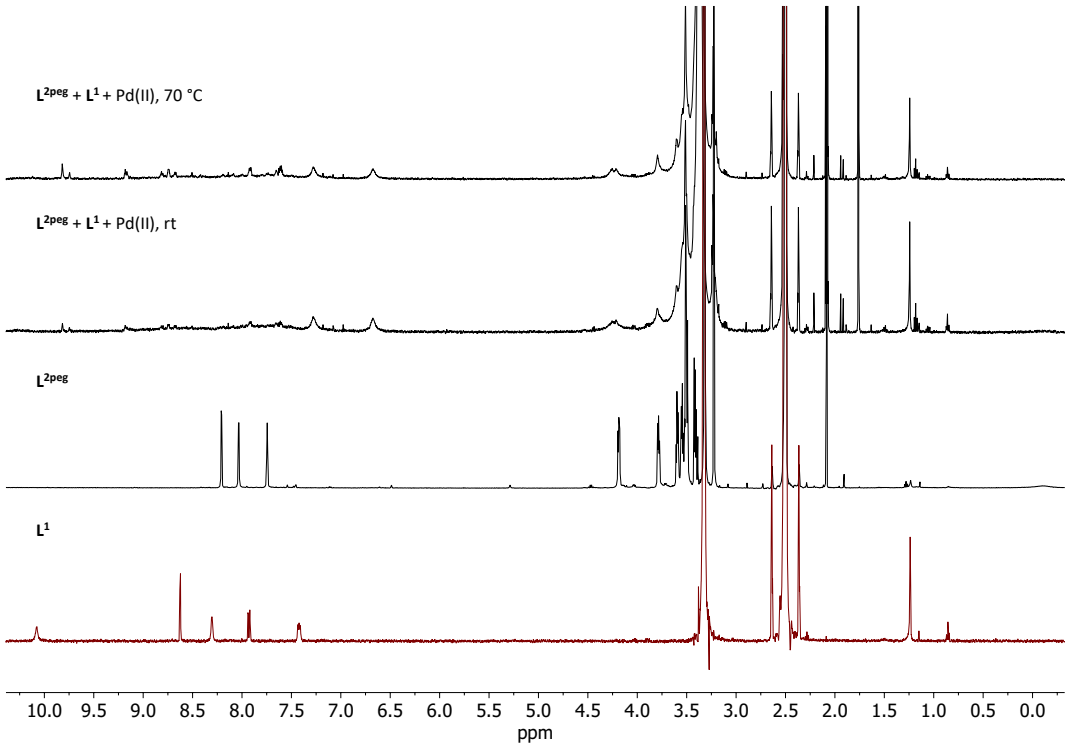

Figure 4.138. ^{1}H-NMR spectrum (500 MHz, 298 K, DMSO$-d_6$) of coordination cage formation of L^{2peg} and L^1 at rt and 70 °C .

ESI-MS measurement did not provide any informations about coordination assembly structure.

4.3.8 Heteroleptic Coordination Cage het1peg Formation with Ligand L^{1peg} and L^{2peg}

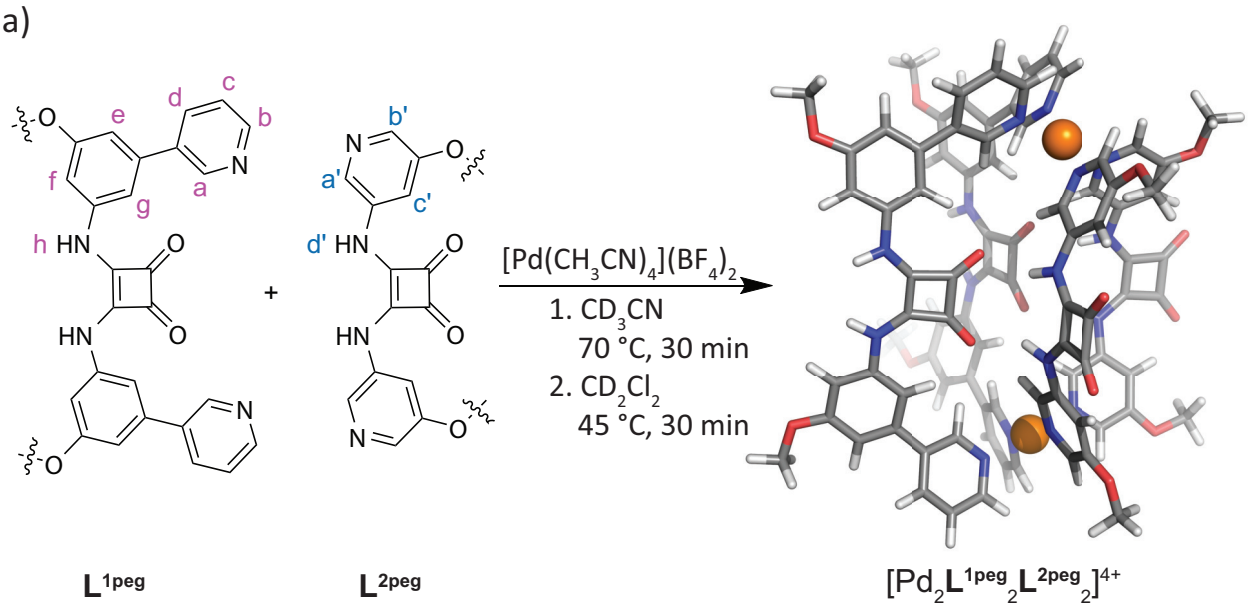

Figure 4.139. Heteroleptic coordination cage formation of $\mathbf{L^{1peg}}$ and $\mathbf{L^{2peg}}$ in CD_2Cl_2. PM6 Level. Peg chain omitted for the calculation and illustration.

A mixture of 270 μL of $\mathbf{L^{1peg}}$ (0.76 mmol, 2.8 mM) and 270 μL of $\mathbf{L^{2peg}}$ (0.76 mmol, 2.8 mM) in CD_3CN has been prepared with 15 mM $[Pd(CH_3CN)_4](BF_4)_2$ (0.90 mmol, 60 μL) and heated for 30 min at 70 °C. Then the solvent was removed *in vacuo* followed by addition of CD_2Cl_2 and heating at 45 °C for 30 min. The chemical shifting of the ^{1}H-NMR signals suggest that a coordination species has been formed. ^{1}H DOSY NMR confirmed that one species was obtained. Mass spectrometry also suggests that the coordination cage is formed. In Addition to that, r_H of $[Pd_2\mathbf{L^{1peg}}_2\mathbf{L^{2peg}}_2]^{4+}$ is 10,5 Å so it can be assumed that it is a $[Pd_2\mathbf{L}_2\mathbf{L'}_2]^{4+}$ species.

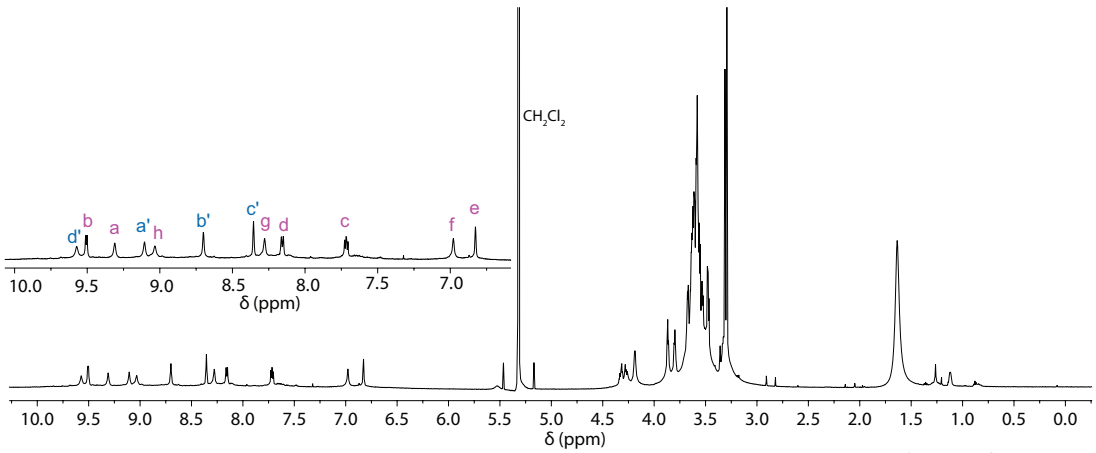

Figure 4.140. ^{1}H-NMR spectrum (500 MHz, 298 K, CD_2Cl_2) of $[Pd_2\mathbf{L^{1peg}}_2\mathbf{L^{2peg}}_2]^{4+}$. The aromatic region is shown zoomed in.

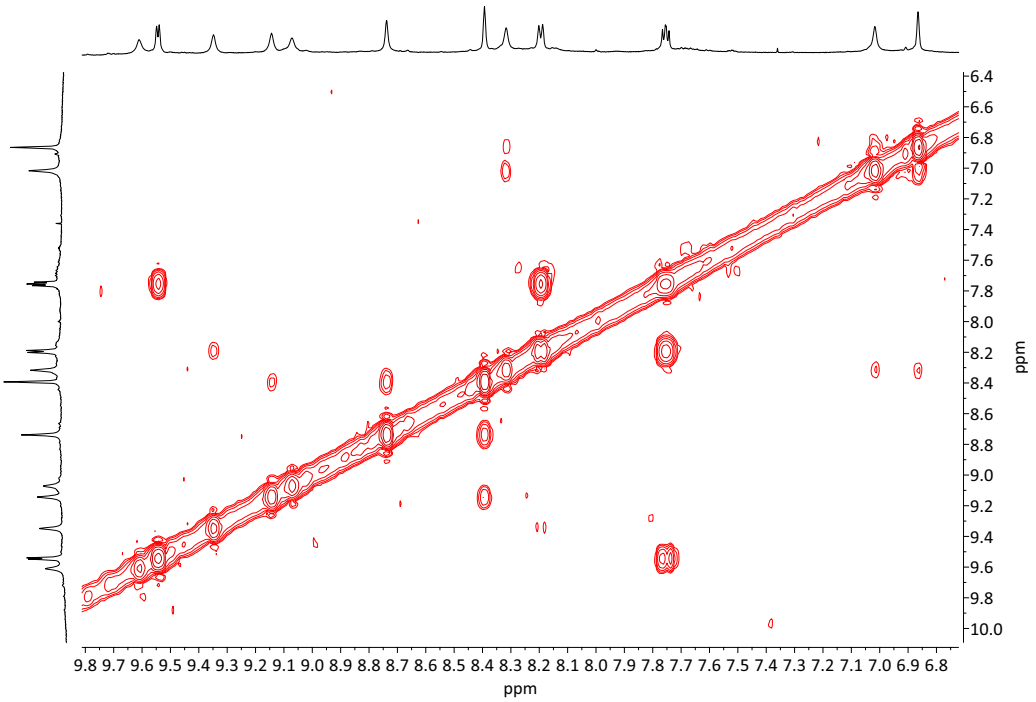

Figure 4.141. ^{1}H-^{1}H COSY spectrum (600 MHz, 298 K, CD_2Cl_2) of spectrum of the cage formation of $\mathbf{L^{2peg}}$ and $\mathbf{L^{1peg}}$.

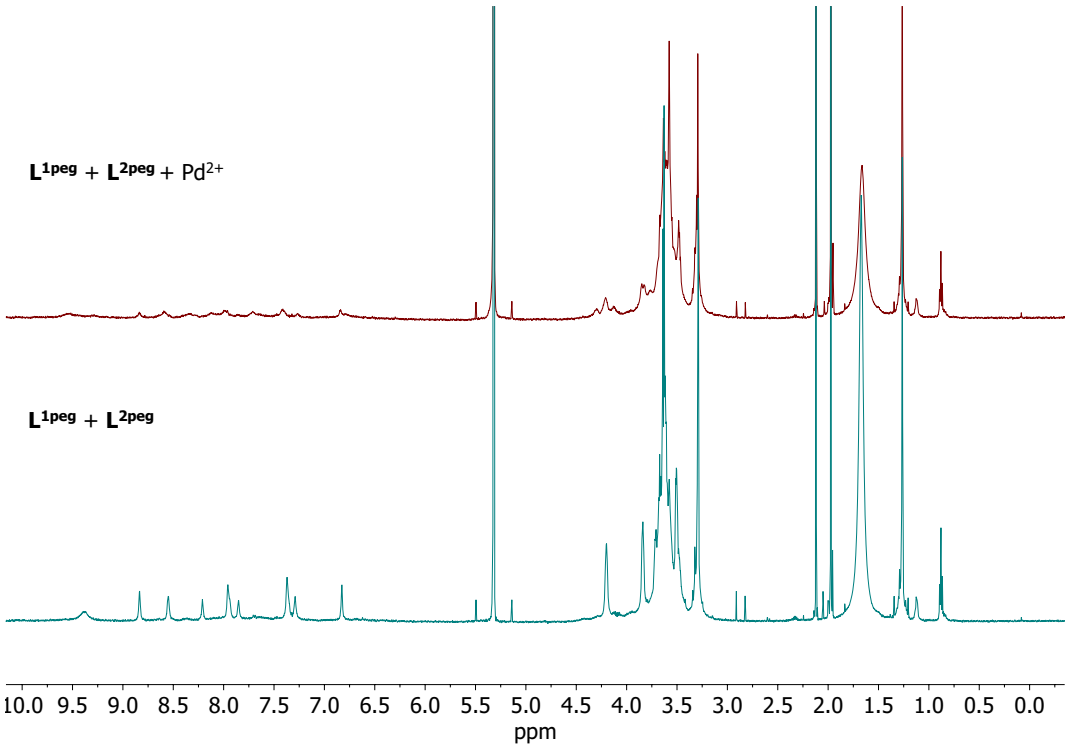

Figure 4.142. ^{1}H-NMR spectra (500 MHz, 298 K, CD_2Cl_2) of coordination cage formation experiment of $\mathbf{L^{2peg}}$ and $\mathbf{L^{1peg}}$ with $[Pd_2(CH_3CN)_4](BF_4)_2$ in CD_2Cl_2.

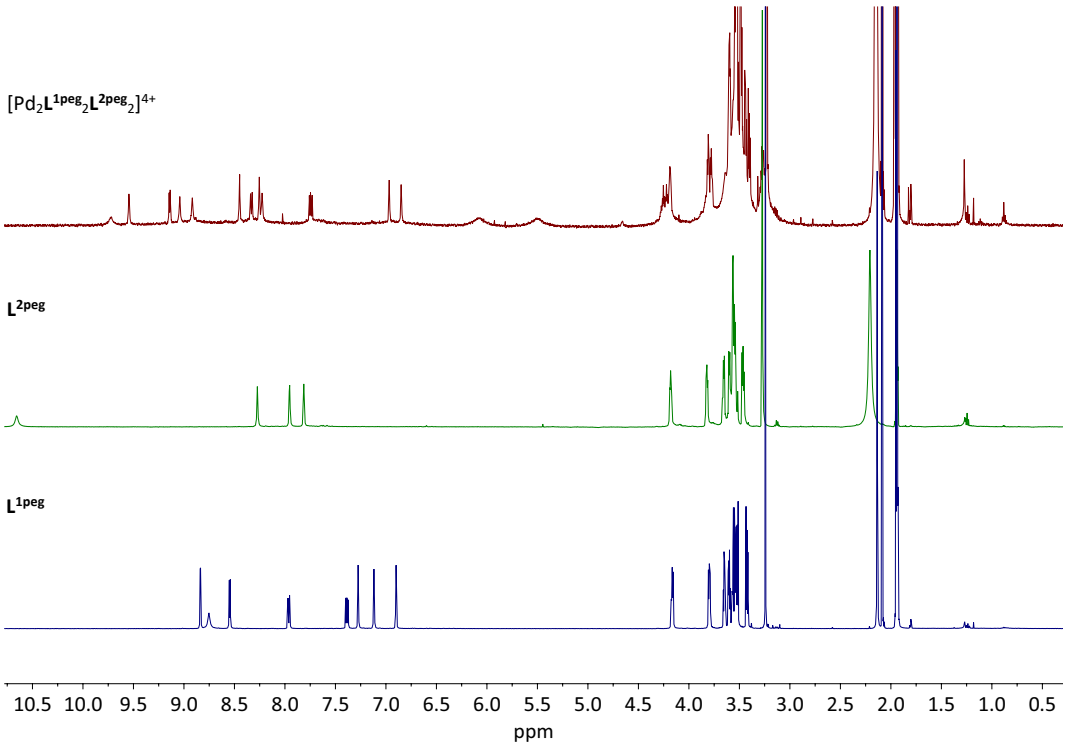

Figure 4.143. ^{1}H-NMR spectra (500 MHz, 298 K, CD_3CN) of coordination cage formation of $[Pd_2\mathbf{L}^{\mathbf{1peg}}{}_2\mathbf{L}^{\mathbf{2peg}}{}_2]^{4+}$.

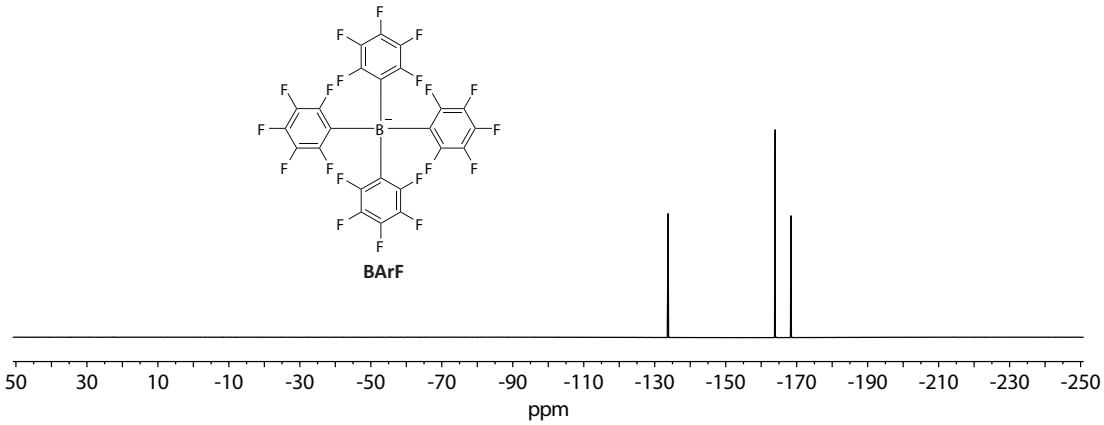

Figure 4.144. ^{19}F-NMR spectrum (400 MHz, 298 K, CD_3CN) of **BArF** with Ag^{+} as a counter ion.

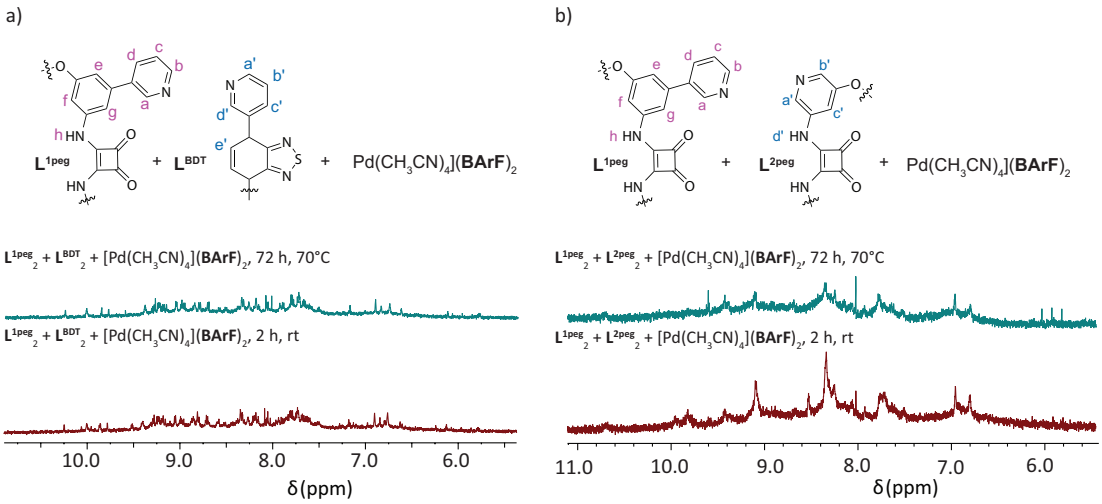

Figure 4.145. ^{1}H-NMR spectra (500 MHz, 298 K, CD_3CN) of cage formation experiment of a) $\mathbf{L^{1peg}}$ and $\mathbf{L^{BDT}}$ with $[Pd(CH_3CN)_4](\mathbf{BArF})_2$. b) $\mathbf{L^{1peg}}$ and $\mathbf{L^{2peg}}$ with $[Pd(CH_3CN)_4](\mathbf{BArF})_2$.

Other counterions such as PF_6^- or OTf^- have been screened for the cage formation of $\mathbf{L^{1peg}}$ and $\mathbf{L^{2peg}}$ in CD_3CN, but the ^{1}H-NMR could be only distinguished for the experiment with BF_4^-.

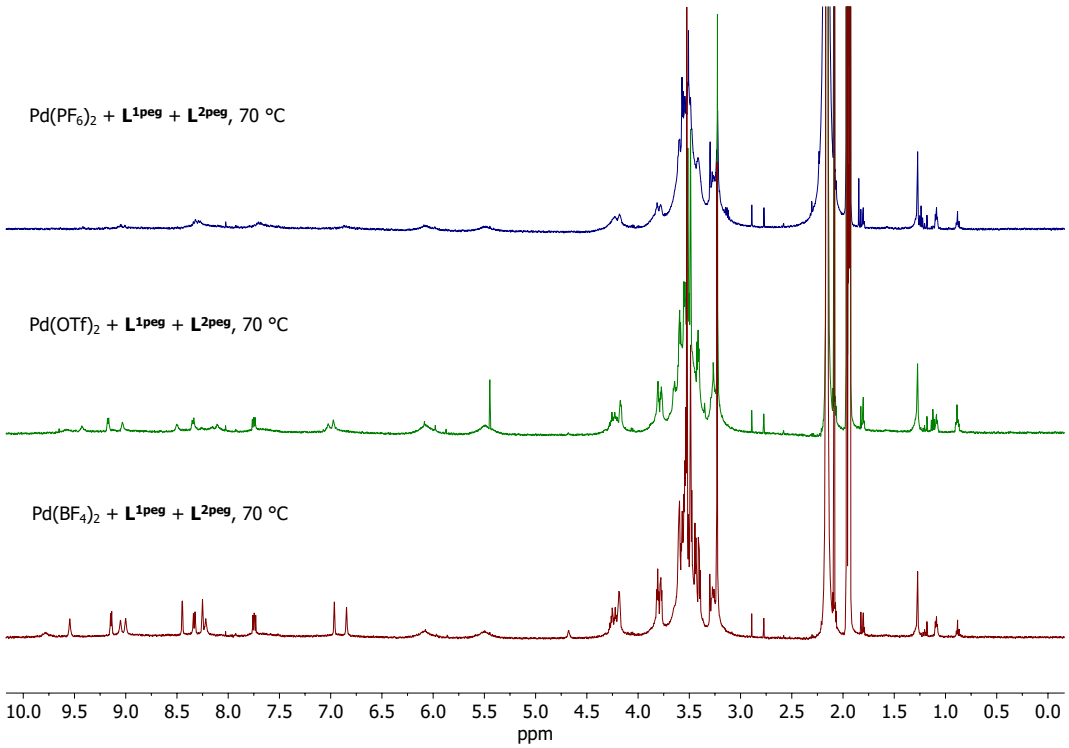

Figure 4.146. ^{1}H-NMR spectra (500 MHz, 298 K, CD_3CN) of coordination cage formation of $\mathbf{L^{2peg}}$ and $\mathbf{L^{1peg}}$ at 70 °C with various counter ions.

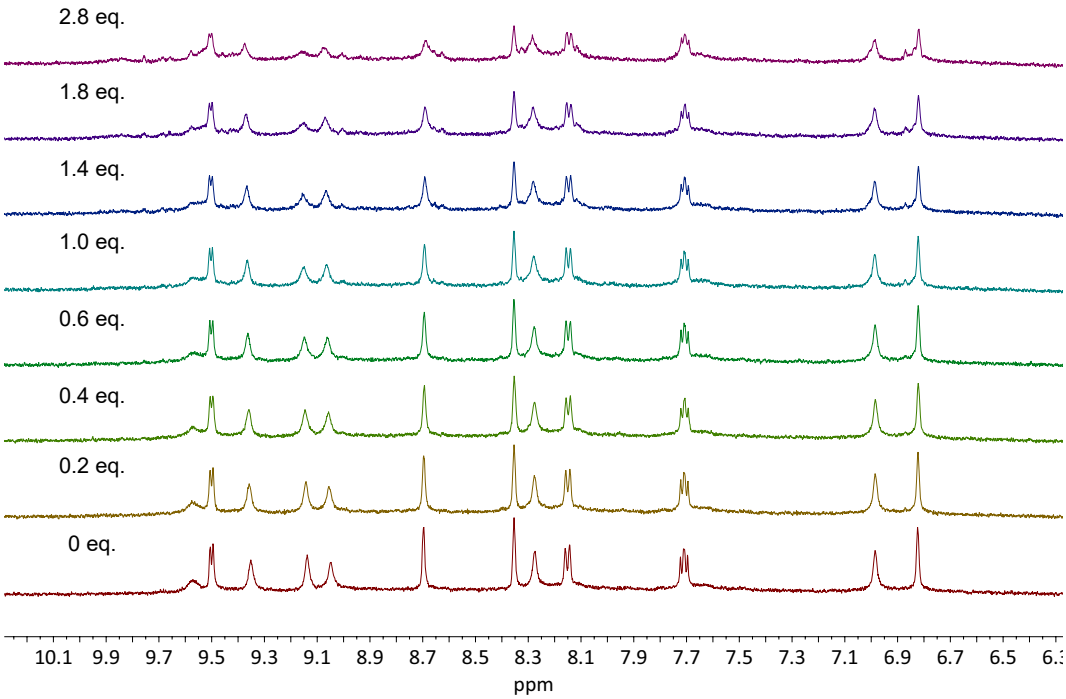

Figure 4.147. ^{1}H-NMR spectrum (500 MHz, 298 K, CD_2Cl_2) of titration of **TBACl** to $[Pd_2\mathbf{L}^{\mathbf{1peg}}{}_2\mathbf{L}^{\mathbf{2peg}}{}_2]^{4+}$.

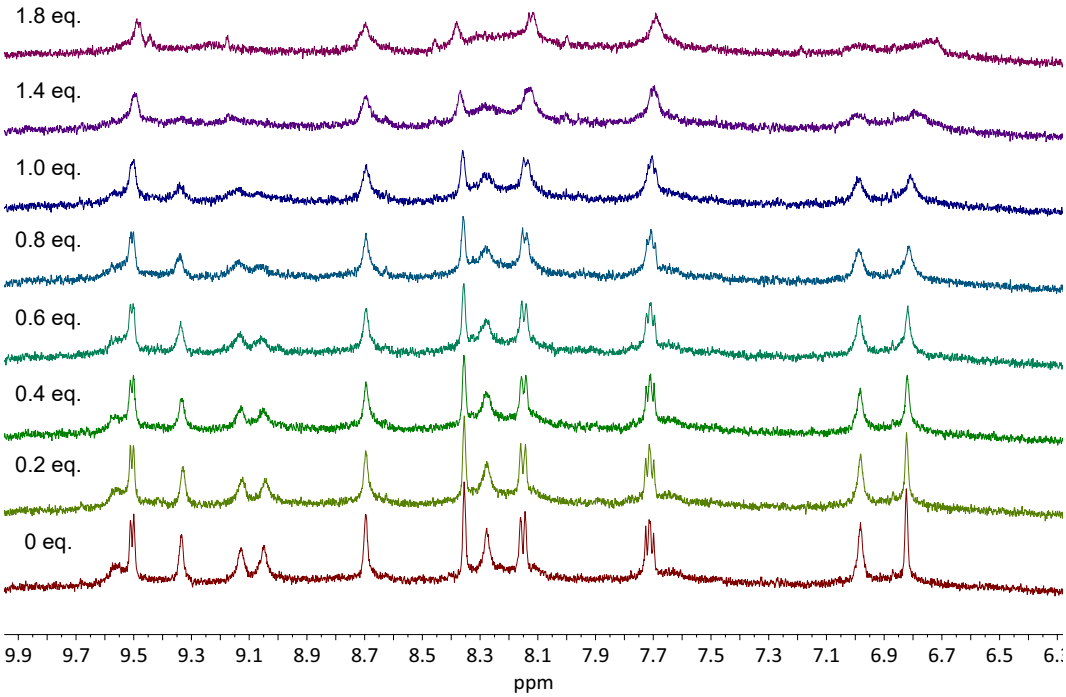

Figure 4.148. ^{1}H-NMR spectrum (500 MHz, 298 K, CD_2Cl_2) of titration of **PDS** to $[Pd_2\mathbf{L}^{\mathbf{1peg}}{}_2\mathbf{L}^{\mathbf{2peg}}{}_2]^{4+}$.

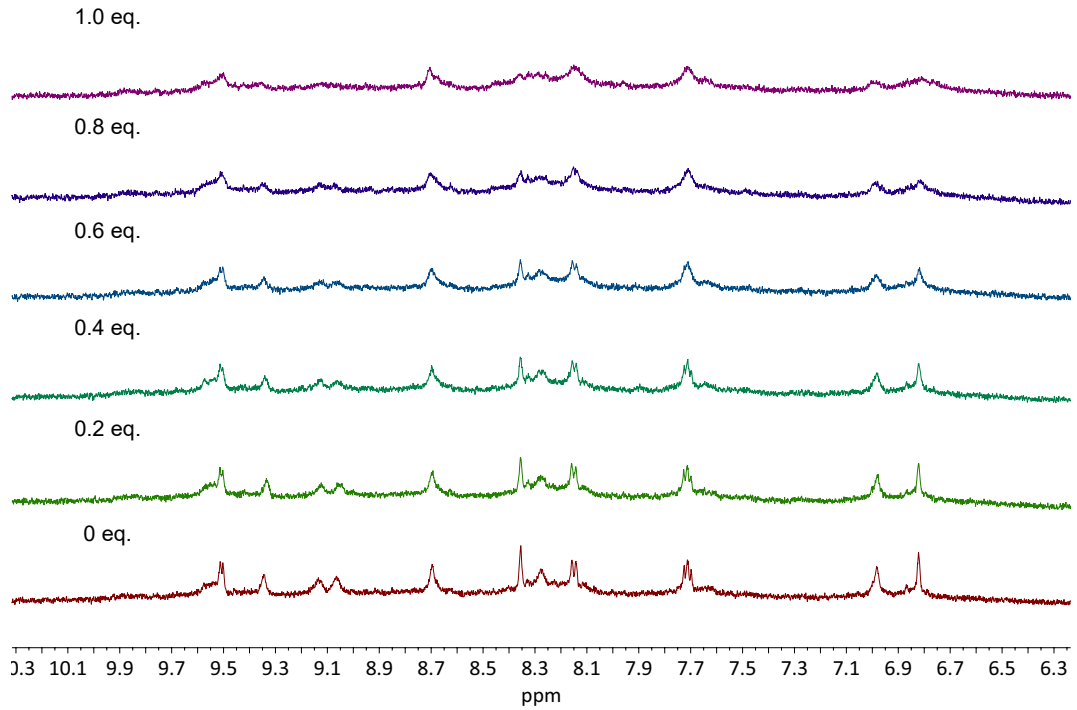

Figure 4.149. ^{1}H-NMR spectrum (500 MHz, 298 K, CD_2Cl_2) of titration of **NDS** to $[Pd_2\mathbf{L}^{\mathbf{1peg}}{}_2\mathbf{L}^{\mathbf{2peg}}{}_2]^{4+}$.

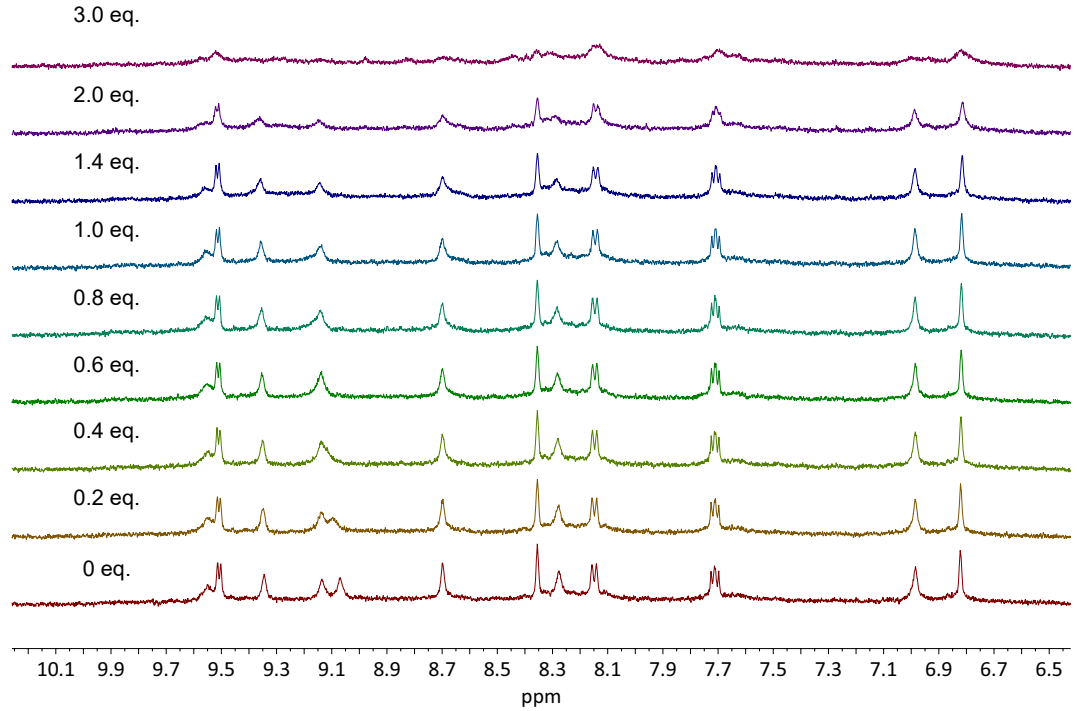

Figure 4.150. ^{1}H-NMR spectrum (500 MHz, 298 K, CD_2Cl_2) of titration of **DEP** to $[Pd_2\mathbf{L}^{\mathbf{1peg}}{}_2\mathbf{L}^{\mathbf{2peg}}{}_2]^{4+}$.

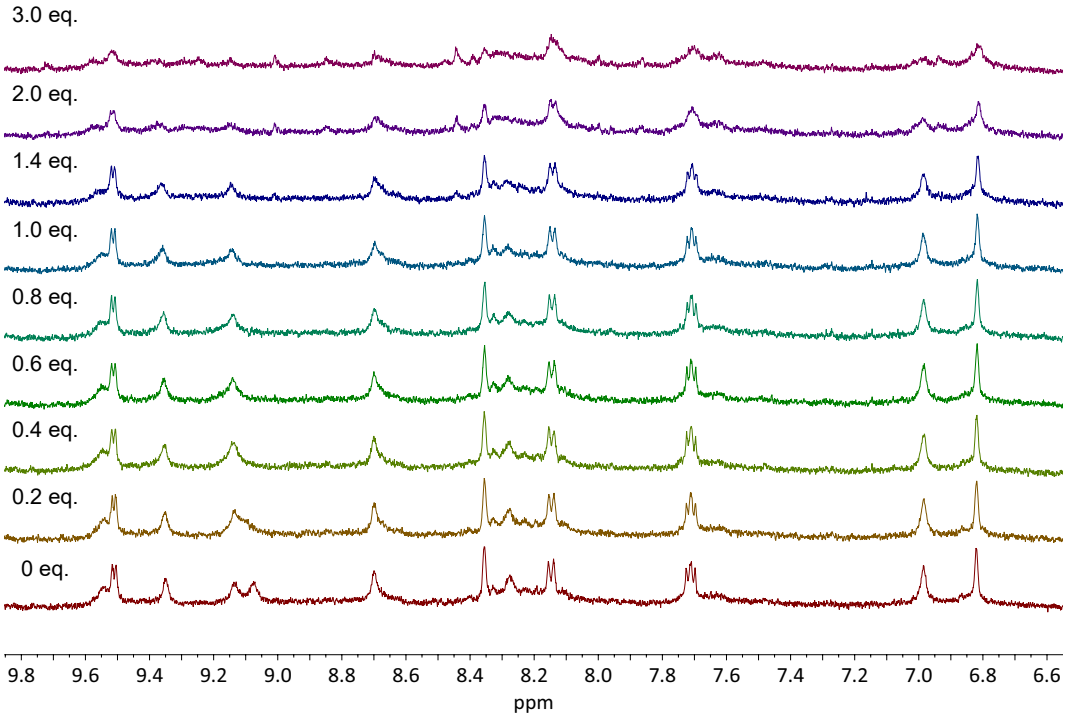

Figure 4.151. ^{1}H-NMR spectrum (500 MHz, 298 K, CD_2Cl_2) of titration of **DBuP** to $[Pd_2\mathbf{L}^{\mathbf{1peg}}{}_2\mathbf{L}^{\mathbf{2peg}}{}_2]^{4+}$.

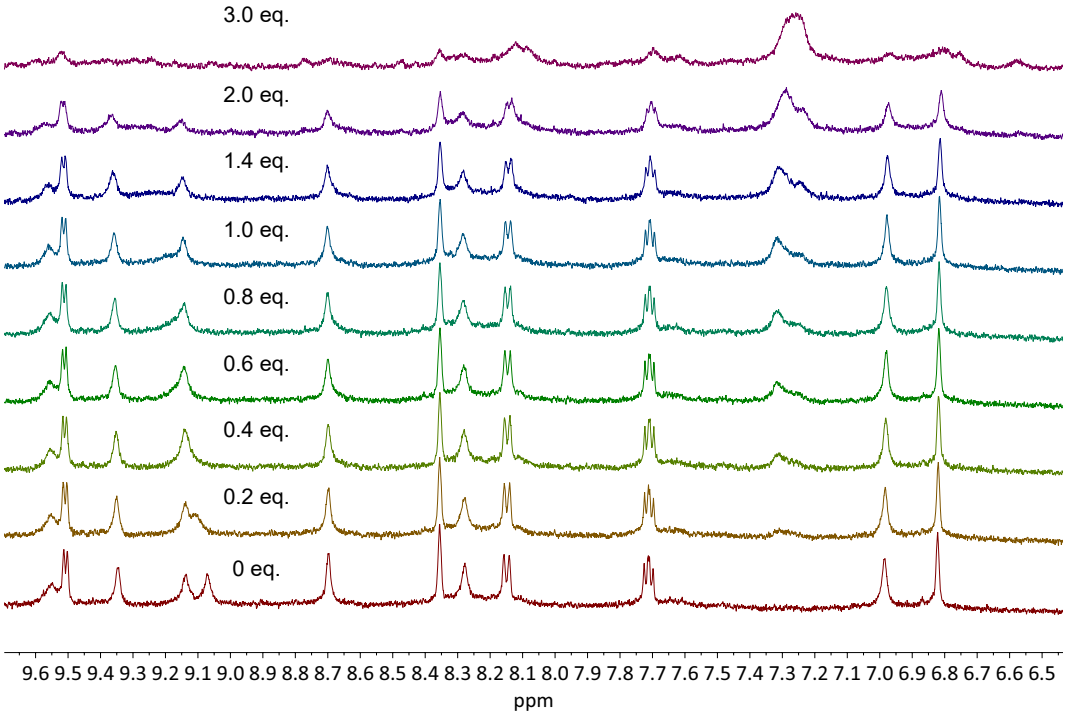

Figure 4.152. ^{1}H-NMR spectrum (500 MHz, 298 K, CD_2Cl_2) of titration of **DBnP** to $[Pd_2\mathbf{L}^{\mathbf{1peg}}{}_2\mathbf{L}^{\mathbf{2peg}}{}_2]^{4+}$.

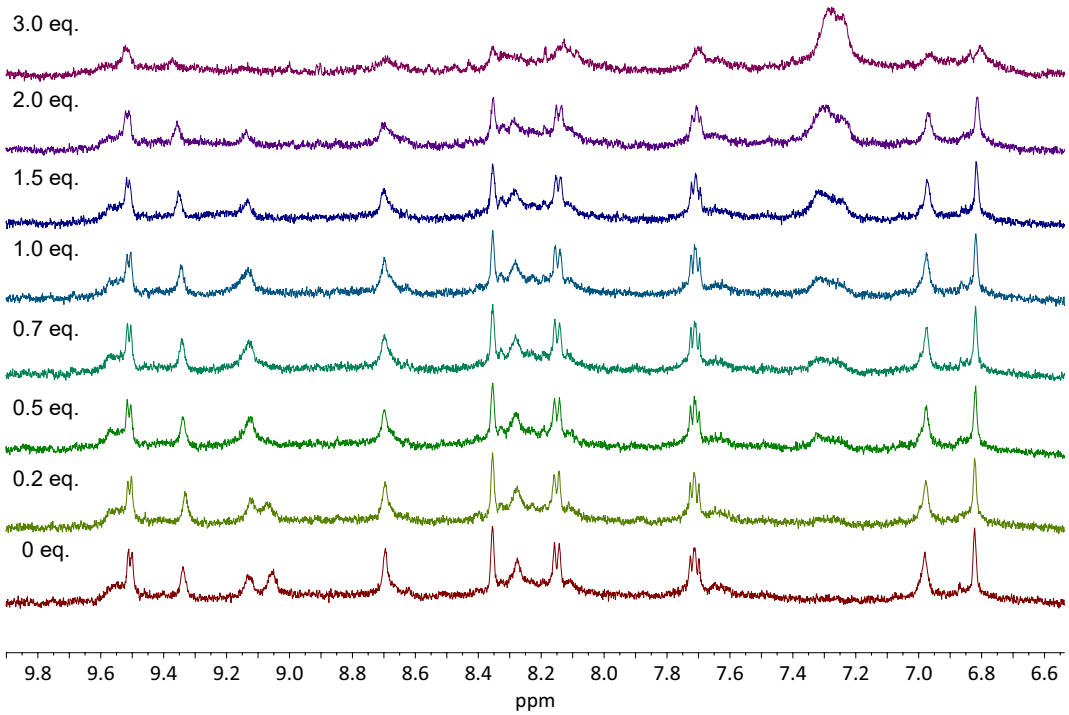

Figure 4.153. ^{1}H-NMR spectrum (500 MHz, 298 K, CD_2Cl_2) of titration of **DPP** to $[Pd_2\mathbf{L}^{\mathbf{1peg}}{}_2\mathbf{L}^{\mathbf{2peg}}{}_2]^{4+}$.

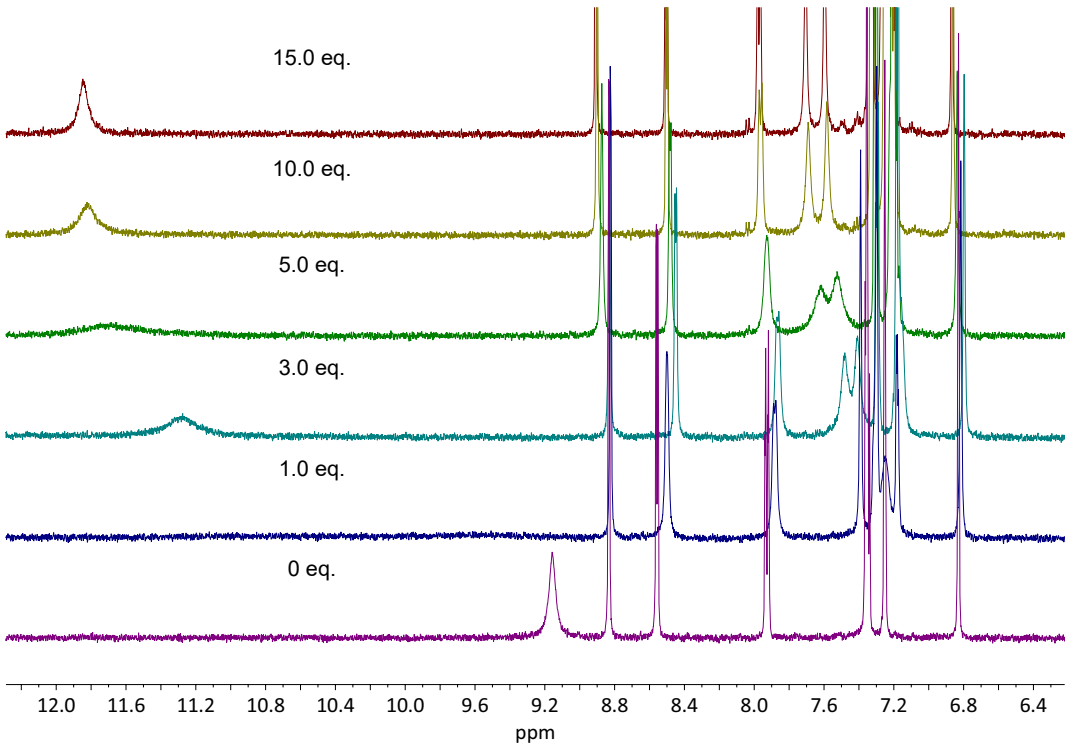

Figure 4.154. ^{1}H-NMR spectrum (500 MHz, 298 K, CD_2Cl_2) of titration of **DBn** to $\mathbf{L}^{\mathbf{1peg}}$.

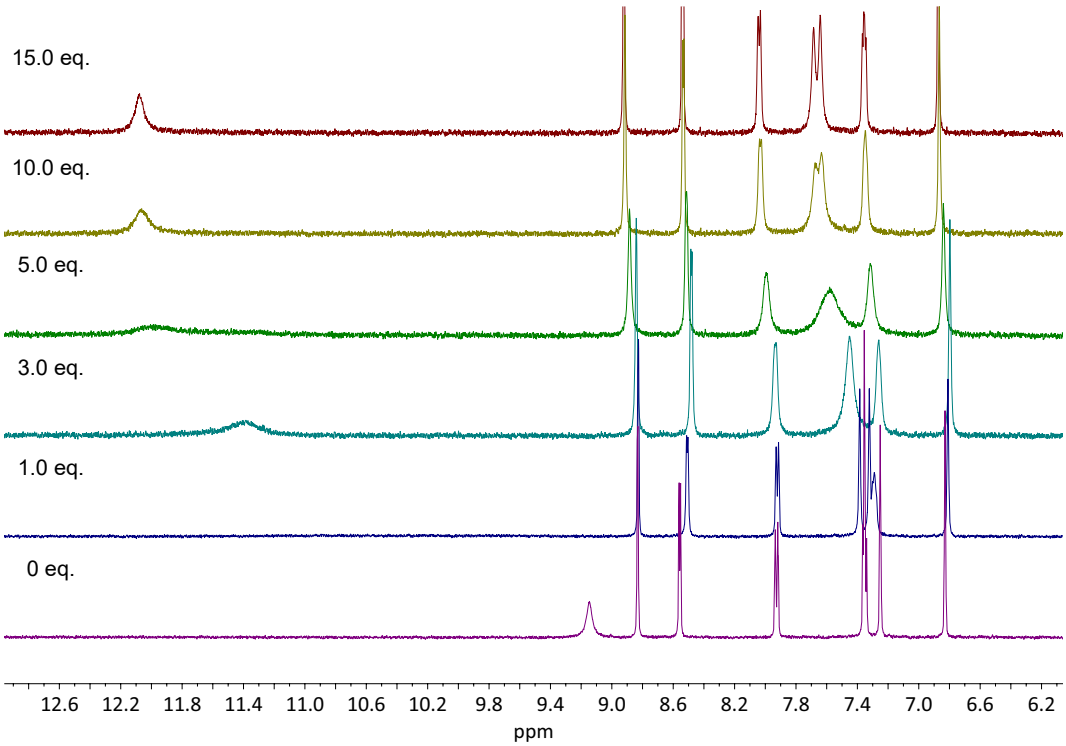

Figure 4.155. ^{1}H-NMR spectrum (500 MHz, 298 K, CD_2Cl_2) of titration of **DBuP** to $\mathbf{L^{1peg}}$.

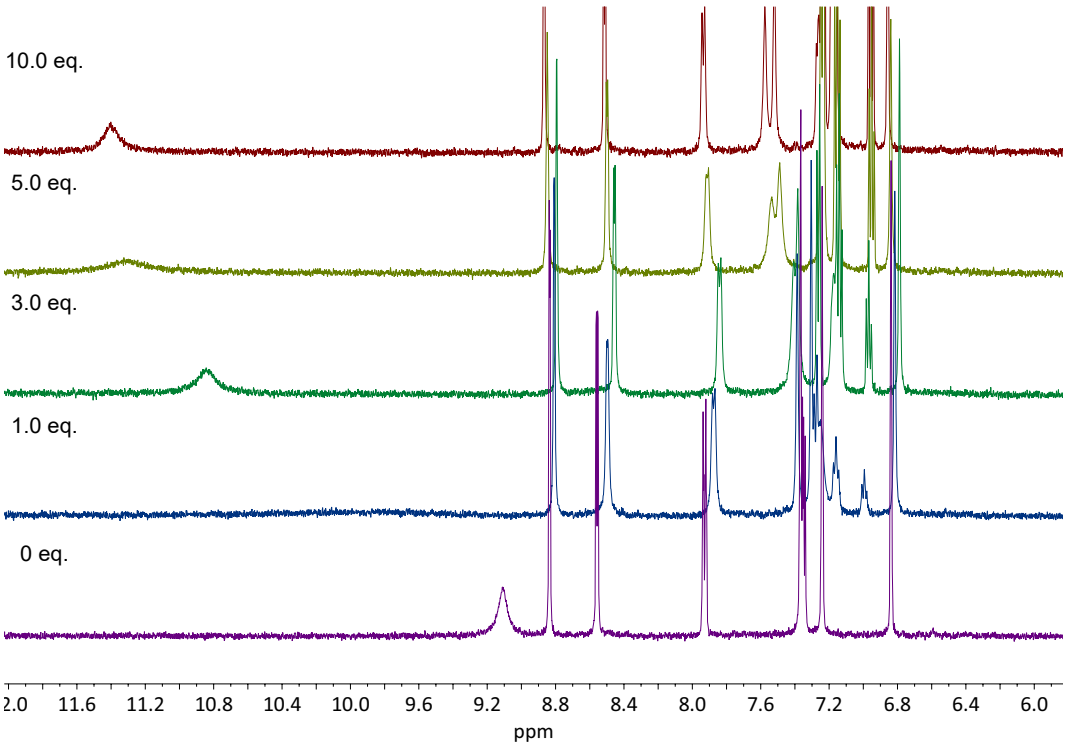

Figure 4.156. ^{1}H-NMR spectrum (500 MHz, 298 K, CD_2Cl_2) of titration of **DPP** to $\mathbf{L^{1peg}}$.

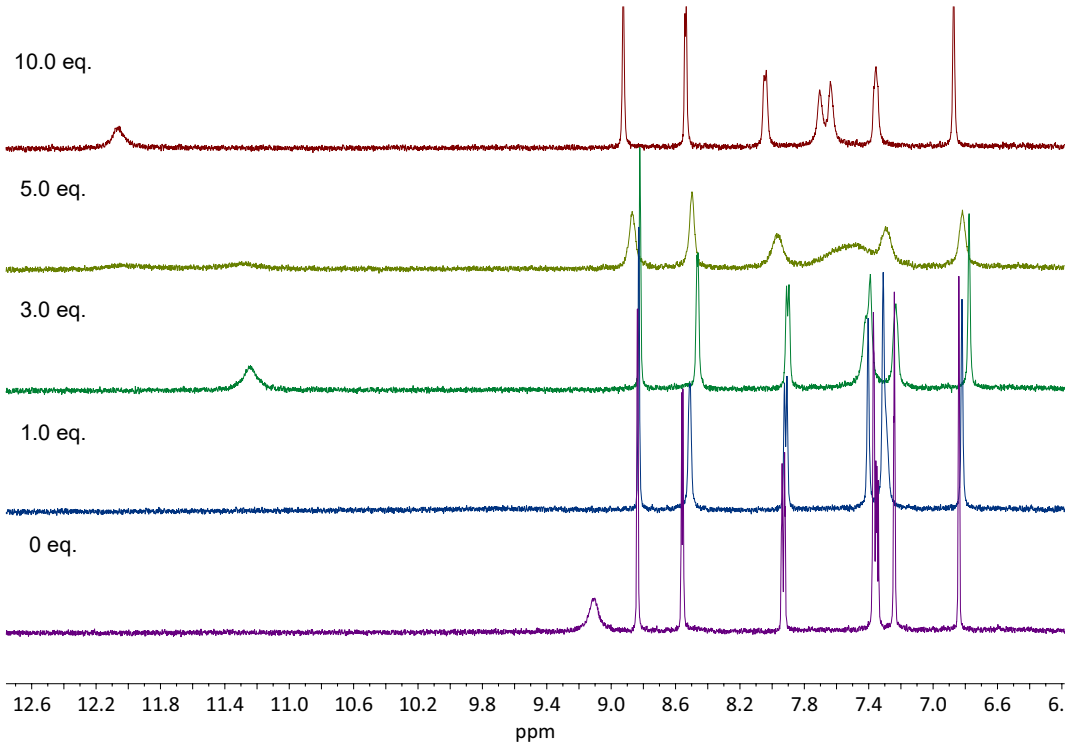

Figure 4.157. ^{1}H-NMR spectrum (500 MHz, 298 K, CD_2Cl_2) of titration of **DEP** to $\mathbf{L^{1peg}}$.

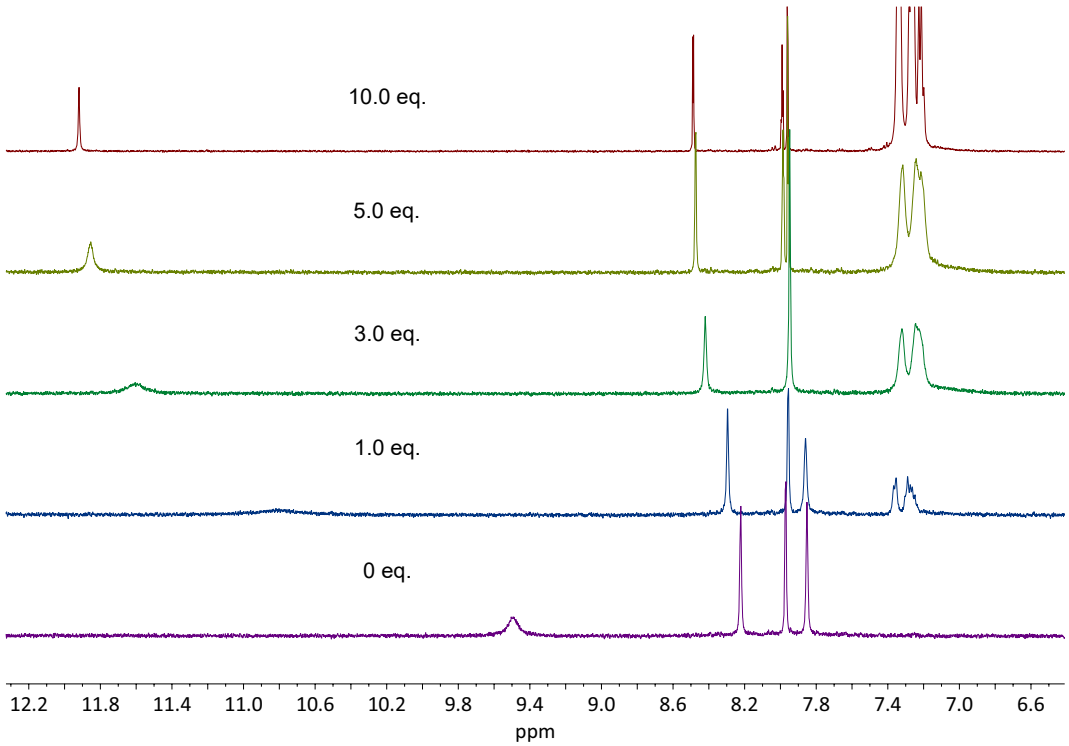

Figure 4.158. ^{1}H-NMR spectrum (500 MHz, 298 K, CD_2Cl_2) of titration of **DBnP** to $\mathbf{L^{2peg}}$.

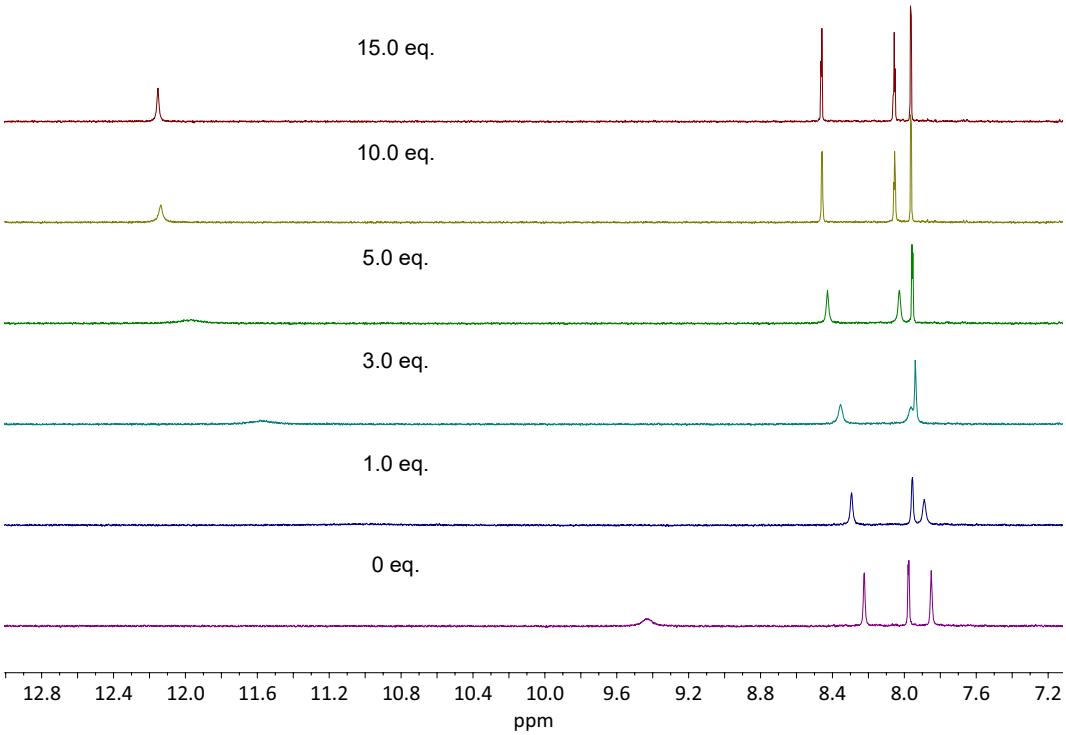

Figure 4.159. ^{1}H-NMR spectrum (500 MHz, 298 K, CD_2Cl_2) of titration of **DBu** to $\mathbf{L^{2peg}}$.

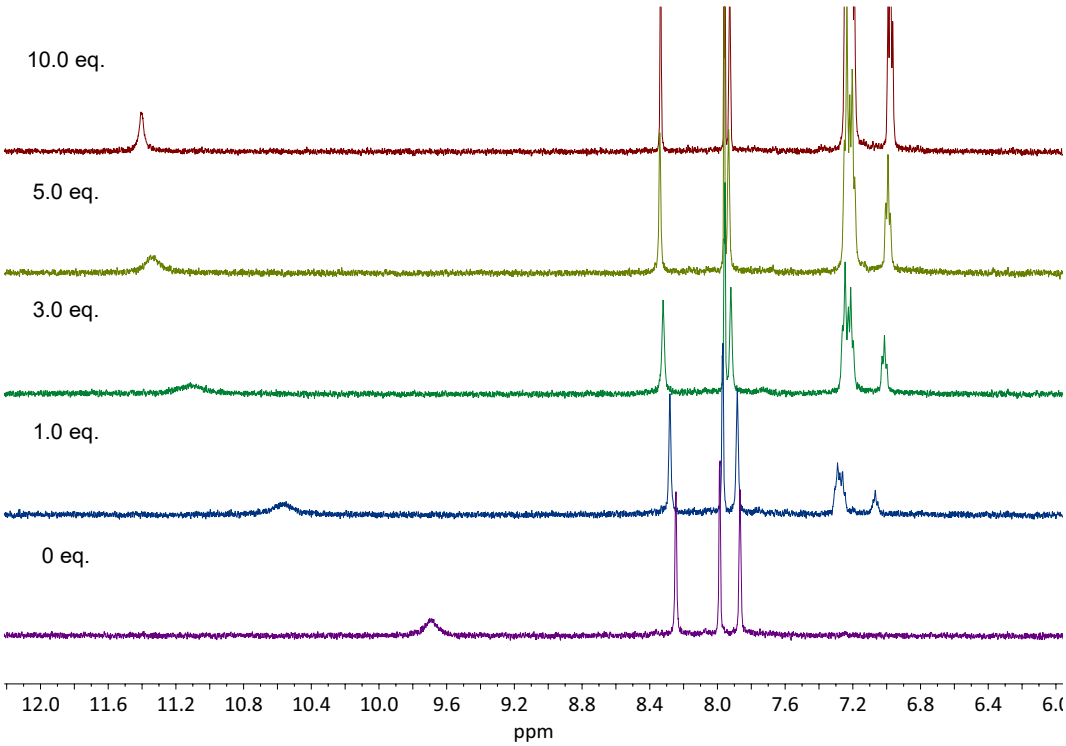

Figure 4.160. ^{1}H-NMR spectrum (500 MHz, 298 K, CD_2Cl_2) of titration of **DPP** to $\mathbf{L^{2peg}}$.

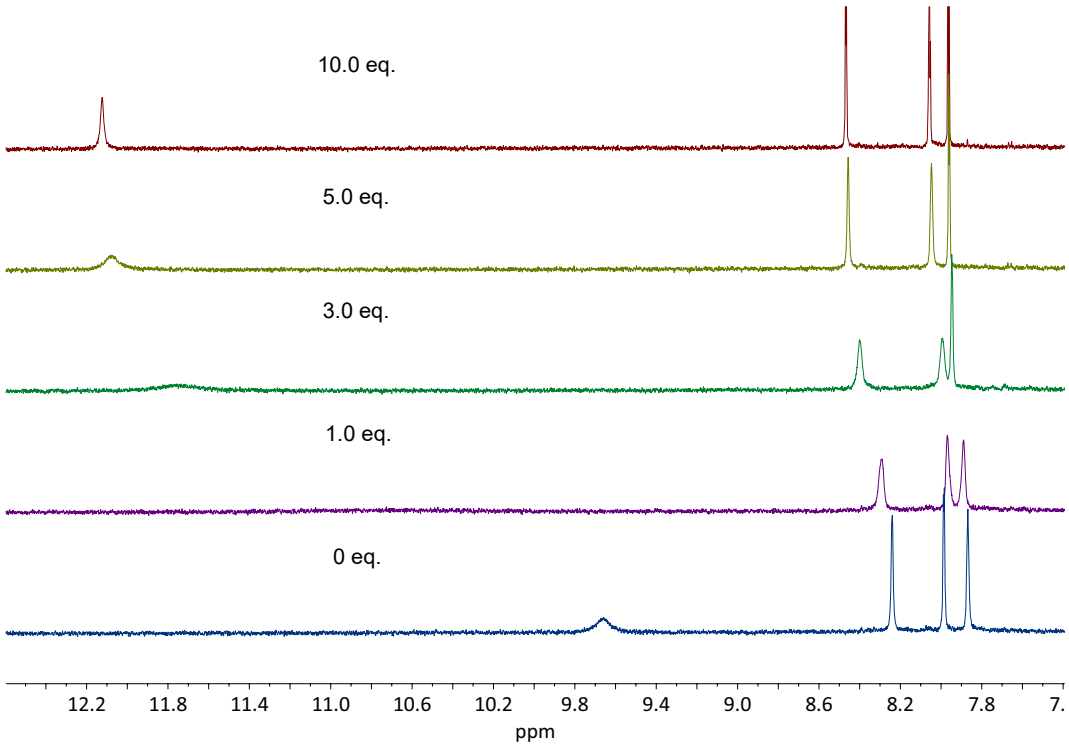

Figure 4.161. ^{1}H-NMR spectrum (500 MHz, 298 K, CD_2Cl_2) of titration of **DEP** to $\mathbf{L^{2peg}}$.

$[Pd_2\mathbf{L^{1peg}}_2\mathbf{L^{2peg}}_2]^{4+}$ was formed with $Pd(NO_3)xH_2O$ in CD_3CN then the solvent was removed and D_2O was added. The signals could be not distinguished (see figure 4.162).

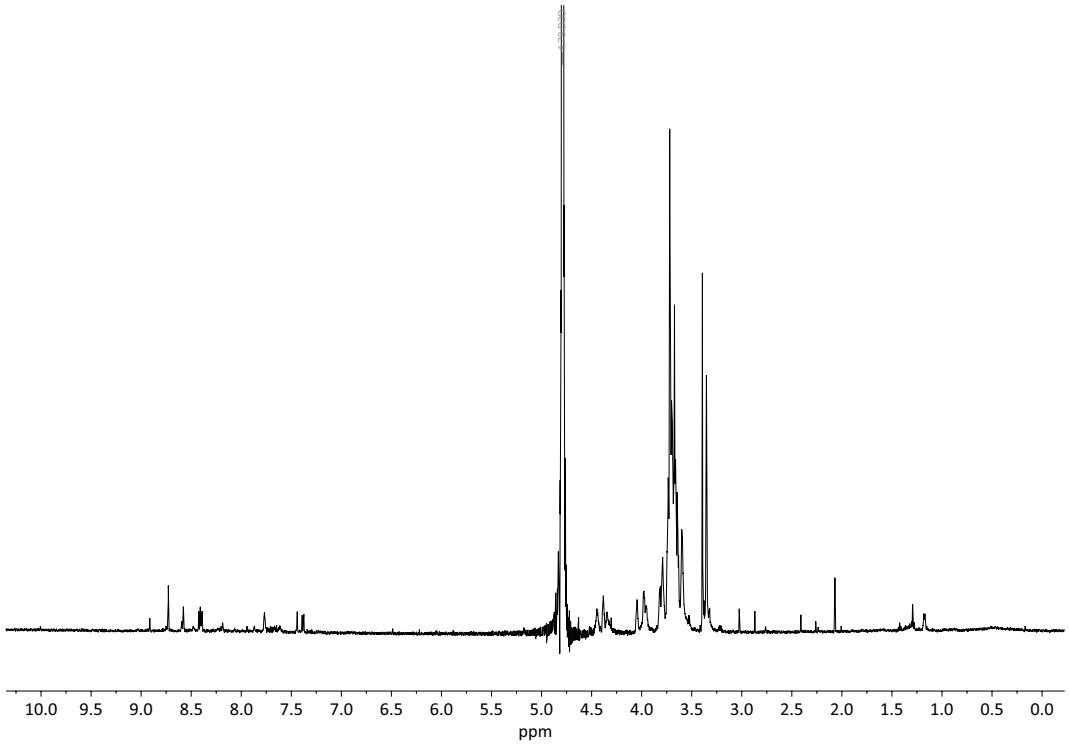

Figure 4.162. ^{1}H-NMR spectrum (500 MHz, 298 K, D_2O) of coordination cage formation of $\mathbf{L^{2peg}}$ and $\mathbf{L^{1peg}}$ with $Pd(NO_3)_2$ at 70 °C.

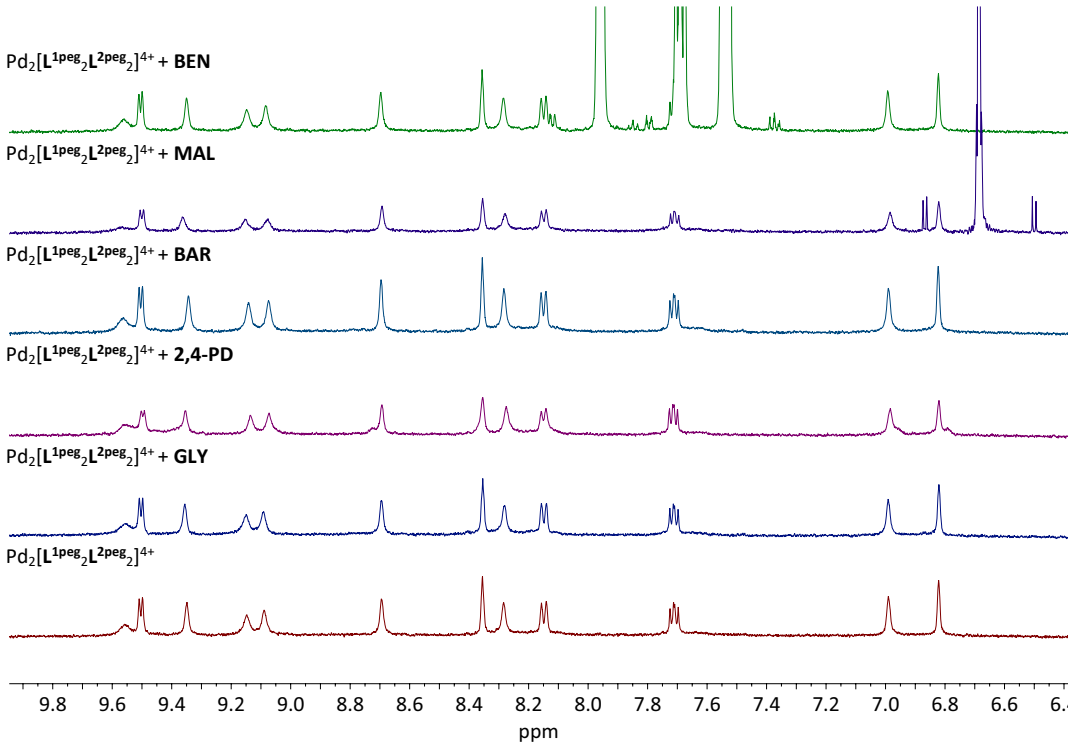

Figure 4.163. ^{1}H-NMR spectrum (500 MHz, 298 K, CD_2Cl_2) screening of neutral molecules to $[Pd_2\mathbf{L^{1peg}}_2\mathbf{L^{2peg}}_2]^{4+}$ by excess addition.

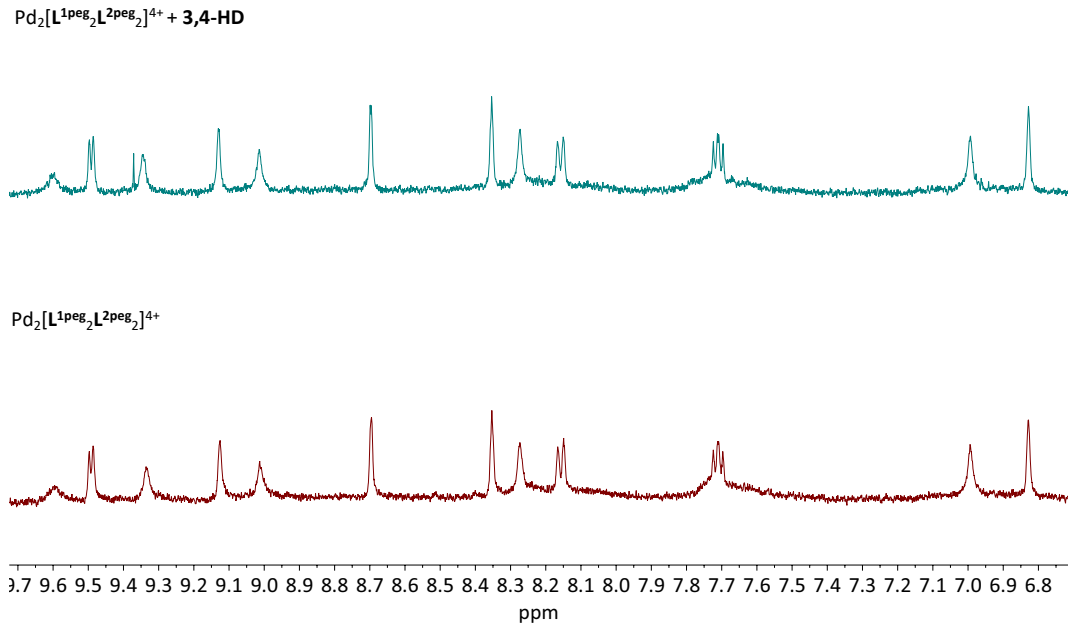

Figure 4.164. ^{1}H-NMR spectrum (500 MHz, 298 K, CD_2Cl_2) screening of **3,4-HD** to $[Pd_2\mathbf{L^{1peg}}_2\mathbf{L^{2peg}}_2]^{4+}$ by excess addition.

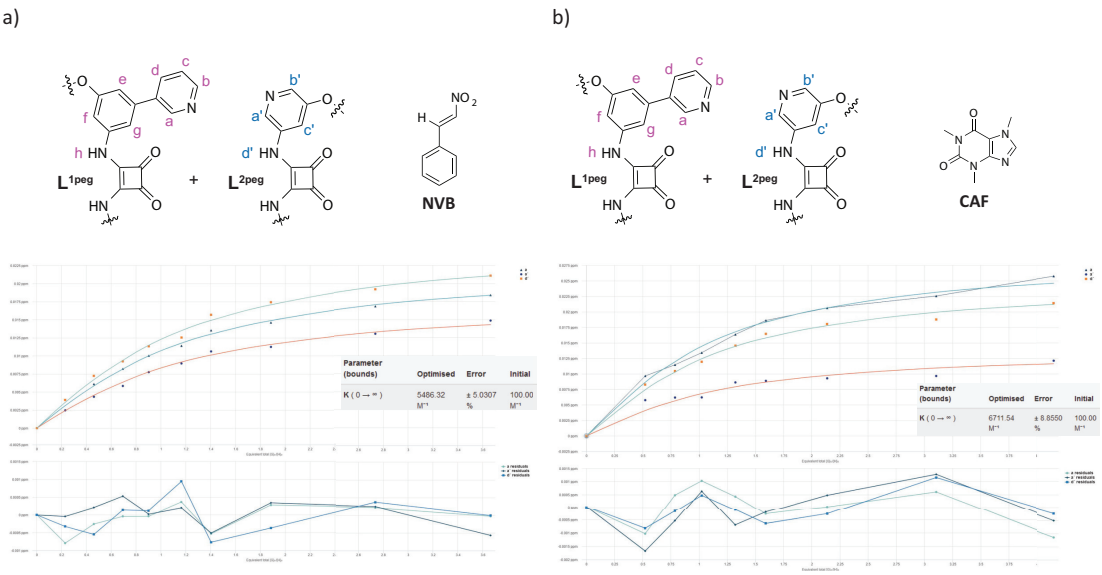

Figure 4.165. Illustration of binding analysis result obtained by BindFit (Fitter: 1:1) titration of **NVB** and **CAF** to $[Pd_2\mathbf{L^{1peg}}_2\mathbf{L^{2peg}}_2]^{4+}$.

Table 4.2: Obtained binding constants K_a for $[Pd_2\mathbf{L^{1peg}}_2\mathbf{L^{2peg}}_2]^{4+}$ in CD_2Cl_2. The concentration of each coordination cage was determined by ^{1}H-NMR spectroscopy using TMB as an internal standard.

K_a (**CAF**)	K_a (**NVB**)	K_a (**DMBM**)	K_a (**2,5-HD**)
$6712\,M^{-1} \pm 9\%$	$5486\,M^{-1} \pm 5\%$	$4394\,M^{-1} \pm 10\%$	$9083\,M^{-1} \pm 7\%$
$6218\,M^{-1} \pm 6\%$	$5072\,M^{-1} \pm 7\%$	$4386\,M^{-1} \pm 18\%$	$8360\,M^{-1} \pm 22\%$
$5625\,M^{-1} \pm 7\%$	$5023\,M^{-1} \pm 7\%$		

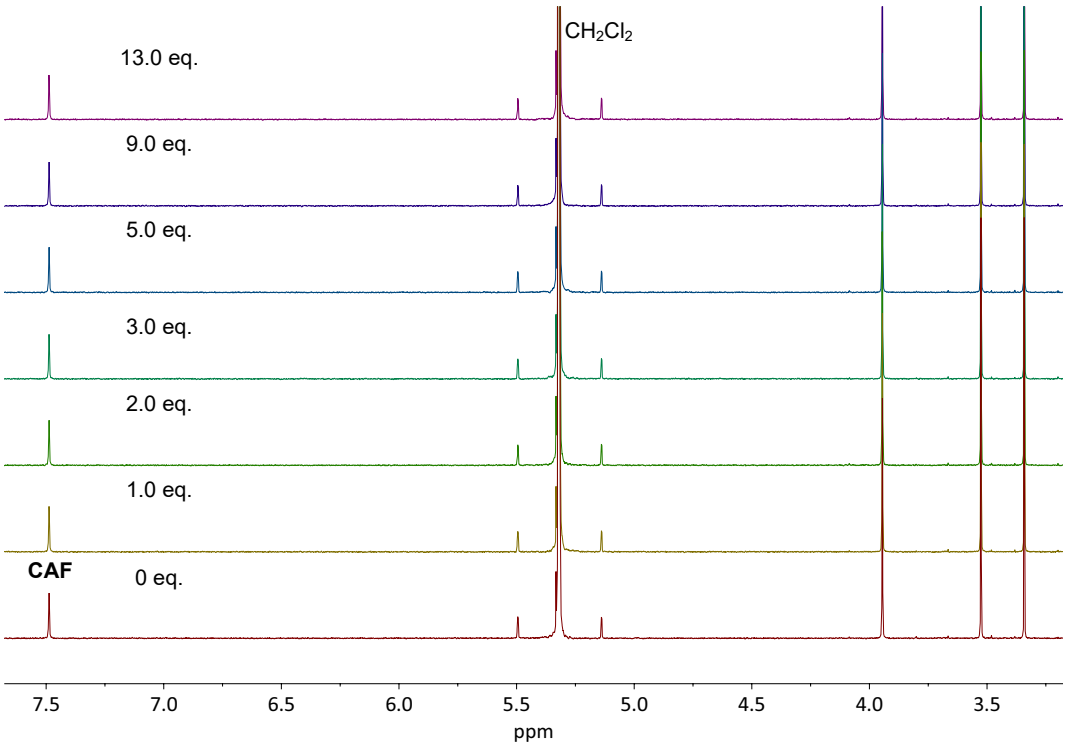

Figure 4.166. ^{1}H-NMR spectrum (500 MHz, 298 K, CD_2Cl_2) the titration of CD_2Cl_2 to **CAF** was adjusted to match the volume of the solvent added during the titrations.

Table 4.3: Values of distances (d_{HB}), normalized contact distance ratio (R_{HB}), angles (Ang), density of all electrons (ρ_{BCP}) at the bond critical points (BCP) and calculated energies corresponding to hydrogen bonding interactions involving squaramide moieties in the X-ray structures of cages. With $R_{HB} = d_{HB}/\sum$vdWr ($\sum$vdWr(O+H) = 2.7 Å) and E_{HB} (kJ/mol)= -(-223.08ρ_{BCP}+0.7423)4.184. [292][216] Calculated by A. S. Mikherdov.

Cage	d_{HB}(H–O) / Å	R_{HB}	Ang(X–H–O) / °	ρ_{BCP} / a.u.	E_{HB} / kJ/mol
$[Pd_2\mathbf{L^1}_2\mathbf{L^2}_2]^{4+}$	1.89	0.70	152.6	0.030	24.4
	1.93	0.71	149.0	0.027	22.5
	1.95	0.72	154.4	0.026	21.2
	1.88	0.70	152.9	0.030	25.1
Total					93.2
$[Pd_2\mathbf{L^1}_2\mathbf{L^{BDT}}_2]^{4+}$	2.26	0.84	156.9	0.014	10.2
	2.31	0.86	154.2	0.013	9.0
	2.41	0.89	162.2	0.011	6.9
	2.30	0.85	149.0	0.013	9.2
Total					35.4

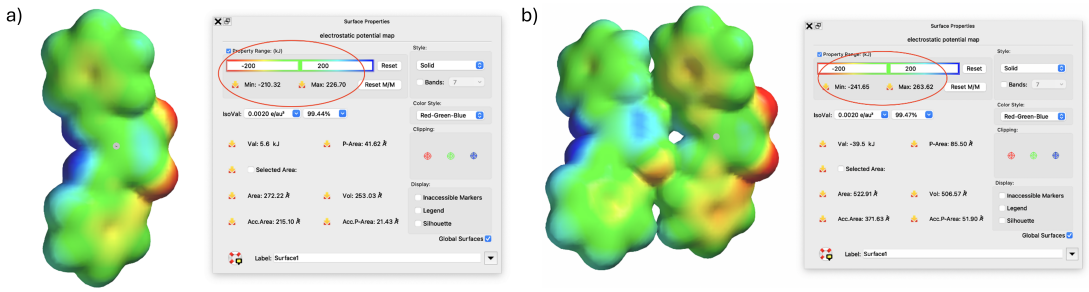

Figure 4.167. Comparison of electrostatic potential maps of a isolated squaramide-based ligand and its dimer. Electrostatic potential maps calculated by G. H. Clever.

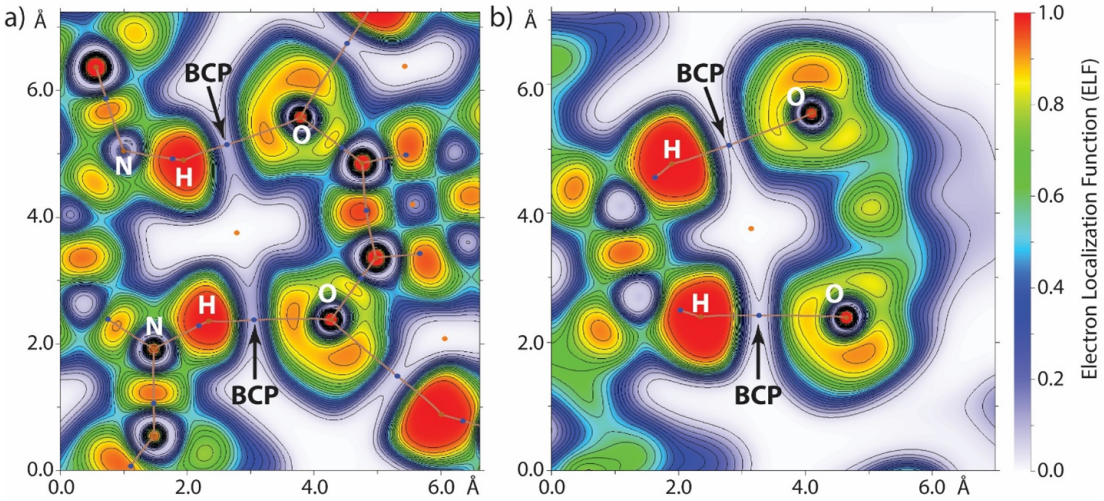

Figure 4.168. Counter map visualization of the electron localization function (ELF), and QTAIM critical points and bond paths for hydrogen bonding interactions involving squaramide fragment in the X-ray structures of cages: a) $[Pd_2\mathbf{L^1}_2\mathbf{L^2}_2]^{4+}$ and b) $[Pd_2\mathbf{L^{1peg}}_2\mathbf{L^{BDT}}_2]^{4+}$. Calculated by A. S. Mikherdov.

4.3.9 Heteroleptic Coordination Cage Formation with Ligand L^{1peg} and L^{BDT}

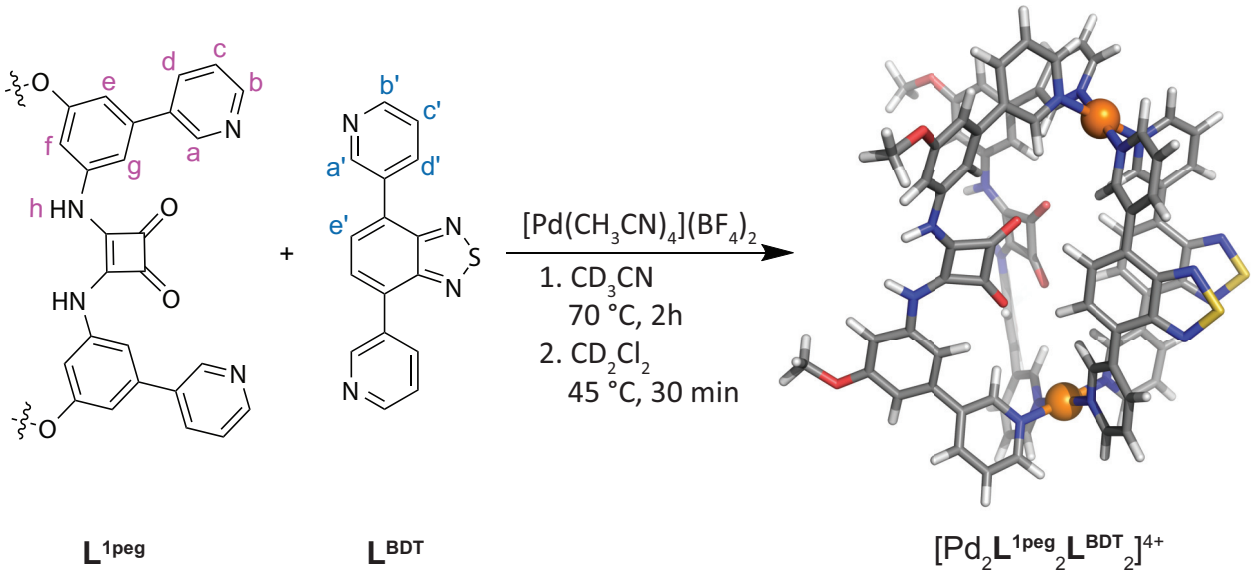

Figure 4.169. Heteroleptic coordination cage formation of $\mathbf{L^{1peg}}$ and $\mathbf{L^{BDT}}$ in CD_2Cl_2.

A mixture of 270 μL of $\mathbf{L^{1peg}}$ (0.76 mmol, 2.8 mM) and 270 μL of $\mathbf{L^{BDT}}$ (0.76 mmol, 2.8 mM) in CD_3CN has been prepared with 15 mM $[Pd(CH_3CN)_4](BF_4)_2$ (0.90 mmol, 60 μL) and heated for 2 h at 70 °C. Then, the solvent was removed *in vacuo* followed by addition of CD_2Cl_2 and heating at 45 °C for 30 min. The chemical shifting of the ^{1}H-NMR signals suggest that a coordination species has been formed. ^{1}H DOSY NMR confirmed that one species was obtained. Mass spectrometry also suggests that the coordination cage is formed. In Addition to that, r_H of $[Pd_2\mathbf{L^{1peg}}_2\mathbf{L^{BDT}}_2]^{4+}$ is 9,61 Å so it can be assumed that it is a $[Pd_2\mathbf{L}_2\mathbf{L'}_2]^{4+}$ species.

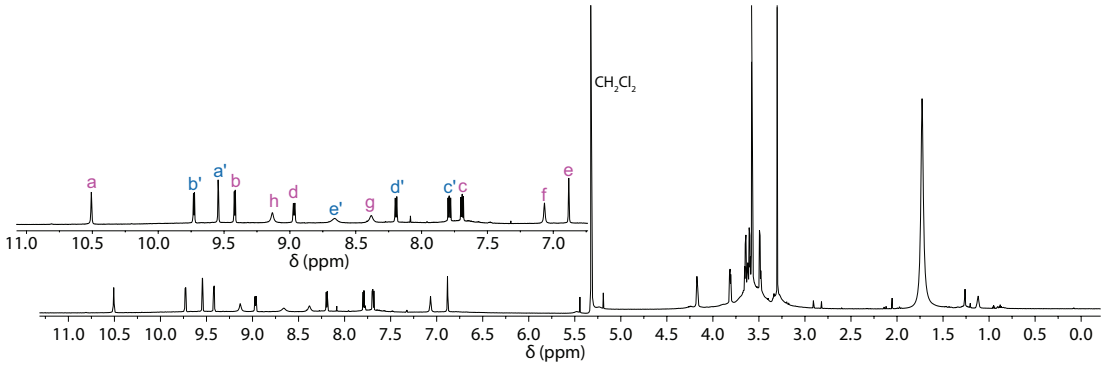

Figure 4.170. ^{1}H-NMR spectrum (500 MHz, 298 K, CD_2Cl_2) of $[Pd_2\mathbf{L^{1peg}}_2\mathbf{L^{BDT}}_2]^{4+}$. The aromatic region is shown zoomed in.

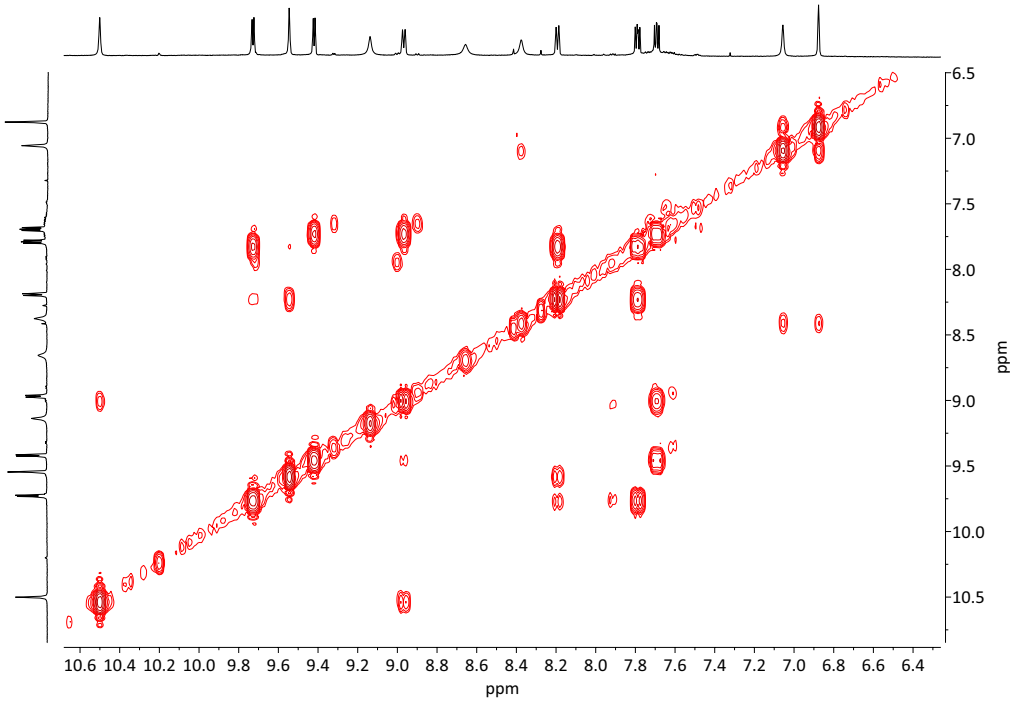

Figure 4.171. ^{1}H-^{1}H COSY spectrum (600 MHz, 298 K, CD_2Cl_2) of $[Pd_2\mathbf{L}^{\mathbf{1peg}}{}_2\mathbf{L}^{\mathbf{BDT}}{}_2]^{4+}$.

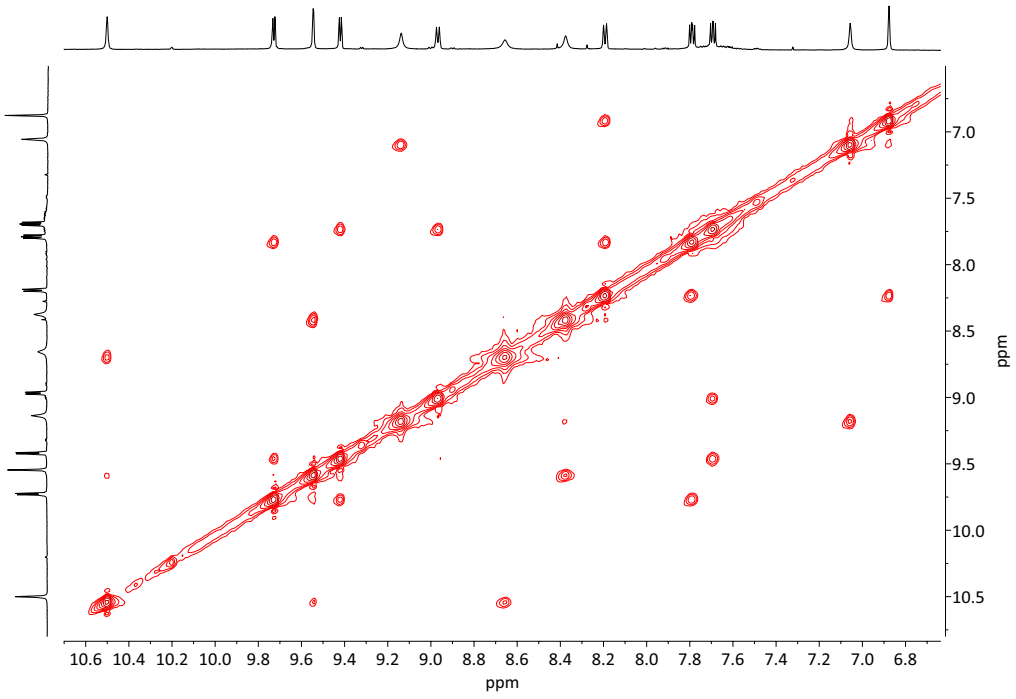

Figure 4.172. ^{1}H-^{1}H NOESY spectrum (600 MHz, 298 K, CD_2Cl_2) of $[Pd_2\mathbf{L}^{\mathbf{1peg}}{}_2\mathbf{L}^{\mathbf{BDT}}{}_2]^{4+}$.

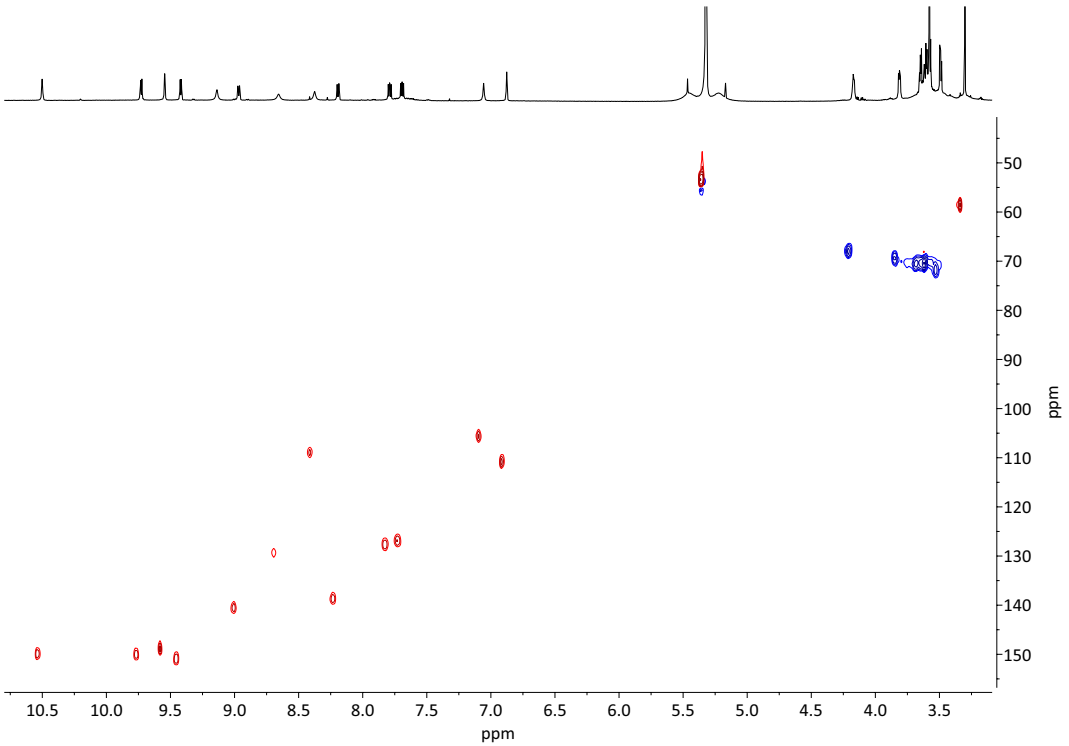

Figure 4.173. ^{1}H-^{13}C HSQC spectrum (600 MHz, 298 K, CD_2Cl_2) of $[Pd_2\mathbf{L}^{\mathbf{1peg}}{}_2\mathbf{L}^{\mathbf{BDT}}{}_2]^{4+}$.

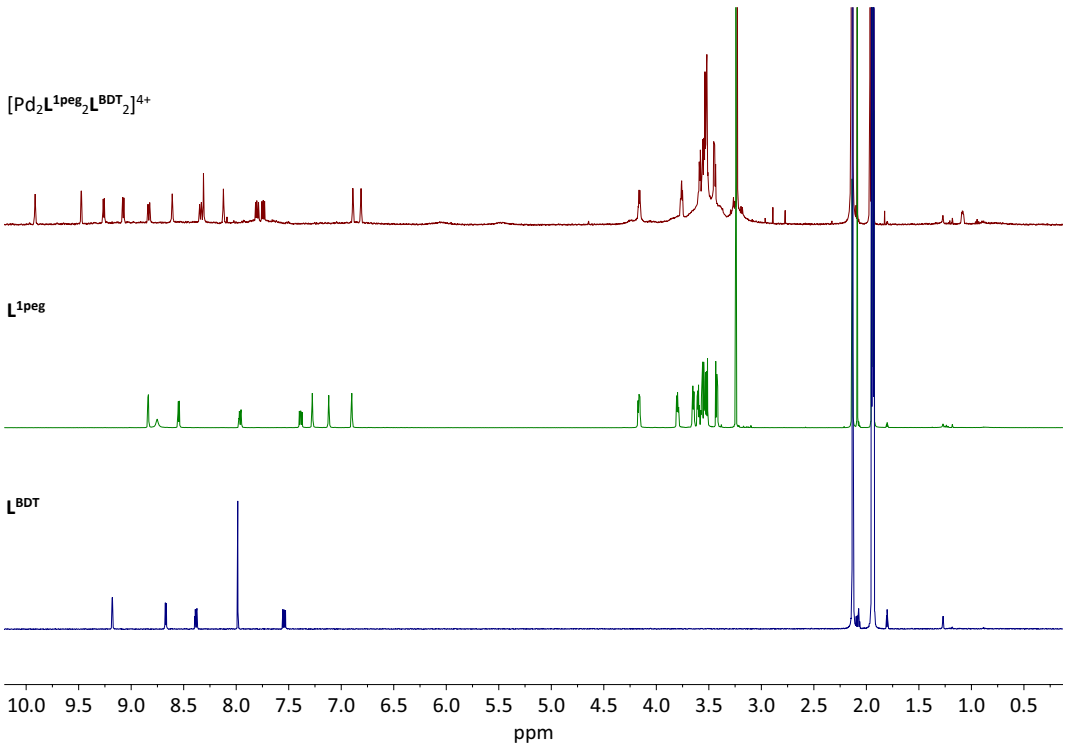

Figure 4.174. ^{1}H-NMR spectra (500 MHz, 298 K, CD_3CN) of coordination cage formation of $[Pd_2\mathbf{L}^{\mathbf{1peg}}{}_2\mathbf{L}^{\mathbf{BDT}}{}_2]^{4+}$.

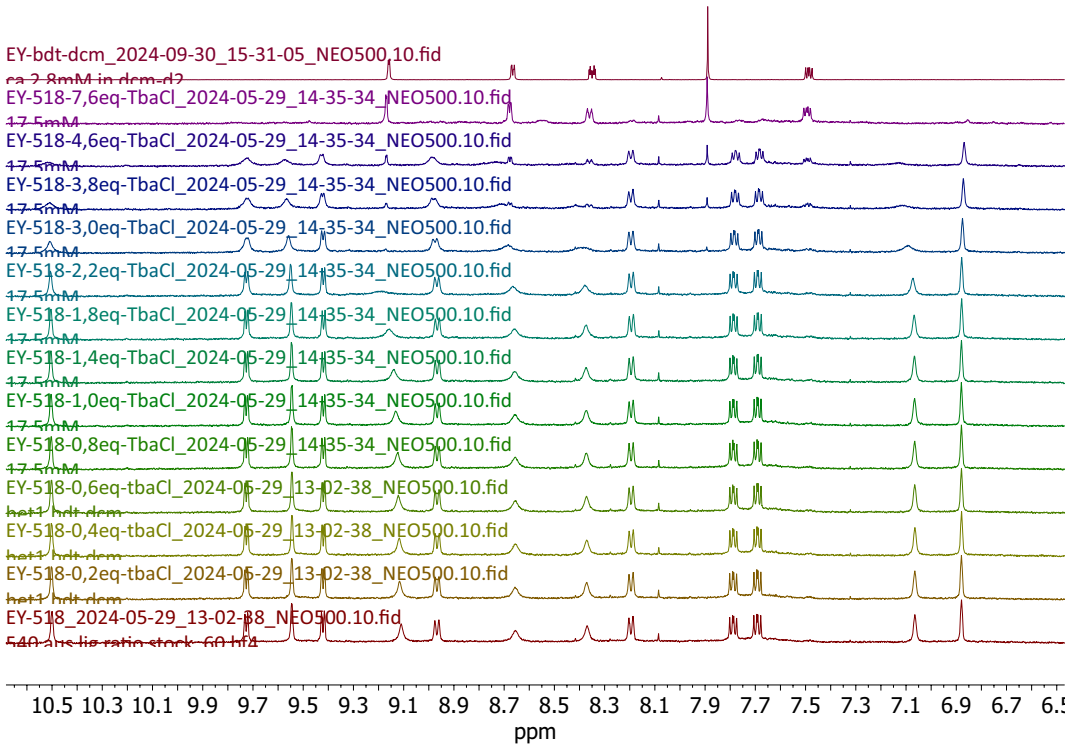

Figure 4.175. ^{1}H-NMR spectrum (500 MHz, 298 K, CD_2Cl_2) of titration of **TBACl** to $[Pd_2\mathbf{L}^{\mathbf{1peg}}{}_2\mathbf{L}^{\mathbf{BDT}}{}_2]^{4+}$.

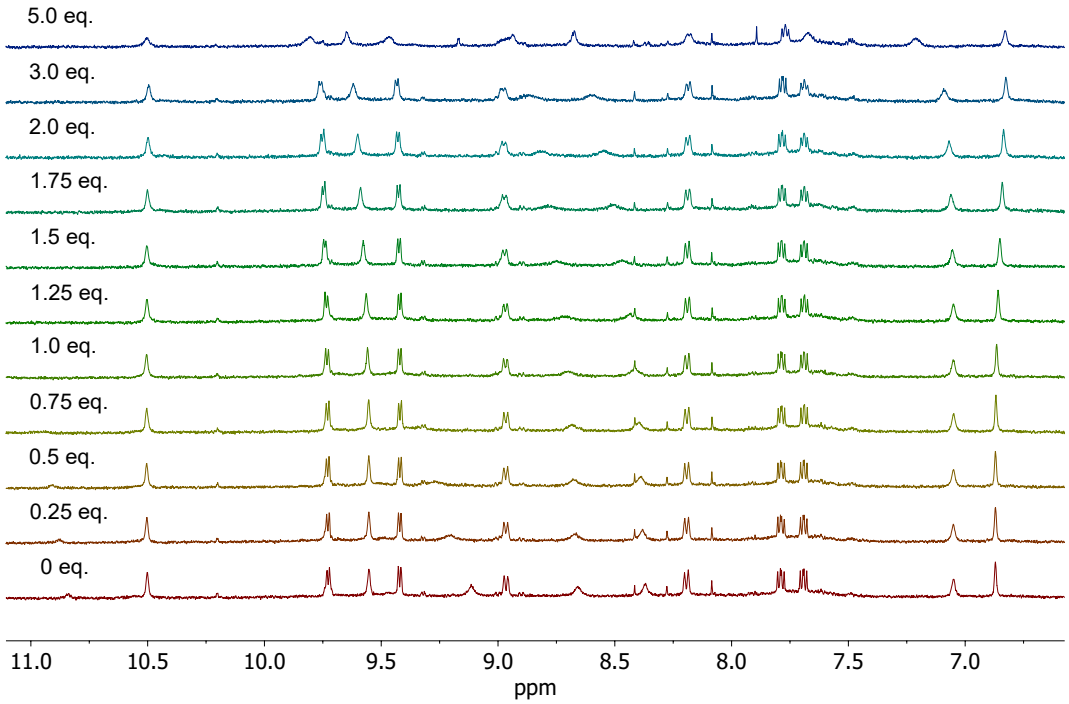

Figure 4.176. ^{1}H-NMR spectrum (500 MHz, 298 K, CD_2Cl_2) of titration of **DEP** to $[Pd_2\mathbf{L}^{\mathbf{1peg}}{}_2\mathbf{L}^{\mathbf{BDT}}{}_2]^{4+}$.

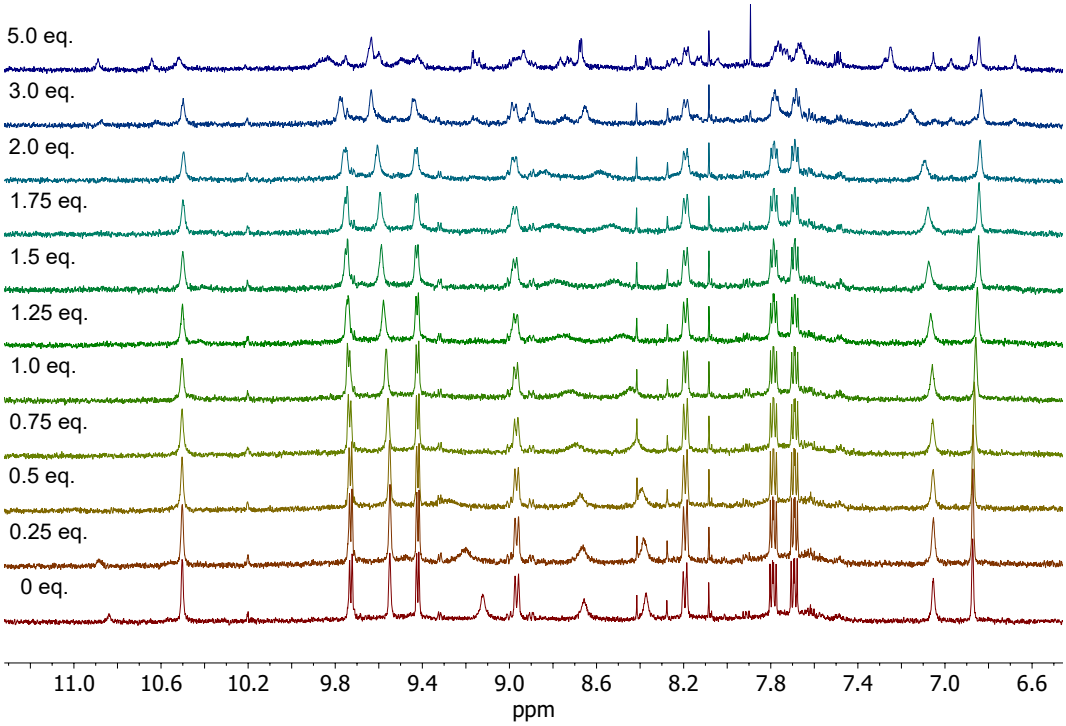

Figure 4.177. ^{1}H-NMR spectrum (500 MHz, 298 K, CD_2Cl_2) of titration of **DBuP** to $[Pd_2\mathbf{L}^{\mathbf{1peg}}{}_2\mathbf{L}^{\mathbf{BDT}}{}_2]^{4+}$.

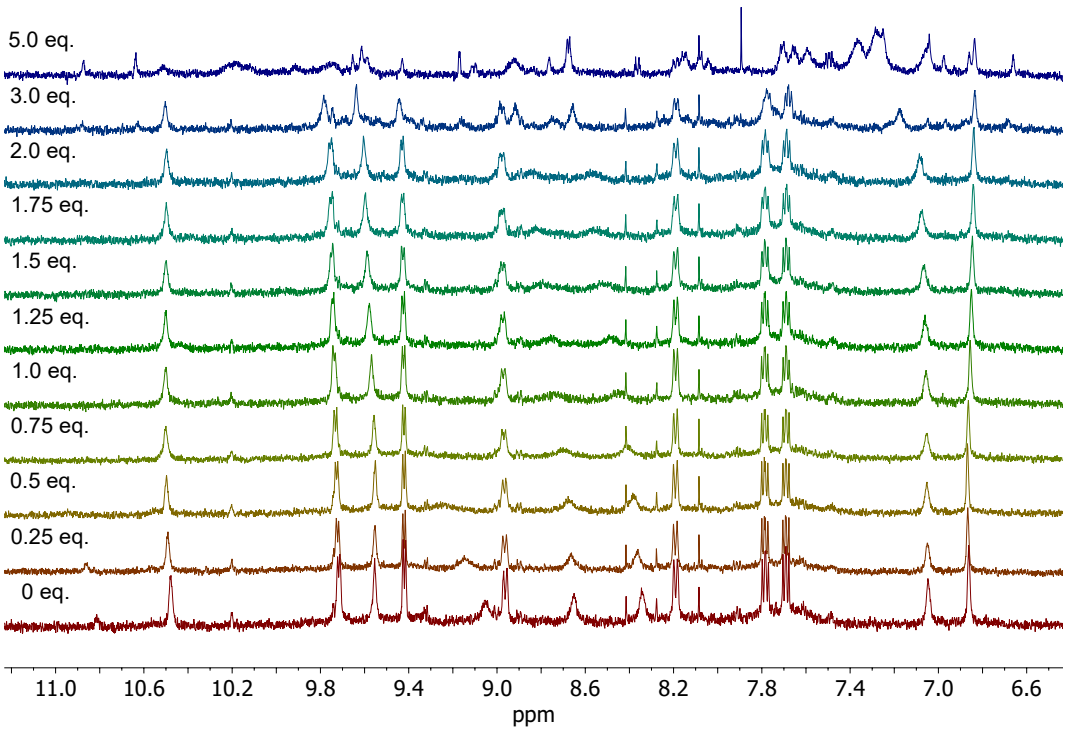

Figure 4.178. ^{1}H-NMR spectrum (500 MHz, 298 K, CD_2Cl_2) of titration of **DBnP** to $[Pd_2\mathbf{L}^{\mathbf{1peg}}{}_2\mathbf{L}^{\mathbf{BDT}}{}_2]^{4+}$.

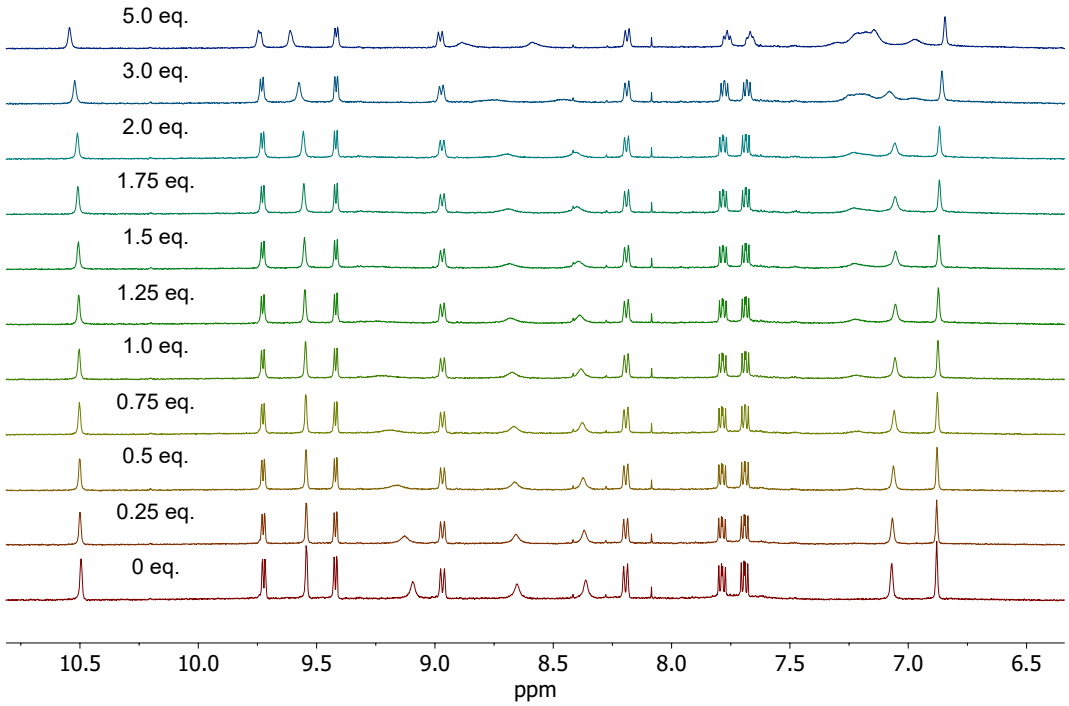

Figure 4.179. ^{1}H-NMR spectrum (500 MHz, 298 K, CD_2Cl_2) of titration of **DPP** to $[Pd_2\mathbf{L}^{\mathbf{1peg}}{}_2\mathbf{L}^{\mathbf{BDT}}{}_2]^{4+}$.

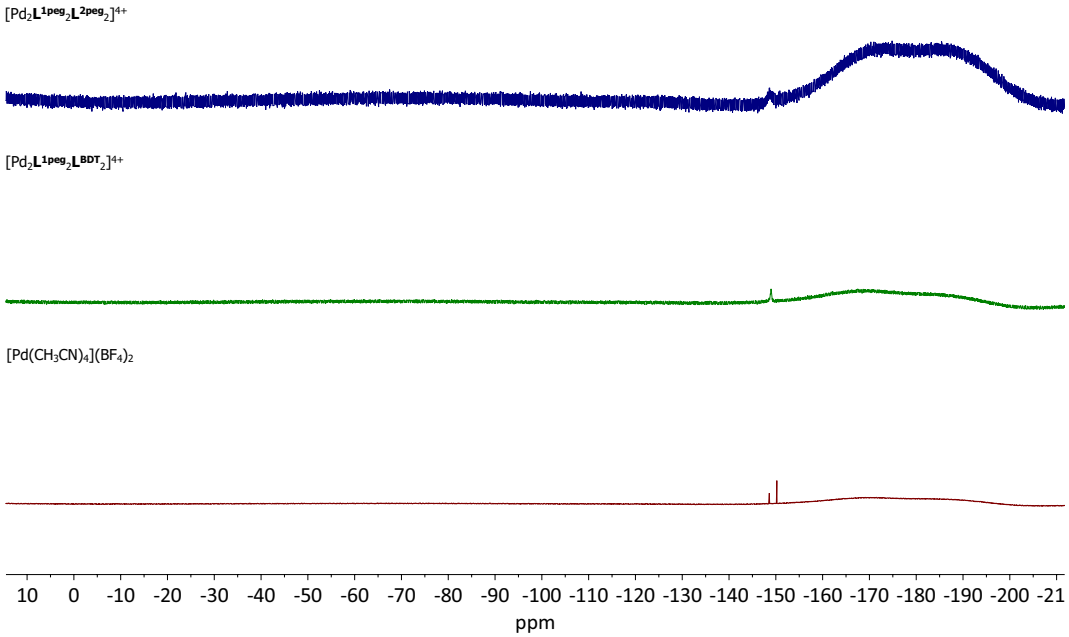

Figure 4.180. ^{19}F-NMR spectrum (400 MHz, 298 K, CD_2Cl_2) of $[Pd_2\mathbf{L}^{\mathbf{1peg}}{}_2\mathbf{L}^{\mathbf{2peg}}{}_2]^{4+}$, $[Pd_2\mathbf{L}^{\mathbf{1peg}}{}_2\mathbf{L}^{\mathbf{BDT}}{}_2]^{4+}$ and $[Pd(CH_3CN)_4](BF_4)_2$.

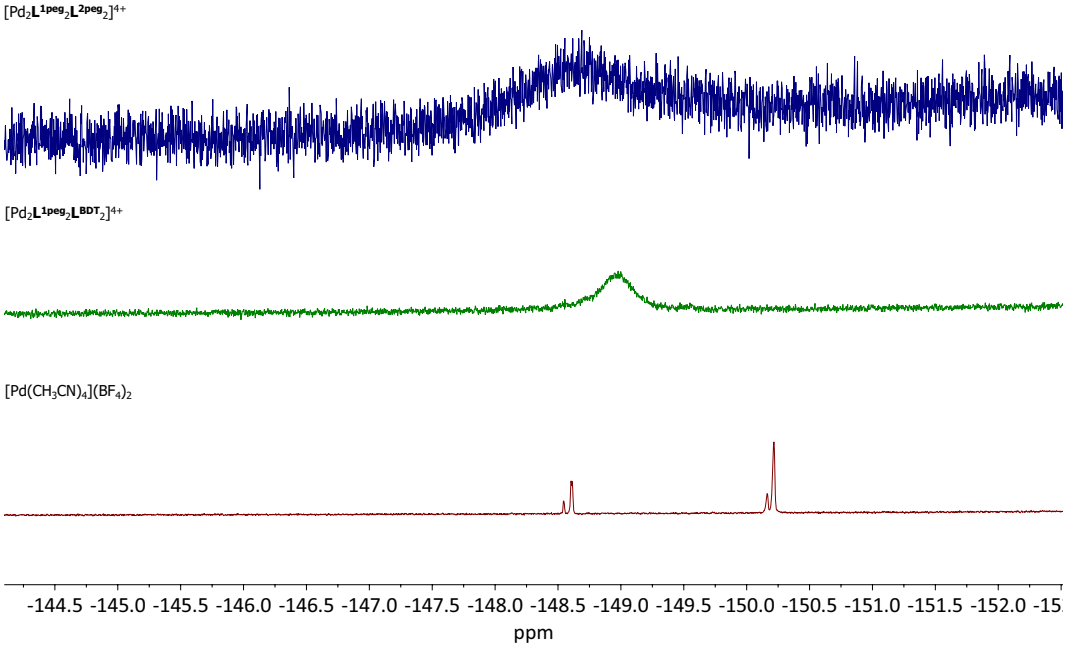

Figure 4.181. Zoomed in ^{19}F-NMR spectrum (400 MHz, 298 K, CD_2Cl_2) of $[Pd_2\mathbf{L^{1peg}}_2\mathbf{L^{2peg}}_2]^{4+}$, $[Pd_2\mathbf{L^{1peg}}_2\mathbf{L^{BDT}}_2]^{4+}$ and $[Pd(CH_3CN)_4](BF_4)_2$.

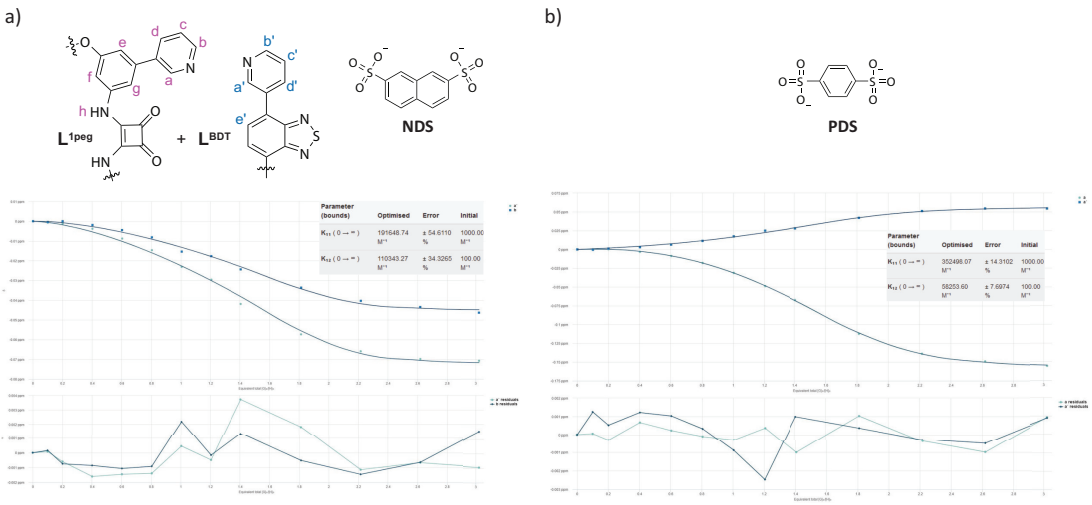

Figure 4.182. Illustration of binding analysis result obtained by BindFit (Fitter: 1:2) titration of **NDS** and **PDS** to $[Pd_2\mathbf{L^{1peg}}_2\mathbf{L^{BDT}}_2]^{4+}$. TBA as counter ions for **NDS** and **PDS**.

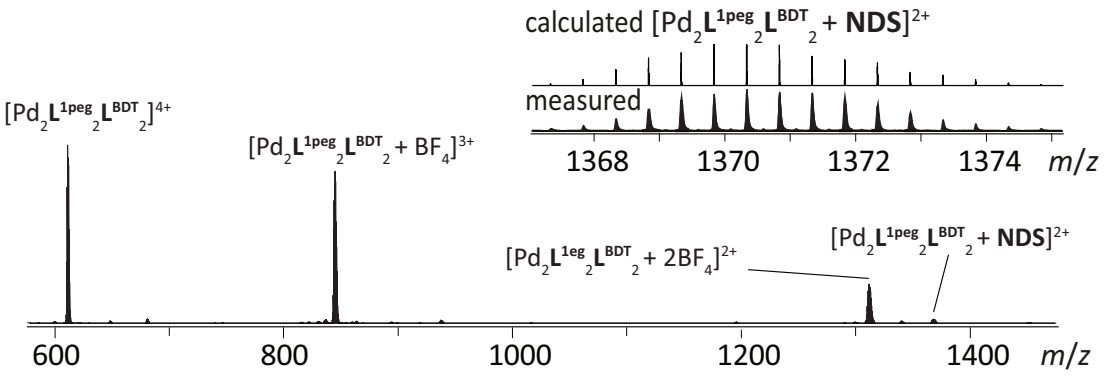

Figure 4.183. Illustration ESI-MS of $[Pd_2\mathbf{L^{1peg}}_2\mathbf{L^{BDT}}_2]^{4+}$ and **NDS**.

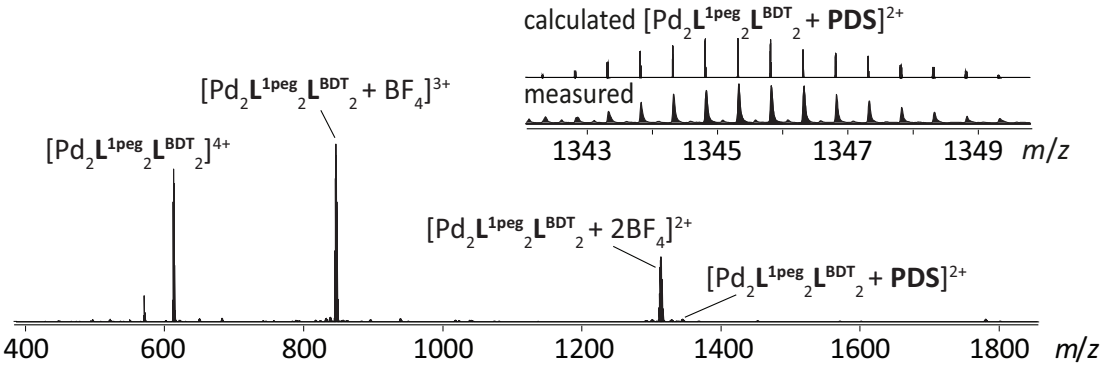

Figure 4.184. Illustration ESI-MS of $[Pd_2\mathbf{L^{1peg}}_2\mathbf{L^{BDT}}_2]^{4+}$ and **NDS**.

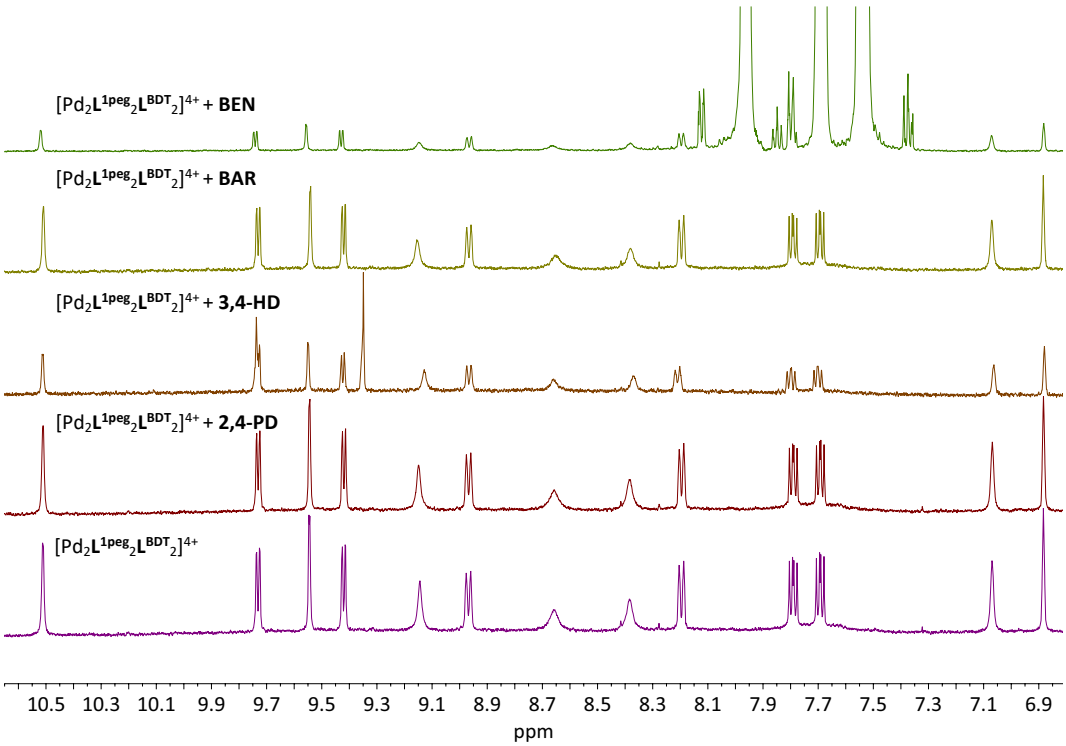

Figure 4.185. ^{1}H-NMR spectrum (500 MHz, 298 K, CD_2Cl_2) screening of neutral molecules to $[Pd_2\mathbf{L^{1peg}}_2\mathbf{L^{BDT}}_2]^{4+}$ by excess addition.

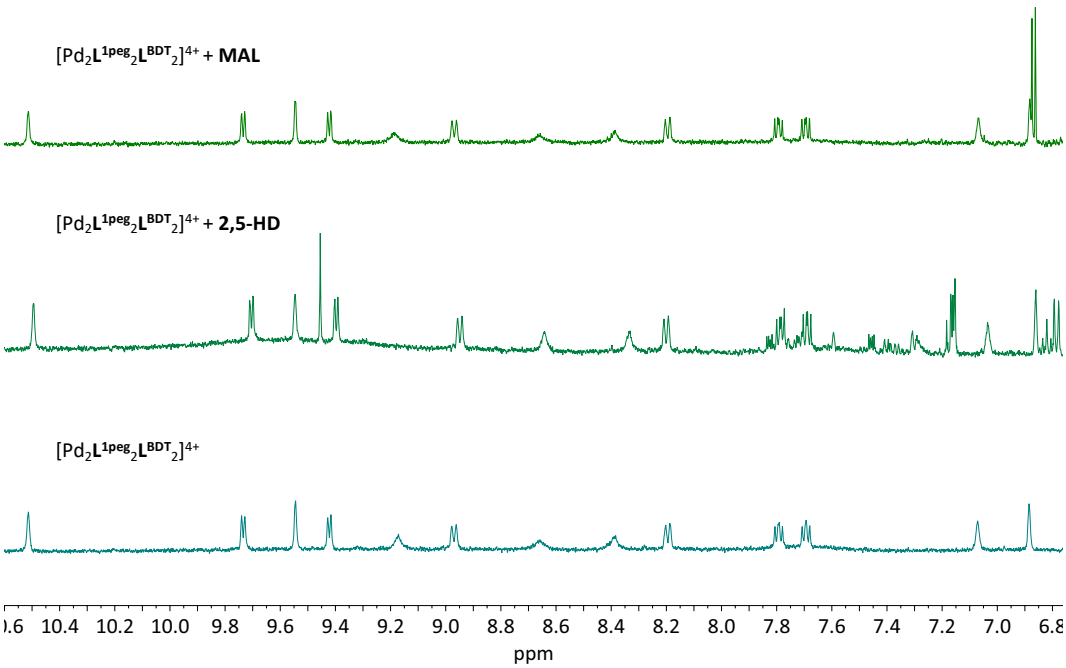

Figure 4.186. ^{1}H-NMR spectrum (500 MHz, 298 K, CD_2Cl_2) screening of neutral molecules to $[Pd_2\mathbf{L^{1peg}}_2\mathbf{L^{BDT}}_2]^{4+}$ by excess addition.

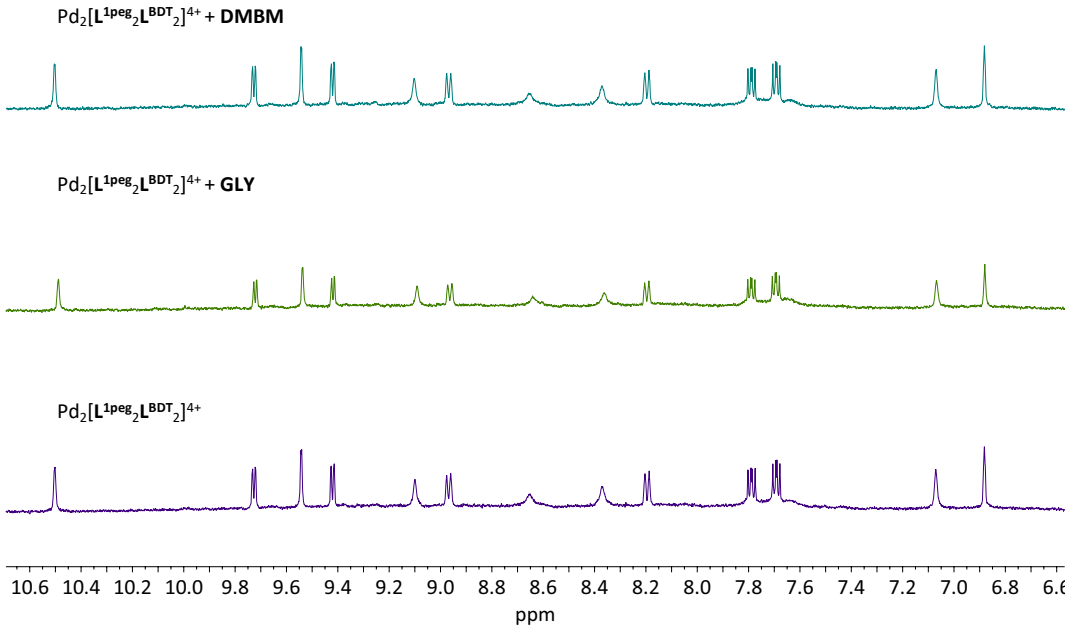

Figure 4.187. ^{1}H-NMR spectrum (500 MHz, 298 K, CD_2Cl_2) screening of neutral molecules to $[Pd_2\mathbf{L}^{\mathbf{1peg}}{}_2\mathbf{L}^{\mathbf{BDT}}{}_2]^{4+}$ by excess addition.

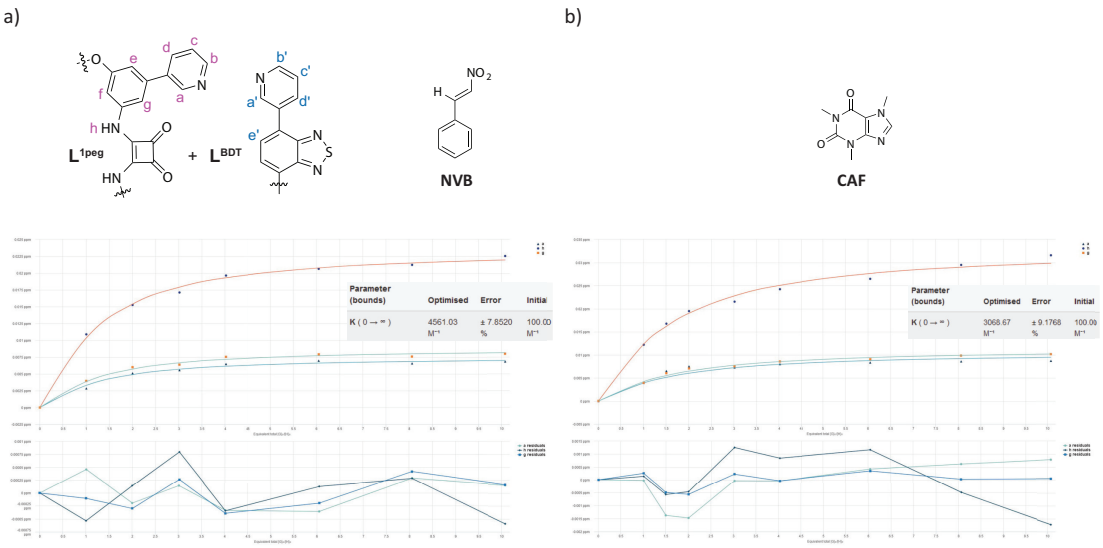

Figure 4.188. Illustration of binding analysis result obtained by BindFit (Fitter: 1:1) titration of **NVB** and **CAF** to $[Pd_2\mathbf{L}^{\mathbf{1peg}}{}_2\mathbf{L}^{\mathbf{BDT}}{}_2]^{4+}$.

Table 4.4: Obtained binding constants K_a for 0.3 mM $[Pd_2\mathbf{L}^{\mathbf{1peg}}{}_2\mathbf{L}^{\mathbf{BDT}}{}_2]^{4+}$ in CD_2Cl_2.

K_a (**CAF**)	K_a (**NVB**)
$3157 \pm 9\%$	$3646\ \mathrm{M}^{-1}$ 13%
$4861\ \mathrm{M}^{-1}$ 9%	$4428\ \mathrm{M}^{-1}$ 14%

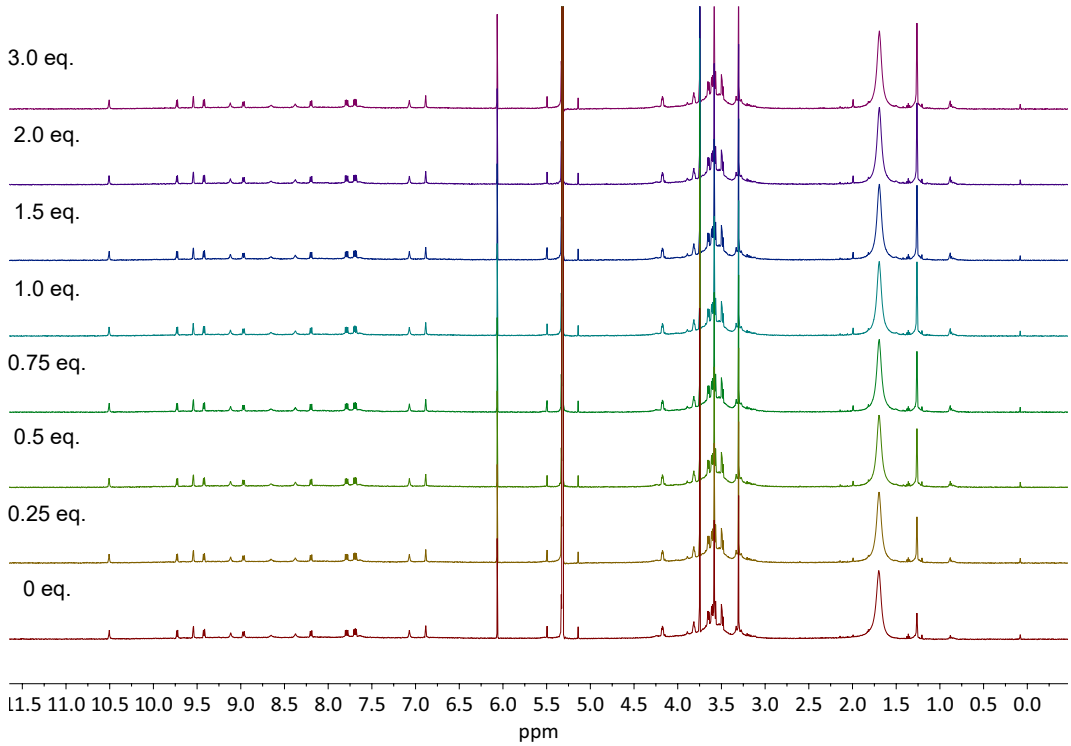

Figure 4.189. ^{1}H-NMR spectrum (500 MHz, 298 K, CD_2Cl_2) adding of CD_2Cl_2 to $[Pd_2\mathbf{L}^{\mathbf{1peg}}{}_2\mathbf{L}^{\mathbf{BDT}}{}_2]^{4+}$.

Crystal data

Structure Tables

	$[Pd_2\mathbf{L^1}_2\mathbf{L^2}_2]^{4+}$	$\mathbf{L^2}$	$[Pd_2\mathbf{L^{1peg}}_2\mathbf{L^{BDT}}_2]^{4+}$
CCDC number			
Empirical formula	$C_{83}H_{65}B_4F_{16}N_{17}O_{10}Pd_2$	$C_{16}H_{16}N_4O_3S$	$C_{106}H_{105}B_3F_{12}N_{17}O_{18}Pd_2S_2$
Formula weight	2020.56	344.39	2442.41
Temperature [K]	100(2)	100(2)	100(2)
Crystal system	triclinic	triclinic	triclinic
Space group (number)	$P\overline{1}$ (2)	$P\overline{1}$ (2)	$P\overline{1}$ (2)
a [Å]	15.662(12)	6.9584(18)	17.990(4)
b [Å]	19.490(13)	10.319(2)	20.572(6)
c [Å]	20.185(13)	11.277(3)	20.692(5)
α [°]	67.529(12)	97.852(8)	106.495(8)
β [°]	76.41(2)	93.441(10)	110.64(9)
γ [°]	72.121(17)	99.592(10)	93.687(13)
Volume [Å^3]	5370(7)	788.1(3)	6755(5)
Z	2	2	2
ρ_{calc} [gcm^{-3}]	1.250	1.451	1.201
μ [mm^{-1}]	0.741	0.229	1.010
F(000)	2036	360	2502
Crystal size [mm^3]	0.040×0.010×0.005	0.260×0.050×0.015	0.040×0.030×0.005
Crystal colour	colourless	colourless	colourless
Crystal shape	plate	needle	plate
Radiation	synchrotron (λ=0.88561 Å)	MoK_α (λ=0.71073 Å)	synchrotron (λ=1.03321 Å)
2Θ range [°]	2.90 to 47.42 (1.10 Å)	5.85 to 57.40 (0.74 Å)	3.05 to 55.36 (1.11 Å)
Index ranges	-14 ≤ h ≤ 14	-9 ≤ h ≤ 9	-15 ≤ h ≤ 15
	-17 ≤ k ≤ 17	-11 ≤ k ≤ 13	-16 ≤ k ≤ 16
	-18 ≤ l ≤ 18	-15 ≤ l ≤ 15	-18 ≤ l ≤ 18
Reflections collected	26985	19322	25776
Independent reflections	7439	4079	7099
	R_{int} = 0.0963	R_{int} = 0.1632	R_{int} = 0.0563
	R_{sigma} = 0.0856	R_{sigma} = 0.1363	R_{sigma} = 0.0498
Completeness	88.4 %	99.8 %	68.9 %
Data / Restraints / Parameters	7439/2286/1235	4079/0/219	7099/3289/1600
Goodness-of-fit on F^2	1.058	1.066	1.301
Final *R* indexes	R_1 = 0.0956	R_1 = 0.0915	R_1 = 0.1015
[I≥2σ(I)]	wR_2 = 0.2663	wR_2 = 0.2106	wR_2 = 0.2799
Final *R* indexes	R_1 = 0.1287	R_1 = 0.1253	R_1 = 0.1202
[all data]	wR_2 = 0.2943	wR_2 = 0.2299	wR_2 = 0.2984
Largest peak/hole [eÅ^{-3}]	1.31/-0.50	0.56/-0.94	0.87/-0.46
Flack X parameter			
Extinction coefficient			

Figure 4.190. Crystal data and structure refinement for $\mathbf{L^2}$, $[Pd_2\mathbf{L^1}_2\mathbf{L^2}_2]^{4+}$ and $[Pd_2\mathbf{L^{1peg}}_2\mathbf{L^{BDT}}_2]^{4+}$.

4.3.10 Homoleptic Coordination Cage Formation of Ligand L^{283}

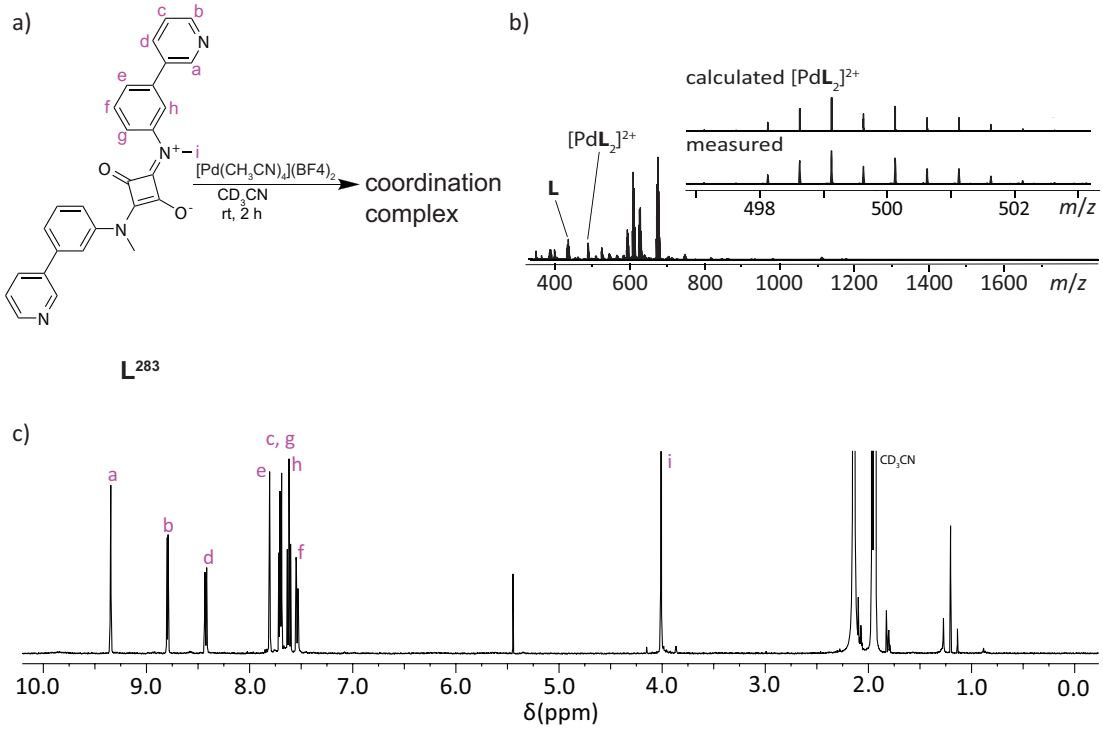

Figure 4.191. a) Homoleptic cage formation of $\mathbf{L^{283}}$, b) ESI-MS of cage formation experiment of $\mathbf{L^{283}}$ and c) ^{1}H-NMR spectrum (500 MHz, 298 K, CD_3CN) spectrum of the cage formation of $\mathbf{L^{283}}$ at rt after 2 h.

The homoleptic cage formation with $[Pd(CH_3CN)_4](BF_4)_2$ was performed analogous to the previous homoleptic cages.

Then ESI-MS was meassured which showed suggests that a mononuclear assembly $[Pd\mathbf{L^{283}}_2]^{2+}$ was observed.

The main signals in the ESI-MS could be not determined. Due to the palladium pattern of the signals it is possible to assume that it is a mononuclear assembly of decomposed $\mathbf{L^{283}}$.

4.3.11 Homoleptic Coordination Cage Formation of Ligand L^4

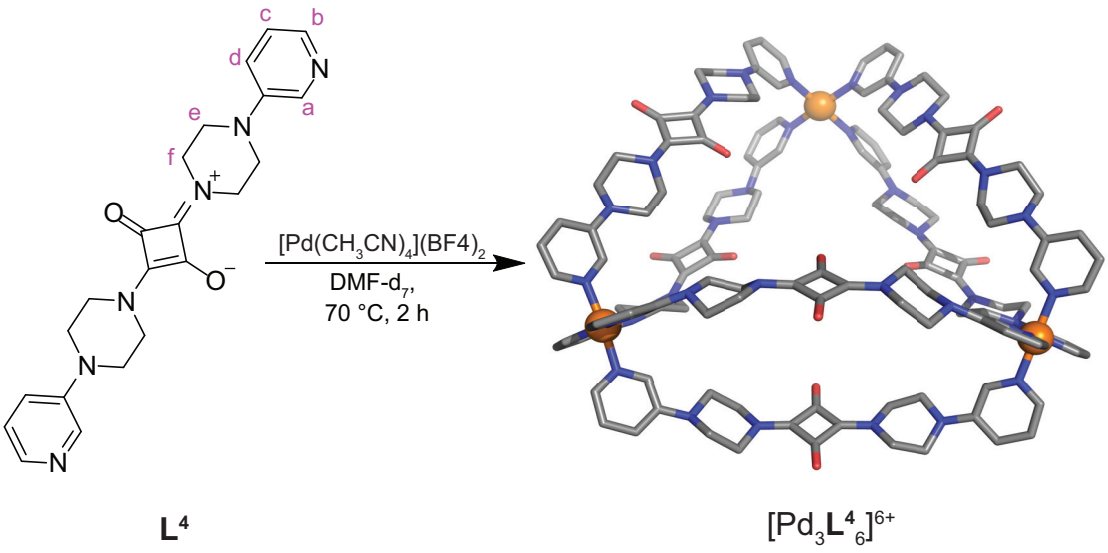

Figure 4.192. Homoleptic cage formation of$\mathbf{L^4}$ in DMF−d_7. Primarily crystal structure.

540 μL of$\mathbf{L^4}$ (1.51 mmol, 2.8 mM) in DMF-d_7 has been prepared with 15 mM $[Pd(CH_3CN)_4](BF_4)_2$ (0.98 mmol, 65 μL) heated at 70 °C for 2 h. The chemical shifting of the ^{1}H-NMR signals suggest that a homoleptic species has been formed. ^{1}H DOSY NMR confirmed that one species was obtained. Mass spectrometry also suggests that the homoleptic species is formed. In addition to that, r_H of $[Pd_3\mathbf{L^4}_6]^{6+}$ is 13,5 Å so it can be assumed that it is a $[Pd_3\mathbf{L}_6]^{6+}$ species.

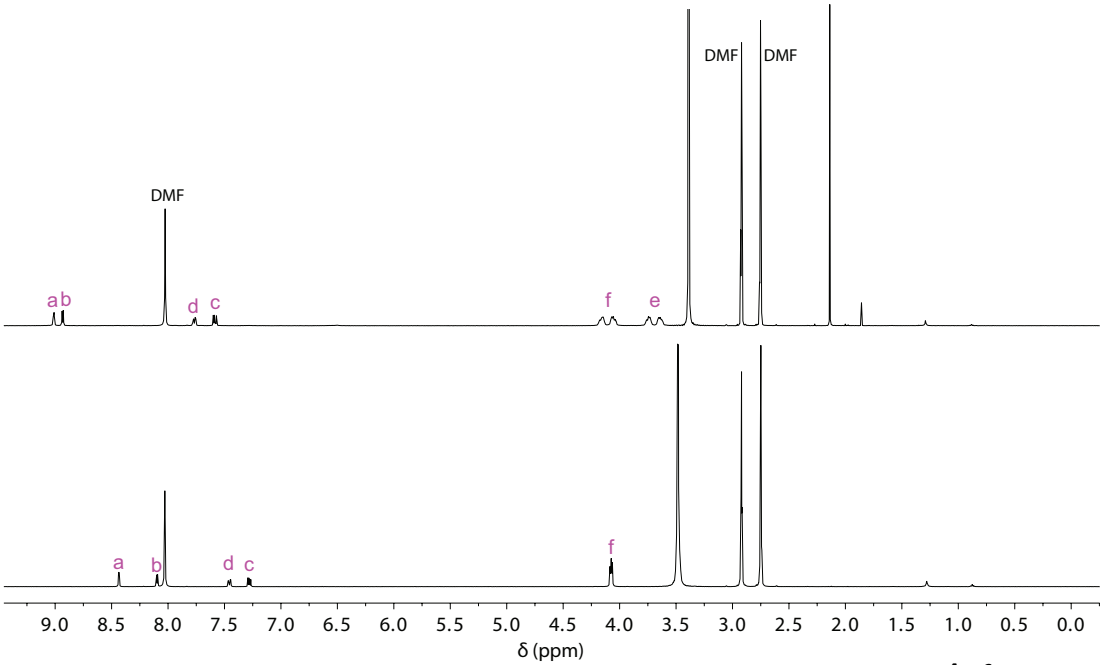

Figure 4.193. ^{1}H-NMR spectrum (500 MHz, 298 K, DMF-d_7) of $[Pd_3\mathbf{L^4}_6]^{6+}$.

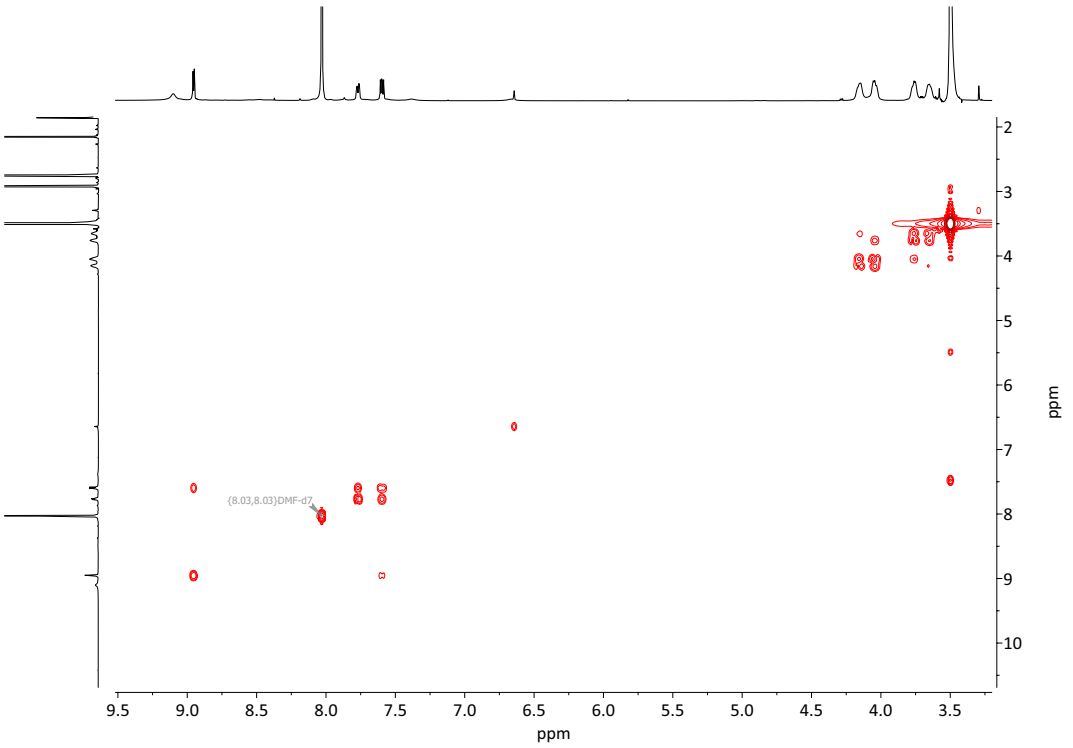

Figure 4.194. ^{1}H-^{1}H COSY spectrum (600 MHz, 298 K, DMF-d_7) of spectrum of $[Pd_3\mathbf{L^4}_6]^{6+}$.

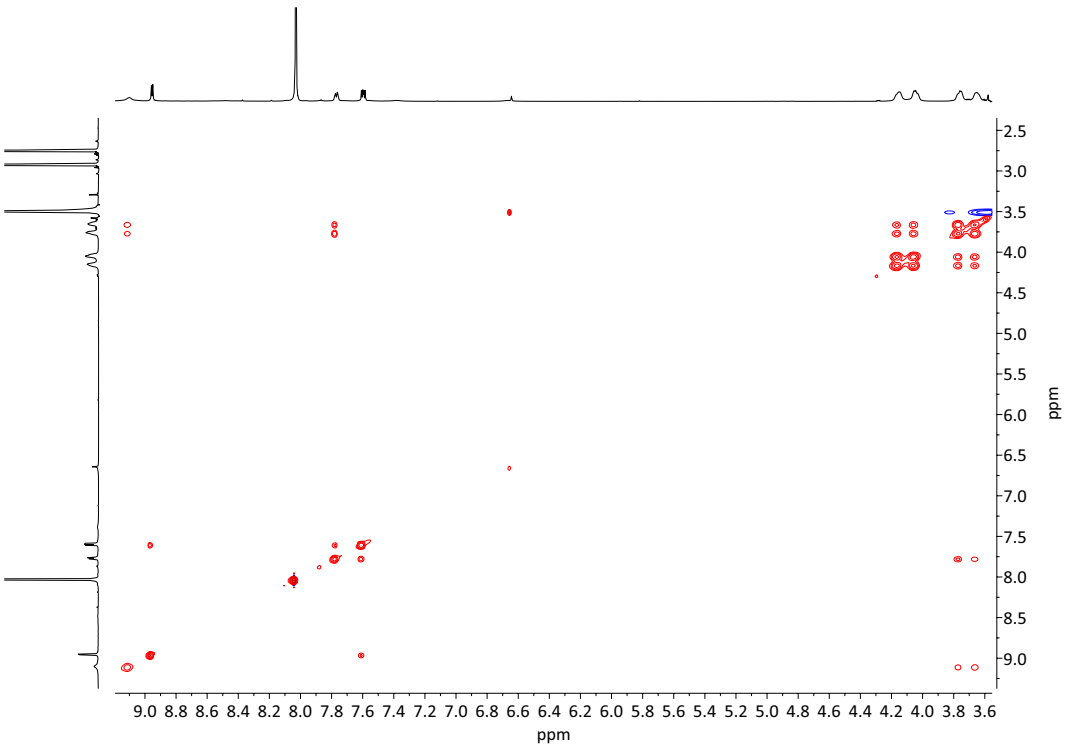

Figure 4.195. ^{1}H-^{1}H NOESY spectrum (600 MHz, 298 K, DMF-d_7) of $[Pd_3\mathbf{L^4}_6]^{6+}$.

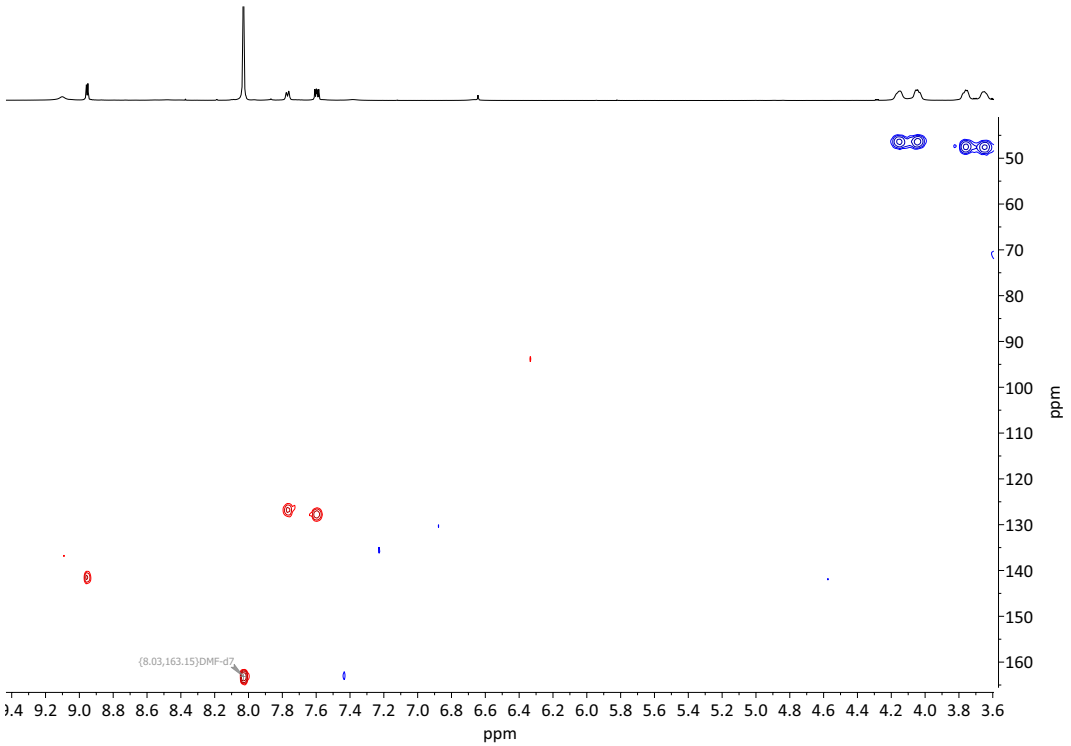

Figure 4.196. ^{1}H-^{13}C HSQC spectrum (600 MHz, 298 K, DMF-d_7) of $[Pd_3\mathbf{L^4}_6]^{6+}$.

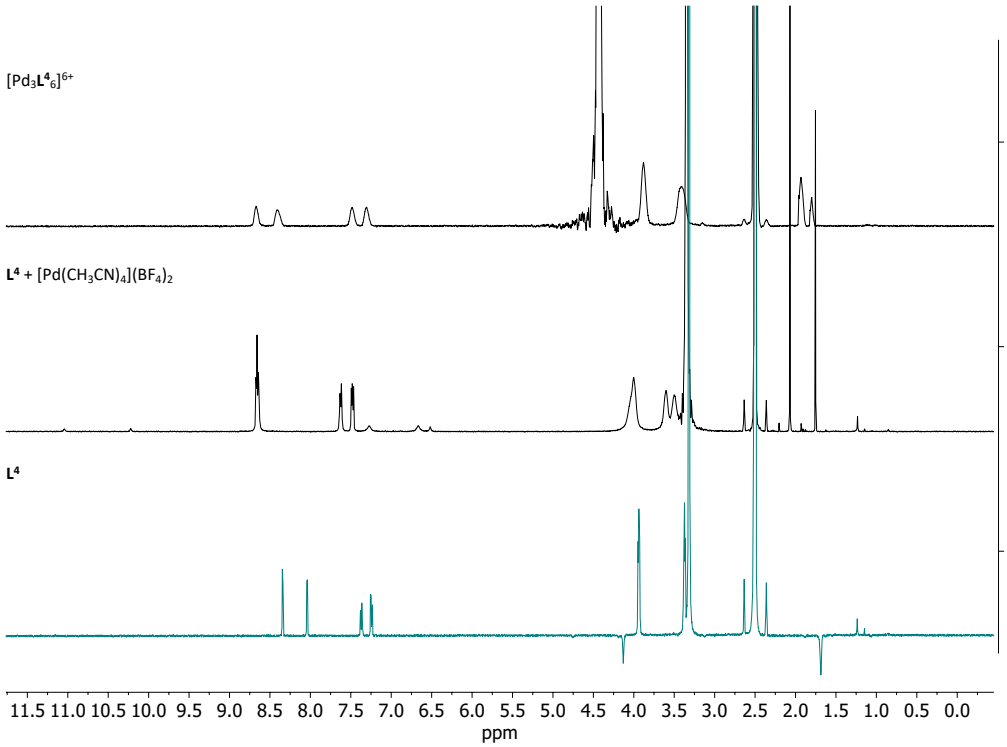

Figure 4.197. ^{1}H-NMR spectra (500 MHz, 298 K) of $[Pd_3\mathbf{L}_6]^{6+}$ in DMSO-d_6 and D_2O:DMSO-d_6 (1:1) mixture stacked with the spectrum of $\mathbf{L^4}$ in DMSO-d_6.

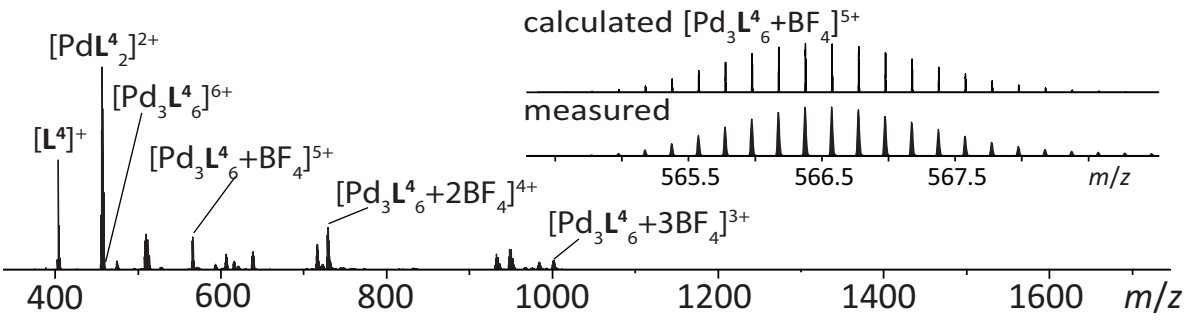

Figure 4.198. Illustration of ESI-MS of cage formation experiment of $\mathbf{L^4}$ in DMSO$-d_6$:D_2O (1:1) mixture.

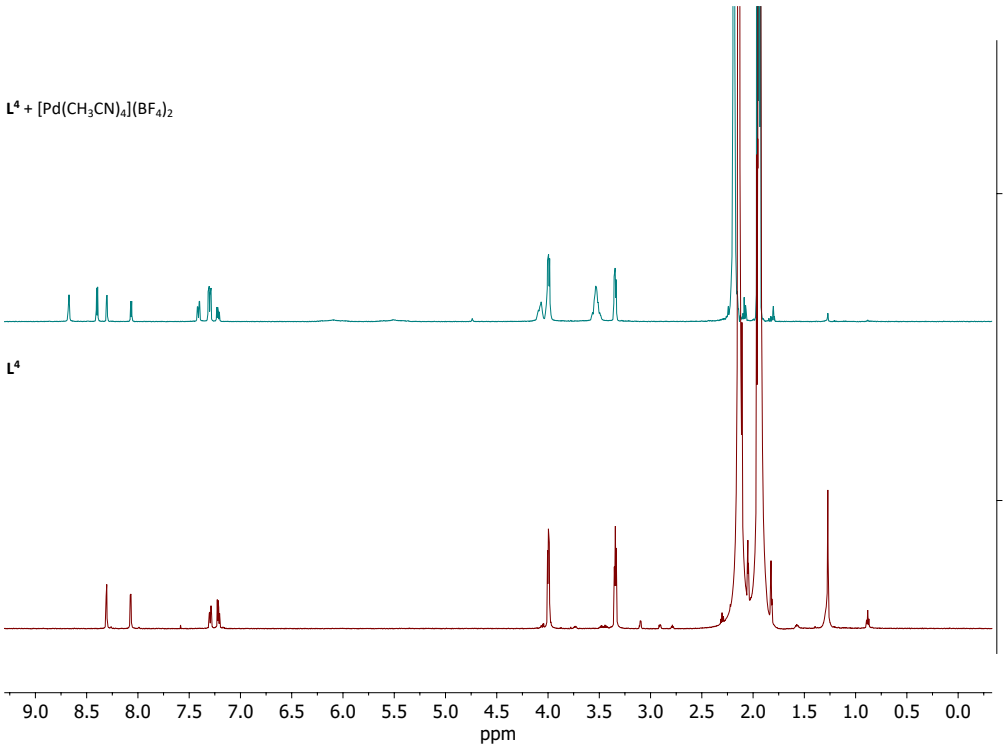

Figure 4.199. ^{1}H-NMR spectrum (500 MHz, 298 K, CD_3CN) of the cage formation experiment of $\mathbf{L^4}$. Cage formation of $\mathbf{L^4}$ in CD_3CN was not observed by ESI-MS.

HG Complex Studies

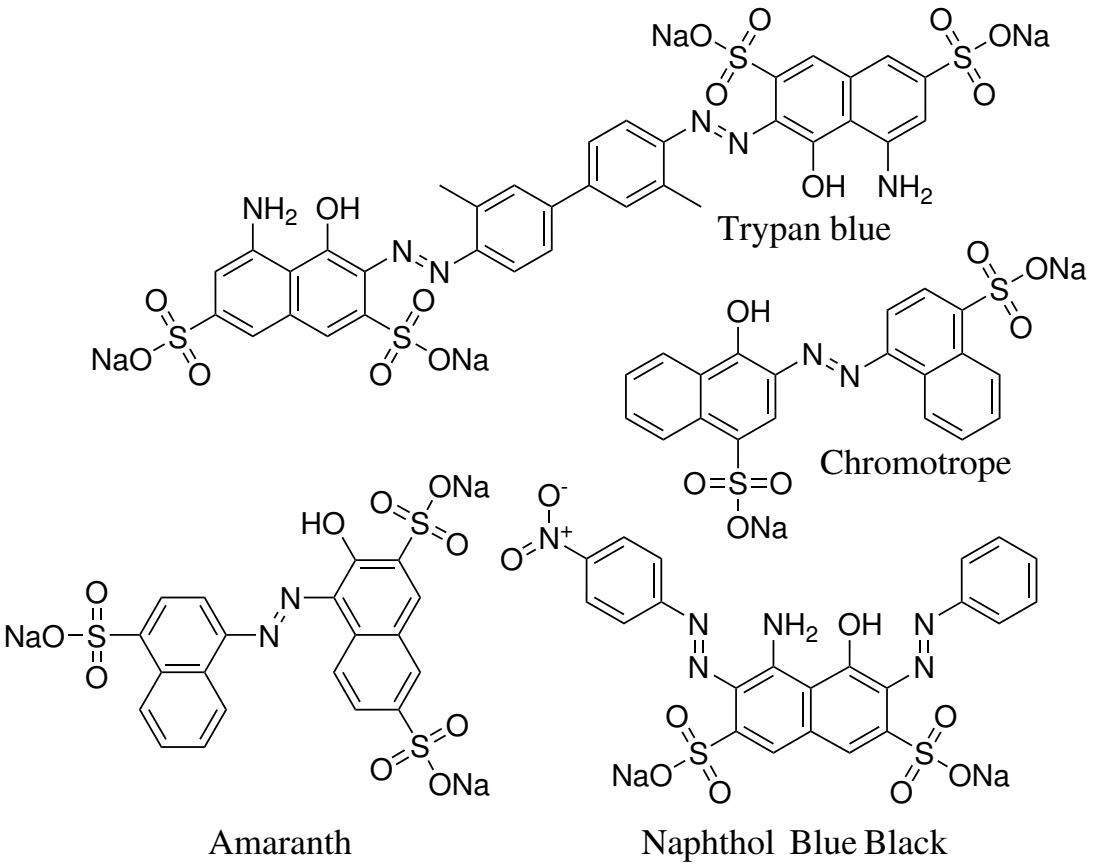

Figure 4.200. Illustration of different azo-dyes, which were screened by ^{1}H-NMR titration to $[Pd_3\mathbf{L^4}_6]^{6+}$.

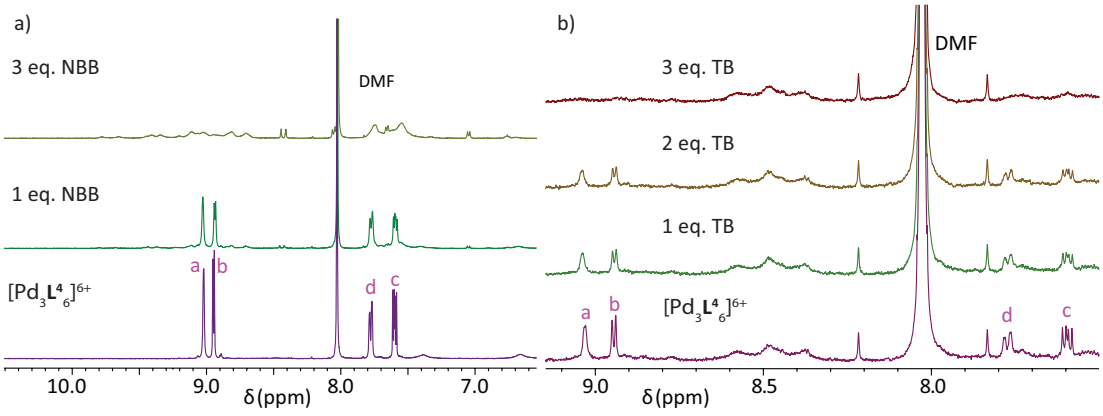

Figure 4.201. Illustration of ^{1}H-NMR spectrum (500 MHz, 298 K, DMF-$d7$) titration of a) naphthol blue black and b) trypan blue to $[Pd_3\mathbf{L^4}_6]^{6+}$.

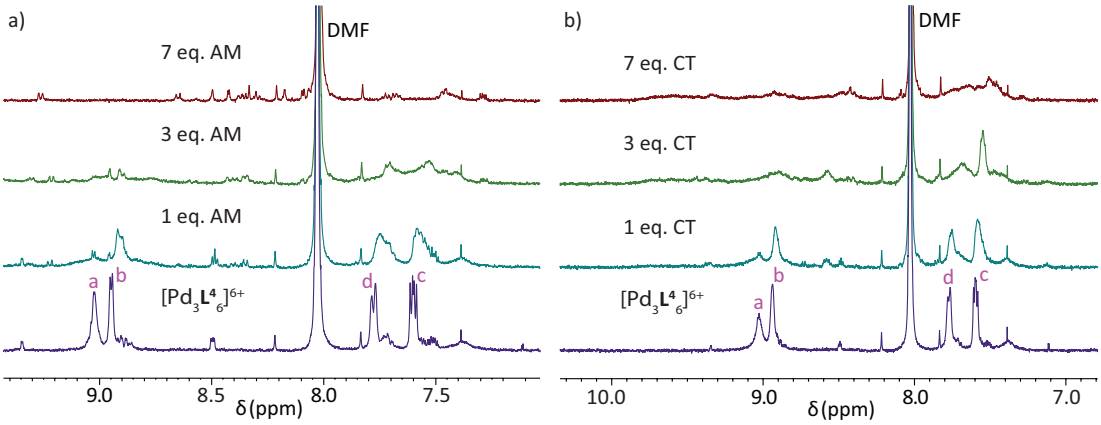

Figure 4.202. Illustration of ^{1}H-NMR spectrum (500 MHz, 298 K, DMF-$d7$) titration of a) amaranth and b) chromotrope to $[Pd_3\mathbf{L^4}_6]^{6+}$.

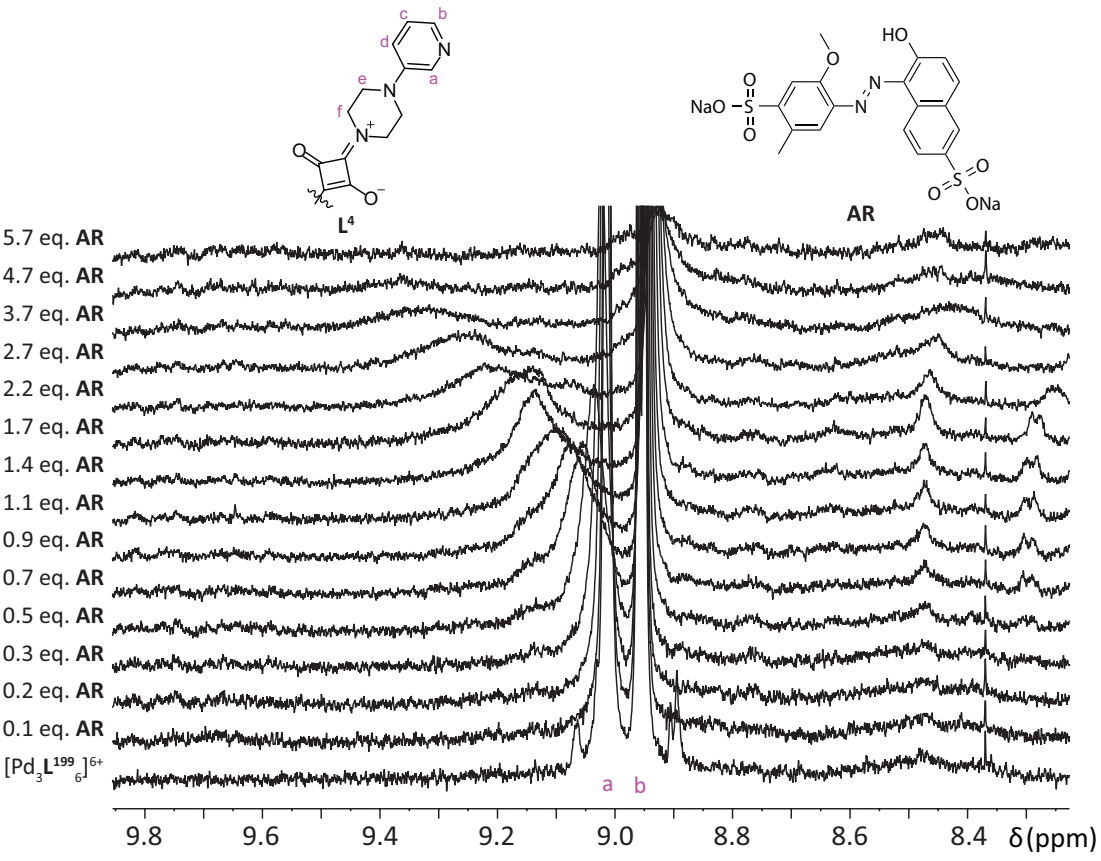

Figure 4.203. Illustration of ^{1}H-NMR titration of allura red (**AR**) to 0.63 mM $[Pd_3\mathbf{L^4}_6]^{6+}$ in DMF-d_7. Shift and broadening of proton a is shown enlarged. Broad signals observed due to fast exchange of **AR** are shown around 8.4 ppm.

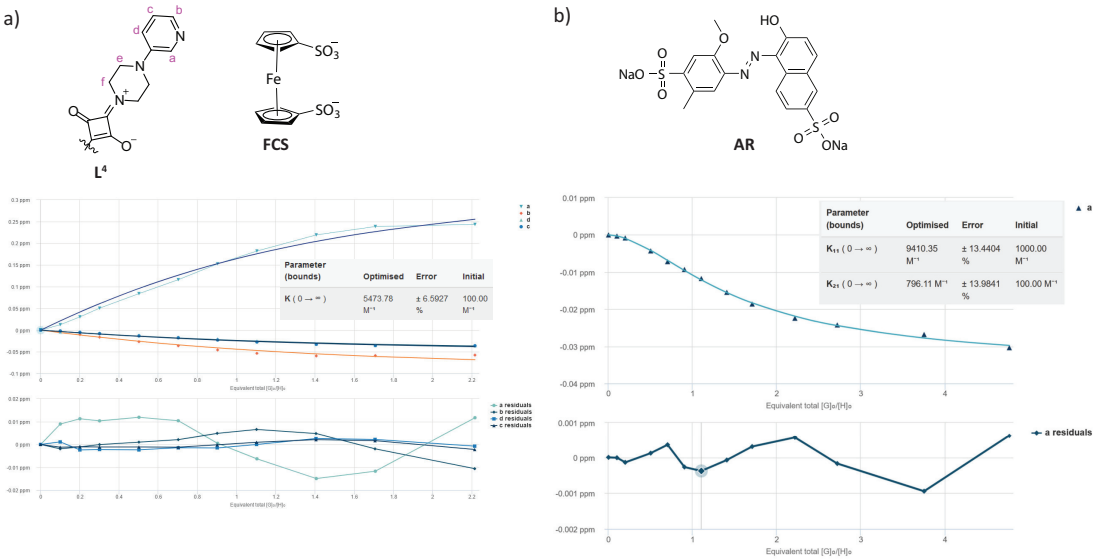

Figure 4.204. Illustration of binding analysis result obtained by BindFit (Fitter: 1:1; titration of allura red (**AR**) and ferrocene-1,1'-disulfonate (**FCS**) to $[Pd_3\mathbf{L^4}_6]^{6+}$. TBA as counter ions for **FCS**.

The host-guest complex of $[Pd_3\mathbf{L^4}_6]^{6+}$ and **BH** leads to a precipitate which dissolved over night but measuring the concentration before and after the addition showed that the c of the host in solution is decaying (see figure 4.205).

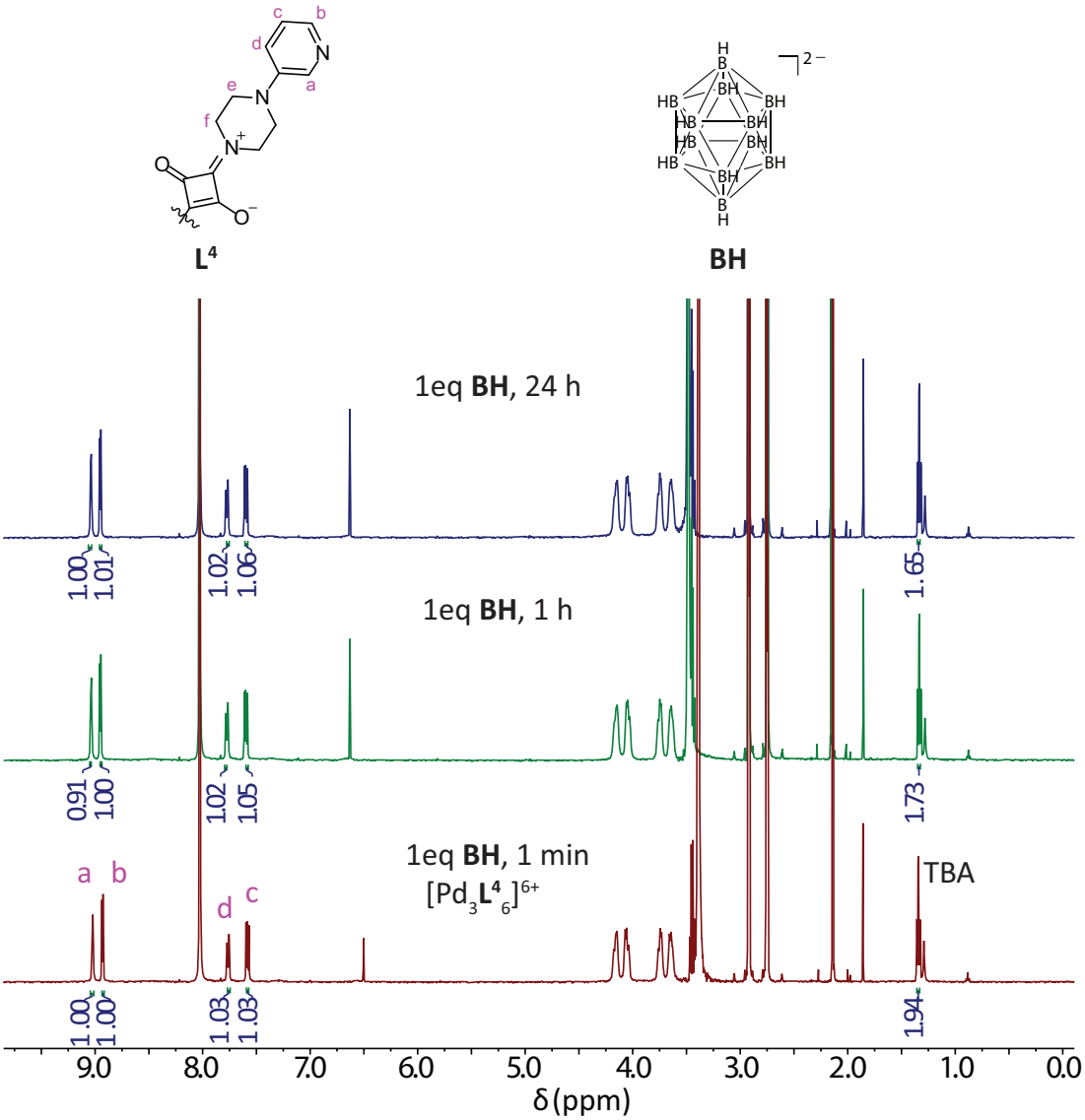

Figure 4.205. Illustration ^{1}H-NMR spectrum (500 MHz, 298 K, DMF-$d7$) spectra of $[Pd_3\mathbf{L^4}_6]^{6+}$ and **BH** at different times after addition of **BH**, such as 1 min, 1 h and 24 h measured after adding of **BH**. TBA as counter ions for **BH**.

UV-Vis Studies

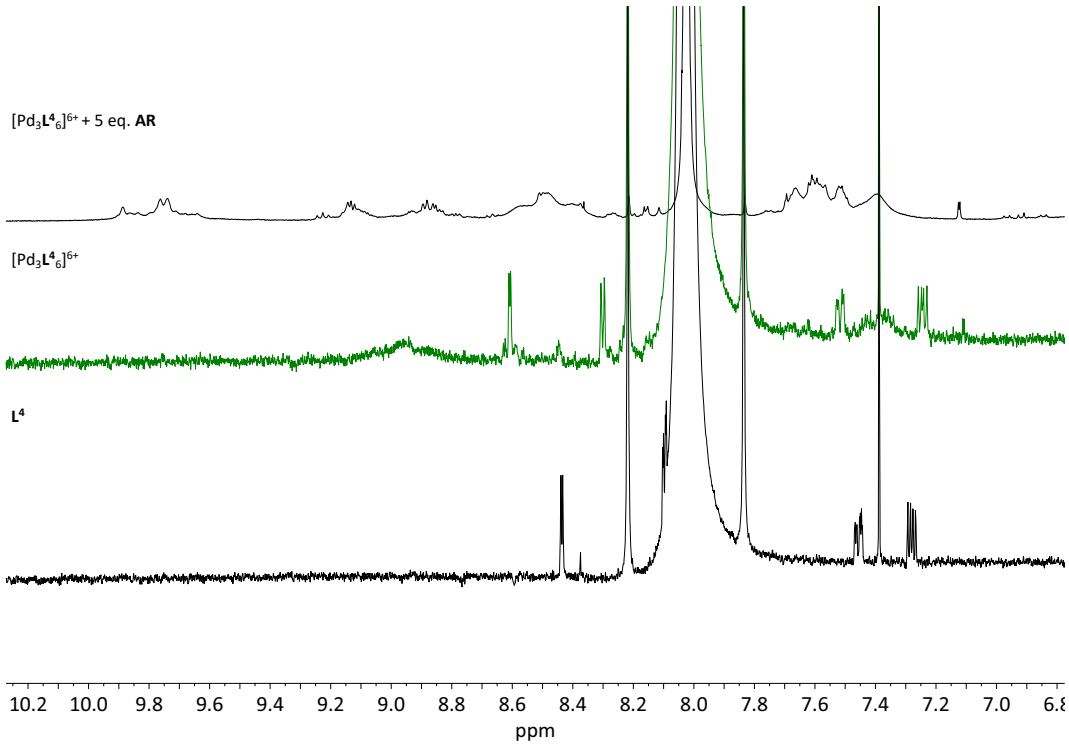

Figure 4.206. Illustration of ^{1}H-NMR of $\mathbf{L}^{4}$, $[Pd_3\mathbf{L}^{\mathbf{4}}{}_6]^{6+}$ and HG complex consisting of 35 μM $[Pd_3\mathbf{L}^{\mathbf{4}}{}_6]^{6+}$ + 5 eq. **AR** in DMF-d_7.

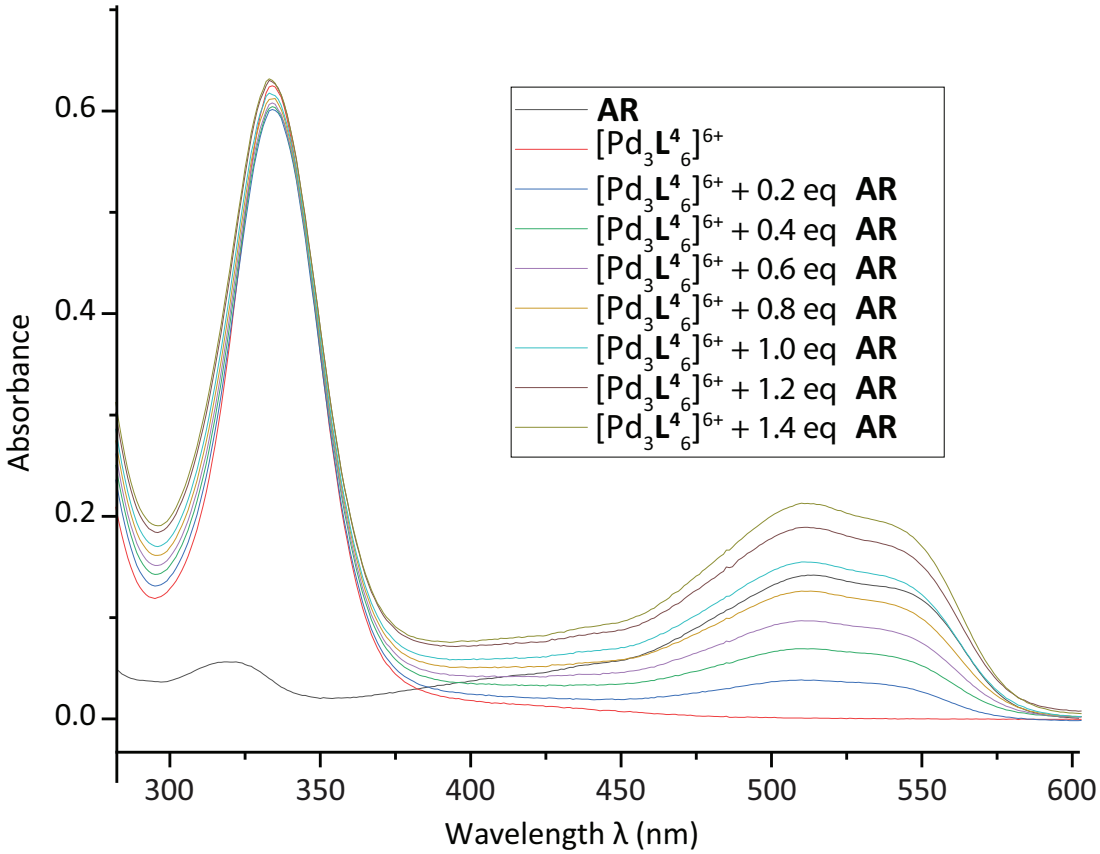

Figure 4.207. Illustration of UV-Vis titration of **AR** to $[Pd_3\mathbf{L^4}_6]^{6+}$ in DMF-d_7. Concentration of 35 μM $[Pd_3\mathbf{L^4}_6]^{6+}$, DMF-d_7 and with a cuvette of 0.2 cm optical path.

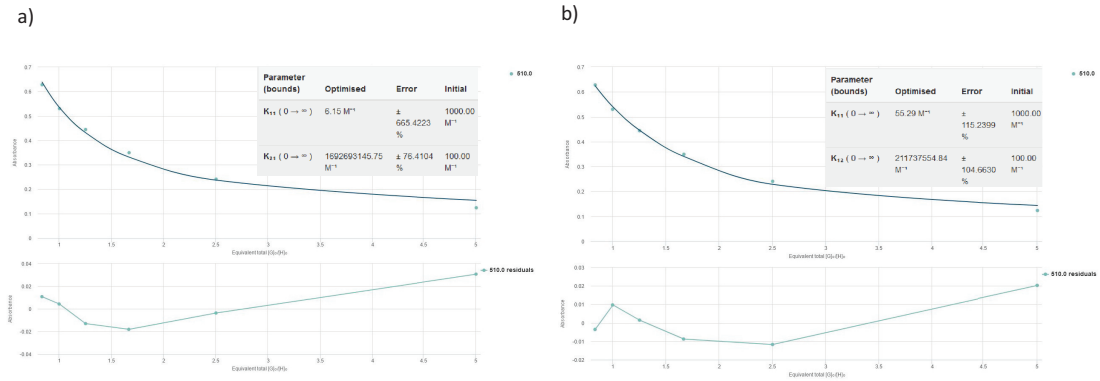

Figure 4.208. Illustration of binding analysis result obtained by BindFit (Fitter: 1:1 failed, a) 2:1 fitter, b) 1:2 fitter. UV-Vis titration of $[Pd_3\mathbf{L^4}_6]^{6+}$ to **AR**. In DMF-d_7 and adding of 35 μM $[Pd_3\mathbf{L^4}_6]^{6+}$. 0.2 cm optical path.

CV Studies

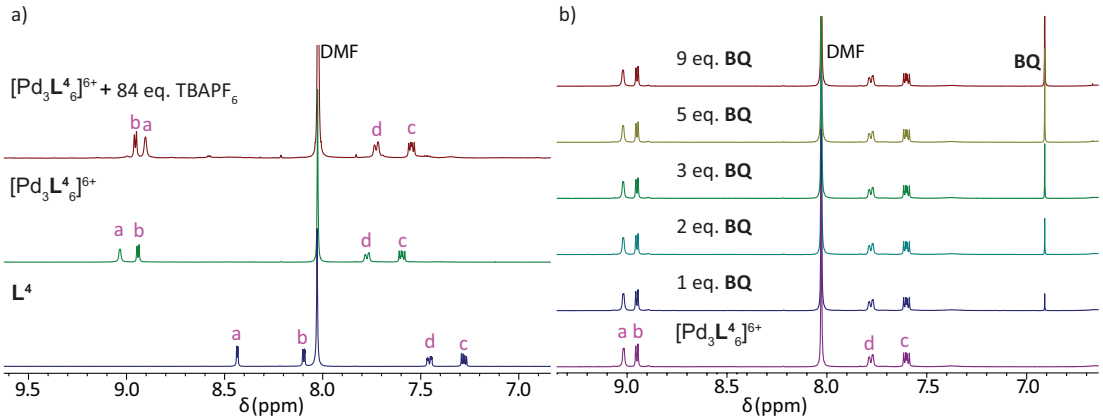

Figure 4.209. Illustration of ^{1}H-NMR spectrum (500 MHz, 298 K, DMF-$d7$) titrated guests a) PF_6^- and b) **BQ** to 0.63 mM $[Pd_3\mathbf{L^4}_6]^{6+}$.

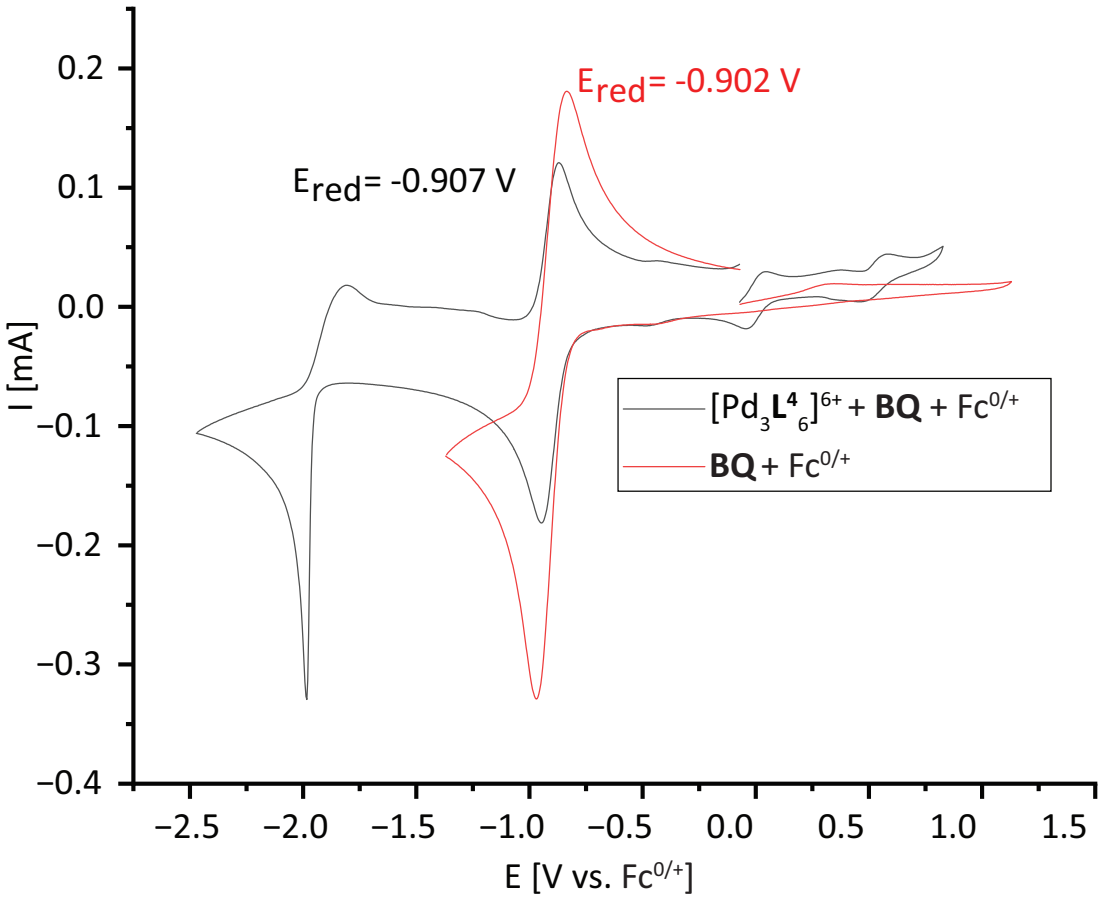

Figure 4.210. Illustration of CV of **BQ** and $[Pd_3\mathbf{L^4}_6]^{6+}$ with **BQ**. 0.63 mM $[Pd_3\mathbf{L^4}_6]^{6+}$ in DMF. 4 eq. **BQ**. Measured at rt (scanned towards anodic potentials). Measured at 200 mV/s (iR compensation = 259 Ohm) and referenced internally against ferrocene (Fc).

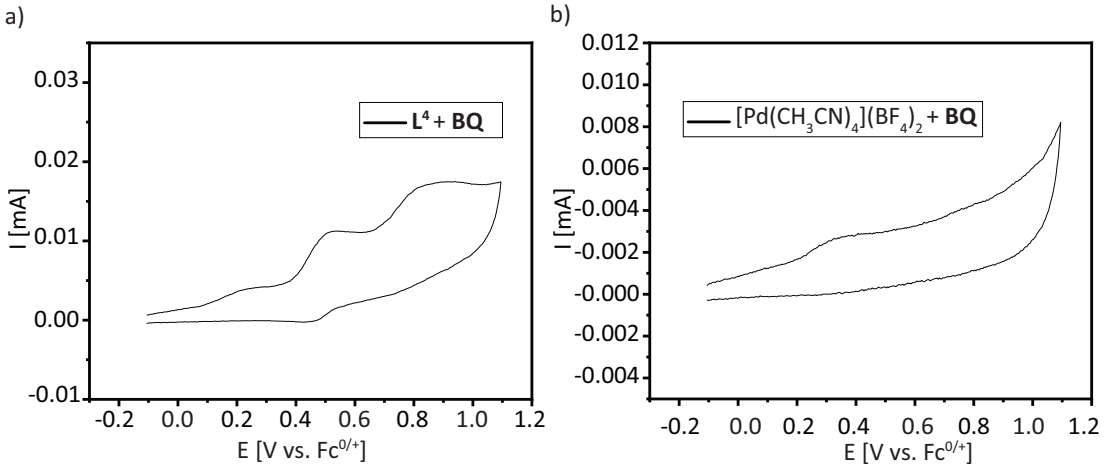

Figure 4.211. Respective control experiment of a) ligand and **BQ** and b) $[Pd(CH_3CN)_4](BF_4)_2$ and **BQ** in DMF. Both cyclic voltammograms are electrochemically irreversible.

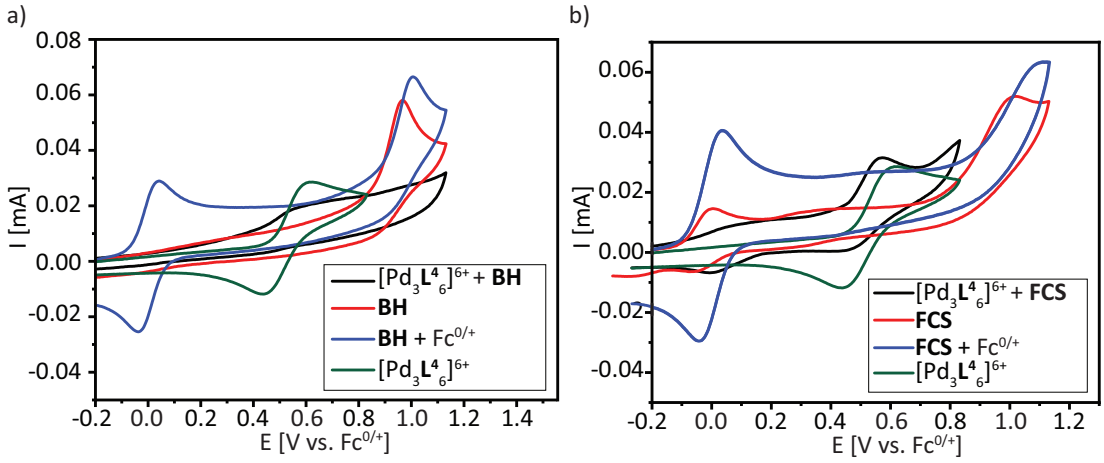

Figure 4.212. Respective HG complexes of $[Pd_3\mathbf{L^4}_6]^{6+}$ with respectively **FCS** and **BH** are showing an electrochemical irreversible cyclic voltammogram. 0.63 mM $[Pd_3\mathbf{L^4}_6]^{6+}$ in DMF. 1 eq **BH** and 2 eq **FCS**. Scanned towards anodic potentials. Measured at 200 mV/s (iR compensation = 259 Ohm) and referenced internally against ferrocene (Fc).

Crystal Data

Structure Tables

	$[Pd_3\mathbf{L^4}_6]^{6+}$	$[Pd_4\mathbf{L^4}_8]^{8+}$	$[Pd_4\mathbf{L^4}_8]^{8+}$
CCDC number			
Empirical formula	$C_{148.50}H_{167.50}B_2F_8N_{36}O_{18}Pd_3S_{1.50}$	$C_{490}H_{532}N_{118}O_{90}Pd_8S_{12}$	$C_{218}H_{234}N_{54}O_{34}Pd_4S_4$
Formula weight	3285.59	10750.22	4708.42
Temperature [K]	100(2)	100(2)	100(2)
Crystal system	triclinic	triclinic	monoclinic
Space group (number)	$P\overline{1}$ (2)	$P\overline{1}$ (2)	$P2_1/c$ (14)
a [Å]	11.874(3)	17.336(4)	24.144(5)
b [Å]	34.417(11)	24.691(5)	37.344(5)
c [Å]	35.129(10)	40.499(5)	16.648(6)
α [°]	118.967(7)	82.036(5)	90
β [°]	92.54(2)	86.315(6)	91.86(3)
γ [°]	97.019(13)	86.876(9)	90
Volume [Å^3]	12377(6)	17114(6)	15002(7)
Z	2	1	2
ρ_{calc} [gcm^{-3}]	0.882	1.043	1.042
μ [mm^{-1}]	0.756	0.827	0.875
F(000)	3397	5578	4880
Crystal size [mm^3]	0.025×0.005×0.005	0.070×0.030×0.020	0.080×0.020×0.005
Crystal colour	orange	colourless	red
Crystal shape	needle	block	plate
Radiation	synchrotron (λ=1.03321 Å)	synchrotron (λ=1.0332 Å)	synchrotron (λ=1.0332 Å)
2Θ range [°]	1.94 to 46.83 (1.30 Å)	1.48 to 55.94 (1.10 Å)	2.45 to 47.95 (1.27 Å)
Index ranges	-9 ≤ h ≤ 9	-13 ≤ h ≤ 13	-18 ≤ h ≤ 18
	-26 ≤ k ≤ 26	-21 ≤ k ≤ 21	-29 ≤ k ≤ 29
	-26 ≤ l ≤ 26	-34 ≤ l ≤ 34	-13 ≤ l ≤ 13
Reflections collected	39205	65713	49958
Independent reflections	10416	17673	7425
	R_{int} = 0.0989	R_{int} = 0.0530	R_{int} = 0.0827
	R_{sigma} = 0.0812	R_{sigma} = 0.0445	R_{sigma} = 0.0480
Completeness	88.3 %	65.9 %	97.4 %
Data / Restraints / Parameters	10416/3753/1941	17673/6544/3232	7425/2941/1415
Goodness-of-fit on F^2	1.499	1.369	1.134
Final *R* indexes	R_1 = 0.1304	R_1 = 0.0963	R_1 = 0.0853
[I≥2σ(I)]	wR_2 = 0.3564	wR_2 = 0.2968	wR_2 = 0.2579
Final *R* indexes	R_1 = 0.1744	R_1 = 0.1137	R_1 = 0.1127
[all data]	wR_2 = 0.3912	wR_2 = 0.3166	wR_2 = 0.2854
Largest peak/hole [eÅ^{-3}]	0.76/-0.41	0.82/-0.35	0.48/-0.21
Flack X parameter			
Extinction coefficient			

Figure 4.213. Crystal data and structure refinement for $[Pd_3\mathbf{L^4}_6]^{6+}$ and $[Pd_4\mathbf{L^4}_8]^{8+}$ + **AR**.

4.3.12 Homoleptic Coordination Cage Formation of Ligand L^{4n}

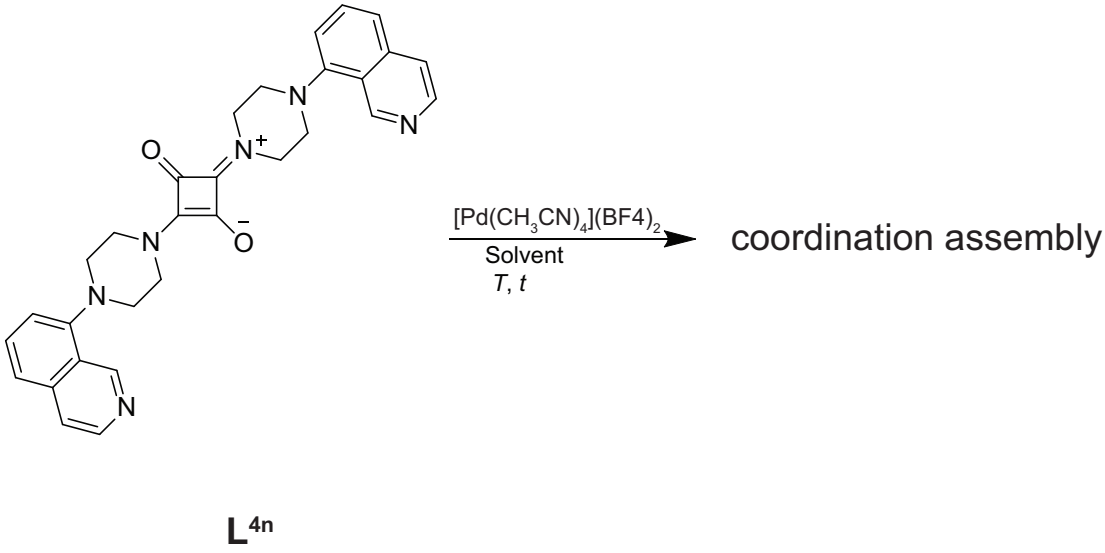

Figure 4.214. Homoleptic cage formation of L^{4n}.

The homoleptic cage formation with $[Pd(CH_3CN)_4](BF_4)_2$ was performed analogous to the previous homoleptic cages. No signals could be distinguished, that would indicate the formation of a clean coordination cage.

The cage formation has been examined in DMSO$-d_6$, CD_3CN and DMF$-d_7$, but no distinct species has been observed. ESI-MS did not provide further information about the cage formation.

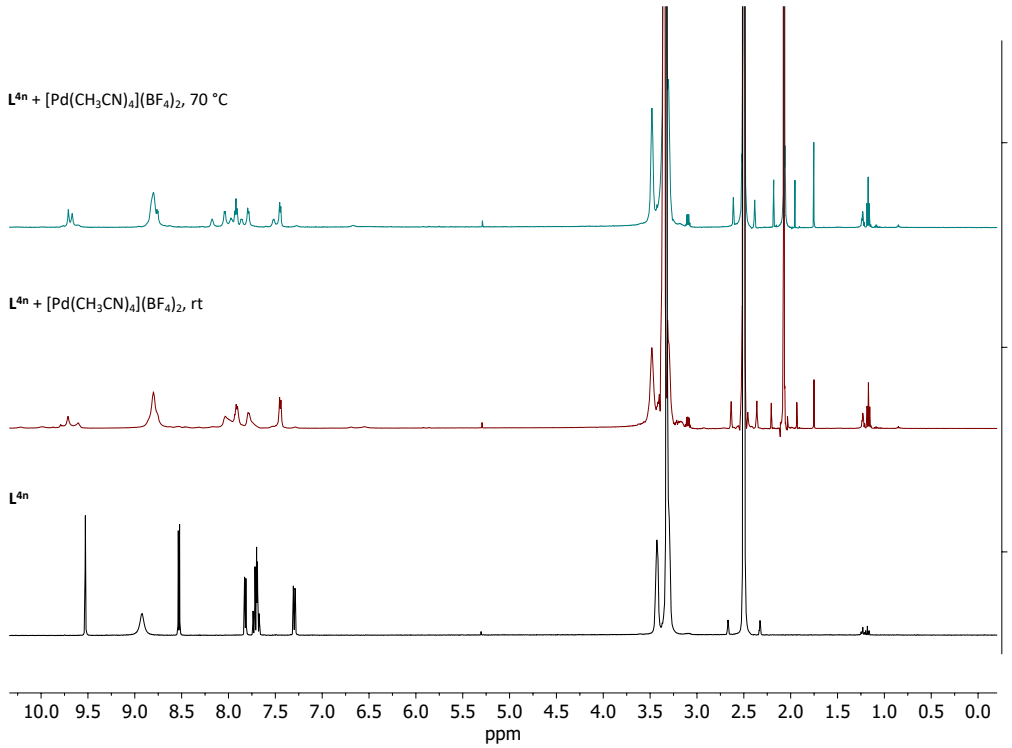

Figure 4.215. ^{1}H-NMR spectrum (500 MHz, 298 K, DMSO$-d_6$) of the cage formation of L^{4n} at rt after 2 h and 70 °C after 12 h.

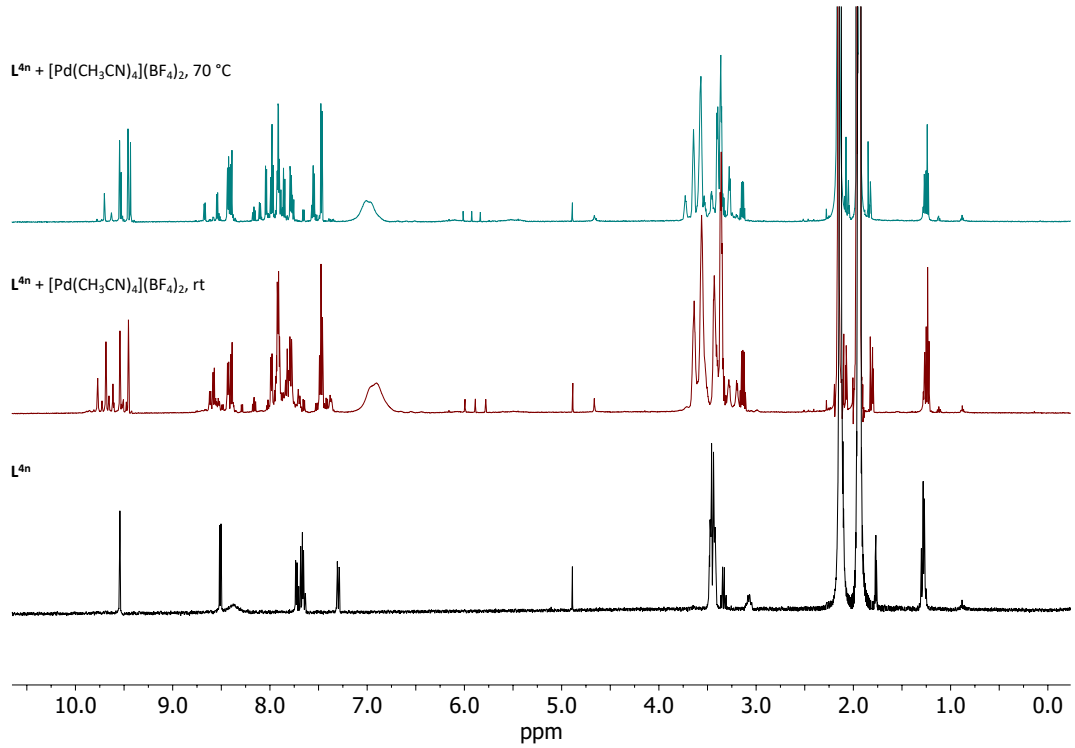

Figure 4.216. ^{1}H-NMR spectrum (500 MHz, 298 K, CD_3CN) of the cage formation of $\mathbf{L^{4n}}$ at rt after 2 h and 70 °C after 12 h.

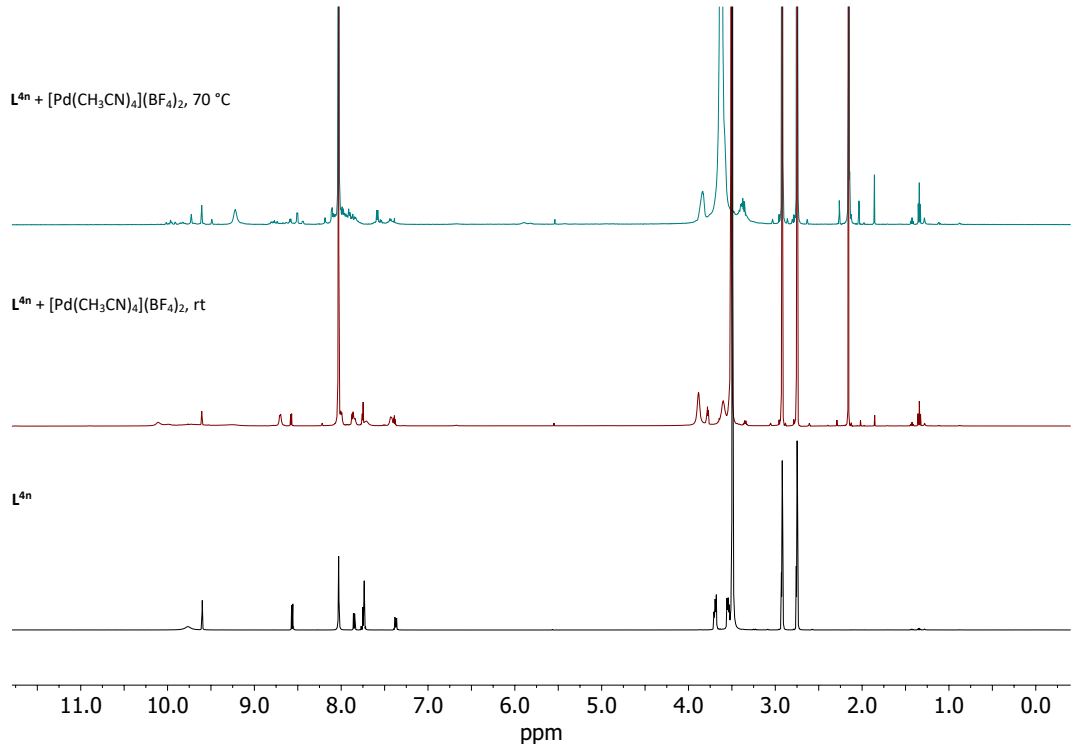

Figure 4.217. ^{1}H-NMR spectrum (500 MHz, 298 K, DMF$-d_7$) of the cage formation of $\mathbf{L^{4n}}$ at rt after 2 h and 70 °C after 12 h

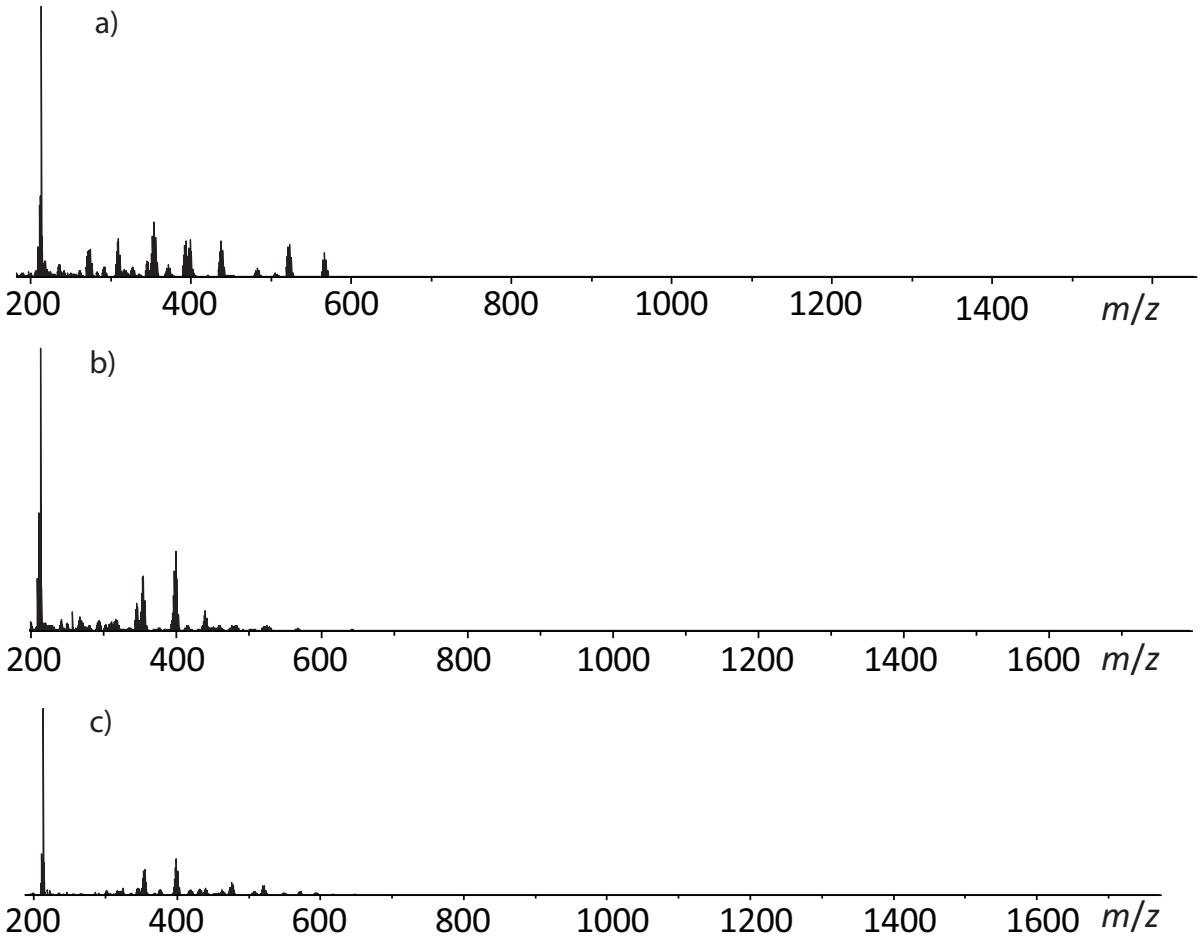

Figure 4.218. Illustration of ESI-MS of the cage formation of $\mathbf{L^{4n}}$ in a) DMSO$-d_6$, b) CD_3CN and c) DMF$-d_7$.

4.3.13 Coordination Cage Formation of Catechol-based Ligands

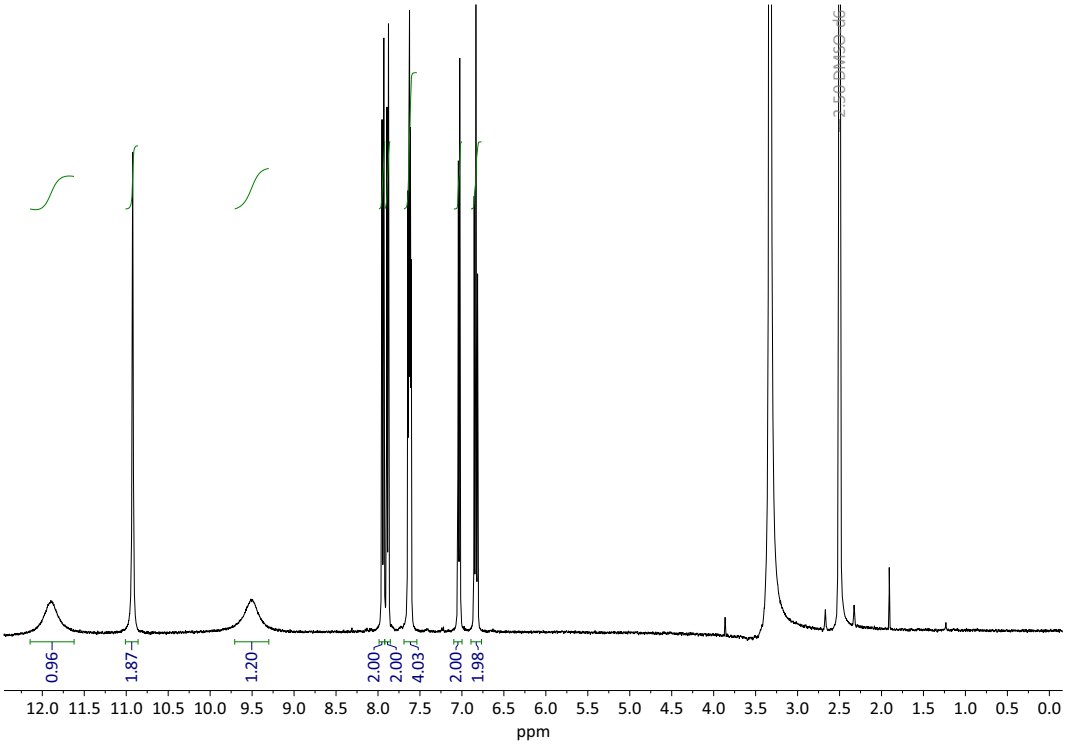

Figure 4.219. ^{1}H-NMR Spectrum (500 MHz, 298 K, DMSO$-d_6$) of ligand $\mathbf{L^5}$.

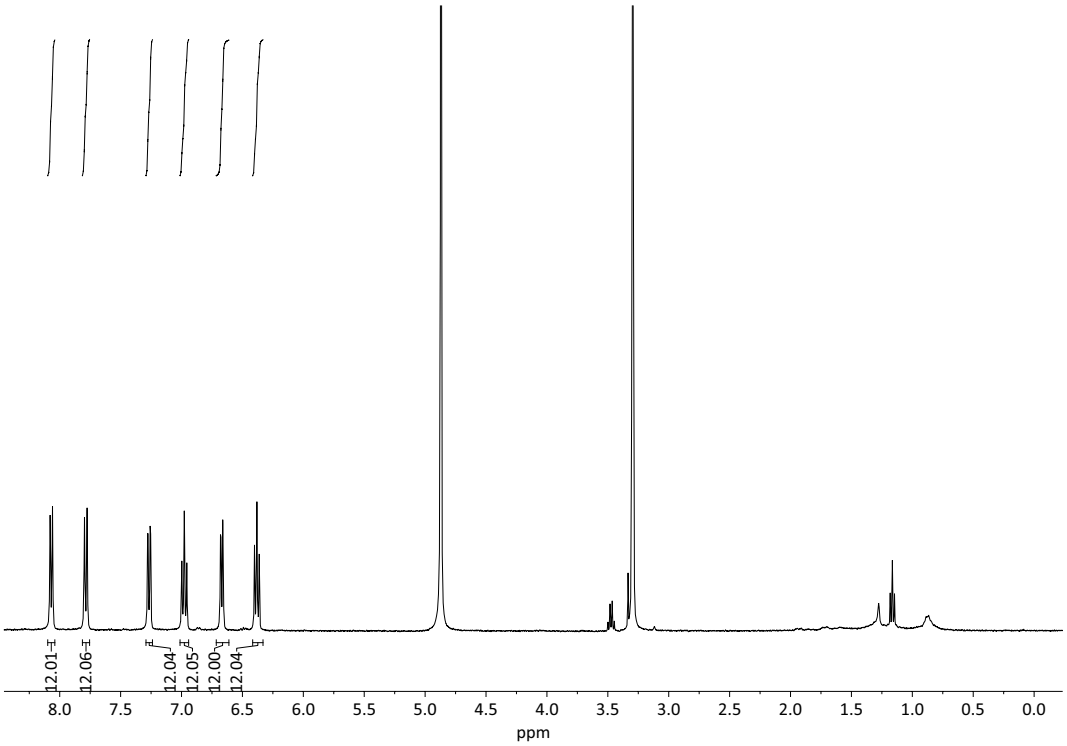

Figure 4.220. ^{1}H-NMR Spectrum (500 MHz, 298 K, CD_3DO) of coordination cage $[Ga_4\mathbf{L^5}_6]_2^{1-}$.

Toste group observed that the reduction of 3-methyl-indole with $[Ga_4\mathbf{L^1}_6]^{12-}$ in buffered D_2O shows deuterium insertion at 45 °C observed by ^{1}H-NMR analysis

even though an acidic ethanol solution as a solvent, without the host did not lead to this observation (see figure 4.221).

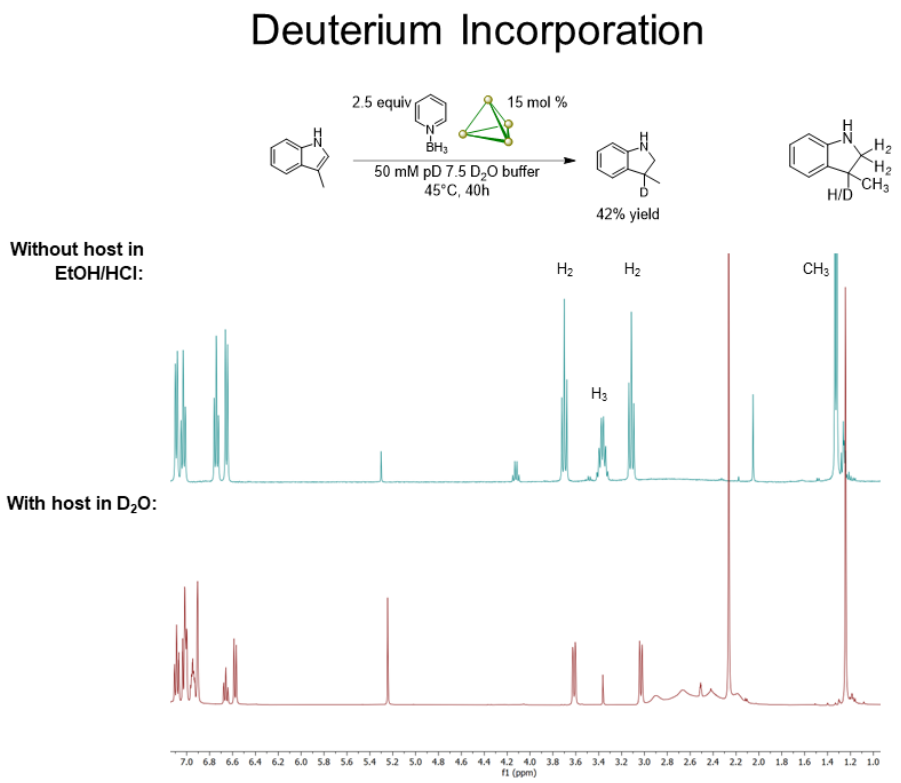

Figure 4.221. ^{1}H-NMR Spectrum (500 MHz, 298 K, D_2O) of racemic cage. Adapted from E. Heather.

In this work the deuterium insertion into 2-methyl-indole was examined by preparing the $[Ga_4\mathbf{L}^{\mathbf{5}}{}_6]^{12-}$ with 2-methyl-indole under inert conditions in a glove box in deuterium. Additionally, a reference sample with the blocked cavity by adding 1 eq. of PET to the cage was prepared, which is reported to be encapsulated by $[Ga_4\mathbf{L}^{\mathbf{5}}{}_6]^{12-}$. [274]

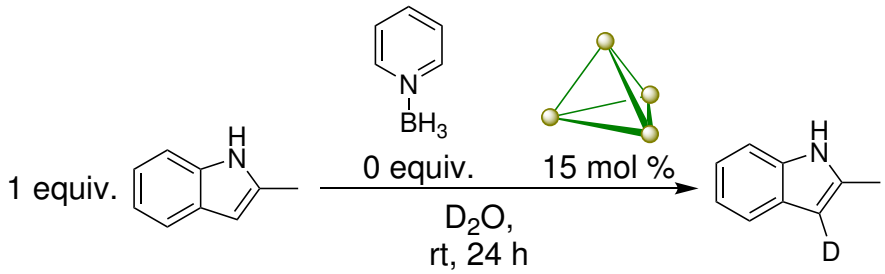

Figure 4.222. Study of deuterium insertion in 2-methyl-indole with racemic cage in D_2O.

Both experiments showed deuterium insertion into 2-methyl-indole, confirming a solvent effect (see figure 4.224). The deuterium insertion into indole is a part of the approximated reduction cycles from Heather et al. (see figure 4.223).

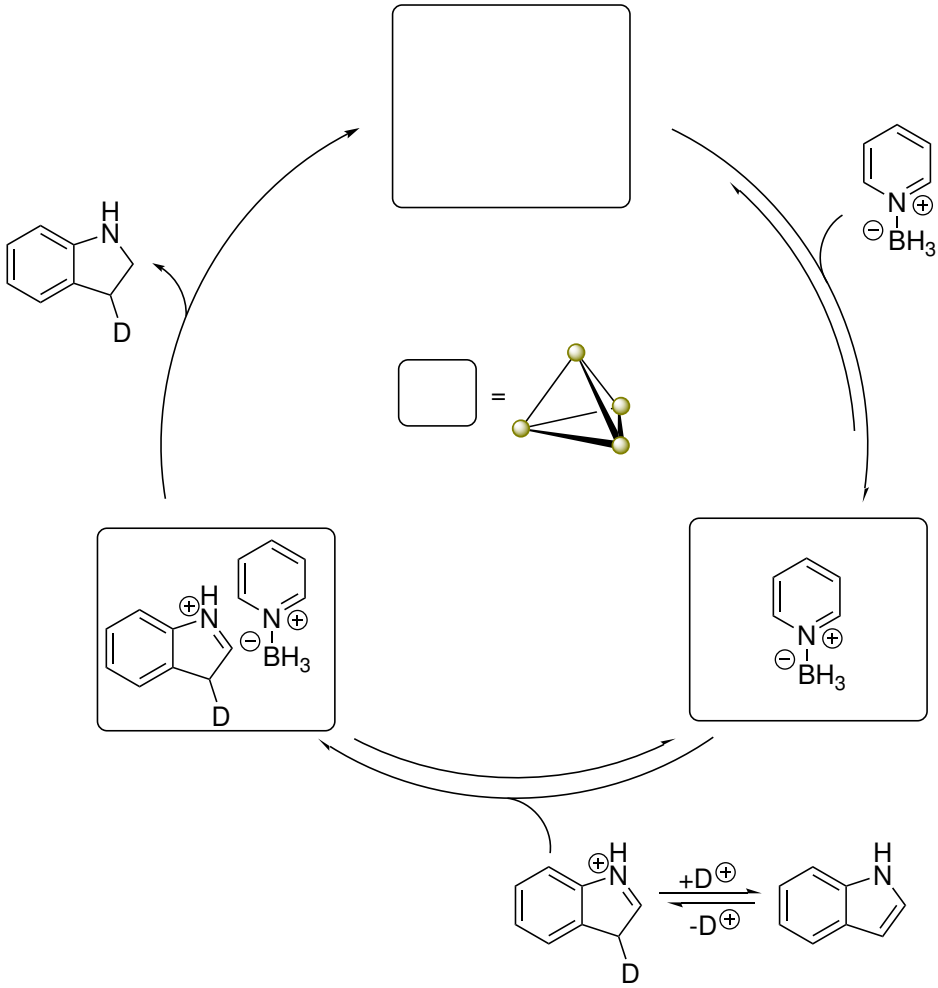

Figure 4.223. Aproximated catalysis cycle by Toste group. Picture adapted from E. Heather. [268]

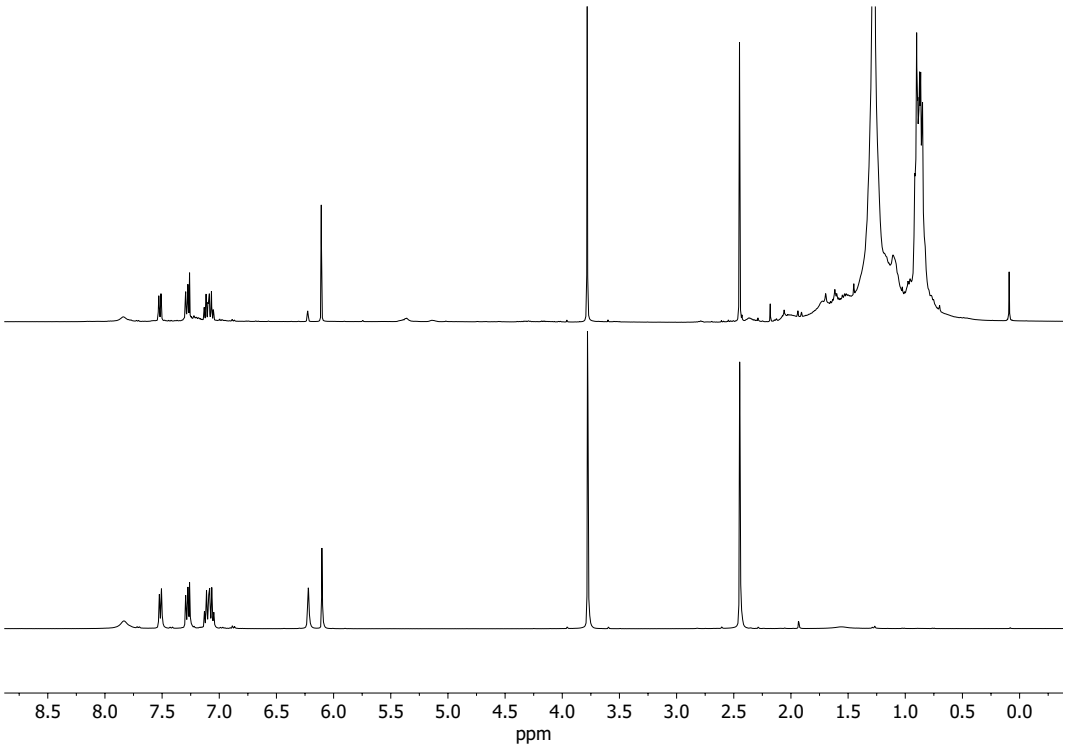

Figure 4.224. Stacked ^{1}H-NMR spectra (500 MHz, 298 K, $CDCl_3$) of blocked and non-blocked racemic cage. The reaction was performed in D_2O and then worked up by extraction with CD_3Cl_3. Then the solvent was removed *in vacuo*. To determine the conversion a fresh solution of internal standard of 1,3,5-trimethoxybenzene in CD_3Cl_3 was used. The difference in conversion can be explained by longer reaction time.

Coordination Cage Formation of Chiral Catechol-based Ligand

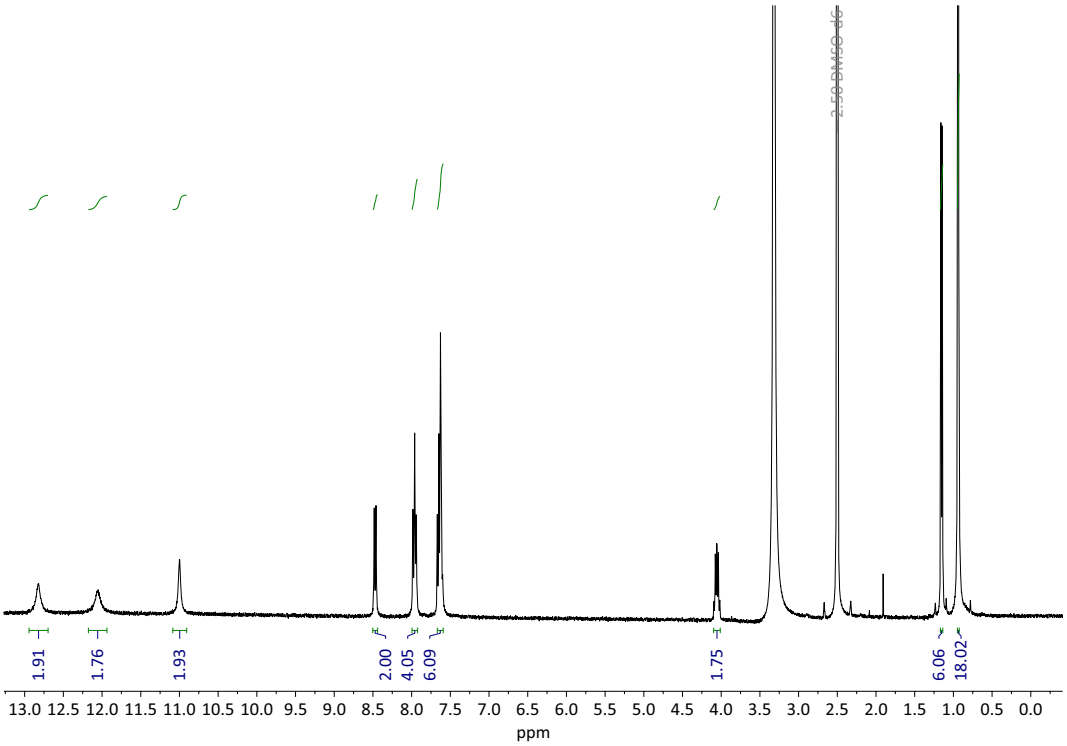

Figure 4.225. ^{1}H-NMR Spectrum (500 MHz, 298 K, DMSO$-d_6$) of $\mathbf{L^6}$.

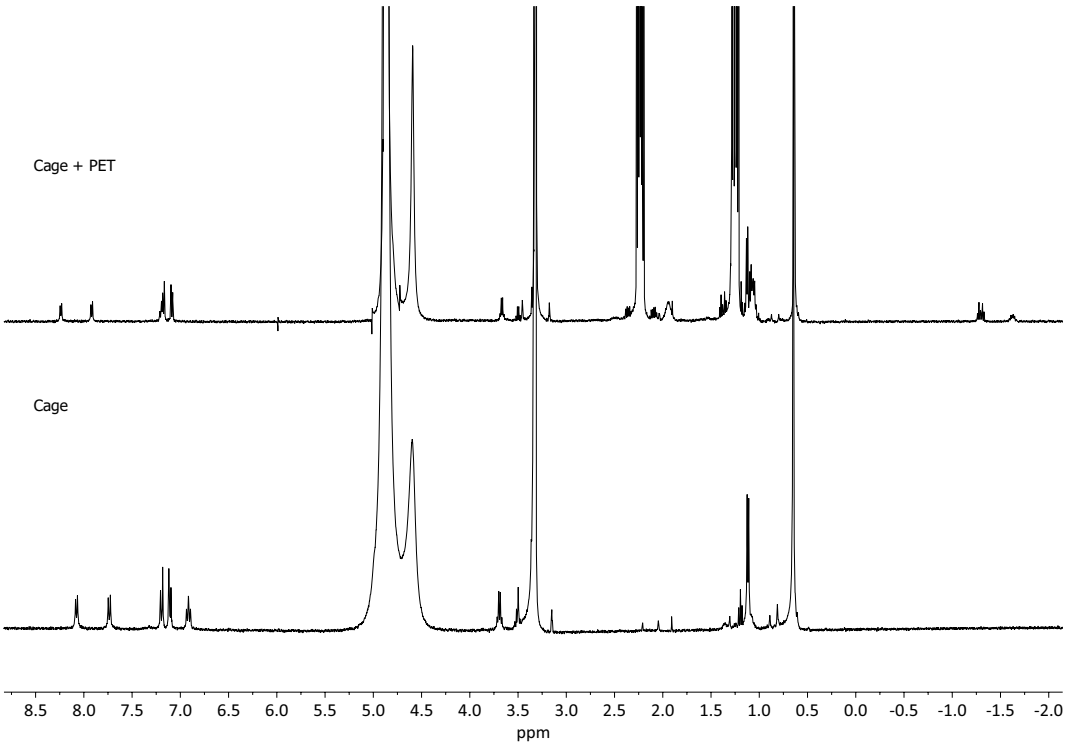

Figure 4.226. ^{1}H-NMR Spectrum (500 MHz, 298 K, CD_3OD). Control experiment for enantiopure cage 2.0 with PET. The cage signals in the aromatic area are shifting after encapsulation and the signals of encapsulated PET are shown at -1,3 ppm and -1,63 ppm. [259]

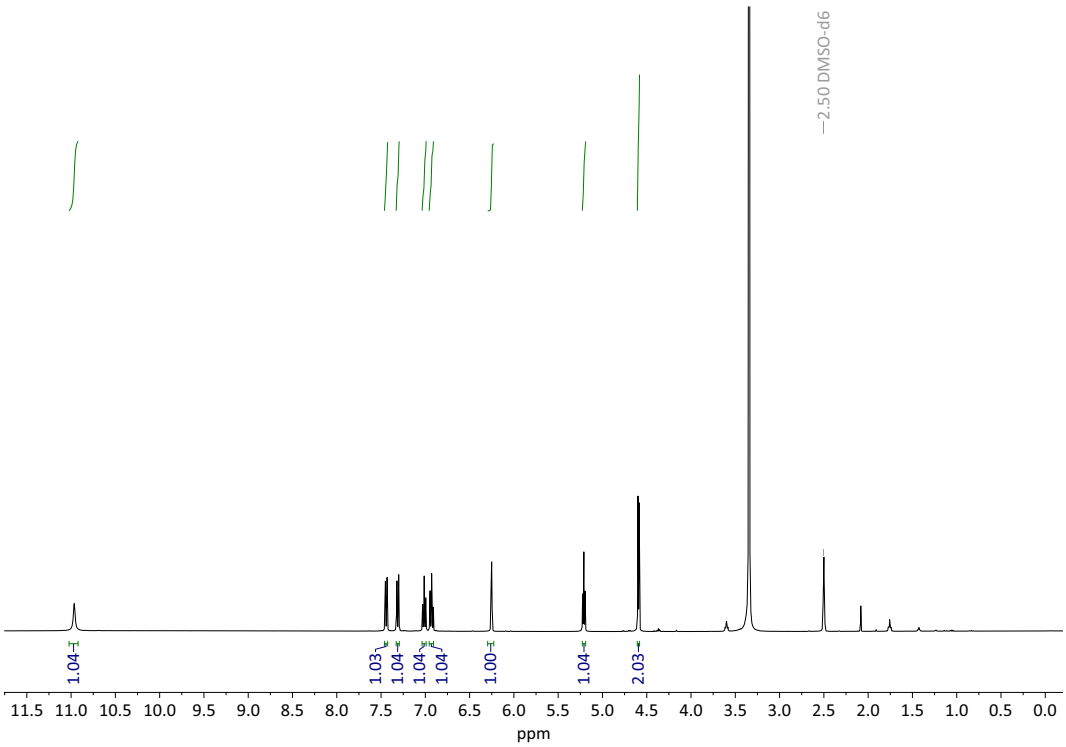

Figure 4.227. ^{1}H-NMR Spectrum (500 MHz, 298 K, DMSO$-d_6$) of **22**.

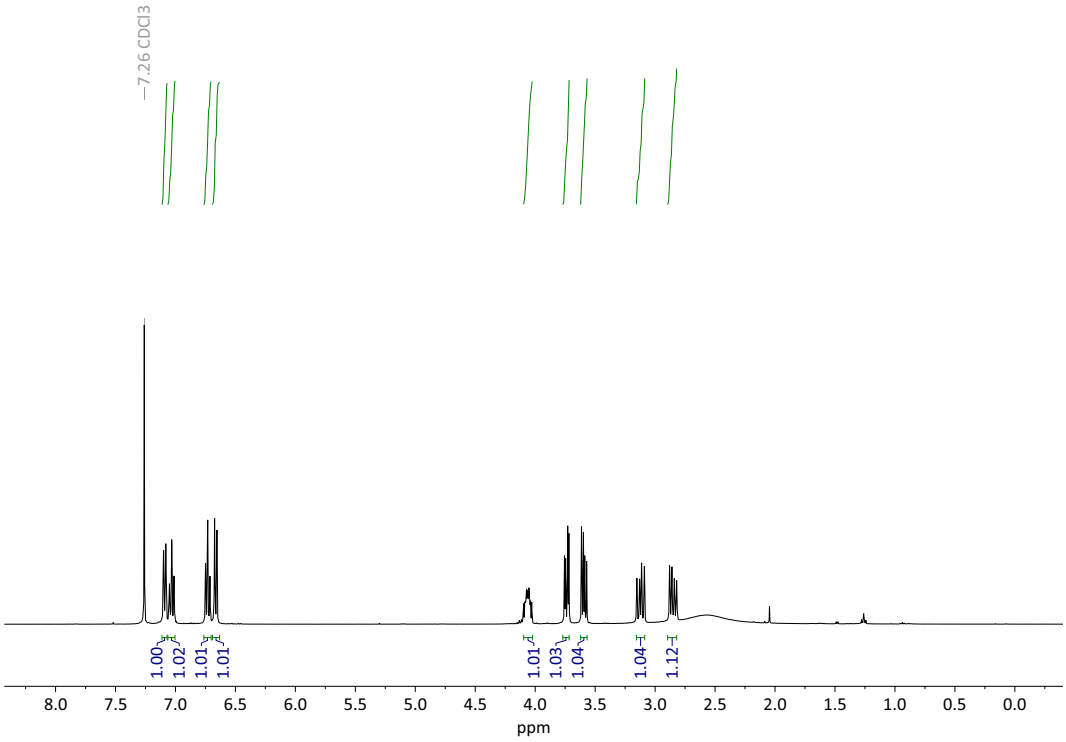

Figure 4.228. ^{1}H-NMR Spectrum (500 MHz, 298 K, $CDCl_3$) of **23**.

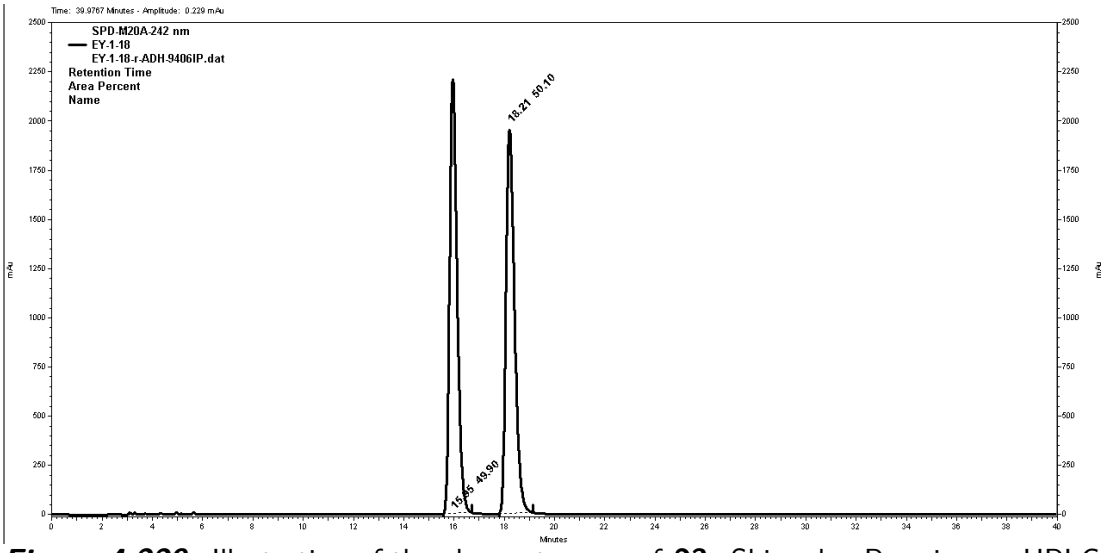

Figure 4.229. Illustration of the chromatogram of **23**. Shimadzu Prominence HPLC system was used. The column used is CHIRALPAK©IA. Samples for the chiral HPLC analysis were prepared in a solution of 95 % hexanes and IPA.

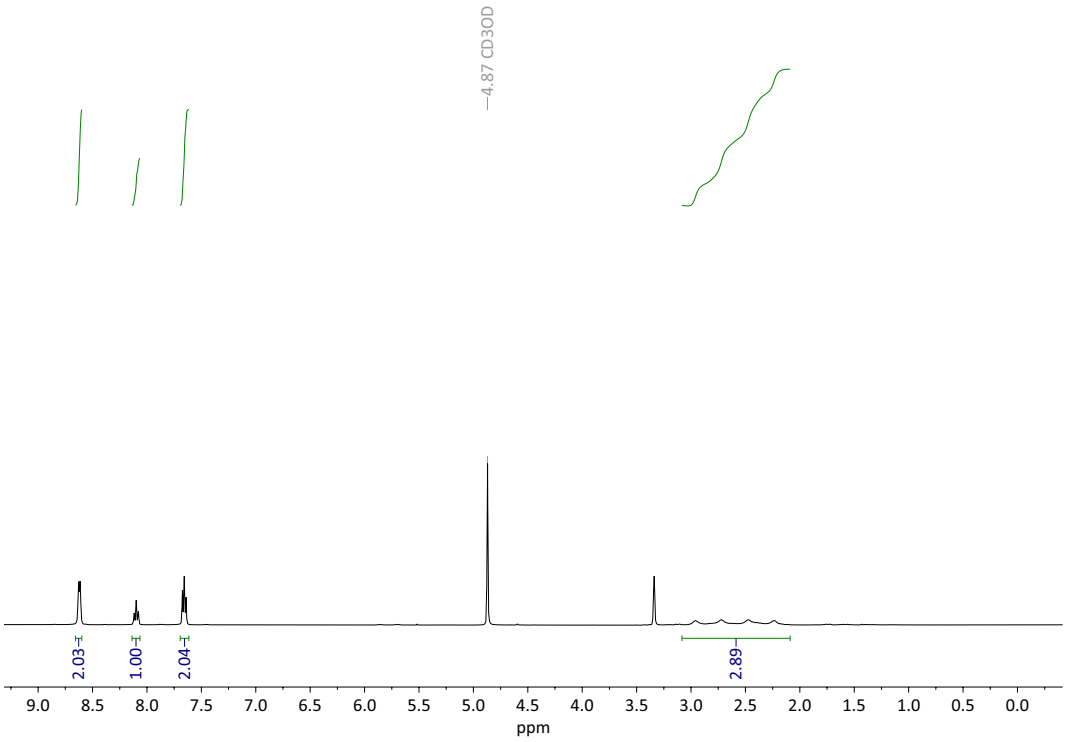

Figure 4.230. ^{1}H-NMR Spectrum (500 MHz, 298 K, CD_3OD) of pyridine borane **24**.

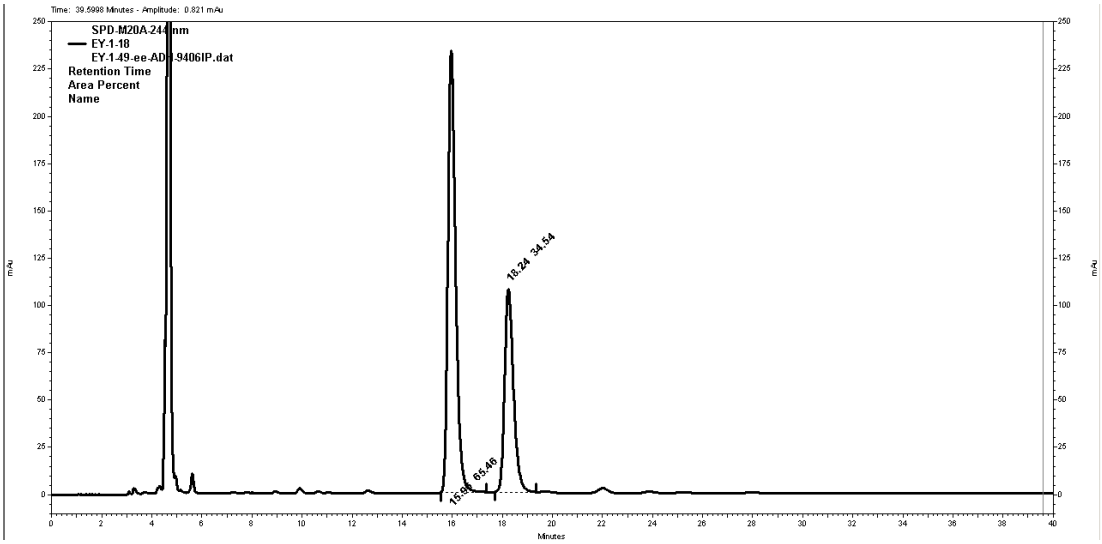

Figure 4.231. Shimadzu Prominence HPLC system was used. The column used is CHIRALPAK©IA. Samples for the chiral HPLC analysis were prepared in a solution of 95 % hexanes and IPA.

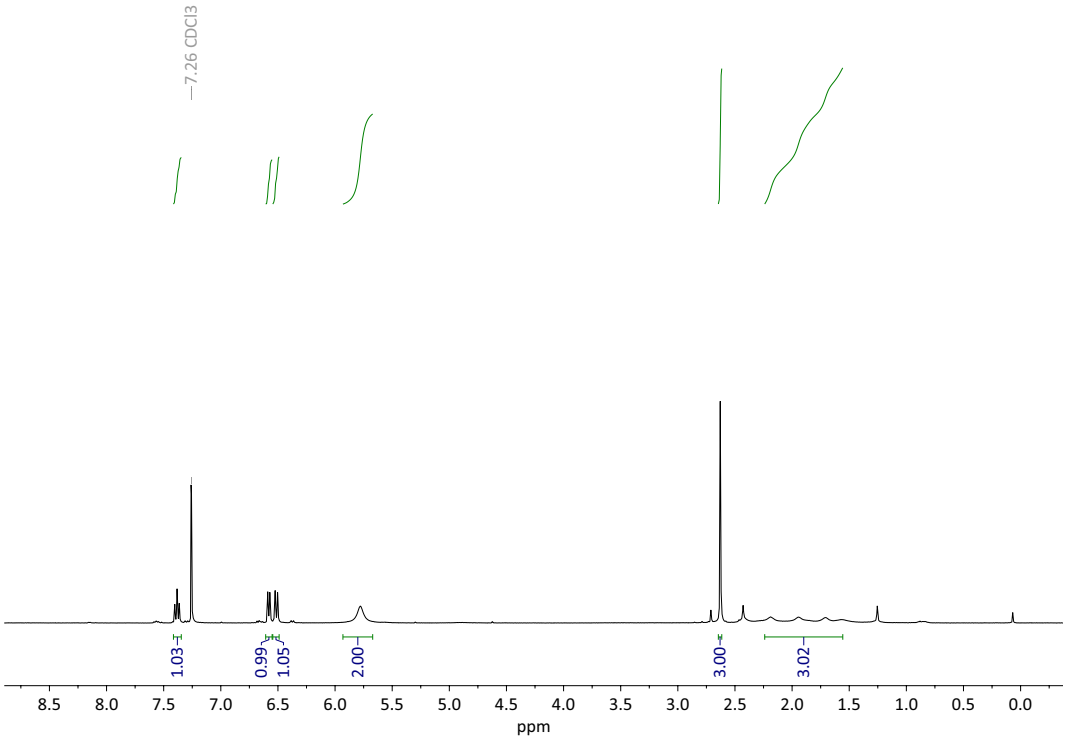

Figure 4.232. ^{1}H-NMR Spectrum (500 MHz, 298 K, $CDCl_3$) of ligand **26**.

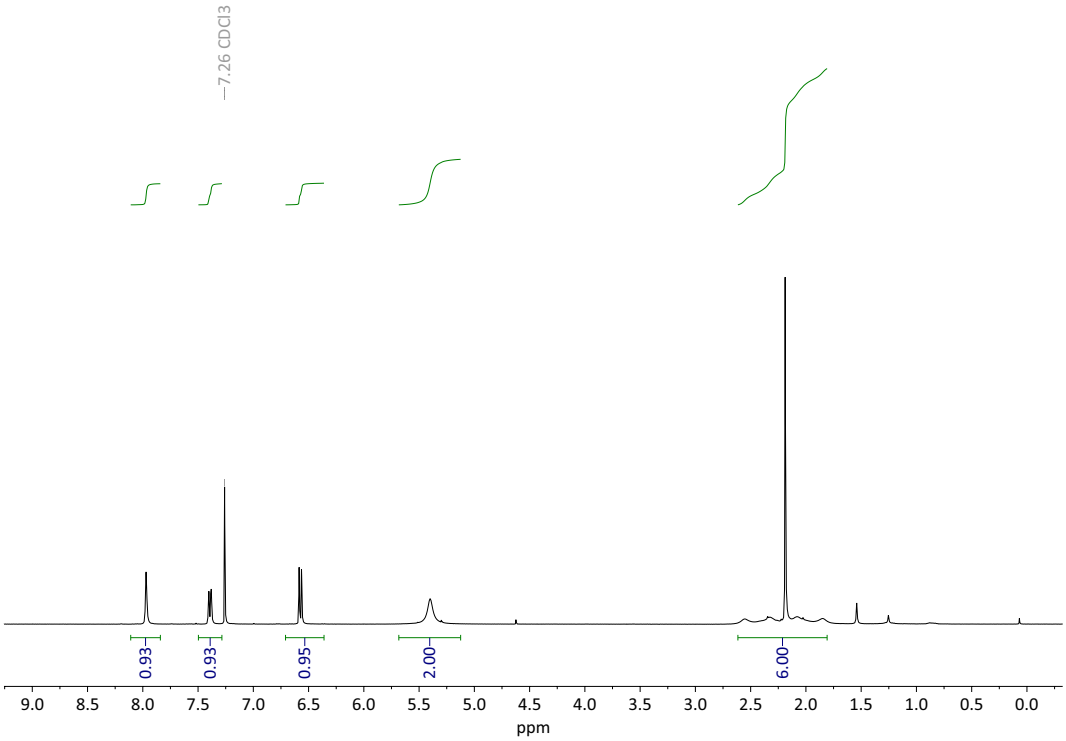

Figure 4.233. ^{1}H-NMR Spectrum (500 MHz, 298 K, $CDCl_3$)of ligand **26**.

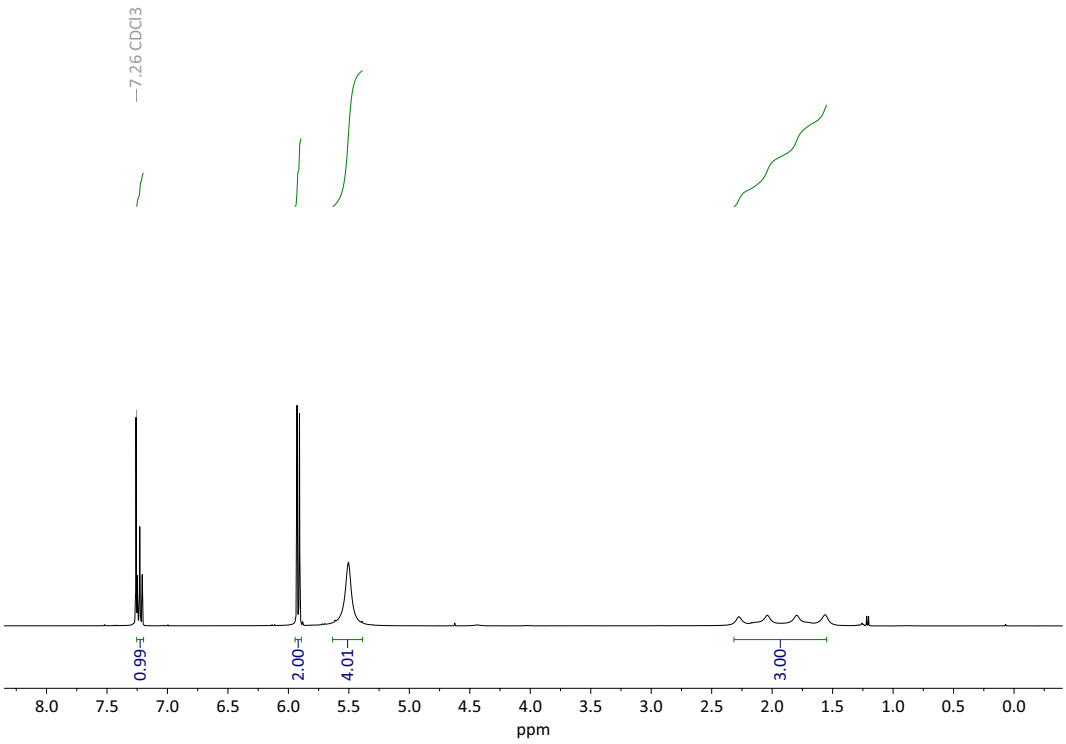

Figure 4.234. ^{1}H-NMR Spectrum (500 MHz, 298 K, $CDCl_3$) of ligand **28**.

4.4 Further Cage Formation Studies

4.4.1 Heterolepic Coordination Cage Formation with L^{TB}

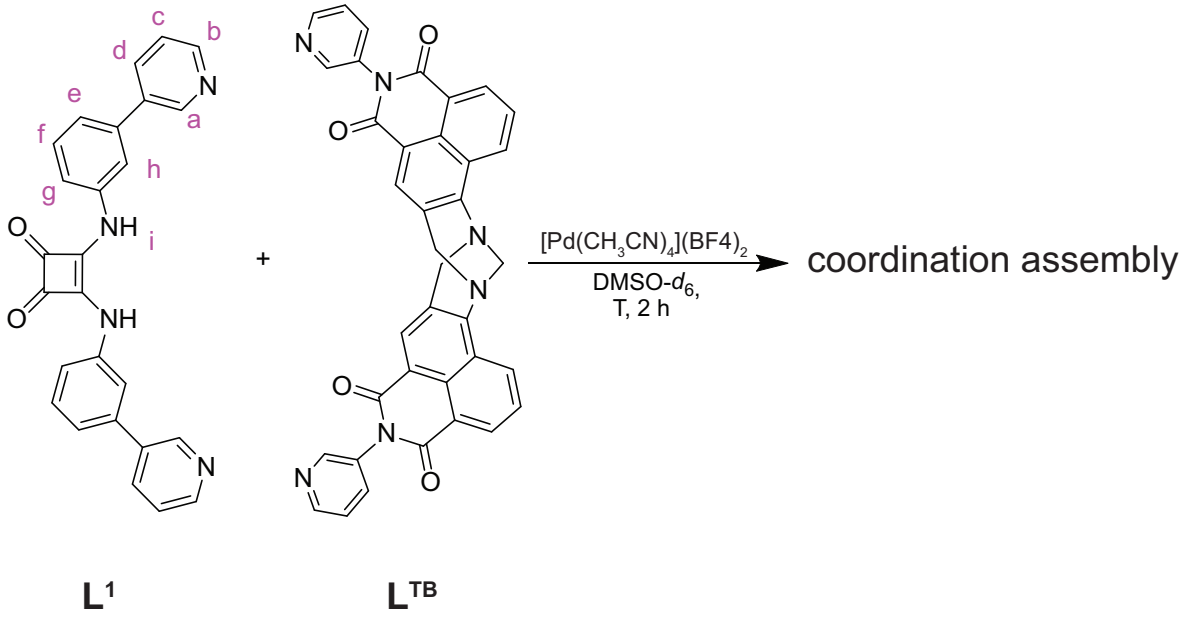

Figure 4.235. Heteroleptic coordination cage formation of $\mathbf{L^1}$ and $\mathbf{L^{TB}}$ in DMSO-d_6.

The heteroletic cage formation with $[Pd(CH_3CN)_4](BF_4)_2$ was performed analogous to the previous heteroleptic cages. ESI-MS showed 4+, 3+ and 2+ species.

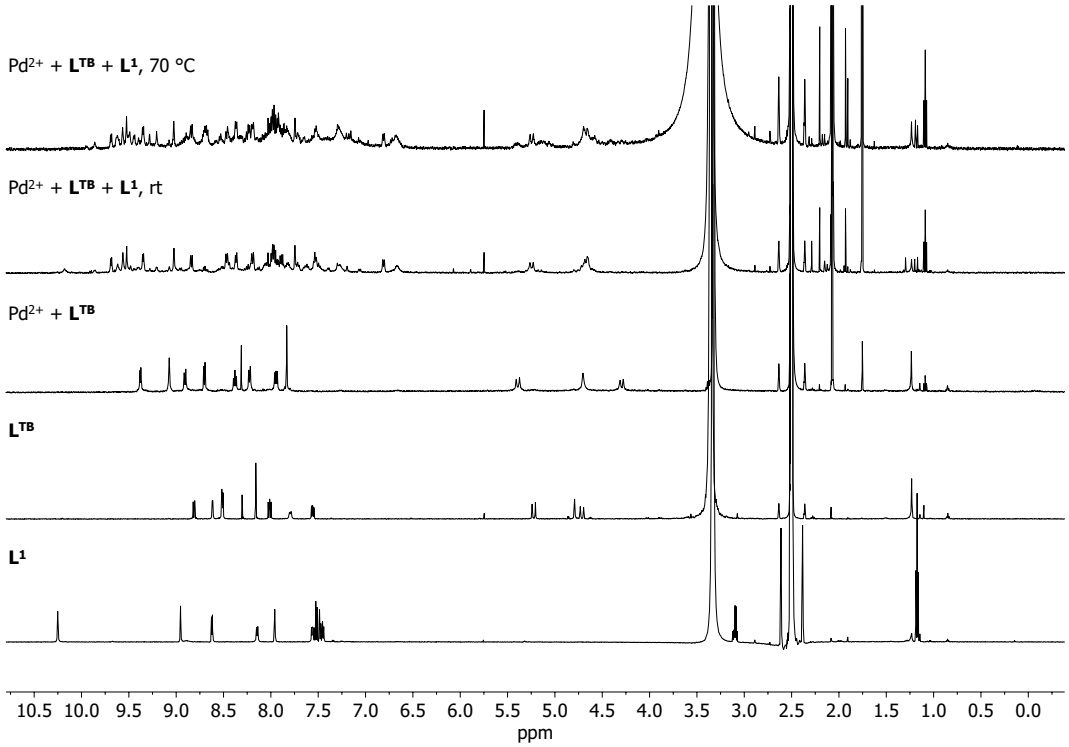

Figure 4.236. ^{1}H-NMR spectrum (500 MHz, 298 K, DMSO-d_6) of $\mathbf{L^1}$ and $\mathbf{L^{TB}}$. Cage formation at rt for 2 h and at 70 °C for 12 h

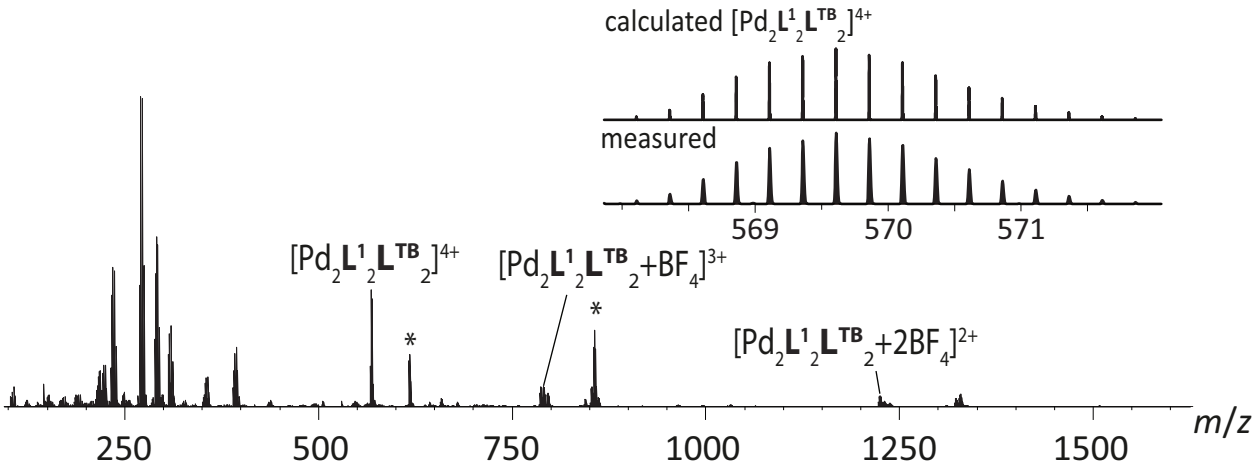

Figure 4.237. Illustration of ESI-MS of $[Pd_2\mathbf{L^1}_2\mathbf{L^{TB}}_2]^{4+}$ in DMSO$-d_6$.

4.4.2 Towards Squaraine Dyes-Based Coordination Cages

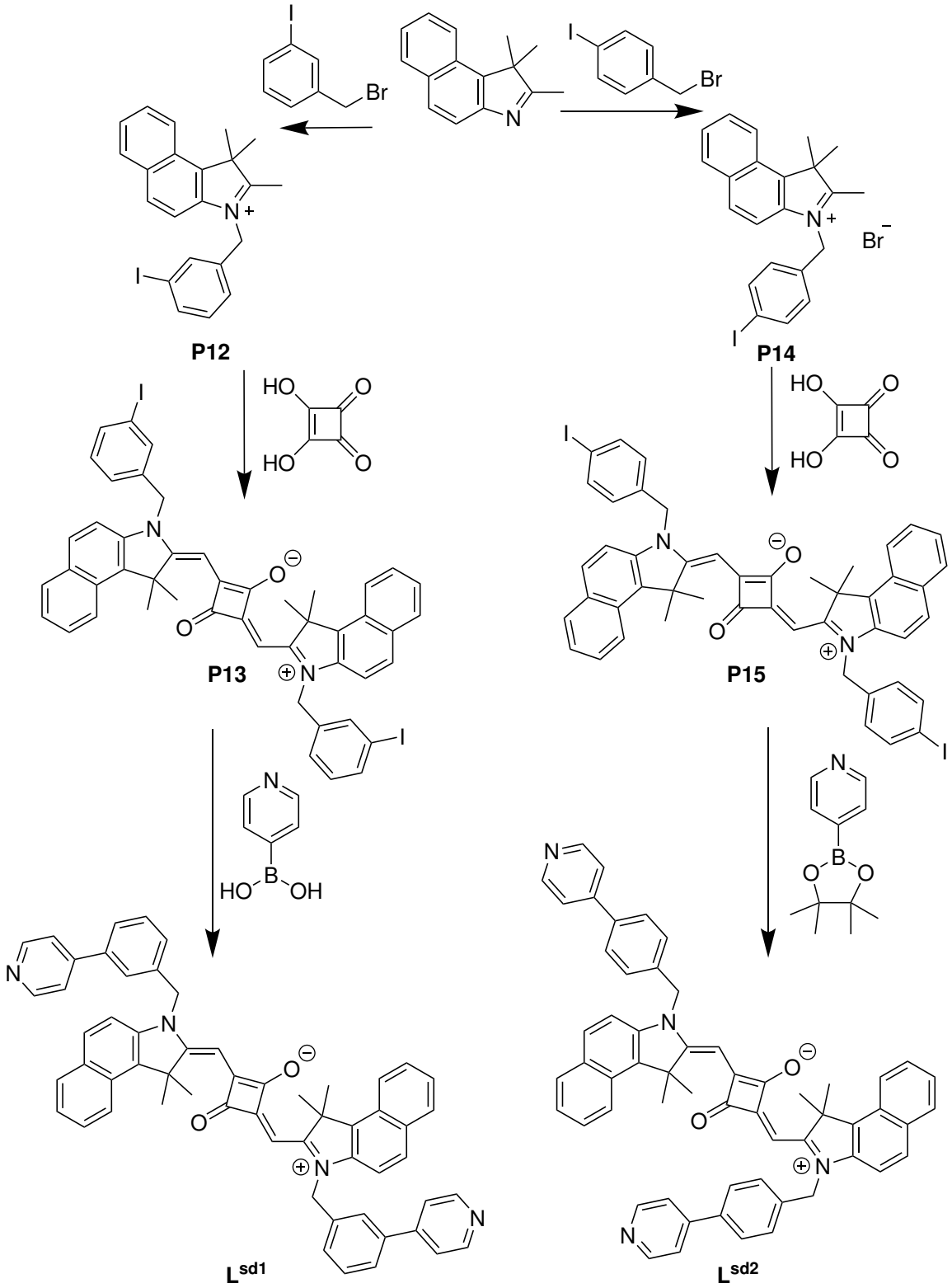

Figure 4.238. Illustration of indole-based squaraine dye ligands $\mathbf{L^{sd1}}$ and $\mathbf{L^{sd2}}$. Details about the synthesis can be found in chapter 4.2.11.

Then the homolpetic cage formation of $\mathbf{L^{sd1}}$ was examined in DMSO$-d_6$, CD_3CN and DMF$-d_7$ with different counterions. However, the cage formation

could be not observed, but mostlikely a chelate was formed since $r_{\mathrm{H}} = 9,24\,\text{Å}$, which is suportted by ESI-MS because a $[\mathrm{PdL_2}]^{2+}$ species was observed.

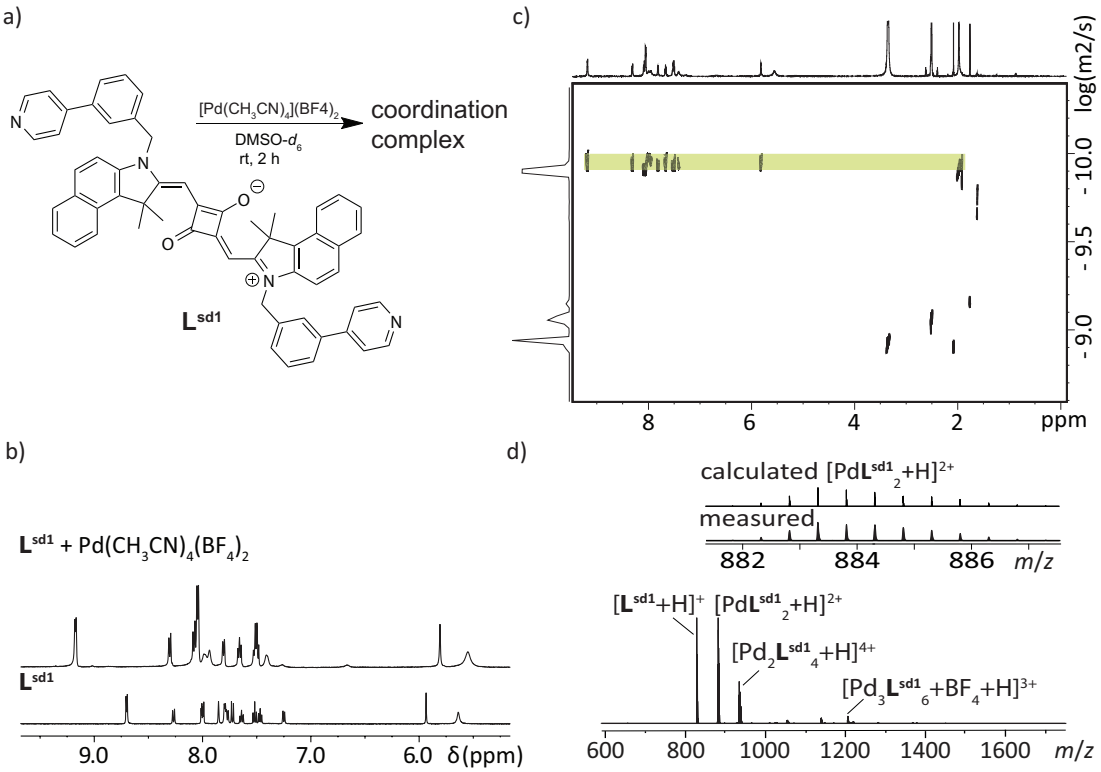

Figure 4.239. a) ESI-MS of cage formation of $\mathbf{L^{sd1}}$. b) ^{1}H DOSY NMR spectrum (500 MHz, 298 K) of the coordination cage formation experiment of $\mathbf{L^{sd1}}$. $D = 1,08 \cdot 10^{-10}\,\frac{\mathrm{m}^2}{\mathrm{s}}$, $r_{\mathrm{H}} = 9,24\,\text{Å}$.

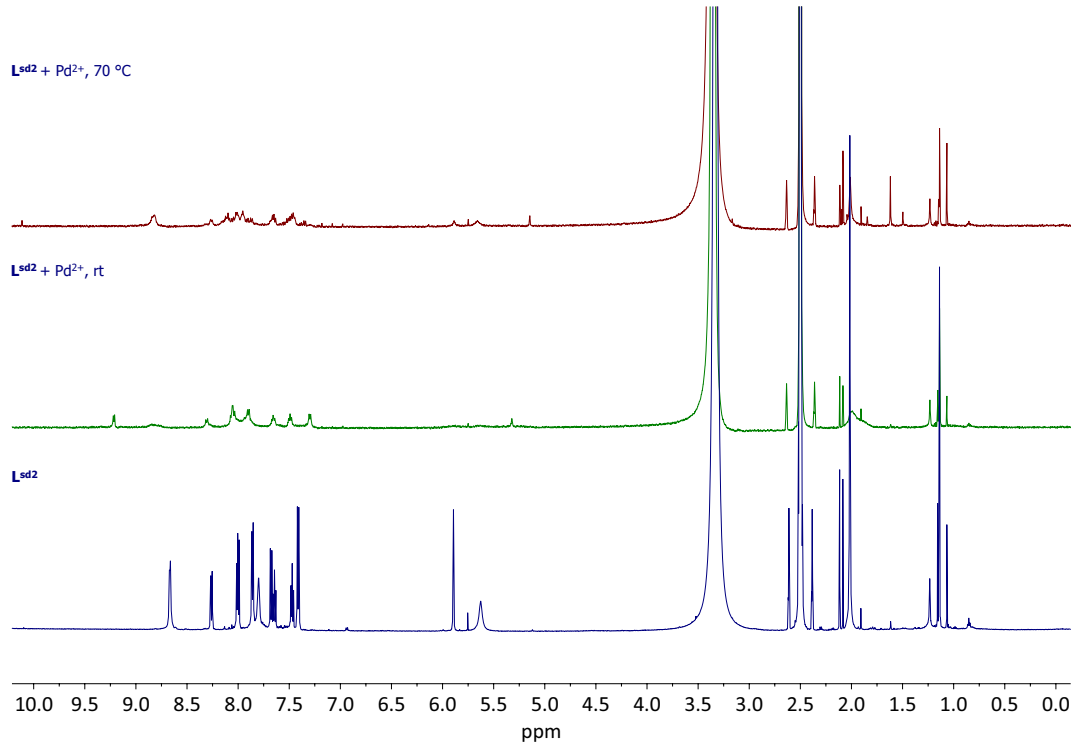

Figure 4.240. ^{1}H-NMR spectra (500 MHz, 298 K, DMSO$-d_6$) cage formation experiment of $\mathbf{L^{sd2}}$ with $Pd(NO_3)_2$. ESI-MS analysis did not suggest any coordination cage formation.

4.4.3 Heteroleptic Coordination Cage Formation with $\mathbf{L^B}$

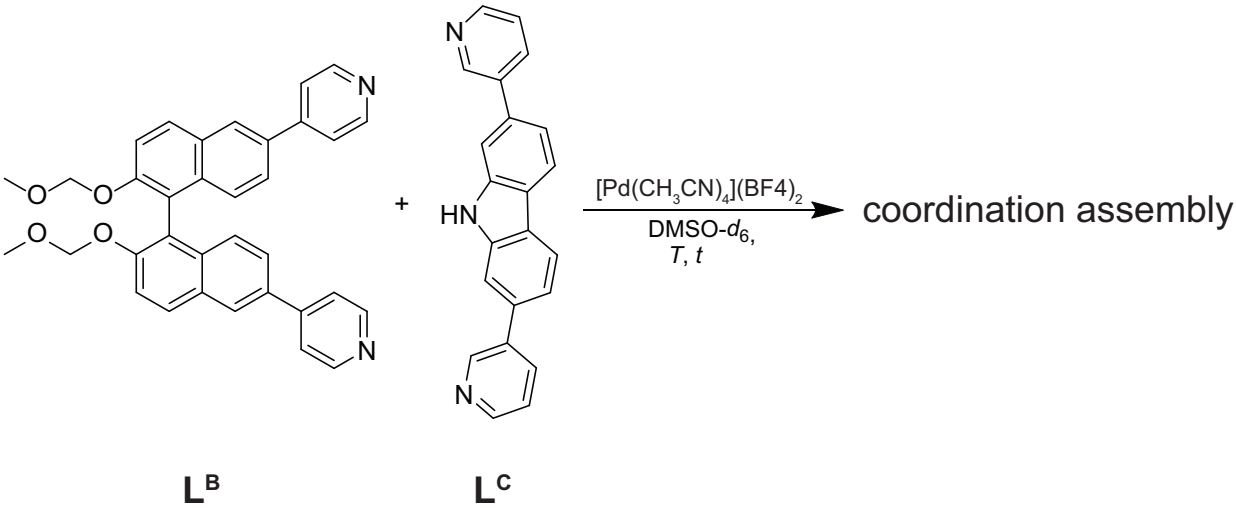

Figure 4.241. Heteroleptic coordination cage formation of $\mathbf{L^B}$ and $\mathbf{L^{LF}}$ in DMSO-d_6.

The heteroleptic cage formation with $[Pd(CH_3CN)_4](BF_4)_2$ was performed analogous to the previous heteroleptic cages. No signals could distinguished to a clear coordination cage formation.

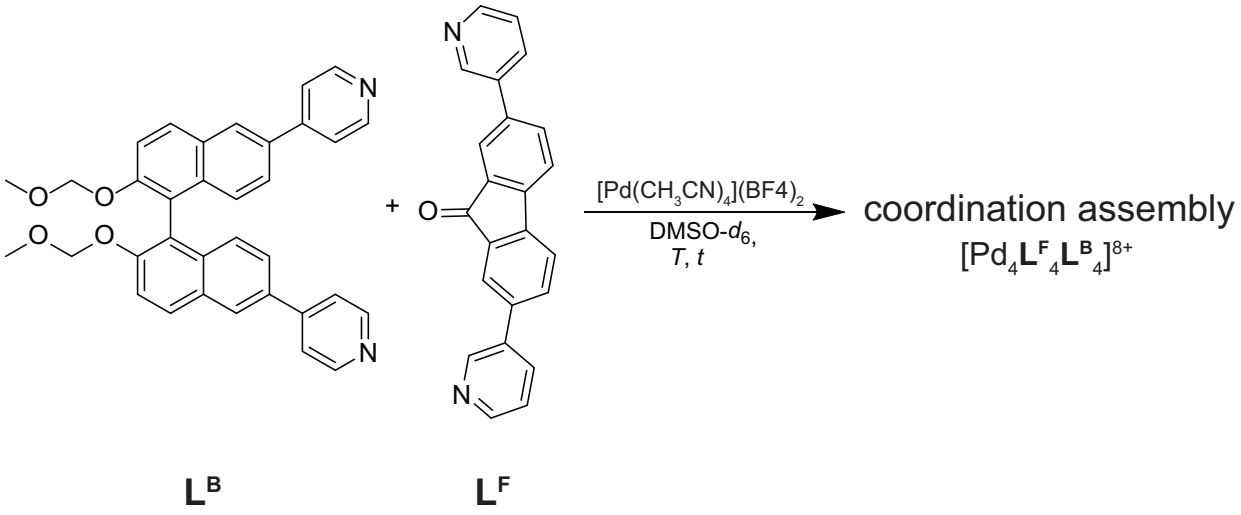

Figure 4.242. Heteroleptic coordination cage formation of $\mathbf{L^B}$ and $\mathbf{L^F}$ in DMSO-d_6.

The heteroleptic cage formation with $[Pd(CH_3CN)_4](BF_4)_2$ was performed analogous to the previous heteroleptic cages. ESI-MS showed 8+, 7+, 6+, 5+ and 4+ species.

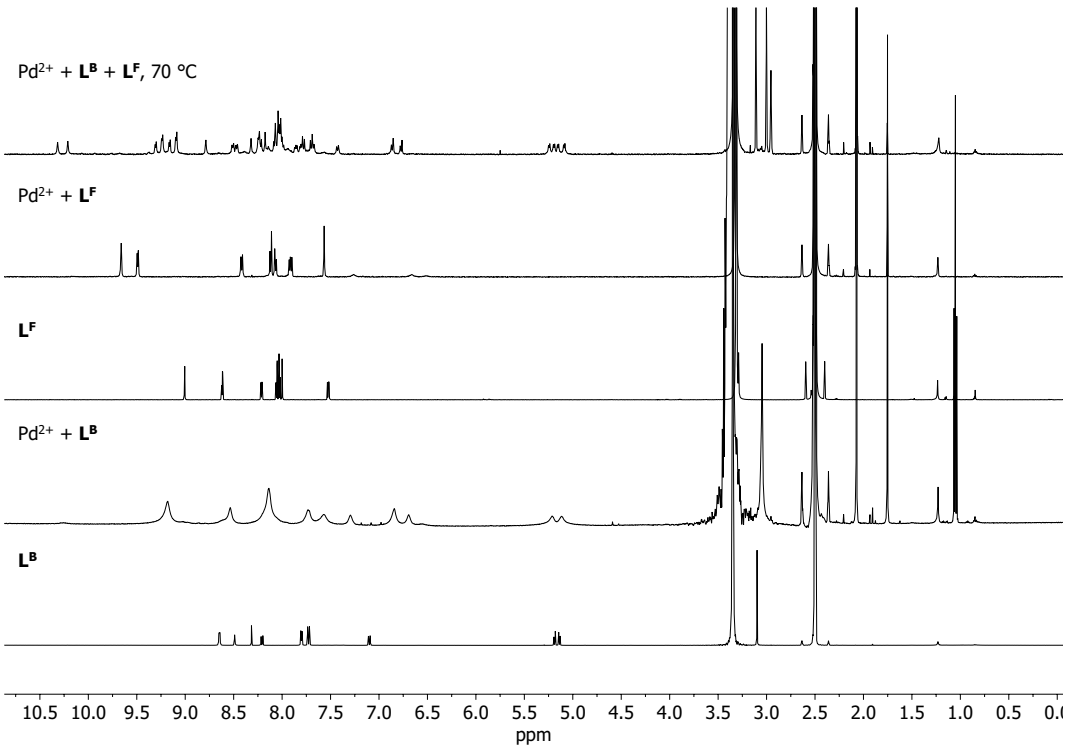

Figure 4.243. ^{1}H-NMR spectrum (500 MHz, 298 K, DMSO-d_6) of $\mathbf{L^B}$ and $\mathbf{L^F}$.

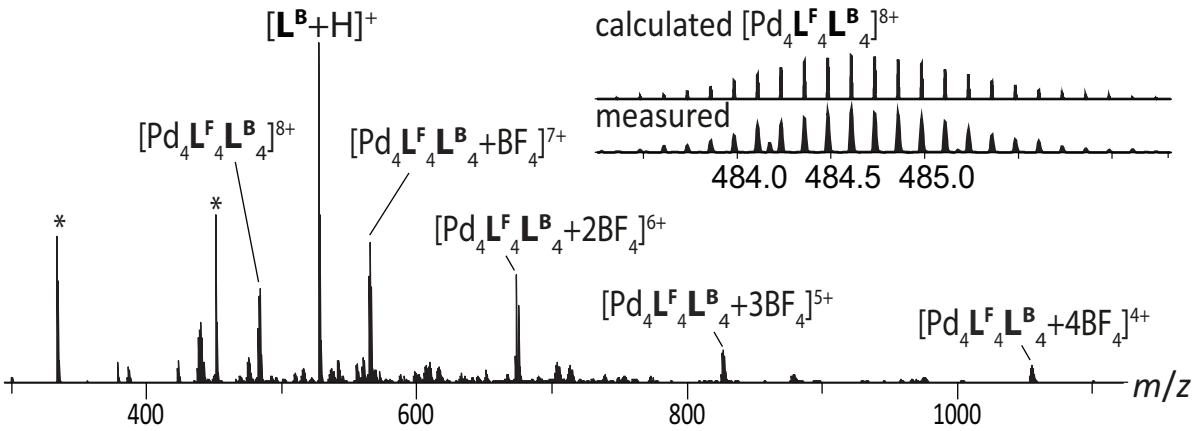

Figure 4.244. Illustration of ESI-MS of $[Pd_4\mathbf{L}^{\mathbf{B}}{}_4\mathbf{L}^{\mathbf{F}}{}_4]^{8+}$ in DMSO$-d_6$.

Part II

Strain Calculation Studies on Coordination Cages

This chapter consist of the previous work of my master thesis and build up on this. [293] Furthermore, the results of Simon Knüver from his "Wahlpflichtpraktikum" are a part of this chapter.

First the general theory of calculation will be briefly introduced and then strain calculation will be explained.

5 Theoretical Methods

Computational simulations are used to study and predict the behavior of complex systems and are widely applied in various fields, such as drug discovery, biotechnology, and toxicology. [294][295][296] They enable the simulation and analysis of biological, chemical, and physical processes without the need for extensive laboratory experiments. [295][297] Such as computer-based methods are called *in silico* models.

5.1 Molecular Geometry optimization

The geometry of an *in silico* molecular model must be optimized, because the initial structure often deviates from the ideal geometry. [298] Additionally, molecules can exist as different conformers. According to Boltzmann statistics, the lower the energy E of a conformer, the higher its probability of occurrence in an experiment. Consequently, minimizing the energy as a function of the nuclear coordinates is essential to identify the most appropriate conformer. [299]

5.1.1 Gradient Descent

The Gradient Descent (GD) method is a widely used algorithm for determining the local minimum of a molecule's potential energy surface.

The simplest case is a diatomic molecule, where energy depends solely on bond length. After selecting an initial bond length and computing its energy, the bond length is adjusted incrementally in one direction. If the energy decreases, adjustments continue in that direction. On the other hand, if the energy increases, the bond length is adjusted in the opposite direction. Ultimately, three adjacent points are identified, where the energy of the central point is lower than that of the other two. These three non-collinear points can be described using a parabola, whose minimum corresponds to the optimal bond length. By step-by-step refining the bond length to either side of the parabolic minimum, the energy can be reduced below a predefined threshold, signifying convergence. Higher-order polynomial equations can also be used by incorporating additional points and adapting step sizes based on previous data. [300]

In multi-dimensional cases, the parabolic minimum is found iteratively. For example, in a triatomic molecule such as LiOH, the process begins with optimizing the Li–O bond, followed by the O–H bond. The Li–O–H bond angle is then optimized while keeping the other two degrees of freedom fixed. This cycle is repeated until convergence is achieved. [300] However, in multi-dimensional systems, optimizing one coordinate at a time is inefficient. A more effective approach involves moving in the direction of the steepest descent of the energy,

which corresponds to the opposite direction of the gradient vector $\vec{g}$. The gradient vector is defined as:

$$\vec{g} = \left(\frac{\partial E}{\partial q_1} \; \frac{\partial E}{\partial q_2} \; \frac{\partial E}{\partial q_3} \; .... \; \frac{\partial E}{\partial q_n} \right)^{\mathrm{T}} \tag{5.1}$$

where q_i represents one coordinate of an atom and n is equal to $3N$ in a Cartesian coordinate system ($n = 3N$-6 in an internal coordinate system). Here, N denotes the number of atoms in the molecule. Depending on the chosen theoretical level, the gradient vector can be calculated numerically or analytically. Subsequently, all coordinates are adjusted in the direction opposite to the gradient vector by a specified step size. The energy of the updated structure is compared with that of the previous one, and the process is repeated until the energy difference falls below a defined convergence criterion. [300][301] It is important to note that GD identifies a local minimum rather than the global minimum. To locate multiple local minima, simulations are performed where the molecule is allowed to move freely within the boundaries of the chosen physical model. In such cases, the search algorithm must incorporate calculations that account for energy increases to overcome local energy barriers. [299]

5.2 Theoretical Models

In section 1.3, supramolecular coordination cages were introduced. These cages present significant challenges for accurate quantum mechanical methods due to their large size, which encompasses numerous degrees of freedom and, consequently, a multitude of local minima. Additionally, the presence of heavy transition metals further complicates the calculations, because relativistic effects must be taken into account. Moreover, metal-mediated supramolecular coordination cages require consideration of noncovalent interactions. To address the macromolecular effects as well as the influence of transition metals, a suitable theoretical model is essential. [299]

5.2.1 Molecular Mechanics

In classical mechanics, covalent bonds are modeled as springs with harmonic potentials, offering the advantage of low computational cost. The stretching of a bond as a harmonic oscillator is described by the function in equation 5.2:

$$V(l) = \frac{k}{2}(l - l_0)^2 \tag{5.2}$$

Here, l represents the internuclear distance, k is the force constant, l_0 is the equilibrium bond length, and $V(l)$ is the potential energy. Additionally, noncovalent interactions can be calculated pairwise by employing potential functions

that depend on distance. The combination of such parameters and functions constitutes a force field. Depending on the specific force field, different levels of specialization, accuracy, and computational cost can be achieved. However, a key limitation of this method is its inability to account for phenomena such as hyperconjugation and charge transfer. Therefore, molecular mechanics cannot account for chemical reactions. For these reasons, models based on quantum mechanical approaches are necessary.

5.2.2 Density Functional Theory

The quantum mechanical state of a non-relativistic system is described by the Schrödinger equation (equation 5.3). [302] However, the Schrödinger equation can only be solved exactly for systems with a single electron. Therefore, several approximations are required to extend its applicability to quantum systems with multiple electrons. The non-relativistic, time-independent Schrödinger equation is expressed as follows:

$$\hat{H}\Psi = E\Psi \tag{5.3}$$

Here, $\hat{H}$ denotes the Hamiltonian operator, Ψ represents the wave function and E is the energy of the system. Another widely used approach is *Density Functional Theory* (DFT). DFT is grounded in the first Hohenberg-Kohn theorem, which posits that the ground-state energy of a system is a functional of the electron density ρ. The second Hohenberg-Kohn theorem further asserts that the electron density that minimizes the total energy corresponds to the exact ground-state density, based on the variational principle. [303] Additionally, the Born-Oppenheimer approximation simplifies calculations by assuming that electronic motion can be treated independently of nuclear motion, as electrons move significantly faster than nuclei.

In DFT, the electron density ρ is determined from several Kohn-Sham single-electron orbitals ϕ_i. To properly account for the interactions between electrons, the exchange-correlation energy $E_{\mathrm{XC}}(\rho)$, is introduced as a functional of the electron density. This term is particularly important, because electrons are indistinguishable particles and interact with each other through Coulomb repulsion, which influences their spatial distribution and probability density. Therefore, selecting an appropriate approximation for E_{XC} is crucial to obtaining accurate and reliable results in DFT calculations.

An approximation for the orbitals ϕ_i can be made using a linear combination of a set of known hydrogenic orbitals. The choice of the set determines the total number of atomic orbitals in the linear combination, their extra features, such as polarization and their overall influence on the calculation. The polarization function accounts for electron density polarization. [300][301]

For DFT calculations, both the exchange-correlation functional and the basis set are required. The accuracy, specificity and computational cost of the calculation depend on these choices. The primary computational demand arises from the linear combinations and the associated coefficients for each Kohn-Sham orbital ϕ_i.

Although DFT methods often involve several parameters, they are generally categorized as *ab initio* methods because they do not rely on empirical data. In contrast, Hartree-Fock (HF) theory, another *ab initio* method, is entirely parameter-free. [304]

5.2.3 Quantum Mechanical Methods

Parameterized Model 6

The semiempirical quantum mechanical (SQM) method achieves a balance between the computational efficiency of force-field methods and the accuracy of *ab initio* methods. SQM employs a minimal basis set and approximates electron integrals while incorporating parameters derived from empirical data to compensate for errors inherent in Hartree-Fock theory or DFT. [305]

Derived from Hartree-Fock theory, the Parameterized Model Number 6 (PM6) includes parameterization for more than 80 elements. [306] Like DFT, Hartree-Fock theory applies the Born-Oppenheimer approximation and the variational principle. However, instead of focusing on electron density, Hartree-Fock theory uses a single Slater determinant to describe the exchange interaction of electrons. In this model, the Coulomb interaction between electrons is approximated as the interaction between each electron and the average charge field of all other electrons. Electron correlation effects, however, are not explicitly accounted for in Hartree-Fock theory. [300][301][304]

In this work, preliminary geometry optimization of structures was performed at the PM6 level to reduce the computation time for geometry optimization at a higher level.

ωB97X-D

As highlighted in section 1.2, non-covalent interactions are critically important in supramolecular chemistry. Therefore, a method that accurately accounts for these interactions is essential. The ωB97X-D functional of the DFT method incorporates empirical atom-atom dispersion corrections and demonstrates moderately better performance compared to well-established DFT-D functionals, such as B97-D, B3LYP-D, BLYP-D and ωB97. [307][308] This conclusion is based on evaluations using independent test data sets, which include atomization energies, reaction energies, non-covalent interaction energies, equilibrium geometries and charge-

transfer excited states. Overall, the long-range corrected ωB97X-D method consistently outperforms its predecessors in general performance. [308]

Beside ωB97 there is also ωB97X. It is worth mentioning that ωB97X is an improved version of ωB97, however, it still lacks explicit dispersion corrections. Nonetheless, ωB97X generally offers better accuracy than ωB97 due to its enhanced treatment of exchange interactions. [309]

A suitable method and basis set is chosen based on certain criteria such as accuracy and computational effort. After that, different studies can be performed based on strain. In section 5.3 the strain calculation will be introduced.

5.3 Strain Calculation

Strain is a measure of the internal stress due to deviations from ideal molecular geometry, particularly in macrocyclic molecules. [310] Strain plays a crucial role in bioorthogonal reactivity within chemical biology and in polymer chemistry during ring-opening metathesis. [311][312]

One of the most prominent methods for calculating strain energy in macrocycles involves comparing the heat of formation of a strained molecule with that of an unstrained counterpart in a theoretical strain-releasing reaction. [313] Here, strain energy represents the potential energy released upon breaking a macrocycle. [314] Hypothetical homodesmic and isodesmic reactions are well-established approaches for determining strain energy, owing to the straightforward accessibility of molecular structures and energy calculations. [313] In an isodesmic reaction, the number and types of bonds remain identical on both the reactant and product sides. A subset of isodesmic reactions, homodesmic reactions, further require the preservation of the number of carbon atoms in each hybridization state throughout the reaction. [313]

Notably, Cowell et al. reported a new computational method for determining strain energy in macrocycles, improving upon homodesmotic reactions by identifying individual strain contributions, such as bond length, bond angle and dihedral angle. [314] However, coordination systems are large and include a transition metal, making the calculations more complex and increasing computational cost.

Therefore, an alternative approach to calculating strain in coordination cages is desirable.

5.3.1 Approaches of Strain Calculations for Coordination Cages

As discussed in section 1.4, one well-known approach to forming coordination cages involves using banana-shaped bis-monodentate ligands with transition metal cations. A key factor influencing the self-assembly of coordination cages is strain, which primarily occurs within the ligands. Consequently, studying strain in self-

assembled coordination cages is essential. Furthermore, understanding the factors that affect the formation of these self-assembled coordination cages is crucial for designing new ones.

For instance, the Gibbs free energy is of significant importance to chemists, as it enables the prediction of the spontaneity of a chemical reaction under constant temperature and pressure. The relationship between the Gibbs free energy change (ΔG), temperature (T), entropy change (ΔS), and enthalpy change (ΔH) is expressed in equation 5.4. Strain contributes directly to the enthalpy of formation.

$$\Delta G = \Delta H - T\Delta S \tag{5.4}$$

The electronic energy (E) is a component of the enthalpy (H) and can be determined through the Zeropoint correction ($H - E$). Additionally, E can be calculated computationally. In cases where the number and type of bonds and atoms remain constant between reactants and products in a chemical reaction, the energy difference is primarily attributed to differences in strain. By assuming negligible entropy contributions and preserving the enthalpy contributions from intramolecular forces, covalent bonds and ionic bonds between reactants and products, the Zeropoint correction can also be disregarded in strain calculations. The energy difference (ΔE) is calculated as the difference between the sum of the electronic energies of the products and reactants and is account for strain change (see equation 5.5).

$$\Delta E = \sum E_{\text{product}} - \sum E_{\text{educt}} \tag{5.5}$$

In chapter 5.4, the approaches to determine the strain in coordination cages will be introduced.

5.4 Strain Calculations in Coordination Cages

As mentioned at the beginning of chapter 5.3, strain has primarily been studied in macrocyclic molecules. [314] However, as previously noted, strain is also expected to play an important role in coordination cage formation. In 2021, during my master's thesis, I began developing an approach to quantify strain and investigate heteroleptic cage formation focusing on the shape-complementarity approach. For this purpose, two methods were applied. [293]

One method to calculate the strain in self-assembled coordination cages involves comparing the electronic energy of a fully relaxed ligand with that of a ligand extracted from the formed coordination cage. This can be applied to both homoleptic and heteroleptic coordination cages. This approach enables a direct comparison of the strain experienced by ligands in their respective homoleptic cages and during heteroleptic cage formation (see a) in figure 5.1).

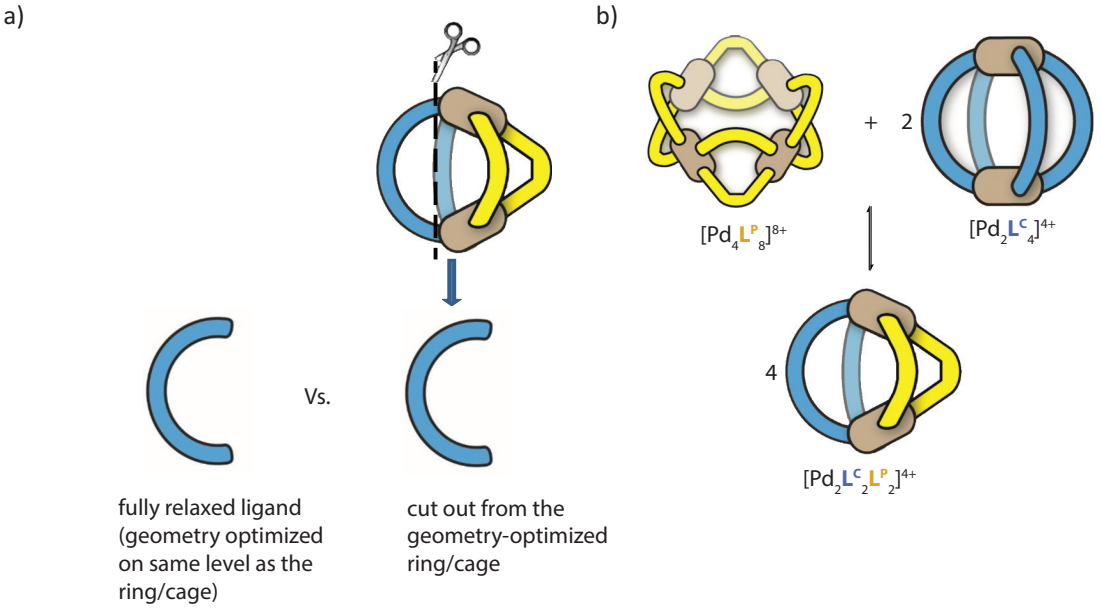

Figure 5.1. Illustration of approaches to determine strain at coordination cages: a) calculation of strain in heteroleptic coordination cages by comparing electronic energies of the fully relaxed ligand and the ligand, which is cut out from the heteroleptic coordination cage. b) cage-to-cage transformation of $[Pd_4\mathbf{L^P}_8]^{8+}$ and $[Pd_2\mathbf{L^C}_2]^{4+}$ to $[Pd_2\mathbf{L^C}_2\mathbf{L^P}_2]^{4+}$. [293]

Another approach to studying strain in self-assembled coordination cages is to determine the energy difference (ΔE) between reactants and products during a cage-to-cage transformation. [161] Figure 5.1 (b)) illustrates the cage-to-cage transformation of the homoleptic cage $[Pd_4\mathbf{L^P}_8]^{8+}$ of $\mathbf{L^P}$ and the homoleptic cage $[Pd_2\mathbf{L^C}_4]^{4+}$ of $\mathbf{L^C}$ into the heteroleptic cage $[Pd_2\mathbf{L^C}_2\mathbf{L^P}_2]^{4+}$. The energy difference primarily reflects the differences in strain and Coulomb repulsion between the species. To accurately attribute this energy difference to strain in the cage-to-cage transformation, Coulomb repulsion should be explicitly considered in the

strain calculation. In the following chapter 6, the previous studies on strain in coordination cages will be discussed.

6 Previous Studies on Strain by Calculations

6.1 Target and Motivation

In 2018, Kristina Ebbert demonstrated in her master's thesis that the extended ligand $\mathbf{L^{PL}}$, which incorporates an alkyne linker and $\mathbf{L^{C}}$ can form a heteroleptic cage. This work parallels the findings of Dr. Witold Bloch, as described in chapter 1.5.1. [315] In figure 6.1, a superposition of the crystal structures of the heteroleptic cages $[Pd_2\mathbf{L^{C}}_2\mathbf{L^{P}}_2]^{4+}$ and $[Pd_2\mathbf{L^{C}}_2\mathbf{L^{PL}}_2]^{4+}$ is depicted.

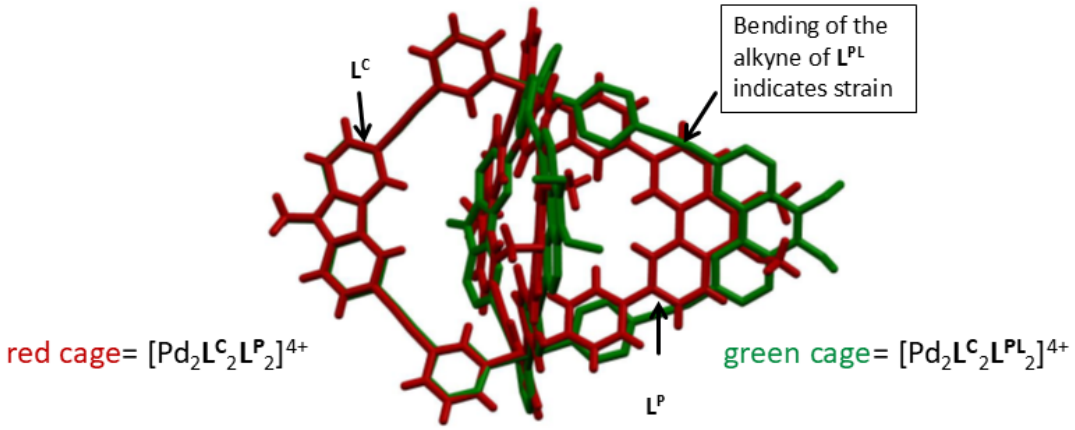

Figure 6.1. Superposition of the crystal structures of $[Pd_2\mathbf{L^{C}}_2\mathbf{L^{P}}_2]^{4+}$ and $[Pd_2\mathbf{L^{C}}_2\mathbf{L^{PL}}_2]^{4+}$ (hydrogen atoms are omitted for clarity). Picture adapted from [315].

Both systems form self-assembled heteroleptic cages, but the elongation of the phenanthrene-based ligand $\mathbf{L^{PL}}$ raises the question of whether strain influences the formation of heteroleptic cages. The superposition of the crystal structures in figure 6.1 suggests that $\mathbf{L^{PL}}$ likely bends to accommodate the heteroleptic coordination cage. This observation supports the hypothesis that $\mathbf{L^{PL}}$ experiences greater strain than $\mathbf{L^{P}}$ in the heteroleptic coordination cage.

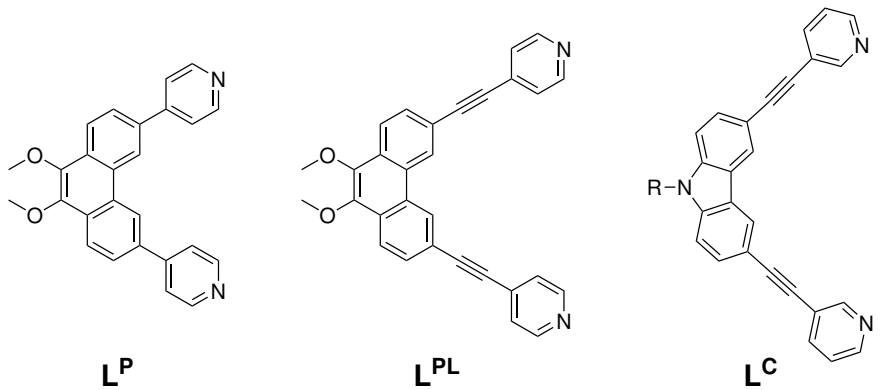

Figure 6.2. Illustration of the ligands $\mathbf{L^{P}}$, $\mathbf{L^{PL}}$ and $\mathbf{L^{C}}$. R= hexyl, but for the calculations it was substituted with a methyl group.

Therefore, the ligands $\mathbf{L^P}$, $\mathbf{L^{PL}}$, and $\mathbf{L^C}$, along with their respective coordination cage systems, were examined in my master's thesis and will be introduced in the following sections.

6.1.1 Consideration of Coulomb Repulsion

Before calculating the cage-to-cage transformations from the respective homoleptic species to the heteroleptic cages $[Pd_2\mathbf{L^C}_2\mathbf{L^P}_2]^{4+}$ and $[Pd_2\mathbf{L^C}_2\mathbf{L^{PL}}_2]^{4+}$, Coulomb repulsion was considered. This consideration is necessary, because the calculations were performed in the gas phase, where no solvent molecules and counter ions were considered. In solution, solvents and counter ions would compensate Coulomb repulsion. [316] To account for the Coulomb repulsion (Pd^{II}-Pd^{II} interactions) in the coordination cages, their energy contributions were determined (see figure 6.3).

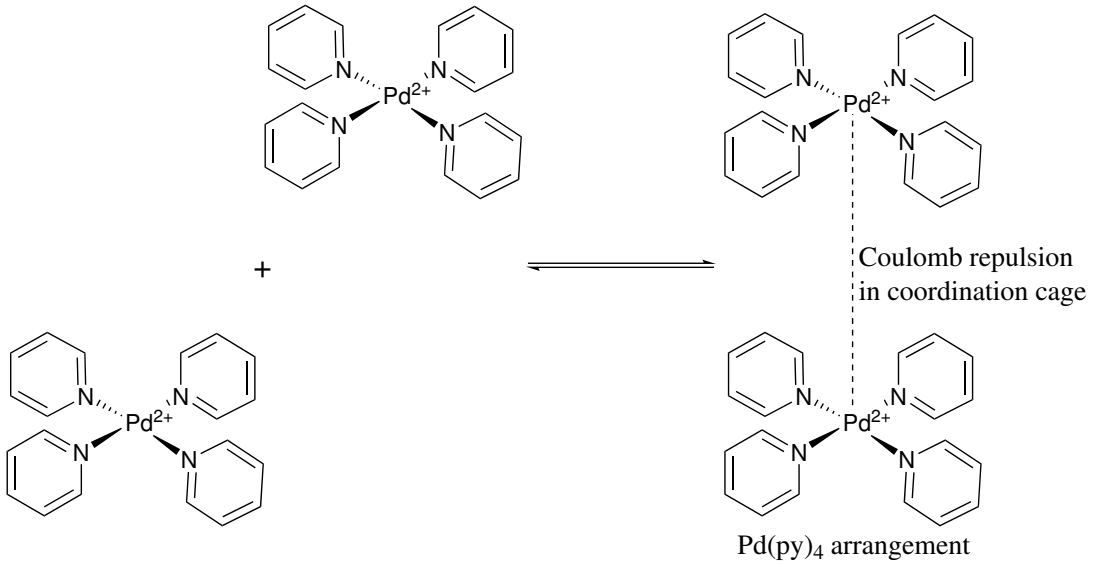

Figure 6.3. Illustration of Coulomb repulsion between $[Pd(py)_4]^{2+}$ of the coordination cages. Py= pyridine.

All bridging parts of the ωB97X-D/def2-SVP geometry-optimized rings and cages were deleted, leaving only the $[Pd(pyridine)_4]^{2+}$ units fixed in space. Truncated connections were saturated with hydrogen substituents. Single-point energies of these arrangements of $[Pd(pyridine)_4]^{2+}$ fragments were then calculated. The sum of the single-point energies of all individual $[Pd(pyridine)_4]^{2+}$ units for each ring or cage was subtracted from the total energy. The results aligned with expectations: Coulomb repulsion is proportional to the magnitude of the charges (see equation 6.1). Consequently, assemblies with higher nuclearity exhibited greater Coulomb repulsion due to the increased number of Pd(II) cations. [317] Another anticipated trend was the increase in Coulomb repulsion as Pd^{II}-Pd^{II} distances decreased in the heteroleptic cages. This is because Coulomb repulsion

is inversely proportional to the square of the distance between the charges, as described by Coulomb's law (see equation 6.1). [317]

$$\left|F_E\right| = k\left|\frac{q_1 q_2}{r^2}\right| \tag{6.1}$$

With electric force F_E, Coulomb´s law constant k (with $k = 9.0 \cdot 10^9 \frac{\mathrm{Nm}^2}{\mathrm{C}^2}$), charges q_1 and q_2 and the distance between the charges r.

The cage-to-cage transformation calculations, which included Coulomb repulsion, revealed that its contribution is significant. Thus, the Coulomb repulsion cannot be neglected, when calculating strain energy during cage-to-cage transformations in gas phase and without considering the solvent and counter ions. [293] After incorporating the Coulomb repulsion, the energy difference in the cage-to-cage transformation was determined. The estimated Coulomb repulsion of the assembled coordination cages was integrated into the strain energy calculations (see chapter 6.1.2).

6.1.2 Cage-to-cage Transformations

The cage-to-cage transformation to the heteroleptic coordination cages from the respective homoleptic cages $[Pd_2\mathbf{L^C}_4]^{4+}$, $[Pd_4\mathbf{L^P}_8]^{8+}$ and $[Pd_3\mathbf{L^{PL}}_6]^{6+}$ are shown in figure 6.4.

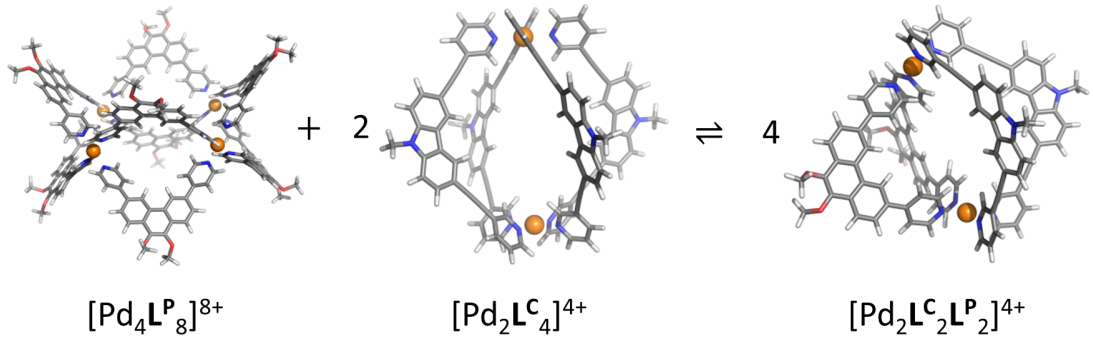

(a) Cage-to-cage transformation of $[Pd_4\mathbf{L^P}_8]^{8+}$ and $[Pd_2\mathbf{L^C}_4]^{4+}$ to $[Pd_2\mathbf{L^C}_2\mathbf{L^P}_2]^{4+}$.

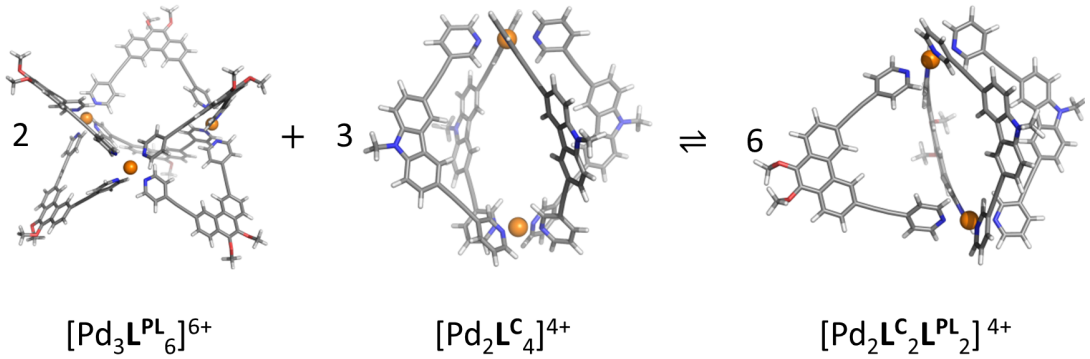

(b) Cage-to-cage transformation of $[Pd_3\mathbf{L^{PL}}_6]^{6+}$ and $[Pd_2\mathbf{L^C}_4]^{4+}$ to $[Pd_2\mathbf{L^C}_2\mathbf{L^{PL}}_2]^{4+}$.

Figure 6.4. Cage-to-cage transformation of geometry optimized structures at ωB97X-D/def2-SVP level (gas phase). Adapted from [293].

Using the single-point energies of the geometry-optimized structures at the ωB97X-D/def2-TZVP level (gas phase), the ΔE of the cage-to-cage transformation of $[Pd_2\mathbf{L^C}_2\mathbf{L^P}_2]^{4+}$ (see figure 6.4a) was calculated as shown in equation 6.2. Furthermore, the cage-to-cage transformation of $[Pd_2\mathbf{L^C}_2\mathbf{L^{PL}}_2]^{4+}$ (see figure 6.4b) is calculated as shown in equation 6.3 (Coulomb repulsion considered).

$$\begin{aligned}\Delta E([Pd_2\mathbf{L^C}_2\mathbf{L^P}_2]^{4+}) &= 2625.5\left(4\,[Pd_2\mathbf{L^C}_2\mathbf{L^P}_2]^{4+} - (2\,[Pd_2\mathbf{L^C}_4]^{4+} + [Pd_4\mathbf{L^P}_8]^{8+})\right)\\ &= -552.4\,\mathrm{kJ/mol}\end{aligned} \tag{6.2}$$

$$\begin{aligned}\Delta E([Pd_2\mathbf{L^C}_2\mathbf{L^{PL}}_2]^{4+}) &= 2625.5\left(6\,[Pd_2\mathbf{L^C}_2\mathbf{L^{PL}}_2]^{4+} - (3\,[Pd_2\mathbf{L^C}_4] + 2\,[Pd_3\mathbf{L^{PL}}_6]^{6+})\right)\\ &= -266.5\,\mathrm{kJ/mol}\end{aligned} \tag{6.3}$$

As demonstrated in equations 6.2 and 6.3, $[Pd_2\mathbf{L^C}_2\mathbf{L^P}_2]^{4+}$ is energetically more favorable than $[Pd_2\mathbf{L^C}_2\mathbf{L^{PL}}_2]^{4+}$. The difference in ΔE between $[Pd_2\mathbf{L^C}_2\mathbf{L^{PL}}_2]^{4+}$ and $[Pd_2\mathbf{L^C}_2\mathbf{L^P}_2]^{4+}$ is 285.8 kJ/mol, which likely accounts for the difference in strain. This indicates that $[Pd_2\mathbf{L^C}_2\mathbf{L^{PL}}_2]^{4+}$ suffers from greater strain compared to $[Pd_2\mathbf{L^C}_2\mathbf{L^P}_2]^{4+}$. One possible explanation is that the coordination angle of $\mathbf{L^{PL}}$ is less optimal, but the flexibility of the alkyne moiety allows for the formation of the heteroleptic coordination cage. On the other hand, $\mathbf{L^P}$ generally fits better into the heteroleptic cage consisting of $\mathbf{L^C}$.

The cage-to-cage transformation offers a straightforward way to investigate trends in coordination cage formation, which could aid in predicting and planning future coordination cage designs. However, this approach does not consider the solvent and counter ion, which can also influence the cage formation.
In 2024, Lewis et al. combined experimental and computational approaches to investigate heteroleptic coordination cage formation. Two sets of ligands, featuring converging and diverging coordination vectors, were systematically evaluated for integrative self-assembly with Pd(II), utilizing the well-established shape-complementarity approach.

The study focused on ligand size and coordination angle to successfully identify shape-complementary ligands. Additionally, a conformational analysis was performed, followed by single-point energy (SPE) calculations, which were used to determine the energy differences between heteroleptic and homoleptic coordination cages. This methodology was analogous to the cage-to-cage approach, but the Coulomb repulsion was not considered. Lewis et al. demonstrated that some heteroleptic coordination cage formations were supported by their calculations. However, they also noted discrepancies between computational predictions and experimental observations, attributing these inconsistencies to the omission of factors such as entropy, solvent effects, counterions and conformational flexibility. [318]

To obtain more precise insights into the strain within a coordination cage, further investigation is necessary. In 2021, in my master's thesis, I also explored strain by comparing the respective ligands to gain a clearer understanding of where the strain is localized within the heteroleptic coordination cage.

6.1.3 Comparison of Respective Ligands

An alternative approach to studying strain in self-assembled coordination cages is to examine the ligands individually. In this approach, the single-point energies of the fully relaxed ligands and the ligands extracted from the optimized cages (with atoms locked in space) were compared to assess the strain induced in the ligands during cage assembly. The entropic contributions were neglected and the electronic energies were calculated in the gas phase.

Table 6.1: Calculated single point energies at def2-TZVP level. The respective cages were geometry optimized at ωB97X-D/def2-SVP level. Adapted from [293].

free ligand (fully relaxed)	ligand cut out from cage	strain per ligand / kJ/mol ($E_{\text{ligand cut out}} - E_{\text{free ligand}}$)
$\mathbf{L^C}$	$[Pd_2\mathbf{L^C}_4]^{4+}$	8.3
	$[Pd_2\mathbf{L^C}_2\mathbf{L^P}_2]^{4+}$	7.8
	$[Pd_2\mathbf{L^C}_2\mathbf{L^{PL}}_2]^{4+}$	7.2
$\mathbf{L^P}$	$[Pd_4\mathbf{L^P}_8]^{8+}$	12.9
	$[Pd_2\mathbf{L^C}_2\mathbf{L^P}_2]^{4+}$	8.7
$\mathbf{L^{PL}}$	$[Pd_3\mathbf{L^{PL}}_6]^{6+}$	13.0
	$[Pd_2\mathbf{L^C}_2\mathbf{L^{PL}}_2]^{4+}$	14.4

The carbazole-based ligand $\mathbf{L^C}$ experiences more strain in the homoleptic cage $[Pd_2\mathbf{L^C}_4]^{4+}$ than in the heteroleptic cages $[Pd_2\mathbf{L^C}_2\mathbf{L^{PL}}_2]^{4+}$ and $[Pd_2\mathbf{L^C}_2\mathbf{L^P}_2]^{4+}$, with strain per ligand decreasing from 8.3 kJ/mol to 7.8 kJ/mol and 7.2 kJ/mol, respectively.

The short phenanthrene ligand $\mathbf{L^P}$ shows a significant decrease in strain, with a reduction of 4.2 kJ/mol from the homoleptic cage $[Pd_4\mathbf{L^P}_8]^{8+}$ to the heteroleptic cage $[Pd_2\mathbf{L^C}_2\mathbf{L^P}_2]^{4+}$.

In contrast, the long phenanthrene ligand $\mathbf{L^{PL}}$ experiences an increase in strain of 1.4 kJ/mol from the homoleptic cage $[Pd_3\mathbf{L^{PL}}_6]^{6+}$ to the heteroleptic cage $[Pd_2\mathbf{L^C}_2\mathbf{L^{PL}}_2]^{4+}$.

It appears that $\mathbf{L^C}$ and $\mathbf{L^P}$ prefer the heteroleptic cages over homoleptic cages to minimize strain. Furthermore, table 6.1 shows that the strain on $\mathbf{L^{PL}}$ increases from the homoleptic cage to the heteroleptic cages. This supports the hypothesis that $\mathbf{L^{PL}}$ must bend to fit into the heteroleptic cage, while $\mathbf{L^P}$ fits more easily.

Additionally, in $[Pd_3\mathbf{L^{PL}}_6]^{6+}$ six ligands of $\mathbf{L^{PL}}$ experience strain, while in $[Pd_2\mathbf{L^{C}}_2\mathbf{L^{PL}}_2]^{4+}$ only two ligands $\mathbf{L^{PL}}$ are strained. Therefore, in total $\mathbf{L^{PL}}$ suffers less strain in the heteroleptic cage than in the homoleptic coordination cage.

So far, two approaches have been introduced in my master's thesis to assess strain in coordination cages: in chapter 6.1.3, strain per ligand was calculated directly (see table 6.1), while in chapter 6.1.2, strain was derived from the energy difference between reactants and products in the cage-to-cage transformation, based on the electronic energies of the respective coordination cages.

Furthermore, the two approaches were combined. This will be explained in chapter 6.1.4, where the energy difference between reactants and products in the cage-to-cage transformation is determined by calculating the respective coordination cage using the summed strain per ligand from table 6.1.

6.1.4 Cage-to-cage Transformation with Balanced Ligands

After examining the ligands individually, the strain per ligand was balanced for the cage-to-cage transformation of the homoleptic species to the heteroleptic cages (see figure 6.4 for the cage-to-cage transformation).

Equations 6.4 and 6.5 show the calculations for the resulting cage-to-cage transformation into the heteroleptic cages with balanced ligands. For this, the strain per ligand energies in kJ/mol from table 6.1 were used for the balancing. Here, $\mathbf{L^{C'}}$ represents the carbazole-based ligand from $[Pd_2\mathbf{L^{C}}_2\mathbf{L^{P}}_2]^{4+}$, and $\mathbf{L^{C''}}$ represents the carbazole-based ligand from $[Pd_2\mathbf{L^{C}}_2\mathbf{L^{PL}}_2]^{4+}$.

$$\begin{aligned}\Delta E([Pd_2\mathbf{L^{C}}_2\mathbf{L^{P}}_2]^{4+}) &= \Big(4\,[2\,E(\mathbf{L^{C'}}) + 2\,E(\mathbf{L^{P}})] - (2\,[4\,E(\mathbf{L^{C}})] + [8\,E(\mathbf{L^{P}})])\Big)\\ &= \Big(4[2\cdot 7.8 + 2\cdot 8.7] - (2[4\cdot 8.3] + [8\cdot 12.9])\Big)\,\mathrm{kJ/mol}\\ &= -37.6\,\mathrm{kJ/mol}\end{aligned} \tag{6.4}$$

$$\begin{aligned}\Delta E([Pd_2\mathbf{L^{C}}_2\mathbf{L^{PL}}_2]^{4+}) &= \Big(6\,[2\,E(\mathbf{L^{C''}}) + 2\,E(\mathbf{L^{PL}})] - (3\,[4\,E(\mathbf{L^{C}})] + 2\,[6\,E(\mathbf{L^{PL}})])\Big)\\ &= \Big(6[2\cdot 7.2 + 2\cdot 14.4] - (3[4\cdot 8.3] + 2[6\cdot 13.0])\Big)\,\mathrm{kJ/mol}\\ &= 3.6\,\mathrm{kJ/mol}\end{aligned} \tag{6.5}$$

This analysis showed that the cage-to-cage transformation from homoleptic to heteroleptic cages is energetically more favorable for the resulting $[Pd_2\mathbf{L^{C}}_2\mathbf{L^{P}}_2]^{4+}$ than for $[Pd_2\mathbf{L^{C}}_2\mathbf{L^{PL}}_2]^{4+}$. This is because $\mathbf{L^{P}}$ reduces strain in the heteroleptic cage compared to the homoleptic cage. This observation aligns with the results obtained from previous approaches. However, the formation of $[Pd_2\mathbf{L^{C}}_2\mathbf{L^{PL}}_2]^{4+}$ is not strain-favorable, as it incurs strain of 3.6 kJ/mol. In this approach, Coulomb repulsion was not considered in the cage-to-cage transformation, because the

strain of the respective coordination cages were calculated by summing the strain contributions of the individual ligands.

The combined approach supported the hypothesis that $[Pd_2\mathbf{L^C}_2\mathbf{L^P}_2]^{4+}$ experiences less strain than $[Pd_2\mathbf{L^C}_2\mathbf{L^{PL}}_2]^{4+}$. It also demonstrated that strain plays a significant role in the self-assembly of coordination cages.

In summary, my master thesis demonstrated that the cage-to-cage transformation approach revealed a substantial influence of Coulomb repulsion on the process. Moreover, this approach indicated a preference for the formation of heteroleptic coordination cages $[Pd_2\mathbf{L^C}_2\mathbf{L^{PL}}_2]^{4+}$ and $[Pd_2\mathbf{L^C}_2\mathbf{L^P}_2]^{4+}$. These findings support the hypothesis, derived from the superposition of the crystal structures of $[Pd_2\mathbf{L^C}_2\mathbf{L^P}_2]^{4+}$ and $[Pd_2\mathbf{L^C}_2\mathbf{L^{PL}}_2]^{4+}$, that the heteroleptic coordination cage containing the elongated ligand $\mathbf{L^{PL}}$ experiences greater strain compared to the cage with the more shape-complementary ligand $\mathbf{L^P}$. Additionally, the ligand-cutting approach confirmed this hypothesis by showing that $\mathbf{L^P}$ alleviates strain in the heteroleptic cage, while $\mathbf{L^{PL}}$ increases strain when paired with $\mathbf{L^C}$. Furthermore, this method revealed that $\mathbf{L^C}$ releases strain at the formation from homoleptic to heteroleptic cages. Finally, a third approach was introduced, combining the cage-to-cage transformation method with the ligand-specific strain calculations. This combined method also confirmed that $[Pd_2\mathbf{L^C}_2\mathbf{L^{PL}}_2]^{4+}$ experiences greater strain than $[Pd_2\mathbf{L^C}_2\mathbf{L^P}_2]^{4+}$.

This work contributes to the expanding study of strain in heteroleptic coordination cages and provides a foundation for investigating additional heteroleptic cage systems with respect to strain. Gas-phase electronic energies will be calculated and compared in a manner analogous to the methods used in this chapter.

7 Results and Discussion

7.1 Strain Calculations

Strain is a crucial factor influencing the self-assembly of coordination cages, primarily occurring within the ligands. To calculate strain, two approaches were detailed in chapter 5.3. The electronic energies were determined in the gas phase without considering counterions.

This chapter expands the study of strain in heteroleptic coordination cages by replacing ligand $\mathbf{L^C}$ with an acridone-based ligand ($\mathbf{L^A}$) and the inverted ligand of $\mathbf{L^C}$ ($\mathbf{L^{IC}}$). For the strain calculations in self-assembled coordination cages, ligands $\mathbf{L^P}$, $\mathbf{L^{PL}}$, $\mathbf{L^{IC}}$ and $\mathbf{L^A}$ were used (see figure 7.1). The respective coordination cages were reported by Clever et al.. [145][315][183] While the homoleptic cage of $\mathbf{L^A}$ was discussed in chapter 1.5.1, no distinct homoleptic cage formation of $\mathbf{L^{IC}}$ has been reported. However, due to its structural similarity to $\mathbf{L^A}$, a $[Pd_2\mathbf{L^{IC}}_4]^{4+}$ cage was assumed as the starting point for this study.

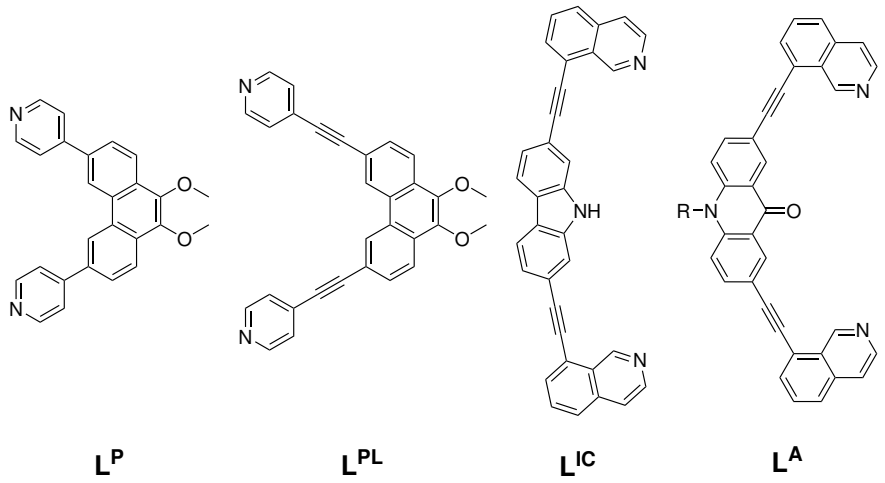

Figure 7.1. Illustration of the ligands $\mathbf{L^P}$, $\mathbf{L^{PL}}$, $\mathbf{L^{IC}}$ and $\mathbf{L^A}$. R= hexyl, but for the calculations it was substituted with a methyl group.

As highlighted in chapter 6.1, Coulomb repulsion must be considered when calculating strain in self-assembled coordination cages via cage-to-cage transformations in the gas phase. Consistent with the methodology described in chapter 6.1, Coulomb repulsion (Pd^{II}-Pd^{II} interaction) was determined for each coordination cage, with the results summarized in tables 7.1 and 7.2.

Table 7.1: Calculated single point energies at ωB97X-D4/def2-TZVP level. Calculated values in kJ/mol. Pd_{diff} is the difference of $Pd(x)_4$ arrangement and sum of isolated $Pd(x)_4$ units. x is respective a pyridine or quinoline group.

	$[Pd_2\mathbf{L^C}_4]^{4+}$	$[Pd_4\mathbf{L^P}_8]^{8+}$	$[Pd_3\mathbf{L^{PL}}_6]^{6+}$	$[Pd_2\mathbf{L^C}_2\mathbf{L^P}_2]^{4+}$	$[Pd_2\mathbf{L^C}_2\mathbf{L^{PL}}_2]^{4+}$
$Pd(py)_4$ arrangement	-5888627.3	-11775026.1	-8832100.1	-5888493.4	-5884420.8
Sum of $Pd(x)_4$ units	-5888994.6	-11777330.3	-8833243.1	-5888955.1	-5884841.7
Pd_{diff}	367.3	2304.2	1143.0	461.7	422.9

For geometry optimization, the theoretical level ωB97X/def2-SVP was employed. The inclusion of dispersion corrections led to unexpected π-stacking interactions between the backbones of $\mathbf{L^A}$ and $\mathbf{L^{PL}}$ within their respective coordination cages, resulting in a deviation from the reported arrangement of ligands in the reported heteroleptic cage. [315] Consequently, all energies for the previously studied coordination cages were recalculated using this updated theoretical level (see table 7.1) Coulomb repulsion for the coordination cages of $\mathbf{L^A}$ and $\mathbf{L^{IC}}$ is provided in table 7.2.

Table 7.2: Calculated single point energies at ωB97X-D4/def2-TZVP level. Calculated values in kJ/mol. Respective coordination cage illustrated in figure 7.2.

	$[Pd_2\mathbf{L^{IC}}_4]^{4+}$	$[Pd_2\mathbf{L^{IC}}_2\mathbf{L^{P}}_2]^{4+}$	$[Pd_2\mathbf{L^{IC}}_2\mathbf{L^{PL}}_2]^{4+}$	$[Pd_2\mathbf{L^{A}}_4]^{4+}$	$[Pd_2\mathbf{L^{A}}_2\mathbf{L^{P}}_2]^{4+}$	$[Pd_2\mathbf{L^{A}}_2\mathbf{L^{PL}}_2]^{4+}$
$Pd(x)_4$ arrangement	-9118582.2	-7503359.7	-7503564.9	-9118514.6	-7503508.4	-7503416.5
Sum of $Pd(x)_4$ units	-9118874.0	-7503765.6	-7503929.3	-9118877.7	-7503923.3	-7503785.0
Pd_{diff}	291.8	405.9	364.4	363.1	414.9	368.5

Tables 7.1 and 7.2 confirm the trend observed in previous work: Coulomb repulsion in coordination cages increases with higher nuclearity and shorter Pd^{II}-Pd^{II} distances. Thus, the Coulomb repulsion in $[Pd_4\mathbf{L^P}_8]^{8+}$ and $[Pd_3\mathbf{L^{PL}}_6]^{6+}$ is significantly higher than in the other assemblies. Furthermore, heteroleptic coordination cages incorporating the elongated ligand $\mathbf{L^{PL}}$ exhibit lower Coulomb repulsion than those with the shorter ligand $\mathbf{L^P}$. These results align with Coulomb's law, as discussed in chapter 6.1. [317]

Equation 7.1 presents the release of Coulomb repulsion during the cage-to-cage transformation of $[Pd_2\mathbf{L^C}_2\mathbf{L^P}_2]^{4+}$.

$$4\,[Pd_2\mathbf{L^C}_2\mathbf{L^P}_2]^{4+} - (2\,[Pd_2\mathbf{L^C}_4]^{4+} + [Pd_4\mathbf{L^P}_8]^{8+}) = -1192.0\,\mathrm{kJ/mol} \tag{7.1}$$

Release of Coulomb repulsion in the cage-to-cage transformation of $[Pd_2\mathbf{L^C}_2\mathbf{L^{PL}}_2]^{4+}$ was also determined by using equation 7.2.

$$6\,[Pd_2\mathbf{L^C}_2\mathbf{L^{PL}}_2]^{4+} - (3\,[Pd_2\mathbf{L^C}_4]^{4+} + 2\,[Pd_3\mathbf{L^{PL}}_6]^{6+}) = -850.3\,\mathrm{kJ/mol} \tag{7.2}$$

Similarly, the release of Coulomb repulsion during the cage-to-cage transformations involving $\mathbf{L^{IC}}$ and $\mathbf{L^A}$ was determined, with the values summarized in table 7.3.

Table 7.3: Calculated release of Coulomb repulsion (CR) per cage in kJ/mol with Pd_{diff} values (tables 7.1 and 7.2) with equations 7.1 and 7.2.

	$[Pd_2\mathbf{L^C}_2\mathbf{L^P}_2]^{4+}$	$[Pd_2\mathbf{L^C}_2\mathbf{L^{PL}}_2]^{4+}$	$[Pd_2\mathbf{L^{IC}}_2\mathbf{L^P}_2]^{4+}$	$[Pd_2\mathbf{L^{IC}}_2\mathbf{L^{PL}}_2]^{4+}$	$[Pd_2\mathbf{L^A}_2\mathbf{L^P}_2]^{4+}$	$[Pd_2\mathbf{L^A}_2\mathbf{L^{PL}}_2]^{4+}$
Release of CR	-298.0	-141.7	-316.1	-162.5	-342.7	-194.0

Table 7.3 illustrates that, for cage-to-cage transformations involving $\mathbf{L^C}$, $\mathbf{L^A}$ and $\mathbf{L^{IC}}$, the heteroleptic cages with $\mathbf{L^P}$ are energetically more favorable compared to those with $\mathbf{L^{PL}}$.

After calculating Coulomb repulsion, the energy differences in the cage-to-cage transformations were determined, incorporating the calculated Coulomb repulsion of the coordination cages as detailed in chapter 7.1.1.

7.1.1 Cage-to-cage Transformations

The cage-to-cage transformation of $[Pd_2\mathbf{L^A}_4]^{4+}$ and $[Pd_2\mathbf{L^{LIC}}_4]^{4+}$ with $[Pd_4\mathbf{L^P}_8]^{8+}$ to the respective heteroleptic cage are shown in figure 7.2.

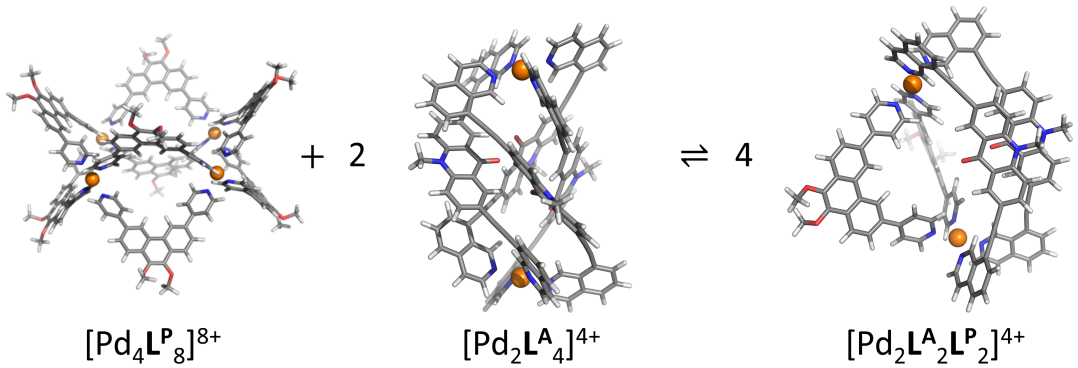

(a) Cage-to-cage transformation of $[Pd_4\mathbf{L^P}_8]^{8+}$ and $[Pd_2\mathbf{L^A}_4]^{4+}$ to $[Pd_2\mathbf{L^A}_2\mathbf{L^P}_2]^{4+}$.

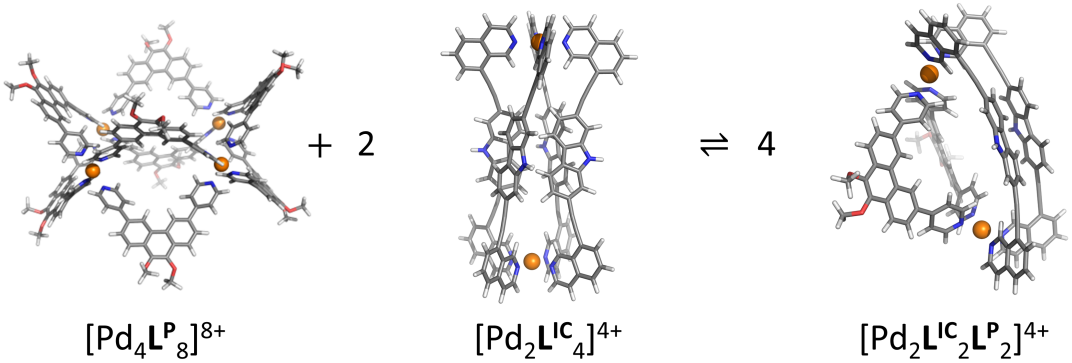

(b) Cage-to-cage transformation of $[Pd_4\mathbf{L^P}_8]^{8+}$ and $[Pd_2\mathbf{L^{IC}}_4]^{4+}$ to $[Pd_2\mathbf{L^{IC}}_2\mathbf{L^P}_2]^{4+}$.

Figure 7.2. Cage-to-cage transformation of geometry optimized structures at ωB97X/def2-SVP level (gas phase).

The respective cage-to-cage transformation with $[Pd_3\mathbf{L^{PL}}_6]^{6+}$ is shown in figure 7.8 in chapter 7.1.5. The obtained single-point energies for the corresponding coordination cages of the geometry-optimized structures at the ωB97X/def2-SVP level (gas phase) are presented in table 7.10 in chapter 7.1.5. ΔE of the cage-to-cage transformation of $[Pd_2\mathbf{L^C}_2\mathbf{L^P}_2]^{4+}$ (see figure 6.2) is calculated as shown in equation 7.3 and of $[Pd_2\mathbf{L^C}_2\mathbf{L^{PL}}_2]^{4+}$ (see figure 6.3) is calculated as shown in equation 7.4 (Coulomb repulsion considered).

$$\begin{aligned}\Delta E([Pd_2\mathbf{L^C}_2\mathbf{L^P}_2]^{4+}) &= 2625.5\left(4\,[Pd_2\mathbf{L^C}_2\mathbf{L^P}_2]^{4+} - (2\,[Pd_2\mathbf{L^C}_4]^{4+} + [Pd_4\mathbf{L^P}_8]^{8+})\right)\\ &= -553.7\,\mathrm{kJ/mol}\end{aligned} \tag{7.3}$$

$$\Delta E([\mathrm{Pd_2}\mathbf{L^C}_2\mathbf{L^{PL}}_2]^{4+}) = 2625.5\left(6\,[\mathrm{Pd_2}\mathbf{L^C}_2\mathbf{L^{PL}}_2]^{4+} - (3\,[\mathrm{Pd_2}\mathbf{L^C}_4] + 2\,[\mathrm{Pd_3}\mathbf{L^{PL}}_6]^{6+})\right)$$
$$= -263.9\,\mathrm{kJ/mol} \tag{7.4}$$

Equation 7.3 and equation 7.4 show that $[\mathrm{Pd_2}\mathbf{L^C}_2\mathbf{L^P}_2]^{4+}$ is energy-wise more favored than $[\mathrm{Pd_2}\mathbf{L^C}_2\mathbf{L^{PL}}_2]^{4+}$. In addition to that, the difference of ΔE which is calculated with $\Delta E([\mathrm{Pd_2}\mathbf{L^C}_2\mathbf{L^{PL}}_2]^{4+}) - \Delta E([\mathrm{Pd_2}\mathbf{L^C}_2\mathbf{L^P}_2]^{4+})$ equates to 289.8 kJ/mol, which should account for the difference in strain. So the trend for the single point energies of the coordination cages with and without dispersion correction at geometry optimization is the same (see chapter 6.1.2). Thereby the determined strain difference between difference of ΔE is 4 kJ/mol. So, calculating strain without the dispersion correction shows no significant difference at the cage-to-cage transformation of $\mathbf{L^C}$-based heteroleptic cages.

ΔE of the cage-to-cage transformation of the $\mathbf{L^A}$- and $\mathbf{L^{IC}}$-based heterolepic coordination cages are shown in table 7.4

Table 7.4: Calculated cage-to-cage transformation energy of respective heteroleptic cage. Single point energies calculated at ωB97X-D4/def2-TZVP level (gas phase).

$\Delta E([\mathrm{Pd_2}\mathbf{L^A}_2\mathbf{L^P}_2]^{4+})$	$\Delta E([\mathrm{Pd_2}\mathbf{L^A}_2\mathbf{L^{PL}}_2]^{4+})$	$\Delta E([\mathrm{Pd_2}\mathbf{L^{IC}}_2\mathbf{L^P}_2]^{4+}$	$\Delta E([\mathrm{Pd_2}\mathbf{L^{IC}}_2\mathbf{L^{PL}}_2]^{4+})$
-619.5 kJ/mol	-275.0 kJ/mol	-565.4 kJ/mol	-270.8 kJ/mol

Table 7.4 shows, that the cage-to-cage transformation of the shown heteroleptic cages are energy-wise favorable. Furthermore, the difference of ΔE for $[\mathrm{Pd_2}\mathbf{L^{IC}}_2\mathbf{L^P}_2]^{4+}$ is 294.7 kJ/mol and for $[\mathrm{Pd_2}\mathbf{L^A}_2\mathbf{L^P}_2]^{4+}$ it is 344.5 kJ/mol. These results show that the heteroleptic cage formations are energy-wise favorable, which confirms the shape-complementarity approach as a useful tool. However, one factor for the difference between the difference of ΔE of the respective heteroleptic coordination cages should account from the difference in strain of the respective ligands. To examine the strain in the heteroleptic coordination cages more precisely, another approach is necessary.

7.1.2 Comparison of Respective Ligands

An alternative approach to studying strain in self-assembled coordination cages involves analyzing the ligands individually (see chapter 5.4). In this method, the single-point energies of the fully relaxed ligand and the ligand extracted from the optimized cage, with its atomic positions locked in space, are compared to assess the strain imposed on the ligand during cage assembly. Notably, entropic contributions are neglected, and the calculated electronic energies pertain to the gas phase.

Table 7.5 demonstrates similar trends for coordination cages composed of $\mathbf{L^C}$, $\mathbf{L^P}$, and $\mathbf{L^{PL}}$ when geometry optimization is performed without dispersion correction. For a detailed discussion of these results see chapter 6.1.

Table 7.5: Calculated single point energies at ωB97X-D4/def2-TZVP level. The respective cages were geometry optimized at ωB97X/def2-SVP level.

free ligand (fully relaxed)	ligand cut out from cage	strain per ligand / kJ/mol ($E_{\text{ligand cut out}} - E_{\text{free ligand}}$)
$\mathbf{L^C}$	$[Pd_2\mathbf{L^C}_4]^{4+}$	8.3
	$[Pd_2\mathbf{L^C}_2\mathbf{L^P}_2]^{4+}$	6.6
	$[Pd_2\mathbf{L^C}_2\mathbf{L^{PL}}_2]^{4+}$	6.3
$\mathbf{L^P}$	$[Pd_4\mathbf{L^P}_8]^{8+}$	12.9
	$[Pd_2\mathbf{L^C}_2\mathbf{L^P}_2]^{4+}$	10.1
	$[Pd_2\mathbf{L^A}_2\mathbf{L^P}_2]^{4+}$	9.0
	$[Pd_2\mathbf{L^{IC}}_2\mathbf{L^P}_2]^{4+}$	10.4
$\mathbf{L^{PL}}$	$[Pd_3\mathbf{L^{PL}}_6]^{6+}$	12.4
	$[Pd_2\mathbf{L^C}_2\mathbf{L^{PL}}_2]^{4+}$	13.5
	$[Pd_2\mathbf{L^A}_2\mathbf{L^{PL}}_2]^{4+}$	7.8
	$[Pd_2\mathbf{L^{IC}}_2\mathbf{L^{PL}}_2]^{4+}$	8.0
$\mathbf{L^A}$	$[Pd_2\mathbf{L^A}_4]^{4+}$	18.6
	$[Pd_2\mathbf{L^A}_2\mathbf{L^P}_2]^{4+}$	17.9
	$[Pd_2\mathbf{L^A}_2\mathbf{L^{PL}}_2]^{4+}$	16.9
$\mathbf{L^{IC}}$	$[Pd_2\mathbf{L^{IC}}_4]^{4+}$	11.7
	$[Pd_2\mathbf{L^{IC}}_2\mathbf{L^P}_2]^{4+}$	16.4
	$[Pd_2\mathbf{L^{IC}}_2\mathbf{L^{PL}}_2]^{4+}$	11.7

In the case of $\mathbf{L^{IC}}$, an increase in strain from the homoleptic cage $[Pd_2\mathbf{L^{IC}}_4]^{4+}$ to the heteroleptic coordination cage $[Pd_2\mathbf{L^{IC}}_2\mathbf{L^P}_2]^{4+}$ is observed, which must be balanced by a significant strain release of $\mathbf{L^P}$. In $[Pd_4\mathbf{L^P}_8]^{8+}$ eight ligands of $\mathbf{L^P}$ experience strain, while in $[Pd_2\mathbf{L^{IC}}_2\mathbf{L^P}_2]^{4+}$ each of two ligands $\mathbf{L^P}$ release strain of 2.5 kJ/mol. Therefore, the total strain release of $\mathbf{L^P}$ could be the driven force to form $[Pd_2\mathbf{L^{IC}}_2\mathbf{L^P}_2]^{4+}$. When forming the elongated heteroleptic cage $[Pd_2\mathbf{L^{IC}}_2\mathbf{L^{PL}}_2]^{4+}$ the strain stays constant for $\mathbf{L^{IC}}$, but very significant strain release for $\mathbf{L^{PL}}$ of 4.4 kJ/mol is observed.

$\mathbf{L^A}$ suffers more strain in the homoleptic cage $[Pd_2\mathbf{L^A}_4]^{4+}$ than in the heteroleptic cages $[Pd_2\mathbf{L^A}_2\mathbf{L^P}_2]^{4+}$ and $[Pd_2\mathbf{L^A}_2\mathbf{L^{PL}}_2]^{4+}$, because the strain decreases respectively of 0.7 kJ/mol and of 1.7 kJ/mol. This shows that $\mathbf{L^A}$ suffers also a less of strain when combined with $\mathbf{L^{PL}}$ than with $\mathbf{L^P}$. The short phenanthrene ligand $\mathbf{L^P}$ shows a significant decrease of strain of 3.9 kJ/mol from the homoleptic cage $[Pd_4\mathbf{L^P}_8]^{8+}$ to the heteroleptic cage $[Pd_2\mathbf{L^A}_2\mathbf{L^P}_2]^{4+}$. Meanwhile, the long phenanthrene ligand $\mathbf{L^{PL}}$ exhibits a higher release strain of 4.6 kJ/mol from the homoleptic cage $[Pd_3\mathbf{L^{PL}}_6]^{6+}$ to the heteroleptic cage $[Pd_2\mathbf{L^A}_2\mathbf{L^{PL}}_2]^{4+}$.

In the heteroleptic cages consisting of $\mathbf{L^A}$ and $\mathbf{L^{IC}}$, the phenanthrene-based ligands show different preferences compared to the heteroleptic cages involving $\mathbf{L^C}$, as discussed in chapter 6.1. One reason for this is the different bite angle of the ligands $\mathbf{L^{IC}}$ and $\mathbf{L^A}$ in comparison to $\mathbf{L^C}$. [161] For example, the bite angle of

$\mathbf{L^C}$ is 75°, while for $\mathbf{L^A}$ it is 60°. [161]$\mathbf{L^P}$ is probably not a shape-complementarity partner for $\mathbf{L^A}$ and $\mathbf{L^{IC}}$. Since $\mathbf{L^{PL}}$ is a more flexible ligand due its alkyne linker in comparison to $\mathbf{L^P}$, it can better adjust to $\mathbf{L^A}$ and $\mathbf{L^{IC}}$ in the heteroleptic coordination cage formation.

In chapter 6.1.4, the energy difference between reactants and products in cage-to-cage transformations was determined by summing the strain contributions per ligand. Similarly, the cage-to-cage transformations of the heteroleptic coordination cages involving $\mathbf{L^{IC}}$ and $\mathbf{L^A}$ were calculated based on the individual strain values of the ligands from table 7.5.

Cage-to-cage Transformation with Balanced Ligands

After analyzing the individual ligands, the strain per ligand was balanced for the cage-to-cage transformation from homoleptic species to heteroleptic cages (see figures 6.4, 7.2, and 7.8 for the cage-to-cage transformation). Analogous to equations 7.3 and 7.4, the calculations for the cage-to-cage transformation into heteroleptic cages with balanced ligands were performed, and the results are presented in table 7.6.

Table 7.6: Obtained strain of cage-to-cage transformation calculated with strain per ligand.

heteroleptic cage	balanced strain per ligand / kJ/mol
$[Pd_2\mathbf{L^C}_2\mathbf{L^{PL}}_2]^{4+}$	-2.0
$[Pd_2\mathbf{L^C}_2\mathbf{L^P}_2]^{4+}$	-9.3
$[Pd_2\mathbf{L^A}_2\mathbf{L^{PL}}_2]^{4+}$	-12.8
$[Pd_2\mathbf{L^A}_2\mathbf{L^P}_2]^{4+}$	-9.4
$[Pd_2\mathbf{L^{IC}}_2\mathbf{L^{PL}}_2]^{4+}$	-8.9
$[Pd_2\mathbf{L^{IC}}_2\mathbf{L^P}_2]^{4+}$	4.2

Table 7.6 demonstrates that, even without applying dispersion corrections during geometry optimization, the formation of $[Pd_2\mathbf{L^C}_2\mathbf{L^P}_2]^{4+}$ remains energetically favorable, consistent with the observed trend. This finding supports that $[Pd_2\mathbf{L^C}_2\mathbf{L^{PL}}_2]^{4+}$ formation from homoleptic cages is favorable from an energetic perspective. In chapter 6.1, the strain associated with $[Pd_2\mathbf{L^C}_2\mathbf{L^{PL}}_2]^{4+}$ using balanced ligands was calculated as 3.6 kJ/mol, suggesting an overall strain increase during heteroleptic cage formation, making the process energetically unfavorable. Table 7.6, however, confirms earlier interpretations, showing that the heteroleptic cage $[Pd_2\mathbf{L^C}_2\mathbf{L^P}_2]^{4+}$ is more favorable than $[Pd_2\mathbf{L^C}_2\mathbf{L^{PL}}_2]^{4+}$ because $\mathbf{L^P}$ reduces strain in the heteroleptic cage compared to its homoleptic counterpart.

Furthermore, table 7.6 indicates that the cage-to-cage transformation from homoleptic to heteroleptic cages is generally energetically favorable, except in the case of $[Pd_2\mathbf{L^{IC}}_2\mathbf{L^P}_2]^{4+}$. It is worth noting that solvent effects and counter ions, which might influence cage formation, are not considered in this approach.

The general trend observed is that $[Pd_2\mathbf{L^A}_2\mathbf{L^{PL}}_2]^{4+}$ and $[Pd_2\mathbf{L^{IC}}_2\mathbf{L^{PL}}_2]^{4+}$ release more strain than their respective shorter heteroleptic coordination cages with $\mathbf{L^P}$. This confirms the previously stated interpretation that $\mathbf{L^A}$ and $\mathbf{L^{IC}}$ prefer $\mathbf{L^{PL}}$ as a partner for heteroleptic cage formation over $\mathbf{L^P}$, due to the greater flexibility and adjustability of $\mathbf{L^{PL}}$.

After completing the approaches to determine strain in various coordination cages, non-phenanthrene-based heteroleptic coordination cages were analyzed. In chapter 7.1.3 (heteroleptic cages with specific arrangements, referred to as figure-eight topology (f8), are examined. The f8 topology was previously introduced in chapter 1.5.1.

7.1.3 Further Heteroleptic Cage Formations: f8 under scope

In the previous chapters (6.1 and 7.1), the cage-to-cage transformation and ligand comparison approaches were successfully applied, supporting the experimentally observed results. However, these studies focused exclusively on *cis*-arranged cages. As the next step, *trans*-arranged cages featuring the so-called figure-eight topology were examined, since strain is also expected to play a significant role in the *trans*-arrangement during cage formation.

For this purpose, various ligands were used (see figure 7.3). The ligand $\mathbf{L^C}$ and its homoleptic cage formation were studied in the previous chapter.

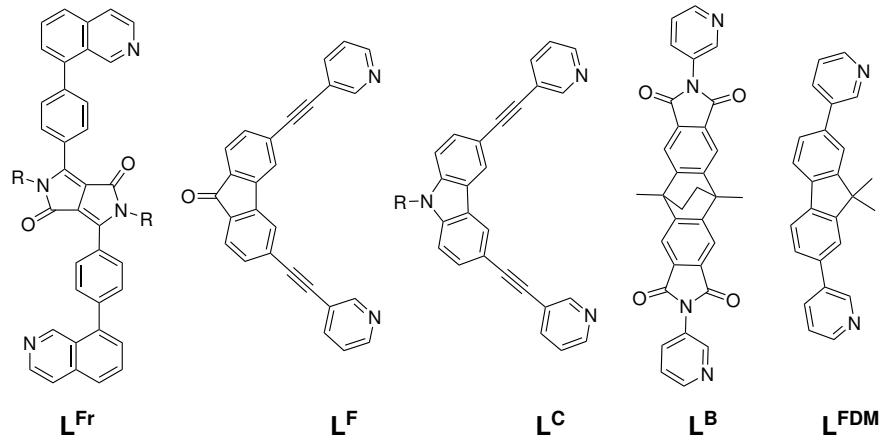

Figure 7.3. Illustration of the ligands $\mathbf{L^{Fr}}$, $\mathbf{L^F}$, $\mathbf{L^C}$ $\mathbf{L^B}$ and $\mathbf{L^{FDM}}$. R= hexyl, but for the calculations it was substituted with a methyl group.

In 2023, I. Regeni examined Pd(II)-mediated self-assembly of diketopyrrolopyrrole (DPP) dyes. [162] Several DPP-based ligands were reported to form self-penetrated motifs with a figure-eight (f8) topology. In these systems, the interlinked homoleptic cage of the DPP-based ligand $\mathbf{L^{Fr}}$ features one coordination site per Pd(II) cation occupied by a solvent molecule due to geometrical constraints (see a) in figure 7.4). [162] Two of the $\mathbf{L^{Fr}}$ ligands adopt an S-shaped conformation in their *trans*-arrangement, enabling π-stacking with a third $\mathbf{L^{Fr}}$ ligand in the homoleptic cage $[Pd_2\mathbf{L^{Fr}}_3(CH_3CN)_2]^{4+}$. [162]

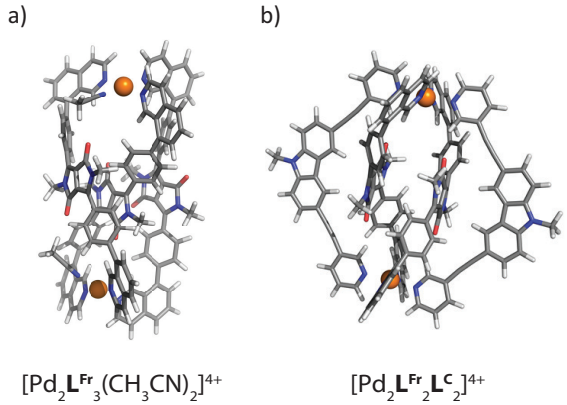

Figure 7.4. a) $[Pd_2\mathbf{L^{Fr}}_3(CH_3CN)_2]^{4+}$ and b) $[Pd_2\mathbf{L^{Fr}}_2\mathbf{L^C}_2]^{4+}$.

In addition, heteroleptic cage formation was also investigated. $\mathbf{L^{Fr}}$ was combined with the carbazole-based ligand $\mathbf{L^{C}}$ to form the heteroleptic coordination cage $[Pd_2\mathbf{L^{Fr}}_2\mathbf{L^{C}}_2]^{4+}$. X-ray analysis confirmed the figure-eight topology of $\mathbf{L^{Fr}}$ in $[Pd_2\mathbf{L^{Fr}}_2\mathbf{L^{C}}_2]^{4+}$, along with π-stacking interaction of two $\mathbf{L^{Fr}}$ ligands (see b) in figure 7.4). [162]

Building on this work, E. Benchimol expanded the series of heteroleptic coordination cages based on $\mathbf{L^{Fr}}$ by combining it with various ligands, including $\mathbf{L^{F}}$, $\mathbf{L^{B}}$ and $\mathbf{L^{FDM}}$ (see figure 7.3). [150] The homoleptic assemblies of $\mathbf{L^{F}}$ and $\mathbf{L^{B}}$ were reported to form lantern-shaped coordination cages $[Pd_2\mathbf{L}_2\mathbf{L'}_2]^{4+}$ (see a) in figure 7.5). [319][279]

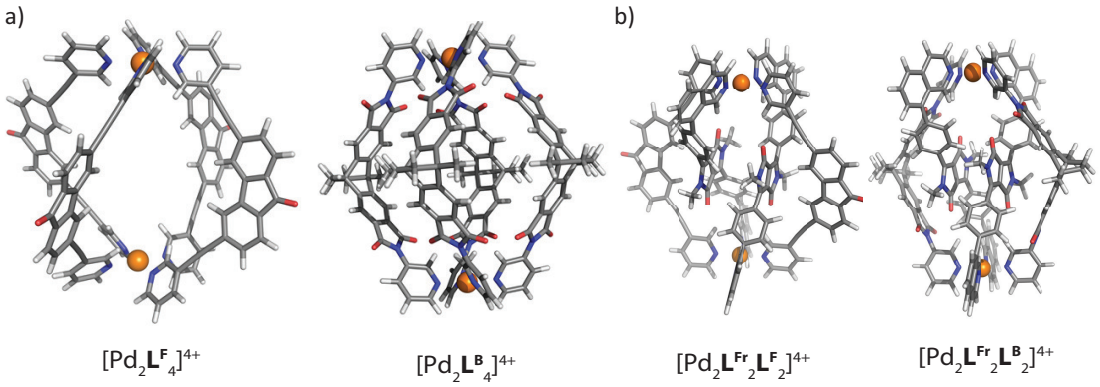

Figure 7.5. a) Homoleptic cages $[Pd_2\mathbf{L^{F}}_4]^{4+}$ and $[Pd_2\mathbf{L^{B}}_4]^{4+}$. b) shown heteroleptic cages $[Pd_2\mathbf{L^{Fr}}_2\mathbf{L^{F}}_2]^{4+}$ and $[Pd_2\mathbf{L^{Fr}}_2\mathbf{L^{B}}_2]^{4+}$.

E. Benchimol further demonstrated that combining $\mathbf{L^{Fr}}$ with $\mathbf{L^{F}}$, $\mathbf{L^{B}}$ or $\mathbf{L^{C}}$ results in heteroleptic cages with an f8 topology and a *trans*-arrangement of $\mathbf{L^{Fr}}$ (see b) in figure 7.5). [150] Another ligand examined for heteroleptic Pd(II)-mediated assemblies with $\mathbf{L^{Fr}}$ was $\mathbf{L^{FDM}}$. The homoleptic assembly of $\mathbf{L^{FDM}}$ resulted in a mixture of a tetrahedron $[Pd_4\mathbf{L^{FDM}}_8]^{8+}$ and a ring $[Pd_3\mathbf{L^{FDM}}_6]^{6+}$ (see a) in figure 7.6). [320]

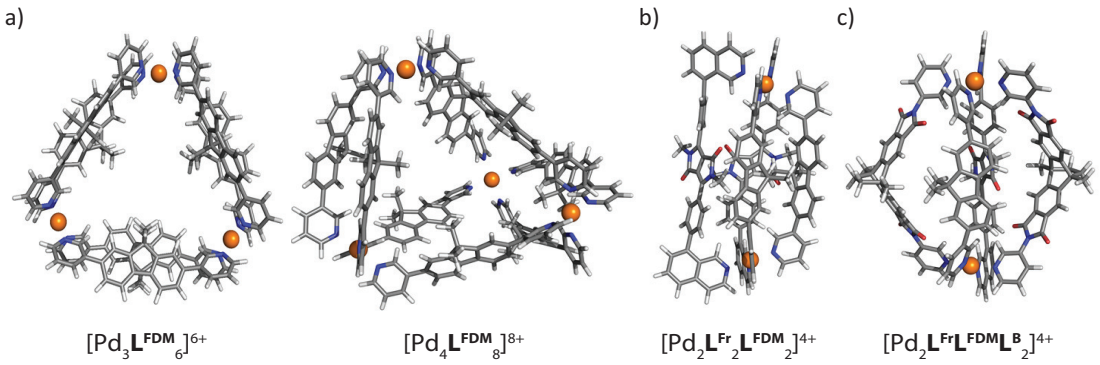

Figure 7.6. a) Homoleptic cages $[Pd_3\mathbf{L^{FDM}}_6]^{6+}$ and $[Pd_4\mathbf{L^{FDM}}_8]^{8+}$. b) shown heteroleptic cages *cis*-$[Pd_2\mathbf{L^{Fr}}_2\mathbf{L^{F}}_2]^{4+}$ and *trans*-$[Pd_2\mathbf{L^{Fr}}\mathbf{L^{FDM}}\mathbf{L^{B}}_2]^{4+}$.

The combination of $\mathbf{L^{Fr}}$ with $\mathbf{L^{FDM}}$ formed a heteroleptic coordination cage with a *cis*-arrangement of the ligands, as confirmed by the X-ray structure of

$[Pd_2\mathbf{L^{Fr}}_2\mathbf{L^{FDM}}_2]^{4+}$ (see b) in figure 7.6). [150] Symmetry breaking of the ligands in the assembly was observed via ^{1}H-NMR analysis, which was attributed to the twisting of $\mathbf{L^{Fr}}$ caused by steric hindrance. [150] Combining $\mathbf{L^{Fr}}$, $\mathbf{L^{FDM}}$ and $\mathbf{L^{B}}$ with Pd(II) in a 1:1:2 ratio yielded the heteroleptic cage $[Pd_2\mathbf{L^{Fr}}\mathbf{L^{FDM}}\mathbf{L^{B}}_2]^{4+}$, with $\mathbf{L^{B}}$ positioned in the *trans*-configuration (see c) in figure 7.6).

A comprehensive series of heteroleptic coordination cages based on $\mathbf{L^{Fr}}$ has been introduced. The f8 topology observed in heteroleptic cages such as $[Pd_2\mathbf{L^{Fr}}_2\mathbf{L^{C}}_2]^{4+}$, $[Pd_2\mathbf{L^{Fr}}_2\mathbf{L^{F}}_2]^{4+}$ and $[Pd_2\mathbf{L^{Fr}}_2\mathbf{L^{B}}_2]^{4+}$ raises the question of whether strain plays a critical role in the formation of these structures.

Furthermore, heteroleptic cage formation experiments revealed that $\mathbf{L^{Fr}}$ combined with $\mathbf{L^{FDM}}$ resulted in a *cis*-arranged cage, $[Pd_2\mathbf{L^{Fr}}_2\mathbf{L^{F}}_2]^{4+}$, while the combination of $\mathbf{L^{Fr}}$, $\mathbf{L^{FDM}}$, and $\mathbf{L^{B}}$ produced a *trans*-arranged cage, $[Pd_2\mathbf{L^{Fr}}\mathbf{L^{FDM}}\mathbf{L^{B}}_2]^{4+}$. This observation raises further questions about whether strain release is a key factor driving the formation of *cis*- and *trans*-cages.

This work focuses on calculating the strain in $\mathbf{L^{Fr}}$-based heteroleptic cages. To achieve this, the cage-to-cage transformation and ligand comparison approaches, analogous to those described in chapters 6.1 and 7.1, were applied.

Calculation of Strain of L^{Fr}-based Heteroleptic Coordination Cages

Before calculating the cage-to-cage transformation from $[Pd_2\mathbf{L}^{\mathbf{Fr}}{}_3(CH_3CN)_2]^{4+}$ to a respective heteroleptic coordination cage with another homoleptic cage, it is essential to consider that CH_3CN coordinates to Pd(II) in the homoleptic cage of $\mathbf{L}^{\mathbf{Fr}}$. This coordination must be accounted for on the product side to ensure stoichiometric balance. Without this consideration, the number of atoms and types of bonds on both sides of the reaction equation would not match, and the resulting energy differences between the heteroleptic and homoleptic coordination cages would not primarily reflect strain. To address this, $Pd(CH_3CN)_4$ was included on the product side to compensate for the CH_3CN molecule and its coordination to Pd(II) in the homoleptic cage. Figure 7.7 illustrates the reaction equations and stoichiometric factors used for strain calculations.

a)

$$4\ [Pd_2\mathbf{L}^{\mathbf{Fr}}{}_3(CH_3CN)_2]^{4+} + 3\ [Pd_2\mathbf{L}_4]^{4+} \rightleftharpoons 6\ [Pd_2\mathbf{L}^{\mathbf{Fr}}{}_2\mathbf{L}_2]^{4+} + 2\ Pd(CH_3CN)_4$$

$$\mathbf{L}=\mathbf{L}^{\mathbf{F}},\mathbf{L}^{\mathbf{C}},\mathbf{L}^{\mathbf{B}}$$

b)

$$10\ [Pd_2\mathbf{L}^{\mathbf{Fr}}{}_3(CH_3CN)_2]^{4+} + 1\ [Pd_3\mathbf{L}^{\mathbf{FDM}}{}_6]^{6+} + 3\ [Pd_4\mathbf{L}^{\mathbf{FDM}}{}_8]^{8+} + 15\ [Pd_2\mathbf{L}^{\mathbf{B}}{}_4]^{4+}$$

$$\downarrow\uparrow$$

$$30\ [Pd_2\mathbf{L}^{\mathbf{Fr}}\mathbf{L}^{\mathbf{FDM}}\mathbf{L}^{\mathbf{B}}{}_2]^{4+} + 5\ Pd(CH_3CN)_4$$

c)

$$10\ [Pd_2\mathbf{L}^{\mathbf{Fr}}{}_3(CH_3CN)_2]^{4+} + 1\ [Pd_3\mathbf{L}^{\mathbf{FDM}}{}_6]^{6+} + 3\ [Pd_4\mathbf{L}^{\mathbf{FDM}}{}_8]^{8+}$$

$$\downarrow\uparrow$$

$$15\ [Pd_2\mathbf{L}^{\mathbf{Fr}}{}_2\mathbf{L}^{\mathbf{FDM}}{}_2]^{4+} + 5\ Pd(CH_3CN)_4$$

Figure 7.7. Illustration of the reaction schemes a)-c) to calculate the strain at the respective coordination cage formation. b) As previous mentioned: the homoleptic assembly of $\mathbf{L}^{\mathbf{FDM}}$ resulted in a mixture of a tetrahedron $[Pd_4\mathbf{L}^{\mathbf{FDM}}{}_8]^{8+}$ and a ring $[Pd_3\mathbf{L}^{\mathbf{FDM}}{}_6]^{6+}$. [320] Therefore both homoleptic cages were used to balance the reaction equation.

As in chapters 6.1 and 7.1, the structures were initially pre-optimized using the PM6 method, followed by geometry optimization at the ωB97X/def2-SVP level (in the gas phase). Single-point energies (SPEs) were subsequently calculated at the ωB97X-D4/def2-TZVP level (in gas phase). These results are presented in chapter 7.1.5 (table 7.11). Furthermore, Coulomb repulsion energies were calculated for the respective assemblies, as shown in chapter 7.1.5 (see table 7.12). The Coulomb repulsion trend mirrors the results from previous systems, as it depends on the number of charges within the assembly. Assemblies with the highest nuclearity exhibit the highest Coulomb repulsion. Specifically, coordination cages

containing three Pd(II) atoms show Coulomb repulsion values of approximately 1000 kJ/mol, while assemblies with four Pd(II) atoms reach nearly 2000 kJ/mol. Cages with two Pd(II) atoms exhibit Coulomb repulsion values around 350 kJ/mol, with variations primarily attributed to the Pd(II)-Pd(II) distance (see table 7.13 in chapter 7.1.5). These results align with trends observed in prior systems. The cage-to-cage transformation of heteroleptic cages of $\mathbf{L^{Fr}}$ were analyzed using the calculated single-point energies, taking Coulomb repulsion into account (see table 7.7).

Table 7.7: Calculated cage-to-cage transformation energy respective of the heteroleptic cages. Single point energies (SPE) calculated at ωB97X-D4/def2-TZVP level (gas phase).

heteroleptic cage	SPE / kJ/mol
$\Delta E([Pd_2\mathbf{L^{Fr}L^{FDM}L^{B}}_2]^{4+})$	-269,3
$\Delta E([Pd_2\mathbf{L^{Fr}}_2\mathbf{L^{FDM}}_2]^{4+})$	-492,3
$\Delta E([Pd_2\mathbf{L^{Fr}}_2\mathbf{L^{C}}_2]^{4+})$	-120,1
$\Delta E([Pd_2\mathbf{L^{Fr}}_2\mathbf{L^{F}}_2]^{4+})$	-126,3
$\Delta E([Pd_2\mathbf{L^{Fr}}_2\mathbf{L^{B}}_2]^{4+})$	-146,2

All heteroleptic coordination cages were found to be energetically more favorable than their homoleptic counterparts, consistent with experimental data. [162][150] Among them, the heteroleptic cages $[Pd_2\mathbf{L^{Fr}}_2\mathbf{L^{FDM}}_2]^{4+}$ and $[Pd_2\mathbf{L^{Fr}L^{FDM}L^{B}}_2]^{4+}$ are over 100 kJ/mol more stable than other heteroleptic cages. The energy difference between these two assemblies is nearly a factor of two, potentially due to strain release within the respective ligands. To examine this strain more precisely, a ligand-centric analysis was employed by using the comparison of ligands approach.

Table 7.8 summarizes the strain per ligand for both homoleptic and heteroleptic assemblies. In the homoleptic cage $[Pd_2\mathbf{L^{Fr}}_3(CH_3CN)_2]^{4+}$, the ligands exhibit two distinct topologies: the f8 topology and the coordination solvent's opposite side, which will be differentiated at the strain examination. Table 7.8 shows that the strain of $\mathbf{L^{Fr}}$ on the side opposite to the coordinating solvent in $[Pd_2\mathbf{L^{Fr}}_3(CH_3CN)_2]^{4+}$, compared to the free $\mathbf{L^{Fr}}$, is 9.5 kJ/mol, while the strain energy for $\mathbf{L^{Fr}}$ with the f8 topology is 43.3 kJ/mol. This f8 topology in $[Pd_2\mathbf{L^{Fr}}_3(CH_3CN)_2]^{4+}$ facilitates π-stacking interactions with a third $\mathbf{L^{Fr}}$ ligand. [162] Thus, while Table 7.8 suggests that $\mathbf{L^{Fr}}$ experiences strain in $[Pd_2\mathbf{L^{Fr}}_3(CH_3CN)_2]^{4+}$, the π-π-stacking interactions help stabilize the system, enabling the formation of the homoleptic cage with $\mathbf{L^{Fr}}$.

For $\mathbf{L^{FDM}}$, a slight strain reduction of 1 kJ/mol was observed from both the ring and double-bridging (DB) ligands in the tetrahedral cage to the $[Pd_2\mathbf{L^{Fr}}_2\mathbf{L^{FDM}}_2]^{4+}$, while the single-bridging (SB) ligands showed no change in strain. In contrast, the outer ligands of $\mathbf{L^{Fr}}$ in $[Pd_2\mathbf{L^{Fr}}_3(CH_3CN)_2]^{4+}$ exhibited a minor strain increase of 1 kJ/mol. However, the strain of $\mathbf{L^{Fr}}$ with the f8 topology in the same cage

was 43.3 kJ/mol, which reduced to 10.5 kJ/mol in $[Pd_2\mathbf{L^{Fr}}_2\mathbf{L^{FDM}}_2]^{4+}$, representing a strain release of approximately 33 kJ/mol per ligand. This significant strain release serves as the primary driving force for the formation of $[Pd_2\mathbf{L^{Fr}}_2\mathbf{L^{FDM}}_2]^{4+}$.

In $[Pd_2\mathbf{L^{Fr}}\mathbf{L^{FDM}}\mathbf{L^{B}}_2]^{4+}$, the strain in $\mathbf{L^{B}}$ decreased by up to 1.7 kJ/mol, whereas $\mathbf{L^{FDM}}$ experienced an increase of up to 7.8 kJ/mol compared to their respective homoleptic cages. The outer $\mathbf{L^{Fr}}$ ligands showed a strain increase of 6 kJ/mol. However, the f8-topology $\mathbf{L^{Fr}}$ ligands released approximately 28 kJ/mol per ligand, again providing the primary driving force for the formation of the heteroleptic assembly $[Pd_2\mathbf{L^{Fr}}\mathbf{L^{FDM}}\mathbf{L^{B}}_2]^{4+}$.

Similarly, in $[Pd_2\mathbf{L^{Fr}}_2\mathbf{L^{B}}_2]^{4+}$, the strain in $\mathbf{L^{B}}$ decreased by 4 kJ/mol, while the outer $\mathbf{L^{Fr}}$ ligands showed a negligible strain increase of 1 kJ/mol. The f8-topology $\mathbf{L^{Fr}}$ ligands released 29 kJ/mol of strain per ligand, driving the formation of this heteroleptic cage. Comparable trends were observed for $[Pd_2\mathbf{L^{Fr}}_2\mathbf{L^{F}}_2]^{4+}$ and $[Pd_2\mathbf{L^{Fr}}_2\mathbf{L^{C}}_2]^{4+}$, where $\mathbf{L^{F}}$ and $\mathbf{L^{C}}$ exhibited strain increases of 5 and 3 kJ/mol, respectively. The release of strain in $\mathbf{L^{Fr}}$ was again the driving force for these transformations.

Table 7.8: Calculated single point energies at ωB97X-D4/def2-TZVP level. The respective cages were geometry optimized at ωB97X/def2-SVP level.

free ligand (fully relaxed)	ligand cut out from cage	strain per ligand / kJ/mol ($E_{\text{ligand cut out}} - E_{\text{free ligand}}$)
$\mathbf{L^{B}}$	$[Pd_2\mathbf{L^{B}}_4]^{4+}$	18,6
	$[Pd_2\mathbf{L^{Fr}}\mathbf{L^{FDM}}\mathbf{L^{B}}_2]^{4+}$	16,9
	$[Pd_2\mathbf{L^{Fr}}_2\mathbf{L^{B}}_2]^{4+}$	14,4
$\mathbf{L^{FDM}}$	$[Pd_3\mathbf{L^{FDM}}_6]^{6+}$	8.7
	$[Pd_4\mathbf{L^{FDM}}_8]^{8+}$ (DB)	8,4
	$[Pd_4\mathbf{L^{FDM}}_8]^{8+}$ (SB)	7,8
	$[Pd_2\mathbf{L^{Fr}}\mathbf{L^{FDM}}\mathbf{L^{B}}_2]^{4+}$	15,6
	$[Pd_2\mathbf{L^{Fr}}_2\mathbf{L^{FDM}}_2]^{4+}$	7,8
$\mathbf{L^{C}}$	$[Pd_2\mathbf{L^{C}}_4]^{4+}$	8,6
	$[Pd_2\mathbf{L^{Fr}}_2\mathbf{L^{C}}_2]^{4+}$	11,7
$\mathbf{L^{F}}$	$[Pd_2\mathbf{L^{F}}_4]^{4+}$	4,0
	$[Pd_2\mathbf{L^{Fr}}_2\mathbf{L^{F}}_2]^{4+}$	9,0
$\mathbf{L^{Fr}}$	$[Pd_2\mathbf{L^{Fr}}_3(CH_3CN)_2]^{4+}$	9,5
	$[Pd_2\mathbf{L^{Fr}}_3(CH_3CN)_2]^{4+}$ (f8)	43,3
	$[Pd_2\mathbf{L^{Fr}}\mathbf{L^{FDM}}\mathbf{L^{B}}_2]^{4+}$	15,6
	$[Pd_2\mathbf{L^{Fr}}_2\mathbf{L^{FDM}}_2]^{4+}$	10,5
	$[Pd_2\mathbf{L^{Fr}}_2\mathbf{L^{C}}_2]^{4+}$	15,0
	$[Pd_2\mathbf{L^{Fr}}_2\mathbf{L^{B}}_2]^{4+}$	14,4
	$[Pd_2\mathbf{L^{Fr}}_2\mathbf{L^{F}}_2]^{4+}$	15,0

Finally, analogous to chapters 6.1 and 7.1, cage-to-cage transformations with balanced ligands were calculated to assess the overall strain changes during heteroleptic cage formation. Table 7.9 demonstrates that all heteroleptic cages are energetically more favorable than their homoleptic counterparts. Notably, $[Pd_2\mathbf{L^{Fr}}\mathbf{L^{FDM}}\mathbf{L^{B}}_2]^{4+}$ emerged as the most stable assembly, followed by $[Pd_2\mathbf{L^{Fr}}_2\mathbf{L^{FDM}}_2]^{4+}$, which aligns with experimental observations where mixing these ligands results in integrative self-sorting to form $[Pd_2\mathbf{L^{Fr}}\mathbf{L^{FDM}}\mathbf{L^{B}}_2]^{4+}$. [150]

Table 7.9: Obtained strain from the cage-to-cage transformation calculated with strain per ligand.

heteroleptic cage	balanced strain per ligand / kJ/mol
$[Pd_2\mathbf{L^{Fr}}\mathbf{L^{FDM}}\mathbf{L^{B}}_2]^{4+}$	-50,0
$[Pd_2\mathbf{L^{Fr}}_2\mathbf{L^{FDM}}_2]^{4+}$	-45,0
$[Pd_2\mathbf{L^{Fr}}_2\mathbf{L^{C}}_2]^{4+}$	-27,7
$[Pd_2\mathbf{L^{Fr}}_2\mathbf{L^{F}}_2]^{4+}$	-19,3
$[Pd_2\mathbf{L^{Fr}}_2\mathbf{L^{B}}_2]^{4+}$	-24,1

After analyzing the heteroleptic cage formations, the questions posed at the beginning of this chapter can now be addressed. The f8 topology observed in heteroleptic cages, such as $[Pd_2\mathbf{L^{Fr}}_2\mathbf{L^{C}}_2]^{4+}$, $[Pd_2\mathbf{L^{Fr}}_2\mathbf{L^{F}}_2]^{4+}$ and $[Pd_2\mathbf{L^{Fr}}_2\mathbf{L^{B}}_2]^{4+}$, demonstrates a significant release of strain compared to the homoleptic cage of $\mathbf{L^{Fr}}$. This suggest that the strain release of $\mathbf{L^{Fr}}$ is the driven force to form the heteroleptic coordination cages.

Similarly, both the *cis*-$[Pd_2\mathbf{L^{Fr}}_2\mathbf{L^{F}}_2]^{4+}$ and *trans*-$[Pd_2\mathbf{L^{Fr}}\mathbf{L^{FDM}}\mathbf{L^{B}}_2]^{4+}$ cage exhibit a significant release of strain for $\mathbf{L^{Fr}}$. These findings, derived from the comparison of the ligand-centered approach aligned with other approaches, clearly indicate that strain is a crucial factor in the formation of $\mathbf{L^{Fr}}$-based heteroleptic cages.

7.1.4 Conclusion and Outlook

In the final part of this thesis, the strain calculations of self-assembled coordination cages with banana-shaped ligands were introduced. Hereby, the strain calculation approach was applied to two different heteroleptic systems to expand the understanding and support experimental observations. The first heteroleptic coordination system involved shape-complementary partners of phenanthrene ligands $\mathbf{L^{PL}}$ and $\mathbf{L^{P}}$ such as $\mathbf{L^{IC}}$ and $\mathbf{L^{A}}$.

The first approach involved calculating the energy difference in the cage-to-cage transformations of the homoleptic cages of $\mathbf{L^{C}}$, $\mathbf{L^{IC}}$, and $\mathbf{L^{A}}$ with the homoleptic ring of $\mathbf{L^{PL}}$ and $\mathbf{L^{P}}$ to the respective heteroleptic cages. These calculations revealed the necessity of accounting for Coulomb repulsion (Pd^{II}-Pd^{II} interactions) when

calculating strain, as it significantly contributes to the electronic energies in gas phase.

The second approach compared the electronic energies of fully relaxed ligands with those of ligands extracted from the cage assemblies. The cage-to-cage transformation calculations indicated that the heteroleptic cages $[Pd_2\mathbf{L^C}_2\mathbf{L^P}_2]^{4+}$, $[Pd_2\mathbf{L^{IC}}_2\mathbf{L^P}_2]^{4+}$, and $[Pd_2\mathbf{L^A}_2\mathbf{L^P}_2]^{4+}$ are energetically more favorable than their elongated heteroleptic counterparts. However, a comparison of the fully relaxed ligands and those extracted from the cages provided more precise insights into the systems. For $[Pd_2\mathbf{L^C}_2\mathbf{L^{PL}}_2]^{4+}$, the strain of $\mathbf{L^{PL}}$ increases from the homoleptic to the heteroleptic cage formation, while the strain of $\mathbf{L^P}$ decreases when forming the respective heteroleptic cage with $\mathbf{L^C}$. In both cases, the strain of $\mathbf{L^C}$ decreases in the heteroleptic cages. These results confirm the hypothesis that in the formation of heteroleptic cages, $\mathbf{L^{PL}}$ must bend to accommodate the cage structure, whereas $\mathbf{L^P}$ fits more naturally into the heteroleptic cage.

The strain trends for heteroleptic cages based on $\mathbf{L^{IC}}$ and $\mathbf{L^A}$ were reversed due to the differing bite angles of these ligands. The flexibility of $\mathbf{L^{PL}}$ allows it to adjust to the respective heteroleptic coordination cage.

Analogous the second system of $\mathbf{L^{Fr}}$-based heteroleptic cages were examined. The f8 topology in heteroleptic cages such as in $[Pd_2\mathbf{L^{Fr}}_2\mathbf{L^C}_2]^{4+}$, $[Pd_2\mathbf{L^{Fr}}_2\mathbf{L^F}_2]^{4+}$ and $[Pd_2\mathbf{L^{Fr}}_2\mathbf{L^B}_2]^{4+}$ were examined. Additionally, the *cis*-$[Pd_2\mathbf{L^{Fr}}_2\mathbf{L^F}_2]^{4+}$ and *trans*-$[Pd_2\mathbf{L^{Fr}L^{FDM}L^B}_2]^{4+}$ cages were analyzed, revealing that the release of strain from $[Pd_2\mathbf{L^{Fr}}_3(CH_3CN)_2]^{4+}$ plays a crucial role in the formation of these heteroleptic coordination cages.

For future studies, strain calculations should be performed stepwise, first incorporating counterions and subsequently solvents, to enhance the accuracy and applicability of the findings.

It is worth mentioning that strain should also occur in the $Pd(Py)_4$ arrangement, which was not examined in previous studies and should be considered in future research.

Moreover, the contributions of π-π-stacking and other non-covalent interactions should be investigated, particularly in $\mathbf{L^{Fr}}$-based coordination cages, where the f8 topology and pronounced π-stacking interactions between the backbones of $\mathbf{L^{Fr}}$ are expected to play a significant role at coordination cage formation.

7.1.5 Supplement

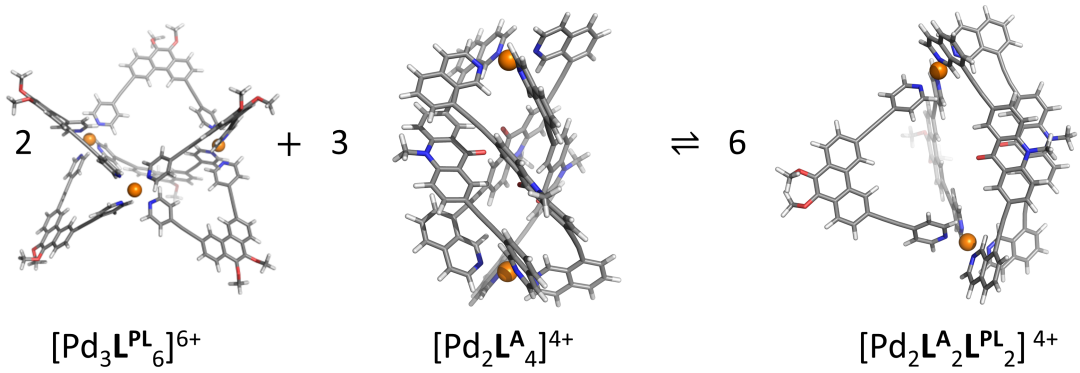

(a) Cage-to-cage transformation of $[Pd_3\mathbf{L}^{\mathbf{PL}}{}_6]^{6+}$ and $[Pd_2\mathbf{L}^{\mathbf{A}}{}_4]^{4+}$ to $[Pd_2\mathbf{L}^{\mathbf{A}}{}_2\mathbf{L}^{\mathbf{PL}}{}_2]^{4+}$.

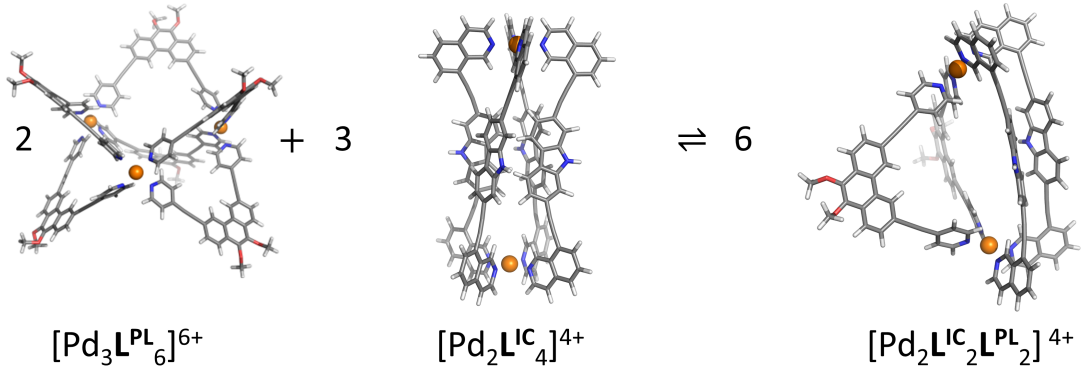

(b) Cage-to-cage transformation of $[Pd_3\mathbf{L}^{\mathbf{PL}}{}_6]^{6+}$ and $[Pd_2\mathbf{L}^{\mathbf{IC}}{}_4]^{4+}$ to $[Pd_2\mathbf{L}^{\mathbf{IC}}{}_2\mathbf{L}^{\mathbf{PL}}{}_2]^{4+}$.

Figure 7.8. Cage-to-cage transformation of geometry optimized structures at ωB97X/def2-SVP level (gas phase).

Table 7.10: Determined single point energies of the geometry-optimized structures at ωB97X/def2-TZVP level (gas phase) for the corresponding cage. The single point energies (SPE) calculated at ωB97X-D4/def2-TZVP level (gas phase).

cage	SPE / Hatree
$[Pd_2\mathbf{L}^{\mathbf{C}}{}_4]^{4+}$	-5071.990842
$[Pd_4\mathbf{L}^{\mathbf{P}}{}_8]^{8+}$	-10619.719571
$[Pd_3\mathbf{L}^{\mathbf{P}}{}_6]^{6+}$	-8879.454891
$[Pd_2\mathbf{L}^{\mathbf{A}}{}_4]^{4+}$	-6755.867561
$[Pd_2\mathbf{L}^{\mathbf{IC}}{}_4]^{4+}$	-6144.840729
$[Pd_2\mathbf{L}^{\mathbf{C}}{}_2\mathbf{L}^{\mathbf{P}}{}_2]^{4+}$	-5191.022693
$[Pd_2\mathbf{L}^{\mathbf{C}}{}_2\mathbf{L}^{\mathbf{PL}}{}_2]^{4+}$	-5495.860243
$[Pd_2\mathbf{L}^{\mathbf{A}}{}_2\mathbf{L}^{\mathbf{P}}{}_2]^{4+}$	-6032.969098
$[Pd_2\mathbf{L}^{\mathbf{A}}{}_2\mathbf{L}^{\mathbf{PL}}{}_2]^{4+}$	-6337.782926
$[Pd_2\mathbf{L}^{\mathbf{IC}}{}_2\mathbf{L}^{\mathbf{P}}{}_2]^{4+}$	-5727.445236
$[Pd_2\mathbf{L}^{\mathbf{IC}}{}_2\mathbf{L}^{\mathbf{PL}}{}_2]^{4+}$	-6032.279889

Table 7.11: Determined single point energies of the geometry-optimized structures at ωB97X/def2-SVP level (gas phase) for the corresponding cage. The single point energies (SPE) calculated at ωB97X-D4/def2-TZVP level (gas phase).

cage	SPE Hatree
$[Pd_2\mathbf{L^B}_4]^{4+}$	-7271,141896
$[Pd_2\mathbf{L^{Fr}}_3(CH_3CN)_2]^{4+}$	-6024,769207
$[Pd_2\mathbf{L^C}_4]^{4+}$	-5071,990842
$[Pd_2\mathbf{L^F}_4]^{4+}$	-5146,505814
$[Pd_3\mathbf{L^{FDM}}_6]^{6+}$	-6833,133805
$[Pd_4\mathbf{L^{FDM}}_8]^{8+}$	-9110,625027
$[Pd_2\mathbf{L^{Fr}L^{FDM}L^B}_2]^{4+}$	-6672,894543
$[Pd_2\mathbf{L^{Fr}}_2\mathbf{L^{FDM}}_2]^{4+}$	-6074,644572
$[Pd_2\mathbf{L^{Fr}}_2\mathbf{L^C}_2]^{4+}$	-6332,893792
$[Pd_2\mathbf{L^{Fr}}_2\mathbf{L^F}_2]^{4+}$	-6370,15204
$[Pd_2\mathbf{L^{Fr}}_2\mathbf{L^B}_2]^{4+}$	-7432,476262

Table 7.12: Calculated single point energies at ωB97X-D4/def2-TZVP level. Calculated values in kJ/mol.

Käfig	Pd_{diff} kJ/mol
$[Pd_2\mathbf{L^B}_4]^{4+}$	351,0
$[Pd_2\mathbf{L^{Fr}}_3(CH_3CN)_2]^{4+}$	342,7
$[Pd_2\mathbf{L^C}_4]^{4+}$	367,3
$[Pd_2\mathbf{L^F}_4]^{4+}$	377,3
$[Pd_3\mathbf{L^{FDM}}_6]^{6+}$	1065,7
$[Pd_4\mathbf{L^{FDM}}_8]^{8+}$	1995,9
$[Pd_2\mathbf{L^{Fr}L^{FDM}L^B}_2]^{4+}$	354,1
$[Pd_2\mathbf{L^{Fr}}_2\mathbf{L^{FDM}}_2]^{4+}$	356,3
$[Pd_2\mathbf{L^{Fr}}_2\mathbf{L^C}_2]^{4+}$	361,4
$[Pd_2\mathbf{L^{Fr}}_2\mathbf{L^F}_2]^{4+}$	362,2
$[Pd_2\mathbf{L^{Fr}}_2\mathbf{L^B}_2]^{4+}$	345,4

Table 7.13: Determined Pd(II)-Pd(II) distance in the geometry-optimized structures at ωB97X-D4/def2-TZVP level (gas phase) for the corresponding cage.

Käfig	Pd(II)-Pd(II) distance / Å
$[Pd_2\mathbf{L^B}_4]^{4+}$	15.421
$[Pd_2\mathbf{L^{Fr}}_3(CH_3CN)_2]^{4+}$	15.606
$[Pd_2\mathbf{L^C}_4]^{4+}$	13.988
$[Pd_2\mathbf{L^F}_4]^{4+}$	13.510
$[Pd_3\mathbf{L^{FDM}}_6]^{6+}$	15.298
$[Pd_4\mathbf{L^{FDM}}_8]^{8+}$	17.088
$[Pd_2\mathbf{L^{Fr}L^{FDM}L^B}_2]^{4+}$	15.242
$[Pd_2\mathbf{L^{Fr}}_2\mathbf{L^{FDM}}_2]^{4+}$	14.857
$[Pd_2\mathbf{L^{Fr}}_2\mathbf{L^C}_2]^{4+}$	14.871
$[Pd_2\mathbf{L^{Fr}}_2\mathbf{L^F}_2]^{4+}$	14.822
$[Pd_2\mathbf{L^{Fr}}_2\mathbf{L^B}_2]^{4+}$	15.478

8 Appendix

8.1 Abbreviations

H-bond	hydrogen bond
THF	tetrahydrofuran
ESI-MS	electrospray ionisation mass spectrometry
DOSY	diffusion ordered spectroscopy
NMR	nuclear magnetic resonance
min	minute
°C	degree Celsius
NEt_3	triethylamine
rt	room temperature
ppm	parts per million
MS	mass spectrometry
GPC	Gel-Permeations-Chromatographie
g	gram
PPh_3	triphenylphosphine
DIPEA	*N,N*-diisopropylethylamine
NTf_2	trifluoromethylsulfonylimide
CSI-TOF-MS	cold-spray ionization time-of-flight mass spectrometry
NOESY	nuclear overhauser enhancement spectroscopy
$P(t-Bu)_3$	tri-*tert*-butylphosphine
cv	cyclic voltammetry
UV-Vis	UV-Visible
DMSO	dimethyl sulfoxide
DMF	dimethylformamide
CH_3CN, ACN	acetonitrile
$CHCl_3$	chloroform
DCM	dichloromethane
Et_2O	diethyl ether
ETOH	ethanol
DABCO	1,4-diazabicyclo[2.2.2]octane
TMS-	trimethylsilyl group
$Pd_2(dba)_3$	tris(dibenzylideneacetone)dipalladium(0)
XPhos	dicyclohexyl[2',4',6'-tris(propan-2-yl)[1,1'-biphenyl]-2-yl]phosp
$Pd(dppf)Cl_2$	[1,1'-bis-(diphenylphosphino)-ferrocen]-dichloro-palladium(II)
$Zn(OTf)_2$,$(CF_3SO_3)_2Zn$	zinc trifluoromethanesulfonate
DMAP	*N,N*-dimethylpyridin-4-amin
IPA	propan-2-ol

TMB	1,3,5-trimethoxybenzene
prep TLC	preparative thin layer chromatography
ee	enantiomeric excess
DIPA	diisopropylamine
Fc	ferrocene
acac	acetylacetonate
1,5-DAN	1,5-Diaminonaphthalene
TBA	tetrabutylammonium

8.2 List of Figures

8.3 List of Tables

9 References

[1] H. Samuel, U. Nweke-Maraizu, E. E. Etim, *Journal of Chemical Reviews* **2023**, *5*, 439–465, DOI 10.48309/jcr.2023.407989.1235.

[2] F. Weinhold, R. A. Klein, *Molecular Physics* **2012**, *110*, 565–579, DOI 10.1080/00268976.2012.661478.

[3] W. M. Latimer, W. H. Rodebush, *Journal of the American Chemical Society* **1920**, *42*, 1419–1433, DOI 10.1021/ja01452a015.

[4] J. Kohler, Robert E., *Historical Studies in the Physical Sciences* **1971**, *3*, 343–376, DOI 10.2307/27757322.

[5] G. Lewis, *Valence and the Structure of Atoms and Molecules*, Chemical Catalog Company, Incorporated, **1923**.

[6] L. J. Karas, C.-H. Wu, R. Das, J. I.-C. Wu, *Computational Molecular Science* **2020**, *10*, DOI 10.1002/wcms.1477.

[7] G. R. Desiraju, *Accounts of Chemical Research* **2002**, *35*, 565–573, DOI 10.1021/ar010054t.

[8] J. D. Watson, F. H. C. Crick, *Nature* **1953**, *171*, 737–738, DOI 10.1038/171737a0.

[9] L. Pauling, R. B. Corey, H. R. Branson, *Proceedings of the National Academy of Sciences* **1951**, *37*, 205–211, DOI 10.1073/pnas.37.4.205.

[10] L. Pauling, R. B. Corey, *Proceedings of the National Academy of Sciences* **1951**, *37*, 251–256, DOI 10.1073/pnas.37.5.251.

[11] J. Donohue, *The Journal of Physical Chemistry* **1952**, *56*, 502–510, DOI 10.1021/j150496a023.

[12] J. Dong, A. P. Davis, *Angewandte Chemie International Edition* **2021**, *60*, 8035–8048, DOI https://doi.org/10.1002/anie.202012315.

[13] A. G. Doyle, E. N. Jacobsen, *Chemical Reviews* **2007**, *107*, 5713–5743, DOI 10.1021/cr068373r.

[14] M. Shoji, Y. Hayashi in *Hydrogen Bonding in Organic Synthesis*, John Wiley & Sons, Ltd, **2009**, Chapter 7, pp. 353–371, DOI https://doi.org/10.1002/9783527627844.ch7.

[15] P. S. Corbin, L. J. Lawless, Z. Li, Y. Ma, M. J. Witmer, S. C. Zimmerman, *Proceedings of the National Academy of Sciences* **2002**, *99*, 5099–5104, DOI 10.1073/pnas.062641199.

[16] R. P. Sijbesma, E. Meijer, *Current Opinion in Colloid & Interface Science* **1999**, *4*, 24–32, DOI 10.1016/s1359-0294(99)00011-4.

[17] V. Farina, J. T. Reeves, C. H. Senanayake, J. J. Song, *Chemical Reviews* **2006**, *106*, 2734–2793, DOI 10.1021/cr040700c.

[18] A. Sampedro, R. Villalonga-Planells, M. Vega, G. Ramis, S. F. d. Mattos, P. Villalonga, A. Costa, C. Rotger, *Bioconjugate Chemistry* **2014**, *25*, 1537–1546, DOI 10.1021/bc500258b.

[19] T. Grus, H. Lahnif, B. Klasen, E.-S. Moon, L. Greifenstein, F. Roesch, *Bioconjugate Chemistry* **2021**, *32*, 1223–1231, DOI 10.1021/acs.bioconjchem.1c00305.

[20] J. P. Malerich, K. Hagihara, V. H. Rawal, *Journal of the American Chemical Society* **2008**, *130*, 14416–14417, DOI 10.1021/ja805693p.

[21] S. D. Shinde, N. Kulkarni, B. Sahu, *ACS Applied Bio Materials* **2023**, *6*, 507–518, DOI 10.1021/acsabm.2c00803.

[22] A. A. Abogunrin, S. A. Healy, O. Fenelon, R. B. P. Elmes, *Chemistry* **2022**, *4*, 1288–1299, DOI 10.3390/chemistry4040085.

[23] S. Cohen, S. G. Cohen, *Journal of the American Chemical Society* **1966**, *88*, 1533–1536, DOI 10.1021/ja00959a040.

[24] A. Rostami, A. Colin, X. Y. Li, M. G. Chudzinski, A. J. Lough, M. S. Taylor, *The Journal of Organic Chemistry* **2010**, *75*, 3983–3992, DOI 10.1021/jo100104g.

[25] L. Hu, Z. Yan, H. Xu, *RSC Advances* **2013**, *3*, 7667–7676, DOI 10.1039/c3ra23048a.

[26] M. Rombola, V. H. Rawal, *Organic Letters* **2018**, *20*, 514–517, DOI 10.1021/acs.orglett.7b03549.

[27] M. Ito, R. West, *Journal of the American Chemical Society* **1963**, *85*, 2580–2584, DOI 10.1021/ja00900a011.

[28] D. Quiñonero, A. Frontera, P. Ballester, P. M. Deyà, *Tetrahedron Letters* **2000**, *41*, 2001–2005, DOI 10.1016/s0040-4039(00)00084-8.

[29] P. v. R. Schleyer, K. Najafian, B. Kiran, H. Jiao, *The Journal of Organic Chemistry* **2000**, *65*, 426–431, DOI 10.1021/jo991267n.

[30] H. Liu, C. S. Tomooka, H. W. Moore, *Synthetic Communications* **1997**, *27*, 2177–2180, DOI 10.1080/00397919708006826.

[31] A. Schmidt*, *Synthesis* **1980**, *1980*, 961–994, DOI 10.1055/s-1980-29291.

[32] L. F. Tietze, M. Arlt, M. Beller, K.-H. G. üsenkamp, E. Jähde, M. F. Rajewsky, *Chemische Berichte* **2010**, *124*, 1215–1221, DOI 10.1002/cber.19911240539.

[33] M. P. Dwyer, Y. Yu, J. Chao, C. Aki, J. Chao, P. Biju, V. Girijavallabhan, D. Rindgen, R. Bond, R. Mayer-Ezel, J. Jakway, R. W. Hipkin, J. Fossetta, W. Gonsiorek, H. Bian, X. Fan, C. Terminelli, J. Fine, D. Lundell, J. R. Merritt, L. L. Rokosz, B. Kaiser, G. Li, W. Wang, T. Stauffer, L. Ozgur, J. Baldwin, A. G. Taveras, *Journal of Medicinal Chemistry* **2006**, *49*, 7603–7606, DOI 10.1021/jm0609622.

[34] R. I. Storer, C. Aciro, L. H. Jones, *Chemical Society Reviews* **2011**, *40*, 2330–2346, DOI 10.1039/c0cs00200c.

[35] S. J. Connon, *Chemistry – A European Journal* **2006**, *12*, 5418–5427, DOI https://doi.org/10.1002/chem.200501076.

[36] J. Alemán, A. Parra, H. Jiang, K. A. Jørgensen, *Chemistry - A European Journal* **2011**, *17*, 6890–6899, DOI 10.1002/chem.201003694.

[37] S. Tomàs, R. Prohens, M. Vega, M. C. Rotger, P. M. Deyà, P. Ballester, A. Costa, *The Journal of Organic Chemistry* **1996**, *61*, 9394–9401, DOI 10.1021/jo9614147.

[38] C. Rotger, B. Soberats, D. Quiñonero, A. Frontera, P. Ballester, J. Benet-Buchholz, P. M. Deyà, A. Costa, *European Journal of Organic Chemistry* **2008**, *2008*, 1864–1868, DOI 10.1002/ejoc.200701209.

[39] D. Quiñonero, R. Prohens, C. Garau, A. Frontera, P. Ballester, A. Costa, P. M. Deyà, *Chemical Physics Letters* **2002**, *351*, 115–120, DOI 10.1016/s0009-2614(01)01295-7.

[40] R. Prohens, A. Portell, M. Font-Bardia, A. Bauzá, A. Frontera, *Crystal Growth & Design* **2014**, *14*, 2578–2587, DOI 10.1021/cg500264k.

[41] L. Brunsveld, B. J. B. Folmer, E. W. Meijer, R. P. Sijbesma, *Chemical Reviews* **2001**, *101*, 4071–4098, DOI 10.1021/cr990125q.

[42] R. Prohens, S. Tomàs, J. Morey, P. M. Deyà, P. Ballester, A. Costa, *Tetrahedron Letters* **1998**, *39*, 1063–1066, DOI 10.1016/s0040-4039(97)10728-6.

[43] A. Frontera, J. Morey, A. Oliver, M. N. Piña, D. Quiñonero, A. Costa, P. Ballester, P. M. Deyà, E. V. Anslyn, *The Journal of Organic Chemistry* **2006**, *71*, 7185–7195, DOI 10.1021/jo0609327.

[44] V. Amendola, G. Bergamaschi, M. Boiocchi, L. Fabbrizzi, M. Milani, *Chemistry - A European Journal* **2010**, *16*, 4368–4380, DOI 10.1002/chem.200903190.

[45] Y. Hoashi, T. Okino, Y. Takemoto, *Angewandte Chemie International Edition* **2005**, *44*, 4032–4035, DOI 10.1002/anie.200500459.

[46] S. J. Edwards, H. Valkenier, N. Busschaert, P. A. Gale, A. P. Davis, *Angewandte Chemie International Edition* **2015**, *54*, 4592–4596, DOI 10.1002/anie.201411805.

[47] A. P. Davis, S. M. Draper, G. Dunne, P. Ashton, *Chemical Communications* **1999**, 2265–2266, DOI 10.1039/a907179b.

[48] M. C. Rotger, M. N. Piña, A. Frontera, G. Martorell, P. Ballester, P. M. Deyà, A. Costa, *The Journal of Organic Chemistry* **2004**, *69*, 2302–2308, DOI 10.1021/jo035546t.

[49] A. Portell, R. Barbas, D. Braga, M. Polito, C. Puigjaner, R. Prohens, *CrystEngComm* **2008**, *11*, 52–54, DOI 10.1039/b813086h.

[50] M. S. Sigman, E. N. Jacobsen, *Journal of the American Chemical Society* **1998**, *120*, 4901–4902, DOI 10.1021/ja980139y.

[51] J. Wang, H. Li, X. Yu, L. Zu, W. Wang, *Organic Letters* **2005**, *7*, 4293–4296, DOI 10.1021/ol051822+.

[52] Y.-Q. Wang, J. Song, R. Hong, H. Li, L. Deng, *Journal of the American Chemical Society* **2006**, *128*, 8156–8157, DOI 10.1021/ja062700v.

[53] Y. Yamaoka, H. Miyabe, Y. Takemoto, *Journal of the American Chemical Society* **2007**, *129*, 6686–6687, DOI 10.1021/ja071470x.

[54] I. T. Raheem, P. S. Thiara, E. A. Peterson, E. N. Jacobsen, *Journal of the American Chemical Society* **2007**, *129*, 13404–13405, DOI 10.1021/ja076179w.

[55] R. P. Singh, K. Bartelson, Y. Wang, H. Su, X. Lu, L. Deng, *Journal of the American Chemical Society* **2008**, *130*, 2422–2423, DOI 10.1021/ja078251w.

[56] Y. Huang, A. K. Unni, A. N. Thadani, V. H. Rawal, *Nature* **2003**, *424*, 146–146, DOI 10.1038/424146a.

[57] J.-i. Oku, S. Inoue, *Journal of the Chemical Society Chemical Communications* **1981**, 229–230.

[58] H. Hiemstra, H. Wynber, *Journal of the American Chemical Society* **1981**, *103*, 417–430.

[59] T. Akiyama, J. Itoh, K. Yokota, K. Fuchibe, *Angewandte Chemie International Edition* **2004**, *43*, 1566–1568, DOI https://doi.org/10.1002/anie.200353240.

[60] E. J. Corey, M. J. Grogan, *Organic Letters* **1999**, *1*, 157–160, DOI 10.1021/ol9906231.

[61] B. M. Nugent, R. A. Yoder, J. N. Johnston, *Journal of the American Chemical Society* **2004**, *126*, 3418–3419, DOI 10.1021/ja031906i.

[62] T. Lu, S. E. Wheeler, *Chemistry – A European Journal* **2013**, *19*, 15141–15147, DOI 10.1002/chem.201302990.

[63] B. M. McVey, J. Rumble, C. E. V. Nathan, I. A. Gass, M. R. Sambrook, P. J. Cragg, *Supramolecular Chemistry* **2024**, *ahead-of-print*, 1–15, DOI 10.1080/10610278.2024.2307016.

[64] S. Vera, A. García-Urricelqui, A. Mielgo, M. Oiarbide, *European Journal of Organic Chemistry* **2023**, *26*, DOI 10.1002/ejoc.202201254.

[65] K. Bera, I. N. N. Namboothiri, *The Journal of Organic Chemistry* **2015**, *80*, 1402–1413, DOI 10.1021/jo502332r.

[66] Ö. Işılar, A. Bulut, A. S. Yaglioglu, İ. Demirtaş, E. Arat, M. Türk, *Carbohydrate Research* **2020**, *492*, 107991, DOI 10.1016/j.carres.2020.107991.

[67] Y. Deng, Z. Dong, F. Gao, Y. Guo, M. Sun, Y. Li, Y. Wang, Q. Chen, K. Wang, W. Yan, *The Journal of Organic Chemistry* **2021**, *86*, 13011–13024, DOI 10.1021/acs.joc.1c01705.

[68] K. Tanabe, W. F. Hölderich, *Applied Catalysis A: General* **1999**, *181*, 399–434, DOI https://doi.org/10.1016/S0926-860X(98)00397-4.

[69] X. Ni, X. Li, Z. Wang, J.-P. Cheng, *Organic Letters* **2014**, *16*, 1786–1789, DOI 10.1021/ol5005017.

[70] M. Žabka, R. Šebesta, *Molecules* **2015**, *20*, 15500–15524, DOI 10.3390/molecules200915500.

[71] F. R. Wurm, H.-A. Klok, *Chemical Society Reviews* **2013**, *42*, 8220–8236, DOI 10.1039/c3cs60153f.

[72] X.-J. Cai, Z. Li, W.-H. Chen, *Mini-Reviews in Organic Chemistry* **2018**, *15*, 148–156, DOI 10.2174/1570193x14666171114115629.

[73] B.-L. Zhao, J.-H. Li, D.-M. Du, *The Chemical Record* **2017**, *17*, 994–1018, DOI https://doi.org/10.1002/tcr.201600140.

[74] L. A. Marchetti, L. K. Kumawat, N. Mao, J. C. Stephens, R. B. Elmes, *Chem* **2019**, *5*, 1398–1485, DOI 10.1016/j.chempr.2019.02.027.

[75] Nobel Prize in Chemistry: Jean-Marie Lehn with Donald J. Cram and Charles J. Pedersen in 1987, *La lettre du Collège de France* **2015**, 11, DOI 10.4000/lettre-cdf.2587.

[76] P. D. Beer, P. A. Gale, D. K. Smith, *Supramolecular chemistry*, Repr, Oxford Univ. Press, Oxford, **2003**.

[77] C. J. Pedersen, *Journal of the American Chemical Society* **1967**, *89*, 7017–7036, DOI 10.1021/ja01002a035.

[78] B. Dietrich, J. M. Lehn, J. P. Sauvage, *Tetrahedron Letters* **1969**, *10*, 2889–2892, DOI 10.1016/S0040-4039(01)88300-3.

[79] D. J. Cram, T. Kaneda, R. C. Helgeson, G. M. Lein, *Journal of the American Chemical Society* **1979**, *101*, 6752–6754, DOI 10.1021/ja00516a048.

[80] K. E. Koenig, G. M. Lein, P. Stuckler, T. Kaneda, D. J. Cram, *Journal of the American Chemical Society* **1979**, *101*, 3553–3566.

[81] D. J. Cram, *Angewandte Chemie International Edition in English* **1986**, *25*, 1039–1057, DOI https://doi.org/10.1002/anie.198610393.

[82] M. M. G. Antonisse, D. N. Reinhoudt, *Chem. Commun.* **1998**, 443–448, DOI 10.1039/A707529D.

[83] L. Qin, A. Hartley, P. Turner, R. B. P. Elmes, K. A. Jolliffe, *Chemical Science* **2016**, *7*, 4563–4572, DOI 10.1039/c6sc01011c.

[84] X. Shu, R. Wang, Y. Fan, S. Li, C. Huang, *Tetrahedron Letters* **2019**, *60*, 729–733, DOI 10.1016/j.tetlet.2019.02.004.

[85] Y. Okumura, S. Murakami, H. Maeda, N. Matsumura, K. Mizuno, *Tetrahedron Letters* **2003**, *44*, 8183–8185, DOI https://doi.org/10.1016/j.tetlet.2003.08.112.

[86] A. J. Sindt, M. D. Smith, P. J. Pellechia, L. S. Shimizu, *Crystal Growth & Design* **2018**, *18*, 1605–1612, DOI 10.1021/acs.cgd.7b01558.

[87] C. Jin, M. Zhang, L. Wu, Y. Guan, Y. Pan, J. Jiang, C. Lin, L. Wang, *Chemical Communications* **2013**, *49*, 2025–2027, DOI 10.1039/c3cc00196b.

[88] D. Jagleniec, M. Wilczek, J. Romański, *Molecules* **2021**, *26*, 2751, DOI 10.3390/molecules26092751.

[89] M. Zaleskaya, Ł. Dobrzycki, J. Romański, *International Journal of Molecular Sciences* **2020**, *21*, 9465, DOI 10.3390/ijms21249465.

[90] C. Dietrich-Buchecker, J. Sauvage, J. Kintzinger, *Tetrahedron Letters* **1983**, *24*, 5095–5098, DOI 10.1016/S0040-4039(00)94050-4.

[91] E. Wasserman, *Journal of the American Chemical Society* **1960**, *82*, 4433–4434, DOI 10.1021/ja01501a082.

[92] Jean-Pierre Sauvage, Sir J. Fraser Stoddart, Bernard L. Feringa, Press release: The Nobel Prize in Chemistry 2016: They developed the world's smallest machines, Stockholm, **2016**, https://www.nobelprize.org/prizes/chemistry/2016/press-release/.

[93] J.-C. Chambron, J.-P. Sauvage, *New J. Chem.* **2013**, *37*, 49–57, DOI 10.1039/c2nj40555e.

[94] C. O. Dietrich-Buchecker, J. P. Sauvage, *Chemical reviews* **1987**, *87*, 795–810, DOI 10.1021/cr00080a007.

[95] C. D. Pentecost, K. S. Chichak, A. J. Peters, G. W. V. Cave, S. J. Cantrill, J. F. Stoddart, *Angewandte Chemie* **2007**, *46*, 218–222, DOI 10.1002/anie.200603521.

[96] K. S. Chichak, S. J. Cantrill, A. R. Pease, S.-H. Chiu, G. W. V. Cave, J. L. Atwood, J. F. Stoddart, *Science* **2004**, *304*, 1308–1312, DOI 10.1126/science.1096914.

[97] G. Rapenne, C. Dietrich-Buchecker, J. Sauvage, *Journal of the American Chemical Society* **1999**, *121*, 994–1001.

[98] C. Dietrich-Buchecker, J.-P. Sauvage, *Molecular catenanes, rotaxanes and knots: A journey through the world of molecular topology*, Wiley-VCH, Weinheim and New York, **1999**, DOI 10.1002/9783527613724.

[99] P. L. Anelli, N. Spencer, J. F. Stoddart, *Journal of the American Chemical Society* **1991**, *113*, 5131–5133, DOI 10.1021/ja00013a096.

[100] Y. Liu, A. H. Flood, P. A. Bonvallet, S. A. Vignon, B. H. Northrop, H.-R. Tseng, J. O. Jeppesen, T. J. Huang, B. Brough, M. Baller, S. Magonov, S. D. Solares, W. A. Goddard, C.-M. Ho, J. F. Stoddart, *Journal of the American Chemical Society* **2005**, *127*, 9745–9759, DOI 10.1021/ja051088p.

[101] J. D. Badjic, C. M. Ronconi, J. F. Stoddart, V. Balzani, S. Silvi, A. Credi, *Journal of the American Chemical Society* **2006**, *128*, 1489–1499, DOI 10.1021/ja0543954.

[102] T. Kudernac, N. Ruangsupapichat, M. Parschau, B. Maciá, N. Katsonis, S. R. Harutyunyan, K.-H. Ernst, B. L. Feringa, *Nature* **2011**, *479*, 208–211, DOI 10.1038/nature10587.

[103] A. Portell, R. Prohens, *Crystal Growth & Design* **2014**, *14*, 397–400, DOI 10.1021/cg401639g.

[104] A. Singh, R. K. Singh, G. N. Patwari, *CrystEngComm* **2021**, *23*, 5331–5336, DOI 10.1039/D1CE00623A.

[105] R. Prohens, A. Portell, C. Puigjaner, S. Tomàs, K. Fujii, K. D. M. Harris, X. Alcobé, M. Font-Bardia, R. Barbas, *Crystal Growth & Design* **2011**, *11*, 3725–3730, DOI 10.1021/cg200772e.

[106] T. Steiner, *Angewandte Chemie International Edition* **2002**, *41*, 48–76, DOI 10.1002/1521-3773(20020104)41:1<48::aid-anie48>3.0.co;2-u.

[107] A. S. Mahadevi, G. N. Sastry, *Chemical Reviews* **2016**, *116*, 2775–2825, DOI 10.1021/cr500344e.

[108] J. Nochebuena, C. Cuautli, J. Ireta, *Physical Chemistry Chemical Physics* **2017**, *19*, 15256–15263, DOI 10.1039/c7cp01695f.

[109] L. d. A. Santos, D. Cesario, P. Vermeeren, S. C. C. v. d. Lubbe, F. Nunzi, C. F. Guerra, *ChemPlusChem* **2022**, *87*, e202100436, DOI 10.1002/cplu.202100436.

[110] J. L. Cook, C. A. Hunter, C. M. R. Low, A. Perez-Velasco, J. G. Vinter, *Angewandte Chemie International Edition* **2007**, *46*, 3706–3709, DOI 10.1002/anie.200604966.

[111] S. Cantekin, T. F. A. d. Greef, A. R. A. Palmans, *Chemical Society Reviews* **2012**, *41*, 6125–6137, DOI 10.1039/c2cs35156k.

[112] M. M. J. Smulders, A. P. H. J. Schenning, E. W. Meijer, *Journal of the American Chemical Society* **2008**, *130*, 606–611, DOI 10.1021/ja075987k.

[113] Y. Toledo-González, J.-M. Sotiropoulos, D. Bécart, G. Guichard, P. Carbonnière, *The Journal of Organic Chemistry* **2022**, *87*, 10726–10735, DOI 10.1021/acs.joc.2c00562.

[114] D. Bécart, V. Diemer, A. Salaün, M. Oiarbide, Y. R. Nelli, B. Kauffmann, L. Fischer, C. Palomo, G. Guichard, *Journal of the American Chemical Society* **2017**, *139*, 12524–12532, DOI 10.1021/jacs.7b05802.

[115] N. Probst, Á. Madarász, A. Valkonen, I. Pápai, K. Rissanen, A. Neuvonen, P. M. Pihko, *Angewandte Chemie International Edition* **2012**, *51*, 8495–8499, DOI 10.1002/anie.201203852.

[116] L. Trevisan, A. D. Bond, C. A. Hunter, *Journal of the American Chemical Society* **2022**, *144*, 19499–19507, DOI 10.1021/jacs.2c08120.

[117] N. Dominelli-Whiteley, J. J. Brown, K. B. Muchowska, I. K. Mati, C. Adam, T. A. Hubbard, A. Elmi, A. J. Brown, I. A. W. Bell, S. L. Cockroft, *Angewandte Chemie International Edition* **2017**, *56*, 7658–7662, DOI 10.1002/anie.201703757.

[118] D. O. Soloviev, F. E. Hanna, M. C. Misuraca, C. A. Hunter, *Chemical Science* **2022**, *13*, 11863–11868, DOI 10.1039/d2sc04271a.

[119] F. E. Hanna, A. J. Root, C. A. Hunter, *Chemical Science* **2023**, *14*, 11151–11157, DOI 10.1039/d3sc03823h.

[120] L. Martínez-Crespo, G. F. S. Whitehead, I. J. Vitórica-Yrezábal, S. J. Webb, *Chemical Science* **2024**, *15*, 17120–17127, DOI 10.1039/d4sc04337e.

[121] T. Sawada, Y. Inomata, K. Shimokawa, M. Fujita, *Nature Communications* **2019**, *10*, 5687, DOI 10.1038/s41467-019-13594-4.

[122] T. Sawada, M. Yamagami, K. Ohara, K. Yamaguchi, M. Fujita, *Angewandte Chemie International Edition* **2016**, *55*, 4519–4522, DOI 10.1002/anie.201600480.

[123] J. L. Atwood, A. Szumna, *Journal of the American Chemical Society* **2002**, *124*, 10646–10647, DOI 10.1021/ja0271911.

[124] L. R. MacGillivray, J. L. Atwood, *Nature* **1997**, *389*, 469–472, DOI 10.1038/38985.

[125] Y. Liu, C. Hu, A. Comotti, M. D. Ward, *Science* **2011**, *333*, 436–440, DOI 10.1126/science.1204369.

[126] W. Zhang, D. Yang, J. Zhao, L. Hou, J. L. Sessler, X.-J. Yang, B. Wu, *Journal of the American Chemical Society* **2018**, *140*, 5248–5256, DOI 10.1021/jacs.8b01488.

[127] O. Mogck, E. F. Paulus, V. Böhmer, I. Thondorf, W. Vogt, *Chemical Communications* **1996**, *0*, 2533–2534, DOI 10.1039/cc9960002533.

[128] M. Fujita, M. Tominaga, A. Hori, B. Therrien, *Accounts of Chemical Research* **2005**, *38*, 369–378, DOI 10.1021/ar040153h.

[129] A. Kumar, S.-S. Sun, A. J. Lees, *Coordination Chemistry Reviews* **2008**, *252*, 922–939, DOI https://doi.org/10.1016/j.ccr.2007.07.023.

[130] B. Therrien, G. Süss-Fink, P. Govindaswamy, A. K. Renfrew, P. J. Dyson, *Angewandte Chemie International Edition* **2008**, *47*, 3773–3776, DOI https://doi.org/10.1002/anie.200800186.

[131] D. J. Tranchemontagne, Z. Ni, M. O'Keeffe, O. M. Yaghi, *Angewandte Chemie* **2008**, *47*, 5136–5147, DOI 10.1002/anie.200705008.

[132] M. M. Conn, J. Rebek, *Chemical reviews* **1997**, *97*, 1647–1668, DOI 10.1021/cr9603800.

[133] R. Custelcean, *Chemical Society reviews* **2014**, *43*, 1813–1824, DOI 10.1039/C3CS60371G.

[134] P. Mal, B. Breiner, K. Rissanen, J. R. Nitschke, *Science* **2009**, *324*, 1697–1699, DOI 10.1126/science.1175313.

[135] S. Turega, M. Whitehead, B. R. Hall, M. F. Haddow, C. A. Hunter, M. D. Ward, *Chemical communications* **2012**, *48*, 2752–2754, DOI 10.1039/C2CC17369G.

[136] C. J. Hastings, M. D. Pluth, R. G. Bergman, K. N. Raymond, *Journal of the American Chemical Society* **2010**, *132*, 6938–6940, DOI 10.1021/ja102633e.

[137] Y. R. Hristova, M. M. J. Smulders, J. K. Clegg, B. Breiner, J. R. Nitschke, *Chem. Sci.* **2011**, *2*, 638–641, DOI 10.1039/C0SC00495B.

[138] I. A. Riddell, M. M. J. Smulders, J. K. Clegg, J. R. Nitschke, *Chemical communications* **2011**, *47*, 457–459, DOI 10.1039/C0CC02573A.

[139] M. Yoshizawa, J. K. Klosterman, M. Fujita, *Angewandte Chemie International Edition* **2009**, *48*, 3418–3438, DOI 10.1002/anie.200805340.

[140] D. M. Vriezema, M. Comellas Aragonès, J. A. A. W. Elemans, J. J. L. M. Cornelissen, A. E. Rowan, R. J. M. Nolte, *Chemical reviews* **2005**, *105*, 1445–1489, DOI 10.1021/cr0300688.

[141] T. Murase, H. Takezawa, M. Fujita, *Chemical communications* **2011**, *47*, 10960–10962, DOI 10.1039/C1CC14523A.

[142] D. Phlip, *Advanced Materials* **1996**, *8*, 866–868, DOI 10.1002/adma.19960081029.

[143] M. Han, D. M. Engelhard, G. H. Clever, *Chemical Society reviews* **2014**, *43*, 1848–1860, DOI 10.1039/c3cs60473j.

[144] E. Riedel, C. Janiak, *Anorganische Chemie*, 8. Aufl., de Gruyter, Berlin, **2011**, DOI 10.1515/9783110225679.

[145] W. M. Bloch, Y. Abe, J. J. Holstein, C. M. Wandtke, B. Dittrich, G. H. Clever, *Journal of the American Chemical Society* **2016**, *138*, 13750–13755, DOI 10.1021/jacs.6b08694.

[146] Susanne Löffler, PhD thesis, Georg–August–Universität Göttingen, Göttingen, **2018**, http://hdl.handle.net/11858/00-1735-0000-002E-E415-6.

[147] H. S. Sahoo, D. K. Chand, *Dalton transactions* **2010**, *39*, 7223–7225, DOI 10.1039/C0DT00337A.

[148] D. M. Engelhard, S. Freye, K. Grohe, M. John, G. H. Clever, *Angewandte Chemie* **2012**, *51*, 4747–4750, DOI 10.1002/anie.201200611.

[149] Z. Bo, PhD thesis, Technische Universität Dortmund, Dortmund, **2019**, https://katalog.ub.tu-dortmund.de/id/ir01388a:ubd.lobid:HT020332415.

[150] E. Benchimol, I. Regeni, B. Zhang, M. Kabiri, J. J. Holstein, G. H. Clever, *Journal of the American Chemical Society* **2024**, DOI 10.1021/jacs.3c14168.

[151] K. Wu, E. Benchimol, A. Baksi, G. H. Clever, *Nature Chemistry* **2024**, 1–8, DOI 10.1038/s41557-023-01415-7.

[152] K. Wu, E. Benchimol, A. Baksi, G. Clever, **2023**, DOI 10.26434/chemrxiv-2023-5gb4q.

[153] L. A. Wessjohann, O. Kreye, D. G. Rivera, *Angewandte Chemie* **2017**, *56*, 3501–3505, DOI 10.1002/anie.201610801.

[154] N. Christinat, R. Scopelliti, K. Severin, *Angewandte Chemie* **2008**, *47*, 1848–1852, DOI 10.1002/anie.200705272.

[155] W. M. Bloch, G. H. Clever, *Chemical communications* **2017**, *53*, 8506–8516, DOI 10.1039/c7cc03379f.

[156] T. K. Ronson, D. A. Roberts, S. P. Black, J. R. Nitschke, *Journal of the American Chemical Society* **2015**, *137*, 14502–14512, DOI 10.1021/jacs.5b09920.

[157] M. Albrecht, M. Schneider, H. Röttele, *Angewandte Chemie International Edition* **1999**, *38*, 557–559, DOI https://doi.org/10.1002/(SICI)1521-3773(19990215)38:4<557::AID-ANIE557>3.0.CO;2-S.

[158] N. Kishi, Z. Li, K. Yoza, M. Akita, M. Yoshizawa, *Journal of the American Chemical Society* **2011**, *133*, 11438–11441, DOI 10.1021/ja2037029.

[159] M. Yamashina, T. Yuki, Y. Sei, M. Akita, M. Yoshizawa, *Chemistry – A European Journal* **2015**, *21*, 4200–4204, DOI 10.1002/chem.201406445.

[160] Q.-F. Sun, S. Sato, M. Fujita, *Angewandte Chemie International Edition* **2014**, *53*, 13510–13513, DOI 10.1002/anie.201408652.

[161] W. M. Bloch, J. J. Holstein, W. Hiller, G. H. Clever, *Angewandte Chemie* **2017**, *56*, 8285–8289, DOI 10.1002/anie.201702573.

[162] I. Regeni, R. Chowdhury, K. Terlinden, S. Horiuchi, J. J. Holstein, S. Feldmann, G. H. Clever, *Angewandte Chemie International Edition* **2023**, *62*, e202308288, DOI 10.1002/anie.202308288.

[163] R. Zhu, W. M. Bloch, J. J. Holstein, S. Mandal, L. V. Schäfer, G. H. Clever, *Chemistry (Weinheim an der Bergstrasse Germany)* **2018**, *24*, 12976–12982, DOI 10.1002/chem.201802188.

[164] S. Turega, M. Whitehead, B. R. Hall, M. F. Haddow, C. A. Hunter, M. D. Ward, *Chemical Communications* **2012**, *48*, 2752–2754, DOI 10.1039/c2cc17369g.

[165] R. Custelcean, *Chemical Society Reviews* **2014**, *43*, 1813–1824, DOI 10.1039/c3cs60371g.

[166] P. Mal, B. Breiner, K. Rissanen, J. R. Nitschke, *Science* **2009**, *324*, 1697–1699, DOI 10.1126/science.1175313.

[167] C. J. Hastings, M. D. Pluth, R. G. Bergman, K. N. Raymond, *Journal of the American Chemical Society* **2010**, *132*, 6938–6940, DOI 10.1021/ja102633e.

[168] M. Röper, *Chemie in unserer Zeit* **2006**, *40*, 126–135, DOI 10.1002/ciuz.200600373.

[169] M. Yoshizawa, M. Tamura, M. Fujita, *Science* **2006**, *312*, 251–254, DOI 10.1126/science.1124985.

[170] M. D. Pluth, R. G. Bergman, K. N. Raymond, *Science* **2007**, *316*, 85–88, DOI 10.1126/science.1138748.

[171] J. Wang, T. A. Young, F. Duarte, P. J. Lusby, *Journal of the American Chemical Society* **2020**, *142*, 17743–17750, DOI 10.1021/jacs.0c08639.

[172] T. Murase, Y. Nishijima, M. Fujita, *Journal of the American Chemical Society* **2012**, *134*, 162–164, DOI 10.1021/ja210068f.

[173] T. Gadzikwa, R. Bellini, H. L. Dekker, J. N. H. Reek, *Journal of the American Chemical Society* **2012**, *134*, 2860–2863, DOI 10.1021/ja211455j.

[174] C. J. Hastings, M. D. Pluth, R. G. Bergman, K. N. Raymond, *Journal of the American Chemical Society* **2010**, *132*, 6938–6940, DOI 10.1021/ja102633e.

[175] D. H. Leung, R. G. Bergman, K. N. Raymond, *Journal of the American Chemical Society* **2007**, *129*, 2746–2747, DOI 10.1021/ja068688o.

[176] R. Wolfenden, M. J. Snider, *Accounts of Chemical Research* **2001**, *34*, 938–945, DOI 10.1021/ar000058i.

[177] S. Horowitz, R. C. Trievel, *Journal of Biological Chemistry* **2012**, *287*, 41576–41582, DOI 10.1074/jbc.r112.418574.

[178] D. P. August, G. S. Nichol, P. J. Lusby, *Angewandte Chemie International Edition* **2016**, *55*, 15022–15026, DOI https://doi.org/10.1002/anie.201608229.

[179] V. Martí-Centelles, A. L. Lawrence, P. J. Lusby, *Journal of the American Chemical Society* **2018**, *140*, 2862–2868, DOI 10.1021/jacs.7b12146.

[180] T. A. Young, V. Martí-Centelles, J. Wang, P. J. Lusby, F. Duarte, *Journal of the American Chemical Society* **2020**, *142*, 1300–1310, DOI 10.1021/jacs.9b10302.

[181] P. Howlader, P. Das, E. Zangrando, P. S. Mukherjee, *Journal of the American Chemical Society* **2016**, *138*, 1668–1676, DOI 10.1021/jacs.5b12237.

[182] A. N. Rollinson, J. Jones, V. Dupont, M. V. Twigg, *Energy Environ. Sci.* **2011**, *4*, 1216–1224, DOI 10.1039/C0EE00705F.

[183] A. Platzek, S. Juber, C. Yurtseven, S. Hasegawa, L. Schneider, C. Drechsler, K. E. Ebbert, R. Rudolf, Q.-Q. Yan, J. J. Holstein, L. V. Schäfer, G. H. Clever, *Angewandte Chemie International Edition* **2022**, *61*, e202209305, DOI 10.1002/anie.202209305.

[184] N. Y. Meredith, S. Borsley, I. V. Smolyar, G. S. Nichol, C. M. Baker, K. B. Ling, S. L. Cockroft, *Angewandte Chemie International Edition* **2022**, *61*, e202206604, DOI 10.1002/anie.202206604.

[185] R.-J. Li, C. Pezzato, C. Berton, K. Severin, *Chemical Science* **2021**, *12*, 4981–4984, DOI 10.1039/d1sc00127b.

[186] K. E. Ebbert, F. Sendzik, L. Neukirch, L. Eberlein, A. Platzek, P. Kibies, S. M. Kast, G. H. Clever, *Angewandte Chemie International Edition* **2024**, e202416076, DOI 10.1002/anie.202416076.

[187] A. Walther, G. Tusha, B. Schmidt, J. J. Holstein, L. V. Schäfer, G. H. Clever, *Journal of the American Chemical Society* **2024**, DOI 10.1021/jacs.4c12525.

[188] H. Jiang, M. W. Paixão, D. Monge, K. A. Jørgensen, *Journal of the American Chemical Society* **2010**, *132*, 2775–2783, DOI 10.1021/ja9097803.

[189] C. Tong, T. Liu, V. S. Talens, W. E. M. Noteborn, T. H. Sharp, M. M. R. M. Hendrix, I. K. Voets, C. L. Mummery, V. V. Orlova, R. E. Kieltyka, *Biomacromolecules* **2018**, *19*, 1091–1099, DOI 10.1021/acs.biomac.7b01614.

[190] S. Mert, Ö. Erdebil, *ACS Omega* **2024**, *9*, 8333–8342, DOI 10.1021/acsomega.3c09094.

[191] A. Arun, A. Docker, H. M. Tay, P. D. Beer, *Chemistry – A European Journal* **2023**, *29*, e202301446, DOI 10.1002/chem.202301446.

[192] A. Einstein, *Annalen der Physik* **1905**, *322*, 549–560, DOI 10.1002/andp.19053220806.

[193] P. W. Atkins, J. de Paula, M. Bär, *Physikalische Chemie*, 5. Aufl., Wiley-VCH Verl., Weinheim, **2013**, DOI 10.1002/3527682899.

[194] Anton Paar, Viscosity of Dimethyl Sulfoxide, https://wiki.anton-paar.com/en/dimethyl-sulfoxide/.

[195] I. Regeni, B. Chen, M. Frank, A. Baksi, J. J. Holstein, G. H. Clever, *Angewandte Chemie International Edition* **2021**, *60*, 5673–5678, DOI https://doi.org/10.1002/anie.202015246.

[196] Kristina Ebbert, PhD thesis, Technische Universität Dortmund, Dortmund, **2024**.

[197] Alexandre Walther, PhD thesis, Technische Universität Dortmund, Dortmund, **2024**.

[198] Y. Marunaka, *The Journal of Physiological Sciences* **2023**, *73*, 31, DOI 10.1186/s12576-023-00889-x.

[199] S. Sudan, D. W. Chen, C. Berton, F. Fadaei-Tirani, K. Severin, *Angewandte Chemie International Edition* **2023**, *62*, e202218072, DOI 10.1002/anie.202218072.

[200] C. M. McGuirk, J. Mendez-Arroyo, A. M. Lifschitz, C. A. Mirkin, *Journal of the American Chemical Society* **2014**, *136*, 16594–16601, DOI 10.1021/ja508804n.

[201] D. Jagleniec, S. Siennicka, Ł. Dobrzycki, M. Karbarz, J. Romański, *Inorganic Chemistry* **2018**, *57*, 12941–12952, DOI 10.1021/acs.inorgchem.8b02163.

[202] V. Ramalingam, M. E. Domaradzki, S. Jang, R. S. Muthyala, *Organic Letters* **2008**, *10*, 3315–3318, DOI 10.1021/ol801204s.

[203] P. Thordarson, Bindfit, http://supramolecular.org/.

[204] L. Cheng, K. Liu, Y. Duan, H. Duan, Y. Li, M. Gao, L. Cao, *CCS Chemistry* **2021**, *3*, 2749–2763, DOI 10.31635/ccschem.020.202000509.

[205] C. Özdemir, A. Güner, *European Polymer Journal* **2007**, *43*, 3068–3093, DOI 10.1016/j.eurpolymj.2007.02.022.

[206] X.-Q. Hou, D.-M. Du, *Advanced Synthesis & Catalysis* **2020**, *362*, 4487–4512, DOI 10.1002/adsc.202000842.

[207] agc-chemicals, Viscosity of DCM, https://www.agc-chemicals.com/file.jsp?id=jp/en/products/pdf/ASAHI_TRICHLOR_EN02.pdf.

[208] M. R. Wright, *An Introduction to Aqueous Electrolyte Solutions*, John Wiley & Sons, **2007**.

[209] K. S. Rao, P. Ramesh, R. Trivedi, M. L. Kantam, *Tetrahedron Letters* **2016**, *57*, 1227–1231, DOI 10.1016/j.tetlet.2016.02.008.

[210] T. J. Mooibroek, *Molecules* **2019**, *24*, 3370, DOI 10.3390/molecules24183370.

[211] C. Drechsler, A. Baksi, A. Platzek, M. Acar, J. J. Holstein, C. J. Stein, G. H. Clever, *Chemical Science* **2024**, DOI 10.1039/d4sc04786a.

[212] A. Kumar, R. Banerjee, E. Zangrando, P. S. Mukherjee, *Inorganic Chemistry* **2022**, *61*, 2368–2377, DOI 10.1021/acs.inorgchem.1c03797.

[213] P. K. Maitra, S. Bhattacharyya, N. Hickey, P. S. Mukherjee, *Journal of the American Chemical Society* **2024**, *146*, 15301–15308, DOI 10.1021/jacs.4c02956.

[214] D. Dalmau, E. P. Urriolabeitia, *Molecules* **2023**, *28*, 2663, DOI 10.3390/molecules28062663.

[215] R. F. W. Bader, *Chemical Reviews* **1991**, *91*, 893–928, DOI 10.1021/cr00005a013.

[216] S. Emamian, T. Lu, H. Kruse, H. Emamian, *Journal of Computational Chemistry* **2019**, *40*, 2868–2881, DOI https://doi.org/10.1002/jcc.26068.

[217] R. Plessius, N. Orth, I. Ivanović-Burmazović, M. A. Siegler, J. N. H. Reek, J. I. van der Vlugt, *Chem. Commun.* **2019**, *55*, 12619–12622, DOI 10.1039/C9CC07138E.

[218] V. Croué, S. Goeb, M. Sallé, *Chemical Communications* **2015**, *51*, 7275–7289, DOI 10.1039/c5cc00597c.

[219] W. Wang, Y.-X. Wang, H.-B. Yang, *Chemical Society Reviews* **2016**, *45*, 2656–2693, DOI 10.1039/c5cs00301f.

[220] A. J. McConnell, C. S. Wood, P. P. Neelakandan, J. R. Nitschke, *Chemical Reviews* **2015**, *115*, 7729–7793, DOI 10.1021/cr500632f.

[221] M.-X. Wu, Q.-Y. Hong, M. Li, W.-L. Jiang, B. Huang, S. Lu, H. Wang, H.-B. Yang, X.-L. Zhao, X. Shi, *Chem. Commun.* **2024**, *60*, 1184–1187, DOI 10.1039/D3CC04864K.

[222] B. Roy, E. Zangrando, P. S. Mukherjee, *Chem. Commun.* **2016**, *52*, 4489–4492, DOI 10.1039/C6CC00042H.

[223] S. Bhattacharyya, S. R. Ali, M. Venkateswarulu, P. Howlader, E. Zangrando, M. De, P. S. Mukherjee, *Journal of the American Chemical Society* **2020**, *142*, 18981–18989, DOI 10.1021/jacs.0c09567.

[224] T. Yamaguchi, M. Fujita, *Angewandte Chemie* **2008**, *120*, 2097–2099, DOI 10.1002/ange.200705139.

[225] D.-N. Yan, L.-X. Cai, S.-J. Hu, Y.-F. Zhou, L.-P. Zhou, Q.-F. Sun, *Angewandte Chemie International Edition* **2022**, DOI 10.1002/anie.202209879.

[226] Y. Furutani, H. Kandori, M. Kawano, K. Nakabayashi, M. Yoshizawa, M. Fujita, *Journal of the American Chemical Society* **2009**, *131*, 4764–4768, DOI 10.1021/ja8089075.

[227] D. M. Dalton, S. R. Ellis, E. M. Nichols, R. A. Mathies, F. D. Toste, R. G. Bergman, K. N. Raymond, *Journal of the American Chemical Society* **2015**, *137*, 10128–10131, DOI 10.1021/jacs.5b06317.

[228] L.-X. Cai, S.-C. Li, D.-N. Yan, L.-P. Zhou, F. Guo, Q.-F. Sun, *Journal of the American Chemical Society* **2018**, *140*, 4869–4876, DOI 10.1021/jacs.8b00394.

[229] W. Cullen, H. Takezawa, M. Fujita, *Angewandte Chemie* **2019**, *131*, 9269–9271, DOI 10.1002/ange.201904752.

[230] G. Szalóki, V. Croué, V. Carré, F. Aubriet, O. Alévêque, E. Levillain, M. Allain, J. Aragó, E. Ortí, S. Goeb, M. Sallé, *Angewandte Chemie* **2017**, *129*, 16490–16494, DOI 10.1002/ange.201709483.

[231] J. Zheng, Y. Yang, T. K. Ronson, D. M. Wood, J. R. Nitschke, *Advanced Materials* **2023**, *35*, e2302580, DOI 10.1002/adma.202302580.

[232] D.-N. Yan, L.-X. Cai, P.-M. Cheng, S.-J. Hu, L.-P. Zhou, Q.-F. Sun, *Journal of the American Chemical Society* **2021**, *143*, 16087–16094, DOI 10.1021/jacs.1c06390.

[233] V. Croué, S. Goeb, G. Szalóki, M. Allain, M. Sallé, *Angewandte Chemie International Edition* **2016**, *55*, 1746–1750, DOI https://doi.org/10.1002/anie.201509265.

[234] F. G. Brunetti, J. L. López, C. Atienza, N. Martín, *Journal of Materials Chemistry* **2012**, *22*, 4188–4205, DOI 10.1039/c2jm15710a.

[235] R. L. Spicer, A. D. Stergiou, T. A. Young, F. Duarte, M. D. Symes, P. J. Lusby, *Journal of the American Chemical Society* **2020**, DOI 10.1021/jacs.9b11273.

[236] B. Huang, M. Zhou, Q.-Y. Hong, M.-X. Wu, X.-L. Zhao, L. Xu, E.-Q. Gao, H.-B. Yang, X. Shi, *Angewandte Chemie International Edition* **2024**, *63*, e202407279, DOI 10.1002/anie.202407279.

[237] M. Frank, J. Ahrens, I. Bejenke, M. Krick, D. Schwarzer, G. H. Clever, *Journal of the American Chemical Society* **2016**, *138*, 8279–8287, DOI 10.1021/jacs.6b04609.

[238] M. Frank, J. Hey, I. Balcioglu, Y.-S. Chen, D. Stalke, T. Suenobu, S. Fukuzumi, H. Frauendorf, G. H. Clever, *Angewandte Chemie International Edition* **2013**, *52*, 10102–10106, DOI https://doi.org/10.1002/anie.201302536.

[239] H.-E. Sprenger, W. Ziegenbein, *Angewandte Chemie International Edition in English* **1968**, *7*, 530–535, DOI 10.1002/anie.196805301.

[240] E. W. Neuse, B. R. Green, *The Journal of Organic Chemistry* **1974**, *39*, 3881–3887, DOI 10.1021/jo00940a018.

[241] S. Hünig, H. Pütter, *Angewandte Chemie* **1972**, *84*, 480–481, DOI 10.1002/ange.19720841012.

[242] K. Deuchert, S. Hünig, *Angewandte Chemie International Edition in English* **1978**, *17*, 875–886, DOI https://doi.org/10.1002/anie.197808753.

[243] M. E. Baumert, V. Le, P.-H. Su, Y. Akae, D. Bresser, P. Théato, M. M. Hansmann, *Journal of the American Chemical Society* **2023**, *145*, 23334–23345, DOI 10.1021/jacs.3c09153.

[244] J. S. Tracy, C. H. Broderick, F. D. Toste, *Journal of the American Chemical Society* **2024**, *146*, 11740–11755, DOI 10.1021/jacs.3c14776.

[245] F. G. Brunetti, J. L. López, C. Atienza, N. Martín, *Journal of Materials Chemistry* **2012**, *22*, 4188–4205, DOI 10.1039/c2jm15710a.

[246] P. Thordarson, *Chemical Society Reviews* **2010**, *40*, 1305–1323, DOI 10.1039/c0cs00062k.

[247] T. Murase, S. Horiuchi, M. Fujita, *Journal of the American Chemical Society* **2010**, *132*, 2866–2867, DOI 10.1021/ja9107275.

[248] D. H. Leung, D. Fiedler, R. G. Bergman, K. N. Raymond, *Angewandte Chemie International Edition* **2004**, *43*, 963–966, DOI https://doi.org/10.1002/anie.200352772.

[249] P. Das, A. Kumar, P. Howlader, P. S. Mukherjee, *Chemistry - A European Journal* **2017**, *23*, 12565–12574, DOI 10.1002/chem.201702263.

[250] W. Cullen, M. C. Misuraca, C. A. Hunter, N. H. Williams, M. D. Ward, *Nature Chemistry* **2016**, *8*, 231–236, DOI 10.1038/nchem.2452.

[251] G. P. Maier, C. M. Bernt, A. Butler, *Biomater. Sci.* **2018**, *6*, 332–339, DOI 10.1039/C7BM00884H.

[252] Q. Lyu, N. Hsueh, C. L. L. Chai, *ACS Biomaterials Science & Engineering* **2019**, *5*, 2708–2724, DOI 10.1021/acsbiomaterials.9b00281.

[253] R. Pinnataip, B. P. Lee, *ACS Omega* **2021**, *6*, 5113–5118, DOI 10.1021/acsomega.1c00006.

[254] E. A. Pillar-Little, R. Zhou, M. I. Guzman, *The Journal of Physical Chemistry A* **2015**, *119*, 10349–10359, DOI 10.1021/acs.jpca.5b07914.

[255] Y. J. Oh, I. H. Cho, H. Lee, K.-J. Park, H. Lee, S. Y. Park, *Chem. Commun.* **2012**, *48*, 11895–11897, DOI 10.1039/C2CC36843A.

[256] E. A. Pillar-Little, M. I. Guzman, *Environmental Science & Technology* **2017**, *51*, 4951–4959, DOI 10.1021/acs.est.7b00232.

[257] A. C. Gómez-Herrero, C. Sánchez-Sánchez, F. Chérioux, J. I. Martínez, J. Abad, L. Floreano, A. Verdini, A. Cossaro, E. Mazaleyrat, V. Guisset, P. David, S. Lisi, J. A. Martín Gago, J. Coraux, *Chem. Sci.* **2021**, *12*, 2257–2267, DOI 10.1039/D0SC04883F.

[258] D. L. Caulder, C. Brückner, R. E. Powers, S. König, T. N. Parac, J. A. Leary, K. N. Raymond, *Journal of the American Chemical Society* **2001**, *123*, 8923–8938, DOI 10.1021/ja0104507.

[259] S. M. Bierschenk, J. Y. Pan, N. S. Settineri, U. Warzok, R. G. Bergman, K. N. Raymond, F. D. Toste, *Journal of the American Chemical Society* **2022**, *144*, 11425–11433, DOI 10.1021/jacs.2c04182.

[260] Z. Rappoport, J. F. Liebman, *The chemistry of hydroxylamines, oximes and hydroxamic acids*, Wiley, **2009**.

[261] J. Mas-Roselló, N. Cramer, *Chemistry – A European Journal* **2022**, *28*, e202103683, DOI 10.1002/chem.202103683.

[262] H. Fang, G. Wang, M. Oestreich, *Organic Chemistry Frontiers* **2021**, *8*, 3280–3285, DOI 10.1039/d1qo00251a.

[263] M. P. Krzemiński, M. Zaidlewicz, *Tetrahedron: Asymmetry* **2003**, *14*, 1463–1466, DOI 10.1016/s0957-4166(03)00314-8.

[264] J. Mas-Roselló, T. Smejkal, N. Cramer, *Science* **2020**, *368*, 1098–1102, DOI 10.1126/science.abb2559.

[265] B. Li, J. Chen, D. Liu, I. D. Gridnev, W. Zhang, *Nature Chemistry* **2022**, *14*, 920–927, DOI 10.1038/s41557-022-00971-8.

[266] F. Wang, Y. Chen, P. Yu, G.-Q. Chen, X. Zhang, *Journal of the American Chemical Society* **2022**, *144*, 17763–17768, DOI 10.1021/jacs.2c07506.

[267] Y. Xia, S. Wang, R. Miao, J. Liao, L. Ouyang, R. Luo, *Organic & Biomolecular Chemistry* **2022**, *20*, 6394–6399, DOI 10.1039/d2ob01084d.

[268] Elizabeth Heafner, PhD thesis, UC Berkeley, Berkeley, **2024**.

[269] T. Sravanthi, S. Manju, *European Journal of Pharmaceutical Sciences* **2016**, *91*, 1–10, DOI https://doi.org/10.1016/j.ejps.2016.05.025.

[270] M. López-Iglesias, E. Busto, V. Gotor, V. Gotor-Fernández, *The Journal of Organic Chemistry* **2012**, *77*, 8049–8055, DOI 10.1021/jo301307q.

[271] F.-H. Tu, S. Lin, Y.-J. Tang, L.-C. Liu, Q. Li, H. Wang, *Tetrahedron Chem* **2023**, *8*, 100052, DOI https://doi.org/10.1016/j.tchem.2023.100052.

[272] I. Kuznetcova, F. Bacher, D. Vegh, H.-Y. Chuang, V. B. Arion, *Beilstein Journal of Organic Chemistry* **2022**, *18*, 143–151, DOI 10.3762/bjoc.18.15.

[273] A. Theodorou, C. G. Kokotos, *Advanced Synthesis & Catalysis* **2017**, *359*, 1577–1581, DOI 10.1002/adsc.201601262.

[274] M. Morimoto, W. Cao, R. G. Bergman, K. N. Raymond, F. D. Toste, *Journal of the American Chemical Society* **2021**, *143*, 2108–2114, DOI 10.1021/jacs.0c12479.

[275] L. S. Fitzgerald, R. L. McNulty, A. Greener, M. L. O'Duill, *The Journal of Organic Chemistry* **2023**, *88*, 10772–10776, DOI 10.1021/acs.joc.3c00819.

[276] T. M. Rolf Voges, J. Richard Heys, *Preparation of compounds labeled with tritium and carbon-14*, Wiley, **2009**.

[277] X.-Y. Zhou, X. Chen, *Organic & Biomolecular Chemistry* **2020**, *19*, 548–551, DOI 10.1039/d0ob02080j.

[278] Y. Okamoto, K. Ogura, T. Kinoshita, M. Shirai, Y. Matsumoto, *Polyhedron* **1987**, *6*, 1183–1189, DOI 10.1016/s0277-5387(00)80867-0.

[279] B. Chen, J. J. Holstein, S. Horiuchi, W. G. Hiller, G. H. Clever, *Journal of the American Chemical Society* **2019**, *141*, 8907–8913, DOI 10.1021/jacs.9b02207.

[280] K. Hirose in *Analytical Methods in Supramolecular Chemistry*, John Wiley & Sons, Ltd, **2012**, Chapter 2, pp. 27–66, DOI https://doi.org/10.1002/9783527644131.ch2.

[281] E. G. Sheetz, D. Van Craen, A. H. Flood in *Anion-Binding Catalysis*, John Wiley & Sons, Ltd, **2022**, Chapter 2, pp. 79–109, DOI https://doi.org/10.1002/9783527830664.ch2.

[282] P. Job, *Ann. chim* **1928**, *9*, 113–134.

[283] D. B. Hibbert, P. Thordarson, *Chemical Communications* **2016**, *52*, 12792–12805, DOI 10.1039/c6cc03888c.

[284] F. Ulatowski, K. Dąbrowa, T. Bałakier, J. Jurczak, *The Journal of Organic Chemistry* **2016**, *81*, 1746–1756, DOI 10.1021/acs.joc.5b02909.

[285] J. A. Nelder, R. Mead, *The Computer Journal* **1965**, *7*, 308–313, DOI 10.1093/comjnl/7.4.308.

[286] K. Amirbekyan, N. Duchemin, E. Benedetti, R. Joseph, A. Colon, S. A. Markarian, L. Bethge, S. Vonhoff, S. Klussmann, J. Cossy, J.-J. Vasseur, S. Arseniyadis, M. Smietana, *ACS Catalysis* **2016**, *6*, 3096–3105, DOI 10.1021/acscatal.6b00495.

[287] W. Chen, S. Wang, G. Yang, S. Chen, K. Ye, Z. Hu, Z. Zhang, Y. Wang, *The Journal of Physical Chemistry C* **2016**, *120*, 587–597, DOI 10.1021/acs.jpcc.5b10954.

[288] A. Rioz-Martínez, J. Oelerich, N. Ségaud, G. Roelfes, *Angewandte Chemie* **2016**, *55*, 14136–14140, DOI 10.1002/anie.201608121.

[289] F. A. Fernandez-Lima, D. A. Kaplan, M. A. Park, *The Review of scientific instruments* **2011**, *82*, 126106, DOI 10.1063/1.3665933.

[290] J.-F. Greisch, J. Chmela, M. E. Harding, D. Wunderlich, B. Schäfer, M. Ruben, W. Klopper, D. Schooss, M. M. Kappes, *Physical chemistry chemical physics : PCCP* **2017**, *19*, 6105–6112, DOI 10.1039/c6cp04656h.

[291] D. R. Hernandez, J. D. Debord, M. E. Ridgeway, D. A. Kaplan, M. A. Park, F. Fernandez-Lima, *The Analyst* **2014**, *139*, 1913–1921, DOI 10.1039/C3AN02174B.

[292] A. Bondi, *The Journal of Physical Chemistry* **1964**, *68*, 441–451, DOI 10.1021/j100785a001.

[293] Ertugrul Yalcin, Master thesis, Technische Universität Dortmund, Dortmund, **2021**.

[294] A. A. Buglak, A. V. Samokhvalov, A. V. Zherdev, B. B. Dzantiev, *International Journal of Molecular Sciences* **2020**, *21*, DOI 10.3390/ijms21228420.

[295] J. Kleynhans, H. Kruger, T. T. Cloete, J. Zeevaart, T. Ebenhan, *Current medicinal chemistry* **2020**, DOI 10.2174/0929867327666200504082256.

[296] E. Benfenati, Q. Chaudhry, G. Gini, J. Dorne, *Environment international* **2019**, *131*, 105060, DOI 10.1016/j.envint.2019.105060.

[297] C. Milne, P.-J. Kim, J. A. Eddy, N. Price, *Biotechnology Journal* **2009**, *4*, DOI 10.1002/biot.200900234.

[298] Mag. Walter Snor, PhD thesis, Universität Wien, Wien, **2009**.

[299] Christoph Drechsler, Master thesis, Technische Universität Dortmund, Dortmund, **2019**.

[300] C. J. Cramer, *Essentials of computational chemistry: Theories and models*, 2. ed., Wiley, Chichester, **2014**.

[301] F. Jensen, *Introduction to computational chemistry*, Third edition, John Wiley & Sons, Chichester, UK and Hoboken, NJ, **2017**.

[302] E. Schrödinger, *Physical Review* **1926**, *28*, 1049–1070, DOI 10.1103/PhysRev.28.1049.

[303] W. Kohn, L. J. Sham, *Physical Review* **1965**, *140*, A1133–A1138, DOI 10.1103/PhysRev.140.A1133.

[304] *Proceedings of the Royal Society of London. Series A - Mathematical and Physical Sciences* **1935**, *150*, 9–33, DOI 10.1098/rspa.1935.0085.

[305] A. S. Christensen, T. Kubař, Q. Cui, M. Elstner, *Chemical reviews* **2016**, *116*, 5301–5337, DOI 10.1021/acs.chemrev.5b00584.

[306] J. Řezáč, J. Fanfrlík, D. Salahub, P. Hobza, *Journal of chemical theory and computation* **2009**, *5*, 1749–1760, DOI 10.1021/ct9000922.

[307] S. Grimme, *Journal of computational chemistry* **2006**, *27*, 1787–1799, DOI 10.1002/jcc.20495.

[308] J.-D. Chai, M. Head-Gordon, *Physical chemistry chemical physics : PCCP* **2008**, *10*, 6615–6620, DOI 10.1039/B810189B.

[309] S. Li, C. L. Guenther, M. S. Kelley, D. A. Dixon, *The Journal of Physical Chemistry C* **2011**, *115*, 8072–8103, DOI 10.1021/jp111031x.

[310] Y. Segawa, H. Omachi, K. Itami, *Organic Letters* **2010**, *12*, 2262–2265, DOI 10.1021/ol1006168.

[311] N. J. Agard, J. A. Prescher, C. R. Bertozzi, *Journal of the American Chemical Society* **2004**, *126*, 15046–15047, DOI 10.1021/ja044996f.

[312] C. W. Bielawski, R. H. Grubbs, *Progress in Polymer Science* **2007**, *32*, 1–29, DOI 10.1016/j.progpolymsci.2006.08.006.

[313] K. J. Daoust, S. M. Hernandez, K. M. Konrad, I. D. Mackie, J. Winstanley, R. P. Johnson, *The Journal of organic chemistry* **2006**, *71*, 5708–5714, DOI 10.1021/jo060698k.

[314] C. E. Colwell, T. W. Price, T. Stauch, R. Jasti, *Chemical Science* **2020**, *11*, 3923–3930, DOI 10.1039/d0sc00629g.

[315] K. Ebbert, Master thesis, Technische Universität Dortmund, Dortmund, **2018**.

[316] Y. Li, H.-L. Dong, J.-S. Zhang, C. Lin, Z.-J. Tan, *Frontiers in Physics* **2021**, *9*, 696104, DOI 10.3389/fphy.2021.696104.

[317] P. G. Huray, *Maxwell's equations*, Wiley IEEE Press and IEEE Xplore, Hoboken, New Jersey and Piscataway, New Jersey, **2011**, DOI 10.1002/9780470549919.

[318] A. Tarzia, W. Shan, V. Posligua, C. J. T. Cox, L. Male, B. D. Egleston, R. L. Greenaway, K. E. Jelfs, J. E. M. Lewis, *Chemistry – A European Journal* **2025**, *31*, e202403336, DOI https://doi.org/10.1002/chem.202403336.

[319] K. E. Ebbert, L. Schneider, A. Platzek, C. Drechsler, B. Chen, R. Rudolf, G. H. Clever, *Dalton Transactions* **2019**, DOI 10.1039/c9dt01814j.

[320] K. Wu, B. Zhang, C. Drechsler, J. J. Holstein, G. H. Clever, *Angewandte Chemie International Edition* **2020**, *60*, 6403–6407, DOI 10.1002/anie.202012425.

Acknowledgement

Firstly, I want to thank Professor Dr. Clever as the first examiner. Then, I want to thank Prof. Dr. Lars Schäfer for taking on the role as co-examiner. Furthermore, I extend my gratitude to the entire research group. In particular, I sincerely thank *Dr. Aleksandr S. Mikherdov* for the fruitful discussions and outstanding support, especially in proofreading. I also extend my gratitude to *Dr. Simon C. Rickert* for his support and assistance with proofreading.
In addition to that, I want to thank F. Dean Toste to accept me as a visiting scholar for my research stay at UC Berkeley and all involed (GRK 2376).
I extend my heartfelt gratitude to all those I encountered throughout my educational journey, may it in Germany, Japan or USA, who embraced faith in my abilities. To those who continue to stand by my side, offering tireless support and encouragement, I am really grateful. I am equally appreciative of those who take pride in my accomplishments, as well as those who challenged me, for they have contributed to my growth and resilience.

A special thank you goes to *Dr. Chak-Shing Kwan.* I appreciate to work with you and to share the lab and office with you. You have a great and humble heart, which makes you even more awesome as a person.

I would like to thank my friends *Lorenz Hündgen* with whom I spend a lot of time in and outside the university. I also want to thank my classmate *Dr. Christen Lin* who accompanied me very loyally to my lessons. Moreover, I want to thank *Dr. Schanth Hacatrjan* for his support and for the enjoyable conversations we had at a coffee break.
Shout-out to *Kosuke Yamaguchi*, my flatmate, lab mate, and first Japanese friend — you're awesome. And to *Tzu-Chun Chien*, known as *Sen*, my best Taiwanese friend: both of you made a lasting impact on my study abroad in Japan. Even after all these years, your unwavering support means the world to me. That's true friendship, and I'm incredibly grateful for it. どうも有難う御座います
I would especially want to thank my very good friend *Dr. Hannan Ahmed* for his support.
Last but not least I would like to thank *my family*, who always supported me. Especially my brothers *Adem* and *Dr. Eyüp.*

"I want to thank me for believing in me, I want to thank me for doing all this hard work. I wanna thank me for having no days off. I wanna thank me for never quitting. I wanna thank me for always being a giver and trying to give more than I receive. I wanna thank me for trying to do more right than wrong."
-Snoop Dogg-

„今日から思い出 (*From today, it will all be memories*)"-Aimer-

Here, I would like to share the most inspiring quotes that have given me strength and guidance throughout my journey.

*"**Das Leben ist kein Geschenk, es ist ein Test**, dieses graue Leben*
Heißt wie viel kann ein Mensch ertragen, ohne aufzugeben
Und der Grund, warum ich dennoch bis heute lebe
Ist, weil ich weiß, dass ich für Selbstmord in's Feuer käme
Und ich bete jeden Tag
Damit ich, wenn es soweit ist, nicht vor dem Tod stehe und sag
Bitte gib mir noch ein Jahr und ich mach alles wieder gut
Vorbei ist vorbei und ich muss in den Himmel kommen
Denn was sind 70 Jahre Lebenszeit, verglichen mit der Ewigkeit
***Wozu Geld und Autos, wenn am Ende nur die Seele bleibt**"*
Kollegah, Felix Martin Andreas Matthias Blume

*"The strong man is not the one who can overpower others; rather, **the strong man is the one who controls himself when he is angry**."*
[Sahih Bukhari - 6114]

*"**Beware of false thought**,*
for false thought is the most untruth speech.
Do not search for the faults of one another, do not spy on one another, do not envy one another, do not turn your backs on one another, do not harbor hatred for one another [...]." [Sahih Bukhari - 6064]

*"**Allah does not burden a soul except [with that within] its capacity**. It will have [the consequence of] what [good] it has gained, and it will bear [the consequence of] what [evil] it has earned. "Our Lord, do not impose blame upon us if we have forgotten or erred. Our Lord, and lay not upon us a burden like that which You laid upon those before us. Our Lord, and burden us not with that which we have no ability to bear. **And pardon us; and forgive us; and have mercy upon us**." [2:286]*

*"**Who is the biggest scholar?**"*
*He replied: "**He who is constantly trying to learn from others, for a scholar is ever hungry for more knowledge**." PBUH*